INNOVATIONS IN THE CLINICAL USE OF OCT

Optical coherence tomography for guiding coronary interventions and assessing the vascular healing response after implantation of intravascular devices

Antonios Karanasos

Financial support for the research performed in this thesis was kindly provided by:

Hellenic Heart Foundation

St. Jude Medical

Printed by: Ridderprint BV

Cover illustration:
Left panel: ‘Prometheus carrying fire’ Cossiers, Jan; 1636-1638; Oil on canvas; Museo Nacional de Prado. Right panels: compilation of images created in the context of this thesis.

ISBN: 978-94-6299-260-3

Innovations in the Clinical Use of OCT

Optical coherence tomography for guiding coronary interventions and assessing the vascular healing response after implantation of intravascular devices

Innovaties in de Klinische Gebruik van OCT

Optische coherentie tomografie voor de leiding van coronaire interventies en de beoordeling van de vasculaire genezingsrespons na implantatie van intravasculaire stents

Proefschrift

Ter verkrijging van de graad van doctor aan de Erasmus Universiteit op gezag van de rector magnificus

Prof.dr. H.A.P. Pols

en volgens besluit van het College voor Promoties.

De openbare verdediging zal plaatsvinden op

dinsdag 12 januari 2016 om 13:30 uur

door

Antonios Karanasos

geboren te Athene, Griekenland

Erasmus University Rotterdam

Doctoral committee

Promotor:	Prof.dr. F. Zijlstra
Reading committee:	Dr. G. van Soest
	Prof.dr. A.P. Kappetein
	Prof.dr. J.J. Piek
Co-promotor:	Dr. E. Regar

For my parents and for my girlfriend

Table of contents

Part VIII. Intravascular imaging assessment in renal denervation.

Introduction and outline

Introduction and outline

The introduction of percutaneous coronary intervention (PCI) has been a major breakthrough in the history of cardiology[1], as today PCI has become one of the most widely used treatment options for obstructive coronary artery disease. The advent of intracoronary stents managed to overcome limitations of balloon angioplasty that was associated with poor procedural outcomes[2] [3]. However, despite the improved outcomes with this technology, new problems such as stent restenosis and stent thrombosis arose, driving continuous innovations and developments in stent design in order to address these issues[4-6]. Since the era of balloon angioplasty and up to today, coronary angiography has traditionally been the tool for the assessment of the coronary anatomy, and evaluation of the treatment effect of the interventions. Intravascular imaging modalities have provided a new paradigm for this evaluation. The introduction of intravascular ultrasound (IVUS) signals a transition from the assessment of the luminal contour to the direct assessment of vessel wall morphology, and direct visualization of the effects of intervention[7]. This kind of comprehensive assessment has allowed us to gain further insight in the development of atherosclerosis and the vascular response to stent implantation[8, 9]. Although IVUS has been the cornerstone of invasive imaging for years, this modality has several limitations in the assessment of coronary atherosclerosis and treatment effects, due to its limited resolution (150-200μm). This has prompted the development of several new intravascular imaging modalities that provide a more detailed visualization of the vascular micro-morphology.

Among these modalities, optical coherence tomography (OCT) has been widely used in clinical practice. OCT is an infrared light-based imaging modality with near-histological resolution (5-15μm) allowing the comprehensive evaluation of the vascular wall and intracoronary devices[10-12]. First generation time domain OCT was soon substituted in clinical practice by frequency domain OCT which simplified the procedure of image acquisition, shortened the required time, and reduced requirements for flashing media[13]. This enabled a more widespread utilization of this imaging modality for the assessment of atherosclerosis and of the impact of interventions on the vascular wall, but also for the guidance of coronary intervention. This thesis will focus on these applications of OCT.

In Part I of this thesis, there is an overview of OCT imaging in clinical practice, while Part II deals with methodological considerations of OCT analysis and describes new developments that can overcome current limitations. Part III describes the role of OCT in the assessment of the pathomechanisms of metallic stent thrombosis. Parts IV to VII focuses on the evaluation of bioresorbable vascular scaffolds by OCT, describing the vascular healing response

with these devices and providing insights into pathomechanisms of bioresorbable scaffold failure. Finally, Part VIII describes the use of OCT in the renal arteries for the assessment of the vascular effects of renal denervation, an innovative treatment for resistant hypertension.

Scope of the thesis

The aim of this thesis is to outline the contemporary use of optical coherence tomography in clinical practice and summarize insights gained by this imaging modality into the acute and chronic vascular response after intravascular interventions.

In specific, this thesis intends to:

- Summarize the current status of OCT in clinical practice
- Describe and validate new analysis tools for optical coherence tomography, that allow to overcome some of the current limitations
- Examine the pathomechanisms of very late metallic stent failure with particular emphasis on the role of neoatherosclerosis
- Assess the acute and chronic vascular healing response after bioresorbable vascular scaffold implantation and provide pilot observations regarding the pathomechanisms of early and late bioresorbable scaffold failure
- Evaluate the acute effects of catheter-based renal denervation on the renal artery integrity

References

1. Gruntzig A. Transluminal dilatation of coronary-artery stenosis. Lancet 1978;**1**(8058):263.
2. Gruntzig AR, Senning A, Siegenthaler WE. Nonoperative dilatation of coronary-artery stenosis: percutaneous transluminal coronary angioplasty. N Engl J Med 1979;**301**(2):61-8.
3. Serruys PW, Strauss BH, Beatt KJ, Bertrand ME, Puel J, Rickards AF, Meier B, Goy JJ, Vogt P, Kappenberger L, et al. Angiographic follow-up after placement of a self-expanding coronary-artery stent. N Engl J Med 1991;**324**(1):13-7.
4. Lagerqvist B, James SK, Stenestrand U, Lindback J, Nilsson T, Wallentin L. Long-term outcomes with drug-eluting stents versus bare-metal stents in Sweden. N Engl J Med 2007;**356**(10):1009-19.
5. Morice MC, Serruys PW, Sousa JE, Fajadet J, Ban Hayashi E, Perin M, Colombo A, Schuler G, Barragan P, Guagliumi G, Molnar F, Falotico R. A randomized comparison of a sirolimus-eluting stent with a standard stent for coronary revascularization. N Engl J Med 2002;**346**(23):1773-80.
6. Ormiston JA, Serruys PW, Regar E, Dudek D, Thuesen L, Webster MW, Onuma Y, Garcia-Garcia HM, McGreevy R, Veldhof S. A bioabsorbable everolimus-eluting coronary stent system for patients with single de-novo coronary artery lesions (ABSORB): a prospective open-label trial. Lancet 2008;**371**(9616):899-907.
7. Hodgson JM, Graham SP, Sheehan H, Savakus AD. Percutaneous intracoronary ultrasound imaging: initial applications in patients. Echocardiography 1990;**7**(4):403-13.
8. McPherson DD, Sirna SJ, Hiratzka LF, Thorpe L, Armstrong ML, Marcus ML, Kerber RE. Coronary arterial remodeling studied by high-frequency epicardial echocardiography: an early compensatory mechanism in patients with obstructive coronary atherosclerosis. J Am Coll Cardiol 1991;**17**(1):79-86.
9. Nakamura S, Colombo A, Gaglione A, Almagor Y, Goldberg SL, Maiello L, Finci L, Tobis JM. Intracoronary ultrasound observations during stent implantation. Circulation 1994;**89**(5):2026-34.
10. Huang D, Swanson EA, Lin CP, Schuman JS, Stinson WG, Chang W, Hee MR, Flotte T, Gregory K, Puliafito CA, et al. Optical coherence tomography. Science 1991;**254**(5035):1178-81.
11. Tearney GJ, Regar E, Akasaka T, Adriaenssens T, Barlis P, Bezerra HG, Bouma B, Bruining N, Cho J-m, Chowdhary S, Costa MA, de Silva R, Dijkstra J, Di Mario C, Dudeck D, Falk E, Feldman MD, Fitzgerald P, Garcia H, Gonzalo N, Granada JF, Guagliumi G, Holm NR, Honda Y, Ikeno F, Kawasaki M, Kochman J, Koltowski L, Kubo T, Kume T, Kyono H, Lam CCS, Lamouche G, Lee DP, Leon MB, Maehara A, Manfrini O, Mintz GS, Mizuno K, Morel M-a, Nadkarni S, Okura H, Otake H, Pietrasik A, Prati F, Räber L, Radu MD, Rieber J, Riga M, Rollins A, Rosenberg M, Sirbu V, Serruys PWJC, Shimada K, Shinke T, Shite J, Siegel E, Sonada S, Suter M, Takarada S, Tanaka A, Terashima M, Troels T, Uemura S, Ughi GJ, van Beusekom HMM, van der Steen AFW, van Es G-A, van Soest G, Virmani R, Waxman S, Weissman NJ, Weisz G. Consensus Standards for Acquisition, Measurement, and Reporting of Intravascular Optical Coherence Tomography Studies: A Report From the International Working Group for Intravascular Optical Coherence Tomography Standardization and Validation. J Am Coll Cardiol 2012;**59**(12):1058-1072.
12. Jang IK, Tearney GJ, MacNeill B, Takano M, Moselewski F, Iftima N, Shishkov M, Houser S, Aretz HT, Halpern EF, Bouma BE. In vivo characterization of coronary atherosclerotic plaque by use of optical coherence tomography. Circulation 2005;**111**(12):1551-5.
13. Gonzalo N, Tearney GJ, Serruys PW, van Soest G, Okamura T, Garcia-Garcia HM, Jan van Geuns R, van der Ent M, Ligthart J, Bouma BE, Regar E. Second-generation optical coherence tomography in clinical practice. High-speed data acquisition is highly reproducible in patients undergoing percutaneous coronary intervention. Rev Esp Cardiol 2010;**63**(8):893-903.

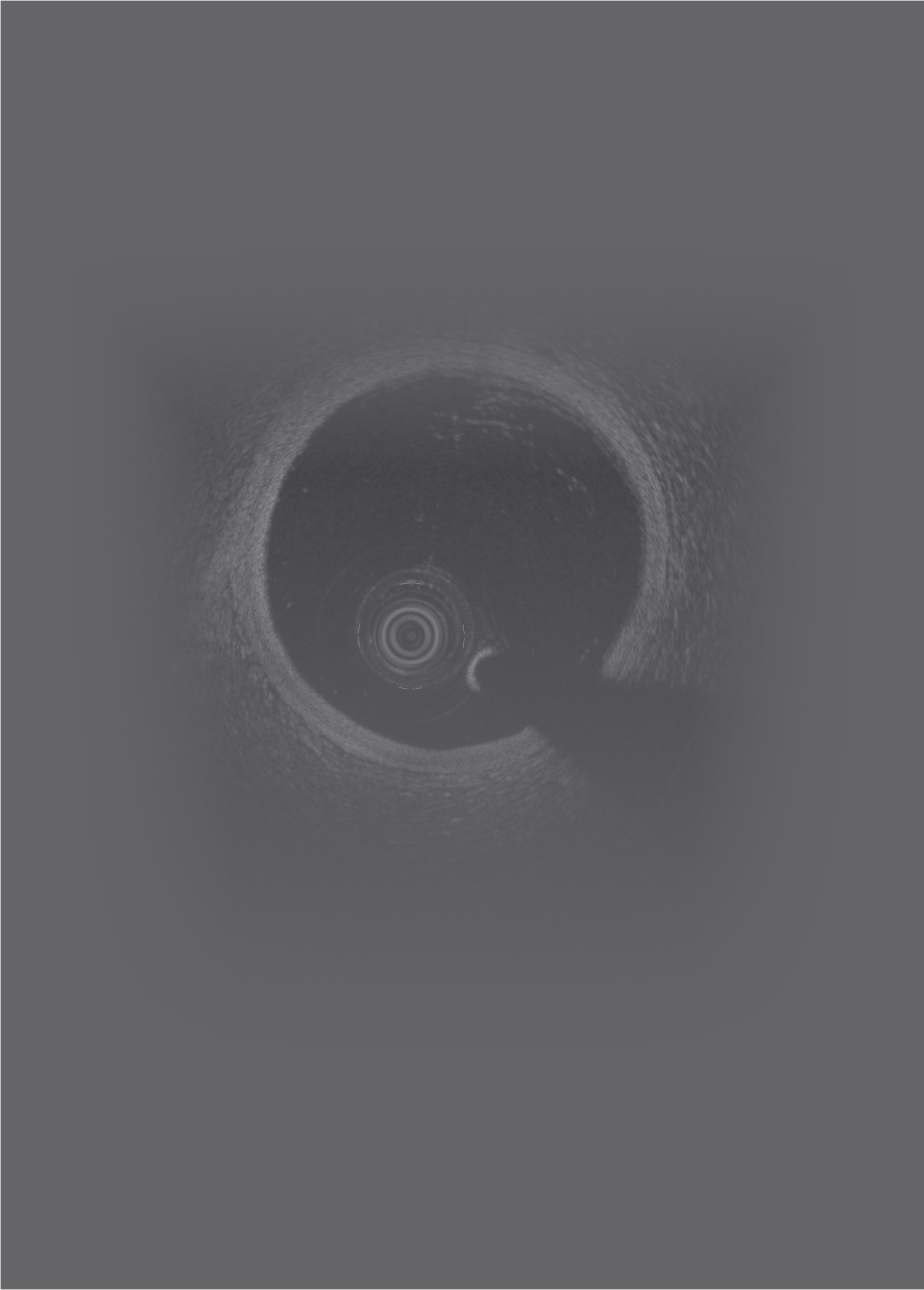

PART I

OCT imaging in clinical practice

Chapter 1.1

Optical Coherence Tomography: Potential Clinical Applications

Karanasos A, Ligthart J, Witberg K, van Soest G, Bruining N, Regar E

Curr Cardiovasc Imaging Rep. 2012;5(4):206-220

Optical Coherence Tomography: Potential Clinical Applications

Antonios Karanasos · Jurgen Ligthart · Karen Witberg · Gijs van Soest · Nico Bruining · Evelyn Regar

Published online: 3 May 2012

Abstract Optical coherence tomography (OCT) is a novel intravascular imaging modality using near-infrared light. By OCT it is possible to obtain high-resolution cross-sectional images of the vascular wall structure and assess the acute and long-term effects of percutaneous coronary intervention. For the time being OCT has been mainly used in research providing new insights into the pathophysiology of the atheromatic plaque and of the vascular response to stenting, however, it seems that there is potential for clinical application of OCT in various fields, such as pre-interventional evaluation of coronary arteries, procedural guidance in coronary interventions, and follow-up assessment of vascular healing after stent implantation. This review will focus on the potential and advantages of OCT in the clinical practice of a catheterization laboratory.

Keywords Optical coherence tomography · Intravascular imaging · Percutaneous coronary intervention · Stent coverage · Restenosis · Stent thrombosis · Fractional flow reserve · Intravascular ultrasound · Procedural guidance · Coronary angiography · Stent · Plaque · Atheromatosis

Introduction

Since the introduction of percutaneous coronary intervention (PCI), coronary angiography has been the tool for assessing the need for revascularization, as well as for assessing the results of the interventions. The advent of intravascular ultrasound (IVUS) has opened a new chapter in PCI guidance, enabling the transition from assessment of the lumen to the direct assessment of plaque and vessel morphology and the evaluation of the vessel wall response to stenting. Utilizing this approach, IVUS studies have provided useful insights into the pathogenesis and prevention of stent failure [1–3] as well as the dynamic nature of atherosclerosis and the impact of medical therapy [4–6]. Despite, however, the enormous contribution of IVUS, it is limited by low axial resolution (100–150 μm) and poor capability to discriminate different plaque components that precludes assessment of specific plaque and stent characteristics. Technological advances have led to the development of new intravascular imaging methods. We will discuss the potential and advantages of optical coherence tomography (OCT) in the clinical practice of a catheterization laboratory. Table 1 summarizes some potential clinical applications of OCT.

A. Karanasos · J. Ligthart · K. Witberg · G. van Soest · N. Bruining · E. Regar (✉)
Department of Cardiology, Erasmus University Medical Center, Thoraxcenter, BA-585, 's Gravendijkwal 230, 3015 CE Rotterdam, The Netherlands
e-mail: e.regar@erasmusmc.nl

Basic Principles of OCT Imaging

OCT is an intravascular imaging method capable of proving cross-sectional images of the vascular wall with a high axial resolution (5–15 μm) and a lateral resolution of approximately 25 μm. This high resolution, however, comes at a cost of reduced penetration depth caused by the rapid attenuation of light waves in the tissue, and of the need to temporarily displace blood during imaging, because of the high scattering of light caused by erythrocytes. OCT in contrast to IVUS is based on emission of near-infrared light rather than acoustic waves for imaging. These infrared light waves reflect off the vascular wall and are then received and processed by the OCT imaging system. As the wavelength of light waves is far greater than those of the intravascular ultrasound, OCT cannot directly interpret the signal, but uses instead a technique called

Table 1 Potential clinical applications of optical coherence tomography (OCT)

Setting	Application
Lesion evaluation	Assessment of culprit lesion in acute coronary syndromes: evaluation for plaque rupture and/or thrombus in patients without angiographically evident culprit lesion
	Evaluation of lesions with angiographic haziness: differential diagnosis between thrombus, dissection, heavy calcification
	Determination about presence or absence of plaque (e.g. in coronary spasm)
Pre-procedural assessment	Luminal measurements for selection of balloon and stent dimensions
	Assessment of plaque morphology in order to guide therapeutic strategy and device selection (rotablation, cutting balloon, etc.)
	Evaluation of the optimal location in the vessel for implantation of a coronary stent
	Use for tracking the exact guidewire position (i.e. in chronic total occlusion or in bifurcation stenting)
	Use in bifurcation intervention (assessment of carina, ostia of side-branches, stent cell geometry)
Post-procedural assessment	Assessment of stent expansion (detection of under-expansion, residual stenosis, incomplete stent apposition)
	Assessment of vascular injury: detection of edge dissections, tissue protrusion, intra-stent thrombus
	Assessment of intervention by adjunctive devices: measurement of luminal enlargement after cutting balloon angioplasty, assessment of the reduction of calcification after rotablation
	Assessment of adjunctive therapies in acute coronary syndromes: evaluation of residual thrombus burden after thrombectomy or selective administration of IIb/IIIa antagonists
Follow-up stent assessment	Mid-term and long-term assessment of stent safety and efficacy: evaluation of stent restenosis (quantitative and qualitative), stent thrombosis, and stent coverage as a surrogate for vessel healing
	Monitoring of the bioresorption and the healing response after implantation of bioresorbable scaffolds

low-coherence interferometry in order to process the reflected signal. By this technique, an interferogram is created that can be analyzed by the imaging system in order to interpret the reflection as temporal delay or as tissue length (A-line) [7••].

Time-Domain and Fourrier-Domain OCT Systems

There are two processing methods that are being used for intravascular OCT imaging: Time Domain OCT (TD-OCT), and the recently introduced Fourier Domain OCT (FD-OCT), which is also known as second generation OCT, Frequency Domain OCT, or Optical Frequency Domain Imaging (OFDI). FD-OCT systems can record A-lines at a very high speed, while improving noise-signal ratios resulting in greater penetration depth, without loss of vital detail or resolution. In this way, imaging acquisition time and contrast used is reduced, while longer pullbacks are acquired [8].

Intravascular FD-OCT Systems and Image Acquisition Technique

Currently available FD-OCT systems are utilizing a short rapid-exchange monorail catheter for mounting of the optical probe. The optical signal is transmitted by a single-mode fiber, automatically mounted on the catheter, the focus of which is approximately 1 mm outside the catheter. In order to scan the vessel lengthwise, the catheter imaging tip is pulled back while rotating, inside a transparent sheath, allowing for retrieval of consecutive cross-sectional images for a length of 50–70 mm from the coronary artery. Both rotary and pullback motion are driven proximally by a motor outside the patient. For image acquisition, the FD-OCT catheter is initially advanced with the aid of a conventional guidewire distally to the desired segment, while the catheter position is indicated by radio-opaque markers. In order to create a blood-free environment during the acquisition, contrast warmed to 37 °C is injected, either manually, or by a power injector at a rate of 3–4 mL/sec. Pullback of the optical fiber is being performed simultaneously with the contrast injection.

Safety and Efficacy of OCT Imaging

The first experimental and human studies of TD-OCT have shown the safety and feasibility of OCT imaging using a proximal occlusion balloon for blood clearance [9]. An alternative technique eliminating the need for proximal occlusion has also demonstrated a favorable safety profile [10]. In the first systematic attempt from a multicenter registry of 468 patients undergoing TD-OCT imaging either with the occlusive or the non-occlusive technique, to record the safety of optical coherence tomography, use of the non-occlusive technique was associated with a reduction in the rate of transient complications during image acquisition such as chest pain and ECG changes [11••]. The introduction of FD-OCT led to a significant improvement in the rate of images of usable quality by simultaneously reducing acquisition time and the rate of transient chest pain and ECG changes [8]. Furthermore, use of a FD-OCT system for guidance of intervention was associated with a favorable safety profile [12].

Plaque Characterization and Quantitative Measurements

OCT is an imaging method that can accurately measure lumen and stent dimensions with high agreement with histological specimens and characterize tissue with high sensitivity and specificity. By OCT, it is possible to visualize all three arterial layers in a normal coronary artery, in accordance with pathological specimens [13]. OCT allows differentiation of fibrous, fibrocalcific, and lipid-rich tissue by visual assessment of the standard intensity image [14]. Briefly, fibrous plaque is seen as a high-intensity, low-attenuation area, lipid as a low-intensity, high-attenuation area with diffuse borders, while calcium as low-intensity, low-attenuation area with sharp borders (Fig. 1) [14]. OCT can also detect thrombus with very high sensitivity and specificity, and allows for distinction between red (erythrocyte-rich) and white (platelet-rich) thrombus [15].

Several studies have validated the ability of OCT to perform quantitative measurements of the lumen and stent area [7••, 16, 17]. Meanwhile, in vivo studies have confirmed that there is high correlation between OCT and IVUS measurements of vessel and stent dimensions, as well as that there is very low intra-observer and inter-observer variability in the assessment of stent and vessel area [18]. Measurements acquired by FD-OCT systems seem to be equally accurate and reproducible [19]. The recent introduction of algorithms allowing for the automated quantitative assessment of lumen dimensions enables the acceleration of the analysis process [20–22]. Various algorithms and software packages have been suggested for this approach [20], while the ability of these automatic quantification programs to detect with high correlation with histology and manual interpretation the luminal and stent borders allows for the rapid online assessment of the degree of stenosis, reference site diameter, and degree of neointimal hyperplasia [21, 22].

Role of OCT in Pre-interventional Decision Making

Intermediate Lesions

Accurate measurements of lumen area by OCT can be used for the evaluation of intermediate lesions. It has been shown in IVUS studies, that angiography often underestimates the

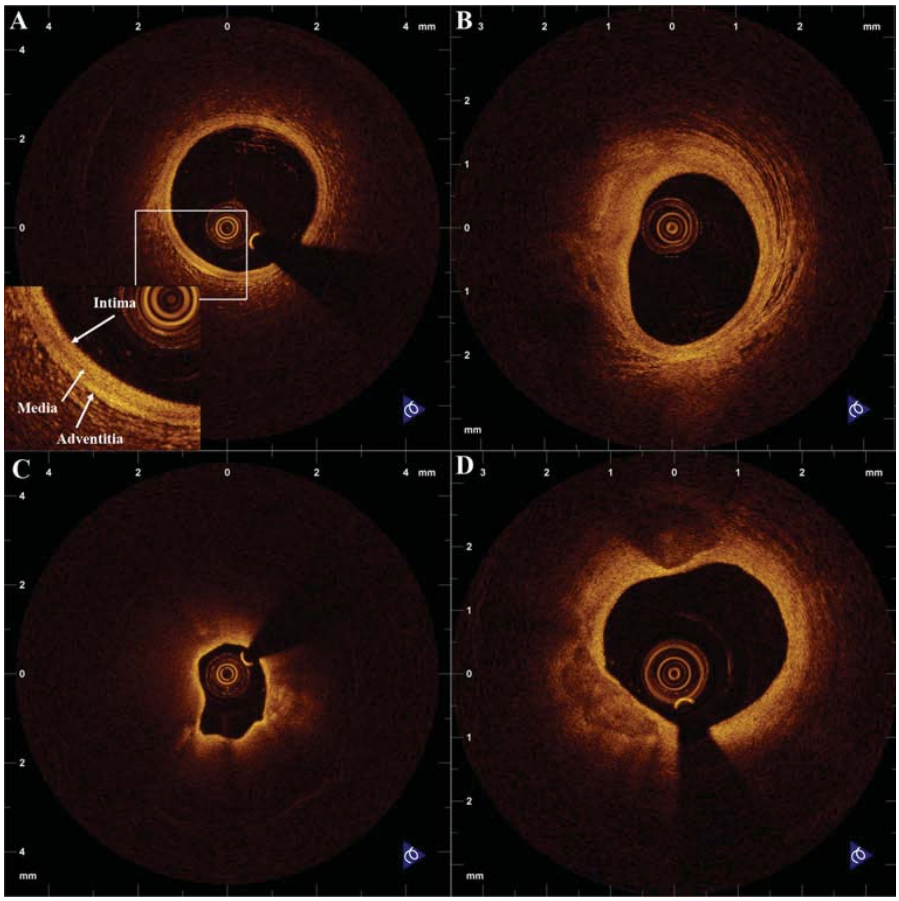

Fig. 1 Representative optical coherence tomography (OCT) cross-sectional images of **a** normal vessel with high-power view demonstrating the three layers of the vascular wall: **b** fibrous plaque; **c** lipid-rich plaque; **d** fibrocalcific plaque

plaque burden and the severity of stenosis [23]. Thus, evaluation of intermediate lesions has been a focus of invasive imaging. Functional assessment of intermediate lesions using fractional flow reserve (FFR) in patients with stable disease has been shown in large-scale studies to be linked with improved outcomes as it overcomes limitations of angiography [24]. Despite the existence of IVUS studies assessing quantitative indices of stenosis as a marker of the functional significance of a lesion, it remains questionable whether functional measurements can be replaced by anatomic measurements by IVUS or OCT. Taking into account, however, that various parameters, such as lesion length, lesion location, and plaque burden are factors also affecting the functional significance of a lesion, it is doubtful that the physiological significance of a lesion can be accurately assessed by measurement of minimal lumen area alone [25]. Moreover, a recent evaluation of IVUS and OCT to assess the physiological significance of a stenosis revealed that despite OCT measurements of minimal lumen area having greater diagnostic potential than IVUS for the assessment of the physiological significance of intermediate stenosis, anatomic lesion assessment by either modality correlates poorly to physiologic measurements performed by FFR [26]. Consequently, the current golden standard to assess hemodynamic relevance in a patient with stable angina is functional measurement by FFR (what to treat?), while OCT is helpful in guiding the procedure (how to treat?) or identification of the culprit and thrombosed lesion in acute coronary syndromes with intermediate lesions.

Angiographic Haziness

A field were OCT could substantially improve preprocedural assessment is in the evaluation of hazy lesions (Fig. 2). It is known that angiographic haziness could be due to a variety of morphological features such as thrombus, heavy calcification, extreme tortuosity, and intimal dissection. There have been several reports of utilizing OCT for the assessment of the nature of haziness, that have ranged from extreme vessel tortuosity to vessel dissection and recanalised thrombus [27–29]. Furthermore, the use of IVUS would be less helpful in such cases, as its diagnostic accuracy for complicated plaque and thrombus detection is limited [30].

Evaluation of Coronary Spasm

Optical coherence tomography can also aid decision making in cases of acute coronary syndromes in patients where coronary spasm appears to be the culprit. Use of OCT in this subset of patients can exclude the presence of culprit atheromatic plaques and/or thrombus. The association of plaque morphology with coronary spasm has been evaluated by OCT, showing that the main underlying morphology is transient intima-media thickening [31]. Multiple lumen irregularities observed during the episode consisting of intimal bumps and intimal gathering disappear after intracoronary nitrate administration, giving place to normal vessel morphology [31].

Assessment of Plaque Morphology

One of the advantages of OCT is that it can assist in the preprocedural evaluation of coronary lesions by providing information about the morphology of the lesions. A small study recently evaluated the complementary use of FD-OCT with FFR in order to assess angiographically ambiguous lesions. In this study, FFR was used in order to provide information about the functional significance of these lesions, while FD-OCT was used in order to assess the presence of unstable plaques and guide decision making in cases of ACS and FFR values >0.80 [32]. Moreover, the underlying plaque type has been associated with the outcome of the intervention. The presence of lipid-rich plaques by OCT has been associated with greater incidence of non-reflow and greater rise in biomarkers of cardiac necrosis in

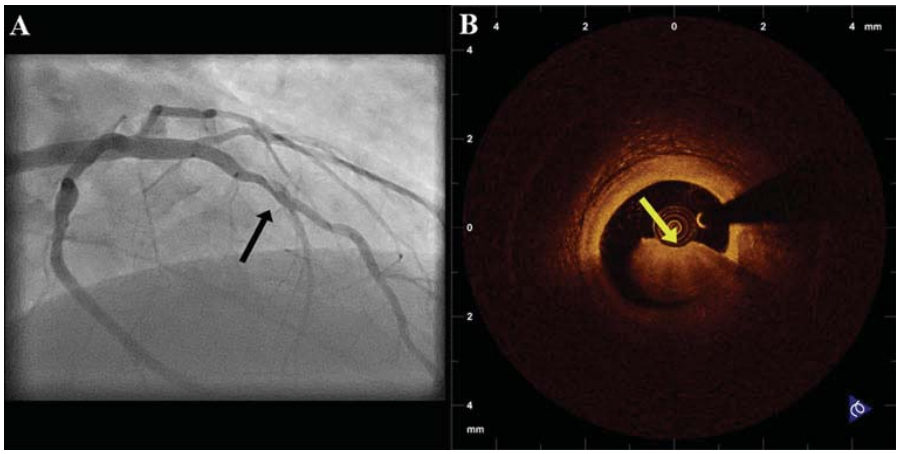

Fig. 2 Evaluation by OCT of a patient with acute coronary syndrome and haziness in the coronary angiogram. OCT revealed the presence of thrombus

several studies [33]. Additionally, patients with unstable angina compared to stable patients had greater rates of acute malapposition and tissue protrusion post PCI, while they had higher rates of malapposition and incomplete coverage at 9-month follow-up, implying an association between complicated plaque morphology—which was more common in the unstable angina group—with impaired vessel healing after stenting [34].

It remains to be proven whether qualitative assessment of non-culprit lesions can guide decision for treatment and improve patient-related outcomes. A recent intravascular ultrasound study suggested an association of the presence of a non-culprit lesion with small lumen area, large plaque burden and plaque morphology, as identified by radiofrequency ultrasound analysis, with subsequent re-hospitalizations and events [6]. However, the prognostic value of intravascular ultrasound with radiofrequency signal analysis for vulnerable plaque identification and risk stratification still needs to be established.

Preprocedural Guidance

Selection of PCI Strategy

OCT can be used in order to guide decisions about treatment before the procedure. As discussed above, OCT can provide precise area measurements not only of the minimal lumen, but of proximal and distal reference sites as well, and define the lesion length. Therefore, preprocedural measurements by OCT can aid in the proper selection of balloon and stent dimensions. Selection of appropriate balloon size using OCT measurements has been performed in a series of patients undergoing cutting balloon angioplasty for the treatment of in-stent restenosis [35]. Furthermore, OCT has also been used for selection of treatment strategy on the basis of lesion morphology. Given that OCT can quantify calcifications of the target site more accurately than IVUS [36], it could better assess the need for targeted therapies (Fig. 3). In a recent study, pre-interventional OCT assessment of plaque morphology guided the selection of dedicated treatments such as rotablation, thrombectomy, and cutting balloon in one third of patients [37•]. In the same study, decision to defer angioplasty was taken in 18 % of the patients using criteria of IVUS guidance [38], for assessing the severity of the lesion.

One of the advantages of OCT guidance is that it can help precisely identify the optimal segment for stent deployment, the so-called “landing zone” (Fig. 4). It has been shown that multiple plaque morphologies may be present in the culprit lesion of a patient with ACS [39]. Moreover, the longitudinal analysis of culprit lesions of ACS has demonstrated that in the majority of cases there is geographic mismatch of the minimal lumen site with the rupture site [40•], indicating the presence

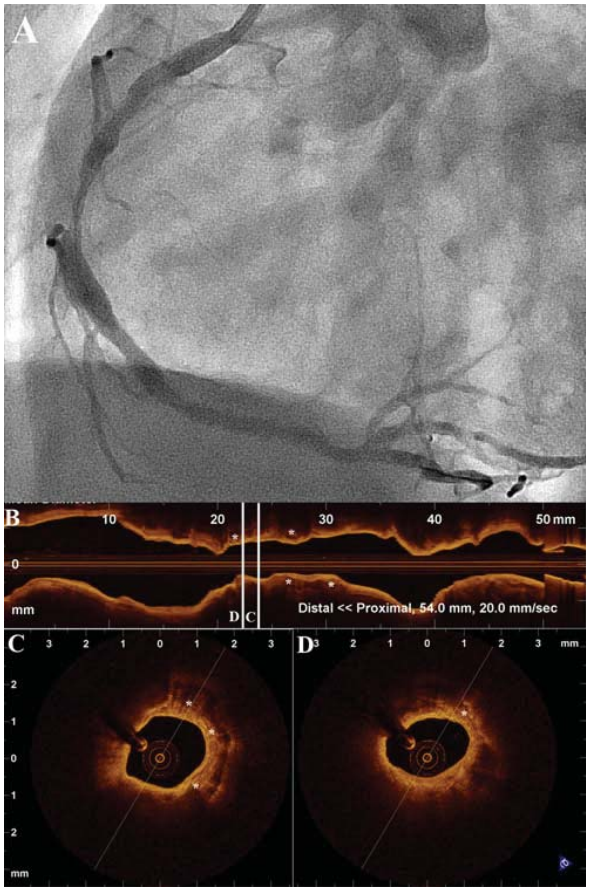

Fig. 3 **a** Angiogram of the right coronary artery of a patient with stable angina. **b** L-mode reconstruction of OCT images demonstrating the longitudinal morphology of the lesion. **c, d** Representative OCT cross-sections showing heavily superficially calcified plaque suggesting the need for targeted therapy such as rotablation. *Asterisks* represent calcific depositions

of necrotic core plaques in sites remote to the site of the greatest stenosis. Although there is not definitive evidence that stenting should also cover lipid-rich plaques located in shoulder areas, it has been shown that presence of such areas in the edge of the stent is associated with edge dissection, as is the presence of fibrocalcific plaques [41]. Additionally, pathologic studies have shown the association of late stent thrombosis with the presence of struts penetrating areas of necrotic core [42], while as mentioned earlier, possible stent-induced disruption of such areas could lead to impaired vascular healing or raise in cardiac necrosis biomarkers [33, 34].

Co-registration of Invasive Imaging and Coronary Angiography

While invasive imaging generally offers high spatial resolution, it can be challenging to consolidate the information

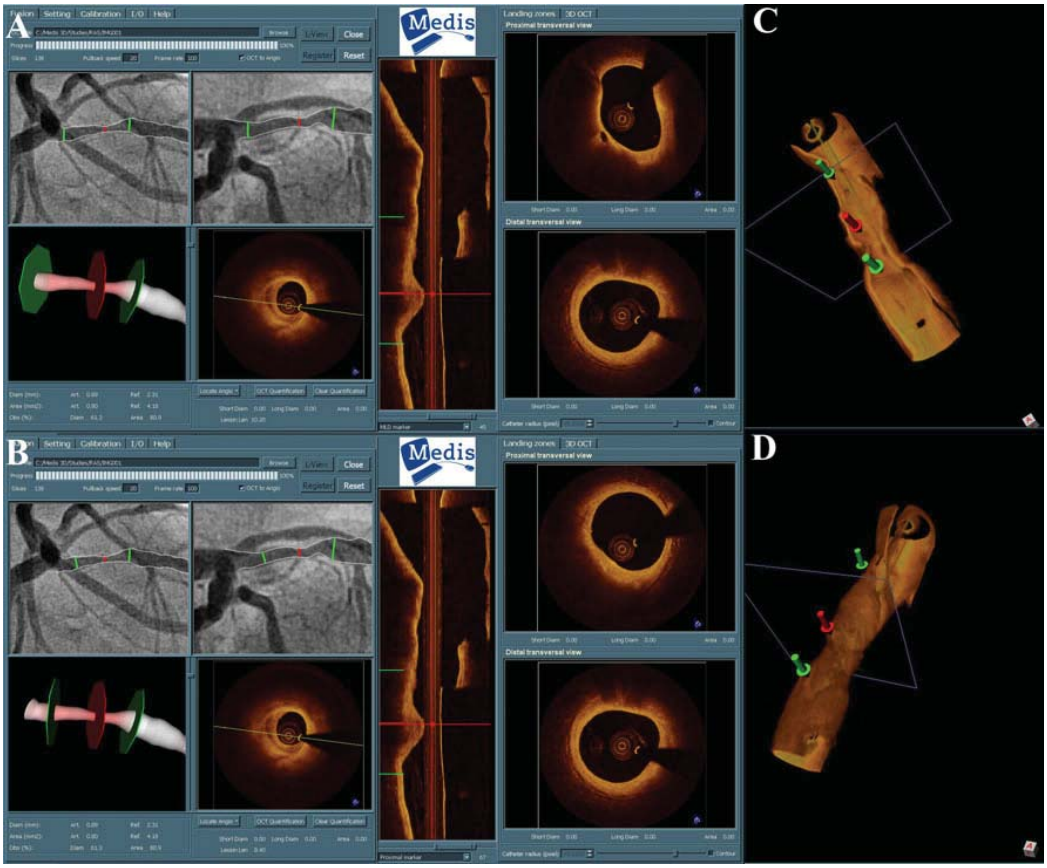

Fig. 4 Registration of 3D QCA and OCT using qAngioOCT (Medis Medical Systems BV, Leiden, The Netherlands). **a** Fibrous cap at the minimal lumen area (*red marker*). Images at the right indicate proximal and distal landing zone. In the proximal landing zone there is a thin cap fibroatheroma. **b** If a shorter stent is selected, the proximal landing zone will be at a site with stable plaque. **c, d** Online three-dimensional reconstructions of the segment generated by the software

gained by invasive imaging technologies with the angiogram, and especially, to ensure correct spatial orientation. This is true for all angiographically silent lesions, whereas this phenomenon might be a consequence of vessel overlap, foreshortening or the inability to visualize a complex three-dimensional structure correctly in a two-dimensional image. Often operators use side branches as observed in both imaging modalities as landmarks. This approach is not always the optimal, as side branch ostia are not always clearly visible by angiography and also the assumed calibre of a particular side branch can be underestimated. Currently, a number of technical solutions to this problem are being developed, including the use of pulsed fluoroscopy to track the imaging catheter in real time (Siemens Medical prototype, Erlangen, Germany) [43] or alternatively, approaches for software enabled synchronization of three-dimensional angiography with invasive imaging pullbacks are being developed (Medis Medical Imaging Systems BV, Leiden, The Netherlands) (Fig. 4) [44]. The ultimate goal is an online co-registration of the invasive imaging modality with the coronary angiogram, allowing the operator to scroll through a synchronized dataset. Such information could be useful for planning of the most appropriate interventional strategy and for the longitudinal assessment of atherosclerotic lesions.

Guidance in Complex Procedures

OCT can also be a tool for guidance during complex procedures. There have been reports of OCT guidance in chronic total occlusions (CTOs) [45]. In such cases, OCT can be used to identify the entry point of the occlusion and to confirm that the guidewire is indeed in the true vessel lumen and has not entered a false lumen. The development of forward-looking OCT catheters will enable the guidance of a CTO crossing by continuous visualization of the position of the guidewire relative to the microchannels.

Bifurcation lesion stenting is another potential application of OCT guidance. By 3-dimensional reconstruction of OCT images it is possible to produce images that indicate the relative position of the main vessel and the side-branch and help select a suitable strategy [46]. Furthermore, three-dimensional models of coronary arteries can help identify the point of re-crossing of a guidewire in a side branch through the cells of a stent implanted in the main vessel, and evaluate possible presence of struts at the ostia of the side branches following kissing balloon dilation [47]. The development of online reconstructions that incorporate three-dimensional angiography and optical coherence tomography images could improve real-time guidance in these subsets of lesions [44, 48•].

Assessment of Acute Effects of PCI

Pathologic studies have indicated the association of implantation characteristics with late events following stent implantation [49]. Stent strut malapposition has been associated with very late stent thrombosis in IVUS studies [1]. Furthermore, postprocedural lesion assessment has shown that stent expansion, tissue protrusion, and dissection are associated with early stent thrombosis [2, 3], while restenosis is also associated with inadequate stent expansion [3]. Indeed, use of standardized criteria for stent expansion using IVUS guidance and additional treatment based on these criteria was associated with a low restenosis rate in the bare metal stent era [38].

OCT can accurately assess the acute vessel wall response to stent implantation. Due to the high resolution of OCT, tissue prolapse, malapposition, intra-stent thrombus formation, and edge dissection can be detected more accurately than with IVUS (Fig. 5), while stent and luminal measurements by the two modalities are not significantly different [7••, 9, 50]. In a study assessing the effects of stenting on vessel wall morphology, it was shown that the presence of dissections, either at the stent edge or inside the stent, and tissue protrusion was observed in almost all the cases, while in the majority of patients there was some degree of stent malapposition [51•]. Thrombus presence inside the stent was also common, both in stable and in ACS patients [51•]. Furthermore, optical coherence tomography is particularly useful in the assessment of malapposition, due to its superior resolution allowing the detection of small degrees of malapposition not detectable by IVUS with low variability between independent measurements. As OCT signal does not penetrate the surface of stent struts, it is important when calculating the distance of the stent strut from the vessel wall, to subtract the thickness of the strut and polymer from the total distance from strut surface to vessel wall. Acute malapposition has been assessed in a variety of studies, and was found to be associated with plaque and stent characteristics, clinical syndrome, and presence of overlapping stents (Fig. 6) [34, 52].

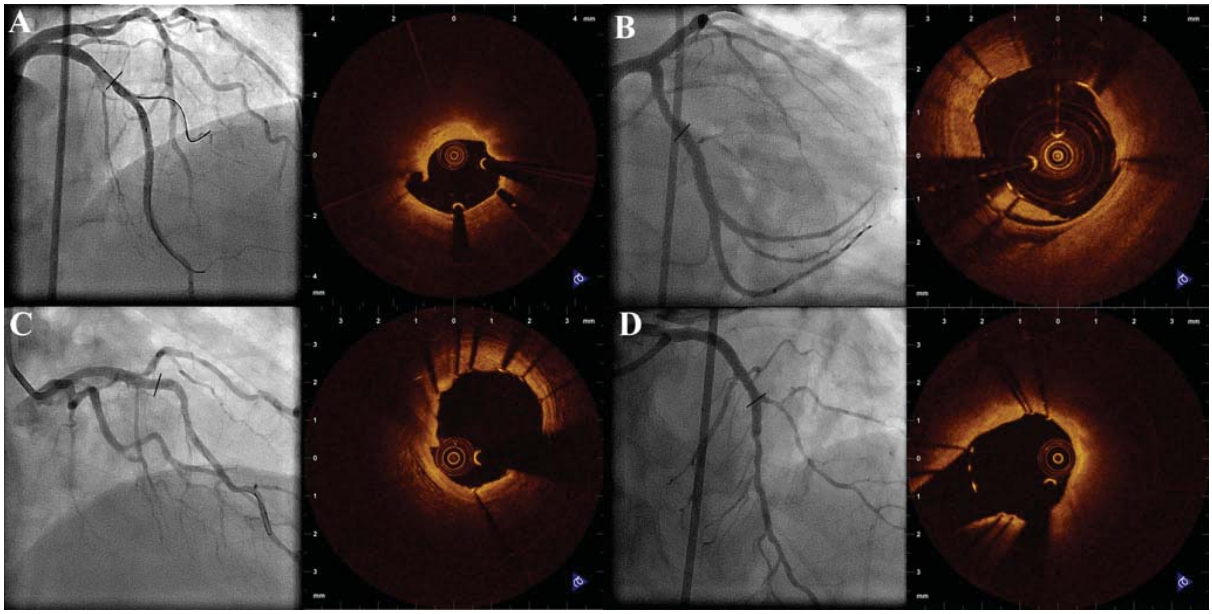

Fig. 5 Assessment of acute effects of intervention. **a** Patient with edge dissection after stent implantation at the bifurcation segment. **b** Intra-stent dissection following stent implantation at the left circumflex artery. **c** Tissue protrusion (9 to 10 o'clock) following stent implantation at the middle left anterior descending artery. **d** Stent protrusion to the diagonal branch following primary percutaneous intervention at the left anterior descending artery without kissing balloon dilation

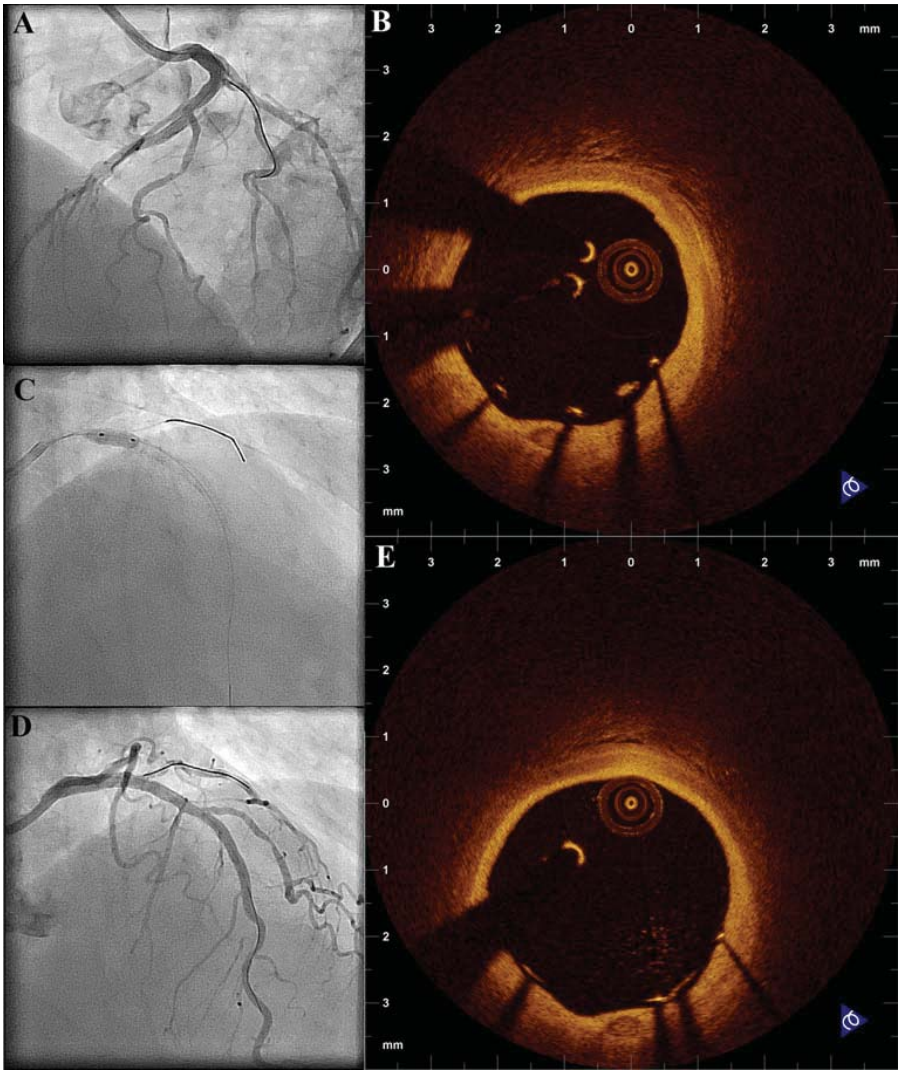

Fig. 6 Correction of malapposition at the proximal LAD following stent implantation. **a** Angiographic result following the initial intervention. **b** OCT demonstrating malapposition at the proximal LAD. **c** Post-dilation was performed with a non-compliant balloon. **d** Final angiographic result. **e** OCT shows correction of malapposition (the distance of the strut surface from the vessel wall is lower than the thickness of the strut and polymer, as provided by the manufacturer)

The significance, however, and prognostic value of the detection of small degrees of malapposition, tissue protrusion, or thrombus that are detectable only with the high-resolution of OCT has not been precisely defined, as with IVUS. Small follow-up studies have tried to assess the impact of these findings with surrogate markers at follow-up [34, 50, 53]. Acute malapposition was more pronounced in implantation compared to follow-up in all of the studies [34, 50, 53]. Conversely, there were cases of initially well-apposed struts that were malapposed at follow-up, possibly due to changes in vessel remodelling [53]. In one of the studies, presence of malapposition was associated with impaired endothelialization and presence of thrombus on struts [53]. Dissections and tissue protrusion, detectable by OCT, tended to resolve at a 6-month follow-up period [50]. Nevertheless, unless larger prospective studies investigate the impact of OCT-detected markers of vessel injury and acute malapposition by OCT on clinical outcome, their role in decision making will remain uncertain.

Post-procedural OCT guidance has not been only used to evaluate vascular injury following stent implantation, but has also been used to assess the effects after PCI with other adjunctive devices such as cutting or scoring balloon and rotational atherectomy [54]. Furthermore, OCT can also be used in ACS in order to assess the role of adjunctive therapies in reducing thrombus burden (Fig. 7) [55, 56].

There is only a handful of studies that have assessed the role of OCT guidance in PCI [12, 35, 37•]. Imola et al. [12] used post-implantation OCT imaging in 74 patients in order to assess the need for further intervention. In 24 patients, additional interventions were performed based on OCT assessment (15 patients with balloon metadilation and 9 patients with additional stent implantation), while in 50 patients the result of the

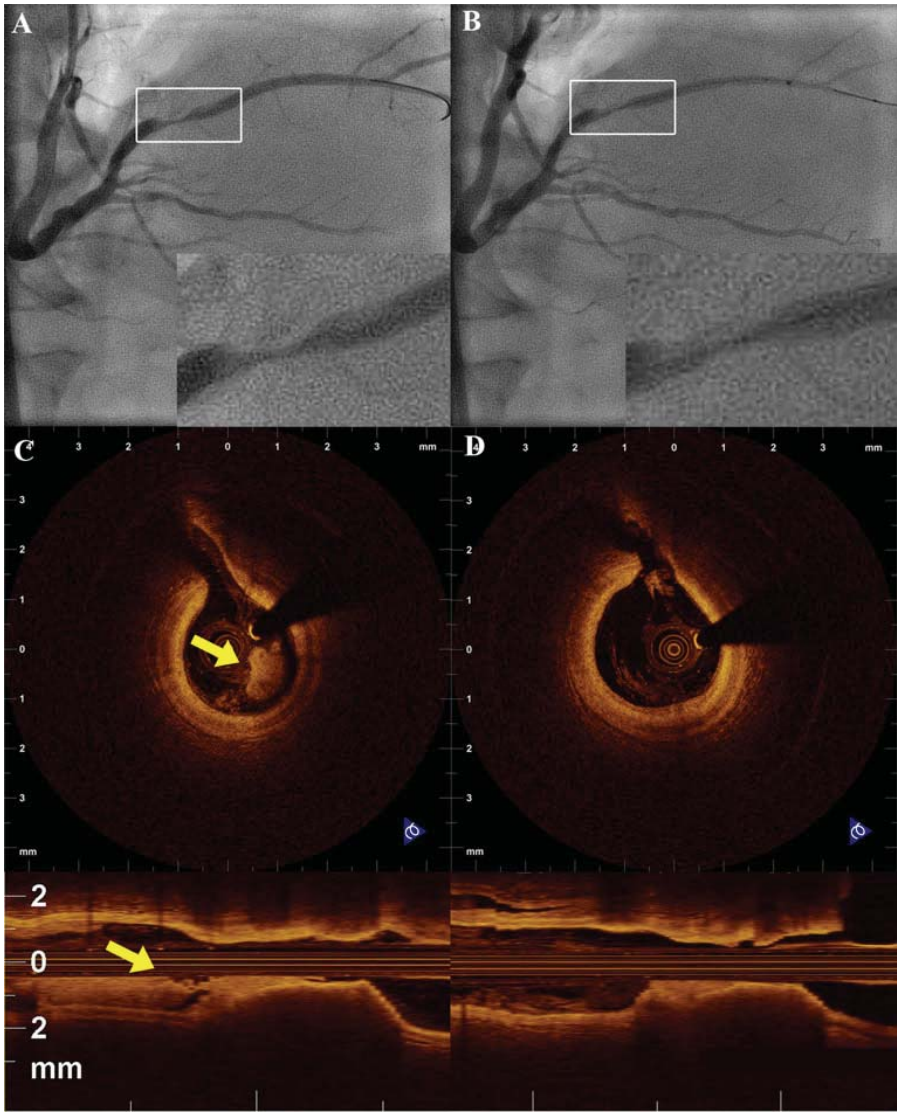

Fig. 7 **a** Coronary angiography of the right posterolateral branch of a patient with myocardial infarction. **b** OCT reveals significant thrombus burden (*yellow arrow*). **c** Angiography after manual thrombus aspiration. **d** OCT shows reduction of the thrombus burden, confirming the effectiveness of thrombus aspiration

interventions was judged satisfactory, leading to an event-free survival of 98 % at 6-month follow-up. Use of OCT in assessing luminal dimensions after cutting balloon angioplasty has led to the safe upsizing of luminal size in patients without coronary stent implantation [35]. Viceconte et al. [37] report on the outcomes of an OCT-guided strategy for procedural guidance, where in 207 cases, OCT suggested the need of a new stent implantation in 29 and further optimization in 64. No major complications were observed in this study, while serial OCT examinations increased procedural time by a mean of 15.4±8.2 min. Thus, it seems that OCT can be safely used for procedural guidance, but the clinical significance of such an approach remains to be assessed in comparative studies.

Assessment of Long-Term Outcome After PCI

OCT can be a valuable tool for follow-up stent assessment. The association of the extent of stent endothelialization with stent thrombosis in pathologic studies have introduced the need for detailed assessment of stent coverage, as a surrogate marker for stent safety. The superior resolution of OCT allows for near-histology assessment of stent coverage, while the ability of OCT to assess and quantify neointimal hyperplasia with greater accordance with histology compared to IVUS, has clearly been documented (Fig. 8) [57]. Furthermore, the high reproducibility for measurements of neointimal hyperplasia makes OCT a reliable tool for objective evaluation of the degree of restenosis. In view of these advantages, OCT has been used for the assessment of the anti-restenotic efficacy of various devices.

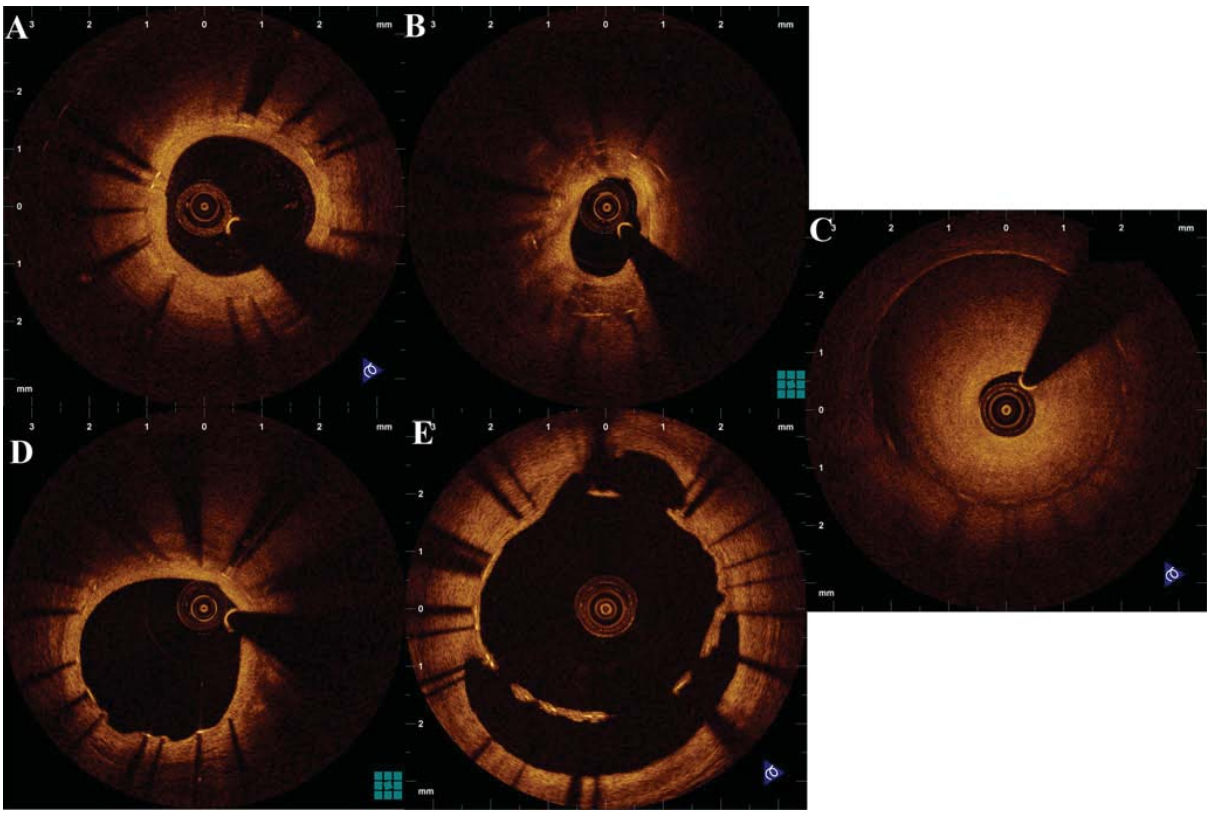

Fig. 8 Various patterns of vessel response at the follow-up of stent implantation. **a** Homogeneous tissue coverage without compromise of the lumen. **b** Heterogeneous coverage with areas resembling lipid plaques 3 years after implantation of a drug-eluting stent. **c** Stent restenosis. **d** Presence of uncovered struts in another site of the stent shown in panel B. **e** Stent malapposition at follow-up, with tissue coverage probably corresponding either to fibrin or endothelial coverage

The assessment of neointimal coverage by OCT constitutes the subject of various studies trying to provide insights into subjects related to stent safety. Stent evaluation by OCT can be used to provide detailed information for stent coverage reported to be associated with stent thrombosis in postmortem studies. It is important to mention that although OCT can detect even minimal tissue coverage at an order of 10 μm, which compares to analysis by optical microscopy, OCT detected coverage could correspond either to true endothelialization or to coverage by fibrin deposits [58]. Therefore, OCT has only about 80 % sensitivity and 95 % specificity for the detection of stent struts lacking endothelial coverage [59]. Nevertheless, due to different optical properties of these components, future developments with characterization based on optical properties [59] may be able to increase the sensitivity for detection of struts without endothelial coverage.

Assessment of tissue coverage has been extensively investigated in the case of the sirolimus-eluting stent, where there are reports from 3 months to 4 years post implantation [60, 61]. All these reports suggest that a small percentage of uncovered struts can be found even 4 years after implantation in sirolimus-eluting stents [61]. Sirolimus-eluting stents, as well as paclitaxel-eluting stents, demonstrate impaired healing compared to bare-metal stents [62, 63]. This does not seem to be the case for the zotarolimus-eluting stent with permanent polymer that is probably the stent with the highest extent of coverage, comparable to that of bare metal stents [64]. Furthermore, comparative studies between sirolimus-eluting and paclitaxel-eluting stents have demonstrated that the latter are associated with an enhanced healing response [65]. A recent OCT substudy of a randomized trial comparing a zotarolimus-stent with biocompatible polymer and the everolimus-eluting stent has shown comparable rates of coverage between these two second-generation stents [66]. Nonetheless, despite the presence of profound differences in vessel healing between different stents, these have not been shown yet to correspond to differences in stent thrombosis, underlining the complexity of mechanisms associated with this entity [67].

Pathologic evidence has shown that bare metal stents are sometimes associated with development of neointimal tissue

with characteristics similar to de novo atherosclerosis [68]. Furthermore, recent observations have shown that this entity is also observed in drug-eluting stents at shorter follow-up intervals [69]. The fact that OCT allows for qualitative assessment of restenotic tissue can be used for elucidating the mechanisms behind late stent failure. Various morphological classifications of restenotic tissue have been proposed by OCT [59, 70, 71], however histologic validation was only available in the recent study by Nakano et al. [59], that proposed the use of a classification similar to the classification used for OCT assessment of de novo atheromatosis. According to this study, the differences in the optical properties of the various tissue components can be used for tissue characterization.

Whether such morphological features are implicated in the pathophysiology of very late stent thrombosis is a subject of investigation. Recent data from OCT studies suggest the existence of two discrete mechanisms associated with stent thrombosis: one involving impaired vessel healing after stent implantation with malapposition and incomplete strut coverage, and one associated with rupture of neoatherosclerotic tissue [72]. Histological examination of thrombus aspirates supports this theory by showing differences in the composition of thrombotic debris between these two mechanisms [72, 73]. However, little is known so far about the incidence and predictors of each mechanism, the "vulnerable" neointimal morphological characteristics, and the differences in clinical outcome in these cases. Future OCT studies will provide new insights into the role of each mechanism in the development of very late stent thrombosis and will assess the clinical significance of evaluation of these mechanisms.

OCT for the Assessment of New Stent Technologies

Due to its superior resolution and the ability to evaluate stent healing and quantify neointimal hyperplasia, OCT is becoming the standard for the assessment of new stent technologies. A new biolimus-eluting stent underwent OCT evaluation in a substudy of the LEADERS trial in order to assess the differences in healing response compared to a sirolimus-eluting stent and was shown to be associated with more complete coverage without increase in neointimal hyperplasia [74]. Moreover, various stents with improvements in release kinetics, coating or matrix design have been evaluated with OCT in order to assess if such improvements correspond to improved healing response as well [75, 76]. Likewise, OCT has been used in a number of studies to evaluate the healing response after treatment with drug-eluting balloons in de novo or in stent restenosis lesions [77].

One of the more fascinating aspects of OCT is the ability to monitor the absorption rate in bioabsorbable stents. OCT has been used for assessment of the biodegradation of the magnesium stent in porcine coronary arteries, as it can demonstrate the reduction in the width of stent struts that is associated with biodegradation [78]. In the case of the bioresorbable everolimus-eluting scaffold (Absorb™, Abbott Vascular, Santa Clara, CA) there have been more extensive animal and human studies [79–81]. Experimental studies have shown that OCT can assess the integration process of the scaffold in long-term observations [81]. In human studies, pilot trials have defined the OCT appearance of various stages of the resorption of the scaffold [79, 80], while OCT has been used for assessment of the vascular healing process and evaluation of differences in resorption and stent strut distribution between the first and the second generation of the scaffold [82], being the best method for measurement of stent length and luminal dimensions [83], as well as assessment of healing in side branches [84].

Future Research Directions

Intravascular OCT is a powerful and easily applicable tool for the assessment of the coronary artery. Today, OCT image interpretation and analysis is based on a color-coded intensity map. Algorithms enabling automated tissue characterization software will allow for a more objective assessment of plaque morphology [85]. New technologies such as polarization-sensitive OCT will enable the distinction of the collagen content of the coronary plaques [86], while the development of micro-OCT will help the better understanding of the pathophysiological mechanisms of acute coronary syndromes [87].

Despite the numerous clinical uses of OCT, and a wealth of case series and clinical observations illustrating potential use in a clinical setting, no clear indications have been established yet. Future studies, focusing either on unselected population or on specific patient and lesion subsets (i.e., acute coronary syndromes, calcified lesions, bifurcations), will determine the role of OCT in procedural guidance.

Furthermore, given that OCT can provide us with an enormous amount of information about plaque morphology and vessel healing following stent implantation, future research will elucidate which are the critical components of plaque and stent "vulnerability" on which we should focus. Finally, natural history studies investigating the impact of vessel morphology and acute procedural complications, as detected by OCT, on future clinical events need to be implemented. And if an association of such OCT findings with clinical outcome is demonstrated, it remains to be seen if treatment based on those findings can lead to an improvement in outcomes.

Conclusions

The introduction of OCT has not only provided new insights in the pathophysiology of the plaque and of the vascular response to stenting, but has also offered interventional cardiology a new tool for procedural guidance. Currently, there are no clear indications for OCT in a clinical setting; however, there are numerous fields where useful decision-guiding information could be provided by OCT. These include pre-interventional evaluation of coronary arteries, procedural guidance in coronary interventions, as well as follow-up assessment of vascular healing after stent implantation. The development of three-dimensional models reconstructed from OCT images could perhaps enhance the role of OCT in procedural guidance [44], while automated tissue characterization software will allow for more objective assessment of plaque morphology [85], strengthening the role of OCT as a tool for implementation of natural history studies. Studies aiming to show an association between OCT imaging and improvement in patient-related outcomes will ultimately define the role of OCT in interventional cardiology.

Disclosure No potential conflicts of interest relevant to this article were reported.

References

Papers of particular interest, published recently, have been highlighted as:
- • Of importance
- •• Of major importance

1. Garcia-Garcia HM, Gonzalo N, Kukreja N, Alfonso F. Greyscale intravascular ultrasound and IVUS-radiofrequency tissue characterisation to improve understanding of the mechanisms of coronary stent thrombosis in drug-eluting stents. EuroIntervention. 2008;4 (Suppl C):C33–8.
2. Choi SY, Witzenbichler B, Maehara A, Lansky AJ, Guagliumi G, Brodie B, et al. Intravascular ultrasound findings of early stent thrombosis after primary percutaneous intervention in acute myocardial infarction: a Harmonizing Outcomes with Revascularization and Stents in Acute Myocardial Infarction (HORIZONS-AMI) substudy. Circ Cardiovasc Interv. 2011;4(3):239–47.
3. Liu X, Doi H, Maehara A, Mintz GS, de Ribamar Costa Jr J, Sano K, et al. A volumetric intravascular ultrasound comparison of early drug-eluting stent thrombosis versus restenosis. JACC Cardiovasc Interv. 2009;2(5):428–34.
4. Nissen SE, Nicholls SJ, Sipahi I, Libby P, Raichlen JS, Ballantyne CM, et al. Effect of very high-intensity statin therapy on regression of coronary atherosclerosis: the ASTEROID trial. JAMA. 2006;295(13):1556–65.
5. Serruys PW, Garcia-Garcia HM, Buszman P, Erne P, Verheye S, Aschermann M, et al. Effects of the direct lipoprotein-associated phospholipase A(2) inhibitor darapladib on human coronary atherosclerotic plaque. Circulation. 2008;118(11):1172–82.
6. Stone GW, Maehara A, Lansky AJ, de Bruyne B, Cristea E, Mintz GS, et al. A prospective natural-history study of coronary atherosclerosis. N Engl J Med. 2011;364(3):226–35.
7. •• Tearney GJ, Regar E, Akasaka T, Adriaenssens T, Barlis P, Bezerra HG, et al. Consensus standards for acquisition, measurement, and reporting of intravascular optical coherence tomography studies: a report from the international working group for intravascular optical coherence tomography standardization and validation. J Am Coll Cardiol. 2012;59(12):1058–72. *This is a consensus document that can be broadly used as a standard reference regarding the current state of the IVOCT imaging modality.*
8. Takarada S, Imanishi T, Liu Y, Ikejima H, Tsujioka H, Kuroi A, et al. Advantage of next-generation frequency-domain optical coherence tomography compared with conventional time-domain system in the assessment of coronary lesion. Catheter Cardiovasc Interv. 2010;75(2):202–6.
9. Bouma BE, Tearney GJ, Yabushita H, Shishkov M, Kauffman CR, DeJoseph Gauthier D, et al. Evaluation of intracoronary stenting by intravascular optical coherence tomography. Heart. 2003;89(3):317–20.
10. Prati F, Cera M, Ramazzotti V, Imola F, Giudice R, Albertucci M. Safety and feasibility of a new non-occlusive technique for facilitated intracoronary optical coherence tomography (OCT) acquisition in various clinical and anatomical scenarios. EuroIntervention. 2007;3(3):365–70.
11. •• Barlis P, Gonzalo N, Di Mario C, Prati F, Buellesfeld L, Rieber J, et al. A multicentre evaluation of the safety of intracoronary optical coherence tomography. EuroIntervention. 2009;5(1):90–5. *This is the first systematic attempt to evaluate the safety of OCT.*
12. Imola F, Mallus MT, Ramazzotti V, Manzoli A, Pappalardo A, Di Giorgio A, et al. Safety and feasibility of frequency domain optical coherence tomography to guide decision making in percutaneous coronary intervention. EuroIntervention. 2010;6(5):575–81.
13. Kume T, Akasaka T, Kawamoto T, Watanabe N, Toyota E, Neishi Y, et al. Assessment of coronary intima–media thickness by optical coherence tomography: comparison with intravascular ultrasound. Circ J. 2005;69(8):903–7.
14. Yabushita H, Bouma BE, Houser SL, Aretz HT, Jang IK, Schlendorf KH, et al. Characterization of human atherosclerosis by optical coherence tomography. Circulation. 2002;106(13):1640–5.
15. Kume T, Akasaka T, Kawamoto T, Ogasawara Y, Watanabe N, Toyota E, et al. Assessment of coronary arterial thrombus by optical coherence tomography. Am J Cardiol. 2006;97(12):1713–7.
16. Murata A, Wallace-Bradley D, Tellez A, Alviar C, Aboodi M, Sheehy A, et al. Accuracy of optical coherence tomography in the evaluation of neointimal coverage after stent implantation. JACC Cardiovasc Imaging. 2010;3(1):76–84.
17. Gonzalo N, Serruys PW, Garcia-Garcia HM, van Soest G, Okamura T, Ligthart J, et al. Quantitative ex vivo and in vivo comparison of lumen dimensions measured by optical coherence tomography and intravascular ultrasound in human coronary arteries. Rev Esp Cardiol. 2009;62(6):615–24.
18. Gonzalo N, Garcia-Garcia HM, Serruys PW, Commissaris KH, Bezerra H, Gobbens P, et al. Reproducibility of quantitative optical coherence tomography for stent analysis. EuroIntervention. 2009;5 (2):224–32.
19. Tahara S, Bezerra HG, Baibars M, Kyono H, Wang W, Pokras S, et al. In vitro validation of new Fourier-domain optical coherence tomography. EuroIntervention. 2011;6(7):875–82.

20. Okamura T, Gonzalo N, Gutierrez-Chico JL, Serruys PW, Bruining N, de Winter S, et al. Reproducibility of coronary Fourier domain optical coherence tomography: quantitative analysis of in vivo stented coronary arteries using three different software packages. EuroIntervention. 2010;6(3):371–9.
21. Sihan K, Botha C, Post F, de Winter S, Gonzalo N, Regar E, et al. Fully automatic three-dimensional quantitative analysis of intracoronary optical coherence tomography: method and Validation. Catheter Cardiovasc Interv. 2009;74(7):1058–65.
22. Tanimoto S, Rodriguez-Granillo G, Barlis P, de Winter S, Bruining N, Hamers R, et al. A novel approach for quantitative analysis of intracoronary optical coherence tomography: high inter-observer agreement with computer-assisted contour detection. Catheter Cardiovasc Interv. 2008;72(2):228–35.
23. Mintz GS, Painter JA, Pichard AD, Kent KM, Satler LF, Popma JJ, et al. Atherosclerosis in angiographically normal coronary-artery reference segments - an intravascular ultrasound study with clinical correlations. J Am Coll Cardiol. 1995;25(7):1479–85.
24. Tonino PA, De Bruyne B, Pijls NH, Siebert U, Ikeno F, van' t Veer M, et al. Fractional flow reserve versus angiography for guiding percutaneous coronary intervention. N Engl J Med. 2009;360 (3):213–24.
25. Kang SJ, Lee JY, Ahn JM, Mintz GS, Kim WJ, Park DW, et al. Validation of intravascular ultrasound-derived parameters with fractional flow reserve for assessment of coronary stenosis severity. Circ Cardiovasc Interv. 2011;4(1):65–71.
26. Gonzalo N, Escaned J, Alfonso F, Nolte C, Rodriguez V, Jimenez-Quevedo P, et al. Morphometric assessment of coronary stenosis relevance with optical coherence tomography: a comparison with fractional flow reserve and intravascular ultrasound. J Am Coll Cardiol. 2012;59(12):1080–9.
27. Toutouzas K, Karanasos A, Stathogiannis K, Synetos A, Tsiamis E, Papadopoulos D, et al. A honeycomb-like structure in the left anterior descending coronary artery: demonstration of recanalized thrombus by optical coherence tomography. JACC Cardiovasc Interv. 2012; (in press).
28. Toutouzas K, Karanasos A, Stefanadis C. Pitfalls of angiography in the assessment of atherosclerosis: The role of optical coherence tomography. J Invasive Cardiol. 2012; (in press).
29. Alfonso F, Paulo M, Gonzalo N, Dutary J, Jimenez-Quevedo P, Lennie V, et al. Diagnosis of spontaneous coronary artery dissection by optical coherence tomography. J Am Coll Cardiol. 2012;59 (12):1073–9.
30. Kubo T, Imanishi T, Takarada S, Kuroi A, Ueno S, Yamano T, et al. Assessment of culprit lesion morphology in acute myocardial infarction: ability of optical coherence tomography compared with intravascular ultrasound and coronary angioscopy. J Am Coll Cardiol. 2007;50(10):933–9.
31. Tanaka A, Shimada K, Tearney GJ, Kitabata H, Taguchi H, Fukuda S, et al. Conformational change in coronary artery structure assessed by optical coherence tomography in patients with vasospastic angina. J Am Coll Cardiol. 2011;58(15):1608–13.
32. Stefano GT, Bezerra HG, Attizzani G, Chamie D, Mehanna E, Yamamoto H, et al. Utilization of frequency domain optical coherence tomography and fractional flow reserve to assess intermediate coronary artery stenoses: conciliating anatomic and physiologic information. Int J Cardiovasc Imaging. 2011;27(2):299–308.
33. Porto I, Di Vito L, Burzotta F, Niccoli G, Trani C, Leone AM, et al. Predictors of periprocedural (Type IVa) myocardial infarction, as assessed by frequency-domain optical coherence tomography. Circ Cardiovasc Interv. 2012;5(1):89–96.
34. Kubo T, Imanishi T, Kitabata H, Kuroi A, Ueno S, Yamano T, et al. Comparison of vascular response after sirolimus-eluting stent implantation between patients with unstable and stable angina pectoris: a serial optical coherence tomography study. JACC Cardiovasc Imaging. 2008;1(4):475–84.
35. Secco GG, Foin N, Viceconte N, Borgia F, De Luca G, Di Mario C. Optical coherence tomography for guidance of treatment of in-stent restenosis with cutting balloons. EuroIntervention. 2011;7 (7):828–34.
36. Kume T, Okura H, Kawamoto T, Yamada R, Miyamoto Y, Hayashida A, et al. Assessment of the coronary calcification by optical coherence tomography. EuroIntervention. 2011;6(6):768–72.
37. • Viceconte N, Chan PH, Barrero EA, Ghilencea L, Lindsay A, Foin N, et al. Frequency domain optical coherence tomography for guidance of coronary stenting. Int J Cardiol. 2011. in press. *A report on the use of OCT for interventional guidance.*
38. de Jaegere P, Mudra H, Figulla H, Almagor Y, Doucet S, Penn I, et al. Intravascular ultrasound-guided optimized stent deployment. Immediate and 6 months clinical and angiographic results from the Multicenter Ultrasound Stenting in Coronaries Study (MUSIC Study). Eur Heart J. 1998;19(8):1214–23.
39. Toutouzas K, Karanasos A, Stefanadis C. Multiple plaque morphologies assessed by optical coherence tomography in a patient with acute coronary syndrome. Heart. 2010;96(16):1335–6.
40. • Toutouzas K, Karanasos A, Tsiamis E, Riga M, Drakopoulou M, Synetos A, et al. New insights by optical coherence tomography into the differences and similarities of culprit ruptured plaque morphology in non-ST-elevation myocardial infarction and ST-elevation myocardial infarction. Am Heart J. 2011;161(6):1192–9. *This study highlights the significance of the longitudinal assessment of coronary plaques with implications in the landing zone concept.*
41. Gonzalo N, Serruys PW, Okamura T, Shen ZJ, Garcia-Garcia HM, Onuma Y, et al. Relation between plaque type and dissections at the edges after stent implantation: an optical coherence tomography study. Int J Cardiol. 2011;150(2):151–5.
42. Joner M, Finn AV, Farb A, Mont EK, Kolodgie FD, Ladich E, et al. Pathology of drug-eluting stents in humans: delayed healing and late thrombotic risk. J Am Coll Cardiol. 2006;48(1):193–202.
43. Hetterich H, Redel T, Lauritsch G, Rohkohl C, Rieber J. New X-ray imaging modalities and their integration with intravascular imaging and interventions. Int J Cardiovasc Imaging. 2010;26 (7):797–808.
44. Tu S, Holm NR, Koning G, Huang Z, Reiber JH. Fusion of 3D QCA and IVUS/OCT. Int J Cardiovasc Imaging. 2011;27(2):197–207.
45. Schultz C, van der Ent M, Serruys PW, Regar E. Optical coherence tomography to guide treatment of chronic occlusions? JACC Cardiovasc Interv. 2009;2(4):366–7.
46. Farooq V, Serruys PW, Heo JH, Gogas BD, Okamura T, Gomez-Lara J, et al. New insights into the coronary artery bifurcation hypothesis-generating concepts utilizing 3-dimensional optical frequency domain imaging. JACC Cardiovasc Interv. 2011;4(8):921–31.
47. Okamura T, Yamada J, Nao T, Suetomi T, Maeda T, Shiraishi K, et al. Three-dimensional optical coherence tomography assessment of coronary wire re-crossing position during bifurcation stenting. EuroIntervention. 2011;7(7):886–7.
48. • Tu S, Xu L, Ligthart J, Xu B, Witberg K, Sun Z, et al. In vivo comparison of arterial lumen dimensions assessed by co-registered three-dimensional (3D) quantitative coronary angiography, intravascular ultrasound and optical coherence tomography. Int J Cardiovasc Imaging. 2012. *This study introduces a new software package for registration of angiography and OCT and for the online reconstruction of three-dimensional models.*
49. Farb A, Burke AP, Kolodgie FD, Virmani R. Pathological mechanisms of fatal late coronary stent thrombosis in humans. Circulation. 2003;108(14):1701–6.
50. Kume T, Okura H, Miyamoto Y, Yamada R, Saito K, Tamada T, et al. Natural history of stent edge dissection, tissue protrusion and incomplete stent apposition detectable only on optical coherence tomography after stent implantation. Circ J. 2012. in press.

51. • Gonzalo N, Serruys PW, Okamura T, Shen ZJ, Onuma Y, Garcia-Garcia HM, et al. Optical coherence tomography assessment of the acute effects of stent implantation on the vessel wall: a systematic quantitative approach. Heart. 2009;95(23):1913–9. *A detailed description of acute vascular wall response to stenting*.
52. Tanigawa J, Barlis P, Dimopoulos K, Dalby M, Moore P, Di Mario C. The influence of strut thickness and cell design on immediate apposition of drug-eluting stents assessed by optical coherence tomography. Int J Cardiol. 2009;134(2):180–8.
53. Ozaki Y, Okumura M, Ismail TF, Naruse H, Hattori K, Kan S, et al. The fate of incomplete stent apposition with drug-eluting stents: an optical coherence tomography-based natural history study. Eur Heart J. 2010;31(12):1470–6.
54. Attizzani GF, Patricio L, Bezerra HG. Optical coherence tomography assessment of calcified plaque modification after rotational atherectomy. Catheter Cardiovasc Interv. 2011.
55. Prati F, Capodanno D, Pawlowski T, Ramazzotti V, Albertucci M, La Manna A, et al. Local delivery versus intracoronary infusion of abciximab in patients with acute coronary syndromes. JACC Cardiovasc Interv. 2010;3(9):928–34.
56. Van Mieghem NM, Kauer F, Regar E. Rheolytic versus aspiration thrombectomy in acute st-segment elevation myocardial infarction judged by OCT. EuroIntervention. 2010;5(8):994.
57. Suzuki Y, Ikeno F, Koizumi T, Tio F, Yeung AC, Yock PG, et al. In vivo comparison between optical coherence tomography and intravascular ultrasound for detecting small degrees of in-stent neointima after stent implantation. JACC Cardiovasc Interv. 2008;1 (2):168–73.
58. Templin C, Meyer M, Muller MF, Djonov V, Hlushchuk R, Dimova I, et al. Coronary optical frequency domain imaging (OFDI) for in vivo evaluation of stent healing: comparison with light and electron microscopy. Eur Heart J. 2010;31(14):1792–801.
59. Nakano M, Vorpahl M, Otsuka F, Taniwaki M, Yazdani SK, Finn AV, et al. Ex vivo assessment of vascular response to coronary stents by optical frequency domain imaging. JACC Cardiovasc Imaging. 2012;5(1):71–82.
60. Takano M, Inami S, Jang IK, Yamamoto M, Murakami D, Seimiya K, et al. Evaluation by optical coherence tomography of neointimal coverage of sirolimus-eluting stent three months after implantation. Am J Cardiol. 2007;99(8):1033–8.
61. Takano M, Yamamoto M, Mizuno M, Murakami D, Inami T, Kimata N, et al. Late vascular responses from 2 to 4 years after implantation of sirolimus-eluting stents: serial observations by intracoronary optical coherence tomography. Circ Cardiovasc Interv. 2010;3(5):476–83.
62. Chen BX, Ma FY, Luo W, Ruan JH, Xie WL, Zhao XZ, et al. Neointimal coverage of bare-metal and sirolimus-eluting stents evaluated with optical coherence tomography. Heart. 2008;94 (5):566–70.
63. Guagliumi G, Costa MA, Sirbu V, Musumeci G, Bezerra HG, Suzuki N, et al. Strut coverage and late malapposition with paclitaxel-eluting stents compared with bare metal stents in acute myocardial infarction: optical coherence tomography substudy of the Harmonizing Outcomes with Revascularization and Stents in Acute Myocardial Infarction (HORIZONS-AMI) Trial. Circulation. 2011;123(3):274–81.
64. Guagliumi G, Sirbu V, Bezerra H, Biondi-Zoccai G, Fiocca L, Musumeci G, et al. Strut coverage and vessel wall response to zotarolimus-eluting and bare-metal stents implanted in patients with ST-segment elevation myocardial infarction: the OCTAMI (Optical Coherence Tomography in Acute Myocardial Infarction) Study. JACC Cardiovasc Interv. 2010;3(6):680–7.
65. Kim JS, Kim JS, Kim TH, Fan C, Lee JM, Kim W, et al. Comparison of neointimal coverage of sirolimus-eluting stents and paclitaxel-eluting stents using optical coherence tomography at 9 months after implantation. Circ J. 2010;74(2):320–6.
66. Gutierrez-Chico JL, van Geuns RJ, Regar E, van der Giessen WJ, Kelbaek H, Saunamaki K, et al. Tissue coverage of a hydrophilic polymer-coated zotarolimus-eluting stent vs. a fluoropolymer-coated everolimus-eluting stent at 13-month follow-up: an optical coherence tomography substudy from the RESOLUTE All Comers trial. Eur Heart J. 2011;32(19):2454–63.
67. Synetos A, Toutouzas K, Karanasos A, Stathogiannis K, Triantafyllou G, Tsiamis E, et al. Differences in drug-eluting stents used in coronary artery disease. Am J Med Sci. 2011;342(5):402–8.
68. Inoue K, Abe K, Ando K, Shirai S, Nishiyama K, Nakanishi M, et al. Pathological analyses of long-term intracoronary Palmaz-Schatz stenting; Is its efficacy permanent? Cardiovasc Pathol. 2004;13(2):109–15.
69. Nakazawa G, Otsuka F, Nakano M, Vorpahl M, Yazdani SK, Ladich E, et al. The pathology of neoatherosclerosis in human coronary implants bare-metal and drug-eluting stents. J Am Coll Cardiol. 2011;57(11):1314–22.
70. Gonzalo N, Serruys PW, Okamura T, van Beusekom HM, Garcia-Garcia HM, van Soest G, et al. Optical coherence tomography patterns of stent restenosis. Am Heart J. 2009;158(2):284–93.
71. Tanimoto S, Aoki J, Serruys PW, Regar E. Paclitaxel-eluting stent restenosis shows three-layer appearance by optical coherence tomography. EuroIntervention. 2006;1(4):484.
72. Guagliumi G, Sirbu V, Musumeci G, Gerber R, Biondi-Zoccai G, Ikejima H, et al. Examination of the in vivo mechanisms of late drug-eluting stent thrombosis: findings from optical coherence tomography and intravascular ultrasound imaging. JACC Cardiovasc Interv. 2012;5(1):12–20.
73. Yamaji K, Inoue K, Nakahashi T, Noguchi M, Domei T, Hyodo M, et al. Bare metal stent thrombosis and in-stent neoatherosclerosis. Circ Cardiovasc Interv. 2012;5(1):47–54.
74. Barlis P, Regar E, Serruys PW, Dimopoulos K, van der Giessen WJ, van Geuns RJ, et al. An optical coherence tomography study of a biodegradable vs. durable polymer-coated limus-eluting stent: a LEADERS trial sub-study. Eur Heart J. 2010;31(2):165–76.
75. Guagliumi G, Sirbu V, Musumeci G, Bezerra HG, Aprile A, Kyono H, et al. Strut coverage and vessel wall response to a new-generation paclitaxel-eluting stent with an ultrathin biodegradable abluminal polymer: Optical Coherence Tomography Drug-Eluting Stent Investigation (OCTDESI). Circ Cardiovasc Interv. 2010;3(4):367–75.
76. Prati F, Stazi F, Dutary J, La Manna A, Di Giorgio A, Pawlosky T, et al. Detection of very early stent healing after primary angioplasty: an optical coherence tomographic observational study of chromium cobaltum and first-generation drug-eluting stents. The DETECTIVE study. Heart. 2011;97(22):1841–6.
77. Gutierrez-Chico JL, van Geuns RJ, Koch KT, Koolen JJ, Duckers H, Regar E, et al. Paclitaxel-coated balloon in combination with bare metal stent for treatment of de novo coronary lesions: an optical coherence tomography first-in-human randomised trial, balloon first vs. stent first. EuroIntervention. 2011;7(6):711–22.
78. Slottow TL, Pakala R, Okabe T, Hellinga D, Lovec RJ, Tio FO, et al. Optical coherence tomography and intravascular ultrasound imaging of bioabsorbable magnesium stent degradation in porcine coronary arteries. Cardiovasc Revasc Med. 2008;9(4):248–54.
79. Serruys PW, Ormiston JA, Onuma Y, Regar E, Gonzalo N, Garcia-Garcia HM, et al. A bioabsorbable everolimus-eluting coronary stent system (ABSORB): 2-year outcomes and results from multiple imaging methods. Lancet. 2009;373(9667):897–910.
80. Serruys PW, Onuma Y, Ormiston JA, de Bruyne B, Regar E, Dudek D, et al. Evaluation of the second generation of a bioresorbable everolimus drug-eluting vascular scaffold for treatment of de novo coronary artery stenosis: six-month clinical and imaging outcomes. Circulation. 2010;122(22):2301–12.

81. Onuma Y, Serruys PW, Perkins LE, Okamura T, Gonzalo N, Garcia-Garcia HM, et al. Intracoronary optical coherence tomography and histology at 1 month and 2, 3, and 4 years after implantation of everolimus-eluting bioresorbable vascular scaffolds in a porcine coronary artery model: an attempt to decipher the human optical coherence tomography images in the ABSORB trial. Circulation. 2010;122(22):2288–300.
82. Gomez-Lara J, Brugaletta S, Diletti R, Garg S, Onuma Y, Gogas BD, et al. A comparative assessment by optical coherence tomography of the performance of the first and second generation of the everolimus-eluting bioresorbable vascular scaffolds. Eur Heart J. 2011;32(3):294–304.
83. Gutierrez-Chico JL, Serruys PW, Girasis C, Garg S, Onuma Y, Brugaletta S, et al. Quantitative multi-modality imaging analysis of a fully bioresorbable stent: a head-to-head comparison between QCA, IVUS and OCT. Int J Cardiovasc Imaging. 2011.
84. Okamura T, Serruys PW, Regar E. Cardiovascular flashlight. The fate of bioresorbable struts located at a side branch ostium: serial three-dimensional optical coherence tomography assessment. Eur Heart J. 2010;31(17):2179.
85. van Soest G, Goderie T, Regar E, Koljenovic S, van Leenders GL, Gonzalo N, et al. Atherosclerotic tissue characterization in vivo by optical coherence tomography attenuation imaging. J Biomed Opt. 2010;15(1):011105.
86. Giattina SD, Courtney BK, Herz PR, Harman M, Shortkroff S, Stamper DL, et al. Assessment of coronary plaque collagen with polarization sensitive optical coherence tomography (PS-OCT). Int J Cardiol. 2006;107(3):400–9.
87. Liu L, Gardecki JA, Nadkarni SK, Toussaint JD, Yagi Y, Bouma BE, et al. Imaging the subcellular structure of human coronary atherosclerosis using micro-optical coherence tomography. Nat Med. 2011;17(8):1010–4.

Chapter 1.2

Optical coherence tomography imaging in acute myocardial infarction

Karanasos A, Toutouzas K, van der Sijde J, van Ditzhuijzen N, Regar E

In: Myocardial infarctions: Risk factors, emergency management and long-term health outcomes. pp 17-52 (Book chapter)

Abstract

Optical coherence tomography (OCT) is a high-resolution intravascular imaging modality able to visualize the micro-environment of the atheromatic plaque and assess intracoronary stents in great detail. As a result, OCT is a valuable research tool for examining the role of morphological characteristics of atheromatic plaque in the progression of coronary artery disease and plaque destabilization, which lead to the clinical manifestation of acute coronary syndromes. Several OCT studies have focused on expanding the current understanding of the pathomechanisms of acute myocardial infarction. Moreover, as OCT is being increasingly used in clinical practice, potential clinical applications of OCT in myocardial infarction are emerging. Despite the lack of established indications for OCT imaging in myocardial infarction thus far, OCT could be potentially of assistance in interventional guidance in several clinical scenarios such as culprit lesion identification, assessment of the underlying mechanisms of stent thrombosis, and guidance of local and systematic antithrombotic therapy. The current chapter summarizes the pathophysiological insights obtained by OCT imaging in acute myocardial infarction, and critically reviews potential areas of clinical application of this imaging modality in myocardial infarction.

Introduction

Acute myocardial infarction (AMI) is a major cause of morbidity and mortality. The almost exclusive cause of acute coronary syndromes (ACS), including unstable angina, AMI with or without ST-segment elevation, and sudden cardiac death is atherothrombosis. Pilot pathologic studies have identified the pathophysiologic processes implicated in the destabilization and thrombosis of atheromatic plaques [1-3]. Although these studies have provided us with the basic understanding of the pathogenetic mechanisms of acute coronary syndromes, the *in vivo* processes and natural history of atherothrombosis remain rather obscure, as post-mortem observations tend to represent the far end of the spectrum of clinical manifestations of atherothrombosis. Developments in intracoronary imaging techniques have managed to overcome limitations of angiography -that is restricted to the study of the lumen of the coronary arteries rather than morphological characteristics of the vessel wall-, and have enabled the *in vivo* visualization of plaque morphology [4].

Among these techniques, optical coherence tomography (OCT) plays a prominent role for the study of plaque morphology due to its very high resolution (~15μm), which enables the identification of the majority of the morphological characteristics of stable and complicated atheromatic plaques [5]. Thus, OCT comprises a valuable tool for obtaining *in vivo* insights into the pathomechanisms of ACS, triggered either by native plaques or by stented arterial segments. Furthermore, OCT can be a useful research tool for studying the effect of treatments applied in AMI and monitoring the vascular healing response. Moreover, as OCT is being increasingly used in clinical practice as a tool for interventional guidance, several potential clinical applications of OCT in AMI have emerged, including culprit lesion identification, assessment of the substrate of stent thrombosis and treatment guidance, and evaluation of the effectiveness of local and systematic antithrombotic therapy [6, 7].

Unstable atherosclerotic plaque: Insights from pathology

Pathomechanisms of Acute Coronary Syndromes

Studies in post-mortem specimens of coronary arteries retrieved from sudden cardiac death victims have identified the major pathologic substrates of coronary thrombosis [1]. These include plaque rupture in 60-70% of the cases, plaque erosion in 20-30% of the cases and thrombosis triggered by calcified nodules in 2-5% [2, 3]. Plaque rupture which is the most frequent mechanism of coronary thrombosis consists of disruption of a thin fibrous cap that overlies a

large necrotic core, causing the thrombogenic contents of the necrotic core to come in contact with the bloodstream and trigger thrombus formation. Plaque erosion is a less well-understood pathologic entity defined as the presence of thrombosis in the absence of plaque thrombosis, more frequently encountered in younger age individuals of female gender [8]. In the majority of the cases with erosion absence of an endothelial layer is observed at the sites of thrombosis [2]. Calcified nodules is a less common cause of coronary thrombosis, more common among men of older age and is characterized by thrombus accumulation on the site of nodular calcification protruding into the lumen through a disrupted thin fibrous cap.

High-risk or 'Vulnerable' Plaque

The term 'vulnerable plaque' has been introduced for denoting plaques that are in high risk to undergo acute thrombosis [9-11]. Traditionally, this term has been used to characterize plaques that bear morphological resemblance to the aforementioned types of thrombosed plaques. As there is debate on whether calcified nodules without thrombosis can be characterized as 'high-risk' plaques, considering a relatively benign prognosis [12], the major types of plaques that are considered vulnerable are these resembling eroded and ruptured plaques. Regarding the eroded plaques, the lack of specific distinct morphological characteristics in such plaques poses a major obstacle for the ad-hoc identification of plaques prone to develop erosion. In contrast to eroded plaques, plaques undergoing rupture have distinct morphological characteristics, including a large necrotic core, a thin (<65μm in pathology series) and inflamed fibrous cap, high plaque size, neovascularization, inflammatory cell infiltration and spotty calcification [13]. These characteristics are also observed in another type of plaque, called thin cap fibroatheroma (TCFA) which is considered the precursor of the ruptured plaque, and thus the main morphological subtype of 'vulnerable plaque' [13]. Therefore, early identification of such plaques has been a topic of intensive research, as this identification -in combination with timely intervention- prior to the occurrence of plaque rupture leading to the manifestation of an acute event, could potentially comprise a treatment strategy for reducing the morbidity and mortality of coronary disease.

It is, nevertheless important to acknowledge that most of the available data concerning the association of plaque morphology and coronary thrombosis are derived from post-mortem studies. Therefore, despite the substantial insights obtained by these studies regarding the substrates of atherothrombosis, and their contribution in the current understanding of atherosclerotic plaque morphology, these studies are associated with several inherent limitations that preclude firm conclusions about the *in vivo* course and mechanisms of atherothrombosis. The

first limitation is the cross-sectional design of these studies that hampers the temporal evaluation of the natural history of plaque morphology and of the responses associated with systematic or local treatment effects. The second limitation is a potential selection bias, given that these studies have focused on deceased patients, thus representing an extreme manifestation of atherothrombosis and therefore findings from these studies are not utterly representative of the actual *in vivo* contribution of these mechanisms in the pathogenesis of ACS. However, technological advances in the field of intracoronary imaging allow to bridge the gap between *post-mortem* and *in vivo* findings and complement current knowledge regarding the mechanisms of atherosclerosis.

In vivo assessment of coronary plaque morphology by OCT

Coronary angiography has traditionally been used for the assessment of coronaries, however not allowing the direct visualization of details of the vessel wall morphology. The development of intravascular imaging techniques enables the direct plaque visualization as it is not restricted to the luminal contour, thus further enabling the *in vivo* assessment of the pathogenetic mechanisms of atherothrombosis. Among intravascular imaging modalities, OCT is the most potent for examining the morphological plaque characteristics associated with acute coronary syndromes, as it can accurately assess the most important aspects of plaque 'vulnerability', including precise measurement of the thickness of the overlying fibrous plaque and a high sensitivity for thrombus detection.

OCT Principle and Image Acquisition in the Cathlab

OCT is an intravascular imaging modality, based on emission and reflectance of near-infrared light from a rotating imaging lens, that can acquire high resolution cross-sectional images of the coronary artery wall [14]. The emitted infrared light waves reflect off the vascular wall and are then received and processed by the OCT imaging system. As the wavelength of light waves is very short, compared to the wavelength of intravascular ultrasound, OCT cannot directly interpret the signal, but uses instead a technique called low-coherence interferometry in order to process the reflected signal. Thereby, OCT can acquire very high axial (~15μm) and lateral (~25 μm) resolution images, but with the disadvantage of a limited penetration with visualization of only the superficial 1–2 mm of the vascular wall, allowing however imaging of the most important elements of plaque vulnerability which are located near the surface of the plaque. Furthermore, during OCT examination it is necessary to temporarily displace blood during imaging, because of the high scattering of light caused by erythrocytes. In currently available

systems, this is achieved through angiographic contrast material injection, warmed to 37°C, through the guide catheter manually or automatically by means of a power injector.

Currently available OCT systems are utilizing a short rapid-exchange monorail catheter for mounting of the optical probe, while the optical signal is transmitted by a single-mode fibre, automatically mounted on the catheter. For image acquisition, the OCT catheter is initially advanced with the aid of a conventional guidewire distally to the target segment, and automated pullback of the optical fibre is performed simultaneously with the contrast injection. The pullback of the catheter imaging tip is performed automatically while rotating inside a transparent sheath, allowing for retrieval of consecutive cross-sectional images for a length of 50-70mm from the coronary artery.

OCT Validation: Stable Coronary Plaques and Fibroatheroma

OCT validation studies performed in post-mortem coronary specimens have focused on defining the optical appearance of the morphological characteristics of the plaque [15-19]. These studies have shown that OCT can be used for plaque characterization with an overall good agreement with histology and high reproducibility. OCT can identify normal wall segments and early atherosclerotic lesions [20, 21], while it can perform tissue characterization in advanced atherosclerotic lesions [5]. The major plaque types discernible by OCT are fibrous plaque, appearing as a signal-rich, homogeneous region with low signal attenuation; fibrocalcific plaque, appearing as a signal-poor heterogeneous region, with sharp borders and low signal attenuation; and necrotic core, which appears as a signal-poor region, with diffuse borders and high signal attenuation within a lesion that is covered by a fibrous cap [5, 15]. Fibroatheroma has been defined as a plaque with necrotic core and a fibrous cap. Importantly, the thickness of the fibrous cap can be measured with precision by OCT [22, 23]. A thin cap fibroatheroma by OCT is defined as a fibroatheroma covered by a thin fibrous cap; the current threshold for defining a cap as thin is the extrapolated by histology value of 65μm, although the optimal threshold remains a matter of debate, that will be discussed more extensively below. Mixed plaques by OCT are characterized as plaques containing more than one plaque morphologies within a single cross-sectional frame. Additional tissue components that can be identified by OCT include macrophages that are characterized by bright reflectance and high signal attenuation, and intimal vasculature that appears as sharply delineated signal-poor voids within the intima [5, 24]. Figure 1 demonstrates the main plaque types and tissue components identified by OCT.

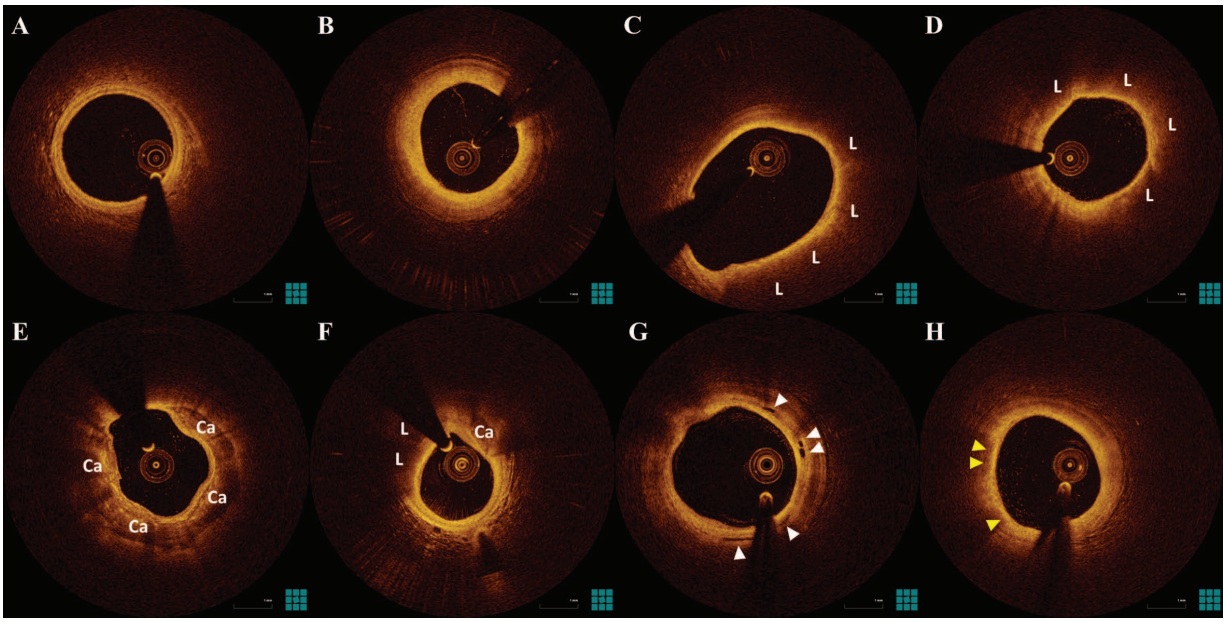

Figure 1. Plaque morphology by OCT.

A. Normal vessel B. Fibrous plaque C. Fibroatheroma (minimum fibrous cap thickness: 120μm) D. Thin cap fibroatheroma (minimum fibrous cap thickness: 40μm) E. Fibrocalcific plaque F. Mixed plaque with necrotic core and calcification G. Intimal microchannels H. Macrophage infiltration.

Annotations: L=necrotic core, Ca=calcifications, white arrowheads=microchannels, yellow arrowheads=macrophages.

Thrombosed Coronary Lesions

Importantly, OCT can also be used for tissue characterization in thrombosed plaques. OCT can identify intracoronary thrombus as an intraluminal mass attached to luminal surface or floating within the lumen, and discriminate between two major types of thrombus: red thrombus (red blood cell–rich) with high backscattering and high attenuation, and white thrombus (platelet-rich) that has lower backscattering, is homogeneous and has low attenuation [25]. Plaque rupture can be identified by OCT as a fibroatheroma with fibrous cap disruption over necrotic core, with or without cavity formation [5]. Plaque erosion is defined as a plaque with thrombus and no evidence of cap rupture evaluated in multiple adjacent frames. It is important to note that in some cases, due to high signal attenuation caused by the presence of red thrombus, the presence of plaque rupture can be obscured, and thus in the presence of red thrombus, the diagnosis of erosion by OCT should be considered presumptive. Thrombosis on the grounds of calcified nodules can be identified as evidence of thrombus in conjunction with calcium protruding into the lumen, frequently forming sharp, jutting angles [26]. Figure 2 demonstrates the main thrombosed plaque morphologies identified by OCT.

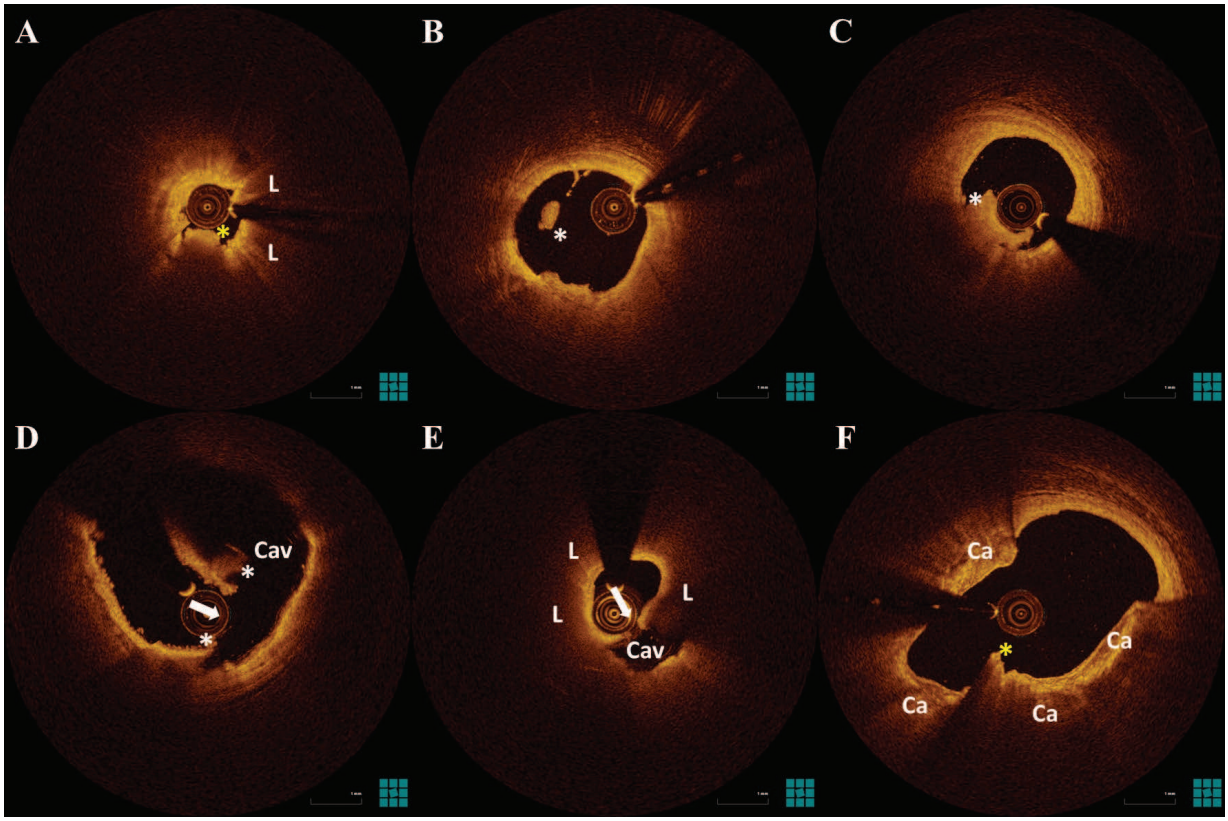

Figure 2. Thrombosed plaque morphology by OCT.

A. Red thrombus B. White thrombus C. Plaque erosion D. Ruptured plaque with large cavity formation E. Ruptured plaque with small cavity formation F. Thrombosed calcified nodules.

Annotations: L=necrotic core, yellow asterisk=red thrombus, white asterisk=white thrombus, Cav=cavity, white arrow=cap disruption, Ca=calcifications.

OCT Insights into the Mechanisms of Plaque Destabilization and Myocardial Infarction

Given the advantages of OCT in characterization of thrombosed plaques, a number of studies have used OCT in order to explore the pathomechanisms of plaque formation, progression and destabilization that will eventually lead to myocardial infarction.

Unstable Plaque Morphology in Culprit Plaques in Patients with ACS

A pilot *in vivo* OCT study focused on the assessment of plaque morphology according to the clinical presentation using three patient groups: patients with stable angina, patients with unstable angina and non-ST-segment elevation myocardial infarction (NSTEMI), and patients with ST-segment elevation myocardial infarction (STEMI) 5 days after thrombolytic therapy

administration [27]. Culprit plaques of patients with unstable angina, NSTEMI and STEMI were associated with lower fibrous cap thickness and higher incidence of TCFA compared to stable lesions. A subsequent study confirmed these findings, showing increased incidence of TCFA, thrombus and plaque rupture in AMI patients compared to stable angina [28].

Superior Assessment of pathomechanisms of ACS

OCT has been also used for the assessment of plaque morphology in the acute phase of ACS, including AMI, after achieving sufficient flow restoration by means of aspiration thrombectomy. A variety of morphological characteristics can be visualized in the culprit lesion of myocardial infarction, as a result of the complexity of atherosclerosis often encountered in these settings [29]. Assessment of the culprit lesion in patients with ACS has shown a superior ability of OCT for the detection of plaque rupture, plaque erosion and intracoronary thrombus compared to intravascular ultrasound (IVUS) or coronary angioscopy [30]. Importantly, in this series of 30 patients, thrombus was successfully visualized by OCT in all cases. Furthermore, this superior visualization of ACS pathomechanisms by OCT enables the evaluation of the incidence of these mechanisms in an *in vivo* setting [31]. In a series of 124 patients with ACS, plaque rupture was identified in 44% of the patients, erosion in 31%, thrombosis of calcified nodules in 8%, and other causes -including subocclusive stenosis, dissection and coronary spasm- in 17% of the cases [32]. Despite a possible misclassification of some cases with plaque rupture as plaque erosion, due to shadowing from residual intraluminal thrombus (in 13% of the cases underlying plaque was not fully visualized classifying them as a probable erosion), this study provides an estimate of the relative contribution of each pathomechanism in patients with ACS, indicating that in an *in vivo* setting, plaque rupture could be accountable for less thrombosis events than what has been previously demonstrated in post-mortem studies. Of note, in this study, plaque rupture was more common among STEMI patients, in contrast to erosion that was more common among non-ST elevation ACS patients and calcified nodules that where exclusively observed among patients with non-ST elevation ACS.

Association between Plaque Morphology and Clinical Presentation

Importantly, morphological characteristics of the ruptured plaque can also differ depending on clinical presentation. It has been independently demonstrated by Toutouzas et al. [33] and Ino et al. [34] that among AMI patients with ruptured culprit plaques, morphological characteristics of the ruptured site differ between ST-segment elevation and non-ST-segment elevation acute myocardial infarction. Specifically, ruptured plaques of patients with STEMI are associated with a

greater extent of cap disruption compared to ruptured plaques of patients with NSTEMI. Also, patients with STEMI had a smaller minimal lumen area compared to patients with NSTEMI [33], showing the importance of residual lumen for the development of more severe vessel occlusion as in STEMI. This finding was further corroborated by the finding of a lower lumen area in patients with culprit ruptured plaques of ACS versus non-culprit plaques in the same patients that had undergone silent rupture [35]. This difference in lumen area of ruptured plaque, both in the rupture site and the minimal lumen area site of the plaque, was also present in a comparison of asymptomatic patients with silent plaque rupture in OCT examination, with non-ST-segment elevation ACS with culprit lesion plaque rupture [36]. Collectively, these studies provide indirect evidence that the degree of the pre-existing lumen narrowing might contribute to the clinical manifestation following plaque rupture.

Moreover, morphological differences have also been found between culprit ruptured plaques of patients with exercise-triggered ACS and culprit ruptured plaques of patients with rest-onset ACS [37]. Patients with exercise-triggered ACS had a higher cap thickness and higher incidence of rupture at the shoulder of the plaque. Finally, in a study of ACS patients, the finding of culprit lesion rupture as pathomechanism by OCT was associated with lower incidence of prodromal symptoms compared to patients without evidence of culprit plaque rupture (36% versus 84%) [38].

Plaque Morphology in ACS – Assessment of Cap Thickness in Plaque Rupture

Additionally, OCT has provided observations regarding culprit plaque morphology in ACS. In a population comprised by both stable patients and ACS patients, positive remodeling of the culprit lesion was associated with TCFA and morphology and evidence of inflammation [39], a finding also observed in a patient subset consisting exclusively by patients with ACS [40]. These observations are in line with pathologic studies indicating plaque remodeling as a component of plaque vulnerability [13] and *in vivo* IVUS studies showing the association of increased local inflammatory activation in ACS patients with positive remodeling and plaque rupture [41]. Furthermore, OCT has been used for identifying a critical value of cap thickness that characterizes rupture-prone plaques *in vivo*. In autopsy series, ruptured caps have a mean thickness of 23μm ± 19μm with 95% of them being thinner than 64μm [1]. However, it is not known whether the same values apply for OCT, as there is a mean overestimation of cap thickness by OCT in comparison with histology of 24μm ± 44μm [22], and also histologic cross-sections are subject to anisotropic tissue shrinkage potentially underestimating measurements [23, 42]. In the study of Tanaka et al. [37], cap thickness in ruptured plaques ranged from 20μm to

160μm, while in the study of Toutouzas et al. [33], 96% of the caps were thinner than 90μm. Furthermore, cap thickness within the plaque was consistently thinner in the rupture site compared to the minimal lumen area site, where cap thickness was as high as 200μm [33]. In an attempt to define a cut-off value for cap thickness, Yonetsu et al. performed cap thickness measurements in 71 ruptured and 111 non-ruptured plaques [43]. As expected fibrous cap thickness was lower for ruptured plaques, a finding observed both for minimal cap thickness of the entire plaque and for minimal cap thickness measured in fixed intervals within the culprit lesion. In 95% of ruptured plaques in this study, minimal cap thickness was below 80μm, whereas a value of 67μm could discriminate ruptured and non-ruptured plaques with 83% sensitivity and 77% specificity. Therefore, despite the current consensus on the utilization of the histology-derived 65μm cut-off for definition of thin-cap fibroatheroma by OCT, it is important to keep in mind that fibroatheromas with higher cap thickness -up to 100μm or even higher- could still be prone to rupture.

OCT Can Identify Spontaneous Coronary Dissection

In addition to insights about morphology of the ruptured plaques, OCT has been used for the study of the morphology of other causes of acute coronary syndromes such as spontaneous dissection and coronary spasm. Indeed, spontaneous dissection can be imaged by OCT as a separation of the intimal layer with formation of a false lumen at the level of the media [44], with or without intramural hematoma formation [45]. In such cases, OCT can also be used clinically in order to facilitate diagnosis and assist in selecting an appropriate management strategy.

OCT Findings in Spontaneous Coronary Spasm and Recanalized Thrombus

Similarly to spontaneous dissection, coronary spasm is another rare cause of acute coronary syndromes. OCT in this setting has demonstrated a variety of morphological changes in the coronary artery comprising intimal notches [46], and transient separation of the coronary artery wall layers [47, 48], that is sometimes accompanied by micro-thrombosis [49]. Finally, recanalized thrombus can be identified by OCT appearing as multiple intraluminal tissue rims, resembling a 'honeycomb' [50, 51].

Localization of High-risk Plaques in the Coronary Tree

OCT studies have also provided important insights concerning the spatial distribution of high-risk plaques in the coronary tree. It is known by angiographic studies that most STEMI events tend to cluster within the proximal portion of coronary artery [52], a distribution similar to the

distribution of coronary atherosclerosis [53]. Pathologic studies have shown that this distribution of occlusions coincides with the distribution of high-risk plaques, where thin cap fibroatheromas and ruptured plaques are localized in focal spots within the proximal third of coronary arteries [54, 55]. Fujii et al. [56] demonstrated in both stable and ACS patients a proximal clustering of both culprit and non-culprit lesion TCFAs, while a small study on ACS patients demonstrated clustering of TCFAs in the proximal segment of the left anterior descending artery (LAD), but an even distribution within the left circumflex artery (LCx) and the right coronary artery (RCA) [37]. In a study of Toutouzas et al. [57, 67] culprit lesions of ACS patients were evaluated by OCT in relation with their spatial distribution in the coronary tree. The distribution of culprit lesions in this study was similar to the distribution described in previous angiographic studies [52]. OCT further demonstrated that among these plaques, culprit plaques located in the proximal 30mm were more often associated with rupture compared to the more distal lesions, indicating that plaque rupture is the main pathomechanism for ACS in these proximal lesions [57]. The distribution of rupture coincided, as expected, with the distribution of thin cap fibroatheromas that were also clustered within the proximal 30mm. Vessel sub-analysis showed that this distribution was evident in the LAD and the LCx, whereas in the RCA there was an even distribution along the coronary artery. A possible explanation for this finding is the presence of multiple side-branches in the proximal segments of the left coronary system, leading to changes in the hemodynamic conditions and development of areas of low shear stress [58, 59], which in turn could lead to the development of unstable plaque phenotypes [60]. This knowledge of the spatial distribution of the high-risk plaques can be potentially useful in the future for the development of preventive treatment strategies [61, 62].

Multiple Coronary Lesion Instability in ACS

Although myocardial infarction is in principle a focal manifestation arising from a single lesion, complex systemic pathophysiologic processes such as inflammation are involved in the pathogenesis, leading to multiple lesion instability [63-65]. Thus, non-culprit lesions of patients with myocardial infarction have a more complex angiographic morphology and are associated with rapid lesion progression and increased event rate at follow-up [66, 67]. This notion is further supported by a recent study, randomizing STEMI patients undergoing primary percutaneous coronary intervention (PCI) of the culprit lesion to additional prophylactic revascularization of non-culprit lesion with >50% stenosis or culprit-only treatment, which demonstrated a reduction in events in the group undergoing prophylactic angioplasty of these non-culprit lesions [68]. These observations have shaped the hypothesis that these non-culprit lesions of ACS have

different morphology than lesions of stable patients. Indeed, OCT studies have lent further evidence to this hypothesis, providing a pathophysiological explanation for these clinical observations. Specifically, non-culprit lesions of patients with AMI were demonstrated to have increased incidence of non-culprit lesion TCFA and thrombus compared to non-culprit lesions of patients with stable angina, and a higher incidence of multiple TCFA lesions [28, 69]. Furthermore, a comparison of the non-culprit lesion of ACS patients with lesions of stable patients showed a higher lipid content, a thinner fibrous cap and a higher incidence of macrophage infiltration and thrombus in non-culprit lesions of ACS patients, in conjunction with higher incidence of TCFA [70]. This effect seems to be derived mainly by patients with rupture of the culprit plaque as pathomechanism for the ACS, as in these patients non-culprit lesions are associated with a higher incidence of TCFA and silent rupture compared to patients without plaque rupture in the culprit lesion [71]. Of note, this evidence of multiple lesions instability in AMI is more pronounced in patients with diabetes, where the incidence of non-culprit lesion TCFA and rupture is more common than in patients without diabetes [72].

Plaque Morphology and Systemic Inflammation

Systemic inflammatory responses have been implicated as potential contributors for the observed lesion instability. Multiple studies have examined a possible association of systemic inflammation, as assessed by circulating inflammatory biomarkers, and culprit plaque morphology in ACS (Table 1) [28, 40, 73-81]. Among these inflammatory markers, C-reactive protein (CRP) is one of the most well studied biomarkers in ACS, as there is an association of its levels with the extent of angiographic disease and ACS [82]. The majority of studies demonstrate the presence of elevated CRP levels in plaque rupture, TCFA and an inverse correlation of CRP levels with cap thickness [28, 40, 73, 76-78, 80], whereas some smaller sample studies failed to detect such a difference [74, 75]. Some other inflammatory biomarkers such as IL-18, MMP-9 and pentraxin-3 have also been associated with TCFA and plaque rupture, while flow cytometry studies have shown increased expression of PSGL-1 in circulating monocytes in plaque rupture. In contrast, plaque erosion has been associated with increased levels of myeloperoxidase (MPO), a hemoprotein released by activated neutrophils [74, 78]. Finally, this association of inflammatory activation plaque morphology by OCT in ACS has also been observed in conjunction with biomarkers representing the influence of risk factors, such as levels of circulating malondialdehyde-modified low-density lipoprotein and the mean amplitude of glycemic excursion (MAGE) [77, 81]. Overall, this association of high-risk plaque morphology with inflammatory molecules and mechanisms

underscores the contribution of inflammation in the pathomechanisms of plaque destabilization in ACS.

Table 1. Association of inflammatory biomarkers and plaque morphology in patients with ACS

Study	Population	Inflammatory marker	Association with plaque morphology
Raffel et al. [80]	32 ACS and 11 SA patients	WBC count	WBC count correlated with cap thickness, macrophage density of the plaque CRP levels higher in TCFA versus non-TCFA lesions
Kashiwagi et al. [40]	47 ACS patients	CRP	CRP levels higher in TCFA versus non-TCFA lesions
Fujii et al. [28]	35 AMI and 20 SA patients	CRP	CRP independent predictor of multiple TCFA in the coronary tree in AMI
Bouki et al. [73]	32 ACS and 14 SA patients	CRP, IL-18	CRP and IL-18 levels higher in TCFA versus non-TCFA lesions CRP and IL-18 levels higher in ruptured plaques versus non-ruptured plaques IL-18 levels lower in plaques with calcification CRP levels independent predictor of ruptured plaque
Li et al. [76]	12 AMI, 23 UA and 11 SA patients	WBC count, CRP, IL-18, TNFα	Cap thickness inversely correlated with WBC count and CRP, IL-18, and TNFα levels WBC count and CRP, IL-18, and TNFα levels higher in TCFA versus non-TCFA lesions No association for any factor with plaque rupture CRP levels independent predictor of TCFA
Nicolli et al. [78]	50 non-ST elevation ACS patients	CRP, MPO, MMP-9, MMP-2, Cystatin-C	CRP and MMP-9 levels higher in plaque rupture compared to erosion and severe stenosis without thrombus MPO levels higher in plaque erosion compared to rupture and severe stenosis without thrombus Cystacin-C levels higher in severe stenosis without thrombus compared to plaque rupture or erosion No association of MMP-2 with plaque morphology

Table 1. (Continued)

Study	Population	Inflammatory marker	Association with plaque morphology
Ferrante et al. [74]	25 AMI patients	CRP, MPO	No difference in CRP levels for plaque rupture versus plaque erosion Elevated MPO levels in plaque erosion versus plaque rupture
Koga et al. [75]	28 ACS and 47 SA patients	CRP, pentraxin-3	Levels of pentraxin-3, but not CRP higher in TCFA versus non-TCFA lesions, both in ACS and SA lesions
Ozaki et al. [79]	25 AMI and 20 UA patients	PSGL-1 expression in circulating monocytes	Increased PSGL-1 expression in circulating monocytes in lesions with plaque rupture
Matsuo et al. [77]	53 ACS and 49 SA patients	MDA-LDL, CRP	Higher CRP levels but no difference in MDA-LDL levels in TCFA versus non-TCFA lesions in ACS Significantly higher MDA-LDL levels in ruptured TCFA versus non-ruptured TCFA in ACS
Teraguchi et al. [81]	37 AMI patients	MAGE, circulating monocytes	Increased MAGE in plaque rupture compared to non-ruptured plaque Increased circulating monocytes in plaque rupture

Abbreviations: WBC=white blood cells, CRP=C-reactive protein, IL=interleukin, TNFα=tumor necrosis factor alpha, MPO=myeloperoxidase, MMP= Matrix metalloproteinase, PSGL-1=P-selectin glycoprotein ligand-1, MDA-LDL=malondialdehyde-modified low-density lipoprotein , MAGE= mean amplitude of glycemic excursion

Culprit lesion Morphology and Outcome of Thrombolysis

Plaque morphology seems also to play an important role in flow restoration after thrombolytic therapy administration. In a series of 55 patients undergoing pharamacological thrombolysis with tenecteplase for the treatment of STEMI, patients with complete flow restoration in the culprit artery after thrombolysis (TIMI flow grade III) had significant differences in plaque morphology with patients with TIMI flow grade 0-II in the culprit lesion [83]. In specific, culprit plaques of patients without complete flow restoration were associated with increased lipid content, thinner fibrous cap, and presented with rupture more often than patients with complete flow restoration. Fibrous cap thickness was the most important factor, having a significant correlation with flow

velocity in the culprit artery, as expressed by the corrected TIMI frame count, and being the only factor independently associated with TIMI flow grade. This observation is in line with the finding of improved reperfusion in patients pre-treated with statins [84], a factor known to increase coronary plaque stability [85]. Although the reason behind this observation is not entirely clear, increased thrombogenicity due to an exaggerated inflammatory reaction has been speculated to play an important role [83]. Furthermore, the residual thrombus pattern after successful administration of thrombolytic therapy in STEMI has also been examined with reference to the pathomechanism of the ACS [86]. In patients with a ruptured culprit lesion, the residual thrombus burden one day after fibrinolysis, as assessed by OCT, was higher than in patients with erosion of the culprit lesion. Ruptured culprit plaques had predominantly white thrombus at the site of the rupture with red thrombus being evenly distributed over the entire culprit lesion length, while in plaques with erosion, white thrombus was mainly found and red thrombus was sparse. Collectively, these findings suggest that underlying plaque morphology in STEMI is a major determinant of the response to thrombolytic therapy.

Myocardial Infarction after Stent Implantation: OCT Insights

An important advantage of OCT is that it can be used for assessing the pathophysiological substrate of ACS in stented arteries, namely stent thrombosis. Although the utilization of stents in PCI, mainly drug-eluting stents, has been a major advancement leading to a reduction of the short-term complications, it has also introduced the need for a long-term vigilance, as events from the stented lesion emerge as late as 15 or more after implantation [87, 88].

Pathologic Findings in Late and Very Late Stent Thrombosis: Impaired Healing and Neoatherosclerosis

The reason behind this ongoing late stent failure is not completely understood, contrary to acute stent thrombosis where procedural factors appear to play a major role [89]. Pathologic studies were the first to identify factors associated with late stent thrombosis [90, 91]. While first studies in bare metal stents (BMS) hinted to the underlying plaque as an important contributor in the pathogenesis, subsequent studies in drug-eluting stents (DES) revealed a very high incidence of uncovered and malapposed struts in patients with events implicating an impaired healing response as the main pathogenetic factor [91]. This impaired healing response was mainly observed in first-generation DES and attributed to a vessel wall toxicity induced by the released drug in the case of paclitaxel-eluting stents or by the polymer in the case of sirolimus-eluting

stents [92]. Consequently, poor strut endothelialization was considered a risk factor for stent thrombosis, and considering the ~10μm resolution of OCT, several OCT studies have focused on exploring the association of impaired healing with stent thrombosis [93]. Simultaneously, *in vivo* OCT observations together with pathologic studies demonstrated a variety in the neointimal patterns observed at the follow-up after stent implantation, resembling components of native atherosclerosis [94-98]. Moreover, OCT observations demonstrating neointimal disruption, in analogy to plaque rupture in native atherosclerosis, have raised questions about the exact role of this mechanism in the pathogenesis of very late stent thrombosis [87].

Neoatherosclerosis with Plaque Rupture as Mechanism of Stent Failure

Several studies have studied the OCT findings in patients with late and very late stent thrombosis, in an attempt to identify the pathomechanisms (Table 2) [99-109]. Despite minor differences in the incidences of each pathomechanism, these studies collectively demonstrate a very high prevalence of plaque rupture as a pathomechanism for very late BMS thrombosis, a process observed at a very late follow-up of BMS [106], and two different mechanisms contributing almost equally [109, 110] in late and very late DES thrombosis: neointimal plaque rupture, and impaired healing response with incomplete stent apposition and low rates of coverage (Figure 3). Neointimal rupture is a mechanism occurring mainly at longer intervals since stent implantation [109, 111], in neointimal regions with high necrotic core content and thin fibrous cap [107], similarly to what is observed in native atherosclerosis, but also with a very high incidence of macrophage infiltration [107].

Delayed Healing and Incomplete Stent Apposition: High Prevalence but Unclear Prognostic Value

Regarding the second mechanism, impaired healing, all studies in DES focusing in patients with events demonstrate a very high incidence of uncovered and malapposed struts, considerably higher than the one reported in control subjects without thrombosis [102, 104], control subjects with stent restenosis [101], or even patients with stent thrombosis due to neointimal rupture [5, 110]. Importantly, these findings are exaggerated within the stent in segments where thrombus is found versus segments without thrombus [104]. Conversely, this association has not been prospectively demonstrated in any study, raising questions about the prognostic significance of such findings [93, 112]. Finally, a third more rare mechanism is also identified in some cases, consisting of a native plaque rupture at the edges of a stent triggering thrombosis within the stented segment [105, 110]. Regarding bioresorbable vascular scaffolds (BVS), the first reports of

scaffold thrombosis are appearing [113], although the exact pathomechanisms are yet be identified for these devices.

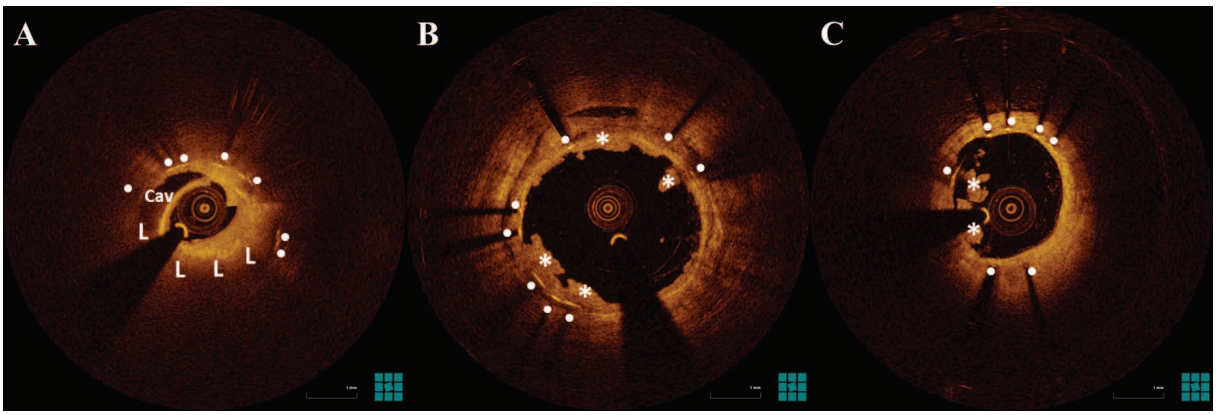

Figure 3. Different pathomechanisms of stent thrombosis.

A. Neointimal rupture with in-stent cavity formation B. Thrombus attached to malapposed struts C. Thrombus attached to an uncovered strut.

Annotations: L=necrotic core, white bullets=stent struts, white asterisk=white thrombus, Cav=cavity.

Table 2. Optical coherence tomography findings in late and very late stent thrombosis

Study	n	DES type	Interval (months)	Uncovered struts(%)	Patients with uncovered struts	Malapposed struts(%)	Patients with malapposed struts	Neointimal rupture	Edge rupture
Ko et al. [99]	18 DES	14 SES/ 3 PES/ 1 EES	40±20	N/A	50%	N/A	39%	22.2%	
Davlouros et al. [100)	7 DES	N/A	8 (3-62)	32%	100%	33%	N/A	BMS 70%/ DES 0%	
Miyazaki et al. [101]	6 DES	5 SES/ 1 PES	37±12	29%	100%	7%	67%	33%	
Guagliumi et al. [102]	18 DES	6 SES/ 10 PES/ 1 EES/ 1 ZES	21 (6-60)	12.3%	84%	10%	78%	11.1%	
Alfonso et al. [105]	8 BMS/ 7 DES	N/A	43±51	N/A	60%	N/A	40%	6.7%	13.3%
Kang et al. [103]	6 BMS/ 27 DES	N/A	74 (46-90)	N/A	17% BMS/ 56% DES	N/A	0% BMS/ 52% DES	BMS 100%/ DES 63%	
Amabile et al. [109]	12 BMS/ 8 DES	N/A	90 (16-210)	32% in 10 cases without rupture	N/A	N/A	N/A	10%	
Parodi et al. [104]	17	N/A	N/A	14%	>10% in 29%	6,7%	>10% in 24%	N/A	
Karanasos et al. [108]	7 BMS/ 32 DES	7 SES/ 19 PES/ 6 EES	63 (21-200)	N/A	66%	N/A	33%	41%	5.1%

Abbreviations: DES=drug eluting stents, BMS=bare metal stent, SES=sirolimus eluting stents, PES=paclitaxel eluting stent, EES=everolimus eluting stents, ZES=zotarolimus eluting stents.

Assessment of the Treatment Effect by OCT

Acute Effects of Stent Implantation in AMI

As OCT is a valuable modality to assess the acute vascular trauma and residual thrombus after stenting [114, 115], but also evaluate stent expansion and apposition [116], it has been used in order to assess the effects of treatment strategies in myocardial infarction [6, 7]. Several studies have investigated the acute results of stent implantation in AMI. Kim et al. examined the acute vascular healing response in 24 patients with stent implantation for the treatment of myocardial infarction, focusing mainly on the incidence of acute incomplete stent apposition (ISA) [117]. The investigators found a very high incidence of incomplete strut apposition ranging for 10% to 28% on a strut-level basis, depending on the type of stent use. When this was assessed on a stent level, the incidence of incomplete stent apposition was 67%, 83%, and 100%, respectively, depending on whether a >10% malapposed struts, >5% malapposed struts, or any malapposed struts definition of incomplete stent apposition was used [117]. In the APPOSITION II trial [118], OCT was used to assess the vascular healing response after implantation of a self-expanding versus a balloon-expandable stent. The use of a self-expanding stent was associated with improved stent apposition (stent-level ISA with >5% malapposed struts definition: 13.9% for self-expanding versus 37.1% for balloon-expandable) and less vascular trauma compared to a balloon expandable stent without significant differences in lumen or stent area. On a strut-level basis, a lower percentage of malapposed stent struts was observed in the self-expanding group than in the balloon-expandable group (2.20 ± 3.92% verus 5.99 ± 7.28%). Importantly, at a three-day follow-up, there were no self-expanding stents with >5% malapposed struts in the self-expanding group, while there was no significant difference over time in the percentage of malapposed struts for the balloon-expandable group.

Evaluation of the Efficacy of Local Antithrombotic Strategies

As OCT can detect and quantify the residual thrombus after stenting [115, 119], it can be also used for the evaluation of various adjunctive therapies aiming at the reduction of distal embolization (Figure 4). The TROFI study was a randomized study that investigated the impact of thrombectomy on the residual flow area (lumen area – prolapse and thrombus area) after 2nd generation stent implantation in myocardial infarction [120]. Only a modest trend was found for higher minimal flow area in the group of thrombectomy, whereas there were no significant differences in morphometric measurements of stent and lumen, residual thrombus or incomplete stent apposition [120]. Similarly, in NSTEMI patients, the use of aspiration thrombectomy failed

to significantly reduce intracoronary thrombus burden, prior to stent implantation [121]. Parodi et al. randomized 80 AMI patients to rheolytic versus aspiration thrombectomy, showing only a trend for lower residual thrombus after rheolytic thrombectomy versus aspiration thrombectomy; however, other markers of reperfusion were better in the rheolytic thrombectomy arm, leading to reduced incidence of malapposed struts at a 6-month follow-up [122]. Another adjunctive treatment for AMI evaluated by OCT is local delivery of IIb/IIIa by means of a dedicated catheter. A comparison of this approach versus intracoronary administration of IIb/IIIa showed a higher reduction of thrombus burden with the local treatment [123], while future studies will aim to investigate what is the impact of this adjunctive treatment in combination with thrombectomy on the residual thrombus burden after stent implantation by OCT [124]. Finally, a small observational study has evaluated potential differences in thrombus burden by OCT among different antiplatelet regimes, however, small numbers preclude the extraction of conclusions [125].

Chronic Arterial Healing Response after Stent Implantation in AMI

Additionally to the acute assessment of intervention, OCT has been used for the assessment of the chronic artery healing response after stent implantation, a factor implicated in the pathogenesis of late events. Gonzalo et al. [126] first demonstrated an impaired healing response at a mid-term follow-up of stents implanted for STEMI compared to stents implanted for stable and unstable angina, with higher rates of uncovered and malapposed struts. This finding was also encountered at the very late (~5 years) OCT follow-up of SIRTAX study, where stent implantation during acute coronary syndrome versus stable angina was associated with higher rate of uncovered struts [127]. This impaired healing response is more pronounced in first-generation DES compared to BMS [128]. These rates appear to be low for second-generation DES and not to be affected by the use of thrombectomy at the baseline procedure [129]. Of note, the amount of coverage in the follow-up of these stents was correlated with the amount of the residual intraluminal material post-stenting showing the important role of thrombus as a mediator of the healing response [129].

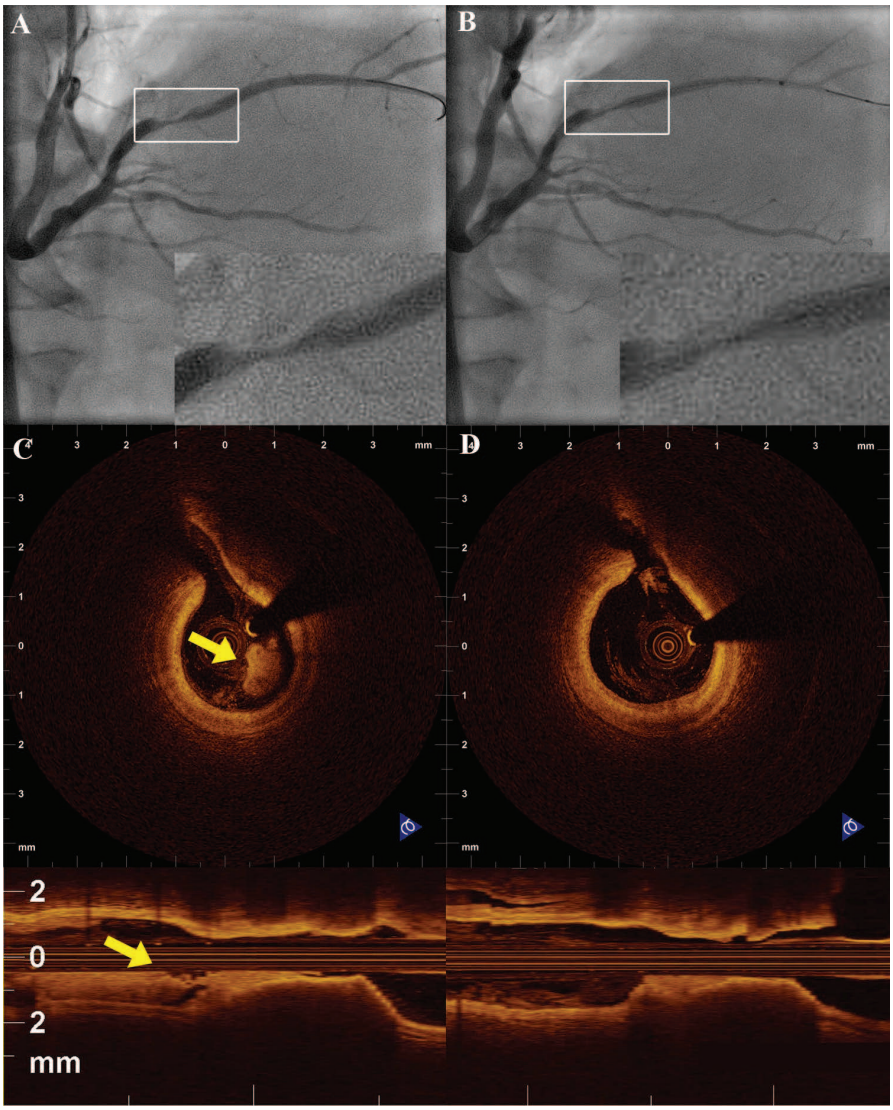

Figure 4. Assessment of thrombectomy result.

A. Coronary angiography of the right posterolateral branch of a patient with myocardial infarction. B. OCT reveals significant thrombus burden (yellow arrow). C. Angiography after manual thrombus aspiration. D. OCT shows reduction of the thrombus burden, confirming the effectiveness of thrombus aspiration.

Reproduced from Karanasos et al, Curr Cardiovasc Imaging Rep. 2012;5:206-220 [6].

Bioresorbable Scaffolds in AMI

As bioresorbable vascular scaffolds are being increasingly used for the treatment of coronary artery disease, AMI patients appear as a patient population that could have higher benefit from the implanatation of these devices [130]. However, given the limited data available on BVS implantation in thrombosed lesions, OCT appears as a useful tool for the study of the acute vascular response [131]. The BVS-STEMI-first study examined the acute vascular response after BVS implantation in 49 patients with myocardial infarction, 31 of whom had an OCT study of

the culprit lesion [132]. The OCT findings were consistent with a good procedural result, without significant lumen compromise or stent underexpansion, a mean percentage of malapposed struts per patient of 2.80 ± 3.90%, and an incidence of scaffolds with >5% malapposed struts of 22.6%. Importantly, despite a high strut thickness of the BVS, a low incidence of angiographic signs of distal embolization was found, while OCT assessment of the tissue prolapse/residual thrombus after scaffold implantation was at similar levels with what has been reported for metal stents [115]. Similar conclusions were reached by an independent study, Prague-19 [133], that also showed good scaffold expansion and apposition in 21 STEMI patients treated with BVS. Although these reports demonstrate that BVS could potentially be a promising treatment for STEMI, data is still fairly limited and OCT studies of the mid- and long-term healing response will be able to give further insight on the effects of such an approach [134-136]

Potential Utility of OCT in Interventional Guidance in Myocardial Infarction

Optimization of Stent Expansion – Reduction of Residual Thrombus Burden

As OCT is being increasingly used in clinical practice, the concept of OCT-guided procedures emerges as an approach for improving the outcome of invasive treatment of coronary artery disease. However, in contrast to IVUS, where numerous studies have investigated the impact of IVUS-guided strategies, only limited data are available for OCT. The main body of evidence for OCT guidance comes from the CLI-OPCI study [137], a non-randomized registry where the outcomes of 335 'all-comer' patients -including ACS patients- undergoing OCT-guided PCI, and the one-year outcomes were compared with the outcomes of 335 matched patients undergoing angiography-guided PCI during the same period. The primary endpoint of 1-year cardiac mortality and myocardial infarction was lower for OCT-guided PCI, both for crude and propensity-matched data, mainly due to a high incidence of events in the angio-guided group [137]. Despite the observational nature of this study, this is the first study that demonstrates a potential benefit from OCT guidance in PCI. Conceptually, such a benefit could be higher for patients with ACS, considering the ability of OCT to detect and quantify thrombus, and simultaneously assess the underlying pathomechanism. The use of OCT in stent thrombosis was discussed earlier; however OCT can also be used in this setting for the assessment of the efficacy of thrombus-reducing strategies as aspiration thrombectomy and rheolytic thrombectomy [138]. A similar assessment can also be performed after stent implantation in AMI caused by native plaque, in order to reduce the residual thrombus burden. Di Giorgio et al. demonstrated the

feasibility of OCT-guided additional balloon dilation in patients with residual in-stent thrombus after PCI in AMI comparing it with no further intervention [139]. Eighty patients were sequentially divided in 2 equal groups treated with the two different strategies. The use of OCT-guided post-dilation was associated with an increase in stent and lumen area, and a decrease in residual thrombus area, without however any significant differences between the OCT-guided group and the control group in OCT morphometric measurements or angiographic markers of distal embolization [139].

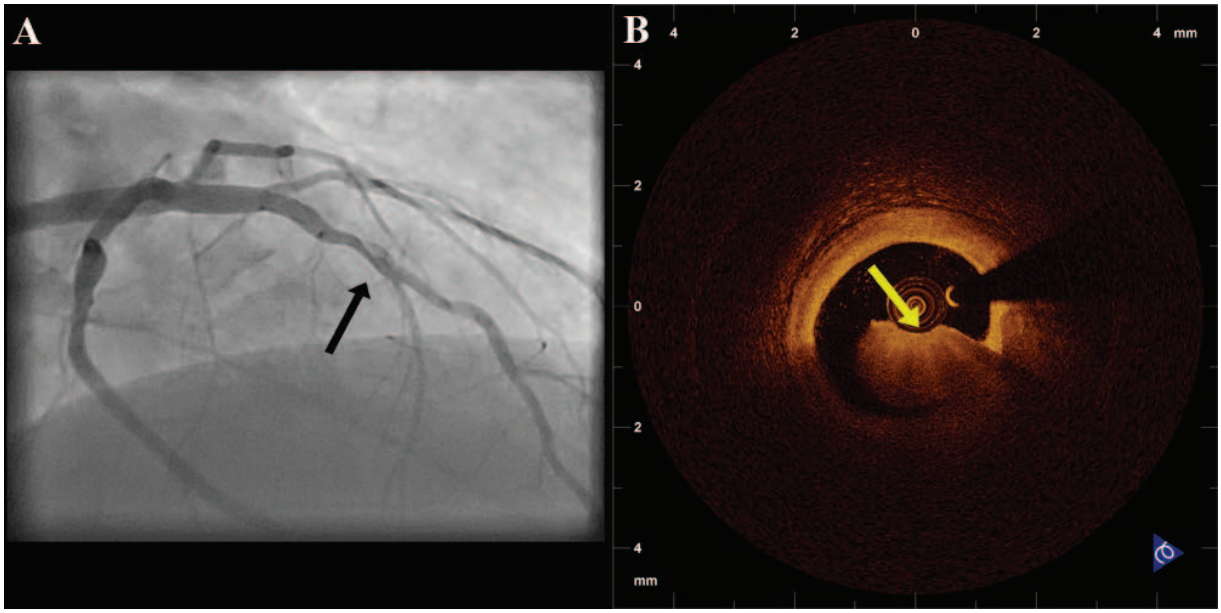

Figure 5. Culprit lesion identification by OCT.

Evaluation by OCT of a patient with acute coronary syndrome and haziness in the coronary angiogram. OCT revealed the presence of thrombus.

Reproduced from Karanasos et al, Curr Cardiovasc Imaging Rep. 2012;5:206-220 [6].

Culprit Lesion Identification in ACS Patients with (Near-)normal Coronaries

Another intriguing potential application for OCT is its use for culprit lesion identification in acute coronary syndromes, without an evident culprit lesion or with doubtful findings such as haziness in the angiogram (Figure 5) [140, 141]. Non-invasive imaging studies have demonstrated that occult atherosclerosis is the cause of ACS in the majority of such cases [142]. Despite a potential utility of such non-invasive approaches in secondary risk stratification of these patients, the lack of guidance during the procedure precludes potential invasive treatment of these lesions and can lead to a mean infarct mass by magnetic resonance imaging of ~10g [142]. Therefore, intravascular imaging by OCT can be used in such scenarios, as it can identify the underlying pathophysiological substrate in the acute phase, and also identify thrombus that constitutes *per se*

a potential target for intervention. So far, several anecdotal reports regarding the utility of OCT in culprit lesion identification in AMI or unstable angina have been published [143-147], but larger series are needed in order to evaluate the potential utility of this modality in this setting.

Assessment of Need for Stent Implantation in AMI Patients Treated with Thrombectomy

Finally, OCT could potentially indicate selection of a less invasive strategy in selected cases of patients with myocardial infarction. Recently, several small series have demonstrated the concept of treatment of the culprit lesion of myocardial infarction with flow restoration by means of thrombectomy, avoiding stent implantation in the acute phase, and evaluation of the need for stent implantation several days after the acute event [148-150]. OCT could be used in this setting for evaluation of the morphology and appraisal of the need for stent implantation either during the acute phase or during the deferred catheterization. Cervinka et al. used OCT for assessing the need of stent implantation in STEMI patients treated by thrombectomy [151]. Among 100 consecutive patients with STEMI treated with thrombus aspiration and IIb/IIIa administration, 20 patients with TIMI flow grade ≥2, absence of ongoing symptoms and presence of a mainly thrombotic stenosis by OCT were treated conservatively without stent implantation. The clinical follow-up showed no major adverse cardiovascular events for either group, while follow-up angiogram and OCT-study at 1 week and 9 months after the event in the thrombectomy-only treated patients showed the presence of non-stenotic lesions (<50% stenosis) with healing of rupture by 9 months [151]. Other investigators have suggested that the presence of plaque erosion and the absence of significant stenosis could constitute a potential criterion for selecting patients that can be treated with thrombectomy alone [152], and the feasibility of such an approach was demonstrated in a highly selected series of 31 patients [153]. Nonetheless, evidence about such approaches is still fairly limited and restricted to proof-of-concept studies, and bigger randomized studies using more objective OCT criteria are warranted to validate the feasibility and potential benefit of such approaches.

Future Directions

From the body of evidence discussed above, it becomes evident that OCT is an imaging modality that has provided useful insights into the pathomechanisms of acute coronary syndromes and that holds promise for application in clinical practice, where it could potentially improve interventional outcomes in patients with acute coronary syndromes. However, it should be kept in mind that the majority of the studies performed up to date are cross-sectional observational studies with small numbers of patients, focused mainly at generating hypotheses about the

pathobiology of atherosclerosis and the potential fields for clinical application of OCT. Therefore, the performance of larger studies aiming at 1) obtaining a better understanding of the natural history of atherosclerosis, the exact mechanisms of plaque progression and destabilization, and treatments that can have an impact on the reduction of the mortality and morbidity of acute coronary syndromes, and 2) evaluating whether OCT can improve patient-oriented outcomes when used for interventional guidance in such settings will be able to define the role of OCT in research and clinical practice.

Several technological developments that could help us achieve these goals are already under way. These technological advances are moving both in the direction of improving plaque characterization using the current technology and in the direction of development of new technologies based on OCT imaging. Towards the first direction, algorithms for the automated measurement of cap thickness can provide a fast and volumetric measure of this critical component of plaque vulnerability, while simultaneously increasing reproducibility of such measurements [154-156], whereas systems for automated tissue characterization in atherosclerotic plaques can be used for a faster, more objective evaluation of atherosclerotic plaque morphology [157-160]. Towards the second direction, the development of ultra-high-speed OCT imaging systems will allow the complete high-resolution assessment of long arterial segments within a heartbeat [161], further allowing the full biomechanical assessment of the hemodynamic environment in the coronary arteries [58, 162]. Furthermore, new imaging systems with resolution comparable to electronic microscopy able to identify (sub-) cellular structures [163], or providing information regarding the collagen content of atherosclerotic plaques [164, 165], or hybrid systems incorporating the ability for detection of molecules targeted with probes simultaneously with plaque imaging [166], are currently under development and are expected to increase our understanding of the pathobiologic processes of acute coronary syndromes.

Conclusions

The development of OCT has allowed us to gain important *in vivo* insights in the mechanisms of atherosclerotic plaque progression and destabilization leading to the manifestation of acute coronary syndromes. Plaque morphology in acute coronary syndromes, the relationship of plaque characteristics with thrombosis and thrombolysis, the role of inflammation in plaque destabilization and the mechanisms of myocardial infarction after stent implantation are some of the areas in which OCT has increased our understanding. This better understanding of atherosclerosis can help in the development of new treatment strategies aiming at an early identification of high-risk plaques and timely intervention that could result in a reduction of the morbidity and mortality of acute coronary syndromes. Meanwhile, the use of OCT as a clinical tool is still an area under investigation. Small-scale clinical studies and reports have demonstrated the potential of OCT as a means for interventional guidance in acute coronary syndromes. Although several potential fields of application have been identified, such as culprit lesion identification and evaluation of the need for local or systematic antithrombotic therapies or for stent implantation, the role of OCT in this setting has yet to be established; future larger scale studies that can show clinical benefit from the use of OCT will ultimately help in establishing appropriate clinical indications for OCT guidance.

References

1. Burke AP, Farb A, Malcom GT, Liang YH, Smialek J, Virmani R. Coronary risk factors and plaque morphology in men with coronary disease who died suddenly. *N. Engl. J. Med.* 1997;336:1276-1282.

2. Falk E, Nakano M, Bentzon JF, Finn AV, Virmani R. Update on acute coronary syndromes: The pathologists' view. *Eur Heart J*. 2013;34:719-728.

3. Virmani R, Kolodgie FD, Burke AP, Farb A, Schwartz SM. Lessons from sudden coronary death a comprehensive morphological classification scheme for atherosclerotic lesions. *Arterioscler. Thromb. Vasc. Biol.* 2000;20:1262-1275.

4. Toutouzas K, Stathogiannis K, Synetos A, Karanasos A, Stefanadis C. Vulnerable atherosclerotic plaque: From the basic research laboratory to the clinic. *Cardiology*. 2012;123:248-253.

5. Tearney GJ, Regar E, Akasaka T, Adriaenssens T, Barlis P, Bezerra HG, Bouma B, Bruining N, Cho JM, Chowdhary S, Costa MA, de Silva R, Dijkstra J, Di Mario C, Dudek D, Falk E, Feldman MD, Fitzgerald P, Garcia-Garcia HM, Gonzalo N, Granada JF, Guagliumi G, Holm NR, Honda Y, Ikeno F, Kawasaki M, Kochman J, Koltowski L, Kubo T, Kume T, Kyono H, Lam CC, Lamouche G, Lee DP, Leon MB, Maehara A, Manfrini O, Mintz GS, Mizuno K, Morel MA, Nadkarni S, Okura H, Otake H, Pietrasik A, Prati F, Raber L, Radu MD, Rieber J, Riga M, Rollins A, Rosenberg M, Sirbu V, Serruys PW, Shimada K, Shinke T, Shite J, Siegel E, Sonoda S, Suter M, Takarada S, Tanaka A, Terashima M, Thim T, Uemura S, Ughi GJ, van Beusekom HM, van der Steen AF, van Es GA, van Soest G, Virmani R, Waxman S, Weissman NJ, Weisz G. Consensus standards for acquisition, measurement, and reporting of intravascular optical coherence tomography studies: A report from the international working group for intravascular optical coherence tomography standardization and validation. *J Am Coll Cardiol.* 2012;59:1058-1072.

6. Karanasos A, Ligthart J, Witberg K, van Soest G, Bruining N, Regar E. Optical coherence tomography: Potential clinical applications. *Curr Cardiovasc Imaging Rep*. 2012;5:206-220.

7. Regar E, van Soest G, Bruining N, Constantinescu AA, van Geuns RJ, van der Giessen W, Serruys PW. Optical coherence tomography in patients with acute coronary syndrome. *EuroIntervention*. 2010;6 Suppl G:G154-160.

8. Kramer MC, Rittersma SZ, de Winter RJ, Ladich ER, Fowler DR, Liang YH, Kutys R, Carter-Monroe N, Kolodgie FD, van der Wal AC, Virmani R. Relationship of thrombus healing to underlying plaque morphology in sudden coronary death. *J Am Coll Cardiol.* 2010;55:122-132.

9. Muller JE, Stone PH, Turi ZG, Rutherford JD, Czeisler CA, Parker C, Poole WK, Passamani E, Roberts R, Robertson T, et al. Circadian variation in the frequency of onset of acute myocardial infarction. *N Engl J Med.* 1985;313:1315-1322.

10. Naghavi M, Libby P, Falk E, Casscells SW, Litovsky S, Rumberger J, Badimon JJ, Stefanadis C, Moreno P, Pasterkamp G, Fayad Z, Stone PH, Waxman S, Raggi P, Madjid M, Zarrabi A, Burke A, Yuan C, Fitzgerald PJ, Siscovick DS, de Korte CL, Aikawa M, Airaksinen KE, Assmann G, Becker CR, Chesebro JH, Farb A, Galis ZS, Jackson C, Jang IK, Koenig W, Lodder RA, March K, Demirovic J, Navab M, Priori SG, Rekhter MD, Bahr R, Grundy SM, Mehran R, Colombo A, Boerwinkle E, Ballantyne C, Insull W, Jr., Schwartz RS, Vogel R, Serruys PW, Hansson GK, Faxon DP, Kaul S, Drexler H, Greenland P, Muller JE, Virmani R, Ridker PM, Zipes DP, Shah PK, Willerson JT. From vulnerable plaque to vulnerable patient: A call for new definitions and risk assessment strategies: Part ii. *Circulation*. 2003;108:1772-1778.

11. Naghavi M, Libby P, Falk E, Casscells SW, Litovsky S, Rumberger J, Badimon JJ, Stefanadis C, Moreno P, Pasterkamp G, Fayad Z, Stone PH, Waxman S, Raggi P, Madjid M, Zarrabi A, Burke A, Yuan C, Fitzgerald PJ, Siscovick DS, de Korte CL, Aikawa M, Juhani Airaksinen KE, Assmann G, Becker CR, Chesebro JH, Farb A, Galis ZS, Jackson C, Jang IK, Koenig W, Lodder RA, March K, Demirovic J, Navab M, Priori SG, Rekhter MD, Bahr R, Grundy SM, Mehran R, Colombo A, Boerwinkle E, Ballantyne C, Insull W, Jr., Schwartz RS, Vogel R, Serruys PW, Hansson GK, Faxon DP, Kaul S, Drexler H, Greenland P, Muller JE, Virmani R, Ridker PM, Zipes DP, Shah PK, Willerson JT. From vulnerable plaque to vulnerable patient: A call for new definitions and risk assessment strategies: Part i. *Circulation*. 2003;108:1664-1672.

12. Xu Y, Mintz GS, Tam A, McPherson JA, Iniguez A, Fajadet J, Fahy M, Weisz G, De Bruyne B, Serruys PW, Stone GW, Maehara A. Prevalence, distribution, predictors, and outcomes of patients with calcified nodules in native coronary arteries: A 3-vessel intravascular ultrasound analysis from providing regional observations to study predictors of events in the coronary tree (prospect). *Circulation*. 2012;126:537-545.

13. Virmani R, Burke AP, Farb A, Kolodgie FD. Pathology of the vulnerable plaque. *J. Am. Coll. Cardiol.* 2006;47:C13-C18.

14. Regar E, Ligthart J, Bruining N, van Soest G. The diagnostic value of intracoronary optical coherence tomography. *Herz*. 2011;36:417-429.

15. Yabushita H, Bouma BE, Houser SL, Aretz HT, Jang IK, Schlendorf KH, Kauffman CR, Shishkov M, Kang DH, Halpern EF, Tearney GJ. Characterization of human atherosclerosis by optical coherence tomography. *Circulation*. 2002;106:1640-1645.

16. Rieber J, Meissner O, Babaryka G, Reim S, Oswald M, Koenig A, Schiele TM, Shapiro M, Theisen K, Reiser MF, Klauss V, Hoffmann U. Diagnostic accuracy of optical coherence tomography and intravascular ultrasound for the detection and characterization of atherosclerotic plaque composition in ex-vivo coronary specimens: A comparison with histology. *Coron Artery Dis*. 2006;17:425-430.

17. Manfrini O, Mont E, Leone O, Arbustini E, Eusebi V, Virmani R, Bugiardini R. Sources of error and interpretation of plaque morphology by optical coherence tomography. *Am J Cardiol*. 2006;98:156-159.

18. Kawasaki M, Bouma BE, Bressner J, Houser SL, Nadkarni SK, MacNeill BD, Jang IK, Fujiwara H, Tearney GJ. Diagnostic accuracy of optical coherence tomography and integrated backscatter intravascular ultrasound images for tissue characterization of human coronary plaques. *J Am Coll Cardiol*. 2006;48:81-88.

19. Kume T, Akasaka T, Kawamoto T, Watanabe N, Toyota E, Neishi Y, Sukmawan R, Sadahira Y, Yoshida K. Assessment of coronary arterial plaque by optical coherence tomography. *Am J Cardiol*. 2006;97:1172-1175.

20. Kume T, Akasaka T, Kawamoto T, Watanabe N, Toyota E, Neishi Y, Sukmawan R, Sadahira Y, Yoshida K. Assessment of coronary intima--media thickness by optical coherence tomography: Comparison with intravascular ultrasound. *Circ J*. 2005;69:903-907.

21. Zimarino M, Prati F, Stabile E, Pizzicannella J, Fouad T, Filippini A, Rabozzi R, Trubiani O, Pizzicannella G, De Caterina R. Optical coherence tomography accurately identifies intermediate atherosclerotic lesions--an *in vivo* evaluation in the rabbit carotid artery. *Atherosclerosis*. 2007;193:94-101.

22. Kume T, Akasaka T, Kawamoto T, Okura H, Watanabe N, Toyota E, Neishi Y, Sukmawan R, Sadahira Y, Yoshida K. Measurement of the thickness of the fibrous cap by optical coherence tomography. *Am Heart J*. 2006;152:755 e751-754.

23. Cilingiroglu M, Oh JH, Sugunan B, Kemp NJ, Kim J, Lee S, Zaatari HN, Escobedo D, Thomsen S, Milner TE, Feldman MD. Detection of vulnerable plaque in a murine model of atherosclerosis with optical coherence tomography. *Catheter Cardiovasc Interv*. 2006;67:915-923.

24. van Soest G, Regar E, Goderie TP, Gonzalo N, Koljenovic S, van Leenders GJ, Serruys PW, van der Steen AF. Pitfalls in plaque characterization by OCT: Image artifacts in native coronary arteries. *JACC Cardiovasc Imaging*. 2011;4:810-813.

25. Kume T, Akasaka T, Kawamoto T, Ogasawara Y, Watanabe N, Toyota E, Neishi Y, Sukmawan R, Sadahira Y, Yoshida K. Assessment of coronary arterial thrombus by optical coherence tomography. *Am. J. Cardiol.* 2006;97:1713-1717.

26. Karanasos A, Ligthart JM, Witberg KT, Regar E. Calcified nodules: An underrated mechanism of coronary thrombosis? *JACC Cardiovasc Imaging*. 2012;5:1071-1072.

27. Jang I-K, Tearney GJ, MacNeill B, Takano M, Moselewski F, Iftima N, Shishkov M, Houser S, Aretz HT, Halpern EF, Bouma BE. *In vivo* characterization of coronary atherosclerotic plaque by use of optical coherence tomography. *Circulation*. 2005;111:1551-1555.

28. Fujii K, Masutani M, Okumura T, Kawasaki D, Akagami T, Ezumi A, Sakoda T, Masuyama T, Ohyanagi M. Frequency and predictor of coronary thin-cap fibroatheroma in patients with acute myocardial infarction and stable angina pectoris a 3-vessel optical coherence tomography study. *J. Am. Coll. Cardiol.* 2008;52:787-788.

29. Toutouzas K, Karanasos A, Stefanadis C. Multiple plaque morphologies assessed by optical coherence tomography in a patient with acute coronary syndrome. *Heart*. 2010;96:1335-1336.

30. Kubo T, Imanishi T, Takarada S, Kuroi A, Ueno S, Yamano T, Tanimoto T, Matsuo Y, Masho T, Kitabata H, Tsuda K, Tomobuchi Y, Akasaka T. Assessment of culprit lesion morphology in acute myocardial infarction: Ability of optical coherence tomography compared with intravascular ultrasound and coronary angioscopy. *J. Am. Coll. Cardiol.* 2007;50:933-939.

31. Gonzalo N, Tearney GJ, van Soest G, Serruys P, Garcia-Garcia HM, Bouma BE, Regar E. Witnessed coronary plaque rupture during cardiac catheterization. *JACC Cardiovasc Imaging*. 2011;4:437-438.

32. Jia H, Abtahian F, Aguirre AD, Lee S, Chia S, Lowe H, Kato K, Yonetsu T, Vergallo R, Hu S, Tian J, Lee H, Park S-J, Jang Y-S, Raffel OC, Mizuno K, Uemura S, Itoh T, Kakuta T, Choi S-Y, Dauerman HL, Prasad A, Toma C, McNulty I, Zhang S, Yu B, Fuster V, Narula J, Virmani R, Jang I-K. *In vivo* diagnosis of plaque erosion and calcified nodule in patients with acute coronary syndrome by intravascular optical coherence tomography. *J. Am. Coll. Cardiol.* 2013;62:1748-1758.

33. Toutouzas K, Karanasos A, Tsiamis E, Riga M, Drakopoulou M, Synetos A, Papanikolaou A, Tsioufis C, Androulakis A, Stefanadi E, Tousoulis D, Stefanadis C. New insights by optical coherence tomography into the differences and similarities of culprit ruptured plaque morphology in non-st-elevation myocardial infarction and st-elevation myocardial infarction. *Am. Heart J.* 2011;161:1192-1199.

34. Ino Y, Kubo T, Tanaka A, Kuroi A, Tsujioka H, Ikejima H, Okouchi K, Kashiwagi M, Takarada S, Kitabata H, Tanimoto T, Komukai K, Ishibashi K, Kimura K, Hirata K, Mizukoshi M, Imanishi T, Akasaka T. Difference of culprit lesion morphologies between st-segment elevation myocardial infarction and non-st-segment elevation acute coronary syndrome: An optical coherence tomography study. *JACC Cardiovasc Interv*. 2011;4:76-82.

35. Tian J, Ren X, Vergallo R, Xing L, Yu H, Jia H, Soeda T, McNulty I, Hu S, Lee H, Yu B, Jang I-K. Distinct morphological features of ruptured culprit plaque for acute coronary events compared to those with silent

rupture and thin-cap fibroatheroma: A combined optical coherence tomography and intravascular ultrasound study. *J. Am. Coll. Cardiol.* 2014;63:2209-2216.

36. Shimamura K, Ino Y, Kubo T, Nishiguchi T, Tanimoto T, Ozaki Y, Satogami K, Orii M, Shiono Y, Komukai K, Yamano T, Matsuo Y, Kitabata H, Yamaguchi T, Hirata K, Tanaka A, Imanishi T, Akasaka T. Difference of ruptured plaque morphology between asymptomatic coronary artery disease and non-st elevation acute coronary syndrome patients: An optical coherence tomography study. *Atherosclerosis.*

37. Tanaka A, Imanishi T, Kitabata H, Kubo T, Takarada S, Tanimoto T, Kuroi A, Tsujioka H, Ikejima H, Ueno S, Kataiwa H, Okouchi K, Kashiwaghi M, Matsumoto H, Takemoto K, Nakamura N, Hirata K, Mizukoshi M, Akasaka T. Morphology of exertion-triggered plaque rupture in patients with acute coronary syndrome: An optical coherence tomography study. *Circulation.* 2008;118:2368-2373.

38. Kato M, Dote K, Sasaki S, Kagawa E, Nakano Y, Watanabe Y, Higashi A, Itakura K, Ochiumi Y, Takiguchi Y. Presentations of acute coronary syndrome related to coronary lesion morphologies as assessed by intravascular ultrasound and optical coherence tomography. *Int. J. Cardiol.* 2013;165:506-511.

39. Raffel OC, Merchant FM, Tearney GJ, Chia S, Gauthier DD, Pomerantsev E, Mizuno K, Bouma BE, Jang I-K. *In vivo* association between positive coronary artery remodelling and coronary plaque characteristics assessed by intravascular optical coherence tomography. *Eur Heart J.* 2008;29:1721-1728.

40. Kashiwagi M, Tanaka A, Kitabata H, Tsujioka H, Matsumoto H, Arita Y, Ookochi K, Kuroi A, Kataiwa H, Tanimoto T, Ikejima H, Takarada S, Kubo T, Hirata K, Nakamura N, Mizukoshi M, Imanishi T, Akasaka T. Relationship between coronary arterial remodeling, fibrous cap thickness and high-sensitivity c-reactive protein levels in patients with acute coronary syndrome. *Circ. J.* 2009;73:1291-1295.

41. Toutouzas K, Synetos A, Stefanadi E, Vaina S, Markou V, Vavuranakis M, Tsiamis E, Tousoulis D, Stefanadis C. Correlation between morphologic characteristics and local temperature differences in culprit lesions of patients with symptomatic coronary artery disease. *J Am Coll Cardiol.* 2007;49:2264-2271.

42. Barlis P, Serruys PW, Gonzalo N, van der Giessen WJ, de Jaegere PJ, Regar E. Assessment of culprit and remote coronary narrowings using optical coherence tomography with long-term outcomes. *Am. J. Cardiol.* 2008;102:391-395.

43. Yonetsu T, Kakuta T, Lee T, Takahashi K, Kawaguchi N, Yamamoto G, Koura K, Hishikari K, Iesaka Y, Fujiwara H, Isobe M. *In vivo* critical fibrous cap thickness for rupture-prone coronary plaques assessed by optical coherence tomography. *Eur Heart J.* 2011;32:1251-1259.

44. Alfonso F, Paulo M, Gonzalo N, Dutary J, Jimenez-Quevedo P, Lennie V, Escaned J, Bañuelos C, Hernandez R, Macaya C. Diagnosis of spontaneous coronary artery dissection by optical coherence tomography. *J. Am. Coll. Cardiol.* 2012;59:1073-1079.

45. Johnson TW, Smith D, Strange JW, Bucciarelli-Ducci C, Lowe R, Baumbach A. Spontaneous multivessel coronary intramural hematoma: An insight with OCT. *JACC Cardiovasc Imaging.* 2012;5:1070-1071.

46. Tanaka A, Shimada K, Tearney GJ, Kitabata H, Taguchi H, Fukuda S, Kashiwagi M, Kubo T, Takarada S, Hirata K, Mizukoshi M, Yoshikawa J, Bouma BE, Akasaka T. Conformational change in coronary artery structure assessed by optical coherence tomography in patients with vasospastic angina. *J. Am. Coll. Cardiol.* 2011;58:1608-1613.

47. Kohno H, Sueda S, Sakaue T. Separation of the intima-media complex from the adventitia during spontaneous coronary artery spasm documented by intracoronary optical coherence tomography. *Int. J. Cardiol.* 2012;154:e4-5.

48. Vizzi V, Johnson TW, Jenkins N, Strange JW, Baumbach A. Dynamic separation of coronary artery medial and adventitial layers with vasospasm: New insights using oct. *Int. J. Cardiol.* 2013;167:2344-2345.

49. Park H-C, Choi SI, Lee JU, Kim S-G, Shin J, Kim H-J. Morphological findings in typical variant angina presenting as acute coronary syndrome using optical coherence tomography. *J Interv Cardiol.* 2013;26:491-500.

50. Kang S-J, Nakano M, Virmani R, Song H-G, Ahn J-M, Kim W-J, Lee J-Y, Park D-W, Lee S-W, Kim Y-H, Lee CW, Park S-W, Park S-J. Oct findings in patients with recanalization of organized thrombi in coronary arteries. *JACC Cardiovasc Imaging.* 2012;5:725-732.

51. Toutouzas K, Karanasos A, Stathogiannis K, Synetos A, Tsiamis E, Papadopoulos D, Stefanadis C. A honeycomb-like structure in the left anterior descending coronary artery: Demonstration of recanalized thrombus by optical coherence tomography. *JACC Cardiovasc Interv.* 2012;5:688-689.

52. Wang JC, Normand S-LT, Mauri L, Kuntz RE. Coronary artery spatial distribution of acute myocardial infarction occlusions. *Circulation.* 2004;110:278-284.

53. Hochman JS, Phillips WJ, Ruggieri D, Ryan SF. The distribution of atherosclerotic lesions in the coronary arterial tree: Relation to cardiac risk factors. *Am. Heart J.* 1988;116:1217-1222.

54. Cheruvu PK, Finn AV, Gardner C, Caplan J, Goldstein J, Stone GW, Virmani R, Muller JE. Frequency and distribution of thin-cap fibroatheroma and ruptured plaques in human coronary arteries: A pathologic study. *J. Am. Coll. Cardiol.* 2007;50:940-949.

55. Kume T, Okura H, Yamada R, Kawamoto T, Watanabe N, Neishi Y, Sadahira Y, Akasaka T, Yoshida K. Frequency and spatial distribution of thin-cap fibroatheroma assessed by 3-vessel intravascular ultrasound and optical coherence tomography: An ex vivo validation and an initial *in vivo* feasibility study. *Circ. J.* 2009;73:1086-1091.

56. Fujii K, Kawasaki D, Masutani M, Okumura T, Akagami T, Sakoda T, Tsujino T, Ohyanagi M, Masuyama T. Oct assessment of thin-cap fibroatheroma distribution in native coronary arteries. *JACC Cardiovasc Imaging.* 2010;3:168-175.

57. Toutouzas K, Karanasos A, Riga M, Tsiamis E, Synetos A, Michelongona A, Papanikolaou A, Triantafyllou G, Tsioufis C, Stefanadis C. Optical coherence tomography assessment of the spatial distribution of culprit ruptured plaques and thin-cap fibroatheromas in acute coronary syndrome. *EuroIntervention.* 2012;8:477-485.

58. Chatzizisis YS, Jonas M, Coskun AU, Beigel R, Stone BV, Maynard C, Gerrity RG, Daley W, Rogers C, Edelman ER, Feldman CL, Stone PH. Prediction of the localization of high-risk coronary atherosclerotic plaques on the basis of low endothelial shear stress: An intravascular ultrasound and histopathology natural history study. *Circulation.* 2008;117:993-1002.

59. Cunningham KS, Gotlieb AI. The role of shear stress in the pathogenesis of atherosclerosis. *Lab. Invest.* 2005;85:9-23.

60. Koskinas KC, Feldman CL, Chatzizisis YS, Coskun AU, Jonas M, Maynard C, Baker AB, Papafaklis MI, Edelman ER, Stone PH. Natural history of experimental coronary atherosclerosis and vascular remodeling in relation to endothelial shear stress: A serial, *in vivo* intravascular ultrasound study. *Circulation.* 2010;121:2092-2101.

61. Karanasos A, Simsek C, Serruys P, Ligthart J, Witberg K, van Geuns RJ, Sianos G, Zijlstra F, Regar E. Five-year optical coherence tomography follow-up of an everolimus-eluting bioresorbable vascular scaffold: Changing the paradigm of coronary stenting? *Circulation.* 2012;126:e89-91.

62. Wykrzykowska JJ, Diletti R, Gutierrez-Chico JL, van Geuns RJ, van der Giessen WJ, Ramcharitar S, Duckers HE, Schultz C, de Feyter P, van der Ent M, Regar E, de Jaegere P, Garcia-Garcia HM, Pawar R, Gonzalo N, Ligthart

J, de Schepper J, van den Berg N, Milewski K, Granada JF, Serruys PW. Plaque sealing and passivation with a mechanical self-expanding low outward force nitinol vshield device for the treatment of ivus and OCT-derived thin cap fibroatheromas (TCFAs) in native coronary arteries: Report of the pilot study vshield evaluated at cardiac hospital in rotterdam for investigation and treatment of TCFA (SECRITT). *EuroIntervention*. 2012;8:945-954.

63. Toutouzas K, Drakopoulou M, Markou V, Karabelas I, Vaina S, Vavuranakis M, Tsiamis E, Tsioufis C, Androulakis A, Stefanadis C. Correlation of systemic inflammation with local inflammatory activity in non-culprit lesions: Beneficial effect of statins. *Int. J. Cardiol.* 2007;119:368-373.

64. Toutouzas K, Drakopoulou M, Mitropoulos J, Tsiamis E, Vaina S, Vavuranakis M, Markou V, Bosinakou E, Stefanadis C. Elevated plaque temperature in non-culprit de novo atheromatous lesions of patients with acute coronary syndromes. *J. Am. Coll. Cardiol.* 2006;47:301-306.

65. Toutouzas K, Drakopoulou M, Vaina S, Stefanadis C. Significance of characterization of non-culprit lesions: An underscored clinical problem. *Atherosclerosis*. 2007;195:236-241.

66. Goldstein JA, Demetriou D, Grines CL, Pica M, Shoukfeh M, O'Neill WW. Multiple complex coronary plaques in patients with acute myocardial infarction. *N. Engl. J. Med.* 2000;343:915-922.

67. Tsiamis E, Toutouzas K, Synetos A, Karambelas J, Karanasos A, Demponeras C, Drakopoulou M, Stefanadi E, Tsioufis C, Tousoulis D, Stefanadis C. Prognostic clinical and angiographic characteristics for the development of a new significant lesion in remote segments after successful percutaneous coronary intervention. *Int. J. Cardiol.* 2010;143:29-34.

68. Wald DS, Morris JK, Wald NJ, Chase AJ, Edwards RJ, Hughes LO, Berry C, Oldroyd KG. Randomized trial of preventive angioplasty in myocardial infarction. *N Engl J Med.* 2013;369:1115-1123.

69. Kubo T, Imanishi T, Kashiwagi M, Ikejima H, Tsujioka H, Kuroi A, Ishibashi K, Komukai K, Tanimoto T, Ino Y, Kitabata H, Takarada S, Tanaka A, Mizukoshi M, Akasaka T. Multiple coronary lesion instability in patients with acute myocardial infarction as determined by optical coherence tomography. *Am. J. Cardiol.* 2010;105:318-322.

70. Kato K, Yonetsu T, Kim S-J, Xing L, Lee H, McNulty I, Yeh RW, Sakhuja R, Zhang S, Uemura S, Yu B, Mizuno K, Jang I-K. Nonculprit plaques in patients with acute coronary syndromes have more vulnerable features compared with those with non-acute coronary syndromes: A 3-vessel optical coherence tomography study. *Circ Cardiovasc Imaging*. 2012;5:433-440.

71. Vergallo R, Ren X, Yonetsu T, Kato K, Uemura S, Yu B, Jia H, Abtahian F, Aguirre AD, Tian J, Hu S, Soeda T, Lee H, McNulty I, Park S-J, Jang Y, Prasad A, Lee S, Zhang S, Porto I, Biasucci LM, Crea F, Jang I-K. Pancoronary plaque vulnerability in patients with acute coronary syndrome and ruptured culprit plaque: A 3-vessel optical coherence tomography study. *Am. Heart J.* 2014;167:59-67.

72. Fukunaga M, Fujii K, Nakata T, Shibuya M, Miki K, Kawasaki D, Masutani M, Kawabata-Lee M, Ohyanagi M, Masuyama T. Multiple complex coronary atherosclerosis in diabetic patients with acute myocardial infarction: A three-vessel optical coherence tomography study. *EuroIntervention*. 2012;8:955-961.

73. Bouki KP, Katsafados MG, Chatzopoulos DN, Psychari SN, Toutouzas KP, Charalampopoulos AF, Sakkali EN, Koudouri AA, Liakos GK, Apostolou TS. Inflammatory markers and plaque morphology: An optical coherence tomography study. *Int. J. Cardiol.* 2012;154:287-292.

74. Ferrante G, Nakano M, Prati F, Niccoli G, Mallus MT, Ramazzotti V, Montone RA, Kolodgie FD, Virmani R, Crea F. High levels of systemic myeloperoxidase are associated with coronary plaque erosion in patients with acute coronary syndromes: A clinicopathological study. *Circulation*. 2010;122:2505-2513.

75. Koga S, Ikeda S, Yoshida T, Nakata T, Takeno M, Masuda N, Koide Y, Kawano H, Maemura K. Elevated levels of systemic pentraxin 3 are associated with thin-cap fibroatheroma in coronary culprit lesions: Assessment by optical coherence tomography and intravascular ultrasound. *JACC Cardiovasc Interv.* 2013;6:945-954.

76. Li QX, Fu QQ, Shi SW, Wang YF, Xie JJ, Yu X, Cheng X, Liao YH. Relationship between plasma inflammatory markers and plaque fibrous cap thickness determined by intravascular optical coherence tomography. *Heart.* 2010;96:196-201.

77. Matsuo Y, Kubo T, Okumoto Y, Ishibashi K, Komukai K, Tanimoto T, Ino Y, Kitabata H, Hirata K, Imanishi T, Akagi H, Akasaka T. Circulating malondialdehyde-modified low-density lipoprotein levels are associated with the presence of thin-cap fibroatheromas determined by optical coherence tomography in coronary artery disease. *Eur Heart J Cardiovasc Imaging.* 2013;14:43-50.

78. Niccoli G, Montone RA, Cataneo L, Cosentino N, Gramegna M, Refaat H, Porto I, Burzotta F, Trani C, Leone AM, Severino A, Crea F. Morphological-biohumoral correlations in acute coronary syndromes: Pathogenetic implications. *Int. J. Cardiol.* 2014;171:463-466.

79. Ozaki Y, Imanishi T, Teraguchi I, Nishiguchi T, Orii M, Shiono Y, Shimamura K, Ishibashi K, Tanimoto T, Yamano T, Ino Y, Yamaguchi T, Kubo T, Akasaka T. Association between p-selectin glycoprotein ligand-1 and pathogenesis in acute coronary syndrome assessed by optical coherence tomography. *Atherosclerosis.* 2014;233:697-703.

80. Raffel OC, Tearney GJ, Gauthier DD, Halpern EF, Bouma BE, Jang I-K. Relationship between a systemic inflammatory marker, plaque inflammation, and plaque characteristics determined by intravascular optical coherence tomography. *Arterioscler. Thromb. Vasc. Biol.* 2007;27:1820-1827.

81. Teraguchi I, Imanishi T, Ozaki Y, Tanimoto T, Orii M, Shiono Y, Shimamura K, Ishibashi K, Yamano T, Ino Y, Yamaguchi T, Hirata K, Kubo T, Akasaka T. Impact of glucose fluctuation and monocyte subsets on coronary plaque rupture. *Nutr Metab Cardiovasc Dis.* 2014;24:309-314.

82. Drakopoulou M, Toutouzas K, Stefanadi E, Tsiamis E, Tousoulis D, Stefanadis C. Association of inflammatory markers with angiographic severity and extent of coronary artery disease. *Atherosclerosis.* 2009;206:335-339.

83. Toutouzas K, Tsiamis E, Karanasos A, Drakopoulou M, Synetos A, Tsioufis C, Tousoulis D, Davlouros P, Alexopoulos D, Bouki K, Apostolou T, Stefanadis C. Morphological characteristics of culprit atheromatic plaque are associated with coronary flow after thrombolytic therapy: New implications of optical coherence tomography from a multicenter study. *JACC Cardiovasc Interv.* 2010;3:507-514.

84. Mytas D, Zairis M, Karanasos A, Kosma L, Arsenos P, Tentolouris C, Pitsavos C, Foussas S, Stefanadis C, Cokkinos D. Effect of statin pretreatment on the outcome of ST-segment elevation myocardial infarction in patients without prior history of coronary artery disease. *Hellenic J Cardiol.* 2013;54:422-428.

85. Takarada S, Imanishi T, Ishibashi K, Tanimoto T, Komukai K, Ino Y, Kitabata H, Kubo T, Tanaka A, Kimura K, Mizukoshi M, Akasaka T. The effect of lipid and inflammatory profiles on the morphological changes of lipid-rich plaques in patients with non-ST-segment elevated acute coronary syndrome: Follow-up study by optical coherence tomography and intravascular ultrasound. *JACC Cardiovasc Interv.* 2010;3:766-772.

86. Hu S, Yonetsu T, Jia H, Karanasos A, Aguirre AD, Tian J, Abtahian F, Vergallo R, Soeda T, Lee H, McNulty I, Kato K, Yu B, Mizuno K, Toutouzas K, Stefanadis C, Jang I-K. Residual thrombus pattern in patients with ST-segment elevation myocardial infarction caused by plaque erosion versus plaque rupture after successful fibrinolysis: An optical coherence tomography study. *J. Am. Coll. Cardiol.* 2014;63:1336-1338.

87. Karanasos A, Ligthart JM, Regar E. In-stent neoatherosclerosis: A cause of late stent thrombosis in a patient with "full metal jacket" 15 years after implantation: Insights from optical coherence tomography. *JACC Cardiovasc Interv*. 2012;5:799-800.

88. Yamaji K, Kimura T, Morimoto T, Nakagawa Y, Inoue K, Soga Y, Arita T, Shirai S, Ando K, Kondo K, Sakai K, Goya M, Iwabuchi M, Yokoi H, Nosaka H, Nobuyoshi M. Very long-term (15 to 20 years) clinical and angiographic outcome after coronary bare metal stent implantation. *Circ Cardiovasc Interv*. 2010;3:468-475.

89. Cheneau E, Leborgne L, Mintz GS, Kotani J, Pichard AD, Satler LF, Canos D, Castagna M, Weissman NJ, Waksman R. Predictors of subacute stent thrombosis: Results of a systematic intravascular ultrasound study. *Circulation*. 2003;108:43-47.

90. Farb A, Burke AP, Kolodgie FD, Virmani R. Pathological mechanisms of fatal late coronary stent thrombosis in humans. *Circulation*. 2003;108:1701-1706.

91. Finn AV, Joner M, Nakazawa G, Kolodgie F, Newell J, John MC, Gold HK, Virmani R. Pathological correlates of late drug-eluting stent thrombosis: Strut coverage as a marker of endothelialization. *Circulation*. 2007;115:2435-2441.

92. Nakazawa G, Finn AV, Vorpahl M, Ladich ER, Kolodgie FD, Virmani R. Coronary responses and differential mechanisms of late stent thrombosis attributed to first-generation sirolimus- and paclitaxel-eluting stents. *J Am Coll Cardiol*. 2011;57:390-398.

93. Gutierrez-Chico JL, Alegria-Barrero E, Teijeiro-Mestre R, Chan PH, Tsujioka H, de Silva R, Viceconte N, Lindsay A, Patterson T, Foin N, Akasaka T, di Mario C. Optical coherence tomography: From research to practice. *Eur Heart J Cardiovasc Imaging*. 2012.

94. Inoue K, Abe K, Ando K, Shirai S, Nishiyama K, Nakanishi M, Yamada T, Sakai K, Nakagawa Y, Hamasaki N, Kimura T, Nobuyoshi M, Miyamoto TA. Pathological analyses of long-term intracoronary palmaz-schatz stenting; is its efficacy permanent? *Cardiovasc. Pathol.* 2004;13:109-115.

95. Nakazawa G, Otsuka F, Nakano M, Vorpahl M, Yazdani SK, Ladich E, Kolodgie FD, Finn AV, Virmani R. The pathology of neoatherosclerosis in human coronary implants bare-metal and drug-eluting stents. *J. Am. Coll. Cardiol.* 2011;57:1314-1322.

96. Gonzalo N, Serruys PW, Okamura T, van Beusekom HM, Garcia-Garcia HM, van Soest G, van der Giessen W, Regar E. Optical coherence tomography patterns of stent restenosis. *Am Heart J*. 2009;158:284-293.

97. Hou J, Qi H, Zhang M, Ma L, Liu H, Han Z, Meng L, Yang S, Zhang S, Yu B, Jang IK. Development of lipid-rich plaque inside bare metal stent: Possible mechanism of late stent thrombosis? An optical coherence tomography study. *Heart*. 2010;96:1187-1190.

98. Tanimoto S, Aoki J, Serruys PW, Regar E. Paclitaxel-eluting stent restenosis shows three-layer appearance by optical coherence tomography. *EuroIntervention*. 2006;1:484.

99. Ko Y-G, Kim D-M, Cho JM, Choi SY, Yoon JH, Kim J-S, Kim B-K, Choi D, Jang Y, Hong M-K. Optical coherence tomography findings of very late stent thrombosis after drug-eluting stent implantation. *Int J Cardiovasc Imaging*. 2012;28:715-723.

100. Davlouros PA, Karantalis V, Xanthopoulou I, Mavronasiou E, Tsigkas G, Toutouzas K, Alexopoulos D. Mechanisms of non-fatal stent-related myocardial infarction late following coronary stenting with drug-eluting stents and bare metal stents. Insights from optical coherence tomography. *Circ. J.* 2011;75:2789-2797.

101. Miyazaki S, Hiasa Y, Takahashi T, Yano Y, Minami T, Murakami N, Mizobe M, Tobetto Y, Nakagawa T, Chen P-M, Ogura R, Miyajima H, Yuba K, Hosokawa S, Kishi K, Ohtani R. *In vivo* optical coherence tomography of very late drug-eluting stent thrombosis compared with late in-stent restenosis. *Circ. J.* 2012;76:390-398.

102. Guagliumi G, Sirbu V, Musumeci G, Gerber R, Biondi-Zoccai G, Ikejima H, Ladich E, Lortkipanidze N, Matiashvili A, Valsecchi O, Virmani R, Stone GW. Examination of the *in vivo* mechanisms of late drug-eluting stent thrombosis: Findings from optical coherence tomography and intravascular ultrasound imaging. *JACC Cardiovasc Interv.* 2012;5:12-20.

103. Kang S-J, Lee CW, Song H, Ahn J-M, Kim W-J, Lee J-Y, Park D-W, Lee S-W, Kim Y-H, Mintz GS, Park S-W, Park S-J. OCT analysis in patients with very late stent thrombosis. *JACC Cardiovasc Imaging.* 2013;6:695-703.

104. Parodi G, La Manna A, Di Vito L, Valgimigli M, Fineschi M, Bellandi B, Niccoli G, Giusti B, Valenti R, Cremonesi A, Biondi-Zoccai G, Prati F. Stent-related defects in patients presenting with stent thrombosis: Differences at optical coherence tomography between subacute and late/very late thrombosis in the mechanism of stent thrombosis (most) study. *EuroIntervention.* 2013;9:936-944.

105. Alfonso F, Dutary J, Paulo M, Gonzalo N, Perez-Vizcayno MJ, Jimenez-Quevedo P, Escaned J, Banuelos C, Hernandez R, Macaya C. Combined use of optical coherence tomography and intravascular ultrasound imaging in patients undergoing coronary interventions for stent thrombosis. *Heart.* 2012;98:1213-1220.

106. Karanasos A, Witberg K, Ligthart J, Toutouzas K, Daemen J, Van Soest G, Gnanadesigan M, Van Mieghem N, Zijlstra F, Regar E. In-stent neoatherosclerosis: Are first generation drug eluting stents different than bare metal stents? An optical coherence tomography study. *Progress in Biomedical Optics and Imaging - Proceedings of SPIE.* 2013;8565.

107. Karanasos A, Ligthart J, Witberg K, Toutouzas K, Daemen J, Van Soest G, Gnanadesigan M, Van Geuns RJ, De Jaegere P, Regar E. Association of neointimal morphology by optical coherence tomography with rupture of neoatherosclerotic plaque very late after coronary stent implantation. *Progress in Biomedical Optics and Imaging - Proceedings of SPIE.* 2013;8565.

108. Karanasos A, Ligthart J, Toutouzas K, Witberg K, van Geuns RJ, Van Mieghem N, Schultz C, Duckers H, De Jaegere P, Regar E. TCT-304 Neoatherosclerosis and impaired vascular healing are associated with clinical presentation late after coronary stent implantation. An optical coherence tomography study. *(abstract) J. Am. Coll. Cardiol.* 2012;60.

109. Amabile N, Souteyrand G, Ghostine S, Combaret N, Slama MS, Barber-Chamoux N, Motreff P, Caussin C. Very late stent thrombosis related to incomplete neointimal coverage or neoatherosclerotic plaque rupture identified by optical coherence tomography imaging. *Eur Heart J Cardiovasc Imaging.* 2014;15:24-31.

110. Karanasos A, Witberg K, Van Geuns RJ, Schultz C, Van Mieghem N, De Jaegere P, Bruining N, Zijlstra F, Regar E. Morphological characteristics by optical coherence tomography of ruptured neoatherosclerotic plaques in patients with very late stent thrombosis. *(abstract) Eur Heart J.* 2012;33:176-176.

111. Karanasos A, Ligthart J, Schultz C, Van Geuns RJ, Van Mieghem N, De Jaegere P, Daemen J, Zijlstra F, Regar E. Clinical and angiographic predictors of neointimal rupture as a culprit for very late stent thrombosis. Insights from optical coherence tomography. *(abstract) Eur Heart J.* 2012;33:399-399.

112. Im E, Kim BK, Ko YG, Shin DH, Kim JS, Choi D, Jang Y, Hong MK. Incidences, predictors, and clinical outcomes of acute and late stent malapposition detected by optical coherence tomography after drug-eluting stent implantation. *Circ Cardiovasc Interv.* 2014;7:88-96.

113. Karanasos A, van Geuns RJ, Zijlstra F, Regar E. Very late bioresorbable scaffold thrombosis after discontinuation of dual antiplatelet therapy. *Eur Heart J*. 2014;35:1781-1781

114. Gonzalo N, Serruys PW, Okamura T, Shen ZJ, Onuma Y, Garcia-Garcia HM, Sarno G, Schultz C, van Geuns RJ, Ligthart J, Regar E. Optical coherence tomography assessment of the acute effects of stent implantation on the vessel wall: A systematic quantitative approach. *Heart*. 2009;95:1913-1919.

115. Magro M, Regar E, Gutiérrez-Chico JL, Garcia-Garcia H, Simsek C, Schultz C, Zijlstra F, Serruys PW, van Geuns RJ. Residual atherothrombotic material after stenting in acute myocardial infarction--an optical coherence tomographic evaluation. *Int. J. Cardiol.* 2013;167:656-663.

116. Karanasos A, Regar E. Standing on solid ground?: Reassessing the role of incomplete strut apposition in drug-eluting stents. *Circ Cardiovasc Interv*. 2014;7:6-8.

117. Kim U, Kim JS, Lee JM, Son JW, Kim J, Ko YG, Choi D, Jang Y. The initial extent of malapposition in st-elevation myocardial infarction treated with drug-eluting stent: The usefulness of optical coherence tomography. *Yonsei Med J*. 2010;51:332-338.

118. van Geuns R-J, Tamburino C, Fajadet J, Vrolix M, Witzenbichler B, Eeckhout E, Spaulding C, Reczuch K, La Manna A, Spaargaren R, García-García HM, Regar E, Capodanno D, Van Langenhove G, Verheye S. Self-expanding versus balloon-expandable stents in acute myocardial infarction: Results from the APPOSITION II study: Self-expanding stents in ST-segment elevation myocardial infarction. *JACC Cardiovasc Interv*. 2012;5:1209-1219.

119. Muramatsu T, García-García HM, Lee IS, Bruining N, Onuma Y, Serruys PW. Quantitative optical frequency domain imaging assessment of in-stent structures in patients with st-segment elevation myocardial infarction: Impact of imaging sampling rate. *Circ. J.* 2012;76:2822-2831.

120. Onuma Y, Thuesen L, van Geuns R-J, van der Ent M, Desch S, Fajadet J, Christiansen E, Smits P, Holm NR, Regar E, van Mieghem N, Borovicanin V, Paunovic D, Senshu K, van Es G-A, Muramatsu T, Lee I-S, Schuler G, Zijlstra F, Garcia-Garcia HM, Serruys PW, Investigators T. Randomized study to assess the effect of thrombus aspiration on flow area in patients with st-elevation myocardial infarction: An optical frequency domain imaging study--TROFI trial. *Eur Heart J*. 2013;34:1050-1060.

121. Wieringa WG, Lexis CPH, Diercks GFH, Lipsic E, Tan E-S, Schurer RAJ, van der Werf HW, van den Heuvel AFM, Suurmeijer AJH, Zijlstra F, de Smet BJGL, Pundziute G. The feasibility of optical coherence tomography guided thrombus aspiration in patients with non-st-elevation myocardial infarction after initial conservative therapy--a pilot study. *Int. J. Cardiol.* 2013;168:4981-4982.

122. Parodi G, Valenti R, Migliorini A, Maehara A, Vergara R, Carrabba N, Mintz GS, Antoniucci D. Comparison of manual thrombus aspiration with rheolytic thrombectomy in acute myocardial infarction. *Circ Cardiovasc Interv*. 2013;6:224-230.

123. Prati F, Capodanno D, Pawlowski T, Ramazzotti V, Albertucci M, La Manna A, Di Salvo M, Gil RJ, Tamburino C. Local delivery versus intracoronary infusion of abciximab in patients with acute coronary syndromes. *JACC Cardiovasc Interv*. 2010;3:928-934.

124. Prati F, Di Vito L, Ramazzotti V, Imola F, Pawlowski T, Materia L, Tavazzi L, Biondi-Zoccai G, Albertucci M. Randomized trial of standard versus clearway-infused abciximab and thrombectomy in myocardial infarction: Rationale and design of the coctail ii study. *J Cardiovasc Med (Hagerstown)*. 2013;14:364-371.

125. Abtahian F, Yonetsu T, Vergallo R, Jia H, Kato K, Tian J, Hu S, McNulty I, Jang I-K. Ticagrelor immediately prior to stenting is associated with smaller residual thrombus in patients with acute coronary syndrome. *Int. J. Cardiol.* 2013;168:3099-3101.

126. Gonzalo N, Barlis P, Serruys PW, Garcia-Garcia HM, Onuma Y, Ligthart J, Regar E. Incomplete stent apposition and delayed tissue coverage are more frequent in drug-eluting stents implanted during primary percutaneous coronary intervention for ST-segment elevation myocardial infarction than in drug-eluting stents implanted for stable/unstable angina: Insights from optical coherence tomography. *JACC Cardiovasc Interv.* 2009;2:445-452.

127. Räber L, Zanchin T, Baumgartner S, Taniwaki M, Kalesan B, Moschovitis A, Garcia-Garcia HM, Justiz J, Pilgrim T, Wenaweser P, Meier B, Jüni P, Windecker S. Differential healing response attributed to culprit lesions of patients with acute coronary syndromes and stable coronary artery after implantation of drug-eluting stents: An optical coherence tomography study. *Int. J. Cardiol.* 2014;173:259-267.

128. Guagliumi G, Costa MA, Sirbu V, Musumeci G, Bezerra HG, Suzuki N, Matiashvili A, Lortkipanidze N, Mihalcsik L, Trivisonno A, Valsecchi O, Mintz GS, Dressler O, Parise H, Maehara A, Cristea E, Lansky AJ, Mehran R, Stone GW. Strut coverage and late malapposition with paclitaxel-eluting stents compared with bare metal stents in acute myocardial infarction: Optical coherence tomography substudy of the harmonizing outcomes with revascularization and stents in acute myocardial infarction (HORIZONS-AMI) trial. *Circulation.* 2011;123:274-281.

129. García-García HM, Muramatsu T, Nakatani S, Lee IS, Holm NR, Thuesen L, van Geuns R-J, van der Ent M, Borovicanin V, Paunovic D, Onuma Y, Serruys PW. Serial optical frequency domain imaging in stemi patients: The follow-up report of TROFI study. *Eur Heart J Cardiovasc Imaging.* 2014.

130. Gori T, Schulz E, Hink U, Wenzel P, Post F, Jabs A, Munzel T. Early outcome after implantation of ABSORB bioresorbable drug-eluting scaffolds in patients with acute coronary syndromes. *EuroIntervention.* 2014;9:1036-1041.

131. Karanasos A, Regar E, Geeve P, van Mieghem NM. Bioresorbable scaffold in myocardial infarction: Has the time come? *Int J Cardiol.* 2013;167:e17-19.

132. Diletti R, Karanasos A, Muramatsu T, Nakatani S, Van Mieghem NM, Onuma Y, Nauta ST, Ishibashi Y, Lenzen MJ, Ligthart J, Schultz C, Regar E, de Jaegere PP, Serruys PW, Zijlstra F, van Geuns RJ. Everolimus-eluting bioresorbable vascular scaffolds for treatment of patients presenting with ST-segment elevation myocardial infarction: BVS STEMI first study. *Eur Heart J.* 2014;35:777-786.

133. Kočka V, Malý M, Toušek P, Buděšínský T, Lisa L, Prodanov P, Jarkovský J, Widimský P. Bioresorbable vascular scaffolds in acute st-segment elevation myocardial infarction: A prospective multicentre study 'Prague 19'. *Eur Heart J.* 2014;35:787-794.

134. Karanasos A, van Mieghem N, Diletti R, Onuma Y, Nauta S, Felix C, Daemen J, Kauer F, de Jaegere P, Serruys P, Regar E, Zijlstra F, van Geuns R. Oct assessment of the mid-term vascular healing response following everolimus-eluting bioresorbable scaffold implantation in myocardial infarction. The bioresorbable scaffolds STEMI-first OCT study. (abstract). *EuroIntervention.* 2014;EuroPCR abstracts 2014:Euro14A-MA072.

135. Simsek C, Karanasos A, Magro M, Garcia-Garcia HM, Onuma Y, Regar E, Boersma E, Serruys P, van Geuns R-J. Long-term invasive follow-up of the everolimus-eluting bioresorbable vascular scaffold: Five-year results of multiple invasive imaging modalities. *EuroIntervention.* 2014;in press.

136. Karanasos A, Gnanadesigan M, van Ditzhuijzen N, simsek c, Freire R, Dijkstra J, Van Soest G, Zijlstra F, van Geuns R, Regar E. Optical coherence tomography assessment of the 5-year vascular healing response following implantation of the everolimus-eluting bioresorbable vascular scaffold (abstract). *Journal of the American College of Cardiology*. 2014;63.

137. Prati F, Di Vito L, Biondi-Zoccai G, Occhipinti M, La Manna A, Tamburino C, Burzotta F, Trani C, Porto I, Ramazzotti V, Imola F, Manzoli A, Materia L, Cremonesi A, Albertucci M. Angiography alone versus angiography plus optical coherence tomography to guide decision-making during percutaneous coronary intervention: The centro per la lotta contro l'infarto-optimisation of percutaneous coronary intervention (CLI-OPCI) study. *EuroIntervention*. 2012;8:823-829.

138. Van Mieghem NM, Kauer F, Regar E. Rheolytic versus aspiration thrombectomy in acute ST-segment elevation myocardial infarction judged by OCT. *EuroIntervention*. 2010;5.

139. Di Giorgio A, Capodanno D, Ramazzotti V, Imola F, Mallus MT, Stazi F, Paoletti G, Biondi-Zoccai G, Tamburino C, Prati F. Optical coherence tomography guided in-stent thrombus removal in patients with acute coronary syndromes. *Int J Cardiovasc Imaging*. 2013;29:989-996.

140. Planer D, Mehran R, Ohman EM, White HD, Newman JD, Xu K, Stone GW. Prognosis of patients with non-ST-segment-elevation myocardial infarction and nonobstructive coronary artery disease: Propensity-matched analysis from the acute catheterization and urgent intervention triage strategy trial. *Circ Cardiovasc Interv*. 2014;7:285-293.

141. Lanza GA, Crea F. Acute coronary syndromes without obstructive coronary atherosclerosis: The tiles of a complex puzzle. *Circ Cardiovasc Interv*. 2014;7:278-281.

142. Aldrovandi A, Cademartiri F, Arduini D, Lina D, Ugo F, Maffei E, Menozzi A, Martini C, Palumbo A, Bontardelli F, Gherli T, Ruffini L, Ardissino D. Computed tomography coronary angiography in patients with acute myocardial infarction without significant coronary stenosis. *Circulation*. 2012;126:3000-3007.

143. Karanasos A, Tsiamis E, Stefanadis C. Myocardial infarction caused by ostial right coronary artery thrombus in the absence of atheromatosis. *J Invasive Cardiol*. 2012;24:E188-189.

144. Toutouzas K, Karanasos A, Stefanadis C. Pitfalls of angiography in the assessment of atherosclerosis: The role of optical coherence tomography. *J Invasive Cardiol*. 2012;24:246-247.

145. Stefano GT, Bezerra HG, Attizzani G, Chamie D, Mehanna E, Yamamoto H, Costa MA. Utilization of frequency domain optical coherence tomography and fractional flow reserve to assess intermediate coronary artery stenoses: Conciliating anatomic and physiologic information. *Int J Cardiovasc Imaging*. 2011;27:299-308.

146. Van Mieghem NM, Ligthart J, Manintveld OC, Regar E. Acute coronary syndrome in 3 dimensions: The culprit exposed. *J. Am. Coll. Cardiol*. 2011;58.

147. McCabe JM, Croce KJ. Optical coherence tomography. *Circulation*. 2012;126:2140-2143.

148. Kramer MC, Verouden NC, Li X, Koch KT, van der Wal AC, Tijssen JG, de Winter RJ. Thrombus aspiration alone during primary percutanous coronary intervention as definitive treatment in acute ST-elevation myocardial infarction. *Catheter Cardiovasc Interv*. 2012;79:860-867.

149. Escaned J, Echavarria-Pinto M, Gorgadze T, Gonzalo N, Armengol F, Hernandez R, Jimenez-Quevedo P, Nunez-Gil IJ, Perez-Vizcayno MJ, Alfonso F, Banuelos C, Ibañez B, Garcia E, Fernandez Ortiz A, Macaya C. Safety of lone thrombus aspiration without concomitant coronary stenting in selected patients with acute myocardial infarction. *EuroIntervention*. 2013;8:1149-1156.

150. Kelbæk H, Engstrøm T, Ahtarovski KA, Lønborg J, Vejlstrup N, Pedersen F, Holmvang L, Helqvist S, Saunamäki K, Jørgensen E, Clemmensen P, Kløvgaard L, Tilsted H-H, Raungaard B, Ravkilde J, Aaroe J, Eggert S, Køber L. Deferred stent implantation in patients with ST-segment elevation myocardial infarction: A pilot study. *EuroIntervention*. 2013;8:1126-1133.

151. Cervinka P, Spaček R, Bystroň M, Kvašňák M, Kupec A, Cervinková M, Kala P. Optical coherence tomography-guided primary percutaneous coronary intervention in ST-segment elevation myocardial infarction patients: A pilot study. *Can J Cardiol*. 2014;30:420-427.

152. Braunwald E. Coronary plaque erosion: Recognition and management. *JACC Cardiovasc Imaging*. 2013;6:288-289.

153. Prati F, Uemura S, Souteyrand G, Virmani R, Motreff P, Di Vito L, Biondi-Zoccai G, Halperin J, Fuster V, Ozaki Y, Narula J. OCT-based diagnosis and management of STEMI associated with intact fibrous cap. *JACC Cardiovasc Imaging*. 2013;6:283-287.

154. Chamié D, Wang Z, Bezerra H, Rollins AM, Costa MA. Optical coherence tomography and fibrous cap characterization. *Curr Cardiovasc Imaging Rep*. 2011;4:276-283.

155. Zahnd G, Karanasos A, van Soest G, Regar E, Niessen WJ, Gijsen F, van Walsum T. Semi-automated quantification of fibrous cap thickness in intracoronary optical coherence tomography. *Information processing in computer-assisted interventions*. Springer; 2014:78-89.

156. Wang Z, Chamie D, Bezerra HG, Yamamoto H, Kanovsky J, Wilson DL, Costa MA, Rollins AM. Volumetric quantification of fibrous caps using intravascular optical coherence tomography. *Biomed Opt Express*. 2012;3:1413-1426.

157. Ughi GJ, Adriaenssens T, Sinnaeve P, Desmet W, D'Hooge J. Automated tissue characterization of *in vivo* atherosclerotic plaques by intravascular optical coherence tomography images. *Biomed Opt Express*. 2013;4:1014-1030.

158. Gnanadesigan M, van Soest G, White S, Scoltock S, Ughi GJ, Baumbach A, van der Steen AFW, Regar E, Johnson TW. Effect of temperature and fixation on the optical properties of atherosclerotic tissue: A validation study of an *ex-vivo* whole heart cadaveric model. *Biomed Opt Express*. 2014;5:1038-1049.

159. Regar E, Gnanadesigan M, Van der Steen AF, van Soest G. Quantitative optical coherence tomography tissue-type imaging for lipid-core plaque detection. *JACC Cardiovasc Interv*. 2013;6:891-892.

160. van Soest G, Goderie T, Regar E, Koljenovic S, van Leenders GL, Gonzalo N, van Noorden S, Okamura T, Bouma BE, Tearney GJ, Oosterhuis JW, Serruys PW, van der Steen AF. Atherosclerotic tissue characterization *in vivo* by optical coherence tomography attenuation imaging. *J Biomed Opt*. 2010;15:011105.

161. Wang T, Wieser W, Springeling G, Beurskens R, Lancee CT, Pfeiffer T, van der Steen AFW, Huber R, van Soest G. Intravascular optical coherence tomography imaging at 3200 frames per second. *Opt Lett*. 2013;38:1715-1717.

162. Karanasos A, Schuurbiers J, Gnanadesigan M, van Ditzhuijzen N, Dijkstra J, Van Soest G, Zijlstra F, van Geuns R, Wentzel J, Regar E. Association of wall shear stress with vascular healing response by oct 5 years after bioresorbable scaffold implantation (abstract). *Journal of the American College of Cardiology*. 2014;63.

163. Liu L, Gardecki JA, Nadkarni SK, Toussaint JD, Yagi Y, Bouma BE, Tearney GJ. Imaging the subcellular structure of human coronary atherosclerosis using micro-optical coherence tomography. *Nat. Med.* 2011;17:1010-1014.

164. Villiger M, Zhang EZ, Nadkarni S, Oh WY, Bouma BE, Vakoc BJ. Artifacts in polarization-sensitive optical coherence tomography caused by polarization mode dispersion. *Opt Lett*. 2013;38:923-925.

165. Nadkarni SK, Pierce MC, Park BH, de Boer JF, Whittaker P, Bouma BE, Bressner JE, Halpern E, Houser SL, Tearney GJ. Measurement of collagen and smooth muscle cell content in atherosclerotic plaques using polarization-sensitive optical coherence tomography. *J Am Coll Cardiol*. 2007;49:1474-1481.

166. Yoo H, Kim JW, Shishkov M, Namati E, Morse T, Shubochkin R, McCarthy JR, Ntziachristos V, Bouma BE, Jaffer FA, Tearney GJ. Intra-arterial catheter for simultaneous microstructural and molecular imaging *in vivo*. *Nat Med*. 2011;17:1680-1684.

Chapter 1.3

Safety of optical coherence tomography in daily practice. A comparison with intravascular ultrasound

van der Sijde JN, **Karanasos A**, van Ditzhuijzen N, van Geuns RJ, Valgimigli M, Ligthart JMR, Witberg KT, Wemelsfelder S, Diletti R, de Jaegere PP, van Mieghem NM, Okamura T, van Soest G, Zijlstra F, van Domburg R, Regar E

Submitted for publication

Abstract

Objective

Previous studies have reported the safety and feasibility of both TD-OCT and FD-OCT in highly selected patients and clinical settings. However, the generalizability of these data is limited and data in unselected patient populations reflecting a routine cathlab practice are lacking. We compared safety of intracoronary Fourier domain optical coherence tomography (OCT) imaging to intravascular ultrasound (IVUS) imaging in a large real world series of consecutive patients who underwent invasive imaging during coronary catheterization in our center.

Methods

This is a prospective, single-center registry of patients scheduled for coronary angiography or intervention undergoing intracoronary imaging with Fourier domain OCT or IVUS between April 2008 and December 2013. Intra-procedural and major in-hospital adverse events that could be possibly related to invasive imaging were registered routinely by the operator as part of our clinical report and prospectively recorded in our database. These events were retrospectively individually adjudicated by an independent safety committee.

Results

Between April 2008 and December 2013, 13,418 diagnostic or interventional coronary catheterization procedures were performed. Of these, 1,142 procedures used OCT and 2,476 procedures used IVUS. Invasive imaging related complications were rare, did not differ between the two imaging methods (OCT: n=7, 0.6%; IVUS: n=12, 0.5%; p=0.6), and were self-limiting after retrieval of the imaging catheter or easily treatable in the catheterization laboratory. No major adverse events, prolongation of hospital stay or permanent patient harm were observed.

Conclusions

Fourier domain optical coherence tomography is safe in an unselected and heterogeneous group of patients with varying clinical settings.

Introduction

Intracoronary optical coherence tomography (OCT) is increasingly used in the catheterization laboratory. Various clinical applications have been proposed, including assessment of plaque morphology in angiographic ambiguous lesions, guidance of stent placement during percutaneous coronary interventions (PCI) and follow-up stent assessment[1, 2]. In the early days of the first generation, time domain OCT (TD-OCT), intracoronary application was hampered by the need for proximal balloon occlusion to limit antegrade blood flow in combination with distal delivery of a translucent flush solution in order to create a blood-free environment during OCT data acquisition[3]. The currently commercially available and widespread used second-generation intracoronary Fourier domain OCT (FD-OCT) was developed to overcome these limitations, allowing for a simplification of the image acquisition procedure. Importantly, the imaging device was redesigned to a monorail OCT imaging catheter that could be introduced into the coronary artery over any PCI guide wire of choice, which substantially facilitated instrumentation. Further, the data acquisition speed was increased by using frequency domain techniques that are capable of acquiring images at high speed (up to 180 frames/sec) and with fast pullback (up to 40mm/sec), alleviating the need for proximal balloon occlusion during imaging and the risk of creating ischemia during imaging[4]. Previous smaller studies[5, 6, 7, 8, 9, 10] have reported the safety and feasibility of both TD-OCT and FD-OCT in highly selected patients and clinical settings. However, the generalizability of these data is limited and data in unselected patient populations reflecting a routine cathlab practice are lacking.

We report safety of intracoronary FD-OCT imaging in a large real world series of consecutive patients that underwent OCT during coronary catheterization in our center since the introduction of FD-OCT imaging in 2008 and compare the results to our intravascular ultrasound (IVUS) safety data from the same time period.

Methods

Study population

This is a single-center study, prospectively evaluating the safety of FD-OCT. Consecutive patients who underwent FD-OCT examination during cardiac catheterization between April 2008 and December 2013 were included. This data was then compared to the cohort of patients that underwent IVUS within the same time period. All consecutive patients who underwent intracoronary OCT or IVUS during the study period were included. Additionally, to assess

generalizability of our data, the indications for catheterization and patient baseline characteristics were also compared to the cohort that, at the discretion of the operators, did not undergo any form of invasive imaging during the same time period. Both OCT and IVUS were performed either as part of various clinical trial protocols or at the discretion of the operators. In the latter case, the exclusion criteria were acute, life-threatening hemodynamic instability and coronary anatomy not deemed suitable for introduction of an imaging catheter, such as extensive tortuosity or calcification or a lumen diameter >5mm, beyond the penetration depth of OCT and lesions considered too tight to allow crossing of a device of approximately 3F. In acute settings, restoration of antegrade flow always was the main priority and had to be secured before introduction of an imaging catheter.

Invasive imaging procedure

Invasive imaging was performed via radial or femoral access according to routine clinical standard in our center using 6F (range 5F-7F) guide catheters. Patients received weight-adjusted intravenous heparin in order to maintain the activated clotting time >300sec and intracoronary administration of 0.2mg nitroglycerin, as standard prior to invasive imaging. Imaging catheters were advanced distally to a region of interest over 0.014-inch conventional angioplasty guide wires, chosen at the discretion of the operators. All the imaging systems have dedicated pullback devices and consoles that allow data processing and storage.

IVUS image acquisition

IVUS images were acquired with different systems (Galaxy I, Galaxy II and iLab: Boston Scientific, Marlborough, MA, USA; In-Vision Gold and S5 imaging system: Volcano Corporation, San Diego, CA, USA). Different types of catheters (range 20-45MHz, 3.2-3.5F) were used with a default motorized pullback speed of 0.5 mm/sec.

OCT image acquisition

OCT imaging was performed with commercially available FD-OCT systems (Lightlab C7XR, Ilumien and Ilumien Optis: St Jude Medical, St Paul, MN, USA; Terumo Lunawave: Terumo, Tokyo, Japan) and in a limited number of patients with several different OCT prototypes (Lightlab M4: St Jude Medical, St Paul, MN, USA; MGH OCT system: The Wellman Center for Photomedicine, Boston, MA, USA; Volcano OCT system: Volcano Corporation, San Diego, CA, USA).

OCT imaging probes had a short monorail design with a fiber-optic imaging core integrated into a catheter. The catheter profile ranged from 2.4Fr to 2.7Fr. During OCT image acquisition the optic imaging core rotated at a rate of 100–180 revolutions per second. OCT pullbacks were performed automated at the pullback speed of generally 20mm/sec (range 10-40mm/sec) during simultaneous flushing of viscous iso-osmolar contrast (Iodixanol 320, Visipaque™, GE Health Care, Cork, Ireland at 37C) through the guiding catheter by use of an automated power injector (Medrad Inc., Warrendale, PA, USA) with a flow rate of 3ml/sec as standard setting, or in selected cases by manual injection.

Safety assessment

Both major in-hospital and intra-procedural adverse events were recorded and considered as potential imaging related complications. Major in-hospital adverse events were defined as cerebrovascular event, emergency revascularization and death. Intra-procedural events were defined as the occurrence of clinical symptoms (new or worsened chest pain or shortness of breath), adverse angiographic outcomes (dissection, perforation, vasospasm, thrombus formation, no-reflow) or electrocardiographic changes (ST-segment elevation, severe bradycardia, ventricular arrhythmias) requiring interruption of the imaging procedure during intracoronary imaging and were routinely registered by the operator as a standard item being part of our clinical PCI report and collected in our PCI database. In addition, all free text comments in the PCI database/reporting system were screened for "OCT" or "IVUS". Comments containing these key words were individually reviewed for any possible association with an adverse event. Major peri-procedural adverse events were also recorded and defined as cerebrovascular event, emergency revascularization and death.

Adjudication

Complications were individually adjudicated by an independent safety committee by thorough review of the patient files, procedural notes, angiogram and intracoronary images. A complication was considered related to the imaging procedure if it would not have occurred if the invasive imaging would not have been performed. "Definitely related" was used for complications that were with great certainty caused by the invasive imaging. If the relation between invasive imaging procedure and registered event was less clear, but could not be completely ruled out, the event was defined as "possibly related". Possible and definite invasive imaging related events were categorized as self-limiting after withdrawal of the imaging catheter, requiring action or major adverse events. The safety committee consisted of two teams that

reviewed the events independently. In case of disagreement, the case was re-evaluated and discussed between both teams until consensus was reached. Each team consisted of a senior invasive cardiologist not directly involved in clinical or research coronary imaging projects and an invasive imaging expert (RJG & JL; MV & KW).

Statistical analysis

Continuous data were expressed as mean values ±SD. An independent-samples t-test was used to analyze continuous data between two groups and ANOVA for more than two groups. Significance of associations of categorical variables were assessed using the chi-square test or Fisher's exact test, as appropriate. Univariate analyses to identify predictors of an adverse event during image acquisition were performed using a logistic regression model. A p-value of <0.05 was considered significant.

Results

Patient population

Between April 2008 and December 2013, 13,418 diagnostic or interventional coronary catheterization procedures were performed in our center. During 1,142 procedures (984 patients with 3,045 pullbacks) FD-OCT was used and during 2,476 procedures (2,054 patients with 5,148 pullbacks) IVUS was used. A combination of OCT and IVUS images were acquired during 307 procedures. Invasive imaging was performed by 13 different senior operators, of whom 11 had more than five years of experience and the other two between one and five years of experience as senior operator in a catheterization laboratory. Baseline demographic characteristics of all patients who underwent OCT or IVUS are displayed in Table 1. Invasive imaging was used in a variety of clinical settings. Patients undergoing OCT had less renal failure (5.3% vs 9.1%, $p<0.001$) when compared to IVUS. OCT imaging was performed more often in patients with ST-elevation myocardial infarction (24.7 vs 14.5, $p<0.001$). Procedural characteristics are given in Table 2. The mean number of pullbacks per procedure was significantly higher in the OCT group compared to IVUS (2.66 vs 2.07, $p<0.001$), which might be explained in part by the shorter artery segment, that can be visualized in one pullback (typically 50mm OCT vs 100mm IVUS). Imaged vessels and lesion types were roughly equal. Clearing of the coronary from blood during OCT imaging was performed with a contrast flush rate of 3ml/sec in 78% and 4ml/sec in 21% of the pullbacks.

Table 1. Characteristics of all consecutive patients undergoing invasive imaging in our center between 2008-2013.

Procedures	OCT	IVUS	P-value
N	1,142	2,476	
Age, years	61.9±11.1	62.6±11.2	0.112
Male	853 (74.7)	1,852 (74.8)	0.967
Risk factors			
Hypertension	589 (53.9)	1,465 (62.0)	<0.001
Diabetes	206 (18.1)	500 (20.5)	0.105
Dyslipidemia	600 (55.3)	1,413 (60.4)	0.006
Current smokers	299 (26.3)	576 (23.5)	0.073
Family history	471 (44.0)	1,025 (44.2)	0.911
History			
Prior myocardial infarction	344 (30.1)	776 (31.3)	0.462
Prior CABG	50 (4.4)	136 (5.5)	0.169
Prior PCI	529 (46.3)	1,058 (42.7)	0.047
Renal Failure	60 (5.3)	224 (9.1)	<0.001
Indications for catheterization			<0.001
Stable angina	433 (37.9)	1,114 (45.0)	<0.001
Unstable angina	180 (15.7)	466 (18.8)	0.028
Non-STEMI	97 (8.5)	233 (9.4)	0.385
STEMI	282 (24.7)	360 (14.5)	<0.001
Other	150 (13.1)	303 (12.2)	0.45

*A combination of OCT and IVUS images were acquired during 307 procedures. Age: mean ± standard deviation, other values: n (%).

Generalizability of invasive imaging cohorts

Table 3 shows the comparison of baseline characteristics the OCT and IVUS cohorts to the population that did not undergo invasive imaging within the same time window. The most pronounced differences were the higher incidence of renal failure (12.7% vs 5.3% vs 9.1%, p<0.001) in the non-imaging group, the lower incidence of patients with a prior PCI (26.9% vs 46.4% vs 42.7%) and the larger number of type C lesions (35.9% vs 25.2% vs 24.1%, p<0.001) when compared to OCT and IVUS, respectively. Figure 1 illustrates three examples of clinical settings that are typically considered difficult for invasive imaging acquisition. OCT images were successfully acquired in all of these cases without complications.

Table 2. Invasive imaging procedure details.

Procedures	OCT	IVUS	P-value
N	1,142	2,476	
Mean number of pullbacks	2.66 ±1.54	2.07 ±1.32	<0.001
Mean number of imaged vessels	1.18 ±0.42	1.28 ±0.51	<0.001
Total pullbacks, n	3,042	5,135	
Pullback distribution among vessels			<0.001
LAD	1,484 (48.8)	2,459 (47.9)	0.436
LCX	577 (19.0)	1,136 (22.1)	0.001
RCA	846 (27.8)	1,266 (24.7)	0.002
Other	135 (4.4)	274 (5.3)	0.074
Lesion type, n	946	1,927	0.584
A	115 (12.2)	214 (11.1)	0.418
B1	235 (24.8)	519 (26.9)	0.241
B2	358 (37.8)	729 (37.8)	1.000
C	238 (25.2)	465 (24.1)	0.549

Values in n (%) or mean (± standard deviation).

Safety assessment

After adjudication, seven (0.6%) complications that occurred during image acquisition were possibly or definitely related to OCT and twelve (0.5%) to IVUS imaging (P=0.6) (Figure 2). Table 4 further specifies the complications as adjudicated. Transient ST-elevation requiring withdrawal of the imaging catheter was seen in 0.26% vs 0.08% (P=0.2), hypotension during image acquisition in 0.18% vs 0.04% (P=0.2), coronary spasm requiring infusion of additional intracoronary nitroglycerin in 0.09% vs 0.04% (P=0.6), thrombus formation in 0.09% vs 0.16% (P=0.6), dissection of the imaged vessel in 0.00% vs 0.12% (P=0.2) and stent deformation in 0.00% vs 0.04% (P=0.5) during OCT and IVUS imaging, respectively. The event rate per pullback was the same for both modalities (0.23%). Figure 3 shows an example of a typical angiographic and OCT image of coronary spasm occurring during image acquisition. A more detailed description of all the complications that were encountered can be found in the supplemental material.

Risk factors for adverse event

All baseline characteristics and indications for catheterization were tested in univariate analyses for the risk of invasive imaging events (Supplementary table 1). The use of both modalities, the

Table 3. Comparison between invasive imaging cohorts and non-imaging population.

	OCT	IVUS	Non-imaging	P-value
N	1,142	2,476	10,107	
Age, years	61.9±11.1	62.6±11.2	63.7±12.8	<0.001
Male	853 (74.7)	1,852 (74.8)	6,992 (69.2)	<0.001
Risk factors				
Hypertension	589 (53.9)	1,465 (62.0)	5,037 (54.6)	<0.001
Diabetes	206 (18.1)	500 (20.5)	1,981 (20.3)	0.210
Dyslipidemia	600 (55.3)	1,413 (60.4)	4,347 (48.0)	<0.001
Current smokers	299 (26.3)	576 (23.5)	2,345 (24.1)	0.180
Family history	471 (44.0)	1,025 (44.2)	3,248 (36.6)	<0.001
History				
Prior myocardial infarction	344 (30.1)	776 (31.3)	2,324 (23.4)	<0.001
Prior CABG	50 (4.4)	136 (5.5)	1,002 (10.1)	<0.001
Prior PCI	529 (46.3)	1,058 (42.7)	2,682 (26.9)	<0.001
Renal Failure	60 (5.3)	224 (9.1)	1,260 (12.7)	<0.001
Indications for catheterization				<0.001
Stable angina	433 (37.9)	1,114 (45.0)	2,768 (27.4)	<0.001
Unstable angina	180 (15.7)	466 (18.8)	1,552 (15.4)	<0.001
Non-STEMI	97 (8.5)	233 (9.4)	1,271 (12.6)	<0.001
STEMI	282 (24.7)	360 (14.5)	2,787 (27.6)	<0.001
Other	150 (13.1)	303 (12.2)	1,729 (17.1)	<0.001
Lesion type, n	946	1,927	7,263	<0.001
A	115 (12.2)	214 (11.1)	571 (7.9)	<0.001
B1	235 (24.8)	519 (26.9)	1,690 (23.3)	0.003
B2	358 (37.8)	729 (37.8)	2,398 (33.0)	<0.001
C	238 (25.2)	465 (24.1)	2,604 (35.9)	<0.001

*A combination of OCT and IVUS images were acquired during 307 procedures. Age: mean (± standard deviation), other values: n (%).

total number of pullbacks and the total number of invasively imaged main vessels were also tested. No predictor of adverse events was identified in the individual OCT and IVUS cohorts, nor in the combined invasive imaging cohort. Additionally, the impact of the interventional cardiologist's experience with the use of invasive imaging on the risk of an adverse event was evaluated. When compared to the most experienced operator, there was no significant increase in risk for every individual senior operator.

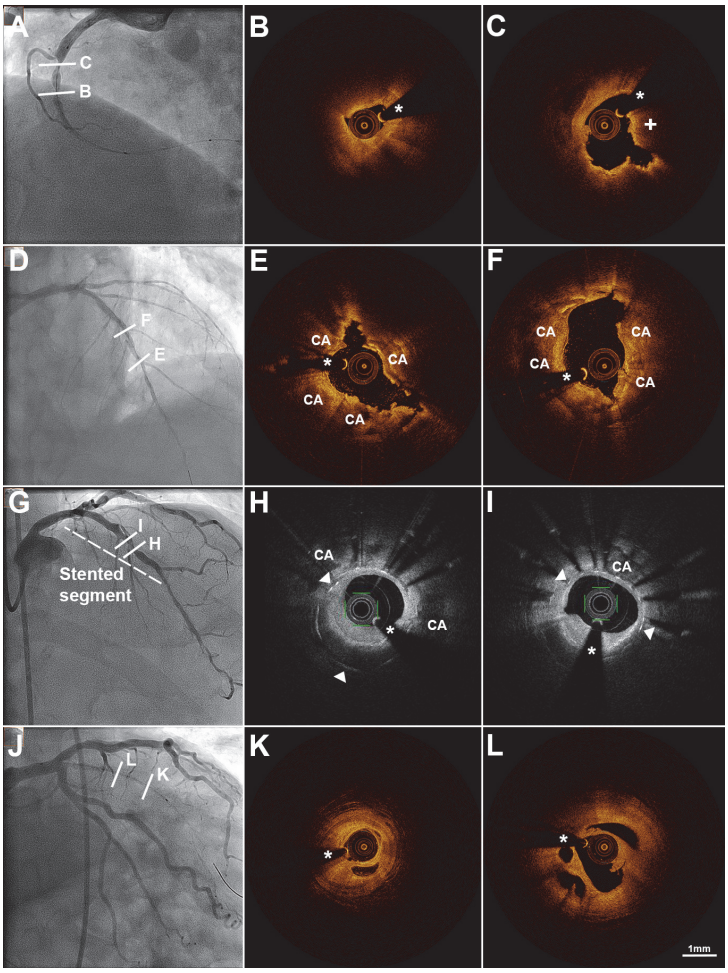

Figure 1: Examples of the use OCT in different clinical settings.

Angiogram (A) of a STEMI patient with corresponding OCT cross-sectional images (B and C) with the presence of thrombus (+). Angiogram (D) of a severely calcified vessel, which is clearly appreciated (CA) on the OCT-images (E and F) after lesion preparation with a cutting balloon and rotablator. Angiogram (G) of a patient with in-stent restenosis. The OCT-images reveal neoatherosclerosis within the stent (H and I). Angiographic (J) and OCT image acquisition (K and L) in a recanalized chronic total occlusion. *Guide wire artefact.

Table 4. Invasive imaging complications after adjudication

	OCT	IVUS	P-value
Transient ST-elevation	3 (0.26)	2 (0.08)	0.2
Bradycardia	2 (0.18)	1 (0.04)	0.2
Coronary spasm	1 (0.09)	1 (0.04)	0.6
Thrombus formation	1 (0.09)	4 (0.16)	0.6
Dissection	0 (0.00)	3 (0.12)	0.2
Stent deformation	0 (0.00)	1 (0.04)	0.5
Major adverse events	0 (0.00)	0 (0.00)	NA

Values in n (%).

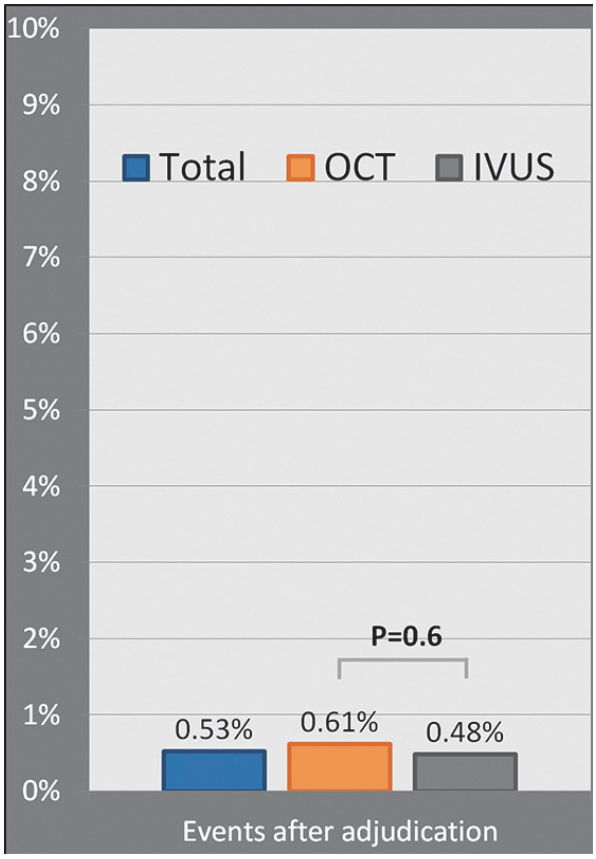

Figure 2: Event rates of intravascular ultrasound and optical coherence tomography after adjudication.

OCT: optical coherence tomography, IVUS: intravascular ultrasound.

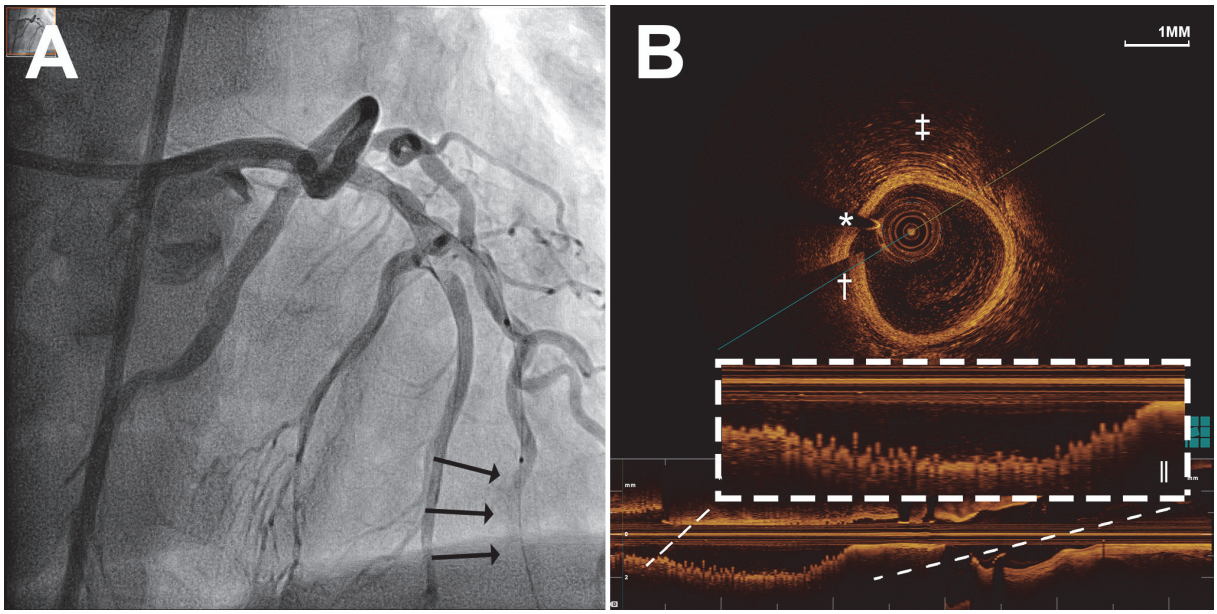

Figure 3: Coronary spasm during optical coherence tomography pullback.

Angiogram (A) and OCT-image (B) of a diagonal branch with coronary spasm. Vasospasm can potentially mimic streaming effect due to poor contrast injection or dissection on the coronary angiogram. The seam-line (†) and non-uniform rotational distortion artefact (‡) on the cross-sectional and the "sawtooth" appearance (‖) on the longitudinal image, together with poor clearing of the artery from blood (arrows) despite good guide catheter position, suggest that coronary spasm could be present. *Guide wire artefact.

Discussion

The present study demonstrates that intracoronary OCT and IVUS imaging is comparably safe in an unselected and heterogeneous group of patients with varying clinical settings, reflecting daily routine catheterization laboratory practice in a tertiary care center. Imaging related events were scarce, with a similar incidence for OCT and IVUS imaging and most importantly, self-limiting after withdrawal of the imaging catheter or easily treatable in the catheterization laboratory. No major adverse events, prolongation of hospital stay or permanent patient harm was observed.

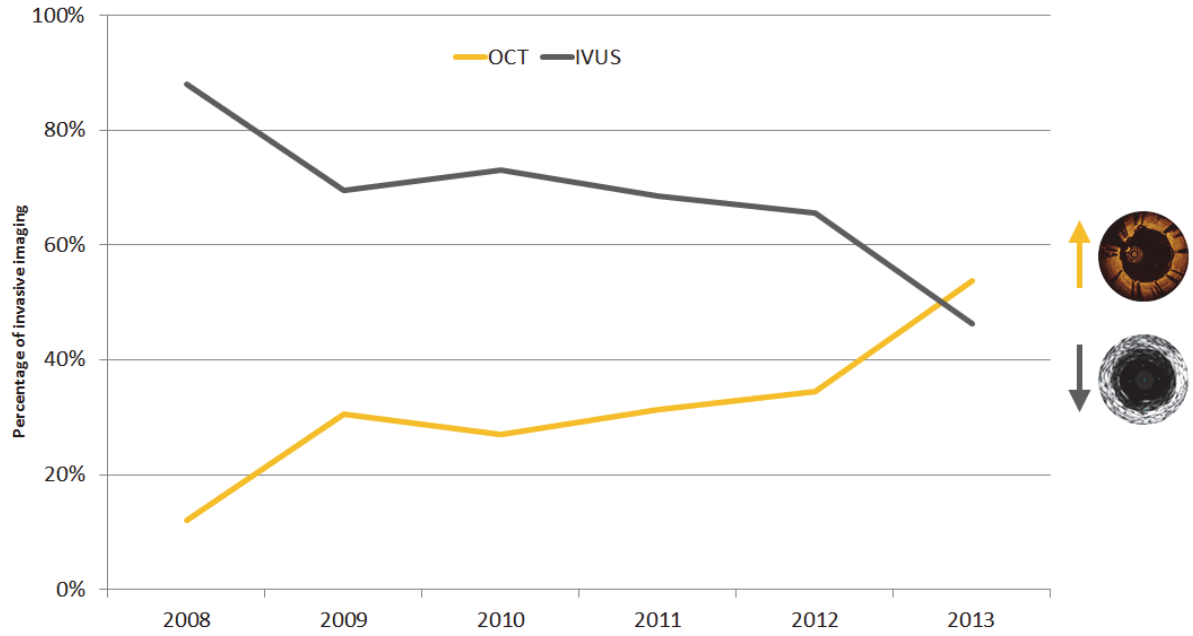

Figure 4: Change of invasive imaging policy during the study period.
The use of IVUS and OCT has balanced over time.

Comparison between the OCT and IVUS cohorts

During the study period, the frequency in the use of OCT and IVUS has changed in our center. In 2008 OCT was not yet CE marked and, thus, infrequently used. In 2013 however, the use of OCT and IVUS has balanced out (Figure 4). While IVUS was more often performed in patients with stable angina, OCT was used more often in STEMI patients. OCT has a higher sensitivity in visualizing thrombus and plaque ruptures, often present in STEMI patients.

OCT and IVUS were used in a heterogeneous population and in several clinical settings. Although most non-imaging variables in Table 3 differ significantly from the OCT and IVUS cohorts, most differences can be explained by the features that are inextricably linked to both modalities. For example, in patients with renal failure, x-ray contrast exposure has to be kept to a

minimum. This explains the smaller numbers of patients with renal impairment in the OCT and, in lesser extent, the IVUS group. In patients with a chronic total occlusion (lesion type C), operators are less inclined to use invasive imaging, while additional imaging can be of great help in complex lesions (type B2), such as bifurcations. We believe that our data reflect the diversity in the use of invasive imaging and its many possible applications.

Previous studies demonstrating the safety of OCT

OCT's need of clearance of blood from the vessel during image acquisition was perceived as the Achilles heel in the early days of intracoronary OCT imaging with time domain technology, limiting its clinical application to a few expert centers. Today, this problem is largely solved by the introduction of FD-OCT technology. With FD-OCT, the need to clear the artery temporarily from blood does not appear as a major drawback anymore. The first studies that reported the safety of OCT[10, 11] used the currently abandoned TD-OCT systems. At that time, OCT image acquisition was relatively slow (framerate 15 frames/sec and pullback speed of 1mm/sec) and thus requiring longer pullback times with temporary occlusion of the proximal vessel segment using a dedicated occlusion balloon. Prati et al.[5] were the first to perform OCT with a pullback speed of 3mm/sec and a non-occlusive technique demonstrating improved feasibility and reduced complication risk. This was then confirmed in a larger multicenter registry[6] comparing the occlusive balloon technique (n=256) to the non-occlusive TD-OCT (n=212) technique. No MACE were observed during or in the 24 hour period following OCT imaging.

The first study to report the safety and feasibility of Fourier Domain OCT was published by Imola et al.[7] in a group of 90 patients with unstable or stable coronary artery disease. In this population, one case of coronary spasm was recorded, but no MACE was observed. Likewise, two other studies[8, 9] reported FD-OCT safety in small, selected groups. Our study presents safety of OCT in a high volume center, over several years. The findings corroborate the results of the prior, smaller studies with complication rates of 0-2%. The few complications that were encountered were all resolved before the patient left the catheterization laboratory. These complications were also in line with individual case reports that described rare adverse events during OCT imaging[12, 13, 14, 15]. Importantly, our large scale, systematic registry can demonstrated that these complications occur very rarely (all <0.2%) in a tertiary, high volume center and seem to happen randomly.

Comparison with IVUS

Although IVUS image acquisition shows many similarities to that of OCT, there are some distinct differences, most importantly IVUS's lack of need for a temporarily blood-free environment. Despite the differences, complications are seen very rarely for both modalities and do not significantly differ. In our study, we report 12 (0.5%) adverse events during IVUS image acquisition.

Large IVUS safety trials have been performed[16, 17], reporting 1-3% complications, a number that may be partially driven by a larger catheter size. The most recent large-scale study implementing IVUS, the PROSPECT[18] study, reported eleven patients (1.6%) with complications that were attributed to IVUS procedures. In contrast to our findings, all events were caused by mechanical damage (10 dissections and 1 perforation) to the vessel wall. The reasons for this difference are unclear. The mean number of vessels that were imaged with IVUS in our cohort is 1.28 per procedure, in contrast to the 3 vessels that were imaged as part of the protocol in the PROSPECT study. Furthermore, in the PROSPECT study images where acquired within a shorter time window and in multiple centers.

Risk factors for adverse event

We did not find any patient characteristics, nor any procedural related characteristics that increase the chance of occurrence of an imaging-related event in the light of our very low event rate. The absence of risk factors most likely demonstrates that adverse events occur infrequently and randomly, implicating that OCT and IVUS can both be used in a large variety of patients and in different clinical settings. We additionally explored if the amount of adverse events declined with increasing experience, however an association between the operator's experience and the number of imaging procedures was not identified, tracking with previous reports[9].

Limitations

A limitation of this study is its design. Collection of data that has been recorded over several years as part of our clinical routine catheterization database. This could possibly cause inconsistency and create bias. Furthermore, reproduction of the procedures associated with adverse events that occurred during coronary catheterizations that were performed years ago can be complex. However, the registration of events is done by experienced operators in a standardized way and for a long period of time. We included every patient undergoing FD-OCT and IVUS within the selected time window and used all available procedural data to reproduce

the procedures with two independent adjudication committees. Therefore we feel that the reported results represent clinical practice. The fact that imaging was acquired at the discretion of very experienced operators could create selection bias. Moreover, the high level of experience in this single-center study does not mean that reported results can be translated less experienced centers. Furthermore, it is of note that it is possible that the differences in clinical characteristics between OCT, IVUS and non-imaging groups as presented in Table 3 were mainly driven by its use in predefined research protocols in specific clinical settings. However, we intentionally included all imaging procedures that have taken place within the specified time window to assure that the presented data represents a modern, real-world catheterization laboratory population.

Another limitation of this study is that we were not able to report the incidence of peri-procedural myocardial infarctions and contrast induced nephropathy, as the majority of our patients are being transferred to the referring hospital within 6 hours after the procedure or dismissed after an uneventful procedure.

Conclusions

Fourier domain optical coherence tomography is safe in an unselected and heterogeneous group of patients with varying clinical settings. Adverse events that occur during image acquisition are rare, and similar to the event rates occurring during IVUS image acquisition.

References

1 Tearney GJ, Regar E, Akasaka T, et al. Consensus standards for acquisition, measurement, and reporting of intravascular optical coherence tomography studies: a report from the International Working Group for Intravascular Optical Coherence Tomography Standardization and Validation. *J Am Coll Cardiol* 2012;**59**:1058-72.

2 Karanasos A, Ligthart J, Witberg K, et al. Optical Coherence Tomography: Potential Clinical Applications. *Curr Cardiovasc Imaging Rep* 2012;**5**:206-20.

3 Prati F, Guagliumi G, Mintz GS, et al. Expert review document part 2: methodology, terminology and clinical applications of optical coherence tomography for the assessment of interventional procedures. *Eur Heart J* 2012;**33**:2513-20.

4 Yun SH, Tearney GJ, Vakoc BJ, et al. Comprehensive volumetric optical microscopy in vivo. *Nat Med* 2006;**12**:1429-33.

5 Prati F, Cera M, Ramazzotti V, et al. Safety and feasibility of a new non-occlusive technique for facilitated intracoronary optical coherence tomography (OCT) acquisition in various clinical and anatomical scenarios. *EuroIntervention* 2007;**3**:365-70.

6 Barlis P, Gonzalo N, Di Mario C, et al. A multicentre evaluation of the safety of intracoronary optical coherence tomography. *EuroIntervention* 2009;**5**:90-5.

7 Imola F, Mallus MT, Ramazzotti V, et al. Safety and feasibility of frequency domain optical coherence tomography to guide decision making in percutaneous coronary intervention. *EuroIntervention* 2010;**6**:575-81.

8 Yoon JH, Di Vito L, Moses JW, et al. Feasibility and safety of the second-generation, frequency domain optical coherence tomography (FD-OCT): a multicenter study. *J Invasive Cardiol* 2012;**24**:206-9.

9 Lehtinen T, Nammas W, Airaksinen JK, et al. Feasibility and safety of frequency-domain optical coherence tomography for coronary artery evaluation: a single-center study. *Int J Cardiovasc Imaging* 2013;**29**:997-1005.

10 Yamaguchi T, Terashima M, Akasaka T, et al. Safety and feasibility of an intravascular optical coherence tomography image wire system in the clinical setting. *Am J Cardiol* 2008;**101**:562-7.

11 Tanigawa J, Barlis P, Di Mario C. Intravascular optical coherence tomography: optimisation of image acquisition and quantitative assessment of stent strut apposition. *EuroIntervention* 2007;**3**:128-36.

12 Koyama K, Yoneyama K, Mitarai T, et al. Periprocedural myocardial injury and right bundle branch block during coronary optical coherence tomography in an acute coronary syndrome patient with severe coronary ectasia. *Int J Cardiol* 2014;**177**:1113-5.

13 Dobarro D, Jiménez-Valero S, Moreno R. Severe coronary spasm induced by OCT wire. There are no innocuous procedures. *J Invasive Cardiol* 2010;**22**:385.

14 Sato K, Panoulas VF, Naganuma T, et al. Bioresorbable vascular scaffold strut disruption after crossing with an optical coherence tomography imaging catheter. *Int J Cardiol* 2014;**174**:e116-9.

15 Smith DK, Bourenane H, Strange JW, et al. Catheter-induced coronary dissection during optical coherence tomography investigation. *EuroIntervention* 2012;**7**:1124-5.

16 Hausmann D, Erbel R, Alibelli-Chemarin MJ, et al. The safety of intracoronary ultrasound. A multicenter survey of 2207 examinations. *Circulation* 1995;**91**:623-30.

17 Batkoff BW, Linker DT. Safety of intracoronary ultrasound: data from a Multicenter European Registry. *Cathet Cardiovasc Diagn* 1996;**38**:238-41.

18 Stone GW, Maehara A, Lansky AJ, et al. A prospective natural-history study of coronary atherosclerosis. *N Engl J Med* 2011;**364**:226-35.

SUPPLEMENTAL MATERIAL

Supplemental results

Complications that occurred during invasive imaging were witnessed very rarely (0.53%) in our center. The adverse events that did occur, however, are described below in more detail.

Transient ST-elevation

Vessel occlusion by the imaging catheter resulting in transient ST-elevation on electrocardiographic (ECG) monitoring requiring withdrawal of the imaging catheter occurred during three OCT and two IVUS image acquisitions. The ECG changes were transient and resolved promptly upon withdrawal of the imaging catheter. Supplemental Figure 1 demonstrates an example of an IVUS imaging procedure of a narrow lesion. Antegrade flow in the coronary artery was occluded by the IVUS catheter which resulted in angina with ST-segment elevations on ECG telemetry. After retrieval of the imaging catheter the electrocardiogram normalized.

Bradycardia

Bradycardia with hypotension was witnessed during two OCT procedures and one IVUS procedure. In two out of three cases, this was secondary to occlusion of flow in the artery by an imaging catheter which resolved upon withdrawal of the catheter. The third case was caused by deep intubation of the guide catheter into the left main coronary artery, possibly to facilitate adequate flushing during OCT image acquisition and resulting in pressure dampening. This led to bradycardia and hypotension which improved upon prompt adjustment of the position of the guide catheter and an intravenous admission of 0.5mg atropine with good response.

Coronary spasm

Severe vasospasm may occur due to the manipulation of the imaging equipment within the coronary vasculature. In severe cases, this may lead to flow reduction. In both reported cases, spasm was resolved by intracoronary infusion of nitrates. Severe cases may mimic dissection. Therefore, early recognition is important. OCT can help differentiate vasospasm from other differential causes. Pullbacks acquired during spasm showed poor blood clearing and a typical pattern of a fast, irregular, saw-tooth artefact (Main paper figure 3), which has previously been described as a "wavy configuration"[1].

Thrombus formation

Thrombus formation on the invasive imaging catheter occurred once during OCT imaging and four times during IVUS imaging. Supplemental figure 2 shows an example of thrombus formation during invasive imaging in a patient undergoing primary PCI for anterior STEMI. The

patient was preloaded with prasugrel, acetylsalicylic acid and heparin according to current guidelines. An emergency coronary angiogram showed that the culprit lesion was in the left anterior descending artery (LAD). The patient subsequently received an extra bolus of 5,000 units of heparin before commencement of PCI. After successful wiring and aspiration thrombectomy of the culprit lesion, there was TIMI-II flow in the LAD. During the passage of the C7 Dragonfly™ OCT-catheter in the LAD, several filling defects with a hazy appearance could be seen on the angiogram, suggesting the presence of thrombus formation. This was confirmed by the appearance of thrombotic material on the OCT images. A Xience™ Xpedition 3.5x23 mm drug-eluting stent (DES) was deployed in the proximal LAD with good angiographic result. Two additional boluses of Grp IIb/IIIa-inhibitor were given.

The mechanism of the thrombus formation is not entirely clear. Possibly causes for the new appearance of thrombus include the migration of thrombotic material during the passage of the imaging catheter within the culprit vessel or insufficient anticoagulation. We did not find any ACT of less than 300 seconds in the cases with thrombus formation during invasive imaging. Furthermore, the interval between admission of intravenous heparin and the introduction of the imaging catheter was a relatively short duration of fourteen minutes, which strengthens the idea that the etiology is related to the acute setting of the procedure rather than a problem with anticoagulation, although the latter cause cannot be ruled out.

Dissection

Three dissections were possibly caused by an IVUS imaging catheter, whereas we could not identify any dissections caused by an OCT catheter. Two of these three dissections were caused by wiring of a vessel to facilitate IVUS imaging. In one case, the dissection occurred at a proximal location which suggested that it was guide catheter related rather than due to the imaging catheter itself. It is, however, possible that the IVUS pullback created additional traction on the guide catheter, thereby possibly damaging the vessel wall (Supplemental Figure 3). Therefore, this dissection was labeled as a possible complication. To treat the dissection, a 4.0x18mm Xience™ Prime drug-eluting DES was implanted to secure vessel patency.

Stent deformation

One case of potential stent deformation involving the use of IVUS (3.5Fr Volcano™ 20Mhz EagleEye Platinum catheter) imaging to assess post deployment result of Xience™ Prime (4.0x28mm) stent in the right coronary artery was recorded in our database. The post deployment IVUS images (Supplemental Figure 4) revealed a proximal stent edge that was circular, not apposed to the vessel wall, with a stent diameter of 2.5mm circularly. Possible explanations for

this appearance include deformation of the stent by the IVUS catheter, deformation of the stent by the guide catheter or simply underexpansion of the stent in its proximal portion.

Further intervention was performed with additional balloon dilatation and implantation of another Xience™ Prime (4.0x8mm) DES, overlapping with the previous stent to assure an optimal mechanical result.

Supplemental Table 1. Univariate analysis for adverse events during invasive-image acquisition.

	OCT	P-value	IVUS	P-value	OCT + IVUS	P-value
N	1,142		2,476		3,311*	
Clinical risk factors						
Age	0.99 (0.93-1.06)	0.869	1.00 (0.95-1.06)	0.884	1.00 (0.96-1.04)	0.985
Male gender	NA (0.00-NA)	0.994	1.69 (0.37-7.73)	0.500	2.95 (0.68-12.8)	0.148
Hypertension	0.64 (0.14-2.87)	0.558	0.61 (0.20-1.90)	0.395	0.61 (0.25-1.50)	0.282
DM	0.75 (0.09-6.27)	0.792	0.35 (0.05-2.73)	0.352	0.48 (0.11-2.06)	0.321
Dyslipidaemia	2.03 (0.39-10.5)	0.399	0.47 (0.15-1.48)	0.195	0.80 (0.32-1.97)	0.625
Smoking	2.11 (0.47-9.50)	0.329	1.08 (0.29-4.02)	0.904	1.42 (0.54-3.75)	0.479
Family history	0.95 (0.21-4.28)	0.950	0.25 (0.06-1.15)	0.074	0.45 (0.16-1.26)	0.131
History						
Prior MI	1.74 (0.39-7.83)	0.469	0.73 (0.20-2.69)	0.631	0.95 (0.39-2.72)	0.952
Prior CABG	3.68 (0.23-31.2)	0.232	1.56 (0.20-12.2)	0.671	2.11 (0.48-9.22)	0.320
Prior PCI	2.90 (0.56-15.0)	0.204	1.34 (0.43-4.15)	0.617	1.79 (0.72-4.47)	0.211
Renal Failure	3.00 (0.36-25.3)	0.313	0.90 (0.12-7.03)	0.923	1.34 (0.31-5.83)	0.696
Indication						
Stable angina	1.00		1.00		1.00	
Unstable angina	0.00 (0.00-NA)	0.996	0.30 (0.04-2.38)	0.253	0.21 (0.03-1.63)	0.136
Non-STEMI	0.00 (0.00-NA)	0.997	1.20 (0.25-5.67)	0.821	0.82 (0.18-3.72)	0.798
STEMI	1.02 (0.17-6.17)	0.980	0.00 (0.00-NA)	0.994	0.41 (0.09-1.87)	0.250
Other	1.94 (0.32-11.7)	0.471	0.46 (0.06-3.67)	0.462	0.92 (0.26-3.32)	0.902
Imaging variables						
Use of both modalities	1.09 (0.21-5.64)	0.920	1.42 (0.31-6.49)	0.655	2.63 (0.87-7.98)	0.087
Total number of pullbacks	0.51 (0.22-1.16)	0.108	1.10 (0.75-1.61)	0.645	1.06 (0.82-1.36)	0.672
Total number of imaged vessels	0.79 (0.11-5.79)	0.820	1.19 (0.43-3.32)	0.737	1.57 (0.88-2.80)	0.130

*307 Patients underwent both OCT and IVUS during the same procedure. Risk values as Hazard Ratio (95% Confidence Interval). OCT: Optical coherence tomography; IVUS: Intravascular ultrasound; DM: Diabetes mellitus; MI: Myocardial infarction; CABG: Coronary artery bypass graft; PCI: Percutaneous coronary intervention.

Lessons learned

When imaging a very tight lesion and the imaging catheter seems occlusive, do not start the pullback too distally because visualization is very poor and time of ischemia will be prolonged. A rather general measure, that is worth repeating however, is that a guide catheter should be positioned coaxially, but wedging should be avoided at all times. Be aware that during invasive imaging, deep intubation of the guide catheter into the vessel may occur resulting in pressure dampening effect or damage to the vessel wall.

All witnessed events appeared isolated events and no systematic contributory cause was detected. Nevertheless, these events are a reminder of the need for caution particularly in view of the large number of intracoronary imaging procedures performed. If these rather general measures are applied, we believe that invasive imaging is a tool that can be of additional value in various clinical situations and can be used safely with low threshold.

Supplemental figures

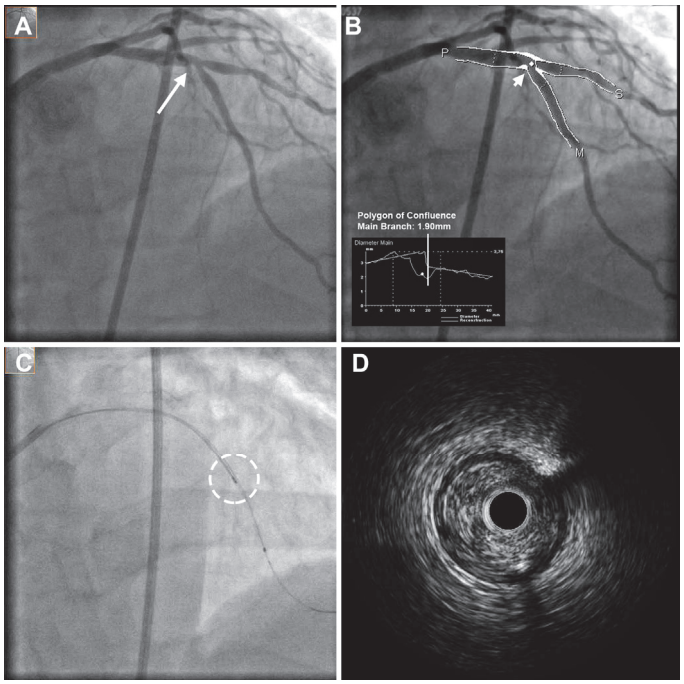

Supplemental Figure 1. Transient ST-elevation caused by occlusive IVUS-catheter.

Lesion (arrow) in the bifurcation of the left descending artery and a diagonal branch (panel A and B). During the IVUS pullback (panel C) the patient develops ST-segment elevation and chest pain from blockage of antegrade flow in the LAD by the IVUS imaging catheter. Although the IVUS shows the 3.5F (= 1.16mm) IVUS-catheter is occlusive (panel D), this was not apparent on angiography (minimum lesion diameter in main branch 1.90mm).

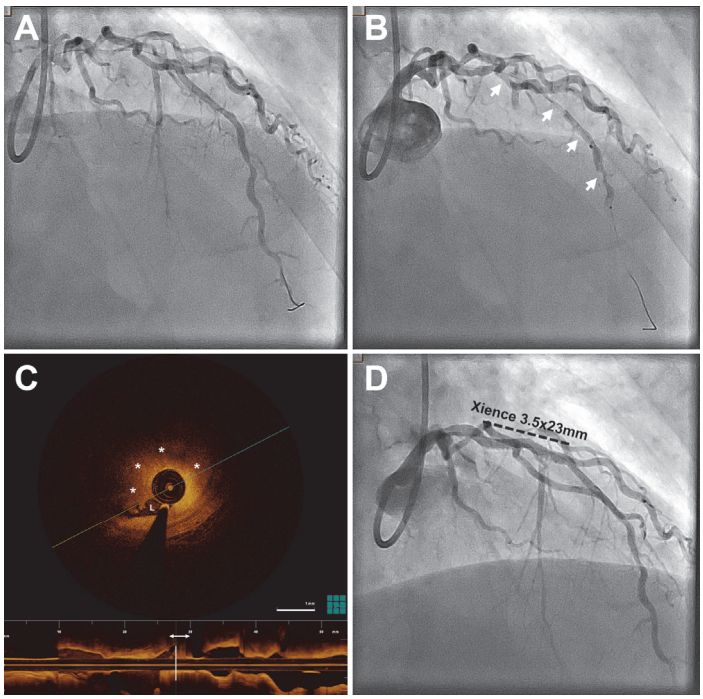

Supplemental Figure 2. Thrombus formation during OCT pullback.

Angiographic image of the left descending artery with TIMI-II flow after successfully wiring and aspiration thrombectomy of the culprit lesion (panel A). During the OCT pullback, several hazy spots appeared (arrows, panel B). On the OCT images (panel C) there is a focal segment (arrow, longitudinal view) with a narrow lumen (L) due to thrombotic material (*). After pre-dilatation, a Xience™ 3.5x23mm stent was deployed with good angiographic result (panel D).

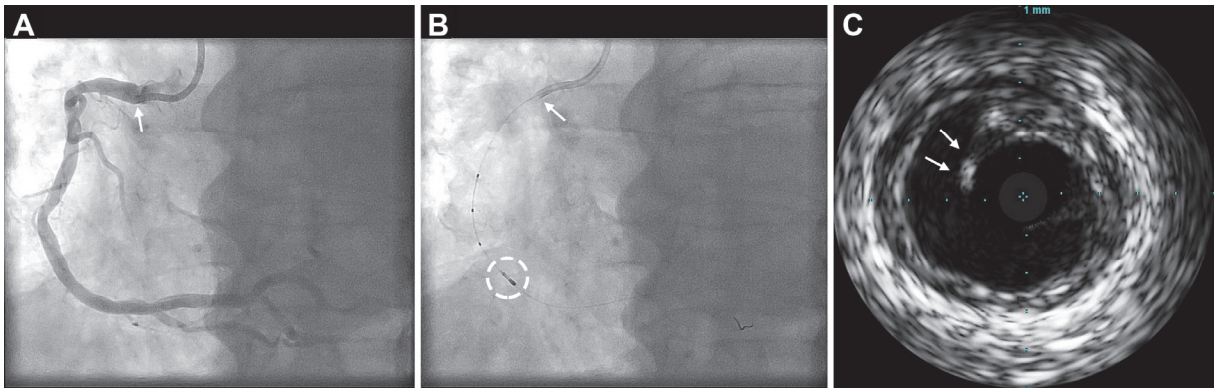

Supplemental Figure 3. Proximal dissection caused by the guide catheter.

Pre-interventional angiographic image of the right coronary artery (panel A) with the arrow indicating the guide catheter position. During the IVUS pullback the guide catheter (arrow, panel B) is pulled distally, possibly creating a proximal dissection as seen on the IVUS cross-sectional image (arrows, panel C).

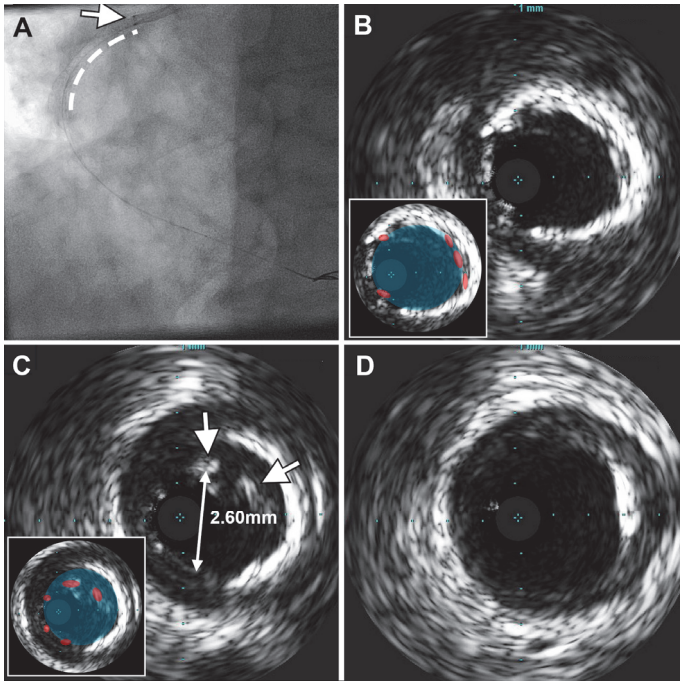

Supplemental Figure 4. Possible stent deformation.

Angiographic image (panel A) of a Xience™ 4.0x28mm stent (dotted line) in the right coronary artery. The guide catheter is in close proximity of the proximal stent (arrow). After IVUS image acquisition, the distal part of the stent is well apposed to the vessel wall (panel B), but the proximal part is malapposed (arrows, panel C), which could either be related to underexpansion or deformation of the stent by the IVUS or guide catheter. The inlayed panels delineate the stent struts in red and the lumen in blue. Panel D shows an IVUS image of the proximal reference area.

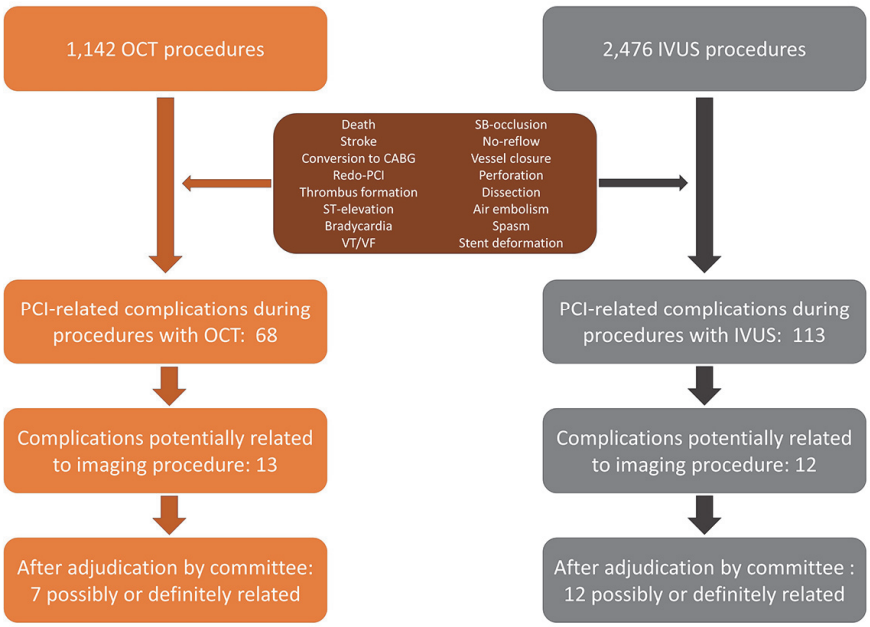

Supplemental Figure 5. Flowchart of the adjudication process.

Adjudication process of all potentially invasive imaging related complications. Four cases of coronary spasm could not directly be related to OCT because spasm occurred during entire procedure, one case of no-reflow could also not directly be related to OCT image acquisition and one case that was registered because the operator could not advance the imaging catheter was also excluded by the adjudication committees.

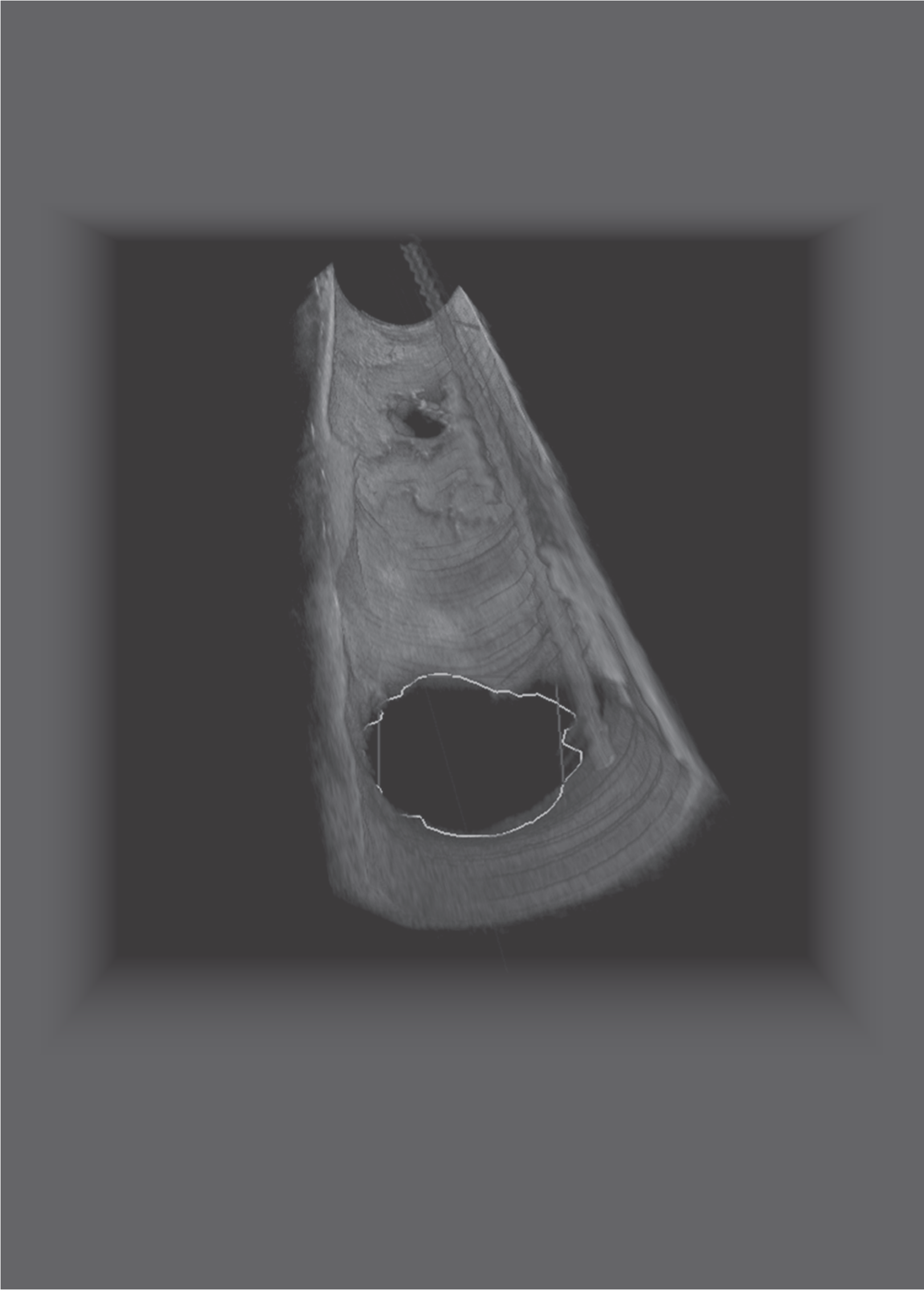

PART II

Methodological aspects of quantitative and qualitative measurements by OCT Technological innovations

Chapter 2.1

The impact of Fourier-Domain optical coherence tomography catheter induced motion artefacts on quantitative measurements of a PLLA-based bioresorbable scaffold

van Ditzhuijzen NS, **Karanasos A**, Bruining N, van den Heuvel M, Sorop O, Ligthart J, Witberg K, Garcia-Garcia HM, Zijlstra F, Duncker DJ, van Beusekom HM, Regar E

Int J Cardiovasc Imaging. 2014 Aug;30(6):1013-26

The impact of Fourier-Domain optical coherence tomography catheter induced motion artefacts on quantitative measurements of a PLLA-based bioresorbable scaffold

N. S. van Ditzhuijzen · A. Karanasos · N. Bruining · M. van den Heuvel · O. Sorop · J. Ligthart · K. Witberg · H. M. Garcia-Garcia · F. Zijlstra · D. J. Duncker · H. M. M. van Beusekom · E. Regar

Received: 26 November 2013 / Accepted: 9 May 2014 / Published online: 16 May 2014

Abstract Intracoronary Fourier-Domain optical coherence tomography (FD-OCT) enables imaging of the coronary artery within 2–4 seconds, a so far unparalleled speed. Despite such fast data acquisition, cardiac and respiratory motion can cause artefacts due to longitudinal displacement of the catheter within the artery. We studied the influence of longitudinal FD-OCT catheter displacement on serial global lumen and scaffold area measurements in coronary arteries of swine that received PLLA-based bioresorbable scaffolds. In 10 swine, 20 scaffolds (18 × 3.0 mm) were randomly implanted in two epicardial coronary arteries. Serial FD-OCT imaging was performed immediately after implantation (T1) and at 3 (T2) and 6 months (T3) follow-up. Two methods for the selection of OCT cross-sections were compared. Method A did not take into account longitudinal displacement of the FD-OCT catheter. Method B accounted for longitudinal displacement of the FD-OCT catheter. Fifty-one OCT pullbacks of 17 scaffolds were serially analyzed. The measured scaffold length differed between time points, up to one fourth of the total scaffold length, indicating the presence of longitudinal catheter displacement. Between method A and B, low error was demonstrated for mean area measurements. Correlations between measurements were high: R^2 ranged from 0.91 to 0.99 for all mean area measurements at all time points. Considerable longitudinal displacement of the FD-OCT catheter was observed, diminishing the number of truly anatomically matching cross-sections in serial investigations. Global OCT dimensions such as mean lumen and scaffold area were not significantly affected by this displacement. Accurate co-registration of cross-sections, however, is mandatory when specific regions, e.g. jailed side branch ostia, are analyzed.

Keywords Optical coherence tomography · OCT · Bioresorbable vascular scaffold · Motion artefact

Abbreviations

OCT	Optical coherence tomography
FD	Fourier-Domain
TD	Time-Domain
PLLA	Poly-L-lactid acid
T	Time point
ROI	Region of interest
LA	Lumen area
SA	Scaffold area
CA	Coverage area
ICC	Intra-class correlation coefficient
IVUS	Intravascular ultrasound

Electronic supplementary material The online version of this article (doi:10.1007/s10554-014-0447-3) contains supplementary material, which is available to authorized users.

N. S. van Ditzhuijzen · A. Karanasos · N. Bruining · M. van den Heuvel · O. Sorop · J. Ligthart · K. Witberg · F. Zijlstra · D. J. Duncker · H. M. M. van Beusekom · E. Regar (✉)
Department of Cardiology, Thoraxcenter, BA-585, Erasmus University Medical Center, 's-Gravendijkwal 230, 3015 CE Rotterdam, The Netherlands
e-mail: e.regar@erasmusmc.nl

N. S. van Ditzhuijzen · M. van den Heuvel · O. Sorop · D. J. Duncker · H. M. M. van Beusekom
Division of Experimental Cardiology, Erasmus University Medical Center, Rotterdam, The Netherlands

N. S. van Ditzhuijzen · A. Karanasos
COEUR Cardiovascular Research School, Erasmus University Medical Center, Rotterdam, The Netherlands

H. M. Garcia-Garcia
Cardialysis B.V., Rotterdam, The Netherlands

3D Three-dimensional

Introduction

Optical coherence tomography (OCT) allows for detailed evaluation of the coronary vessel wall. One of the main advantages of OCT is the high resolution allowing for detailed evaluation of therapeutic devices used for the treatment of coronary artery disease, e.g. coronary stents and scaffolds [1, 2]. Recently, the second generation Fourier Domain (FD)-OCT has been introduced. FD-OCT enables unparalleled fast imaging of the coronary artery employing a wavelength-swept laser as a light source allowing for a high A-line and frame rate (typically ≥100 frames/s) and fast automated catheter pullback speed (≥20 mm/s) [3–5]. Despite the fast pullback speed of the FD-OCT catheter, the catheter can longitudinally move within the coronary artery during the cardiac cycle and can therefore cause distortions in the representation of the data. Little is known about the magnitude of longitudinal catheter displacement in vivo. To study the influence of longitudinal displacement of the FD-OCT catheter on serial mean lumen and scaffold area measurements, we performed serial FD-OCT imaging of PLLA-based bioresorbable scaffolds implanted in atherosclerotic swine, and compared two OCT data analysis methods. Method A did not account for longitudinal displacement of the FD-OCT catheter, method B accounted for longitudinal displacement of the FD-OCT catheter.

Materials and methods

Experimental design

This study was approved by the Erasmus MC Animal Care committee and was performed in accordance with the Guide for the Care and Use of Laboratory Animals (National Institutes of Health Publication 85-23, 1996).

Ten male crossbred (Yorkshire × Landrace) swine fed a high-cholesterol diet were included [6]. Following 2 mg isosorbide dinitrate, twenty 18 × 3.0 mm bioresorbable scaffolds (Abbott Vascular, Santa Clara, CA) were implanted randomly in two of three epicardial coronary arteries of anesthetized swine [7, 8]. Serial FD-OCT (C7XR Fourier-Domain system, St. Jude Medical, Westford, MA, USA) was performed in the anesthetized swine immediately after implantation (T1), 3 (T2) and 6 months (T3) after implantation of the scaffolds, while care was taken to keep the heart rate (average 106 ± 27 bpm) and blood pressure (mean arterial pressure 87 ± 17 mmHg) stable at all time points. The influence of longitudinal catheter displacement on serial mean lumen, scaffold and coverage area measurements was evaluated by comparing two different approaches for the selection of OCT cross-sections (method A and method B).

OCT image acquisition

The OCT catheter was advanced distally to the scaffold through an 8F guiding catheter. The OCT catheter was withdrawn automatically with a pullback speed of 20 mm/s and a frame rate of 100 frames/s during continuous flushing, using a power injector (Mark V ProVis, Medrad, Inc, Indianola, Pa), with 5 or 6 ml/s contrast agent preheated to 37 °C (iodixanol 370; Visipaque, GE Health Care, Cork, Ireland). Since the maximum length of the pullback was 54 mm, the total pullback consists of 270 frames (cross-sections). Moreover, the interval between two consecutive cross-sections corresponds to 0.2 mm.

OCT image analysis

Selection of OCT cross-sections

Analysis method A is the most often employed method for the selection of OCT cross-sections and has been widely described in studies evaluating bioresorbable scaffolds [7, 9]. At each analysis time point, cross-sectional images were selected independently and manually at 1-mm intervals within the ROI. Thus, per timepoint, every five cross-sections, one cross-section was selected independently.

Analysis method B employed a computerized matching method for the selection of serially corresponding cross-sections. OCT pullbacks were digitally saved in DICOM format to allow for matching of corresponding cross-sections by dedicated software (CURAD vessel analysis, CURAD BV, Wijk bij Duurstede, The Netherlands) (Fig. 1) [10]. OCT pullbacks acquired at different time points were tiled horizontally onto one single screen, allowing for accurate matching of the ROI. The pullbacks were divided into three sub-segments within the ROI: (1) the distal segment of the scaffold: starting at the most distal OCT cross-section containing any scaffold strut extending to the first OCT cross-section in which the opening of a distal side branch was clearly visible, (2) the mid segment of the scaffold: starting at the last OCT cross-section in which the opening of the distal side branch was clearly visible, extending to the first OCT cross-section in which the opening of a proximal side branch was clearly visible and (3) the proximal segment of the scaffold: starting at the last OCT cross-section in which the opening of the proximal side branch was clearly visible, extending to the most proximal OCT cross-section containing any scaffold strut.

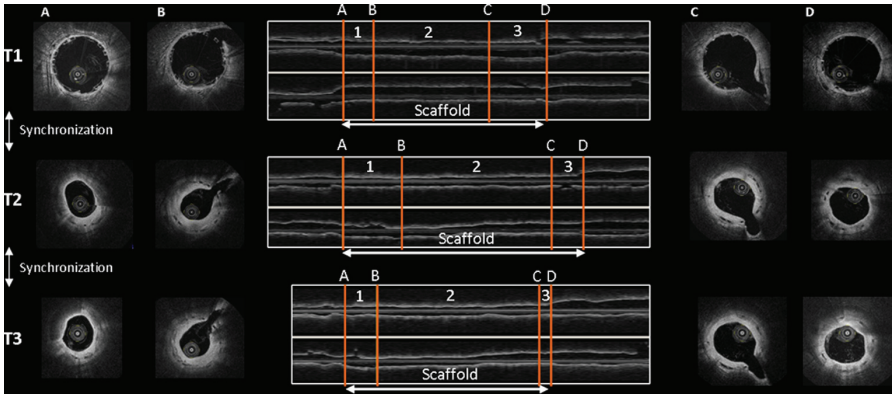

Fig. 1 Matching of a scaffolded segment using dedicated analysis software (CURAD vessel analysis, CURAD BV, Wijk bij Duurstede, The Netherlands). The OCT cross-sections **a**–**d** correspond to the letters *A*–*D* of the longitudinal view in the center of the figure (*A*–*D* = the ROI). The numbers *1*–*3* correspond to the distal (*1*), mid (*2*) and proximal (*3*) segment of the scaffold, which are matched within the different time points using side branches as landmarks. *T1* time-point 1: immediately after scaffold implantation, *T2* time-point 2: 3 months after scaffold implantation, *T3* time-point 3: 6 months after scaffold implantation

In order to allow for serial matching of corresponding segments irrespective to the uniformity of the pullback, the vessel analysis software provides synchronization of the sub-segments within the three time points (Fig. 1). Within these synchronized segments, corresponding OCT cross-sections were manually selected in 1-mm intervals for quantitative OCT analysis.

Quantitative OCT analysis

Quantitative OCT analysis was performed on the OCT cross-sections selected by method A or method B using proprietary software for off-line OCT analysis (St. Jude medical, Westford, MA, USA).

The Z-offset is a manually adjustable image calibration that is critical for accurate measurements. When the sheath of the OCT catheter is aligned with the four yellow fiducials in the OCT image, the Z-offset is correctly adjusted. During image acquisition the optical fibers can however stretch, resulting in possible changes in the size of the Z-offset. Therefore, before off-line OCT analysis, the Z-offset was checked and modified if necessary in all pullbacks, and OCT pullbacks with poor image quality were excluded from the analysis.

The region of interest (ROI) was defined as the region containing the scaffold, delineated by the most distal OCT cross-section containing any scaffold strut until the most proximal OCT cross-section containing any scaffold strut. The length of the ROI—the scaffold length—was measured at all time points using the longitudinal view (l-mode) of the proprietary software for off-line OCT analysis.

Quantitative OCT area measurements included lumen area (LA), scaffold area (SA) and coverage area (CA), according to previously described methodology [11]. Contour tracing of the lumen, scaffold and coverage area are depicted in Fig. 2. Immediately after implantation (T1), lumen area can be imaged because of the translucency of the polymeric struts, and is delineated by the endoluminal contour of the vessel wall behind the struts. At T2 and T3, contours of the lumen area can be drawn by following the endoluminal contour of the coverage between and on top of the struts. The contours for lumen area were obtained by a semi-automated detection algorithm and additional manual corrections were performed if necessary. At all time points the contour of the scaffold area is measured by joining the middle point of the abluminal side of the black core of the struts [7–9]. Coverage area was determined at follow-up (T2 and T3) and defined as scaffold area minus lumen area [CA = SA − LA] [11].

Longitudinal catheter displacement

To evaluate the extent of longitudinal displacement of the FD-OCT catheter, we compared the scaffold length, as measured in the l-mode of the off-line OCT analysis software, between the various time points. Furthermore, we compared the amount of cross-sections selected according to method A between the various time points.

To determine the effect of longitudinal catheter displacement on serial mean lumen, scaffold and coverage area measurements, we performed inter-method reproducibility analysis for the measurements per time point (T1, T2 and T3) and for the measurements between time points (ΔT1 − T2 and ΔT2 − T3). Moreover, we compared the mean area measurements obtained by method A—employing no co-registration of the OCT cross-sections between time points and therefore not taking into account longitudinal displacement of the OCT catheter—with the

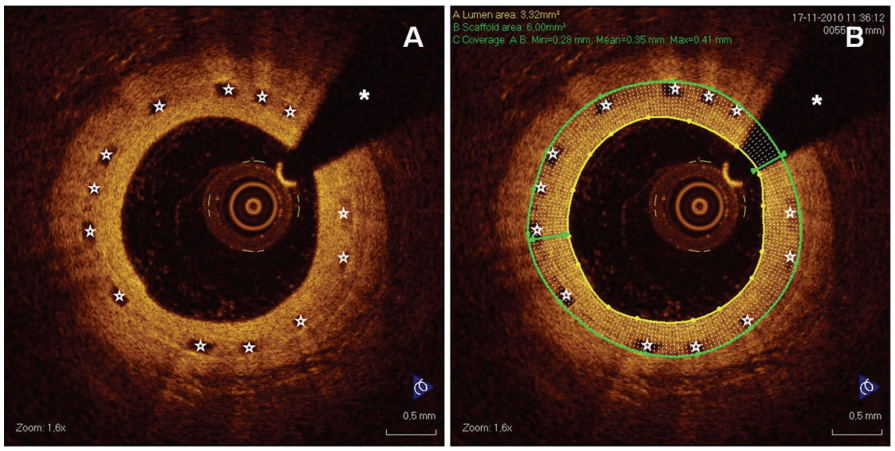

Fig. 2 Lumen, scaffold and coverage area measurements at T2. OCT cross-sections of the scaffold at T2 **a** without and **b** with the lumen area (LA), scaffold area (SA), and coverage area (CA) measurement contours. The '*open*' *stars* indicate the scaffold struts, the *asterisk* indicates the guide wire artefact. The *yellow line* in **b** indicates the contour of the LA, the *green line* the contour of the SA and the area between LA and SA is the CA (*white dotted area*)

mean area measurements obtained by method B—employing co-registration of OCT cross-sections within time points and therefore taking into account longitudinal displacement of the OCT catheter.

To evaluate the effect of longitudinal catheter displacement on the analysis of specific scaffold regions, the amount of OCT cross-sections containing a side branch selected according to method A were compared between the various time points. This analysis was only performed for method A because cross-sections were selected independently at the various time points. By method B corresponding cross-sections were, per protocol, carefully selected and therefore no difference in the amount of selected cross-sections containing a side branch is present between the various time points.

Inter- and intra-observer reproducibility

Two experienced observers independently analyzed five scaffolds at T1, T2 and T3 to assess the inter-observer reproducibility for the quantitative OCT area measurements. To assess the intra-observer reproducibility of the quantitative area measurements, one experienced observer repeated the analysis in all five scaffolds with $\geq$3 months between the first and second analysis. For both the inter-and intra-observer reproducibility analysis, the selection of OCT cross-sections was performed according to method B.

Statistical analysis

GraphPad Prism version 5.00 for Windows (GraphPad Software, San Diego, CA, USA) and SPSS version 20.0 (SPSS Inc., Chicago, IL) were used for statistical analysis. To analyze the difference between time points, repeated measures analysis was performed by GEE modeling using a linear response model with an autoregressive [AR(1)] structure for the within-cluster correlation matrix. GEE is a statistical method that accounts for the clustered nature of >1 scaffold analyzed from one swine, which might result in unknown correlations among measurements within these scaffold clusters. The agreement between method A and B for the analysis of quantitative OCT parameters was determined by Bland–Altman analysis, setting the limits of agreement to 1.96 standard deviations of the mean difference. The Bland–Altman plots show the absolute difference between method A and B ([A − B]; y-axis) versus the average of method A and B ([(A + B)/2]; x-axis) [12]. Linear regression analysis was performed to show the correlation between the two methods.

The inter- and intra-observer reproducibility for quantitative area measurements were assessed using the intra-class correlation coefficient (ICC) for absolute agreement. An ICC < 0.4 indicates poor agreement, an ICC between 0.4 and 0.75 indicates moderate agreement, and ICC values >0.75 indicate excellent agreement [13]. Bland–Altman plots were used to illustrate the agreement between inter- and intra-observer reproducibility measurements at cross-sectional level [12]. A P value of <0.05 indicates statistical significance.

Results

The presence of longitudinal catheter displacement

Fifty-one OCT pullbacks of 17 scaffolds were included in the analysis. Six scaffolds were implanted in the LAD, six in the

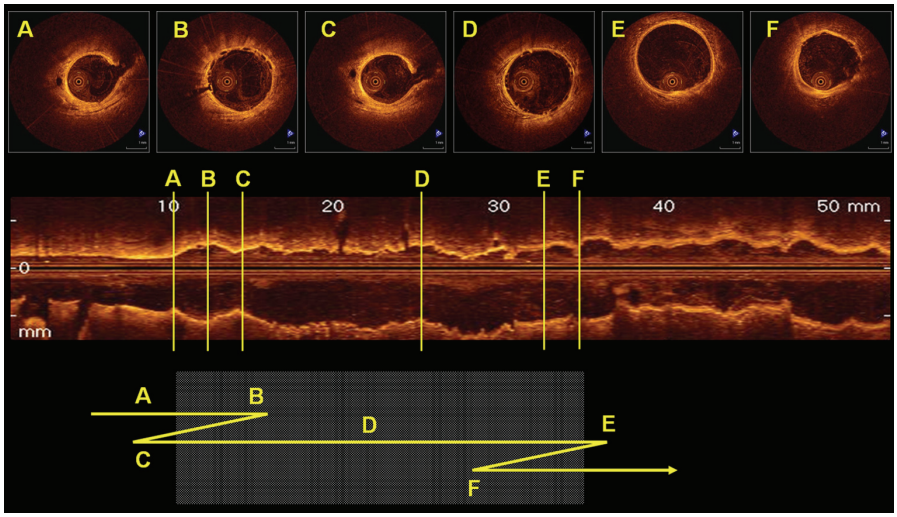

Fig. 3 Representation of longitudinal displacement of the OCT catheter. The *middle panel* demonstrates the l-mode view of the OCT pullback. The *letters A–F* indicate the OCT cross-sections that are visualized in the upper panel of the figure. In the *lower panel* of the figure the displacement of the OCT catheter is schematically depicted, with the *letters* (*A–F*) corresponding to the *letters* in the OCT cross-sections and the longitudinal view of the pullback

LCX and five in the RCA. Mean measured scaffold length was similar between LAD, LCX and RCA at all time points (P = NS), indicating that the extent of longitudinal catheter displacement was similar in the various coronary arteries. Moreover, mean scaffold length as measured in the LAD was 17 ± 2 mm at T1, 15 ± 1 mm at T2 and 17 ± 2 mm at T3, in LCX 18 ± 2 mm at T1, 16 ± 2 mm at T2, 16 ± 1 mm at T3 and in the RCA 18 ± 2 mm at T1, 17 ± 1 mm at T2 and 17 ± 1 mm at T3. All scaffolds demonstrated some difference between measured and nominal scaffold length (18 mm), indicating the presence of longitudinal FD-OCT catheter displacement. Moreover, the greatest difference between measured and nominal scaffold length was 5.2 mm, whereas the smallest difference between measured and nominal scaffold length was 0.1 mm. A schematic representation of longitudinal displacement of the OCT catheter is demonstrated in Fig. 3.

As expected from the scaffold length measurements documented above, the number of OCT cross-sections selected by method A differed between the three time points, with the greatest difference between T1 and T2 [median (IQR) was 19 (18;21) at T1, 17 (16;19) at T2 and 18 (17;19) at T3; $P < 0.01$]. Figure 4 demonstrates a 3D reconstruction of the scaffold in which repetition of the same struts (indicated in yellow) can be observed, as has been described previously [14].

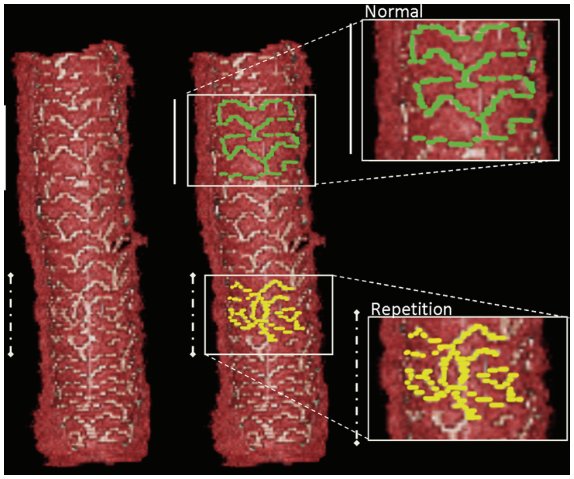

Fig. 4 Three dimensional reconstruction of one of the PLLA-based bioresorbable scaffolds. Because of forward and backward displacement of the FD-OCT catheter, repetition of the same struts (indicated in *yellow*) can be observed, as has been described previously [14]. In the *upper right* a magnification of a normal appearance of the scaffold struts can be observed (indicated in *green*), in the *lower right* a magnification of the repetition can be observed (indicated in *yellow*)

The effect of longitudinal catheter displacement

The results of the quantitative OCT global area measurements are summarized in Table 1. The greatest difference between method A and B was small and observed for the mean coverage area measurement at T3 (absolute difference 0.29 ± 0.15 mm^2). The smallest difference was observed for the mean lumen area measurement at T2 (0.02 ± 0.08 mm^2). The Bland–Altman analyses demonstrate high agreement between both methods for all mean

Table 1 Inter-method reproducibility at scaffold level

	Method A	Method B	Difference (A − B)	Relative difference	Limits of agreement		Linear regression analysis			
	Mean ± SD (mm^2)	Mean ± SD (mm^2)	Mean ± SD (mm^2)	(Method A/ method B)	Lower	Upper	Slope	Intercept	R^2	*P*
Mean lumen area										
T1	8.36 ± 0.61	8.22 ± 0.59	0.14 ± 0.11	1.02	−0.07	0.35	0.95	0.20	0.97	<0.01
T2	3.36 ± 0.79	3.38 ± 0.80	−0.02 ± 0.08	1.00	−0.18	0.14	1.00	0.01	0.99	<0.01
T3	3.16 ± 0.66	3.20 ± 0.64	−0.04 ± 0.09	0.99	−0.22	0.14	0.97	0.10	0.98	<0.01
ΔT1 − T2	5.00 ± 0.65	4.84 ± 0.69	0.16 ± 0.13	1.04	−0.10	0.42	1.04	−0.40	0.96	<0.01
ΔT2 − T3	0.20 ± 0.47	0.17 ± 0.52	0.02 ± 0.12	0.64	−0.22	0.25	1.08	−0.03	0.95	<0.01
Mean scaffold area										
T1	8.53 ± 0.62	8.25 ± 0.58	0.28 ± 0.11	1.03	0.07	0.48	0.93	0.30	0.97	<0.01
T2	7.54 ± 0.60	7.40 ± 0.61	0.14 ± 0.11	1.02	−0.07	0.35	0.99	−0.10	0.97	<0.01
T3	7.55 ± 0.71	7.38 ± 0.72	0.27 ± 0.21	1.04	−0.14	0.68	1.00	−0.30	0.92	<0.01
ΔT1 − T2	0.98 ± 0.40	0.85 ± 0.46	0.13 ± 0.13	1.27	−0.12	0.38	1.11	−0.20	0.93	<0.01
ΔT2 − T3	−0.12 ± 0.31	0.02 ± 0.28	−0.13 ± 0.23	2.76	−0.59	0.32	0.58	−0.10	0.45	<0.01
Mean coverage area										
T2	4.15 ± 0.55	4.00 ± 0.61	0.15 ± 0.17	1.04	−0.18	0.48	1.07	−0.50	0.93	<0.01
T3	4.30 ± 0.51	4.09 ± 0.48	0.29 ± 0.15	1.07	−0.01	0.58	0.88	0.20	0.91	<0.01
ΔT2 − T3	−0.16 ± 0.39	−0.05 ± 0.47	−0.12 ± 0.26	0.49	−0.62	0.39	1.00	−0.10	0.97	<0.01

Bland–Altman limits of agreement defined as mean ± 1.96 SD of absolute difference

T1 time point 1: immediately after scaffold implantation, *T2* time point 2: 3 months after scaffold implantation, *T3* time point 3: 6 months after scaffold implantation, *SD* standard deviation

area measurements at and between all time points (Figs. 5, 6, 7, 8, 9, 10). Linear regression analysis demonstrated excellent correlations with small overall differences between the two methods per time point: R^2 ranged from 0.91 to 0.99 for all mean area measurements (Table 1; Figs. 5, 7, 9). For the measurements between T1 and T2, also excellent correlations were observed: R^2 was 0.96 and 0.93 for mean lumen and scaffold area respectively. For the change in mean lumen area and mean coverage area between T2 and T3, good correlations were observed (R^2 0.95 and 0.70) and for the change in mean scaffold area between T2 and T3 a moderate correlation was observed (R^2 0.45) (Figs. 6, 8, 10).

The amount of selected cross-sections containing a side branch differed between the three time points, however, not statistically significant [median (IQR) was 2 (2;3) at T1, 2 (1;3) at T2 and 2 (1;3) at T3; $P = 0.48$].

Inter-and intra-observer reproducibility

A total of 92 OCT cross-sections per time point were included in the inter- and intra-observer analysis (Tables 2, 3, 4, 5). Bland–Altman analyses for inter-observer reproducibility demonstrated excellent agreement between both observers for all area measurements at all time points (Fig. 11). Intra-class correlation coefficients ranged from 0.89 to 1.00 at cross-sectional level and from 0.90 to 1.00 at scaffold level (Tables 2, 3). For the intra-observer reproducibility, Bland–Altman analyses demonstrated excellent agreement between the two observations for all mean area measurements at all time points (Fig. 12). Intra-class correlation coefficients ranged from 0.96 to 1.00 at cross-sectional level and from 0.95 to 1.00 at scaffold level (Tables 4, 5).

Discussion

In the present study we observed considerable variation in the imaged length of the scaffolded segment, indicating longitudinal displacement of the OCT catheter during pullback acquisition in swine treated with PLLA-based bioresorbable scaffolds. The observed catheter displacement did not affect the reliability of global quantitative OCT area measurements such as mean lumen, mean scaffold and mean coverage area. When not accounted for by the analysis method, however, imaging catheter displacement can cause considerable variation in scaffold length measurements and in the measurements of specific scaffold regions such as side branch take offs.

The presence of longitudinal displacement of the imaging catheter is a long-known pitfall of intravascular

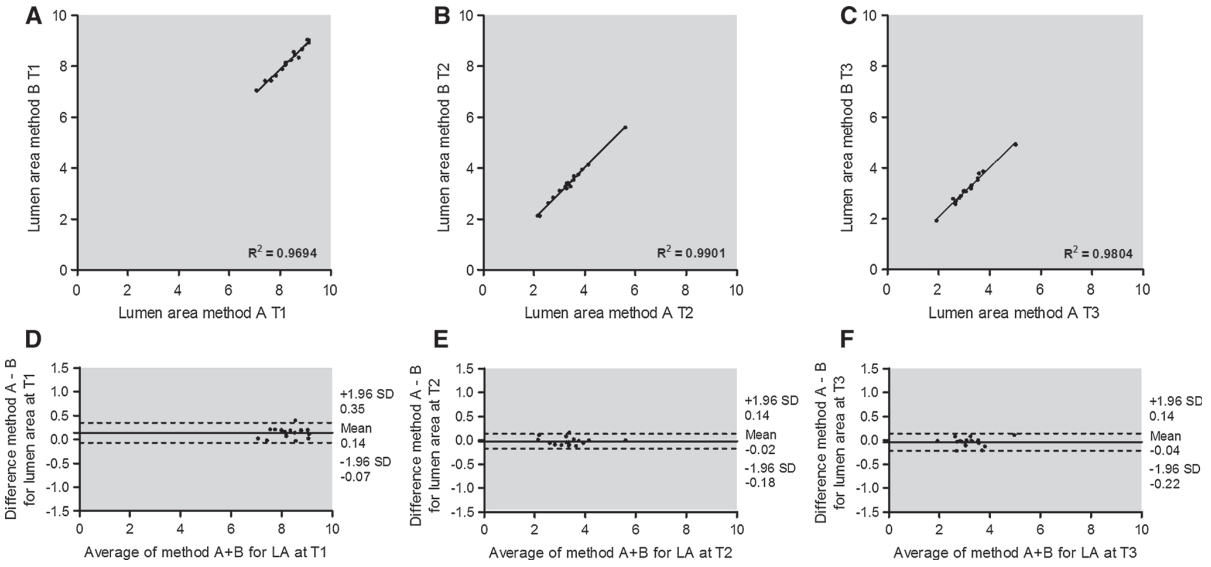

Fig. 5 Inter-method variability for lumen area (mm^2) measurements. The linear regression analysis demonstrates very high correlation between method A and B for mean lumen area (mm^2) at T1 (**a**), T2 (**b**) and T3 (**c**). The Bland–Altman plots demonstrate the inter-method variability for mean lumen area (LA; mm^2) at T1 (**d**), T2 (**e**) and T3 (**f**)

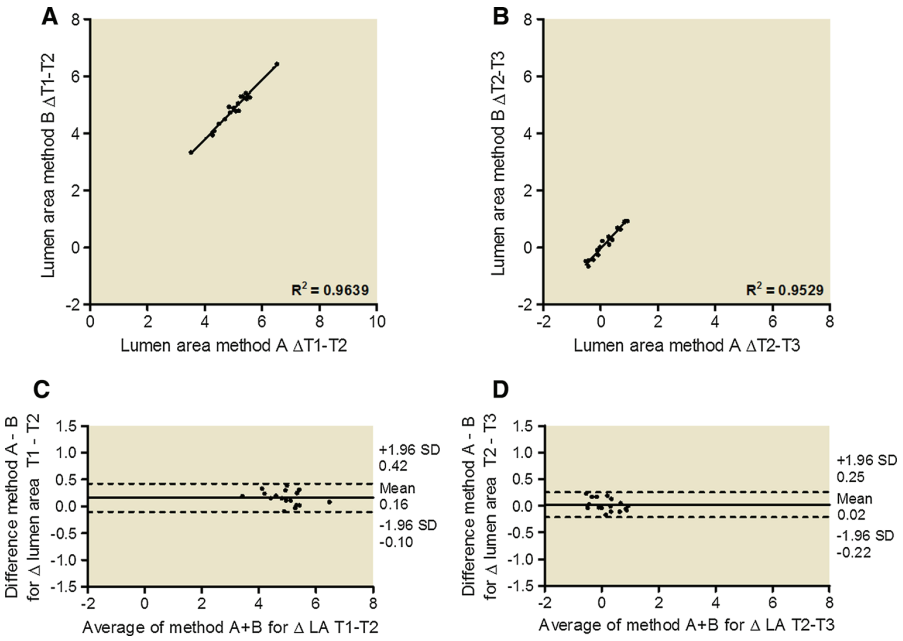

Fig. 6 Inter-method variability for the difference in mean lumen area measurements between T1 and T2 and T2 and T3. The linear regression analysis demonstrates high correlation between method A and B for the difference in mean lumen area measurement between T1 and T2 (ΔT1 − T2) (**a**), and between T2 and T3 (ΔT2 − T3) (**b**). The Bland–Altman plots demonstrate the inter-method variability for the difference in mean lumen area between T1 and T2 (ΔT1 − T2) (**c**) and T2 and T3 (ΔT2 − T3) (**d**)

imaging and can be attributed to the pullback speed and the catheter's frame acquisition rate. In studies evaluating intravascular ultrasound (IVUS)—that typically uses automated catheter pullback speeds of 0.5–1.0 mm/s and a frame rate of 10–30 frames/s [15]—the longitudinal catheter displacement has been described as a consequence of the relative slow pullback speed [16]. When there is a slow pullback speed, the catheter can be displaced during pullback acquisition due to the dynamic movement of the coronary arteries within the cardiac and respiratory cycle. Likewise, longitudinal displacement of the imaging catheter has been observed for the first generation, Time Domain (TD)-OCT catheter. TD-OCT applies higher pullback speeds (1.0–3.0 mm/s) but lower frame rates

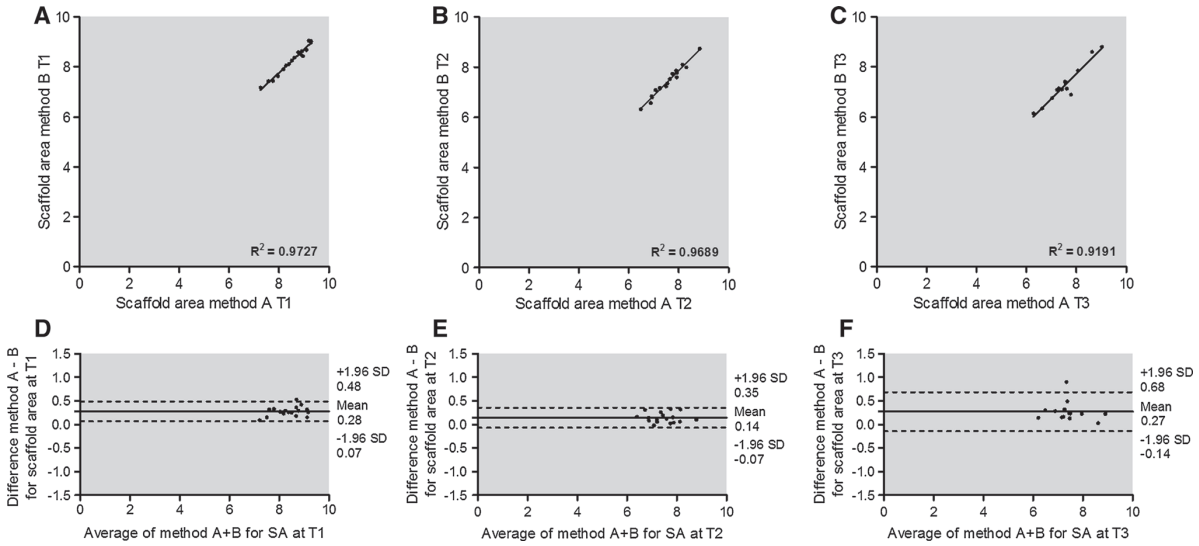

Fig. 7 Inter-method variability for scaffold area (mm^2) measurements. The linear regression analysis demonstrates very high correlation between method A and B for mean scaffold area (mm^2) at T1 (**a**), T2 (**b**), T3 (**c**). The Bland–Altman plots demonstrate the inter-method variability for mean scaffold area (SA; mm^2) at T1 (**d**), T2 (**e**) and T3 (**f**)

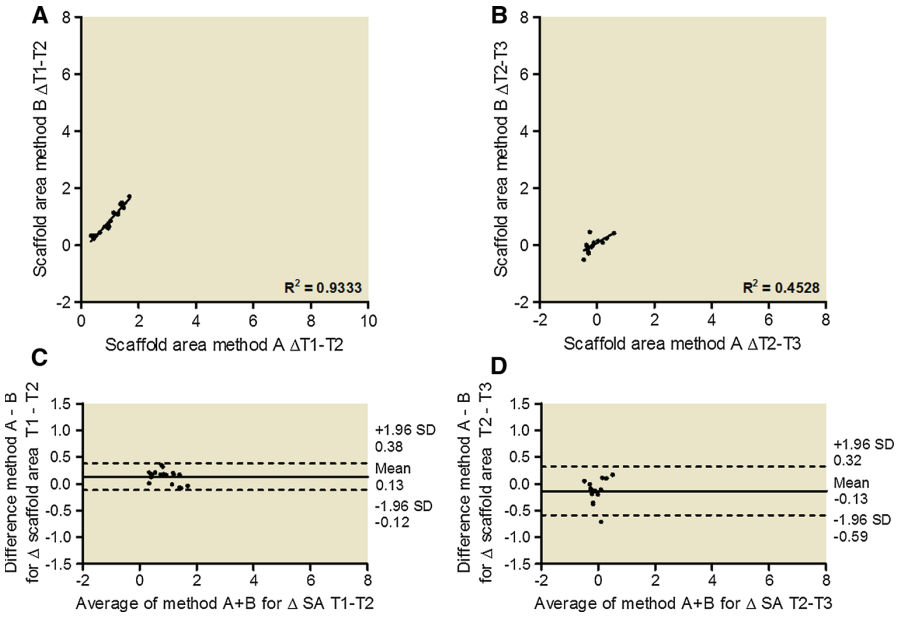

Fig. 8 Inter-method variability for the difference in mean scaffold area measurements between T1 and T2 and T2 and T3. The linear regression analysis demonstrates high correlation between method A and B for the difference in mean scaffold area measurement between T1 and T2 (ΔT1 − T2) (**a**), and between T2 and T3 (ΔT2 − T3) (**b**). The Bland–Altman plots demonstrate the inter-method variability for the difference in scaffold lumen area between T1 and T2 (ΔT1 − T2) (**c**) and T2 and T3 (ΔT2 − T3) (**d**)

(5–20 frames/s) than IVUS. Despite the higher pullback speed compared to IVUS, longitudinal catheter displacement is not alleviated. Consequently, longitudinal catheter displacement during pullback acquisition can cause difficulties interpreting serial stent or scaffold analysis data [17]. FD-OCT, evaluated in the present study, applies a faster pullback speed (20 mm/s) and frame rate (100 frames/s) than both IVUS and TD-OCT. Despite the fast data acquisition, we demonstrated the presence of considerable longitudinal catheter displacement. Scaffold length measurements differed between the various time points, with the greatest length difference between two time points corresponding to 29 % of the total scaffold length (5.2 of 18 mm total scaffold length).

Serial global lumen and scaffold area measurements were however not significantly affected by the longitudinal

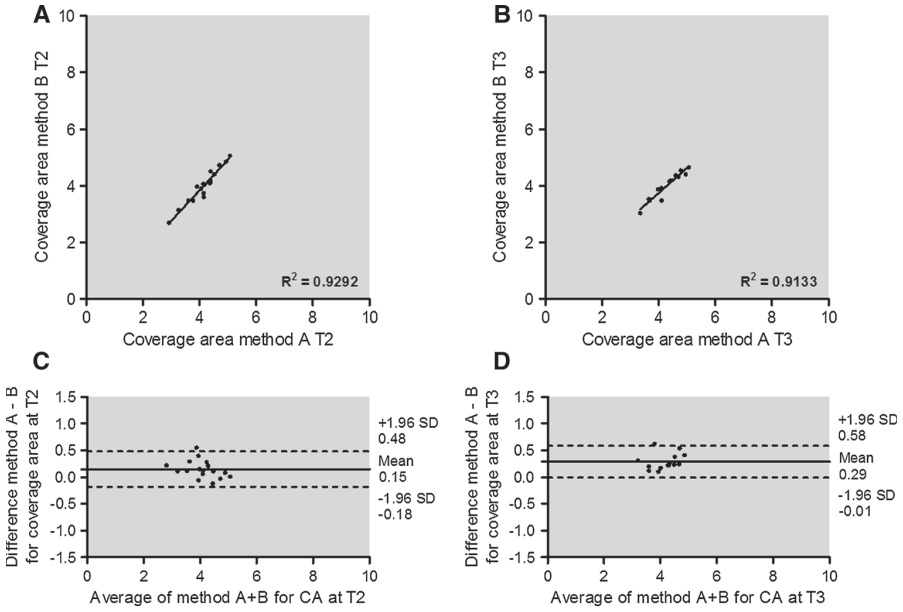

Fig. 9 Inter-method variability for coverage area (mm^2) measurements. The linear regression analysis demonstrates high correlation between method A and B for mean coverage area (mm^2) at T2 (**a**) and T3 (**b**). The Bland–Altman plots demonstrate the inter-method variability for mean coverage area (CA; mm^2) at T2 (**c**) and T3 (**d**)

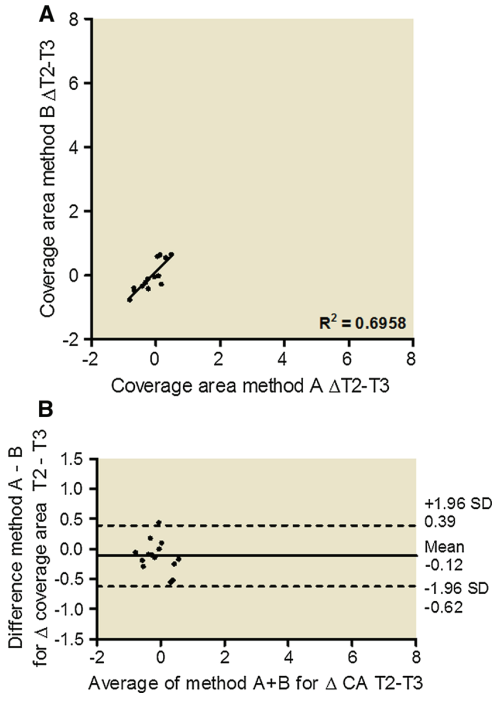

Fig. 10 Inter-method variability for the difference in mean coverage area measurements between T1 and T2 and T2 and T3. The linear regression analysis demonstrates high correlation between method A and B for the difference in mean coverage area measurement between T2 and T3 (ΔT2 − T3) (**a**). The Bland–Altman plots demonstrate the inter-method variability for the difference in mean coverage area between T2 and T3 (ΔT2 − T3) (**b**)

displacement of the FD-OCT catheter. By comparing two methods for the selection of OCT cross-sections—one commonly used method employing random selection of OCT cross-sections at the consecutive time points (method A), not taking into account the effect of longitudinal catheter displacement, and one method employing accurate co-registration of the cross-sections within the consecutive time points (method B), taking into account longitudinal displacement of the catheter—we demonstrated that there was high agreement between the methods for global in vivo quantitative area measurements. Okamura et al. examined the agreement between two consecutively acquired FD-OCT pullbacks from patients treated with elective coronary stent implantation. The ROI was determined in the two FD-OCT pullbacks, and in the corresponding ROI OCT cross-sections were selected at 1-mm longitudinal intervals, not taking into account longitudinal displacement of the FD-OCT catheter. The agreement for mean lumen and scaffold area measurements between the two consecutively acquired pullbacks was high [18]. Jamil et al. [19] evaluated the inter-study variability of FD-OCT by independently analyzing every single cross-section of two repeated pullbacks acquired from patients immediately after stent placement. Per-stent analysis demonstrated small differences between measurements for mean lumen area (relative difference 0.81 %) and mean stent area (relative difference 0.93 %), demonstrating high reproducibility of two consecutively acquired FD-OCT pullbacks. We observed a comparable high agreement between the two methods for the selection

Table 2 Inter-observer reproducibility at cross-sectional level

	Observer 1 Mean ± SD (mm^2)	Observer 2 Mean ± SD (mm^2)	Difference (Obs 1 − Obs 2) Mean ± SD (mm^2)	Relative difference (Obs1/Obs2)	ICC
Mean lumen area					
T1	8.15 ± 0.95	8.08 ± 0.93	0.07 ± 0.10	1.01	1.00
T2	3.70 ± 1.27	3.70 ± 1.27	0.00 ± 0.04	1.00	0.99
T3	3.66 ± 0.99	3.66 ± 1.00	0.00 ± 0.05	1.00	1.00
Mean scaffold area					
T1	8.18 ± 0.92	8.16 ± 0.90	0.08 ± 0.11	1.01	0.99
T2	7.45 ± 0.85	7.27 ± 0.87	0.19 ± 0.13	1.03	0.97
T3	7.53 ± 0.90	7.41 ± 0.95	0.18 ± 0.17	1.03	0.96
Mean coverage area					
T2	3.75 ± 0.61	3.52 ± 0.60	0.19 ± 0.13	1.06	0.93
T3	3.90 ± 0.52	3.72 ± 0.55	0.18 ± 0.17	1.05	0.89

ICC intra-class correlation coefficient for absolute agreement, *T1* time point 1: immediately after scaffold implantation, *T2* time point 2: 3 months after scaffold implantation, *T3* time point 3: 6 months after scaffold implantation, *Obs* observer, *SD* standard deviation

Table 3 Inter-observer reproducibility at scaffold level

	Observer 1 Mean ± SD (mm^2)	Observer 2 Mean ± SD (mm^2)	Difference (Obs 1 − Obs 2) Mean ± SD (mm^2)	Relative difference (Obs1/Obs2)	ICC
Mean lumen area					
T1	8.14 ± 0.88	8.07 ± 0.87	0.07 ± 0.04	1.01	1.00
T2	3.68 ± 1.29	3.68 ± 1.29	−0.00 ± 0.02	1.00	1.00
T3	3.65 ± 0.88	3.65 ± 0.89	−0.00 ± 0.02	1.00	1.00
Mean scaffold area					
T1	8.17 ± 0.85	8.13 ± 0.84	0.04 ± 0.08	1.01	1.00
T2	7.43 ± 0.80	7.24 ± 0.78	0.19 ± 0.06	1.03	0.97
T3	7.48 ± 0.78	7.35 ± 0.83	0.13 ± 0.09	1.02	0.98
Mean coverage area					
T2	3.76 ± 0.61	3.55 ± 0.61	0.21 ± 0.02	1.06	0.94
T3	3.90 ± 0.39	3.71 ± 0.42	0.19 ± 0.05	1.05	0.90

ICC intra-class correlation coefficient for absolute agreement, *T1* time point 1: immediately after scaffold implantation, *T2* time point 2: 3 months after scaffold implantation, *T3* time point 3: 6 months after scaffold implantation, *Obs* observer, *SD* standard deviation

Table 4 Intra-observer reproducibility at cross-sectional level

	Analysis 1 Mean ± SD (mm^2)	Analysis 2 Mean ± SD (mm^2)	Difference (An1 – An2) Mean ± SD (mm^2)	Relative difference (An1/An2)	ICC
Mean lumen area					
T1	8.15 ± 0.95	8.17 ± 0.93	−0.02 ± 0.10	1.00	0.99
T2	3.70 ± 1.27	3.70 ± 1.27	0.00 ± 0.02	1.00	1.00
T3	3.66 ± 0.99	3.66 ± 1.00	−0.01 ± 0.04	1.00	1.00
Mean scaffold area					
T1	8.18 ± 0.92	8.17 ± 0.93	0,02 ± 0.09	1.00	1.00
T2	7.45 ± 0.85	7.49 ± 0.87	−0.03 ± 0.12	1.00	0.99
T3	7.53 ± 0.90	7.62 ± 0.99	−0.09 ± 0.12	0.99	0.99
Mean coverage area					
T2	3.75 ± 0.61	3.77 ± 0.61	−0.03 ± 0.12	0.99	0.98
T3	3.90 ± 0.52	3.99 ± 0.56	−0.09 ± 0.12	0.98	0.96

ICC intra-class correlation coefficient for absolute agreement, *T1* time point 1: immediately after scaffold implantation, *T2* time point 2: 3 months after scaffold implantation, *T3* time point 3: 6 months after scaffold implantation, *An* analysis, *SD* standard deviation

of OCT cross-sections, suggesting minor influence of longitudinal catheter displacement on serial global dimension measurements. The differences between measurements for mean lumen and mean stent area assessed by Jamil et al. were however slightly smaller than what we observed, suggesting that a smaller interval of analysis may reduce the effect of longitudinal catheter displacement.

We furthermore examined the impact of longitudinal catheter displacement on the analysis of specific scaffold regions. The PLLA-based bioresorbable scaffolds are

Table 5 Intra-observer reproducibility at scaffold level

	Analysis 1 Mean ± SD (mm^2)	Analysis 2 Mean ± SD (mm^2)	Difference (An1 − An2) Mean ± SD (mm^2)	Relative difference (An1/An2)	ICC
Mean lumen area					
T1	8.14 ± 0.88	8.16 ± 0.86	−0.02 ± 0.02	1.00	1.00
T2	3.68 ± 1.29	3.69 ± 1.29	−0.00 ± 0.01	1.00	1.00
T3	3.65 ± 0.88	3.66 ± 0.89	−0.01 ± 0.01	1.00	1.00
Mean scaffold area					
T1	8.17 ± 0.85	8.16 ± 0.86	0.02 ± 0.03	1.00	1.00
T2	7.43 ± 0.80	7.47 ± 0.82	−0.04 ± 0.04	0.99	1.00
T3	7.48 ± 0.78	7.59 ± 0.89	−0.11 ± 0.11	0.99	0.99
Mean coverage area					
T2	3.76 ± 0.61	3.79 ± 0.61	−0.03 ± 0.05	0.99	1.00
T3	3.90 ± 0.39	3.99 ± 0.43	0.09 ± 0.12	0.98	0.95

ICC intra-class correlation coefficient for absolute agreement, *T1* time point 1: immediately after scaffold implantation, *T2* time point 2: 3 months after scaffold implantation, *T3* time point 3: 6 months after scaffold implantation, *An* analysis, *SD* standard deviation

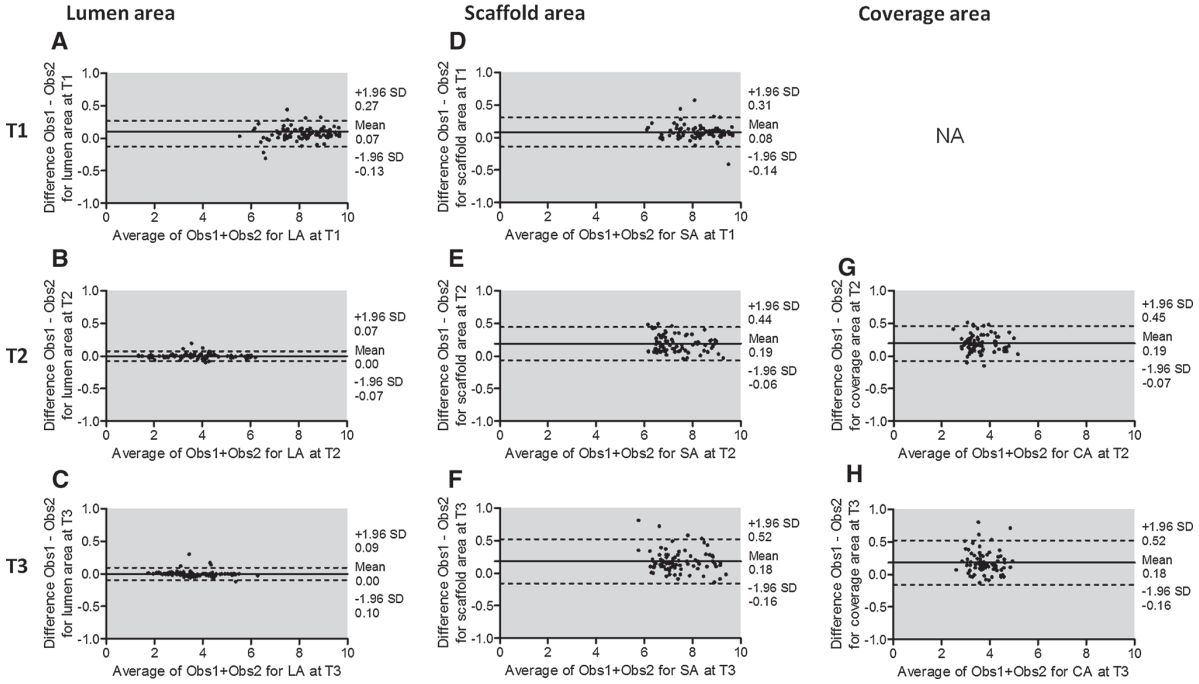

Fig. 11 Inter-observer reproducibility. Bland–Altman plots for the inter-observer variability for mean lumen (**a**–**c**), mean scaffold (**d**–**f**) and mean coverage area (**g**, **h**) at the various time points. *T* time point, *Obs* observer, *LA* lumen area (mm^2), *SA* scaffold area (mm^2), *CA* coverage area (mm^2), *SD* standard deviation

increasingly used in clinical practice outside of controlled studies, resulting in the treatment of patients with more complex lesions, including treatment of longer lesions and treatment with overlapping scaffolds [20]. The accurate evaluation of specific scaffold regions is therefore becoming increasingly important. In the present study, the amount of OCT cross-sections containing a side-branch selected by method A differed, however not statistically significant, between the time points: from T1 to T2, the number of selected OCT cross-sections containing a side branch decreased, whereas from T2 to T3, the number of selected OCT cross-sections increased. Important to note is that the reduction in OCT cross-sections containing a side branch from T1 to T2 could be attributed to neointimal growth at T2, possibly resulting in a diameter reduction of the side branch opening [21]. From T2 to T3, however, the number of OCT cross-sections containing a side branch increased, suggesting that longitudinal catheter displacement can truly affect the assessment of specific scaffold regions when accurate matching of corresponding cross-

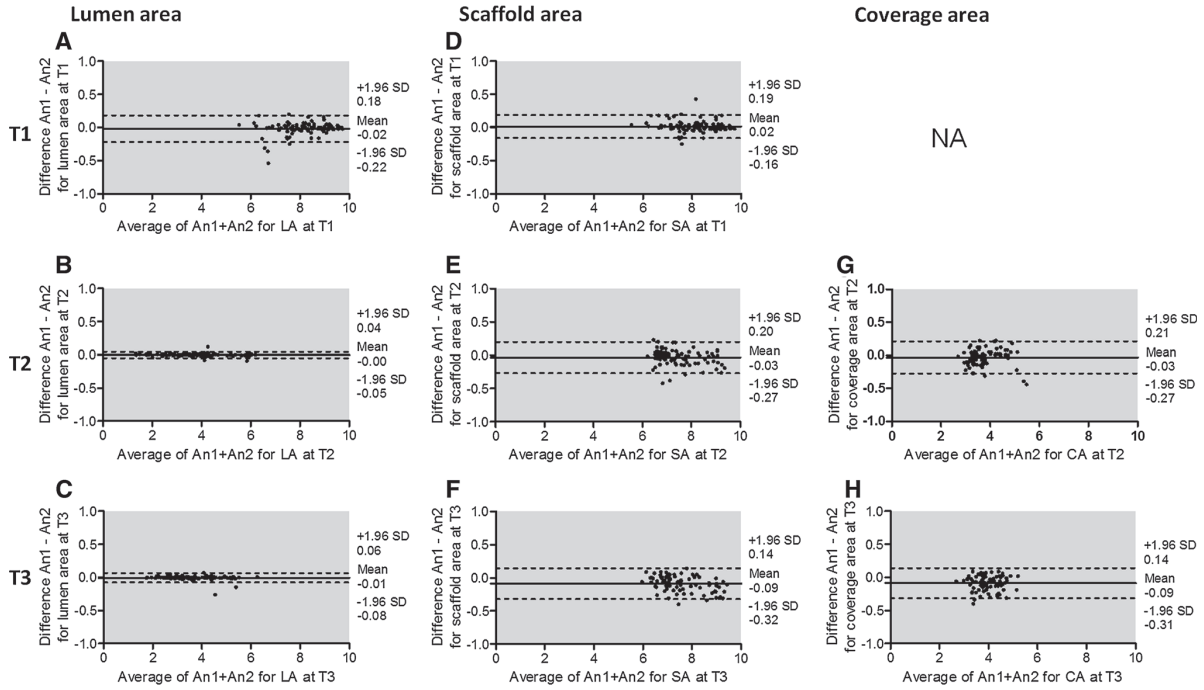

Fig. 12 Intra-observer reproducibility. Bland–Altman plots for the intra-observer variability for mean lumen (**a**–**c**), mean scaffold (**d**–**f**) and mean coverage area (**g**, **h**) at the various time points. *T* time point, *An* analysis, *LA* lumen area (mm^2), *SA* scaffold area (mm^2), *CA* coverage area (mm^2), *SD* standard deviation

sections is not performed. More importantly, the fact that the number of selected OCT cross-sections containing a side branch differed between the several time points suggests that for the analysis of specific scaffold regions either a smaller interval of analysis may be beneficial, as has been eluted to by Mehanna et al. [22], who suggested that analysis of specific stent regions should be performed by analyzing all frames, or an analysis method such as method B should be considered.

Important to note is the shortcoming to reconstruct three-dimensional (3D) images when longitudinal catheter displacement is present. The accurate reconstruction of the 3D vessel structure including the scaffold, could enable a more comprehensive assessment of scaffold strut coverage, apposition and side-branch jailing [23, 24]. A study assessing the impact of cardiac motion artefacts on 3D reconstructions of FD-OCT pullbacks demonstrated that faster pullback acquisition with higher frame rates reduces the amount of artefacts caused by cardiac motion [14]. The development of high-speed OCT imaging with faster pullback speeds and higher frame rates might therefore improve the understanding of scaffold strut coverage, apposition and side-branch jailing because of the ability to accurately reconstruct the volumetric 3D vessel including the scaffold [25].

Inter- and intra-observer reproducibility of quantitative OCT area measurements

The present study demonstrates that FD-OCT allows for the serial analysis of PLLA-based bioresorbable scaffolds in a highly reproducible way. The inter- and intra-observer differences on cross-sectional and scaffold level were low (Tables 2, 3, 4, 5). Likewise, Gomez-Lara et al. [26] reported excellent inter- and intra-observer reproducibility of OCT in assessing bioresorbable vascular scaffolds (ICC for quantitative OCT measurements >0.97). Gonzalo et al. [27] reported on inter- and intra-observer differences in patients undergoing intracoronary OCT after treatment with sirolimus and biolimus-eluting stents. They, similar to what we observed, demonstrated low inter- and intra-observer differences for lumen area measurements and slightly greater for stent area measurements. Okamura et al. evaluated inter- and intra-observer correlation coefficients for lumen area measurements in non-stented coronary arteries of swine. They demonstrated excellent (>0.75) intra-class correlation coefficients, similar to the intra-class correlation coefficients documented in the present study (Tables 2, 3, 4, 5) [14]. Concerning scaffold area, the inter-observer analysis of the present study demonstrated low differences for scaffold area at T1, and

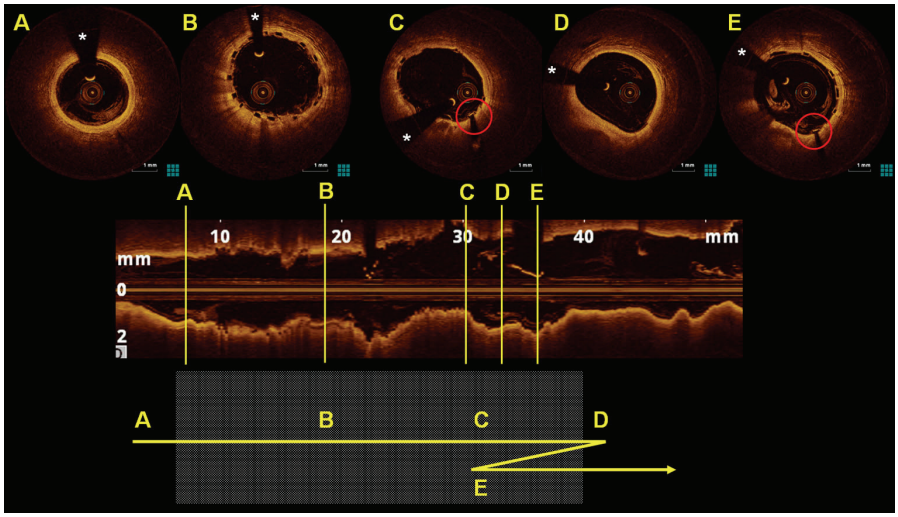

Fig. 13 Representation of longitudinal FD-OCT catheter displacement in a patient. The *middle panel* demonstrates the l-mode of the OCT pullback. The *letters A–E* indicate the OCT cross-sections that are visualized in the *upper panel* of the figure. In the *lower panel* of the figure the displacement of the OCT catheter is schematically depicted, with the *letters* (*A–E*) corresponding to the *letters* in the OCT cross-sections and the longitudinal view of the pullback. In OCT cross-sections **c** and **e** the proximal marker of the scaffold is visible (*red circle*). The *asterisk* indicates the shadow artefact caused by the guide wire

slightly greater differences at T2 and T3. The intra-observer analysis demonstrated similar results for scaffold area, with the lowest intra-observer variability at T1 and slightly greater variability at T2 and T3. This finding is not surprising as the use of a semi-automatic contour detection for lumen area helped diminish inter- and intra-observer reproducibility, whereas for scaffold area measurements at follow-up, the manual tracing of the contours and the relatively high amount of coverage could be associated with higher variability. Notably, the coverage observed in the present study was relatively high (coverage area >2 mm^2), potentially leading to the inability to segment the scaffold area because of the limited penetration depth of OCT.

Limitations

Swine typically have a higher heart rate compared to humans [28]—the average heart rate of the anesthetized swine in the present study was 109 ± 28 beats/min—resulting in a possibly greater longitudinal displacement of the OCT catheter during pullback acquisition. A previously published study that evaluated the three-dimensional motion of coronary arteries by cine-magnetic resonance imaging (MRI), however, demonstrated that the swine RCA, LAD and LCX displacements appear qualitatively similar to those seen in humans, despite differing heart rates [29]. Furthermore, the presence of longitudinal displacement of the OCT catheter has also been described in humans (Fig. 13), limiting the accurate reconstruction of the 3D vessel structure [30]. In the electronic supplementary material an angiogram and OCT pullback of longitudinal displacement of the FD-OCT catheter in a patient is demonstrated (Online Resource 1 and 2).

Off-line, manual tracing of scaffold areas after coronary scaffolding is feasible for experienced observers with acceptable reproducibility. It is however time consuming. In the present study, semi-automatic contour detection of the lumen area demonstrated advantages for reproducibility of the data. For scaffold contour and coverage area measurements we demonstrated a slightly higher inter- and intra-observer variability, possibly due to the lack of algorithms for the automatic detection of polymeric scaffold struts. For the automatic detection of metallic stent struts, algorithms have been developed that show high accuracy and high inter-observer agreement [31, 32]. Further development of contour detection algorithms for the detection of polymeric scaffold struts by OCT might help eliminating the remaining small observer-related variability observed in the present study.

Conclusion

Considerable longitudinal displacement of the FD-OCT catheter was observed, diminishing the number of truly anatomically matching cross-sections in serial investigations. The longitudinal catheter displacement, however, did not affect global dimension measurements such as mean lumen area and mean scaffold area.

Conflict of interest None.

References

1. Huang D, Swanson EA, Lin CP et al (1991) Optical coherence tomography. Science 254(5035):1178–1181
2. Regar E, Schaar JA, Mont E, Virmani R, Serruys PW (2003) Optical coherence tomography. Cardiovasc Radiat Med 4(4):198–204. doi:10.1016/j.carrad.2003.12.003
3. Choma M, Sarunic M, Yang C, Izatt J (2003) Sensitivity advantage of swept source and Fourier domain optical coherence tomography. Opt Express 11(18):2183–2189
4. Yun SH, Tearney GJ, Vakoc BJ et al (2006) Comprehensive volumetric optical microscopy in vivo. Nat Med 12(12):1429–1433. doi:10.1038/nm1450
5. Liu B, Brezinski ME (2007) Theoretical and practical considerations on detection performance of time domain, Fourier domain, and swept source optical coherence tomography. J Biomed Opt 12(4):044007. doi:10.1117/1.2753410
6. van Ditzhuijzen NS, van den Heuvel M, Sorop O et al (2011) Invasive coronary imaging in animal models of atherosclerosis. Neth Heart J 19(10):442–446. doi:10.1007/s12471-011-0187-0
7. Ormiston JA, Serruys PW, Regar E et al (2008) A bioabsorbable everolimus-eluting coronary stent system for patients with single de-novo coronary artery lesions (ABSORB): a prospective open-label trial. Lancet 371(9616):899–907. doi:10.1016/S0140-6736(08)60415-8
8. Serruys PW, Ormiston JA, Onuma Y et al (2009) A bioabsorbable everolimus-eluting coronary stent system (ABSORB): 2-year outcomes and results from multiple imaging methods. Lancet 373(9667):897–910. doi:10.1016/S0140-6736(09)60325-1
9. Serruys PW, Onuma Y, Ormiston JA et al (2010) Evaluation of the second generation of a bioresorbable everolimus drug-eluting vascular scaffold for treatment of de novo coronary artery stenosis: six-month clinical and imaging outcomes. Circulation 122(22):2301–2312. doi:10.1161/CIRCULATIONAHA.110.970772
10. Hamers R, Bruining N, Knook M, Sabate M, Roelandt JRTC (2001) A novel approach to quantitative analysis of intravascular ultrasound images. Comput Cardiol (28)589–592
11. Brugaletta S, Radu MD, Garcia-Garcia HM et al (2012) Circumferential evaluation of the neointima by optical coherence tomography after ABSORB bioresorbable vascular scaffold implantation: can the scaffold cap the plaque? Atherosclerosis 221(1):106–112. doi:10.1016/j.atherosclerosis.2011.12.008
12. Bland JM, Altman DG (1986) Statistical methods for assessing agreement between two methods of clinical measurement. Lancet 1(8476):307–310
13. Haber M, Barnhart HX (2006) Coefficients of agreement for fixed observers. Stat Methods Med Res 15(3):255–271
14. Okamura T, Onuma Y, Garcia-Garcia HM, Bruining N, Serruys PW (2012) High-speed intracoronary optical frequency domain imaging: implications for three-dimensional reconstruction and quantitative analysis. EuroIntervention 7(10):1216–1226. doi:10.4244/EIJV7I10A194
15. Regar E (2011) Invasive imaging technologies: can we reconcile light and sound? J Cardiovasc Med 12(8):562–570
16. Arbab-Zadeh A, DeMaria AN, Penny WF, Russo RJ, Kimura BJ, Bhargava V (1999) Axial movement of the intravascular ultrasound probe during the cardiac cycle: implications for three-dimensional reconstruction and measurements of coronary dimensions. Am Heart J 138(5 Pt 1):865–872
17. Sihan K, Botha C, Post F et al (2011) Retrospective image-based gating of intracoronary optical coherence tomography: implications for quantitative analysis. EuroIntervention 6(9):1098–1103. doi:10.4244/EIJV6I9A191
18. Okamura T, Garg S, Gutierrez-Chico JL et al (2010) In vivo evaluation of stent strut distribution patterns in the bioabsorbable everolimus-eluting device: an OCT ad hoc analysis of the revision 1.0 and revision 1.1 stent design in the ABSORB clinical trial. EuroIntervention 5(8):932–938
19. Jamil Z, Tearney G, Bruining N et al (2013) Interstudy reproducibility of the second generation, Fourier domain optical coherence tomography in patients with coronary artery disease and comparison with intravascular ultrasound: a study applying automated contour detection. Int J Cardiovasc Imaging 29(1):39–51. doi:10.1007/s10554-012-0067-8
20. Farooq V, Gogas BD, Okamura T et al (2013) Three-dimensional optical frequency domain imaging in conventional percutaneous coronary intervention: the potential for clinical application. Eur Heart J 34(12):875–885
21. Kyono H, Guagliumi G, Sirbu V et al (2010) Optical coherence tomography (OCT) strut-level analysis of drug-eluting stents (DES) in human coronary bifurcations. EuroIntervention 6(1):69–77
22. Mehanna EA, Attizzani GF, Kyono H, Hake M, Bezerra HG (2011) Assessment of coronary stent by optical coherence tomography, methodology and definitions. Int J Cardiovasc Imaging 27(2):259–269
23. Farooq V, Serruys PW, Heo JH et al (2013) Intracoronary optical coherence tomography and histology of overlapping everolimus-eluting bioresorbable vascular scaffolds in a porcine coronary artery model: the potential implications for clinical practice. JACC 6(5):523–532
24. Karanasos A, Tu S, van der Linden M, van Weenen S, Ligthart J, Regar E (2012) Online 3-dimensional rendering of optical coherence tomography images for the assessment of bifurcation intervention. Can J Cardiol 28(6):759e751–759e753
25. Wang T, Wieser W, Springeling G et al (2013) Intravascular optical coherence tomography imaging at 3200 frames per second. Opt Lett 38(10):1715–1717
26. Gomez-Lara J, Brugaletta S, Diletti R et al (2011) Agreement and reproducibility of gray-scale intravascular ultrasound and optical coherence tomography for the analysis of the bioresorbable vascular scaffold. Catheter Cardiovasc Interv 79(6):890–902
27. Gonzalo N, Garcia-Garcia HM, Serruys PW et al (2009) Reproducibility of quantitative optical coherence tomography for stent analysis. EuroIntervention 5(2):224–232
28. van den Heuvel M, Sorop O, Koopmans SJ et al (2012) Coronary microvascular dysfunction in a porcine model of early atherosclerosis and diabetes. Am J Physiol Heart Circ Physiol 302(1):H85–H94. doi:10.1152/ajpheart.00311.2011
29. Schmidt EJ, Yoneyama R, Dumoulin CL et al (2009) 3D coronary motion tracking in swine models with MR tracking catheters. J Magn Reson Imaging 29(1):86–98
30. Ha J, Yoo H, Tearney GJ, Bouma BE (2012) Compensation of motion artifacts in intracoronary optical frequency domain imaging and optical coherence tomography. Int J Cardiovasc Imaging 28(6):1299–1304. doi:10.1007/s10554-011-9953-8
31. Wang A, Eggermont J, Dekker N et al (2013) Automatic stent strut detection in intravascular optical coherence tomographic pullback runs. Int J Cardiovasc Imaging 29(1):29–38. doi:10.1007/s10554-012-0064-y
32. Xu C, Schmitt JM, Akasaka T, Kubo T, Huang K (2011) Automatic detection of stent struts with thick neointimal growth in intravascular optical coherence tomography image sequences. Phys Med Biol 56(20):6665–6675. doi:10.1088/0031-9155/56/20/010

Chapter 2.2

Quantification of fibrous cap thickness in intracoronary optical coherence tomography with a contour segmentation method based on dynamic programming

Zahnd G, **Karanasos A**, van Soest G, Regar E, Niessen W, Gijsen F, van Walsum T

Int J Comput Assist Radiol Surg 2015 Sep;10(9):1383-94.

Quantification of fibrous cap thickness in intracoronary optical coherence tomography with a contour segmentation method based on dynamic programming

Guillaume Zahnd · Antonios Karanasos · Gijs van Soest · Evelyn Regar · Wiro Niessen · Frank Gijsen · Theo van Walsum

Received: 12 December 2014 / Accepted: 13 February 2015

Abstract
Objectives Fibrous cap thickness is the most critical component of plaque stability. Therefore, in vivo quantification of cap thickness could yield valuable information for estimating the risk of plaque rupture. In the context of preoperative planning and perioperative decision making, intracoronary optical coherence tomography imaging can provide a very detailed characterization of the arterial wall structure. However, visual interpretation of the images is laborious, subject to variability, and therefore not always sufficiently reliable for immediate decision of treatment.
Methods A novel semiautomatic segmentation method to quantify coronary fibrous cap thickness in optical coherence tomography is introduced. To cope with the most challenging issue when estimating cap thickness (namely the diffuse appearance of the anatomical abluminal interface to be detected), the proposed method is based on a robust dynamic programming framework using a geometrical a priori. To determine the optimal parameter settings, a training phase was conducted on 10 patients.
Results Validated on a dataset of 179 images from 21 patients, the present framework could successfully extract the fibrous cap contours. When assessing minimal cap thickness, segmentation results from the proposed method were in good agreement with the reference tracings performed by a medical expert (mean absolute error and standard deviation of $22 \pm 18\,\mu m$, $R = .73$) and were similar to inter-observer reproducibility ($21 \pm 19\,\mu m$, $R = .74$), while being significantly faster and fully reproducible.
Conclusion The proposed framework demonstrated promising performances and could potentially be used for online identification of high-risk plaques.

Keywords Coronary artery · Optical coherence tomography · Interventional imaging · Thin-cap fibroatheroma · Contour segmentation · Dynamic programming · Preoperative planning

G. Zahnd (✉) · W. Niessen · T. van Walsum
Biomedical Imaging Group Rotterdam, Departments of Radiology and Medical Informatics, Erasmus Medical Center, P.O. Box 2040, 3000 CA Rotterdam, The Netherlands
e-mail: g.zahnd@erasmusmc.nl

A. Karanasos · E. Regar
Department of Interventional Cardiology, Thorax Center, Erasmus MC, Rotterdam, The Netherlands

G. van Soest · F. Gijsen
Department of Biomedical Engineering, Thorax Center, Erasmus MC, Rotterdam, The Netherlands

Introduction

Coronary artery disease is the most common cause of human mortality and morbidity in industrialized countries. Acute coronary syndrome (ACS), the most severe manifestation of atherosclerotic disease, is principally caused by acute coronary thrombosis, which is mainly provoked by plaque rupture [17]. The morphological characteristics of such plaques that are prone to rupture (also dubbed "high-risk" or "vulnerable" plaques) are (1) a large lipid necrotic core, (2) an overlying thin fibrous cap, and (3) dense macrophage infiltration (Fig. 1a) [4]. These plaques are also known as thin-cap fibroatheromas (TCFAs) and are considered the precursor phenotype of plaque rupture. The most critical component of plaque stability is fibrous cap thickness, i.e., thinner caps being more prone to rupture than thicker caps, and the threshold of $65\,\mu m$ has been widely adopted to identify high-risk lesions [11]. Accordingly, identification

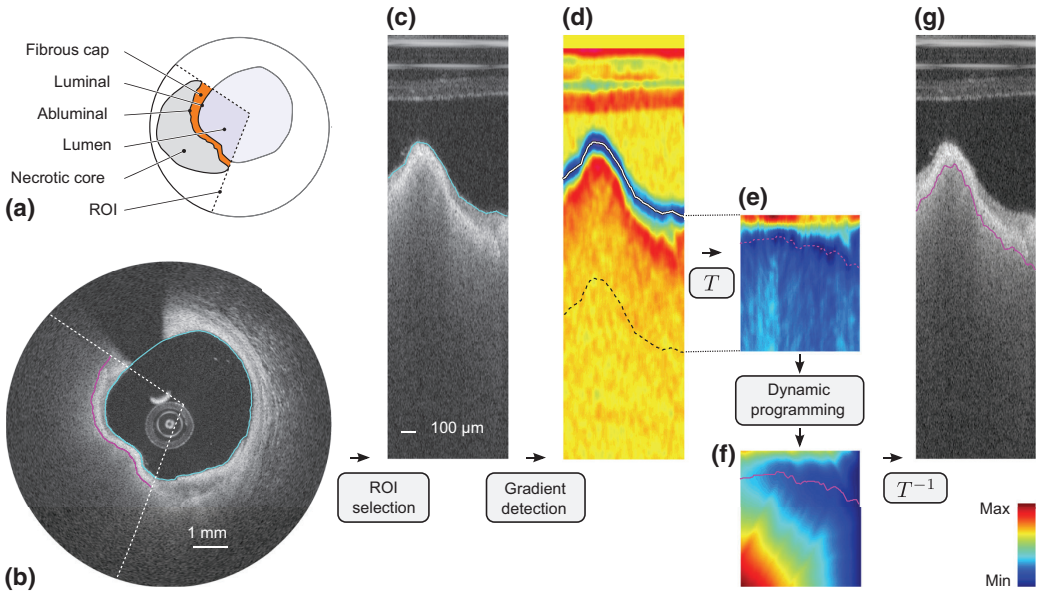

Fig. 1 Segmentation framework. **a** Cartoon depicting the region of interest (ROI, *dashed lines*) encompassing the fibrous cap. **b** OCT image of an in vivo human coronary artery, in Cartesian coordinates, with the resulting luminal (*cyan line*) and abluminal (*magenta line*) segmentation contours. **c** ROI in polar coordinates, with the luminal contour (*cyan line*). **d** Gradient image I_G. **e** Transformed cost image $\mathcal{C}_T$. **f** Cumulated cost $\mathbb{C}$, with the optimal path (*magenta line*). **g** Resulting abluminal segmentation contour

of vulnerable plaques could potentially guide appropriate surgical treatments such as percutaneous coronary intervention (e.g., balloon angioplasty or stent placement) prior to the occurrence of an event. Therefore, in vivo quantification of fibrous cap thickness represents a major clinical challenge.

Intravascular optical coherence tomography (OCT) is a catheter-based imaging modality that enables tissues to be visualized in vivo at a near-histology resolution (10–20 µm) and in a minimally invasive way [3]. In a similar fashion as intravascular ultrasound, the inner circumference of the vessel is investigated by the probe spinning along its axis while being pulled back. At each angular step, a so-called A-line signal is acquired via the emission and reception of near-infrared light (center wavelength of 1280–1350 nm). A stack of consecutive cross-sectional images along the length of the assessed artery segment is then reconstructed by converting the intensity and echo time of all A-lines into a gray-scale representation (Fig. 1b). The very high spatial resolution of OCT enables an accurate characterization of the structure of the most superficial layers of the arterial wall and can indicate the degree of subclinical atherosclerotic lesion formation [14]. Moreover, OCT is currently the only in vivo imaging modality with which fibrous cap thickness, the most critical component of plaque stability, can be assessed accurately [10]. Therefore, OCT can potentially be used for in vivo identification of high-risk plaques.

Although OCT images are acquired online during intervention, fibrous cap thickness quantification is currently performed manually offline [2,14]. The two major drawbacks that hinder such manual image analysis are (1) the procedure is cumbersome and time-consuming, and (2) results are subject to a certain degree of variability between different analysts [9,10]. Moreover, segmentation of the fibrous cap abluminal interface is a challenging task, as fibroatheromas consist of progressively unraveling tissues and are visualized in OCT as signal-poor regions with diffuse contours and high signal attenuation (Fig. 1a,b) [14]. Therefore, the clinical need of immediate and reliable information is not fully met by current procedures based on manual image analysis.

Aiming to provide reliable and quantified information during OCT analysis in the intervention room, various (semi)automated computerized methods have recently been proposed. The attenuation coefficient of the backscattered light has been used in several classification-based approaches [12,16,20]. These methods were successfully used to identify and locate different types of tissues (i.e., healthy wall sections, lipid, calcific and fibrous tissues). Nevertheless, such techniques are not devised to provide information regarding the actual delineation of anatomical interfaces and could not be used to assess fibrous cap thickness. A seminal

study was proposed to specifically assess fibrous cap thickness [19]. This method, based on contour segmentation by means of dynamic programming, was applied to extract both luminal and abluminal interfaces of the fibroatheromas and could quantify cap thickness. However, since this method did not exploit geometrical a priori features, results could have potentially been hindered in images with an eccentric catheter position within the lumen. Another semiautomatic method was introduced to identify the different tissue types and segment the wall layers [5]. In this approach, contour segmentation was based on intensity thresholding. Nevertheless, although the results of this study look promising, fibrous cap thickness was not investigated per se.

The present study aims at introducing and evaluating a framework designed to quantify fibrous cap thickness of fibroatheromas in intracoronary OCT. The principal contribution of this work is a robust contour segmentation method devised to extract the fuzzy abluminal interface of the fibrous cap. This novel framework is based on a dynamic programming approach that previously showed successful results on the common carotid artery wall in B-mode ultrasound [24]. The accuracy of the present method was validated in a set of 179 cross-sectional OCT images acquired in vivo from 21 different patients and demonstrated a similar accuracy compared to the tracings manually performed by two experienced analysts.

Materials and methods

The present segmentation framework is based on three principal phases, (1) a manual initialization aiming to indicate the presence of the fibrous cap to be analyzed, (2) the automatic extraction of the luminal interface in the objective to localize the wall contour, and (3) the automatic extraction of the abluminal interface, which is subsequently exploited to assess the actual cap thickness. An overview of the method is presented in Fig. 1. The outline of this section is the following. First, we introduce a contour segmentation scheme based on dynamic programming, which is exploited in the phases (2) and (3) of our framework. Then, we detail the three principal phases of our framework.

Dynamic programming

Dynamic programming is an efficient method to find the globally optimal solution in combinatory analysis [1]. In the present context, contour segmentation is performed in the polar domain. Given an image I, the anatomical interface to be extracted corresponds to a curve running from the left to the right border of the image, as depicted in Fig. 1c. We thus address the issue of determining, among all the potential candidate contours, the one that best describes the actual (1) location and (2) shape (i.e., smoothness) of the anatomical interface. Toward this objective, we propose a specific implementation of a dynamic programming framework based on front propagation [6].

Cost function

Since the anatomical interfaces to be extracted are located on regions of the image showing a strong intensity transition, the first step consists in locally enhancing the vertical intensity gradient of the image. One should notice that this transition is positive for the luminal interface (i.e., from dark lumen to bright tissues) and negative for the abluminal interface (i.e., from bright fibrous tissues to dark lipid pool), as depicted in Fig. 1c,d. The gradient image I_G is then built according to:

$$I_G = \pm G' * I, \tag{1}$$

with $(*)$ the convolution operator and G' the first derivative of a Gaussian function of standard deviation σ. The $\pm$ sign corresponds to the gradient orientation and is determined according to the processed interface, namely it is positive for the luminal contour and negative for the abluminal contour. Finally, a cost function $\mathcal{C}$ is built such as:

$$\mathcal{C} = \mathcal{N}_{[0,1]}(-I_G), \tag{2}$$

with $\mathcal{N}_{[0,1]}$ representing the normalization of a set of values to the positive interval $[0, 1]$ (viz.: the set is first linearly scaled in such way that the minimum value becomes equal to zero, and then the set is divided by the maximum value). In this image $\mathcal{C}$, the points most likely to represent the location of the analyzed interface correspond to the points with the lowest cost (Fig. 1e).

Front propagation

We now present a dynamic programming strategy to determine the path that runs in the cost image $\mathcal{C}$ from left-to-right with the minimum cumulated cost $\mathbb{C}$. A schematic representation of this front propagation approach is displayed in Fig. 2. The proposed approach extends a previously proposed method [23,24] and takes into account both the image feature (i.e., strong intensity gradient locally corresponding to a low cost in $\mathcal{C}$) and a geometrical constraint (i.e., the shape a priori that describes a smooth structure). Therefore, high cost values as well as vertical displacement are penalized when generating the cumulated cost function $\mathbb{C}$, as detailed in Eq. 3 (Fig. 1f).

$$\mathbb{C}(r, \theta + 1) = \min_{d_r \in \{-N, \ldots 0, \ldots N\}} \Big\{ \mathbb{C}(r + d_r, \theta) + \big(\mathcal{C}(r, \theta + 1) + \mathcal{C}(r + d_r, \theta)\big) \cdot \big(1 + \alpha \cdot d_r^{\beta}\big) \Big\}, \tag{3}$$

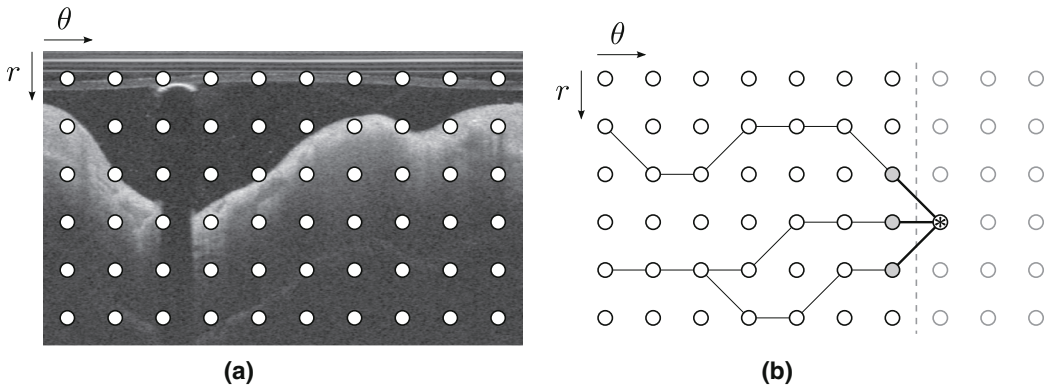

Fig. 2 Schematic representation of the front propagation scheme, corresponding to the panel (f) in Fig. 1. **a** Original polar image, with the pixels represented by the *nodes* (in this example, the layout is coarse for improved visibility). **b** Left-to-right front propagation, with the current location of the front indicated by the *vertical dashed line*. The current node is indicated by an *asterisk*, and the connected gray nodes correspond to the set of potential neighbors. In this example, the number $2N+1$ of horizontally reachable neighbors is equal to 3. The *black lines* connecting the nodes represent the successive backtracking steps from a given node to the left border of the image. Please note that in the case of segmenting the luminal interface, the nodes of the upper row correspond to the top of the polar image (as shown in this example), whereas in the case of the segmenting the abluminal interface, the nodes of the upper row correspond to the luminal interface

with (r, θ) the vertical and horizontal coordinates, d_r the vertical displacement of the path between two consecutive points, and $2N+1$ the number of reachable neighbors. The smoothness of the path is ruled by the positive parameters α and β. More specifically, the overall flexibility of the path is controlled by α (i.e., small α values enable vertical transitions of the path, and large α values favor long horizontal plateaus), and the roughness of the path is controlled by β (i.e., small β values yield contours that are locally spiky, and large β values impose smooth contours).

Prior to computation, the left column of $\mathbb{C}$ (i.e., $\theta = 1$) is initialized to zero: in this implementation, each node on the left border acts as a seed and is a potential starting point for the final optimal path. It is also noteworthy that the weight of each candidate link depends on the cost of the edge connecting the currently evaluated node with the candidate node (viz.: $\mathcal{C}(r, \theta+1)+\mathcal{C}(r+d_r, \theta)$ in Eq. 3), rather than the cost of the current node alone (viz.: $\mathcal{C}(r, \theta+1)$). Therefore, this implementation is independent of the direction (i.e., left-to-right or right-to-left) of the front propagation.

Back tracking

In the objective to extract the globally optimal path, a backtracking scheme is adopted. Since $\mathbb{C}$ is constructed using a penalty that depends of the vertical distance between the nodes (Eq. 3), a classical gradient descent in $\mathbb{C}$ cannot be performed to extract the minimal cost path. Instead, during the previously described propagation of the front, for each node $\mathcal{C}(r, \theta+1)$, neighboring information is memorized by storing the vertical coordinate $r+dr$ of the best candidate node $\mathcal{C}(r+dr, \theta)$, as shown in Fig. 2. Once the cumulated cost function $\mathbb{C}$ is entirely built, the ending point of the path is determined by the node with the minimal cumulated cost located on the right border of the image. Finally, the total path is extracted via backtracking by iteratively connecting the nodes using the stored neighboring information, from the right to the left border of the image.

Initialization and preprocessing

The present framework starts with the user manually performing a quick and simple initialization phase. For a given pullback, this operation consists in (1) visually detecting the presence of a necrotic core covered by a fibrous cap and (2) manually indicating the region of interest (ROI) to be analyzed. The ROI was defined by an arc encompassing the fibrous cap, as displayed in Fig. 1a, b. After this operation has been performed, the region shadowed by the guidewire is easily masked out using an approach similar to the one proposed in [19].

Lumen segmentation

The luminal interface is represented by a positive intensity transition (i.e., from dark lumen to bright tissues) and is generally well perceptible. The luminal contour is easily extracted by applying the previously described dynamic programming approach to the image I.

Abluminal interface segmentation

The abluminal interface is represented by a negative intensity transition (i.e., from bright fibrous tissues to dark lipid pool) and is generally more diffuse and fuzzy. Prior to applying the dynamic programming segmentation method, the ROI manually selected by the user is extracted from the image I, as depicted in Fig. 1c. Then, a spatial transformation T is applied to the ROI. The aim of this transformation T is to generate a sub-image $\mathcal{C}_T$ in which the luminal interface corresponds to a straight horizontal line in the polar domain (Fig. 1e). The cost function $\mathcal{C}$ is thus shifted line-by-line to match the vertical origin with respect to the luminal contour rather than to the probe location. The rationale of our approach is based on the fact that as the fibrous cap thickness does not undergo large variations within adjacent sites, we can exploit a geometrical a priori to cope with the diffuse appearance of the anatomical interface. In the transformed sub-image $\mathcal{C}_T$, the abluminal contour that needs to be extracted is henceforth expected to correspond to a nearly horizontal structure. Subsequently, the dynamic programming segmentation method is applied to $\mathcal{C}_T$. Finally, the actual location of the abluminal interface in the original image is determined by applying the corresponding inverse spatial transformation T^{-1} onto the extracted optimal path (Fig. 1g).

Experiments

Data collection and study population

The OCT imaging database of Thoraxenter, Erasmus MC (Rotterdam, The Netherlands), was screened for native coronary artery OCT pullbacks containing fibroatheromas. Fibroatheromas were defined as necrotic core containing regions with the maximum circumferential extent (arc) exceeding one quadrant of the cross section. Thirty one patients (mean age 61.3 $\pm$ 8.4 years old, 25 males) suffering from coronary artery disease were randomly selected from the database and included in our study. The only inclusion criterion was the presence of fibroatheromas in the acquired pullbacks. Informed consent was acquired from the patients for the use of their imaging data. All procedures followed were in accordance with the ethical standards of the responsible committee on human experimentation (institutional and national) and with the Helsinki Declaration of 1975, as revised in 2008 (5). Pullbacks were acquired in the catheterization laboratory of Erasmus MC for clinical indications, using the C7XR frequency-domain system and the Dragonfly intracoronary imaging catheter (Lightlab/St Jude, Minneapolis, MN, USA). Image acquisition was performed with a previously described non-occlusive technique [14]. Briefly, after positioning the OCT catheter distally to the segment of interest, it was pulled back automatically at 20 mm/s with simultaneous contrast infusion through the guiding catheter by a power injector (flush rate 3-4 ml/s). Images were acquired at the rate of 100 frames/s (corresponding to 54000 A-lines/s), over an average total length of 54 mm along the vessel, resulting in a stack of 271 frames. The central bandwidth of the near-infrared light was 1310 nm, and the spatial resolution of the system was 20 and 30 μm in the axial and lateral directions, respectively. The depth of the scan range was 4.3 mm, and acquired images were sampled at 504 $\times$ 968 pixels per frame, with an isotropic pixel size of 4.5 μm.

Image analysis procedure

For each analyzed pullback, an analyst $\mathcal{A}_1$ selected a series of consecutive images where a necrotic core with an overlying fibrous cap could be observed visually. Definition of image features identifying a necrotic core was signal-poor regions with diffuse contours and high signal attenuation [14]. Subsequently, $\mathcal{A}_1$ indicated, in each selected frame, the limits of the ROI encompassing the fibrous cap (Fig. 1a, b). All that information was stored and subsequently used by the automatic segmentation method, the expert $\mathcal{A}_1$, as well as an additional analyst $\mathcal{A}_2$ to perform, blinded to the results of others, the extraction of the abluminal interface of the fibrous cap. All tracings realized by the human analysts were performed in the Cartesian domain via an effective graphical interface that was developed in-house for this purpose. The two experts are specialists in vascular imaging and OCT. They received identical instructions and were trained on the new segmentation software during 1 month prior to this study.

Parameter settings

Luminal interface

Segmentation of the luminal interface does not present any particular challenge. The proposed segmentation framework was therefore applied on the entire circumference of all images with the following heuristically determined parameter settings: smoothness parameters, $\alpha = 0.1$ and $\beta = 1$; standard deviation of the Gaussian filter, $\sigma = 90$ μm; number of reachable neighbors, $2N + 1 = 41$.

Abluminal interface

Aiming to accurately extract the abluminal contour of the fibrous cap, the optimal parameter settings were determined by means of a training phase. In this purpose, a training set was generated by randomly selecting a subsample of $\Omega_1 = 10$ pullbacks among the cohort of 31 participants. During the training phase, the proposed framework was repeat-

Table 1 Values of the parameter settings used during the training phase of the method

Parameter	Number of different values	Min	Max	Increment step
α	10	0.2	2.0	0.2
β	10	0.2	2.0	0.2
σ	10	9 µm	90 µm	9 µm

edly applied to the training set, with 1000 different sets of $\{\alpha, \beta, \sigma\}$ parameter settings, as displayed in Table 1. The number $2N + 1$ of reachable neighbors was equal to 41 to reduce the search space while still allowing the path to follow the curvature of the analyzed interface. A score was then attributed to each set of parameter settings, by calculating, for every frame of the training set, the mean error between the reference abluminal contour manually traced by $\mathcal{A}_1$ and the corresponding segmentation contour resulting from the proposed framework. Finally, the optimal set of $\{\alpha, \beta, \sigma\}$ parameter settings was determined by visually inspecting the contours of the 10 best ranked sets and selecting the configuration yielding the contours with the most realistic appearance. The selected configuration was the ninth best ranked set, with a mean absolute error of 32 ± 40 µm. The parameters corresponding to the chosen set were as follows: smoothness parameters, $\alpha = 0.2$ and $\beta = 1.8$; standard deviation of the Gaussian filter, $\sigma = 45$ µm. For comparison purpose, the mean absolute error corresponded to 31 ± 41 µm for the best ranked set ($\{\alpha, \beta, \sigma\} = \{0.4, 1.0, 36$ µm$\}$), and to 57 ± 74 µm for the worst ranked set ($\{\alpha, \beta, \sigma\} = \{2.0, 2.0, 9$ µm$\}$). Moreover, the difference between the error distributions corresponding to the chosen set and the best ranked set yielded a zero bias and a 95 % confidence interval equal to $[-3, 3]$ µm. By defining a zone of clinical indifference equal to 9 µm (i.e., ± 1 pixel), we can conclude that the accuracy of the chosen set is statistically equivalent to the accuracy of the best ranked set. Resulting errors in function of the $\{\alpha, \beta, \sigma\}$ parameter settings are displayed in Fig. 3.

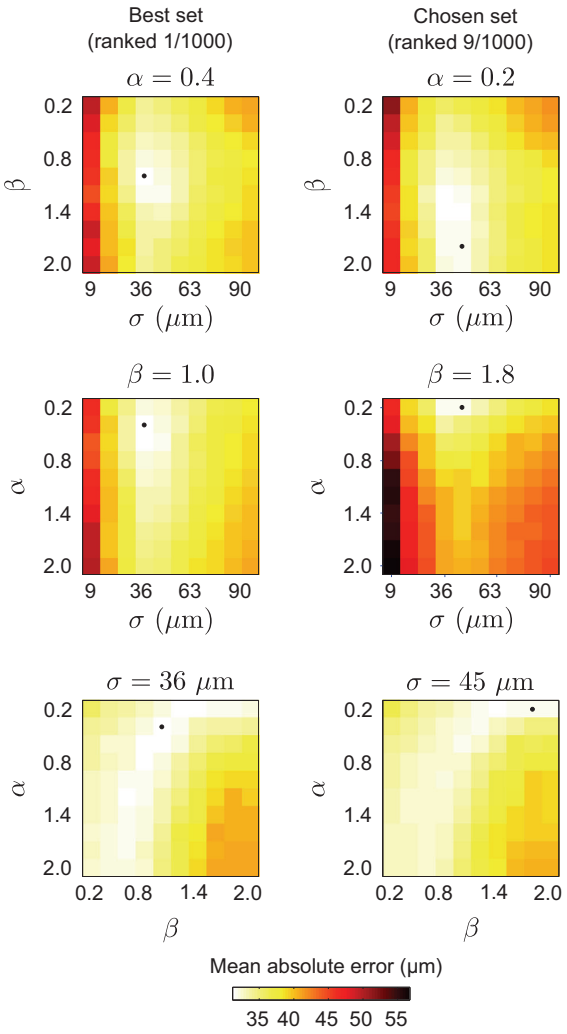

Fig. 3 Mean absolute segmentation error of the fibrous cap abluminal interface, between the automatic framework and the manual tracings of the analyst $\mathcal{A}_1$, in function of the parameter settings $\{\alpha, \beta, \sigma\}$. In each panel, the location of the minimal error is indicated by the *black dot*

Fibrous cap thickness evaluation

The performance of the proposed segmentation framework was evaluated as follow: a testing set was generated with the remaining $\Omega_2 = 21$ pullbacks, and then the segmen-tation framework was applied onto the testing set with the previously determined optimal parameter settings. For each analyzed image, thickness of the fibrous cap was assessed in the Cartesian domain, for our automatic method as well as the two analysts $\mathcal{A}_1$ and $\mathcal{A}_2$. For a given point of the abluminal interface of the fibrous cap, the measure was performed on the line going through the center of the lumen and the assessed point. Cap thickness corresponded to the distance between the two points defined by the intersection of this line with both luminal and abluminal interfaces. For each image, two different measurements were realized to evaluate cap thickness, namely (i) as a vector describing each A-line of the analyzed ROI, and (ii) as the thinnest portion within the frame.

Manual correction of the abluminal contour

The robustness of the proposed segmentation method was also evaluated in the training set by the expert $\mathcal{A}_2$ visually assessing each resulting segmentation contour of the

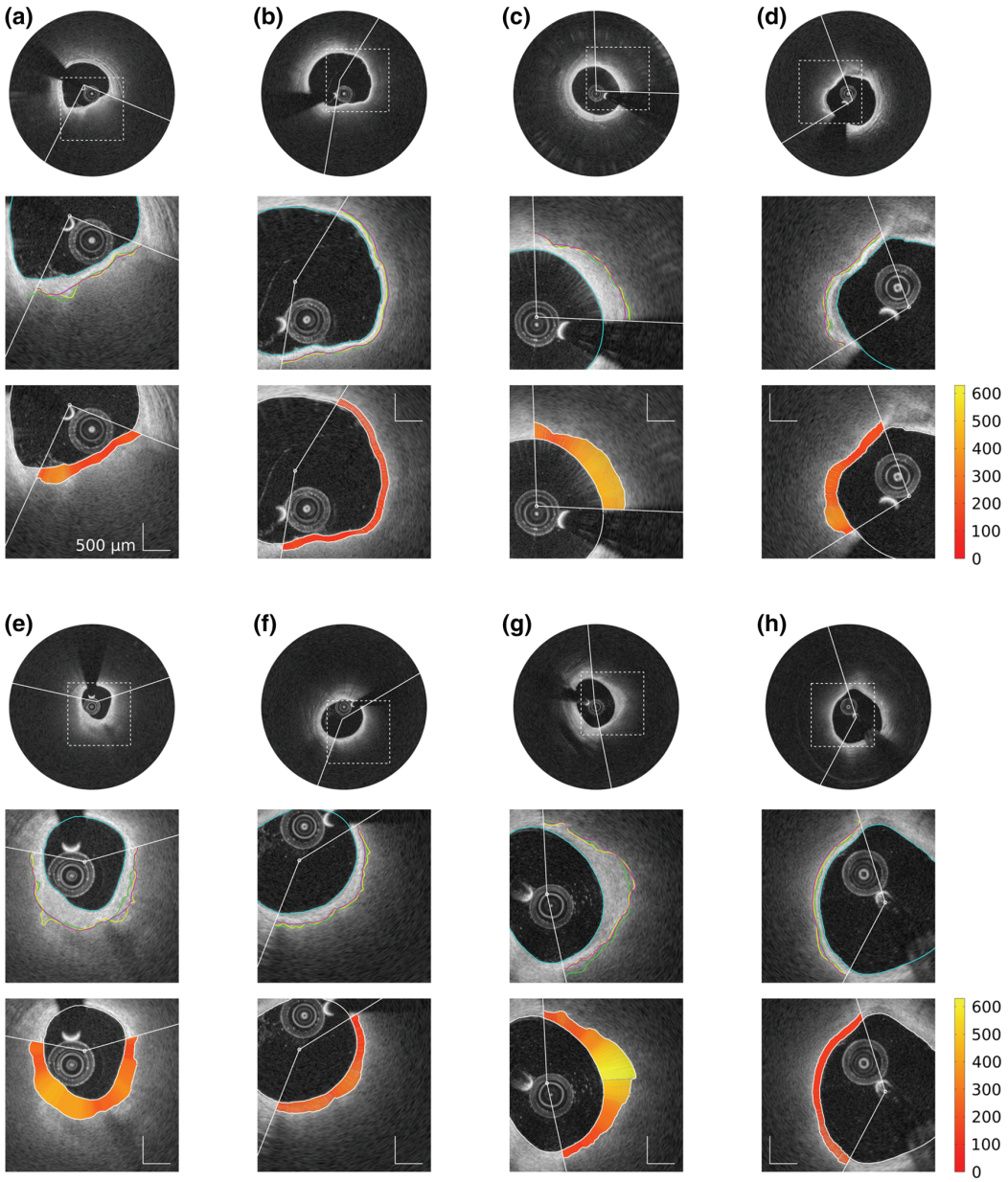

Fig. 4 Representative results of the segmentation framework on eight frames from different pullbacks. For each example, the panel composition is the following. The *top row* displays the full image with the region of interest (ROI, *white arc*). The *middle row* displays an enlarged view of the region delimited by the *dashed square* in the *top row*. The automatic lumen segmentation is represented by the *cyan line*. Within the ROI, tracings of the abluminal interface performed by the segmentation method and the analysts $\mathcal{A}_1$ and $\mathcal{A}_2$ are represented by the *magenta*, *yellow*, and *green lines*, respectively. The *bottom row* displays the cap thickness (scale in µm), automatically computed within the ROI as the distance between the luminal and abluminal contours that were extracted by the segmentation method

abluminal interface and manually correcting it if necessary. More precisely, one or several control points were manually placed by $\mathcal{A}_2$ to correct the automatic segmentation when the analyst did not agree with the original resulting contour. The corrected segmentation contour was generated by means of a modified implementation of the dynamic programming method detailed in "Dynamic programming". Immediately after the generation of the cost

Table 2 Absolute segmentation errors (mean ± standard deviation) of the abluminal interface of the fibrous cap, for the automatic method (Auto) and the two analysts ($\mathcal{A}_1$ and $\mathcal{A}_2$)

Errors (μm)	Auto versus $\mathcal{A}_1$	Auto versus $\mathcal{A}_2$	$\mathcal{A}_1$ versus $\mathcal{A}_2$
Testing set ($\Omega_2 = 21$)	31 ± 38	37 ± 41	30 ± 39
Training set ($\Omega_1 = 10$)	31 ± 39	33 ± 33	34 ± 43

function $\mathcal{C}$, a modified cost function $\mathcal{C}'$ was built using the following approach. For each manually defined control point $p(\theta, r)$, the node (θ, r) of the cost function $\mathcal{C}'$ was set to zero, and all other nodes of the column θ were set to an infinity value (Fig. 2). The following steps of the dynamic programming method were then applied to the cost function $\mathcal{C}'$. As a consequence, the resulting contour corresponded to a path going through all the control points while still performing a search in the regions that were not corrected.[1]

Results

Among the 31 involved patients, the average number of analyzed images per individual pullback was 8.4 ± 1.7 (range 5–10) consecutive frames, with a total of 261 analyzed images. The average length of the analyzed arc per image was 30 ± 16 % of the entire vessel circumference (range 4–78 %). The training set was generated with $\Omega_1 = 10$ random pullbacks (corresponding to 82 images), and the testing set was generated from the remaining $\Omega_2 = 21$ pullbacks (corresponding to 179 images).

For each analyzed frame of both training and testing sets, the luminal interface was automatically extracted for the entire vessel circumference, and the abluminal interface of the fibrous cap was automatically extracted within the ROI defined by the expert $\mathcal{A}_1$ (Fig. 1a, b). Representative examples of resulting segmentation contours are displayed in Fig. 4. The results of our segmentation method, compared to the tracings of both observers $\mathcal{A}_1$ and $\mathcal{A}_2$, are presented alongside to the corresponding inter-observer variability in Table 2.

Quantification of fibrous cap thickness was derived from the segmented contours of both luminal and abluminal interfaces. Including each analyzed A-line per frame, the average cap thickness was 210 ± 82 μm for the 179 images of the testing set and 228 ± 88 μm for the 82 images of the training set. The mean minimal cap thickness (i.e., the thinnest point in a given frame) was 126 ± 37 μm for the testing set, and 161 ± 64 μm for the training set. Results of cap thickness derived from the automatic framework were evaluated against the manual references performed by the two analysts, as presented in Table 3. The Bland-Altman plots (Fig. 5) show an overall good agreement between the present method and the two experts when assessing minimal cap thickness.

It is also insightful to quantify the absolute error of the proposed segmentation framework normalized by the cap thickness. Calculating, for each analyzed A-line, the ratio between the absolute segmentation error and the corresponding cap thickness and putting all these ratios together, the mean values were 16 ± 19 % for the 179 images of the testing set and 15 ± 22 % for the 82 images of the training set. When calculating the relative errors corresponding to the minimal cap thickness, the mean values were 19 ± 18 % for the testing set and 24 ± 31 % for the training set.

Reviewing the resulting abluminal interface segmentation contours of the testing set, the expert $\mathcal{A}_2$ performed a correction of the automatic contours with which he disagreed, as detailed in "Manual correction of the abluminal contour". A total of 20 frames out of 179 were corrected, corresponding to seven pullbacks out of 21. For all these corrected frames, the mean number of manually added control points was 1.8 ± 1.1 (range 1–4). The two main factors motivating this manual corrections were (1) image artifacts hampering the automatic segmentation and (2) the presence of several interface-like structures attracting the contour. Examples of such manual correction of erroneous contours are depicted in Fig. 6. Assessing the fibrous cap with the corrected contours yielded an overall reduced cap thickness (bias of −26 μm, Bland-Altman 95 % limits of agreement of [−95, 147] μm). Comparing, for the 20 corrected frames, the bias (and 95 % limits of agreement) of the cap thickness estimation resulting from the automatic segmentation and the manually corrected segmentation, it decreased from 22 μm ([−142, 187] μm) to −4 μm ([−125, 117] μm) when evaluated against the reference tracings of $\mathcal{A}_2$, but increased from 1 μm ([−133, 134] μm) to −26 μm ([−159, 108] μm) with $\mathcal{A}_1$. This discrepancy, reflecting the subjectivity of human analysts, is also visible through the bias between the two experts, which was equal to 21 μm ([−124, 166] μm) in these 20 frames.

As for the computational speed, the present framework required on average 0.5 s to perform the contour extraction of both luminal and abluminal interfaces and evaluate its thickness for a single image, while the corresponding manual operation required on average 190 s. In both cases and additionally, the average time (per frame) required by the user to define the ROI was 20 s.

[1] Please note that in the remaining of this manuscript, any reference to segmentation contour and all results are related to the original automatic contours (i.e., non manually corrected), except when explicitly specified.

Table 3 Evaluation of fibrous cap thickness, with absolute error (mean ± standard deviation), bias, 95 % limits of agreement (Lim), and Pearson coefficient (R), for the automatic method (Auto) and the two analysts ($\mathcal{A}_1$ and $\mathcal{A}_2$)

Errors (μm)	Overall cap thickness over the entire ROI				Minimal cap thickness per frame			
	Absolute	Bias	Lim	R	Absolute	Bias	Lim	R
Testing set ($\Omega_2 = 21$)								
Auto versus $\mathcal{A}_1$	30 ± 37	1.4	$[-92, 95]$	0.85	22 ± 18	8.4	$[-46, 63]$	0.73
Auto versus $\mathcal{A}_2$	36 ± 41	4.9	$[-101, 111]$	0.81	26 ± 22	4.6	$[-61, 70]$	0.62
$\mathcal{A}_1$ versus $\mathcal{A}_2$	36 ± 41	3.6	$[-102, 109]$	0.82	21 ± 19	−3.8	$[-59, 52]$	0.74
Training set ($\Omega_1 = 10$)								
Auto versus $\mathcal{A}_1$	31 ± 39	−1.4	$[-99, 96]$	0.86	30 ± 27	2.4	$[-77, 82]$	0.82
Auto versus $\mathcal{A}_2$	32 ± 33	−1.8	$[-91, 87]$	0.87	29 ± 27	2.0	$[-75, 79]$	0.85

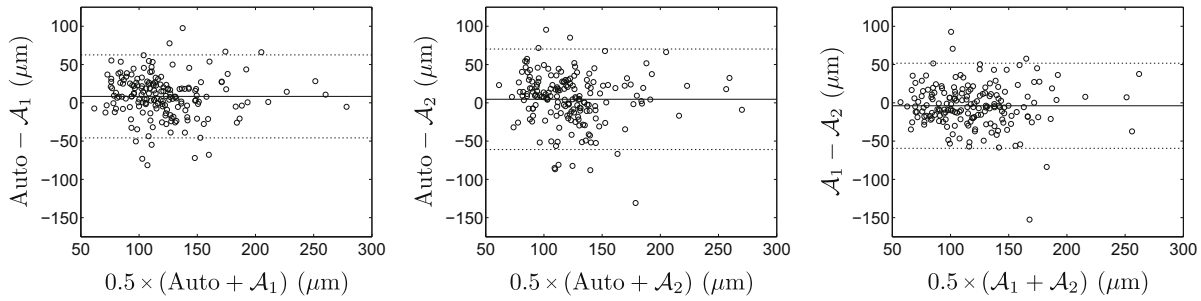

Fig. 5 Bland-Altman plots, comparing the results of minimal cap thickness assessed in the training set, for the proposed automatic method and the manual tracings performed by the two analysts $\mathcal{A}_1$ and $\mathcal{A}_2$. The *solid* and *dashed lines* represent the bias and the 95 % limits of agreement, respectively

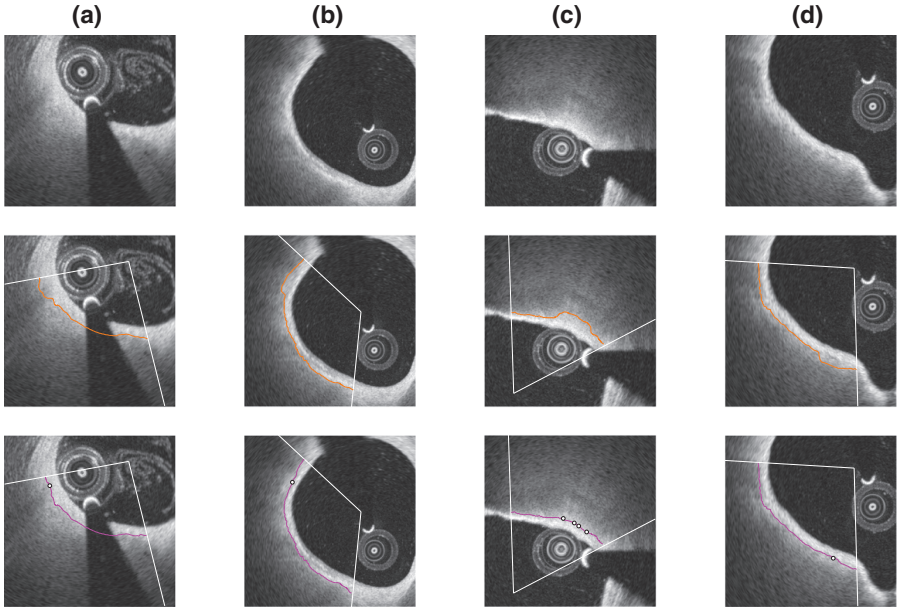

Fig. 6 Example of manual contour correction, on four frames from different pullbacks. The *top*, *middle*, and *bottom rows* display the original image, the automatic segmentation contour of the fibrous cap (*orange line*), and the corrected segmentation contour (*magenta line*), respectively. In the *bottom row*, the control points that were manually indicated by the analyst are represented by the *black dots*

Discussion

The principal aim of this study was to introduce a contour segmentation method devised to quantify fibrous cap thickness in cross-sectional OCT images. Since cap thickness is the most critical component of plaque stability [11], its quantification is likely to provide crucial information about the risk of plaque rupture. The proposed framework was trained in 82 images from 10 patients and subsequently validated in 179 images from 21 other patients.

The evaluation of the proposed segmentation framework was conducted against reference segmentation contours manually generated by two expert analysts in a set of 179 images. The mean absolute error of the automatic method versus both analysts (i.e., 22 ± 18 and 26 ± 22 μm) was similar to the inter-observer variability (i.e., 21 ± 19 μm), as presented in Table 3, which indicates that the present method performs at least as well as an experienced observer when assessing the cap thickness. It is also noteworthy that these errors are relatively small compared to the spatial resolution of the system, which was 20 μm. When assessing the thinnest portion of the fibrous cap in the image, an overall low positive bias was observed between the automatic method and the experts (i.e., 8.4 μm w.r.t. $\mathcal{A}_1$, and 4.6 μm w.r.t. $\mathcal{A}_2$), showing that cap thickness is slightly over-estimated by the computerized method. Furthermore, an accuracy improvement of roughly 30 % could be observed when quantifying, in a given frame, the thinnest portion of the cap rather than the overall thickness of the entire cap (i.e., 22 ± 18 vs. 30 ± 37 μm, Table 3). This performance discrepancy can be explained by the fact that thinnest portions tend to present sharper and more defined contours, whereas thickest portions of the cap often present more fuzzy contours (i.e., due to a greater attenuation of the signal in deeper tissues or to a decrease in the lateral spatial definition along the distance from the probe in the Cartesian domain). We consider the higher accuracy in detection of minimal cap thickness favorable, as the minimal value of cap thickness is the most clinically relevant information [11]. It is also noteworthy that the ability of OCT to quantify cap thickness was previously evaluated in a study where cap thickness was measured manually in OCT images and compared to the corresponding ex vivo histopathologic segments [10]. Results from that study demonstrated a mean signed error of -22 ± 44 μm when measuring the thinnest portion of the cap. This magnitude can thus be understood as the systematic uncertainty that is introduced when analyzing cap thickness in OCT images. The level of accuracy of the proposed method can be validated by the fact that the mean signed error is small in comparison to that uncertainty, namely -8.4 ± 28 μm (Table 3).

A training phase was carried out on a subsample of $\Omega_1 = 10$ pullbacks to determine the optimal set of the $\{\alpha, \beta, \sigma\}$ parameters for the extraction of the fibrous cap abluminal interface. Despite the fact that the method was optimized with respect to the manual tracings of the expert $\mathcal{A}_1$, results show that the errors of the automatic method versus both analysts were close to each other as well as to the inter-observer variability, for contour segmentation (Table 2) as well as cap thickness assessment (Table 3). Moreover, both automatic and manual errors generated from the training set were similar to the errors resulting from the testing phase (Tables 2, 3), which confirms the robustness of the proposed framework against new images. In a few challenging cases (i.e., 20 images out of 179), automatic segmentation of the abluminal interface failed, due to the presence of bright image artifacts or several interface-like structures. To cope with these issues, a correction scheme was proposed. This task is performed easily and quickly by the user visually assessing the resulting segmentation, and indicating, if necessary, one or several control points to modify the contour, as displayed in Fig. 6. As opposed to the abluminal contour, segmentation of the luminal interface does not present any particular challenge, as the location of the anatomical boundary is well perceptible (Fig. 1b). This is testified by the fact that the parameter settings used for the luminal segmentation assign less weight on the shape constraint and more weight on the image data (i.e., $\{\alpha, \beta, \sigma\} = \{0.1, 1.0, 90\ \mu\text{m}\}$), compared to the abluminal parameter settings (i.e., $\{\alpha, \beta, \sigma\} = \{0.2, 1.8, 45\ \mu\text{m}\}$).

The clinical context of our work relates to perioperative decision making rather than patient screening: the severity of the case is averred, and invasive imaging is required. The rationale of the present study is to assess plaque stability via quantifying the thickness of the overlying fibrous cap. Indeed, it has been demonstrated that cap thickness is the most critical component of plaque stability [11] and that lesion morphology is associated with future events [13]. The error introduced by the present framework when assessing minimal cap thickness corresponded to 22 ± 18 μm. This is relatively large compared to the threshold of 65 μm used to identify rupture-prone sites [17]. Nevertheless, the error of the automatic method was similar to the agreement between the two experts, which was 21 ± 19 μm. One should also notice that the empirical 65 μm threshold may be underevaluated, since ex vivo tissues can undergo variable shrinkage rate during histological preparation [14,17]. Indeed, it has recently been demonstrated that ruptured plaques in ACS are often associated with a fibrous cap thickness of up to 100 μm [15] and that the best cutoff to predict rupture was 151 μm for most representative fibrous caps [21]. Accordingly, the clinical applicability of the proposed method is supported by a relatively accurate quantification of cap thickness.

To the best of our knowledge, the study presented by Wang et al. [19] is the only one to report a semiautomatic segmentation scheme dedicated to quantify fibrous cap thickness in coronary OCT. The accuracy of that method was slightly better than that of the present framework, namely the mean

absolute errors (± standard deviation) were 25 (±31) μm versus 31 (±38) μm for the abluminal interface of the cap, and 27 (±27) μm versus 30 (±37) μm for the overall cap thickness. Nevertheless, the pertinence of such comparison is limited by the fact that our method was applied onto a different dataset, using a different OCT scanner, and that the protocol followed by the expert $\mathcal{A}_1$ to determine the fibrous caps to be analyzed may also have differed. Moreover, the finding of a higher inter-observer variability as well in our study could imply the presence of challenging cases in our dataset.

A limitation of this study is that the cap thickness validation was performed against tracings manually generated by expert analysts, but not against ex vivo histopathologic specimens. Therefore, the actual ground truth is lacking, and further validation is warranted. However, as a variable shrinkage rate often occurs during histological preparation of the tissues [14,17], validation on ex vivo data is also expected to involve a certain amount of uncertainty. Another limitation of this study is that a manual initialization phase is required to be performed by the user to indicate the location of the ROI encompassing the fibrous cap to be analyzed. A certain amount of variability is to be expected in between two selections from the same experts, or in between the selection of two different experts, thus hindering clinical applicability. This could be remedied by a more automated way of detecting these locations. Therefore, future work will focus on fully automatic detection of such diseased regions, using an approach based on machine learning [22]. One should also notice that since the spatial resolution along the z-axis is rather coarse compared to the axial resolution (i.e., 200 vs. 20 μm), a three-dimensional segmentation approach is not expected to greatly improve the overall accuracy. For this reason, the proposed framework is based on two-dimensional cross-sectional images. This issue could be addressed in further work by upsampling the acquired data using an ultrafast OCT system at 3200 frames per second [18]. To cope with the diffuse appearance of the abluminal contours, multiple texture features could also be extracted in addition to the intensity gradient in order to generate a multi-dimensional cost function $\mathcal{C}$. Future perspectives will also aim at investigating the association of wall shear stress with cap thickness using a fusion of imaging parameters with OCT and biplane angiography, in the objective to assess the risk of plaque rupture with improved performances. Potential applications could also include automated assessment of device-induced vascular responses [7,8].

Conclusion

The context of this study is to assess rupture-prone plaques by quantifying the thickness of the overlying fibrous cap in cross-sectional coronary OCT imaging. A segmentation framework devised to extract the contours of the cap was proposed. In the objective to localize the diffuse and fuzzy abluminal interface, the introduced method is based on a specific dynamic programming approach that integrates a geometrical a priori. Validated on in vivo data in 21 patients suffering from coronary artery disease, the method provided robust and accurate results, in a clinically acceptable computational time. The automatic framework performed as well as two expert analysts, while being substantially faster. Accordingly, the proposed approach could provide a useful aid for interventional planning and decision making in the catheterization laboratory.

Acknowledgments This work was partially supported by the STW Carisma 11635 funding.

Conflict of interest The authors declare that they have no conflict of interest.

References

1. Bellman R (1966) Dynamic programming. Science 153(3731):34–37
2. Bezerra HG, Costa MA, Guagliumi G, Rollins AM, Simon DI (2009) Intracoronary optical coherence tomography: a comprehensive review. J Am Coll Cardiol Cardiovasc Interv 2(11):1035–1046
3. Brezinski ME (2002) Optical coherence tomography for identifying unstable coronary plaque. Int J Cardiol 102(2):154–165
4. Burke AP, Farb A, Malcom GT, Liang YH, Smialek J, Virmani R (1997) Coronary risk factors and plaque morphology in men with coronary disease who died suddenly. New Engl J Med 336(18):1276–1282
5. Celi S, Berti S (2014) In-vivo segmentation and quantification of coronary lesions by optical coherence tomography images for a lesion type definition and stenosis grading. Med Image Anal 18(7):1157–1168
6. Cohen L (2006) Minimal paths and fast marching methods for image analysis. In: Paragios N, Chen Y, Faugeras O (eds) Handbook of mathematical models in computer vision. Springer, pp 97–111
7. Karanasos A, Ligthart J, Witberg K, Toutouzas K, Daemen J, van Soest G, Gnanadesigan M, van Geuns RJ, de Jaegere P, Regar E (2013) Association of neointimal morphology by optical coherence tomography with rupture of neoatherosclerotic plaque very late after coronary stent implantation. SPIE Conf Proc. doi:10.1117/12.2006331
8. Karanasos A, Simsek C, Gnanadesigan M, van Ditzhuijzen NS, Freire R, Dijkstra J, Tu S, van Mieghem N, van Soest G, de Jaegere P, Serruys PW, Zijlstra F, van Geuns RJ, Regar E (2014) Oct assessment of the long-term vascular healing response 5 years after everolimus-eluting bioresorbable vascular scaffold. J Am Coll Cardiol 64(22):2343–2356
9. Kubo T, Imanishi T, Takarada S, Kuroi A, Ueno S, Yamano T, Tanimoto T, Matsuo Y, Masho T, Kitabata H, Tsuda K, Tomobuchi Y, Akasaka T (2007) Assessment of culprit lesion morphology in acute myocardial infarction: ability of optical coherence

tomography compared with intravascular ultrasound and coronary angioscopy. J Am Coll Cardiol 50(10):933–939
10. Kume T, Akasaka T, Kawamoto T, Okura H, Watanabe N, Toyota E, Neishi Y, Sukmawan R, Sadahira Y, Yoshida K (2006) Measurement of the thickness of the fibrous cap by optical coherence tomography. Am Heart J 152(4):755e1–755e4
11. Narula J, Nakano M, Virmani R, Kolodgie FD, Petersen R, Newcomb R, Malik S, Fuster V, Finn AV (2013) Histopathologic characteristics of atherosclerotic coronary disease and implications of the findings for the invasive and noninvasive detection of vulnerable plaques. J Am Coll Cardiol 61(10):1041–1051
12. van Soest G, Goderie T, Regar E, Koljenovic S, van Leenders GLJH, Gonzalo N, van Noorden S, Okamura T, Bouma BE, Tearney GJ, Serruys PW, van der Steen AFW (2010) Atherosclerotic tissue characterization in vivo by optical coherence tomography attenuation imaging. J Biomed Opt 15:011105-1
13. Stone GW, Maehara A, Lansky AJ (2011) A prospective natural-history study of coronary atherosclerosis. New Engl J Med 364(3):226–235
14. Tearney GJ, Regar E, Akasaka T et al (2012) Consensus standards for acquisition, measurement, and reporting of intravascular optical coherence tomography studies. J Am Coll Cardiol 59(12):1058–1072
15. Toutouzas K, Karanasos A, Tsiamis E, Riga M, Drakopoulou M, Synetos A, Papanikolaou A, Tsioufis C, Androulakis A, Stefanadi E, Tousoulis D, Stefanadis C (2011) New insights by optical coherence tomography into the differences and similarities of culprit ruptured plaque morphology in non-ST-elevation myocardial infarction and ST-elevation myocardial infarction. Am Heart J 161(6):1192–1199
16. Ughi GJ, Steigerwald K, Adriaenssens T, Desmet W, Guagliumi G, Joner M, D'hooge J (2013) Automatic characterization of neointimal tissue by intravascular optical coherence tomography. J Biomed Opt 19:021104
17. Virmani R, Kolodgie FD, Burke AP, Farb A, Schwartz SM (2000) Lessons from sudden coronary death: a comprehensive morphological classification scheme for atherosclerotic lesions. Arterioscler Thromb Vasc Biol 20(5):1262–1275
18. Wang T, Wieser W, Springeling G, Beurskens R, Lancee CT, Pfeiffer T, van der Steen AFW, Huber R, van Soest G (2013) Intravascular optical coherence tomography imaging at 3200 frames per second. Opt lett 38(10):1715–1717
19. Wang Z, Chamie D, Bezerra HG, Yamamoto H, Kanovsky J, Wilson DL, Costa MA, Rollins AM (2012) Volumetric quantification of fibrous caps using intravascular optical coherence tomography. Biomed Opt Express 3:1413–1426
20. Xu C, Schmitt JM, Carlier SG, Virmani R (2008) Characterization of atherosclerosis plaques by measuring both backscattering and attenuation coefficients in optical coherence tomography. J Biomed Opt 13:034003
21. Yonetsu T, Kakuta T, Lee T, Takahashi K, Kawaguchi N, Yamamoto G, Koura K, Hishikari K, Iesaka Y, Fujiwara H, Isobe M (2011) In vivo critical fibrous cap thickness for rupture-prone coronary plaques assessed by optical coherence tomography. Eur Heart J 32(10):1251–1259
22. Zahnd G, Karanasos A, van Soest G, Regar E, Niessen WJ, Gijsen FJH, van Walsum T (2014) Fully automated detection of healthy wall sections in intracoronary optical coherence tomography. In: MICCAI CVII-STENT Workshop. Springer, Berlin, Heidelberg (in press)
23. Zahnd G, Karanasos A, van Soest G, Regar E, Niessen WJ, Gijsen FJH, van Walsum T (2014) Semi-automated quantification of fibrous cap thickness in intracoronary optical coherence tomography. International conference on information processing in computer-assisted interventions p 78–89
24. Zahnd G, Orkisz M, Sérusclat A, Moulin P, Vray D (2013) Simultaneous extraction of carotid artery intima-media interfaces in ultrasound images: assessment of wall thickness temporal variation during the cardiac cycle. Int J Comput Assist Radiol Surg 9(4):645–658

Chapter 2.3

A novel method to assess coronary artery bifurcations by OCT: cut-plane analysis for side-branch ostial assessment from a main-vessel pullback

Karanasos A, Tu S, van Ditzhuijzen NS, Ligthart JM, Witberg K, Van Mieghem N, van Geuns RJ, de Jaegere P, Zijlstra F, Reiber JH, Regar E

Eur Heart J Cardiovasc Imaging. 2015 Feb;16(2):177-89

A novel method to assess coronary artery bifurcations by OCT: cut-plane analysis for side-branch ostial assessment from a main-vessel pullback

Antonios Karanasos[1], Shengxian Tu[2], Nienke S. van Ditzhuijzen[1], Jurgen M.R. Ligthart[1], Karen Witberg[1], Nicolas Van Mieghem[1], Robert-Jan van Geuns[1], Peter de Jaegere[1], Felix Zijlstra[1], Johan H.C. Reiber[2], and Evelyn Regar[1]*

[1]Department of Interventional Cardiology, Thoraxcentre, BA-585, Erasmus University Medical Centre, Gravendijkwal 230, 3015 CE Rotterdam, The Netherlands; and
[2]Division of Image Processing, Department of Radiology, Leiden University Medical Centre, Leiden, The Netherlands

Received 25 April 2014; accepted after revision 10 August 2014

Aims In coronary bifurcations assessment, evaluation of side-branch (SB) ostia by an optical coherence tomography (OCT) pullback performed in the main branch (MB) could speed up lesion evaluation and minimize contrast volume. Dedicated software that reconstructs the cross-sections perpendicular to the SB centreline could improve this assessment. We aimed to validate a new method for assessing the SB ostium from an OCT pullback performed in the MB.

Methods and results Thirty-one sets of frequency-domain OCT pullbacks from 28 patients, both from the MB and the SB of a coronary artery bifurcation were analysed. Measurements of the SB ostium from the SB pullback were used as a reference. Measurements of the SB ostium from the MB pullback were then performed in a laboratory setting by (i) conventional analysis and (ii) cut-plane analysis, and the measurement error for each analysis was estimated. Correlations of SB ostium measurements acquired from the MB pullback in comparison with reference measurements acquired from the SB pullback were higher with cut-plane analysis compared with conventional analysis, albeit not reaching statistical significance (area: $r_{\text{cut-plane}} = 0.927$ vs. $r_{\text{conventional}} = 0.870$, $P = 0.256$; mean diameter: $r_{\text{cut-plane}} = 0.918$ vs. $r_{\text{conventional}} = 0.788$, $P = 0.056$; minimum diameter: $r_{\text{cut-plane}} = 0.841$ vs. $r_{\text{conventional}} = 0.812$, $P = 0.734$; maximum diameter: $r_{\text{cut-plane}} = 0.770$ vs. $r_{\text{conventional}} = 0.635$, $P = 0.316$). Cut-plane analysis was associated with lower absolute error than conventional analysis (area: 0.56 ± 0.45, vs. 1.50 ± 1.31 mm^2, $P < 0.001$; mean diameter: 0.18 ± 0.14 vs. 0.44 ± 0.30 mm, $P < 0.001$).

Conclusion Measurements of SB ostium performed in a laboratory setting by cut-plane analysis of an OCT pullback of the main branch have high correlation with reference measurements performed in a SB OCT pullback and lower error compared with conventional analysis.

Keywords optical coherence tomography • coronary artery interventions • intravascular imaging • intravascular ultrasound • percutaneous coronary intervention • coronary stents

Introduction

Bifurcation lesions are associated with increased events following percutaneous coronary intervention (PCI). Factors contributing to this adverse outcome include limitations of angiography in assessment of side-branch (SB) disease severity[1] and the lack of established angiographic predictors of SB patency and lumen compromise.

Intravascular imaging has provided new understanding of mechanisms associated with SB compromise following bifurcation PCI.[2–5] Optical coherence tomography (OCT) is an intravascular imaging modality that can potentially be used for bifurcation PCI guidance.[6,7] For the accurate characterization of bifurcation lesions, two OCT pullbacks are typically required: one from the main branch (MB) and a second separate OCT pullback from the SB. In clinical practice,

* Corresponding author. Tel: +31 10 7035232; fax: +31 10 7035046, Email: e.regar@erasmusmc.nl

however, it would be highly desirable to also obtain crucial information for the SB ostium from a single MB pullback. In the past, SB ostial assessment from the MB was subject to significant errors due to the misalignment of the imaging catheter relative to the SB centreline (*Figure 1*).[8–11] To overcome this limitation, a novel approach has been developed. The QAngioOCT 1.0 (Medis Specials Bv, Leiden, the Netherlands) is a new software that can reconstruct the cross-sections perpendicular to the SB centreline and enable more accurate assessment of SB ostia from MB pullbacks.[12]

We aimed to validate ostial SB measurements from a main-branch OCT pullback, performed with QAngioOCT, against measurements of the SB ostium obtained from an OCT pullback from the SB.

Methods

Study population

The OCT imaging database of Erasmus MC was reviewed for identification of OCT pullback sets suitable for inclusion in the study. A set of pullbacks was included when good quality frequency-domain OCT pullbacks from both branches were available. The exclusion criteria were invasive treatment of the imaged bifurcation taking place between acquisition of the two pullbacks, poor image quality or image artefacts (e.g. guidewire shadow) hampering SB ostium visualization, and incomplete SB visualization in the range of the OCT system (10 mm) at the level of the carina. After review of studies acquired in the interval between 1 October 2009 and 1 July 2013, 98 sets of OCT pullbacks with visualization of a bifurcation from both branches were considered for inclusion. Sixteen sets of pullbacks (16.3%) were excluded due to the presence of artefacts hampering visualization of the SB ostium (incomplete flushing, guidewire shadow, shadowing by stent struts, thrombus). Fifty-one additional pullbacks (52%) were excluded because of out-of-view artefact hampering complete visualization of the SB ostium, and thus conventional analysis. Thirty-one sets (31.6%) retrieved by 28 patients with bifurcation lesions were finally deemed suitable for inclusion. Informed consent was acquired from the patients for use of their imaging data and the study complies with the declaration of Helsinki.

To demonstrate the feasibility of SB ostium analysis by QAngioOCT, even in cases where conventional analysis of the MB pullback is not feasible due to incomplete SB visualization at the carina, a finding very common in left main bifurcations, an additional representative series of 12 consecutive sets of MB and SB pullbacks, in which SB ostium is not completely visualized in the MB pullback, was analysed by QAngioOCT.

Three-dimensional QCA analysis

In all cases with two suitable angiographic projections and an angle between the two projections >25°, three-dimensional quantitative coronary angiography (3D-QCA) was performed using QAngio XA 3D (bifurcation edition 1.0; Medis Specials bv). The imaged bifurcation was identified, analysed by 3D-QCA, and the measurements of proximal and distal bifurcation angle, proximal and distal reference diameters, as well as luminal areas and diameters at the ostia of the SB and MB were obtained.[13]

OCT image acquisition

OCT pullbacks were acquired using second-generation OCT systems: (i) the C7XR system (St Jude/LightLab Imaging, Inc., Westford, MA, USA) with Dragonfly catheter (St Jude) ($n = 28$) and (ii) the Lunawave system (Terumo Corporation, Tokyo, Japan) with Fastview catheter (Terumo Corporation) ($n = 3$). The OCT catheter was advanced and positioned distal to the imaged bifurcation at the MB or at the SB. A continuous flush of contrast (Iodixanol 370, Visipaque™, GE HealthCare, Ireland) through the guiding catheter at 3–4 mL/s was used for blood clearance, while an automated OCT pullback was performed at 20 mm/s. The procedure was then repeated for the other branch. Images were digitally stored and analysed offline.

OCT image analysis

The principle of analysis is presented in *Figure 2*. All measurements were performed in a laboratory setting, meaning offline analysis performed by

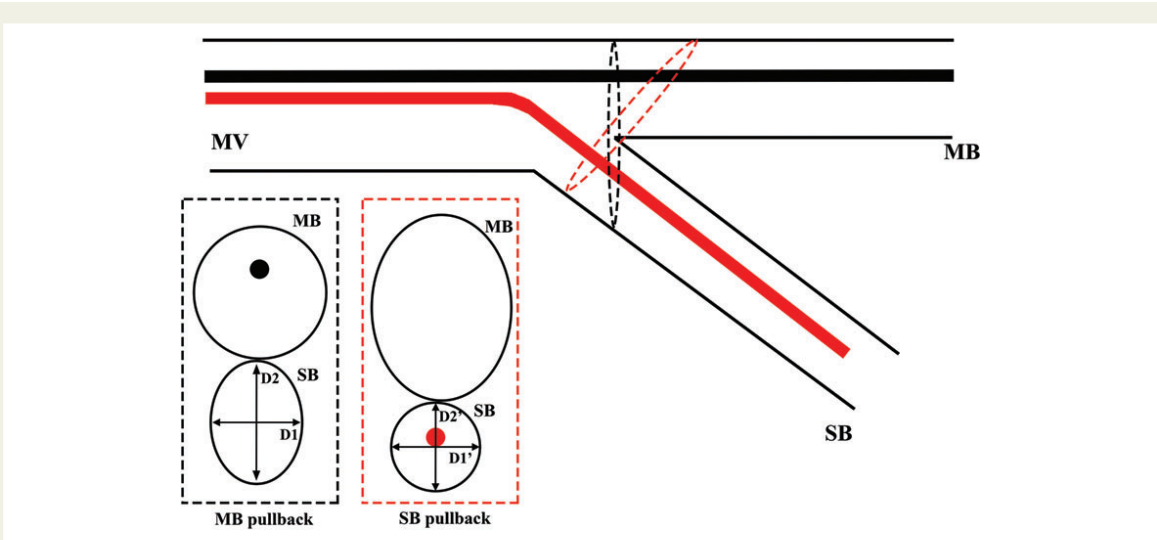

Figure 1: Potential error in ostial SB assessment. When the pullback is performed from the MB (black line), the plane at the level of the carina does not correspond to the true SB ostium, which can be visualized when the pullback is performed from the SB (red line). D1, short diameter; D2, long diameter; MB, main-branch; MV, main vessel; OCT, optical coherence tomography; SB, side-branch.

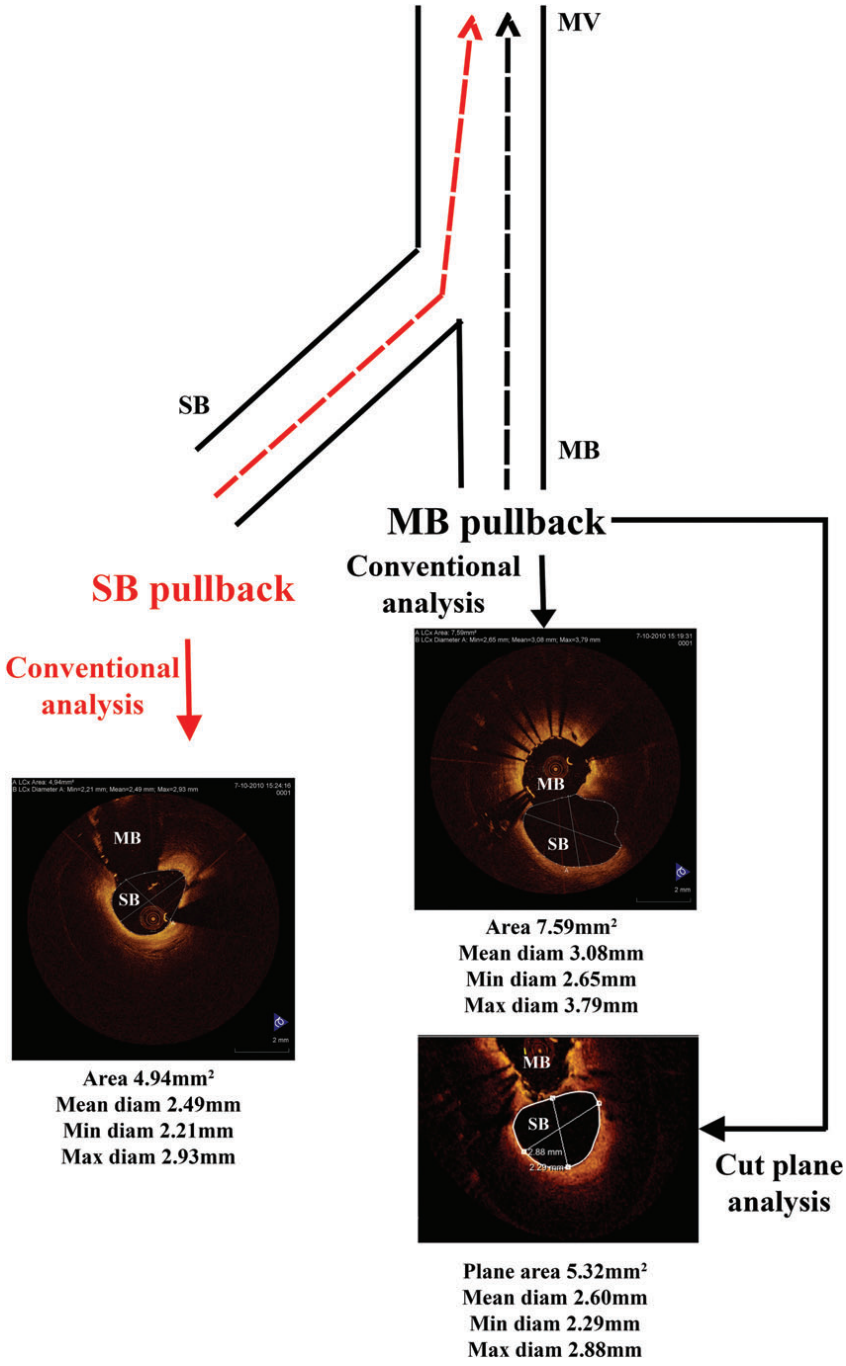

Figure 2: Study diagram. Two OCT studies corresponding to the same bifurcation were available: one with pullback from the SB (red dashed line) and the other with pullback from the MB (black dashed line). Conventional SB ostium measurements were performed from the SB pullback. Measurements of the SB ostium from the MB pullback were performed by (1) conventional analysis and (2) cut-plane analysis. The measurement error for each analysis was then estimated using the SB pullback as a reference. Note the lumen shape similarity between the actual SB ostium and the cut-plane reconstruction of the SB ostium from the MB. Abbreviations as in *Figure 1*.

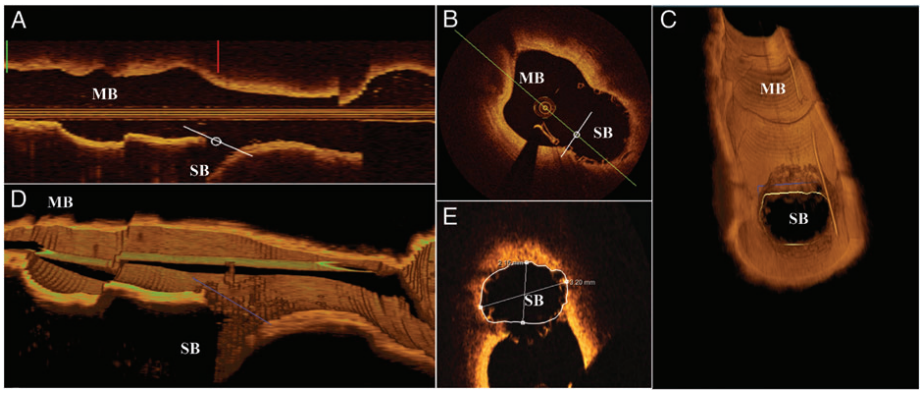

Figure 3: Cut-plane analysis in a patient with ostial bioresorbable scaffold implantation in the SB. The SB is identified in the (*A*) l-mode and the (*B*) cross-sectional OCT images, and the white lines (cut-plane) are rotated by the user so that they become perpendicular to the SB centreline. The position of the plane can be confirmed in the three-dimensional renderings (blue line in *C* and *D*) and further adjusted. The image generated in *E* corresponds to this plane and manual lumen segmentation can be performed. Abbreviations as in *Figure 1*.

Table 1 Baseline characteristics

Number of patients, *n*	28
Age (years)	63.7 ± 11.2
Gender (male), *n* (%)	17 (60.7)
Clinical presentation (*n* = 31 pullback sets)	
Stable angina, *n* (%)	20 (64.5)
Unstable angina, *n* (%)	2 (6.5)
Myocardial infarction, *n* (%)	4 (12.9)
Asymptomatic; follow-up evaluation, *n* (%)	5 (16.1)
Indication for imaging (*n* = 31 pullback sets)	
Pre-interventional, *n* (%)	10 (32.3)
Post-interventional, *n* (%)	15 (48.4)
Follow-up evaluation, *n* (%)	6 (19.4)
Coronary risk factors, *n* (%)	
Diabetes mellitus	7 (25.0)
Dyslipidaemia	14 (50.0)
Hypertension	16 (57.1)
Smoking	7 (25.0)
Family history for coronary disease	14 (50.0)
Previous cerebrovascular accident, *n* (%)	3 (9.7)
Previous myocardial infarction, *n* (%)	7 (25.0)

All values presented as *n* (%) or mean ± SD.

Table 2 Angiographic characteristics and 3D-QCA

Angiographic characteristics (*n* = 31 pullback sets)	
Imaged bifurcation, *n* (%)	
Left main	1 (3.2)
LAD diagonal	24 (77.4)
LCx-OM	5 (16.1)
RPD-RPL	1 (3.2)
Stent in MB, *n* (%)	15 (48.4)
Bioresorbable scaffold in MB, *n* (%)	2 (6.5)
Stent in SB, *n* (%)	10 (32.3)
Bioresorbable scaffold in SB, *n* (%)	3 (9.7)
3D-QCA analysis (*n* = 28 pullback sets)	
Proximal bifurcation angle (°)	155.1 ± 11.6
Distal bifurcation angle (°)	44.2 ± 8.8
Proximal reference diameter (mm)	3.23 ± 0.57
Distal reference diameter in MB (mm)	2.68 ± 0.46
Reference SB diameter (mm)	2.43 ± 0.46
MB ostium area (mm)	4.03 ± 2.16
MB ostium diameter (mm)	2.18 ± 0.61
SB ostium area (mm)	2.98 ± 1.71
SB ostium diameter (mm)	1.88 ± 0.53

All values presented as *n* (%) or mean ± SD.
3D-QCA, three-dimensional quantitative coronary angiography; LAD, left anterior descending artery; LCx, left circumflex artery; MB, main-branch; OM, obtuse marginal branch; RPD, right posterior descending artery; RPL, right posterolateral branch; SB, side-branch.

an experienced observer (A.K.). Measurements were performed (i) by conventional analysis of the SB pullback; (ii) by conventional analysis of the MB pullback; and (iii) by cut-plane analysis of the MB pullback. Conventional analysis measurements from the SB pullback were used as a reference. Measurements included SB diameter and area, which were defined as the diameter and area, respectively, of the SB ostium. The SB ostium for the purposes of the analysis was defined as the first frame with carina visualization. SB diameter measurements included the minimum, maximum, and mean lumen diameters.

SB pullback: conventional analysis

The SB ostium was identified and diameter and area measurements were performed using the St Jude/Lightlab offline software for C7XR pullbacks and the QCU-CMS software (Medis Specials bv) for Lunawave pullbacks.

MB pullback: conventional analysis

The SB ostium was identified in the MB pullback. Diameter and area measurements were performed in the SB ostium using the St Jude/Lightlab offline software for C7XR pullbacks and the QCU-CMS for Lunawave pullbacks.

MB pullback: cut-plane analysis

The MB pullbacks were saved as DICOM files and imported in the QAngioOCT software. The imaged SB was identified and analysed by the 'cut-plane' analysis module in the software. Image data on the cut-plane were reconstructed and visualized in 3D. The position and orientation of the cut-plane can be easily manipulated by using the cross-sectional and longitudinal images so that the cut-plane is adjusted to capture the true vessel morphology perpendicular to the SB centreline. Quantification can be then directly performed from the cut-plane image. An example is presented in *Figure 3*.

Variability assessment

All QAngioOCT measurements were assessed for intra-observer and inter-observer variability. Intra-observer variability was assessed by re-analysis of all studies by the same observer after 2 weeks. Inter-observer variability was assessed by reanalysis of all studies by a second independent observer (N.v.D.).

Statistical analysis

All analyses were performed using the SPSS 20.0 (IBM, Chicago, IL, USA). The Pearson correlation coefficient was used to assess correlations of measurements acquired from the SB with measurements acquired by the MB with conventional or cut-plane analysis, and the significance of the difference of the derived correlation coefficients was assessed by the *z*-test, following Fisher's *r*-to-*z* transformation. The measurement error for each method compared with reference measurements was assessed by Bland–Altman plots. Differences in the absolute measurement error were assessed with the paired *t*-test. Intra-class correlation coefficients (ICCs) for absolute agreement and Bland–Altman statistics were used to assess intra- and inter-observer variability. A univariate logistic regression analysis was performed to identify variables independently associated with measurement error of the SB area. All variables with a *P*-value of <0.15 in the univariate analysis were examined with multi-adjusted linear regression analysis with backward elimination, after excluding variables with high collinearity. A *P*-value of <0.05 indicated statistical significance.

Results

Baseline and angiographic results

Baseline characteristics are summarized in *Table 1*. Angiographic characteristics and 3D-QCA are described in *Table 2*. Three patients had two separate sets of OCT examinations: in two cases they were performed pre- and post-stent implantation and in the other case the first set was performed after stent implantation and the second for follow-up evaluation. 3D-QCA was performed in 28/31 cases, where two angiographic views with $>25^\circ$ difference in the projection angle were available. The mean proximal reference diameter was 3.23 ± 0.57 mm, mean reference diameter in distal MB was 2.68 ± 0.46 mm, mean reference SB diameter was 2.43 ± 0.46 mm, mean proximal bifurcation angle was $155.1^\circ \pm 11.6^\circ$, and mean distal bifurcation angle was $44.2^\circ \pm 8.8^\circ$.

Table 3 Optical coherence tomography measurements and corresponding errors

	SB pullback: conventional analysis	MB pullback: conventional analysis			MB pullback: cut-plane analysis		
	Reference measurement (mean ± SD)	Measurement (mean ± SD)	Error (95% limits of agreement)	Pearson correlation coefficient (95% CI)	Measurement (mean ± SD)	Error (95% limits of agreement)	Pearson correlation coefficient (95% CI)
SB ostium lumen area (mm^2)	3.51 ± 1.70	4.43 ± 3.06	0.92 (−2.66 to 4.49)	0.870 (0.745 to 0.936)	3.57 ± 1.92	0.06 (−1.37 to 1.50)	0.927 (0.853 to 0.964)
SB ostium mean diameter (mm)	2.06 ± 0.56	2.20 ± 0.82	0.14 (−0.89 to 1.17)	0.788 (0.602 to 0.893)	2.05 ± 0.58	−0.01 (−0.47 to 0.46)	0.918 (0.835 to 0.960)
SB ostium minimum diameter (mm)	1.72 ± 0.57	1.80 ± 0.80	0.08 (−0.88 to 1.03)	0.812 (0.643 to 0.906)	1.64 ± 0.62	−0.08 (−0.76 to 0.60)	0.841 (0.690 to 0.922)
SB ostium maximum diameter (mm)	2.53 ± 0.61	2.71 ± 0.85	0.19 (−1.14 to 1.51)	0.635 (0.362 to 0.808)	2.48 ± 0.61	0.00 (−0.80 to 0.81)	0.770 (0.567 to 0.885)

CI, confidence intervals; MB, main-branch; SB, side-branch.

OCT analysis

OCT measurements are presented in *Table 3*, together with the measurement errors and correlation coefficients. Correlations of area and diameters of the SB ostium, acquired from the MB pullback in comparison with those acquired from the SB pullback, were higher with cut-plane analysis than with conventional analysis, albeit not reaching significance (area: $r_{\text{cut-plane}} = 0.927$ vs. $r_{\text{conventional}} = 0.870$, $P = 0.256$; mean diameter: $r_{\text{cut-plane}} = 0.918$ vs. $r_{\text{conventional}} = 0.788$, $P = 0.056$; minimum diameter: $r_{\text{cut-plane}} = 0.841$ vs. $r_{\text{conventional}} = 0.812$, $P = 0.734$; maximum diameter: $r_{\text{cut-plane}} = 0.770$ vs. $r_{\text{conventional}} = 0.635$, $P = 0.316$).

As seen in the Bland–Altman plots, conventional measurements of SB ostium area, mean diameter, minimum diameter, and maximum diameter from the MB pullback were associated with significant error (*Figures 3–7*). Cut-plane analysis was associated with higher reliability, which can be appreciated by the lower mean error and the narrower limits of agreement (*Figures 3–7*). The absolute value of the error in SB ostium measurements was reduced from 1.50 ± 1.31 to 0.56 ± 0.45 mm^2 for area ($P < 0.001$), from 0.44 ± 0.30 to 0.18 ± 0.14 mm for mean diameter ($P < 0.001$), from 0.39 ± 0.29 to 0.22 ± 0.27 mm for minimum diameter ($P = 0.007$), and from 0.59 ± 0.37 to 0.30 ± 0.26 mm for maximum diameter ($P < 0.001$), when cut-plane analysis was used instead of conventional analysis (*Figure 8*).

In conventional analysis from the MB pullback, the measurement error of the SB area was independently associated with the distal reference diameter in SB and the presence of SB stent. However, the per cent measurement error (measurement error/SB ostium area in SB pullback × 100) was associated only with the distal bifurcation angle (*Tables 4* and *5*).

Variability analysis

Intra- and inter-observer agreement is presented in *Table 6*. Intra-observer agreement was very high for all measurements (all ICCs > 0.90). Inter-observer agreement was also very high (ICCs > 0.90),

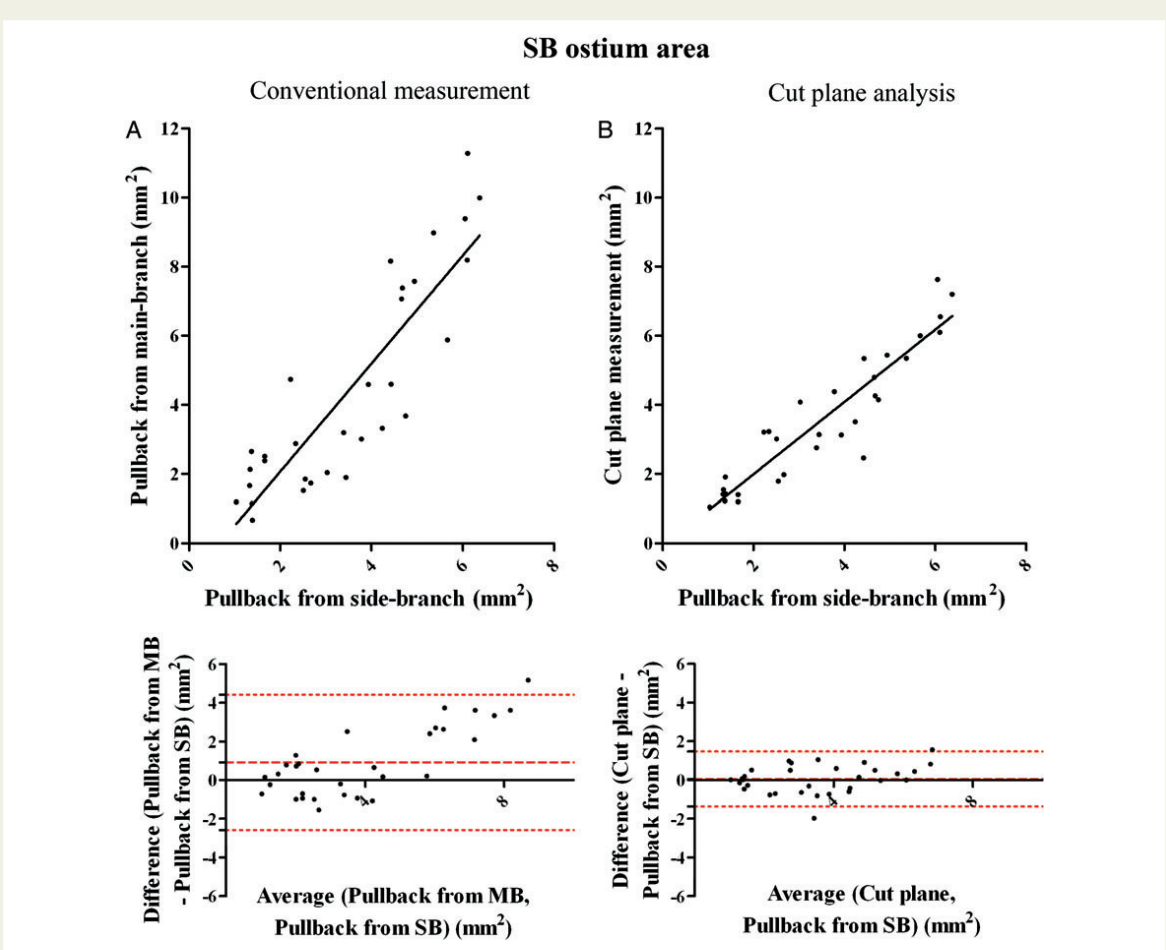

Figure 4: Correlation and Bland–Altman plots of SB ostium area by (*A*) conventional analysis and (*B*) cut-plane analysis of MB pullback. Area measurements from the SB pullback are used as a reference. Red dashed lines correspond to measurement error and red dotted lines to 95% confidence intervals. Abbreviations as in *Figure 1*.

with the exception of maximum diameter where it was relatively good (ICC = 0.79).

Analysis of pullbacks with incomplete SB visualization

Cut-plane analysis was successful in all 12 cases with incomplete SB visualization at the MB pullback. This series comprised nine left main bifurcations and three left anterior descending-diagonal bifurcations with a mean distal bifurcation angle of 55.7 ± 13.0°. Reference measurements were 5.58 ± 2.29 mm^2 for the SB area and 2.59 ± 0.56 mm for the mean SB diameter. The SB area by cut-plane analysis was 5.66 ± 2.69 mm^2 and the mean SB diameter 2.63 ± 0.59 mm. Correlation coefficients of the SB area and the mean SB diameter by cut-plane analysis with reference measurements were 0.876 and 0.915, respectively. The respective measurement errors and 95% limits of agreement were 0.09 mm^2 (−2.51 to 2.69 mm^2) for the SB area and 0.04 mm (−0.48 to 0.55 mm) for the mean SB diameter. An example of a case without SB ostium visualization at the level of the carina is portrayed in *Figure 9*.

Discussion

The main findings of this study are that in OCT assessment of SBs in coronary bifurcations: (i) there is high error when SB ostial measurements are obtained by conventional analysis of pullbacks performed in the MB; (ii) use of dedicated software that reconstructs the cross-sections perpendicular to the SB centreline can significantly reduce the error in assessment of SB ostium luminal dimensions and provide highly reliable measurements; and (iii) this analysis is highly reproducible with low intra- and inter-observer differences. Thus, this novel approach could alleviate the need for an additional OCT pullback and help avoid SB instrumentation.

Assessment of bifurcation lesions and treatment strategy planning remains challenging. In daily practice, strategy planning often depends on whether or not there is a significant lesion at the SB ostium requiring treatment. Angiography is often hampered to answer this question, as vessel overlap, flow phenomena and foreshortening limit angiographic image interpretation, despite major advances such as dedicated quantitative online analysis and 3D rendering.[13] Therefore, we are interested to understand the potential of invasive imaging methods to overcome this limitation.

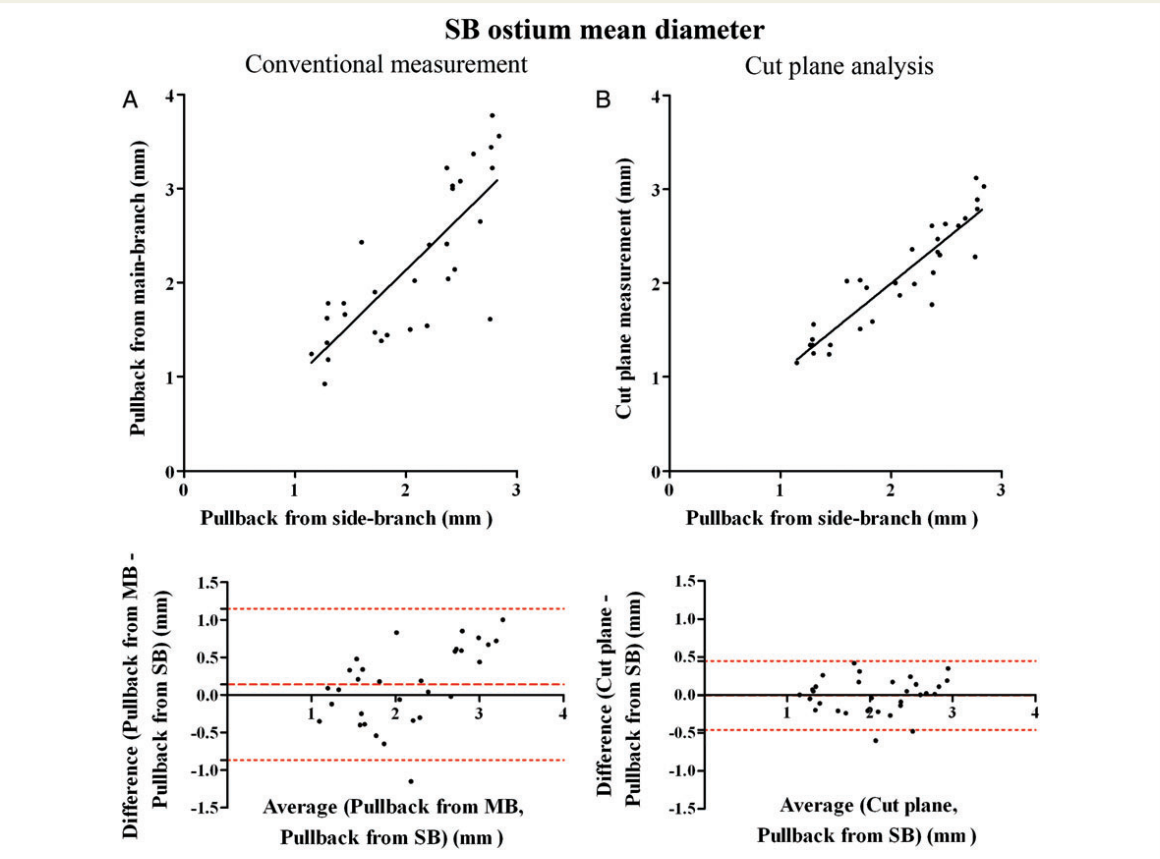

Figure 5: Correlation and Bland–Altman plots of SB ostium mean diameter by (*A*) conventional analysis and (*B*) cut-plane analysis of MB pullback. Mean diameter measurements from the SB pullback are used as a reference. Red dashed lines correspond to measurement error and red dotted lines to 95% confidence intervals. Abbreviations as in *Figure 1*.

Previous intravascular ultrasound (IVUS) studies have studied the accuracy of SB evaluation from a main-branch pullback, showing that lumen and plaque measurements are subject to significant error depending on the relative position of the IVUS catheter.[9] Similarly, in OCT studies of non-bifurcated segments, errors in luminal measurements are common, especially for the maximum diameter, due to misalignment of the imaging catheter with the lumen centreline.[8,11] Likewise, in our study, SB ostial measurements obtained by conventional analysis of a MB pullback were subject to significant error. This error was markedly high with wide limits of agreement, with an absolute value of 1.50 ± 1.31 mm^2 for area and 0.44 ± 0.30 mm for mean diameter. Importantly, in 50% of cases, the absolute error in SB ostium diameter measurement was >0.4 mm (*Figure 8B*). This could have important implications in the therapeutic approach, as such a difference could lead to suboptimal sizing when SB treatment is required. Moreover, while the main determinant of SB area measurement error was the SB reference diameter—with larger SBs associated with higher measurement errors—when the per cent SB area measurement error was assessed, the distal bifurcation angle was the only variable with a significant association. Therefore, assessment of the SB ostium area from the MB pullback using conventional analysis should be avoided in cases with high distal bifurcation angle, as the error can be particularly high. This finding is in accordance with *ex vivo* and *in vitro* IVUS studies showing significant variability in measurements, depending on the angle of incidence of the ultrasound beam.[14,15] Furthermore, in conventional assessment there was a mean overestimation of the SB area by 0.92 mm^2 and of the mean diameter by 0.14 mm. A possible explanation for this overestimation lies in the non-coaxial position of the catheter relative to the SB, at least in not severely diseased or extremely angulated vessels, as illustrated in *Figure 1*.

In our study, dedicated analysis was associated with a lower measurement error, and demonstrated high agreement with reference measurements. In contrast to conventional assessment there was no significant overestimation, as the mean error was 0.06 mm^2 for area and −0.01 mm for the mean diameter, with relatively narrow limits of agreement. In almost all cases, the absolute error was <2.00 mm^2 for area and 0.5 mm for diameter (*Figure 8A* and *B*), indicating that cut-plane assessment can provide a good estimate for SB ostial dimensions. Notably, this finding seems rather robust, as this

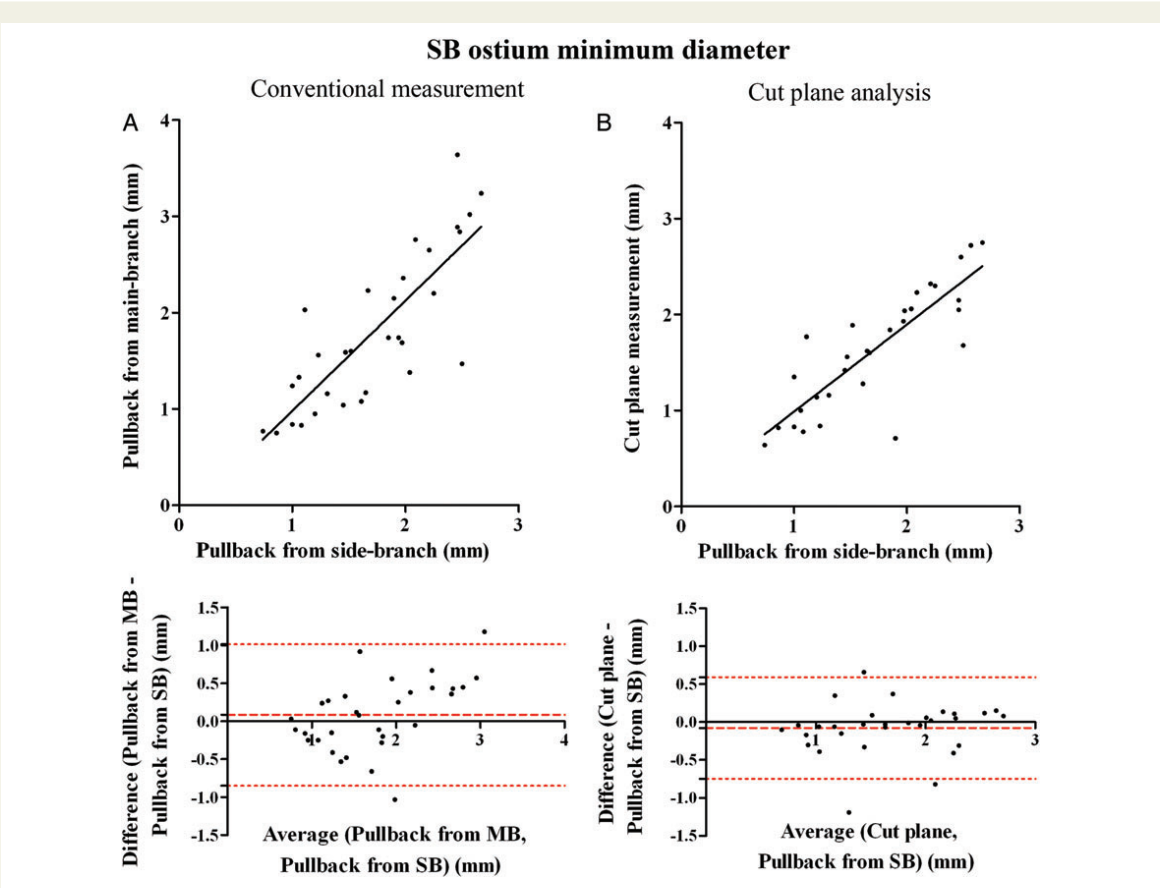

Figure 6: Correlation and Bland–Altman plots of SB ostium minimum diameter by (*A*) conventional analysis and (*B*) cut-plane analysis of MB pullback. Minimum diameter measurements from the SB pullback are used as a reference. Red dashed lines correspond to measurement error and red dotted lines to 95% confidence intervals. Abbreviations as in *Figure 1*.

was observed in OCT pullback sets acquired for different imaging indications, in different clinical settings, with different imaging systems, and both in native and stented coronary arteries (half of the patients had stent in the MB at the carina level and one-third in the SB), reflecting real-world clinical scenarios. This 3D-OCT reconstruction and cut-plane analysis could be readily available after transferring the OCT pullback to the workstation, thus allowing implementation in the daily cath-lab practice.

Despite, however, the better association with reference measurements compared with conventional analysis, the limits of agreement were somewhat wider for minimal and maximal diameter. This was more pronounced for maximal diameter, where intra- and inter-observer agreement were also lower (intra-observer ICC = 0.93; inter-observer ICC = 0.79). A number of reasons may account for these minor discrepancies. First, the selection of a plane perpendicular to the SB is performed by visual estimation of the SB centreline by the observer, and thus subject to error. Secondly, as shown in *Figure 1*, maximal diameter measurements are highly dependent on the catheter position. This variability is also found in inter-study comparisons of OCT and IVUS pullbacks.[8,10] Thus, even reference measurements of minimal and maximal diameter are subject to error as the catheter tends to follow the outer vessel curve. Thirdly, OCT studies are subject to sampling bias due to (i) longitudinal resolution of 100–200 μm, depending on sampling rate and (ii) coronary artery movement,[16] making therefore exact anatomic matching of the ostium not always possible. Nevertheless, the overall error was relatively low (mean absolute error of 0.18 mm for the minimum diameter and 0.30 for the maximum diameter) and in any case significantly lower that the error encountered in conventional analysis of MB pullbacks.

In our study, we included only a small percentage of patients (31 out of 98) with imaging of both the MB and the SB. It is important to note that the reason for excluding a large number of cases from this study was that conventional measurements were used for comparison. As a consequence, a large number of pullback sets ($n = 51$), mainly with left main bifurcations, was excluded from this study due to out-of-view artefact resulting in incomplete visualization of the SB ostium from the MB pullback. Nevertheless, as demonstrated by our additional series of 12 patients, assessment of the SB ostium is also feasible by cut-plane analysis in these cases with larger SBs (mean SB ostium diameter: 2.59 ± 0.56 mm) and higher bifurcation angle

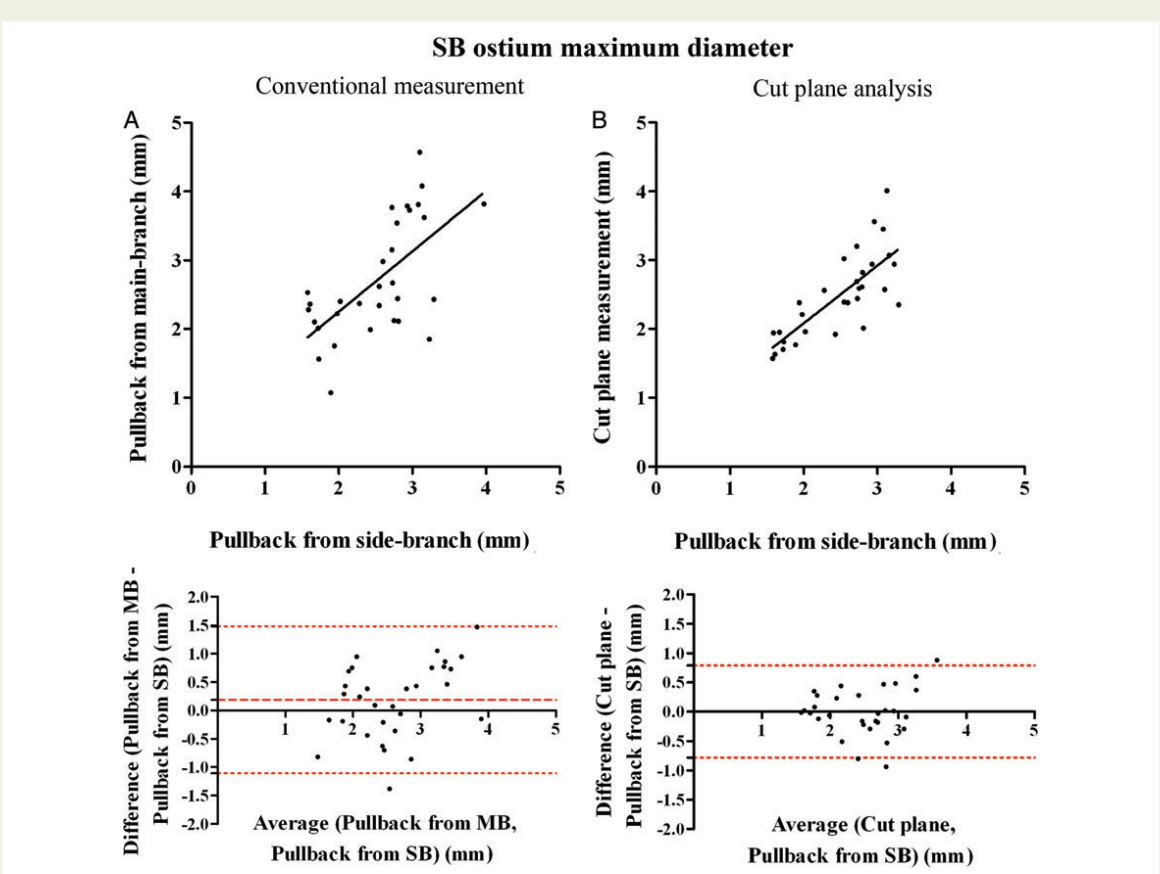

Figure 7: Correlation and Bland–Altman plots of SB ostium maximum diameter by (*A*) conventional analysis and (*B*) cut-plane analysis of MB pullback. Maximum diameter measurements from the SB pullback are used as a reference. Red dashed lines correspond to measurement error and red dotted lines to 95% confidence intervals. Abbreviations as in *Figure 1*.

(mean: 55.7 ± 13.0°), with a relatively low measurement error compared with reference measurements. Therefore, cut-plane analysis can be potentially used for the evaluation of a higher percentage of pullbacks that comprise 84% of cases in this series, whereas conventional analysis can only be performed in a much lower percentage.

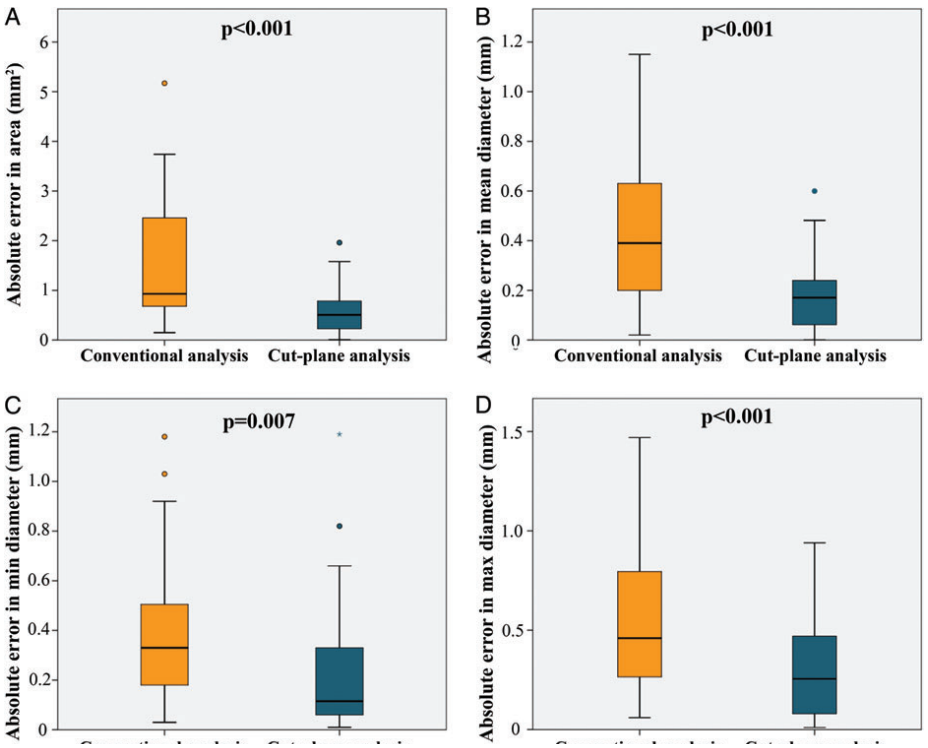

Figure 8: Box plots of absolute values of measurement error in (*A*) area, (*B*) mean diameter, (*C*) minimum diameter, and (*D*) maximum diameter for conventional vs. cut-plane analysis. The top and bottom of boxes correspond to first and third quartiles respectively, with the line representing the median. Abbreviations as in *Figure 1*.

Table 4 Unadjusted and multi-adjusted predictors of absolute measurement error in SB ostial area measurements from a MB pullback

	Measurement error in SB area					
	Unadjusted analysis			Multi-adjusted analysis		
	b	95% CI	*P* value	*b*	95% CI	*P* value
Proximal bifurcation angle (°)	−0.035	−0.095 to 0.026	0.247			
Distal bifurcation angle (°)	**0.072**	**−0.005** to **0.148**	**0.065**	Eliminated		0.103
Proximal reference diameter (3D-QCA) (mm)	**1.230**	**0.395** to **2.064**	**0.006**	Eliminated		0.731
Distal reference diameter in MB (3D-QCA) (mm)	**0.947**	**−0.205** to **2.099**	**0.103**	Eliminated		0.847
Reference SB diameter (3D-QCA) (mm)	**1.969**	**0.634** to **3.303**	**0.005**	**1.593**	**0.407** to **3.033**	**0.012**
MB stent	−0.022	−1.126 to 1.082	0.968			
SB stent	**1.153**	**0.250** to **2.056**	**0.014**	**0.772**	**−0.105** to **1.648**	**0.082**

Variables entered and included in the final model are indicated in bold.
3D-QCA, three-dimensional quantitative coronary angiography; CI, confidence intervals; MB, main-branch; SB, side-branch.

Table 5 **Unadjusted and multi-adjusted predictors of per cent measurement error in SB ostial area measurements from a MB pullback**

	Per cent measurement error in SB area					
	Unadjusted analysis			Multi-adjusted analysis		
	b	95% CI	*P* value	*b*	95% CI	*P* value
Proximal bifurcation angle (°)	−0.715	−2.180 to 0.750	0.325			
Distal bifurcation angle (°)	**2.175**	**0.412** to **3.938**	**0.018**	**2.175**	**0.412** to **3.938**	**0.018**
Proximal reference diameter (3D-QCA)(mm)	0.940	−0.596 to 2.476	0.220			
Distal reference diameter in MB (3D-QCA)(mm)	8.208	−29.651 to 46.106	0.659			
Reference SB diameter (3D-QCA)(mm)	22.797	−13.375 to 58.969	0.207			
MB stent	−2.458	−30.635 to 25.718	0.860			
SB stent	15.262	−9.700 to 40.224	0.221			

Variables entered and included in the final model are indicated in bold.
3D-QCA, three-dimensional quantitative coronary angiography; CI, confidence intervals; MB, main-branch; SB, side-branch.

Table 6 **Intra- and inter-observer variability**

	Observer 1—Measurement 1	Observer 1—Measurement 2	Difference (Measurement 1—Measurement 2)	ICC (95% CI)	Observer 2	Difference (Observer 1—Observer 2)	ICC (95% CI)
SB ostium lumen area (mm^2)	3.57 ± 1.92	3.53 ± 1.91	0.04 (−0.92 to 1.00)	0.97 (0.94 to 0.98)	3.38 ± 1.83	0.18 (−1.08 to 1.45)	0.94 (0.88 to 0.97)
SB ostium mean diameter (mm)	2.05 ± 0.58	2.04 ± 0.58	0.01 (−0.25 to 0.27)	0.98 (0.95 to 0.99)	2.00 ± 0.57	0.05 (−0.32 to 0.42)	0.95 (0.89 to 0.97)
SB ostium minimum diameter (mm)	1.64 ± 0.62	1.65 ± 0.58	0.00 (−0.27 to 0.33)	0.97 (0.94 to 0.99)	1.60 ± 0.59	0.08 (−0.42 to 0.58)	0.91 (0.81 to 0.96)
SB ostium maximum diameter (mm)	2.48 ± 0.61	2.51 ± 0.58	0.00 (−0.47 to 0.47)	0.93 (0.85 to 0.97)	2.47 ± 0.62	0.04 (−0.76 to 0.84)	0.79 (0.61 to 0.90)

Values are presented as mean ± SD, or mean (95% limits of agreement).
CI, confidence intervals; ICC, intra-class correlation coefficient; SB, side-branch.

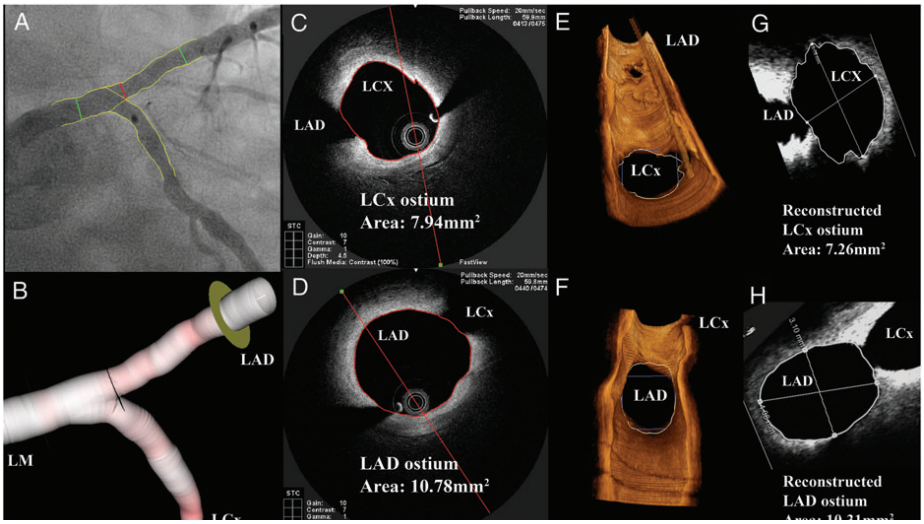

Figure 9: OCT evaluation of left main bifurcation with high distal bifurcation angle (64°) from original and reconstructed OCT pullbacks. (*A* and *B*) 2-D and 3-D angiographic views of the imaged left main bifurcation. (*C* and *D*) Ostia of the LCx and the LAD, respectively, as visualized by OCT pullbacks performed in the ipsilateral branch. Note that ostia of the contralateral branch are not completely visualized in the cross-sectional images. (*E* and *F*) Three-dimensional renderings showing the contralateral branch ostium. (*G* and *H*) Cut-plane analysis showing reconstructed ostia, generated by the contralateral branch pullback. LAD, left anterior descending artery; LCx, left circumflex artery; OCT, optical coherence tomography.

Clinical implications

These findings are clinically remarkable as they suggest that this novel approach could basically alleviate the need for additional OCT pullback in the SB, taking into account the accuracy of the obtained measurements and the therapeutic options, where stent diameters are typically sized at 0.5 mm incremental steps. Consequently, the demonstrated reliable SB assessment with the potential to limit SB instrumentation could significantly reduce procedural complexity, improve treatment strategy planning and potentially improve outcome of bifurcation lesions in the future.

Limitations

Limitations of this study include the relatively small sample size and that it mainly consisted of LAD-diagonal bifurcations, thus not completely representative of all bifurcation subsets. Nevertheless, as mentioned this is mainly a result of limitations of the conventional analysis that was used for comparison, and cut-plane analysis can also be applied in the majority of these cases. Inter- and intra-observer agreement in our measurements, performed in a laboratory setting, was excellent for lumen area and mean diameter with narrow limits of agreement. However, since the selection of a plane perpendicular to the SB involves a user-dependent factor which is the visual estimation of the SB centreline, the possibility of a higher variability in measurements performed by less experienced analysts cannot be excluded. Finally, as this is a retrospective study, selection bias cannot be excluded. A potential selection bias could explain the relatively low bifurcation angle (55.7 $\pm$ 13.0°) in our additional consecutive series of patients compared with previously reported values of 80 $\pm$ 21° for the left main and 48 $\pm$ 16° for LAD-diagonal bifurcations.[13]

Conclusions

In OCT assessment of SB ostia from a main-branch pullback there is high error when the SB area and diameters are measured by conventional analysis. Assessment in a laboratory setting by dedicated software that can reconstruct the cross-sections perpendicular to the SB centreline is associated with a significantly lower error and has a high correlation with reference measurements performed from a SB pullback. This approach could potentially limit the need for SB instrumentation and thereby reduce procedural complexity in the assessment of bifurcation lesions.

Conflict of interest: S.T. is employed by Medis and has a research appointment at Leiden University Medical Center. J.H.C.R. is the CEO of Medis, and has a part-time appointment at Leiden University Medical Center as Professor of Medical Imaging.

Funding

A.K. would like to acknowledge the funding support of the Hellenic Heart Foundation and St Jude Medical.

References

1. Koo BK, Kang HJ, Youn TJ, Chae IH, Choi DJ, Kim HS *et al.* Physiologic assessment of jailed side branch lesions using fractional flow reserve. *J Am Coll Cardiol* 2005;**46**:633–7.
2. Karanasos A, Tu S, van der Heide E, Reiber JH, Regar E. Carina shift as a mechanism for sidebranch compromise following main vessel intervention: insights from three-dimensional optical coherence tomography. *Cardiovasc Diagn Ther* 2012;**2**:173–7.

3. Farooq V, Serruys PW, Heo JH, Gogas BD, Okamura T, Gomez-Lara J *et al.* New insights into the coronary artery bifurcation hypothesis-generating concepts utilizing 3-dimensional optical frequency domain imaging. *JACC Cardiovasc Interv* 2011;**4**: 921–31.
4. Koo BK, Waseda K, Kang HJ, Kim HS, Nam CW, Hur SH *et al.* Anatomic and functional evaluation of bifurcation lesions undergoing percutaneous coronary intervention. *Circ Cardiovasc Interv* 2010;**3**:113–9.
5. Suarez de Lezo J, Medina A, Martin P, Novoa J, Pan M, Caballero E *et al.* Predictors of ostial side branch damage during provisional stenting of coronary bifurcation lesions not involving the side branch origin: an ultrasonographic study. *EuroIntervention* 2012; **7**:1147–54.
6. Di Mario C, Iakovou I, van der Giessen WJ, Foin N, Adrianssens T, Tyczynski P *et al.* Optical coherence tomography for guidance in bifurcation lesion treatment. *EuroIntervention* 2010;**6**(Suppl. J):J99–J106.
7. Karanasos A, Tu S, van der Linden M, van Weenen S, Ligthart J, Regar E. Online 3-dimensional rendering of optical coherence tomography images for the assessment of bifurcation intervention. *Can J Cardiol* 2012;**28**:759e1–3.
8. Sawada T, Shite J, Negi N, Shinke T, Tanino Y, Ogasawara D *et al.* Factors that influence measurements and accurate evaluation of stent apposition by optical coherence tomography. Assessment using a phantom model. *Circ J* 2009;**73**:1841–7.
9. Oviedo C, Maehara A, Mintz GS, Tsujita K, Kubo T, Doi H *et al.* Is accurate intravascular ultrasound evaluation of the left circumflex ostium from a left anterior descending to left main pullback possible? *Am J Cardiol* 2010;**105**:948–54.
10. Suter Y, Schoenenberger AW, Toggweiler S, Jamshidi P, Resink T, Erne P. Intravascular ultrasound-based left main coronary artery assessment: comparison between pullback from left anterior descending and circumflex arteries. *J Invasive Cardiol* 2009;**21**:457–60.
11. Tu S, Xu L, Ligthart J, Xu B, Witberg K, Sun Z *et al.* In vivo comparison of arterial lumen dimensions assessed by co-registered three-dimensional (3D) quantitative coronary angiography, intravascular ultrasound and optical coherence tomography. *Int J Cardiovasc Imaging* 2012;**28**:1315–27.
12. Tu S, Holm NR, Christiansen EH, Reiber JH. First presentation of 3-dimensional reconstruction and centerline-guided assessment of coronary bifurcation by fusion of X-ray angiography and optical coherence tomography. *JACC Cardiovasc Interv* 2012;**5**: 884–5.
13. Tu S, Jing J, Holm NR, Onsea K, Zhang T, Adriaenssens T *et al.* In vivo assessment of bifurcation optimal viewing angles and bifurcation angles by three-dimensional (3D) quantitative coronary angiography. *Int J Cardiovasc Imaging* 2012;**28**:1617–25.
14. Di Mario C, Madretsma S, Linker D, The SH, Bom N, Serruys PW *et al.* The angle of incidence of the ultrasonic beam: a critical factor for the image quality in intravascular ultrasonography. *Am Heart J* 1993;**125**(2 Pt 1):442–8.
15. Chae JS, Brisken AF, Maurer G, Siegel RJ. Geometric accuracy of intravascular ultrasound imaging. *J Am Soc Echocardiogr* 1992;**5**:577–87.
16. Wang T, Wieser W, Springeling G, Beurskens R, Lancee CT, Pfeiffer T *et al.* Intravascular optical coherence tomography imaging at 3200 frames per second. *Opt Lett* 2013;**38**:1715–7.

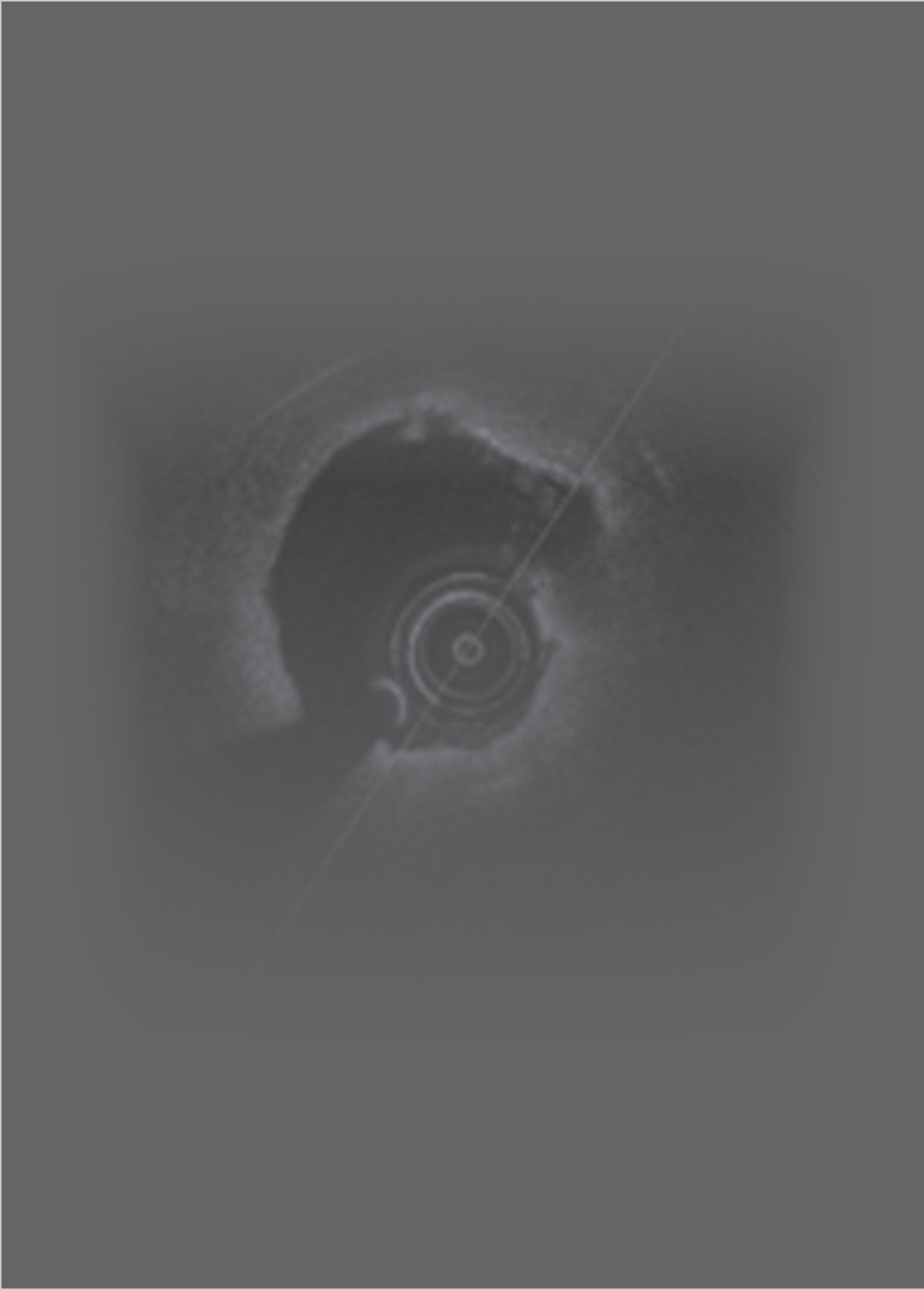

PART III

Optical coherence tomography in the assessment of late metallic stent failure

Chapter 3.1

In-stent neoatherosclerosis: a cause of late stent thrombosis in a patient with “full metal jacket” 15 years after implantation: insights from optical coherence tomography

Karanasos A, Ligthart JM, Regar E

JACC Cardiovasc Interv. 2012 Jul;5(7):799-800

IMAGES IN INTERVENTION

In-Stent Neoatherosclerosis

A Cause of Late Stent Thrombosis in a Patient With "Full Metal Jacket" 15 Years After Implantation: Insights From Optical Coherence Tomography

Antonios Karanasos, MD, Jurgen M. R. Ligthart, BSc, Evelyn Regar, MD, PhD

Rotterdam, the Netherlands

A 62-year-old man presented with inferior ST-segment elevation myocardial infarction for primary percutaneous coronary intervention. He had a history of myocardial infarction 15 years ago and had a bare-metal stent implanted in the right coronary artery. Upon presentation, coronary angiography revealed total occlusion of the right coronary artery, which was covered at its full length with stents (Fig. 1A). We performed thrombus aspiration with partial restoration of antegrade flow (Fig. 1B) and proceeded with optical coherence tomography imaging of the vessel.

Optical coherence tomography (Fig. 2, Online Video 1) revealed a highly heterogeneous tissue coverage, presenting with several features that resemble native atherosclerosis, such as calcific depositions and thin-cap fibroatheroma (1,2). A rupture was detected in the neointima with mural thrombus at the rupture site protruding into the lumen. The neointima had high variability across the stent demonstrating different patterns of coverage (3), as well as a peristrut low-intensity area, reported to correspond to areas of fibrin accumulation (4). Although, there have been pathological reports demonstrating growth of de novo

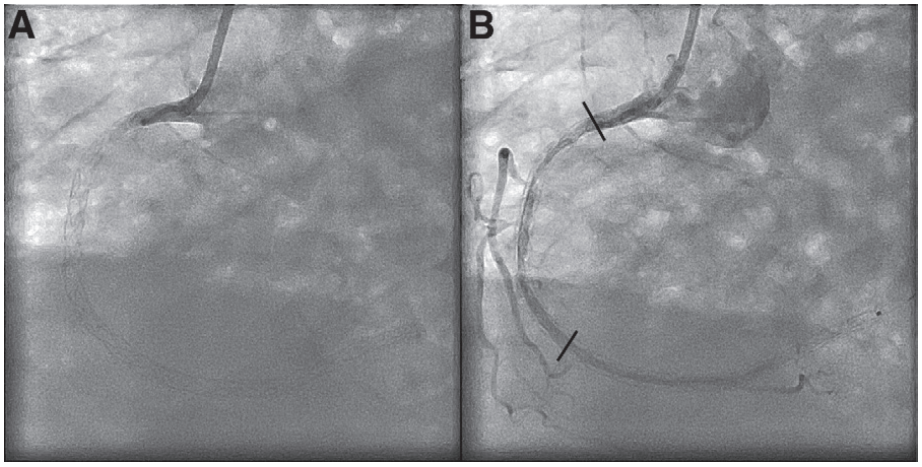

Figure 1. Coronary Angiography of the Right Coronary Artery Pre-and Post-Manual Thrombus Aspiration

(A) Pre- and **(B)** post-manual thrombus aspiration. **Black lines** indicate optical coherence tomography pullback.

From the Department of Cardiology, Thoraxcenter, Erasmus Medical Center, Rotterdam, the Netherlands. Dr. Karanasos was supported by a grant from the Hellenic Heart Foundation. Dr. Ligthart is a consultant for Volcano Corp., Boston Scientific, and St. Jude Medical. Dr. Regar has reported that she has no relationships relevant to the contents of this paper to disclose.

Manuscript received February 9, 2012, accepted February 18, 2012.

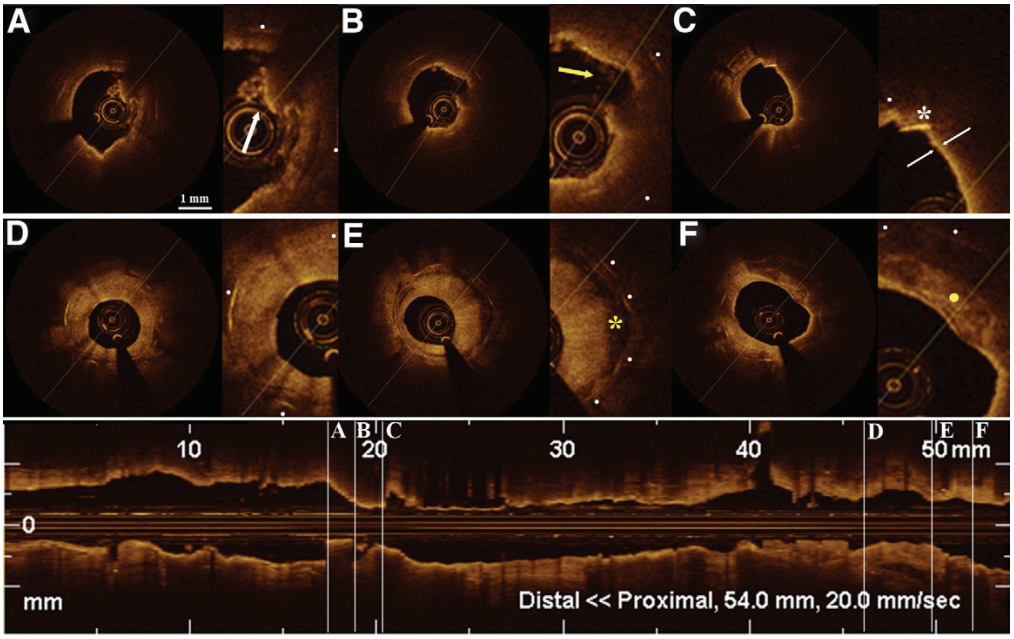

Figure 2. Optical Coherence Tomography Cross-Sectional Images With Magnification and L-Mode Reconstruction

White dots mark the stent struts. **(A)** Neointimal rupture with mural thrombus protrusion **(white arrow). (B)** Neointimal rupture **(yellow arrow). (C)** Layered pattern consistent with thin-cap fibroatheroma (cap thickness: 40 μm) with high-intensity signal, possibly corresponding to macrophage infiltration or cholesterol crystal protrusion **(white asterisk). (D)** Heterogeneous pattern of tissue coverage. **(E)** Homogeneous pattern of tissue coverage with peristrut low-intensity area **(yellow asterisk). (F)** Layered pattern consistent with fibrocalcific plaque **(yellow dot).**

atheromatic tissue inside stents (1), now with optical coherence tomography, it is feasible to unravel the complexity of this entity in vivo, as well as the mechanisms of thrombus formations in such cases.

Reprint requests and correspondence: Dr. Evelyn Regar, Department of Cardiology, Thoraxcenter, BA-585, Erasmus University Medical Centre's Gravendijkwal 230, 3015 CE Rotterdam, the Netherlands. E-mail: e.regar@erasmusmc.nl.

REFERENCES

1. Inoue K, Abe K, Ando K, et al. Pathological analyses of long-term intracoronary Palmaz-Schatz stenting; is its efficacy permanent? Cardiovasc Pathol 2004;13:109–15.
2. Kang SJ, Mintz GS, Akasaka T, et al. Optical coherence tomographic analysis of in-stent neoatherosclerosis after drug-eluting stent implantation. Circulation 2011;123:2954–63.
3. Gonzalo N, Serruys PW, Okamura T, et al. Optical coherence tomography patterns of stent restenosis. Am Heart J 2009;158:284–93.
4. Otake H, Shite J, Ikeno F, et al. Evaluation of the peri-strut low intensity area following sirolimus- and paclitaxel-eluting stents implantation: insights from an optical coherence tomography study in humans. Int J Cardiol 2010;157:38–42.

Chapter 3.2

OCT demonstrating neoatherosclerosis as part of the continuous process of coronary artery disease

Zhang BC, **Karanasos A**, Regar E

Herz 2015 Sep;40(6):845-854

B.-C. Zhang[1,2] · A. Karanasos[1] · E. Regar[1]

[1] Department of Cardiology, Thorax Center, Erasmus Medical Center, Rotterdam, The Netherlands [2] Department of Cardiology, The Affiliated Hospital of Xuzhou Medical College, Jiangsu, China

OCT demonstrating neoatherosclerosis as part of the continuous process of coronary artery disease

Drug-eluting stents (DES) have reduced the rates of target vessel revascularization and comprise the mainstay of treatment in percutaneous coronary intervention. However, despite the excellent short- and mid-term results with the current DES generation, ongoing stent failure with both bare metal stents (BMS) and DES is a frequent finding very late after stent implantation [1–3]. Very late stent failure clinically manifests as very late restenosis or stent thrombosis. Although the pathogenesis of (very) late stent failure appears to be multifactorial [4, 5], one of the major mechanisms that have been implicated is the de novo development of atherosclerosis within the neointimal region, called neoatherosclerosis [6, 7]. Observations of neoatherosclerosis have been documented both in ex vivo pathological observations and in vivo by intravascular imaging.

Among several imaging modalities that have been used to identify neoatherosclerosis [8–11], optical coherence tomography (OCT) can provide the most comprehensive assessment of the neointimal tissue. OCT allows for the visualization of the micromorphology of coronary arteries with near-histological resolution, differentiating between individual plaque components and providing important quantitative plaque information as the thickness of the fibrous plaque [12, 13]. Thus, by OCT it is possible to assess distinct morphological characteristics of

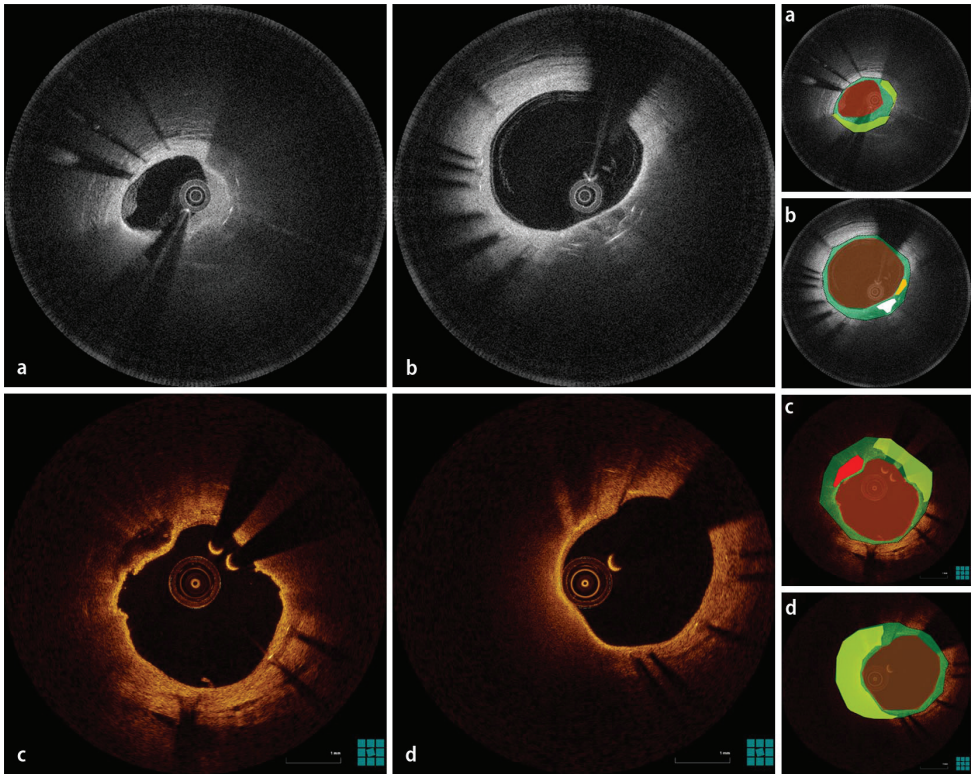

Fig. 1 ◄ Morphological characteristics of in-stent neoatherosclerosis on optical coherence tomography images. **a** In-stent necrotic core (*yellow*) within the neointima (*green*). **b** In-stent calcification (*white*) and macrophage infiltration (orange). **c** Neointimal rupture. **d** In-stent necrotic core (*yellow*) with thin overlying fibrous cap. Panels on the right are color-coded cartoons of the corresponding OCT images, explaining the composition of the neointimal tissue.

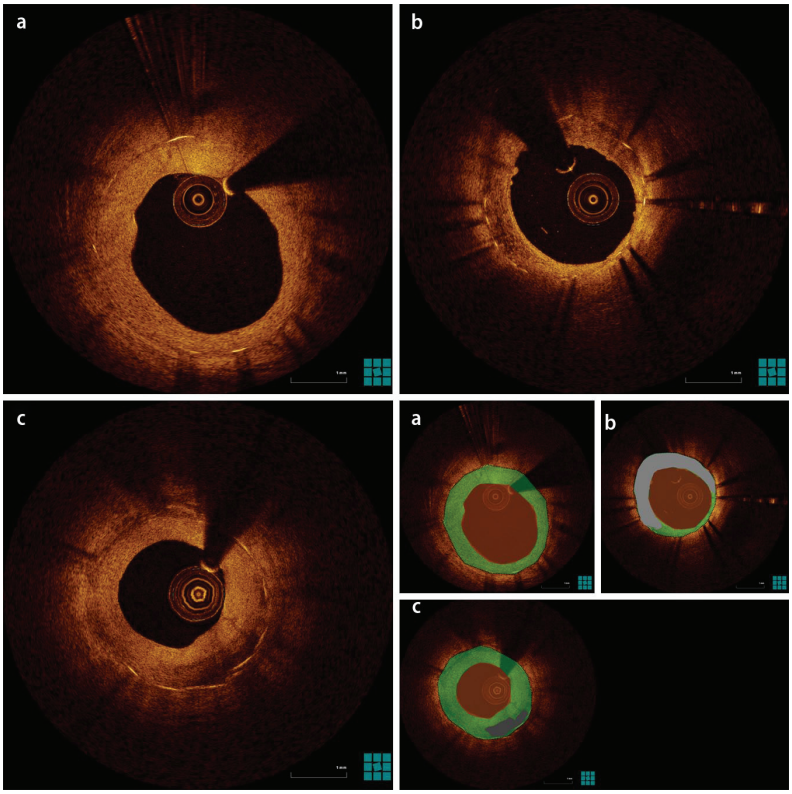

Fig. 2 ▲ Patterns of neointimal coverage as visualized on optical coherence tomography images. **a** Homogeneous pattern (*green*); **b** heterogeneous pattern (*light gray*); **c** layered pattern (*dark gray*). Panels on the bottom right are color-coded cartoons of the corresponding OCT images, explaining the composition of the neointimal tissue.

neoatherosclerosis, such as macrophage infiltration, lipid accumulation, in-stent calcification, or neointimal rupture. Consequently, in vivo OCT studies have focused on studying in-stent neoatherosclerosis and its association with late stent failure. This review summarizes the current insights into neoatherosclerosis obtained with OCT and discusses the implications of neoatherosclerosis on long-term outcome after stent implantation.

Definition and OCT imaging evidence of in-stent neoatherosclerosis

Neoatherosclerosis refers to an atherosclerotic change in neointimal tissue, first described in pathologic specimens of BMS, and more recently in pathologic specimens of DES as well [6, 7]. Although observations of neoatherosclerosis had been sporadically documented from the early application of OCT [14, 15], the tissue properties of the observed neointimal tissue patterns were unknown. Pathological studies were the first to provide more comprehensive insights regarding the histological composition of this entity. These studies defined neoatherosclerosis as the presence of clusters of lipid-laden foamy macrophages with or without necrotic core formation and/or calcification within the neointimal tissue of stented segments [6]. The presence of morphological components of native atherosclerosis within the neointimal tissue implies that these features can be identified by OCT, which has a high accuracy for detection of these characteristics in native atherosclerotic plaques. This hypothesis has been corroborated by a pathologic study of ex vivo stented coronary arteries, imaged by OCT, which showed that the OCT appearance of these characteristics is similar to that in native atherosclerosis [16]. Components of neoatherosclerosis that can be visualized by OCT include macrophage infiltration, necrotic core, in-stent calcifications, and neoatherosclerotic plaque rupture [17]. An in-stent necrotic core visualized by OCT is defined as the presence of signal-poor, highly attenuating regions with poorly delineated borders within the neointima, while in-stent calcifications are defined as well-delineated, signal-poor regions with sharp borders [16]. In accordance with native atherosclerosis, macrophages on OCT appear as a thin signal-bright layer causing high attenuation, while neointimal plaque rupture appears as a discontinuation in the luminal surface with formation of a cavity burrowing into the neointima [16]. Representative OCT images of in-stent neoatherosclerosis are shown in **Fig. 1**.

At this point it is important to emphasize the difference of neoatherosclerosis with the previously reported heterogeneous and layered patterns of coverage [18]. These patterns are respectively defined as neointimal tissue with focally changing optical properties and varying backscattering patterns, and as neointimal tissue with concentric layers having different optical properties (an adluminal high scattering layer and an abluminal low scattering layer). Such patterns are often encountered in the context of in-stent restenosis, and although the pathological substrate is not well characterized, histological findings from atherectomy specimens, autopsy, and animal experiments include organized thrombus, fibrin, and myxomatous extracellular matrix with sporadic evidence of inflammation [16, 19–21]. The association of these patterns with neoatherosclerosis is yet unknown, however there is evidence that these patterns similar to the homogeneous pattern may subsequently be replaced by neoatherosclerotic tissue [22, 23]. Representative OCT images of different neointimal coverage patterns are shown in **Fig. 2**.

Although OCT can discern the distinct morphological characteristics of neoatherosclerosis, caution should be applied to image interpretation. This is because macrophage infiltration can sometimes appear as in-stent necrotic core, and vice versa [24]. Also, the distinction of a layered pattern of coverage with in-stent necrotic core can also be challenging some-

Abstract · Zusammenfassung

Herz 2015 · 40:845–854 DOI 10.1007/s00059-015-4343-y

B.-C. Zhang · A. Karanasos · E. Regar

OCT demonstrating neoatherosclerosis as part of the continuous process of coronary artery disease

Abstract

Although the advent of drug-eluting stents has reduced the rates of target vessel revascularization, there are observations of ongoing stent failure occurring very late after stent implantation and presenting as very late restenosis or as very late stent thrombosis. The de novo development of atherosclerosis within the neointimal region, called neoatherosclerosis, has been identified as one of the pathomechanisms of these observed late stent failures. The mechanisms of neoatherosclerosis development and its association with stent failure are currently the subject of intensive research. Optical coherence tomography (OCT) is an invasive imaging modality that allows us to visualize the micromorphology of coronary arteries with near-histological resolution, thus providing detailed assessment of the morphological characteristics of the neointima after stent implantation, including neoatherosclerosis. Several OCT studies have tried to provide in vivo insights in the mechanisms of neoatherosclerosis development and its association with late stent failure. This review summarizes the current insights into neoatherosclerosis obtained with OCT and discusses the association of neoatherosclerosis with late stent failure.

Keywords

Atherosclerosis · Optical coherence tomography · Percutaneous coronary intervention · Drug-eluting stents · Bare metal stents

OCT-Nachweis einer Neoatherosklerose als Teil des fortlaufenden Prozesses der koronaren Herzkrankheit

Zusammenfassung

Zwar ist es durch das Aufkommen medikamentenbeschichteter Stents zu einer Senkung der Rate von Zielgefäßrevaskularisierungen gekommen, aber es wurden Fälle fortlaufenden Stentversagens beobachtet, die erst sehr spät nach Stentimplantation auftreten und sich mit großer zeitlicher Verzögerung als Restenosierung oder als sehr späte Stentthrombose manifestieren. Das De-novo-Auftreten einer Atherosklerose innerhalb der neointimalen Region, als Neoatherosklerose bezeichnet, hat sich als einer der Pathomechanismen dieser späten Fälle von Stentversagen herausgestellt. Die Mechanismen der Neoatheroskleroseentstehung und ihr Zusammenhang mit einem Stentversagen werden derzeit noch intensiv untersucht. Die optische Kohärenztomographie (OCT) ist ein invasives bildgebendes Verfahren, mit dem sich die Mikromorphologie der Koronararterien in nahezu histologischer Auflösung darstellen lässt und das somit eine detaillierte Beurteilung der morphologischen Merkmale der Neointima nach Stentimplantation, einschließlich Neoatherosklerose, ermöglicht. Im Rahmen verschiedener OCT-Studien wurde versucht, in vivo einen Einblick in die Mechanismen der Neoatheroskleroseentstehung und ihren Zusammenhang mit spätem Stentversagen zu erhalten. In der vorliegenden Übersichtsarbeit wurde der Schwerpunkt auf die zusammenfassende Darstellung aktueller Erkenntnisse aus der OCT in Bezug auf die Neoatherosklerose gelegt und der Zusammenhang der Neoatherosklerose mit spätem Stentversagen erörtert.

Schlüsselwörter

Atherosklerose · Optische Kohärenztomographie · Perkutane Koronarintervention · Medikamentenbeschichtete Stents · Reine Metallstents

times, although the low attenuation observed in the case of the layered pattern can be used to discriminate between these two entities [16]. Finally, with OCT it is not possible to distinguish between true adluminal atherosclerosis from the progression of an abluminal underlying necrotic core into the neointima. Nevertheless, the latter mechanism appears to be less prevalent [25], while it is unclear what the clinical significance of such a discrimination would be.

In vivo prevalence of neoatherosclerosis in BMS and DES with OCT

Several studies have tried to investigate the prevalence of neoatherosclerosis late after BMS or DES implantation using OCT (**Table 1**). The reported prevalence varies highly between the studies. As these studies differ significantly in stent type, in the interval between stent implantation and follow-up, and in the clinical presentation, this difference in prevalence appears to reflect differences in the composition of the studied population. The first reports of in-stent neoatherosclerosis report a prevalence of 67 % in patients with BMS implantation beyond 5 years [15]. Subsequent studies have shown lower prevalence ranging between 30 and 50 % in long-term follow-up of asymptomatic patients with BMS [26–28]; however, this incidence could be as high as 100 % in BMS restenosis more than 10 years since implantation [29]. With regard to neoatherosclerosis within DES, a prevalence of more than 50 % has been reported in a very late follow-up [27, 28], which can be even higher in stents with failure [14]. These rates tend to generally be in accordance with rates reported by pathological studies, which show a prevalence of 13–65 % depending on stent type and stent age [25].

Major factors associated with in-stent neoatherosclerosis

Stent type and age

Pathological studies were the first to indicate a potential association of stent type and stent age with the prevalence of neoatherosclerosis [6]. DES appear to have a higher prevalence of neoatherosclerosis compared with BMS. Moreover, irrespective of stent type, the interval from implantation appears to be strongly associated with neoatherosclerosis development, an interval which is much lower than the interval required for development of native atherosclerotic plaques [25]. Nakazawa et al. [6] first demonstrated an increased prevalence of neoatherosclerosis in autopsy specimens of first-generation DES compared with BMS despite a shorter interval from implantation. Importantly, in both groups, the prevalence of neoatherosclerosis increased with the inter-

Table 1 Reported prevalence of neoatherosclerosis assessed by OCT in late stent follow-up studies

Study	Indication (*n*)	Stent type (*n*)	Follow-up duration	Prevalence (%)
Takano et al. [15]	Follow-up (21)	BMS (21)	≥5 years	67
Kitabata et al. [27]	Follow-up (36)	1st and 2nd DES (19) BMS (17)	60 months 126 months	59 42
Kim et al. [22]	Follow-up (76)	1st and 2nd DES (76)	9 months 2 years	15 28
Kozuki et al. [23]	Follow-up (62)	1st DES (62)	3–12 months 36–80 months	3 23
Yonetsu et al. [30]	Follow-up (138)	1st and 2nd DES (82) BMS (56)	9 months 9–48 months ≥48 months 9 months 9–48 months ≥48 months	37 63 75 8 28 77
Kuramitsu et al. [34]	Follow-up (33)	2nd DES (12) 1st DES (11) BMS (10)	5 years	2 (frames) 10 (frames) 2 (frames)
Kitabata et al. [41]	Follow-up (46)	BMS (46)	≥4 years	47
Tian et al. [36]	Follow-up (109)	DES (109)	1 year	13.8
Hou et al. [26]	Follow-up (60)	BMS (60)	7±1 years	33
Kang et al. [9]	Restenosis (50)	1st and 2nd DES (50)	32 (9–52) months	90
Kang et al. [29]	Restenosis (22)	BMS (22)	132±31 months	100
Ino et al. [38]	Restenosis (48)	1st DES (48)	8±1 months 34±14 months	27 83
Ali et al. [8]	Restenosis (65)	1st and 2nd DES (51) BMS (14)	33 (16–60) months 36 (15–113) months	68 36
Habara et al. [45]	Restenosis (86)	1st DES (86)	1 year 1–3 years 3 years	2 14 35
Lee et al. [33]	Restenosis (212)	1st DES (111) 2nd DES (101)	55 months 12 months	46 11
Ko et al. [54]	Stent thrombosis (18)	1st and 2nd DES (18)	42±21 months	22
Amabile et al. [50]	Stent thrombosis (20)	1st DES (4) and BMS(16)	8 (1–18) years	50
Amioka et al. [51]	Stent thrombosis (23)	1st DES (13) BMS (10)	1,750±770 days 3,224±1,380 days	46 50
Kang et al. [52]	Stent thrombosis (33)	1st DES (27) BMS (6)	Median: 62 months Median: 110 months	56 100
Alfonso et al. [67]	Stent thrombosis (15)	BMS(8) and DES (7)	Median: 347 days	27
Karanasos et al. [49]	Follow-up (22) Restenosis (13) Thrombosis (39)	BMS (13)/1st and 2nd DES (61)	≥18 months Median: 63 months	32 85 67

BMS bare metal stents, *1st DES* first-generation drug-eluting stents, *2nd DES* second-generation drug-eluting stents, *OCT* optical coherence tomography.

val since implantation [6]. In vivo OCT studies have been in line with pathological studies showing an increased prevalence of neoatherosclerosis in DES at a follow-up of up to 4 years, although at a very long-term follow-up the prevalence is similarly high for both stent types [30]. Furthermore, serial imaging observations in first- and second-generation DES demonstrate that neointimas with a homogeneous or heterogeneous pattern of coverage might develop neoatherosclerosis over time with the prevalence of neoatherosclerosis increasing from 15% at 9 months to 28% at 24 months since implantation [22]. This was further corroborated by another serial imaging study in first-generation DES where the incidence of neoatherosclerosis increased from 3% at mid-phase observations (3–12 months after stent implantation) to 23% at late-phase observations [23].

Although DES in general appear to have a higher prevalence of neoatherosclerosis than BMS, it is not clear whether the prevalence of neoatherosclerosis differs between first- and second-generation DES. Second-generation DES have improved biocompatibility due to thinner struts and more biocompatible or bioabsorbable polymers, which translates to lower vascular toxicity and hypersensitivity reactions [31, 32]. However, a human autopsy study did not demonstrate any significant difference in the prevalence of neoatherosclerosis between a second-generation DES, cobalt-chromium everolimus-eluting stent (CoCr-EES), and first-generation paclitaxel-eluting (PES) or sirolimus-eluting stent (SES): CoCr-EES = 29%; SES = 35%; PES = 19% [32]. Conversely, an in vivo OCT study in 212 DES-treated patients with >50% stenosis (101 patients had a first-generation and 111 patients had a second-generation DES) demonstrated a significantly lower prevalence of neoatherosclerosis in the second-generation DES group (10.8 vs. 45.5%, $p<0.001$); however, this difference was not significant after adjusting for time since implantation [33]. Similar findings were observed with OCT in a comparison of the coronary arterial response in biodegradable polymer biolimus-eluting stents (BES) versus durable polymer SES and BMS at the 5-year follow-up. The number of cross sections with neoatherosclerosis within BES was similar to BMS (BES = 2.26% vs. BMS = 2.23%, $p=0.98$) and tended to be lower than SES (BES = 2.26% vs. SES = 9.90%, $p=0.07$) [34].

The reasons why the temporal course of atherosclerosis within stents is accelerated are not well understood; however, dysfunction of endothelial cells, which are barriers that prevent lipid infiltration and

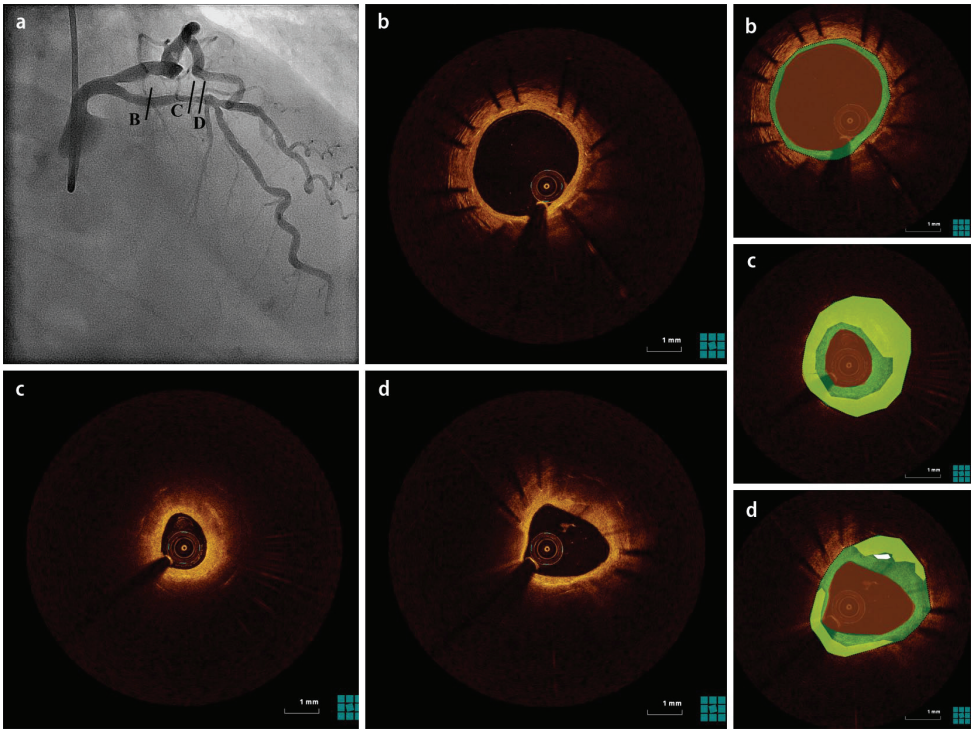

Fig. 3 ◀ Late restenosis due to neoatherosclerosis. **a** Angiogram of patient presenting with stable angina 15 years after sirolimus-eluting stent implantation reveals a possible restenotic lesion in the site of the previously implanted stent. Optical coherence tomography study reveals a homogeneous pattern of coverage (*green*) proximal to the stent (**b**), but with neoatherosclerosis development (*yellow*) at the distal segment (**c** and **d**) causing lumen compromise. Panels on the right are color-coded cartoons of the corresponding OCT images, explaining the composition of the neointimal tissue.

migration of inflammatory cells, has been considered to be the main mechanism. This mechanism can also explain the increased prevalence of neoatherosclerosis observed in DES, where local drug delivery inhibits neointimal hyperplasia, causing delayed coverage and dysfunction of endothelial cells [35].

Clinical factors

In addition to the stent type and age, several patient characteristics have been associated with neoatherosclerosis. Two registries of late stent follow-up have both identified chronic kidney disease as a factor independently associated with neoatherosclerosis [28, 33]. Other identified factors included low-density lipoprotein cholesterol >70 mg/dl [33], current smoking, and lack of treatment with angiotensin-converting enzyme inhibitors or angiotensin II receptor blockers [28]. In another study, the presence of diabetes mellitus was associated with a higher incidence of neoatherosclerosis at a late DES follow-up (18.3 vs. 5.5 %, $p=0.03$) [36]. Further subgroup analysis showed that elevated glycated hemoglobin (HbA_{1c}) levels (>7 %) in patients with diabetes mellitus were associated with a higher incidence of neoatherosclerosis (28 vs. 7 %, $p=0.048$).

Plaque and stent characteristics

Plaque characteristics have also been implicated in the neoatherosclerotic process. Microvessels play a key role in advanced atherosclerosis, which is closely associated with plaque hemorrhage and plaque rupture [37], while previous investigations have demonstrated a higher incidence of microvessels in late in-stent restenotic tissue, suggesting that neovessels might be a trigger for in-stent neoatherosclerosis [38, 39]. Moreover, a spatial correspondence of neoatherosclerosis and microvessels was identified at a follow-up OCT examination of BMS and DES [40], supporting the hypothesis of microvessel involvement in neoatherosclerosis development. In the same study, neoatherosclerosis was more frequently identified in the proximal and distal stent sections, also associated with the morphology of the adjacent vessel segment. Specifically, the presence of lipid plaque in the adjacent stent edges was associated with the presence of neoatherosclerosis at the stent edges, implying that progression of native disease might also contribute to neoatherosclerosis. Apart from plaque characteristics, stent characteristics such as strut thickness seem to play a role even among the same stent type. In a study assessing the prevalence of neoatherosclerosis in BMS at a long-term follow-up (≥4 years after implantation), thick-strut stents (≥100 μm) had a higher prevalence of neoatherosclerosis compared with thin-strut stents (70 vs. 32 %, $p=0.02$) [41].

Neoatherosclerosis and in-stent restenosis

Although early in-stent restenosis mainly results from aggressive neointimal proliferation [42], recent data also suggest that neoatherosclerosis may play an important pathophysiological role, especially in late restenosis. Pathological studies have demonstrated that neoatherosclerosis represents a common substrate in patients with late stent failure [43], while in vivo OCT studies have further elucidated the role of neoatherosclerosis in the development of late stent failure (**Fig. 3**). The presence of neoatherosclerosis has been

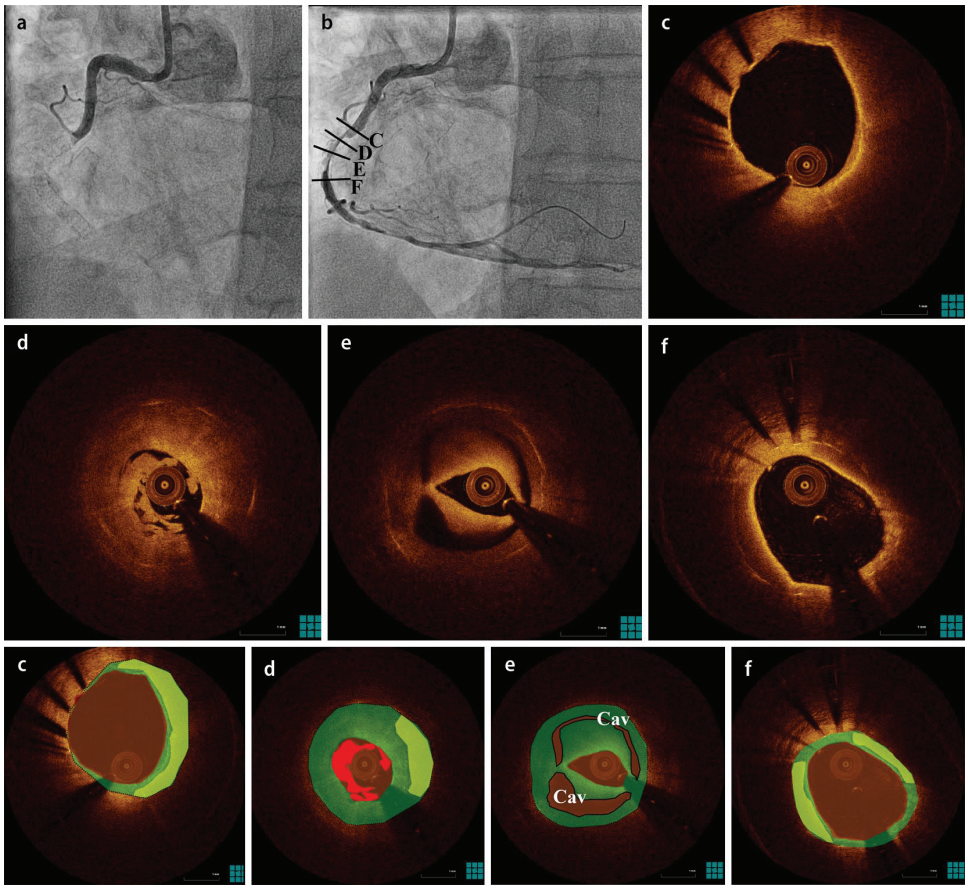

Fig. 4 ◀ Very late thrombosis due to neoatherosclerosis. **a** Angiogram of patient presenting with ST-elevation myocardial infarction 7 years after everolimus-eluting stent implantation in the right coronary artery showing total occlusion. After thrombus aspiration an in-stent lesion is obvious (**b**), while optical coherence tomography study shows neoatherosclerosis development (*yellow*) with neointimal rupture leading to cavity formation (*Cav*) and thrombus (*red*) (**c**–**f**). Homogeneous neointima is indicated in *green*. Panels on the bottom are color-coded cartoons of the corresponding OCT images, explaining the composition of the neointimal tissue.

associated with a higher degree of neointimal hyperplasia, independent from stent type and time since implantation [44]. Although during the early phases after DES implantation, homogeneous or heterogeneous patterns of coverage are the predominant pathology in in-stent restenosis, in later follow-up intervals restenosis is often associated with the presence of neoatherosclerosis [38, 45]. A study focusing on 50 patients with DES restenosis at a median follow-up of 32 months since implantation showed a prevalence of neoatherosclerosis of 52 % [9]. Also, in lesions with very late BMS restenosis beyond 10 years since implantation, neoatherosclerosis was detected in 100 % of the stents with a high frequency of neointimal rupture and neointimal thrombi [29]. However, a comparison of restenotic lesions of DES and BMS showed that neoatherosclerosis occurs earlier in DES compared with BMS and develops more diffusely along stented vessels with thinner cap and greater total lipid core [8]. Whether the contribution of neoatherosclerosis in restenosis of second-generation DES is similar to that of first-generation DES is not well established; however, observations of restenosis due to neoatherosclerosis have also been reported for second-generation DES [33].

Neoatherosclerosis and stent thrombosis

Neoatherosclerosis also appears to contribute to the development of (very) late stent thrombosis (**Fig. 4**). Initial pathological studies demonstrated a role for the underlying plaque in BMS thrombosis, while subsequent studies in DES incriminated an impaired healing response with high rates of uncovered struts and vascular toxicity-associated malapposition as the main pathogenetic factor [46, 47]. Nevertheless, more recent pathological and intracoronary imaging data support the hypothesis that neoatherosclerosis is an active causal mechanism in a high percentage of cases with late stent thrombosis [32, 48, 49]. Autopsy studies have shown that thrombosis might develop on the grounds of neointimal plaque rupture [32], while thrombus aspirate samples from patients with very late BMS thrombosis demonstrate the presence of atherosclerotic plaque components such as foamy macrophages and cholesterol crystals within the aspirates [48]. Simultaneously, a number of studies have examined the OCT findings in patients with late and very late stent thrombosis, in an attempt to identify the pathomechanisms [50–54]. Despite minor discrepancies in the exact prevalence of neoatherosclerosis and the relative contribution of neointimal plaque rupture in each study, these studies collectively demonstrate a very high prevalence of plaque rupture as a pathomechanism for very late BMS thrombosis [55], and an almost equal contribution for neo-

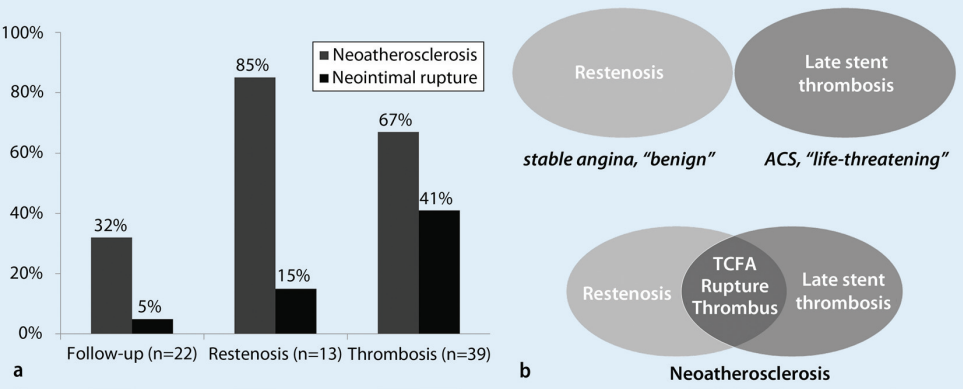

Fig. 5 ▲ **a** Prevalence of neoatherosclerosis and neointimal rupture according to clinical presentation [49]. **b** Change in the understanding of stent failure by intravascular imaging insights. Although stent restenosis had traditionally been considered a benign entity associated with stable symptoms and stent thrombosis had been considered a life-threatening entity associated with acute presentation, intravascular imaging has disclosed the participation of neoatherosclerosis in both entities, with several imaging findings such as in-stent necrotic core, neointimal rupture, and thrombus being common between them

intimal plaque rupture and impaired healing in (very) late DES thrombosis [50, 52, 53]. Compared to an impaired healing response, neointimal rupture is a mechanism occurring mainly at longer intervals since stent implantation [50, 56], in neointimal regions with high necrotic core content and thin fibrous cap, similarly to what is observed in native atherosclerosis, but also with a very high incidence of macrophage infiltration [49].

Evidence also suggests that the clinical presentation of late stent failure is not exclusively affected by the presence of neoatherosclerosis but also by the morphological characteristics. In patients with in-stent restenosis, a higher incidence of OCT-defined thin-cap fibroatheroma, intimal rupture, and thrombi was identified in patients presenting with unstable angina compared with patients with stable symptoms [9]. Our group investigated the differences in the prevalence of neoatherosclerosis with regard to the clinical presentation [49]. Both stent restenosis and stent thrombosis had a higher prevalence of neoatherosclerosis compared with the asymptomatic group (stent thrombosis: 67 % vs. restenosis: 85 % vs. asymptomatic: 32 %; $p < 0.001$). However, the prevalence of neointimal rupture was higher in the stent thrombosis group (stent thrombosis: 41 % vs. restenosis: 15 % vs. asymptomatic: 5 %; $p < 0.001$) (**Fig. 5a**). This finding underscores the contribution of neoatherosclerosis development in the pathogenesis of late stent failure, while it indicates that neointimal rupture is mainly associated with acute presentation, although not infrequently encountered in stable or asymptomatic in-stent lesions.

Overall, intravascular imaging has changed the understanding of the pathogenesis of late restenosis and thrombosis by disclosing that neoatherosclerosis is a common pathomechanism in both entities (**Fig. 5b**). Stent restenosis had traditionally been considered a rather benign entity associated with stable symptoms, while stent thrombosis was seen as a life-threatening entity associated with acute presentation, with these two entities considered to be associated with different pathogenetic substrates. However, the presence—to a different extent—of common imaging findings such as in-stent necrotic core, neointimal rupture, and thrombus in both entities implies that these two presentations can occur as different manifestations of the same unfavorable healing process.

Neoatherosclerosis and bioresorbable scaffolds

Bioresorbable vascular scaffolds (BVS) are a new technology for percutaneous revascularization that are resorbed after an interval of 2–4 years since implantation. Conceptually, after this interval, the permanent vessel caging with the associated endothelial dysfunction disappears and this can lead to a reduction of stent-induced complications such as hypersensitivity reactions or neoatherosclerosis. First-in-man studies of BRS have demonstrated a favorable healing response at a very long-term follow-up with complete strut reabsorption, late luminal enlargement, and a potentially favorable plaque modification, while no cases of necrotic core accumulation of adluminal origin were observed [57]. As after bioresorption, the area corresponding to struts and neointima is consolidated with the underlying plaque, it resembles a native atherosclerotic plaque that is now well separated by the lumen by a signal-rich layer, a process modulated by hemodynamic factors [58] (**Fig. 6**). Nevertheless, as these first-in-man studies have focused on simple lesions, data on more complex lesions including thrombotic lesions are scarce [59]. Studies on more complex populations are ongoing, without, however, any worrying signs regarding neoatherosclerosis development in human studies of BVS thus far. Moreover, studies reporting on (very) late BVS thrombosis have not shown any evidence of scaffold thrombosis due to neointimal plaque rupture [60]. Therefore, the further development and implementation in the clinical practice of bioresorbable technologies might allow these complications to be overcome, although more long-term data are needed to confirm a potential benefit of this technology.

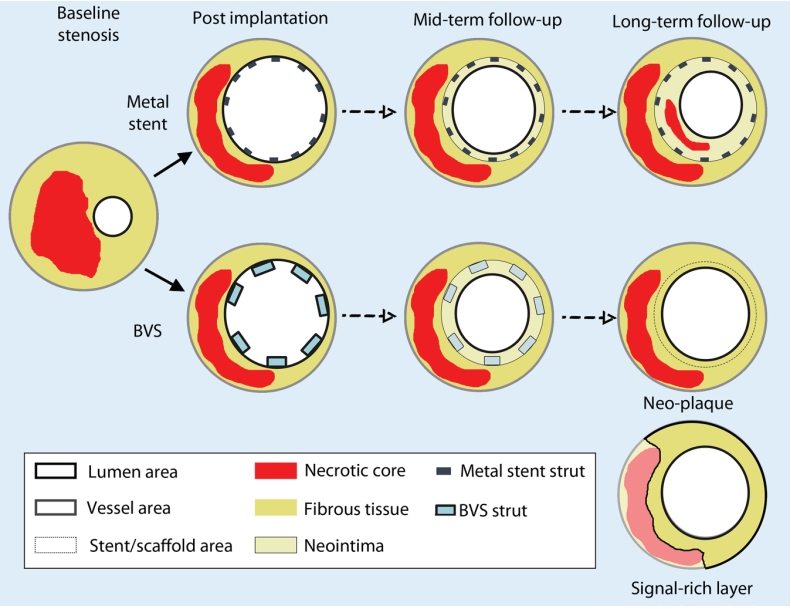

Fig. 6 ▲ Paradigm of healing response in metal stents and bioresorbable scaffolds. After metal stent implantation, struts are preserved and the neointimal area is clearly delineated between the stent and lumen contour even at long-term follow-up, with possible development of neoatherosclerosis within the neointima. Conversely, in long-term follow-up of bioresorbable scaffolds, neointimal boundaries are unclear after bioresorption (*dotted line*), and the intima resembles a native plaque, defined as neoplaque. The signal-rich layer is the layer that separates the underlying plaque components from the lumen. *BVS* bioresorbable vascular scaffold. (Adapted from Karanasos et al. [57])

Newer OCT techniques for assessment of neoatherosclerosis

As previously mentioned, OCT is associated with some limitations in assessment of neoatherosclerosis. Nevertheless, new developments in OCT could improve in-stent tissue characterization and provide an enhanced and more objective neointimal tissue characterization. One of these developments is quantitative attenuation imaging. Tissue properties such as attenuation have been shown in ex vivo studies to be associated with the presence of macrophages and/or necrotic core [61, 62], while in vivo studies have demonstrated the potential of this technique for the detection of lipid plaques and fibroatheromas [63]. Therefore, this technique could be used for the assessment of neoatherosclerosis, since the optical properties of tissue components such as macrophages and a necrotic core are similar between native atherosclerosis and neoatherosclerosis. OCT assessment of neoatherosclerosis can also be improved through software for automated fibrous cap thickness measurement that can reduce human variability in the assessment of in-stent fibroatheromas [64]. Furthermore, the application of technologies such as polarization-sensitive OCT in humans can provide further structural information such as collagen and smooth muscle content of neointimal tissue [65], while high-speed OCT catheters will be able to acquire images from an entire coronary artery in less than 1 s [66].

Conclusion and perspectives

Recent evidence has highlighted the significance of in-stent neoatherosclerosis as a disease entity that comprises an important substrate for late adverse cardiac events after stent implantation and is one of the major pitfalls of the current generation of metallic stents. Pathological studies have demonstrated that infiltration of lipid-laden foamy macrophages with or without necrotic core and/or calcification formation constitutes the pathological substrate. A number of in vivo studies have used OCT—an imaging modality that can accurately identify morphological characteristics such as in-stent necrotic core, in-stent calcification, macrophage infiltration, and neointimal plaque rupture—in order to assess the in vivo characteristics and implications of this disease entity. These have demonstrated that neoatherosclerosis appears earlier and more frequently in drug-eluting stents compared with bare metal stents, is associated with several clinical and morphological factors, while its prevalence increases over time. Importantly, an association of neoatherosclerosis with late stent failure has been demonstrated, manifesting either as late restenosis, or in cases with neointimal plaque rupture as late stent thrombosis. Bioresorbable technologies hold promise for the reduction of this entity; however, their long-term healing response needs to be better documented. Further studies are needed so as to demonstrate what the prognostic implications of neoatherosclerosis detection are, and whether the natural history of this disease entity can be modified. Meanwhile, new devices for percutaneous revascularization need to be developed that can alleviate this entity, in order to be able to reduce the incidence of very late events after percutaneous coronary intervention.

Corresponding address

E. Regar MD, PhD
Department of Cardiology, Thorax Center
Erasmus Medical Center, Room Ba-585
's-Gravendijkwal 230
3015 Rotterdam
e.regar@erasmusmc.nl

Compliance with ethical guidelines

Conflict of interest. B.C. Zhang, A. Karanasos, and E. Regar state that there are no conflicts of interest. The accompanying manuscript does not include studies on humans or animals.

References

1. Daemen J, Wenaweser P, Tsuchida K et al (2007) Early and late coronary stent thrombosis of sirolimus-eluting and paclitaxel-eluting stents in routine clinical practice: data from a large two-institutional cohort study. Lancet 369:667–678
2. Räber L, Magro M, Stefanini GG et al (2012) Very late coronary stent thrombosis of a newer-generation everolimus-eluting stent compared with early-generation drug-eluting stents a prospective cohort study. Circulation 125:1110–1121
3. Yamaji K, Kimura T, Morimoto T et al (2010) Very long-term (15–20 years) clinical and angiographic outcome after coronary bare metal stent implantation. Circ Cardiovasc Interv 3:468–475
4. Holmes DR Jr, Kereiakes DJ, Garg S et al (2010) Stent thrombosis. J Am Coll Cardiol 56:1357–1365
5. Windecker S, Meier B (2007) Late coronary stent thrombosis. Circulation 116:1952–1965
6. Nakazawa G, Otsuka F, Nakano M et al (2011) The pathology of neoatherosclerosis in human coronary implants bare-metal and drug-eluting stents. J Am Coll Cardiol 57:1314–1322
7. Inoue K, Abe K, Ando K et al (2004) Pathological analyses of long-term intracoronary Palmaz-Schatz stenting; is its efficacy permanent? Cardiovasc Pathol 13:109–115
8. Ali ZA, Roleder T, Narula J et al (2013) Increased thin-cap neoatheroma and periprocedural myocardial infarction in drug-eluting stent restenosis: multimodality intravascular imaging of drug-eluting and bare-metal stents. Circ Cardiovasc Interv 6:507–517
9. Kang SJ, Mintz GS, Akasaka T et al (2011) Optical coherence tomographic analysis of in-stent neoatherosclerosis after drug-eluting stent implantation. Circulation 123:2954–2963
10. Muraoka Y, Sonoda S, Kashiyama K et al (2012) Evaluation of in-stent neointimal tissue components using integrated backscatter intravascular ultrasound: comparison of drug-eluting stents and bare-metal stents. Int J Cardiovasc Imaging 28:1635–1641
11. Yokoyama S, Takano M, Yamamoto M et al (2009) Extended follow-up by serial angioscopic observation for bare-metal stents in native coronary arteries: from healing response to atherosclerotic transformation of neointima. Circ Cardiovasc Interv 2:205–212
12. Tearney GJ, Regar E, Akasaka T et al (2012) Consensus standards for acquisition, measurement, and reporting of intravascular optical coherence tomography studies: a report from the International Working Group for Intravascular Optical Coherence Tomography Standardization and Validation. J Am Coll Cardiol 59:1058–1072
13. Karanasos A, Ligthart J, Witberg K et al (2012) Optical coherence tomography: potential clinical applications. Curr Cardiovasc Imaging Rep 5:206–220
14. Tanimoto S, Aoki J, Serruys PW et al (2006) Paclitaxel-eluting stent restenosis shows three-layer appearance by optical coherence tomography. EuroIntervention 1:484
15. Takano M, Yamamoto M, Inami S et al (2009) Appearance of lipid-laden intima and neovascularization after implantation of bare-metal stents extended late-phase observation by intracoronary optical coherence tomography. J Am Coll Cardiol 55:26–32
16. Nakano M, Vorpahl M, Otsuka F et al (2012) Ex vivo assessment of vascular response to coronary stents by optical frequency domain imaging. JACC Cardiovasc Imaging 5:71–82
17. Karanasos A, Ligthart JM, Regar E (2012) In-stent neoatherosclerosis: a cause of late stent thrombosis in a patient with "full metal jacket" 15 years after implantation: insights from optical coherence tomography. JACC Cardiovasc Interv 5:799–800
18. Gonzalo N, Serruys PW, Okamura T et al (2009) Optical coherence tomography patterns of stent restenosis. Am Heart J 158:284–293
19. Nagai H, Ishibashi-Ueda H, Fujii K (2010) Histology of highly echolucent regions in optical coherence tomography images from two patients with sirolimus-eluting stent restenosis. Catheter Cardiovasc Interv 75:961–963
20. Tellez A, Afari ME, Buszman PP et al (2014) Peristrut low-intensity areas in optical coherence tomography correlate with peri-strut inflammation and neointimal proliferation: an in-vivo correlation study in the familial hypercholesterolemic coronary swine model of in-stent restenosis. Coron Artery Dis 25:595–601
21. Kim JS, Afari ME, Ha J et al (2014) Neointimal patterns obtained by optical coherence tomography correlate with specific histological components and neointimal proliferation in a swine model of restenosis. Eur Heart J Cardiovasc Imaging 15:292–298
22. Kim JS, Hong MK, Shin DH et al (2012) Quantitative and qualitative changes in DES-related neointimal tissue based on serial OCT. JACC Cardiovasc Imaging 5:1147–1155
23. Kozuki A, Shinke T, Otake H et al (2013) Temporal course of vessel healing and neoatherosclerosis after DES implantation. JACC Cardiovasc Imaging 6:1121–1123
24. Van Soest G, Regar E, Goderie TP et al (2011) Pitfalls in plaque characterization by OCT: image artifacts in native coronary arteries. JACC Cardiovasc Imaging 4:810–813
25. Otsuka F, Byrne RA, Yahagi K et al (2015) Neoatherosclerosis: overview of histopathologic findings and implications for intravascular imaging assessment. Eur Heart J. pii: ehv205. 2015 May 20. [EPub ahead of print]
26. Hou J, Qi H, Zhang M et al (2010) Development of lipid-rich plaque inside bare metal stent: possible mechanism of late stent thrombosis? An optical coherence tomography study. Heart 96:1187–1190
27. Kitabata H, Loh JP, Pendyala LK et al (2014) Intra-stent tissue evaluation within bare metal and drug-eluting stents > 3 years since implantation in patients with mild to moderate neointimal proliferation using optical coherence tomography and virtual histology intravascular ultrasound. Cardiovasc Revasc Med 15:149–155
28. Yonetsu T, Kato K, Kim SJ et al (2012) Predictors for neoatherosclerosis: a retrospective observational study from the optical coherence tomography registry. Circ Cardiovasc Imaging 5:660–666
29. Kang SJ, Song HG, Ahn JM et al (2012) OCT-verified neoatherosclerosis in BMS restenosis at 10 years. JACC Cardiovasc Imaging 5:1267–1268
30. Yonetsu T, Kim JS, Kato K et al (2012) Comparison of incidence and time course of neoatherosclerosis between bare metal stents and drug-eluting stents using optical coherence tomography. Am J Cardiol 110:933–939
31. Kim JS, Kim JS, Shin DH et al (2012) Optical coherence tomographic comparison of neointimal coverage between sirolimus- and resolute zotarolimus-eluting stents at 9 months after stent implantation. Int J Cardiovasc Imaging 28:1281–1287
32. Otsuka F, Vorpahl M, Nakano M et al (2014) Pathology of second-generation everolimus-eluting stents versus first-generation sirolimus- and paclitaxel-eluting stents in humans. Circulation 129:211–223
33. Lee SY, Hur SH, Lee SG et al (2015) Optical coherence tomographic observation of in-stent neoatherosclerosis in lesions with more than 50% neointimal area stenosis after second-generation drug-eluting stent implantation. Circ Cardiovasc Interv 8:e001878
34. Kuramitsu S, Sonoda S, Yokoi H et al (2014) Long-term coronary arterial response to biodegradable polymer biolimus-eluting stents in comparison with durable polymer sirolimus-eluting stents and bare-metal stents: five-year follow-up optical coherence tomography study. Atherosclerosis 237:23–29
35. Joner M, Nakazawa G, Finn AV et al (2008) Endothelial cell recovery between comparator polymer-based drug-eluting stents. J Am Coll Cardiol 52:333–342
36. Tian F, Chen Y, Liu H et al (2014) Assessment of characteristics of neointimal hyperplasia after drug-eluting stent implantation in patients with diabetes mellitus: an optical coherence tomography analysis. Cardiology 128:34–40
37. Virmani R, Kolodgie FD, Burke AP et al (2005) Atherosclerotic plaque progression and vulnerability to rupture: angiogenesis as a source of intraplaque hemorrhage. Arterioscler Thromb Vasc Biol 25:2054–2061
38. Ino Y, Kubo T, Kitabata H et al (2013) Difference in neointimal appearance between early and late restenosis after sirolimus-eluting stent implantation assessed by optical coherence tomography. Coron Artery Dis 24:95–101
39. Kim BK, Kim JS, Shin DH et al (2012) Optical coherence tomography evaluation of in-stent restenotic lesions with visible microvessels. J Invasive Cardiol 24:116–120
40. Tian J, Ren X, Uemura S et al (2014) Spatial heterogeneity of neoatherosclerosis and its relationship with neovascularization and adjacent plaque characteristics: optical coherence tomography study. Am Heart J 167:884–892.e882
41. Kitabata H, Kubo T, Komukai K et al (2012) Effect of strut thickness on neointimal atherosclerotic change over an extended follow-up period (≥ 4 years) after bare-metal stent implantation: intracoronary optical coherence tomography examination. Am Heart J 163:608–616
42. Toutouzas K, Karanasos A, Stefanadis C (2013) Inflammatory mechanisms of adverse reactions to BMS. Curr Vasc Pharmacol 11:379–391
43. Park SJ, Kang SJ, Virmani R et al (2012) In-stent neoatherosclerosis: a final common pathway of late stent failure. J Am Coll Cardiol 59:2051–2057
44. Vergallo R, Yonetsu T, Uemura S et al (2013) Correlation between degree of neointimal hyperplasia and incidence and characteristics of neoatherosclerosis as assessed by optical coherence tomography. Am J Cardiol 112:1315–1321
45. Habara M, Terashima M, Nasu K et al (2013) Morphological differences of tissue characteristics between early, late, and very late restenosis lesions after first generation drug-eluting stent implantation: an optical coherence tomography study. Eur Heart J Cardiovasc Imaging 14:276–284
46. Farb A, Burke AP, Kolodgie FD et al (2003) Pathological mechanisms of fatal late coronary stent thrombosis in humans. Circulation 108:1701–1706

47. Finn AV, Joner M, Nakazawa G et al (2007) Pathological correlates of late drug-eluting stent thrombosis: strut coverage as a marker of endothelialization. Circulation 115:2435–2441
48. Yamaji K, Inoue K, Nakahashi T et al (2012) Bare metal stent thrombosis and in-stent neoatherosclerosis. Circ Cardiovasc Interv 5:47–54
49. Karanasos A, Ligthart J, Witberg K et al (2013) Association of neointimal morphology by optical coherence tomography with rupture of neoatherosclerotic plaque very late after coronary stent implantation. In: Progress in Biomedical Optics and Imaging – Proceedings of SPIE. p 856542
50. Amabile N, Souteyrand G, Ghostine S et al (2014) Very late stent thrombosis related to incomplete neointimal coverage or neoatherosclerotic plaque rupture identified by optical coherence tomography imaging. Eur Heart J Cardiovasc Imaging 15:24–31
51. Amioka M, Shiode N, Kawase T et al (2014) Causes of very late stent thrombosis investigated using optical coherence tomography. Intern Med 53:2031–2039
52. Kang S-J, Lee CW, Song H et al (2013) OCT analysis in patients with very late stent thrombosis. JACC Cardiovasc Interv 6:695–703
53. Karanasos A, Witberg K, Van Geuns RJ et al (2012) Morphological characteristics by optical coherence tomography of ruptured neoatherosclerotic plaques in patients with very late stent thrombosis (abstract). Eur Heart J 33:176–176
54. Ko YG, Kim DM, Cho JM et al (2012) Optical coherence tomography findings of very late stent thrombosis after drug-eluting stent implantation. Int J Cardiovasc Imaging 28:715–723
55. Karanasos A, Witberg K, Ligthart J et al (2013) In-stent neoatherosclerosis: Are first generation drug eluting stents different than bare metal stents? An optical coherence tomography study. In: Progress in Biomedical Optics and Imaging – Proceedings of SPIE. p 856543
56. Karanasos A, Ligthart J, Schultz C et al (2012) Clinical and angiographic predictors of neointimal rupture as a culprit for very late stent thrombosis. Insights from optical coherence tomography (abstract). Eur Heart J 33:399–399
57. Karanasos A, Simsek C, Gnanadesigan M et al (2014) OCT assessment of the long-term vascular healing response 5 years after everolimus-eluting bioresorbable vascular scaffold. J Am Coll Cardiol 64:2343–2356
58. Karanasos A, Schuurbiers JC, Garcia-Garcia HM et al (2015) Association of wall shear stress with long-term vascular healing response following bioresorbable vascular scaffold implantation. Int J Cardiol 191:279–283
59. Karanasos A, Muramatsu T, Diletti R et al (2015) Early and late optical coherence tomography findings following everolimus-eluting bioresorbable vascular scaffold implantation in myocardial infarction: a preliminary report. Hellenic J Cardiol 56:125–135
60. Karanasos A, Van Mieghem N, Van Ditzhuijzen N et al (2015) Angiographic and optical coherence tomography insights into bioresorbable scaffold thrombosis: single-center experience. Circ Cardiovasc Interv 8:e002369
61. Van Soest G, Goderie T, Regar E et al (2010) Atherosclerotic tissue characterization in vivo by optical coherence tomography attenuation imaging. J Biomed Opt 15:011105
62. Gnanadesigan M, Van Soest G, White S et al (2014) Effect of temperature and fixation on the optical properties of atherosclerotic tissue: a validation study of an ex-vivo whole heart cadaveric model. Biomed Opt Express 5:1038–1049
63. Regar E, Gnanadesigan M, Van Der Steen AF et al (2013) Quantitative optical coherence tomography tissue-type imaging for lipid-core plaque detection. JACC Cardiovasc Interv 6:891–892
64. Zahnd G, Karanasos A, Van Soest G et al (2015) Quantification of fibrous cap thickness in intracoronary optical coherence tomography with a contour segmentation method based on dynamic programming. Int J Comput Assist Radiol Surg. doi:10.1007/s11548-015-1164-7
65. Nadkarni SK, Pierce MC, Park BH et al (2007) Measurement of collagen and smooth muscle cell content in atherosclerotic plaques using polarization-sensitive optical coherence tomography. J Am Coll Cardiol 49:1474–1481
66. Wang T, Wieser W, Springeling G et al (2013) Intravascular optical coherence tomography imaging at 3200 frames per second. Opt Lett 38:1715–1717
67. Alfonso F, Dutary J, Paulo M et al (2012) Combined use of optical coherence tomography and intravascular ultrasound imaging in patients undergoing coronary interventions for stent thrombosis. Heart 98:1213–1220

Chapter 3.3

Association of neointimal morphology by optical coherence tomography with rupture of neoatherosclerotic plaque very late after coronary stent implantation

Karanasos A, Ligthart J, Witberg K, Toutouzas K, Daemen J, van Soest G, Gnanadesigan M, van Geuns RJ, de Jaegere P, Regar E

Based on data presented in SPIE Photonics West 2013

Abstract

Purpose: Neoatherosclerosis within a stent has been recently described as a culprit of late stent failure. We investigated by optical coherence tomography (OCT) the association of neoatherosclerotic plaque morphology with neointimal rupture (NR) and clinical presentation in patients late after coronary stent implantation.

Methods: From 1/1/2007 to 31/1/2012, 74 patients from two institutions underwent OCT assessment of a coronary stent implanted at least 18 months prior to OCT study. Native atherosclerosis criteria were used for neointimal characterization.

Results: Neoatherosclerosis was observed in 59.5% of the stents (n=44). Stents with neoatherosclerosis were more often associated with symptoms compared to stents without neoatherosclerosis (59.1% acute coronary syndrome (ACS), 25% stable angina (SA), and 15.9% asymptomatic versus 43.3% ACS, 6.7% SA, 50% asymptomatic, $p<0.01$). Among neoatherosclerotic lesions (n=44), NR was detected in 19 (43.2%) and had higher incidence in ACS (61.5%) than in SA (18.2%) and asymptomatic (14.3%) ($p<0.05$). Thrombus was detected in all NR cases. Fibrous cap thickness was lower in NR lesions compared to lesions without NR ($48\pm21\mu m$ versus $104\pm58\mu m$, $p<0.01$). Lipid content tended to be higher in lesions with NR (260 ± 103^{o} versus 203 ± 85^{o}, $p=0.051$). Lesions with NR had more often dense macrophage infiltration (84.2% versus 44.0%, $p<0.05$). There were no differences in neovascularization or calcifications between lesions with or without NR.

Conclusions: Neoatherosclerosis is frequent and more common among symptomatic patients. Importantly, neointimal rupture is associated with ACS late after stent implantation. Specific morphological characteristics, such as cap thickness and macrophage infiltration are associated with rupture of neoatherosclerotic plaques.

Introduction

Very late stent failure presenting either as stent restenosis or stent thrombosis is a vexing problem in everyday clinical practice[1, 2]. The pathomechanisms underlying this entity are complex and have not yet been completely elucidated. Recent pathological observations and preliminary in vivo evidence has implicated the development of atherosclerosis with accelerated pace within the stented segment, called neoatherosclerosis, as a potential predisposing factor for very late stent failure[3]. However, the exact role of neoatherosclerosis in the pathogenesis of very late stent failure remains to be elucidated. In particular, it has not been established whether the presence of neoatherosclerosis or neointimal rupture is related to the clinical presentation of the patients and whether neointimal rupture is associated with specific morphological characteristics of the neoatherosclerotic plaque.

Optical coherence tomography (OCT) is an invasive imaging modality, able to visualize the micromorphology of coronary arteries with near-histological resolution[4]. OCT can be used for assessing the vascular healing response following intracoronary stent implantation and also for assessing the morphological features of neointimal tissue[5]. By OCT, we can visualize various components of neoatherosclerosis (macrophage infiltration, necrotic core, in-stent calcifications and neoatherosclerotic plaque rupture)[6].

The aim of the study was to assess the differences in the incidence of neoatherosclerosis and neointimal rupture by OCT among patients that had undergone stent implantation ≥18 months ago with regard to the clinical presentation. Furthermore, in these patients we assessed the specific morphological characteristics of neoatherosclerosis associated with rupture of the neoatherosclerotic plaque.

Methods

Study procedure.

Between 1/1/2007 and 31/1/2012, seventy seven patients from two institutions (Thoraxcenter, Erasmus Medical Center, Rotterdam, The Netherlands and Hippokration Hospital, Athens, Greece) underwent OCT imaging of an intracoronary stent implanted ≥18 months prior to the OCT examination and were included in the study. The culprit lesion was clearly identified in patients with ACS by a combination of ECG, wall motion abnormalities seen in cardiac ultrasound, and coronary angiogram, and in patients with stable angina by a combination of ECG, non-invasive functional study and coronary angiogram. Patients, in whom the culprit lesion could not be clearly identified, were excluded from the study. According to the clinical

presentation, patients were categorized in three groups: 1) acute coronary syndrome (ACS) group consisting of patients with ACS (ST-elevation myocardial infarction and non-ST-elevation acute coronary syndrome) attributed to the stent; 2) stable angina (SA) group consisting of patients with SA attributed to the coronary stent; and 3) asymptomatic group consisting of asymptomatic patients with follow-up stent evaluation or symptomatic patients with a culprit lesion in a different vessel or in the stented vessel with distance greater than 5mm from the proximal and distal stent edges. Demographic data were collected at the time of the presentation and data from the index procedure were collected retrospectively.

OCT image acquisition

OCT image acquisition was performed with 1) a time-domain system with a non-occlusive image acquisition technique (Lightlab M3™ imaging system/ Image-wire™ intravascular imaging catheter) (n=8) and 2) a frequency-domain system (Lightlab C7XR™ imaging system/Dragonfly™ intravascular imaging catheter) (n=69), when the latter became available (all systems: Lighlab Imaging/St Jude, St. Paul, Minnesota, USA). Image acquisition protocols for both techniques have been previously described[4, 7]. Acquired images were digitally stored and analyzed offline.

In the ACS group, OCT was performed during primary percutaneous intervention in patients with ST-elevation myocardial infarction, and within 48 hours from admission in patients with non-ST-elevation acute coronary syndrome. In patients with impaired flow, thrombus aspiration was performed in the culprit lesion prior to OCT image acquisition. In cases where the flow was not restored in the culprit vessel following thrombus aspiration or cases with high residual thrombus burden in angiography or in the OCT examination, rheolytic thrombectomy was applied (Angiojet™, Possis Medical, Inc., Minneapolis, Minnesota, USA). All OCT images in the ACS group were performed prior to any stent implantation. No intervention was performed before OCT image acquisition in the SA or in the asymptomatic group. Further treatment following the OCT image acquisition, in the ACS and SA groups, was left to the discretion of the operator.

OCT image analysis

Off-line analysis was performed with the dedicated LightLab offline analysis software by an experienced analyst. The region of analysis was defined by the stented region. Patients with poor flush quality or high residual thrombus burden precluding analysis of the complete vessel circumference were excluded. The presence of neoatherosclerosis was assessed in all stents.

Neoatherosclerosis was defined as the presence of necrotic core in the neointimal region; necrotic core was defined as signal-poor regions separated by the overlying signal-rich layer by diffuse borders, in line with definitions used in native atherosclerosis[4, 8]. The presence of in-stent thrombus, neointimal rupture, macrophage infiltration, calcifications and neovascularization were recorded. These features were also defined in accordance to native atherosclerosis: macrophage infiltration was defined as a superficial thin bright layer with high signal attenuation, calcifications were defined as signal-poor regions with low attenuation and sharp borders and neovascularization was defined as the presence of signal-void regions in the neointima. The thickness of the fibrous cap overlying the in-stent necrotic core was measured at the thinnest site and the size of the in-stent necrotic core was semi-quantified by measuring the maximum arc that it occupies in the cross-sectional image. Representative examples of OCT image analysis are presented in Figure 1.

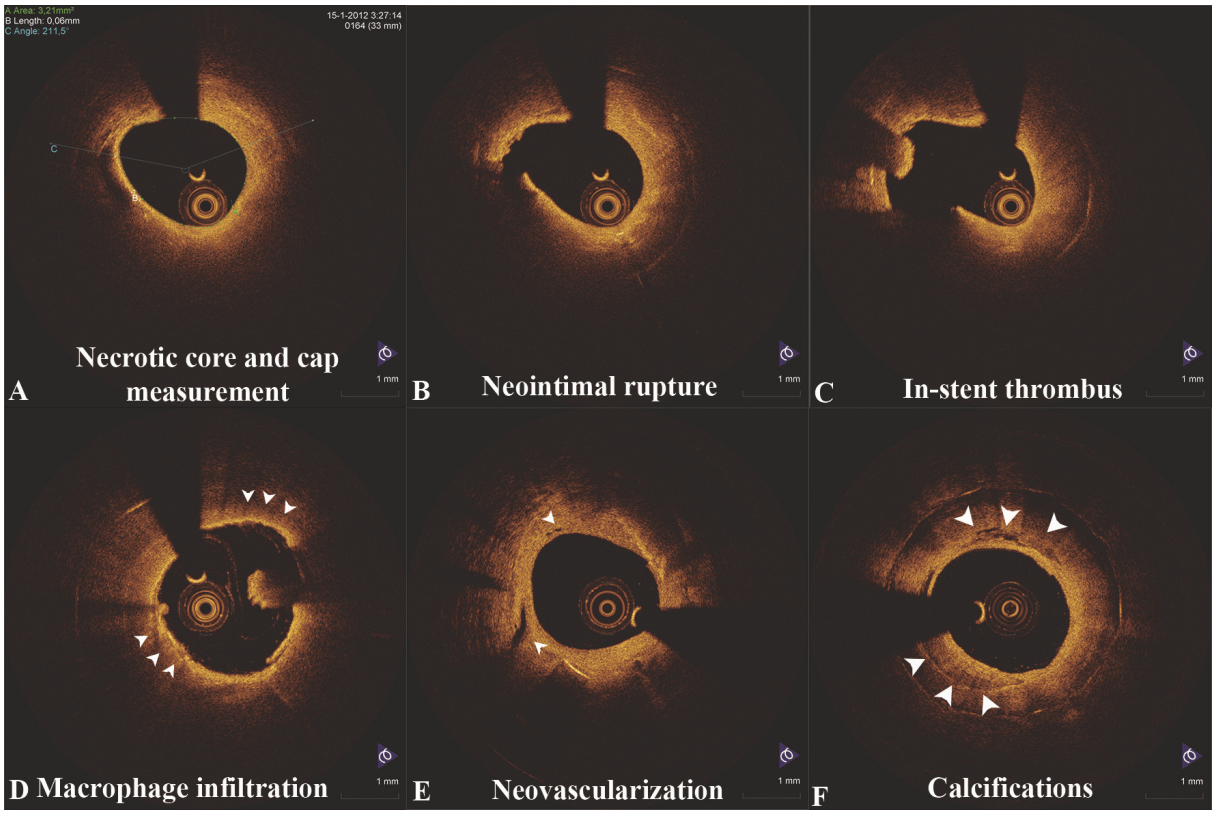

Figure 1. Representative OCT features of in-stent neoatherosclerosis.

Statistical analysis

Qualitative characteristics are reported as n (%) and quantitative as mean±SD. Statistical comparisons were performed with the chi-square test or Fisher's exact test for categorical variables and with the analysis of variance (ANOVA) or the unpaired t-test for continuous variables. A p value <0.05 indicated statistical significance.

Results

Clinical and angiographic characteristics.

After exclusion of 3 patients (2 with high residual thrombus burden and 1 with poor flush quality precluding the assessment), seventy four patients were included in the analysis: 39 (52.7%) in the ACS group, 13 (17.6%) in the SA group, and 22 (29.7%) in the asymptomatic group. The baseline clinical and angiographic characteristics of the patients stratified by clinical presentation are presented in Table 1. There were no significant difference in baseline characteristics among the groups, except for the incidence of smoking that was higher in the ACS and SA groups. The vast majority of the studied stents were drug-eluting stents (n=61, 82.4%), while the mean interval since initial implantation was 70.2±43.0 months (median: 63 months, range: 21-200 months).

Neoatherosclerosis and clinical syndrome.

Neoatherosclerosis was observed in 59.5% of the stents (n=44). Stents with neoatherosclerosis were more often associated with symptomatic presentation compared to stents without neoatherosclerosis. Specifically, 59.1% of the stents with neoatherosclerosis were in the ACS group, 25% in the SA group, and 15.9% in the asymptomatic group versus 43.3% in the ACS group, 6.7% in the SA group, and 50% in the asymptomatic group ($p<0.01$).

In the subset of stents with neoatherosclerosis (n=44), rupture of the neoatherosclerotic plaque was detected in 19 stents (43.2%) and the incidence was higher in the ACS group (61.5%) compared to the SA group (18.2%) and the asymptomatic group (14.3%; $p<0.05$).

Comparison of morphological characteristics in lesions with and without neointimal rupture.

In the subset of patients with neoatherosclerosis, in-stent thrombus was detected in all neointimal rupture cases, regardless of clinical presentation (16 stents in the ACS group, 2 stents in the SA group and 1 stent in the asymptomatic group). Fibrous cap thickness was lower in neointimal rupture lesions compared to lesions without neointimal rupture (48±21μm versus 104±58μm, $p<0.01$). Necrotic core content tended to be higher in lesions with neointimal rupture (260±103° versus 203±85°, $p=0.051$). Lesions with neointimal rupture had more often dense macrophage infiltration (84.2% versus 44.0%, $p<0.05$). There were no differences in neovascularization or calcifications between lesions with or without neointimal rupture. Table 2 contains the OCT morphological characteristics of neoatherosclerosis by OCT in ruptured and non-ruptured neoatherosclerotic plaques.

Table 1. Baseline clinical, angiographic and procedural characteristics stratified by clinical presentation

	ACS group	SA group	Asymptomatic group	p value
n	39	13	22	
Age (years)	61.5±14.0	61.8±8.6	64.6±10.6	0.64
Male gender (%)	29 (74.4)	10 (76.9)	19 (86.4)	0.54
Risk factors				
Hypertension (%)	19 (48.7)	6 (46.2)	14 (63.6)	0.47
Dyslipidemia (%)	28 (71.8)	8 (61.5)	14 (63.6)	0.71
Diabetes mellitus (%)	14 (35.9)	6 (46.2)	4 (18.2)	0.19
Smoking (%)	21 (53.8)	7 (53.8)	5 (22.7)	0.048
Thrombus aspiration (%)	26 (66.7)	1 (7.7)	0 (0)	<0.001
Rheolytic thrombectomy (%)	8 (20.5)	0 (0)	0 (0)	0.018
Index procedure				
Interval since initial implantation (months)	72.2±45.9	61.8±39.4	62.6±40.9	0.55
Syndrome at initial presentation				0.09
Stable angina (%)	18 (46.2)	8 (61.5)	12 (54.5)	
Unstable angina (%)	3 (7.7)	1 (7.7)	6 (27.3)	
Acute myocardial infarction (%)	18 (46.2)	4 (15.4)	4 (18.2)	
Vessel				0.19
Left anterior descending artery (%)	21 (53.8)	4 (30.8)	10 (45.5)	
Left circumflex artery (%)	4 (10.3)	3 (23.1)	7 (31.8)	
Right coronary artery (%)	14 (35.9)	6 (46.2)	5 (22.7)	
Type of stent				0.77
Bare metal stent (%)	7 (17.9)	3 (23.1)	3 (13.6)	
Drug-eluting stent (%)	32 (82.1)	10 (76.9)	19 (86.4)	

Values are presented as mean ± SD or n (%).

Table 2. OCT morphological characteristics of neoatherosclerosis in patients with and without neointimal rupture.

	Neointimal rupture (n=19)	No neointimal rupture (n=25)	p value
Fibrous cap thickness (μm)	48±21	104±58	<0.001
Necrotic core arc (º)	260±103	203±85	0.051
Macrophage infiltration (%)	16 (84.2)	11 (44.0)	0.012
Neovascularization (%)	2 (10.5)	2 (8.0)	0.99
Calcification (%)	7 (36.8)	7 (28.0)	0.74

Values are presented as mean ± SD or n (%).

Discussion

The main findings of this study are that 1) neoatherosclerosis is a relatively common finding at the late follow-up of intracoronary stents, especially in stents associated with clinical symptoms; 2) among stents with neoatherosclerosis, rupture of the neoatherosclerotic plaque is predominantly observed in stents associated with ACS, but can occasionally occur clinically silently and 3) the morphological characteristics that are associated with neointimal rupture are similar to those observed in native atherosclerosis.

Neoatherosclerosis was first described in pathologic specimens of bare metal stents, and more recently in pathologic specimens of drug-eluting stents as well[9, 10]. Furthermore, it was demonstrated *in vivo* by OCT that qualitative changes of the neointima can be observed late after stent implantation[11, 12], and that distinct patterns of restenosis are observed in stents with restenosis[13]. Subsequent trials have shown a high incidence of neoatherosclerosis in stents presenting with late restenosis in both bare metal and drug-eluting stents[14, 15]. Furthermore, small scale studies and numerous reports have also demonstrated individual cases of late stent thrombosis in the setting of a ruptured neoatherosclerotic plaque[6, 16, 17]. Our study expands these observations and shows that more than half of the stents have developed neoatherosclerosis at a mean follow-up of 6 years after implantation. Moreover, the incidence of neoatherosclerosis was higher in stents related with symptomatic patient presentation. Although neoatherosclerosis *per se* was observed with high prevalence both in the ACS and in the SA group compared to the asymptomatic group, analysis of stents with neoatherosclerosis revealed that neointimal rupture was mainly observed in the ACS group. Our observation is corroborated by the detection of in-stent thrombus in all cases of neointimal rupture, regardless of the syndrome. This finding bears resemblance to native atheromatosis[18], where rupture of a native plaque constitutes the main substrate for coronary thrombosis[19], but can also be witnessed in patients with stable angina or in asymptomatic patients[20].

In our study, neointimal rupture was associated with specific morphological characteristics of the neointima. Not surprisingly, similar characteristics have been recognized as determinants of plaque instability in native atheromatosis. Ruptured native plaques are associated with higher incidence of a thin fibrous cap, a large necrotic core, neovascularization, macrophage infiltration, reduced calcification and eccentric remodeling compared to stable native plaques[21, 22]. In our study, the finding of lower fibrous cap thickness and increased macrophage infiltration in ruptured neoatherosclerotic plaques suggests that these characteristics may be implicated in the pathogenesis of neointimal rupture, in analogy to native atheromatosis. Similarly, necrotic core content was higher in stents with neointimal rupture, although this difference did not reach

statistical significance. Finally, contrary to native atheromatosis, neovascularization and calcification were not associated with neointimal rupture. This finding could reflect a differential impact of these characteristics in plaque rupture between native atheromatosis and neoatherosclerosis, error due to small sample size, or could partially be explained by the limitation of OCT to detect microvessels located behind necrotic core.

This study had limitations. Firstly, we cannot exclude selection bias due to the non-consecutive enrollment of patients undergoing OCT examination. Secondly, patients with ACS late after stent implantation is a relatively heterogeneous group, containing also cases with thrombosis associated with impaired vascular healing or other pathomechanisms. Thus, we confined the analysis in the association of morphological characteristics of the neointima with the presence of neointimal rupture, rather than with clinical presentation. Thirdly, OCT characteristics of neoatherosclerosis have been validated against histology only in one study with limited sample size. Fourthly, due to the rapid adaptation of drug-eluting stent use by our institutions during the last decade, the number of bare metal stents examined is limited. Finally, patients in the ACS group often had red thrombus that can impair the assessment of the neointima. Nevertheless, the use of thrombus aspiration and rheolytic thrombectomy in these patients enhanced the visualization of the thrombosed region.

Conclusions

Neoatherosclerosis by OCT very late after stent implantation is a frequent finding. Importantly, neointimal rupture is associated with acute coronary syndrome late after stent implantation. Specific morphological characteristics of the neoatherosclerotic neointima, such as thin fibrous cap and infiltration by macrophages are associated with rupture of neoatherosclerotic plaques.

Acknowledgements

Antonios Karanasos would like to acknowledge the funding support of the Hellenic Heart Foundation.

References

1. Yamaji K, Kimura T, Morimoto T, Nakagawa Y, Inoue K, Soga Y, Arita T, Shirai S, Ando K, Kondo K, Sakai K, Goya M, Iwabuchi M, Yokoi H, Nosaka H, Nobuyoshi M. Very long-term (15 to 20 years) clinical and angiographic outcome after coronary bare metal stent implantation. Circulation. Cardiovascular interventions 2010;**3**(5):468-475.

2. Daemen J, Wenaweser P, Tsuchida K, Abrecht L, Vaina S, Morger C, Kukreja N, Juni P, Sianos G, Hellige G, van Domburg RT, Hess OM, Boersma E, Meier B, Windecker S, Serruys PW. Early and late coronary stent thrombosis of sirolimus-eluting and paclitaxel-eluting stents in routine clinical practice: data from a large two-institutional cohort study. Lancet 2007;**369**(9562):667-78.

3. Park S-J, Kang S-J, Virmani R, Nakano M, Ueda Y. In-stent neoatherosclerosis: a final common pathway of late stent failure. Journal of the American College of Cardiology 2012;**59**(23):2051-2057.

4. Tearney GJ, Regar E, Akasaka T, Adriaenssens T, Barlis P, Bezerra HG, Bouma B, Bruining N, Cho J-m, Chowdhary S, Costa MA, de Silva R, Dijkstra J, Di Mario C, Dudek D, Dudeck D, Falk E, Falk E, Feldman MD, Fitzgerald P, Garcia-Garcia HM, Garcia H, Gonzalo N, Granada JF, Guagliumi G, Holm NR, Honda Y, Ikeno F, Kawasaki M, Kochman J, Koltowski L, Kubo T, Kume T, Kyono H, Lam CCS, Lamouche G, Lee DP, Leon MB, Maehara A, Manfrini O, Mintz GS, Mizuno K, Morel M-a, Nadkarni S, Okura H, Otake H, Pietrasik A, Prati F, Räber L, Radu MD, Rieber J, Riga M, Rollins A, Rosenberg M, Sirbu V, Serruys PWJC, Shimada K, Shinke T, Shite J, Siegel E, Sonoda S, Sonada S, Suter M, Takarada S, Tanaka A, Terashima M, Thim T, Troels T, Uemura S, Ughi GJ, van Beusekom HMM, van der Steen AFW, van Es G-A, van Es G-A, van Soest G, Virmani R, Waxman S, Weissman NJ, Weisz G. Consensus standards for acquisition, measurement, and reporting of intravascular optical coherence tomography studies: a report from the International Working Group for Intravascular Optical Coherence Tomography Standardization and Validation. Journal of the American College of Cardiology 2012;**59**(12):1058-1072.

5. Karanasos A, Ligthart J, Witberg K, van Soest G, Bruining N, Regar E. Optical Coherence Tomography: Potential Clinical Applications. Current cardiovascular imaging reports 2012;**5**(4):206-220.

6. Karanasos A, Ligthart JMR, Regar E. In-stent neoatherosclerosis: a cause of late stent thrombosis in a patient with "full metal jacket" 15 years after implantation: insights from optical coherence tomography. JACC. Cardiovascular interventions 2012;**5**(7):799-800.

7. Prati F, Cera M, Ramazzotti V, Imola F, Giudice R, Albertucci M. Safety and feasibility of a new non-occlusive technique for facilitated intracoronary optical coherence tomography (OCT) acquisition in various clinical and anatomical scenarios. EuroIntervention: journal of EuroPCR in collaboration with the Working Group on Interventional Cardiology of the European Society of Cardiology 2007;**3**(3):365-370.

8. Nakano M, Vorpahl M, Otsuka F, Taniwaki M, Yazdani SK, Finn AV, Ladich ER, Kolodgie FD, Virmani R. Ex vivo assessment of vascular response to coronary stents by optical frequency domain imaging. JACC. Cardiovascular imaging 2012;**5**(1):71-82.

9. Inoue K, Abe K, Ando K, Shirai S, Nishiyama K, Nakanishi M, Yamada T, Sakai K, Nakagawa Y, Hamasaki N, Kimura T, Nobuyoshi M, Miyamoto TA. Pathological analyses of long-term intracoronary Palmaz-Schatz stenting; Is its efficacy permanent? Cardiovascular pathology: the official journal of the Society for Cardiovascular Pathology 2004;**13**(2):109-115.

10. Nakazawa G, Otsuka F, Nakano M, Vorpahl M, Yazdani SK, Ladich E, Kolodgie FD, Finn AV, Virmani R. The pathology of neoatherosclerosis in human coronary implants bare-metal and drug-eluting stents. Journal of the American College of Cardiology 2011;**57**(11):1314-1322.

11. Takano M, Yamamoto M, Inami S, Murakami D, Ohba T, Seino Y, Mizuno K. Appearance of lipid-laden intima and neovascularization after implantation of bare-metal stents extended late-phase observation by intracoronary optical coherence tomography. J Am Coll Cardiol 2009;**55**(1):26-32.

12. Tanimoto S, Aoki J, Serruys PW, Regar E. Paclitaxel-eluting stent restenosis shows three-layer appearance by optical coherence tomography. EuroIntervention: journal of EuroPCR in collaboration with the Working Group on Interventional Cardiology of the European Society of Cardiology 2006;**1**(4).

13. Gonzalo N, Serruys PW, Okamura T, van Beusekom HM, Garcia-Garcia HM, van Soest G, van der Giessen W, Regar E. Optical coherence tomography patterns of stent restenosis. American heart journal 2009;**158**(2):284-293.

14. Kang S-J, Mintz GS, Akasaka T, Park D-W, Lee J-Y, Kim W-J, Lee S-W, Kim Y-H, Lee CW, Park S-W, Park S-J. Optical Coherence Tomographic Analysis of In-Stent Neoatherosclerosis After Drug–Eluting Stent ImplantationClinical Perspective. Circulation 2011;**123**(25):2954-2963.

15. Kang S-J, Song H-G, Ahn J-M, Kim W-J, Lee J-Y, Park D-W, Lee S-W, Kim Y-H, Lee CW, Park S-W, Park S-J. OCT-Verified Neoatherosclerosis in BMS Restenosis at 10 Years. JACC. Cardiovascular imaging 2012;**5**(12):1267-1268.

16. Davlouros PA, Karantalis V, Xanthopoulou I, Mavronasiou E, Tsigkas G, Toutouzas K, Alexopoulos D. Mechanisms of non-fatal stent-related myocardial infarction late following coronary stenting with drug-eluting stents and bare metal stents. Insights from optical coherence tomography. Circulation journal: official journal of the Japanese Circulation Society 2011;**75**(12):2789-2797.

17. Miyazaki S, Hiasa Y, Takahashi T, Yano Y, Minami T, Murakami N, Mizobe M, Tobetto Y, Nakagawa T, Chen P-M, Ogura R, Miyajima H, Yuba K, Hosokawa S, Kishi K, Ohtani R. In vivo optical coherence tomography of very late drug-eluting stent thrombosis compared with late in-stent restenosis. Circulation journal: official journal of the Japanese Circulation Society 2012;**76**(2):390-398.

18. Jang I-K, Tearney GJ, MacNeill B, Takano M, Moselewski F, Iftima N, Shishkov M, Houser S, Aretz HT, Halpern EF, Bouma BE. In vivo characterization of coronary atherosclerotic plaque by use of optical coherence tomography. Circulation 2005;**111**(12):1551-1555.

19. Burke AP, Farb A, Malcom GT, Liang Y-h, Smialek J, Virmani R. Coronary Risk Factors and Plaque Morphology in Men with Coronary Disease Who Died Suddenly. New England Journal of Medicine 1997;**336**(18):1276-1282.

20. Falk E, Nakano M, Benton JF, Finn AV, Virmani R. Update on acute coronary syndromes: the pathologists' view. European heart journal 2012.

21. Yonetsu T, Kakuta T, Lee T, Takahashi K, Kawaguchi N, Yamamoto G, Koura K, Hishikari K, Iesaka Y, Fujiwara H, Isobe M. In vivo critical fibrous cap thickness for rupture-prone coronary plaques assessed by optical coherence tomography. European heart journal 2011;**32**(10):1251-1259.

22. Virmani R, Burke AP, Farb A, Kolodgie FD. Pathology of the Vulnerable Plaque. Journal of the American College of Cardiology 2006;**47**(8, Supplement):C13-C18.

Chapter 3.4

In-stent neoatherosclerosis: are first generation drug eluting stents different than bare metal stents? An optical coherence tomography study

Karanasos A, Witberg K, Ligthart J, Toutouzas K, Daemen J, van Soest G, Gnanadesigan M, van Mieghem N, Zijlstra F, Regar E

Based on data presented in SPIE Photonics West 2013

Abstract

Purpose: In-stent neoatherosclerosis has been recognised in pathologic specimens of bare metal stents (BMS), and recently in first generation drug eluting stents (1st-DES), as well. However, in vivo data are scarce. By optical coherence tomography, we investigated the incidence and morphological characteristics of neoatherosclerosis (NA) very late after BMS or 1st-DES implantation.

Methods: From 1/1/2007 to 31/1/2012, 52 patients from two institutions underwent >24 months follow-up OCT assessment of a BMS or a 1st-DES (13 BMS – 39 1st-DES). NA was characterized using criteria for native atherosclerosis.

Results: BMS had longer follow-up interval but no differences in clinical presentation at follow-up. No significant differences were evident in the incidence of NA, neointimal rupture, lipid content, neovascularization or macrophage infiltration between BMS and 1st-DES. There was however a trend for lower fibrous cap thickness (FCT) and for higher calcification in BMS (FCT: 51±31μm vs. 92±59μm, p=0.057; calcifications: 46.2% vs. 15.4%, p=0.051). 1st-DES with neoatherosclerosis had longer interval from implantation compared to 1st-DES with homogeneous coverage [Median 71 months (range 25-130) vs. 57 months (24-68), p<0.05], but there was no difference for BMS with or without neoatherosclerosis [Median 125 months (range 90-201) vs. 168 months (132-168), p=0.63].

Conclusions: The incidence and morphological characteristics of NA are similar between 1st-DES and BMS of more prolonged follow-up. Our findings suggest a time-dependent pattern in the incidence of NA in 1st-DES with 2-11 years follow-up.

Introduction

In-stent neoatherosclerosis has been recognised in pathologic specimens of bare metal stents (BMS), and recently in first generation drug eluting stents (1st-DES) as well[1, 2]. Pathologic data indicate that the development of neoatherosclerosis in 1st-DES is observed in shorter follow-up intervals than in BMS[2]. Importantly, *in vivo* studies have linked neoatherosclerosis with late stent complications such as late restenosis or late thrombosis[3-7]. However, data about the incidence of neoatherosclerosis in BMS and DES very late after stent implantation are scarce.

Optical coherence tomography (OCT) is an invasive imaging modality, providing near-histological resolution images of the vascular wall. OCT can be used for assessing the vascular healing response following intracoronary stent implantation and also for assessing the morphological features of neointimal tissue[8]. By OCT, it is possible to visualize the various components of neoatherosclerosis (macrophage infiltration, necrotic core, in-stent calcifications and neoatherosclerotic plaque rupture)[9].

The aim of the current study was to assess by OCT the differences in the incidence and morphological characteristics of neoatherosclerosis between bare metal stents and first generation drug eluting stents at a very late follow-up (>24 months).

Methods

Study procedure.

Between 1/1/2007 and 31/1/2012, fifty five patients from two institutions (Thoraxcenter, Erasmus Medical Center, Rotterdam, The Netherlands and Hippokration Hospital, Athens, Greece), who underwent OCT imaging of a bare metal stent (BMS) or a first-generation drug-eluting stent (1st-DES) implanted ≥24 months prior to the OCT examination, were included in the study. First-generation drug-eluting stents included sirolimus-eluting stents (Cypher™, Cordis, Johnson & Johnson, Bridgewater, NJ, USA) and paclitaxel-eluting stents (Taxus Express™ and Taxus Liberte™, Boston Scientific, Natick, MA, USA). Reasons for evaluation included 1) acute coronary syndrome (ST-elevation myocardial infarction and non-ST-elevation acute coronary syndrome) attributed to the stent; 2) stable angina attributed to the stent; and 3) asymptomatic patients with follow-up stent evaluation or symptomatic patients with a culprit lesion in a different vessel or in the stented vessel with distance greater than 5mm from the proximal and distal stent edges. The culprit lesion of the angiogram was clearly identified in patients with acute coronary syndrome by a combination of ECG, wall motion abnormalities seen in cardiac ultrasound, and coronary angiogram, and in patients with stable angina by a

combination of ECG, non-invasive functional study and coronary angiogram. Demographic data were collected at the time of presentation and data from the index procedure were collected retrospectively.

OCT image acquisition

OCT image acquisition was performed with 1) a time-domain system with non-occlusive image acquisition technique (Lightlab M3™ imaging system/ Image-wire™ intravascular imaging catheter) (n=8) and 2) a frequency-domain system (Lightlab C7XR™ imaging system/Dragonfly™ intravascular imaging catheter) (n=47), when the latter became available (all systems: Lighlab Imaging/St Jude, St. Paul, Minnesota, USA). Image acquisition protocols for both techniques have been previously described[10, 11]. Images were digitally stored and analyzed offline.

In the ACS group, OCT was performed during primary percutaneous intervention in patients with ST-elevation myocardial infarction, and within 48 hours from admission in patients with non-ST-elevation acute coronary syndrome. In patients with impaired coronary flow, thrombus aspiration was performed in the culprit lesion prior to OCT image acquisition. In cases where the flow was not restored in the culprit vessel following thrombus aspiration or cases with high residual thrombus burden by angiography or OCT, rheolytic thrombectomy was applied (Angiojet™, Possis Medical, Inc., Minneapolis, Minnesota, USA). All OCT images in the ACS group were performed prior to any stent implantation. No intervention was performed before OCT image acquisition in the SA or in the asymptomatic group. Further treatment following the OCT image acquisition, in the ACS and SA groups, was left to the discretion of the operator.

OCT image analysis

Off-line analysis was performed with the dedicated LightLab offline analysis software by an experienced analyst. The region of analysis was defined by the stented region. Patients with poor flush quality or high residual thrombus burden precluding analysis of the complete vessel circumference were excluded. The presence of neoatherosclerosis, neointimal rupture, macrophage infiltration, calcifications, neovascularization and in-stent thrombus was assessed in all stents. For the characterization of neoatherosclerosis, definitions similar to native atherosclerosis were applied[9, 11]. Neoatherosclerosis was defined as presence of necrotic core inside the stent; necrotic core was defined as signal-poor regions separated by the overlying signal-rich layer by diffuse borders, macrophage infiltration as a superficial thin bright layer with high signal attenuation, calcifications as signal-poor regions with low attenuation and sharp

borders and neovascularization as the presence of signal-void regions in the neointima. In stents with neoatherosclerosis, the thickness of the fibrous cap overlying the in-stent necrotic core was measured at the thinnest site and the size of the in-stent necrotic core was semi-quantified by measuring the largest arc that it occupies in the cross-sectional image.

Statistical analysis

Qualitative characteristics are reported as n (%) and quantitative as mean±SD or median (interquartile range [IQR]). Statistical comparisons were performed with the chi-square or the Fisher's exact test for categorical variables and with the unpaired t-test for normally distributed continuous variables. Comparisons of the interval since implantation that was non-normally distributed were assessed with the Mann-Whitney test. A p value <0.05 indicated statistical significance

Results

Clinical and angiographic characteristics.

After exclusion of 3 patients (2 with high residual thrombus burden and 1 with poor flush quality precluding the assessment), fifty two patients were included in the analysis: 31 (59.6%) with ACS attributed to the studied stent, 9 (17.3%) with SA attributed to the studied stent, and 12 (23.1%) asymptomatic patients or non-culprit stent examination. The baseline clinical, angiographic and procedural characteristics of the patients stratified by stent type are described in Table 1. There were no significant differences in the clinical presentation between BMS and 1st-DES. Median interval since implantation for the BMS was 132 months (range 90-201), while for 1st-DES 65 months (range 24-130; p<0.001). All other baseline variables were similar between the groups.

Morphological characterization of the neointima in BMS and 1st-DES.

The incidence of neoatherosclerosis was high in both groups (69.2%). The differences morphological classification of neoatherosclerosis by OCT in BMS and 1st-DES is presented in Table 2. There were no significant differences in the incidence of neointimal rupture between BMS and 1st-DES. Necrotic core content, neovascularization and macrophage infiltration were also similar between the groups. There was however a trend for lower fibrous cap thickness (FCT) and for higher calcification in BMS (FCT: 51±31μm vs. 92±59μm, p=0.057; calcifications: 46.2% vs. 15.4%, p=0.051).

Table 1. Baseline clinical, angiographic and procedural characteristics stratified by type of stent

	Bare metal stents	First generation drug-eluting stents	p value
n	13	39	
Age (years)	61.7±11.7	62.9±11.7	0.23
Male gender (%)	10 (76.9)	31 (79.5)	0.99
Clinical presentation			0.81
Culprit of acute coronary syndrome	7 (53.8)	24 (61.5)	
Culprit of stable angina	3 (23.1)	6 (15.4)	
Non-culprit stent or asymptomatic	3 (23.1)	9 (23.1)	
Risk factors			
Hypertension (%)	5 (38.5)	21 (53.8)	0.52
Dyslipidemia (%)	7 (53.8)	28 (71.8)	0.31
Diabetes mellitus (%)	7 (53.8)	12 (30.8)	0.19
Smoking (%)	5 (38.5)	18 (46.2)	0.75
Thrombus aspiration (%)	3 (23.1)	18 (46.2)	0.20
Rheolytic thrombectomy (%)	0 (0)	5 (12.8)	0.31
Index procedure			
Interval since initial implantation (months)	132 (90-201)	65 (24-130)	<0.001
Syndrome at initial presentation			0.73
Stable angina (%)	8 (61.5)	20 (51.3)	
Unstable angina (%)	1 (7.7)	6 (15.4)	
Acute myocardial infarction (%)	4 (30.8)	13 (33.3)	
Vessel			0.32
Left anterior descending artery (%)	5 (38.5)	21 (53.8)	
Left circumflex artery (%)	4 (30.8)	5 (12.8)	
Right coronary artery (%)	4 (30.8)	13 (33.3)	

Values are presented as n(%), mean±SD or median (range).

Interval since implantation and neoatherosclerosis

First generation drug-eluting stents with neoatherosclerosis had longer interval from implantation compared to 1st-DES with homogeneous coverage [Median 71 months (range 24-130) vs. 57 months (24-68), p=0.016], but there was no difference for BMS with or without neoatherosclerosis [Median 125 months (range 90-201) vs. 168 months (132-168), p=0.63; Figure 1].

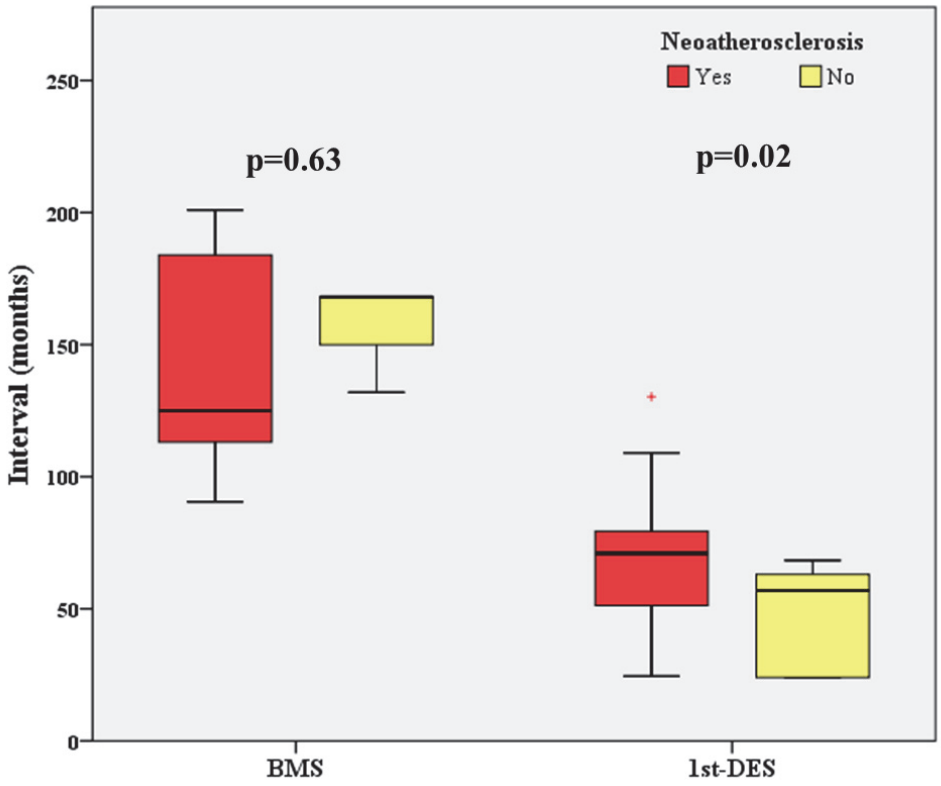

Figure 1. Box plots of interval since implantation in BMS and 1st-DES.

The bottom of the box represents the first quartile and the top of the box represents the third quartile, with the line in the box representing the median. Whiskers represent range.

Table 2. OCT morphological characteristics of the neointima in bare metal and drug-eluting stents

	Bare metal stents (n=13)	First generation drug-eluting stents (n=39)	p value
Neoatherosclerosis (%)	9 (69.2)	27 (69.2)	0.99
Neointimal rupture (%)	6 (46.2)	12 (30.8)	0.33
In-stent thrombus	8 (61.5)	27 (69.2)	0.73
Fibrous cap thickness (μm)	51±31	92±59	0.057
Necrotic core arc (º)	268±119	226±95	0.28
Macrophage infiltration (%)	7 (53.8)	16 (41.0)	0.52
Neovascularization (%)	2 (15.4)	2 (5.1)	0.26
Calcification (%)	6 (46.2)	6 (15.4)	0.051

Values are presented as n (%) or mean±SD.

Discussion

The main findings of this study are that 1) the incidence and morphological characteristics of neoatherosclerosis are similar between bare metal stents and first generation drug-eluting stents, although the follow-up period is significantly shorter in the latter group; and 2) first generation drug-eluting stents with neoatherosclerosis are associated with longer interval since the original implantation.

In our study, 70% of the stents from both groups had developed neoatherosclerosis, at a median follow-up of 11 years in BMS and 5.5 years in 1st-DES . Interestingly, the morphological characteristics of the neointima did not differ between the two groups. Pathologic studies were the first to show that elements of atherosclerosis such as macrophage infiltration and foam cell accumulation were observed in bare metal stents as soon as 2 years since implantation, although they were more prominent in longer follow-up intervals[1]. Recently, the development of neoatherosclerosis was also demonstrated in first-generation DES, but in shorter follow-up intervals compared to bare metal stents[2]. In vivo OCT studies have also verified that neoatherosclerosis is observed both in BMS and 1st-DES[12, 13]. In a sub-analysis of an OCT registry, in a small number of BMS and DES with interval since implantation higher than 2 years, the incidence and morphology of neoatherosclerosis was similar between the two groups, with the only morphological difference being the lower fibrous cap thickness in the BMS group[13]. Moreover, in another sub-analysis from the same registry there was also an association of the interval since implantation with the incidence of in-stent calcification[12]. In the current study, we found a trend towards lower fibrous cap thickness and higher calcification in the BMS group, a finding that requires further validation, as it could also be associated either with the type of stent or the follow-up interval. It is important to note that our study expands the current understanding about the incidence of neoatherosclerosis and differences between BMS and 1st-DES in a population with high incidence of stent-related complications (75%) occurring very late after stent implantation.

Recently, an association of the incidence of neoatherosclerosis with the time interval since stent implantation has been reported in drug-eluting stent restenosis[14]. In our study, we observe a similar association in first generation DES , that is, however, extending far beyond the first two years after implantation, namely up to 11 years. Our findings clearly indicate that this time-dependent neoatheroclerosis pattern continues in 1st DES and that it can occur clinically silently, as we observed this phenomenon not only in stents associated with ACS or SA but in non-culprit stents as well. In contrast, BMS showed no significant interaction of the time interval since implantation and neoatherosclerosis. This could be attributed to the very high time interval since

implantation in the BMS group. A small OCT study has demonstrated that in BMS with restenosis and similar interval since implantation with BMS examined in the current study, the incidence of neoatherosclerosis was 100%[15]. Nakazawa et al[2] on the other hand, in post-mortem specimens have found evidence of neoatherosclerosis only in BMS with implantation interval >2 years and the incidence was higher in stents with implantation interval >6 years. Thus, the temporal pattern of neoatherosclerosis development in BMS remains elusive and larger studies with varying follow-up intervals will be required for addressing this issue.

For our study a number of limitations needs to be addressed. Firstly, we cannot exclude selection bias due to the non-consecutive enrollment of patients undergoing OCT examination. Secondly, the number of bare metal stents examined is limited due to the high adaptation of drug-eluting stent use by our institutions during the last decade. This is also accountable for the important baseline differences in the interval from implantation that hampers the evaluation of the differential vascular response in BMS and 1st-DES with similar implantation interval. Thirdly, OCT characteristics of neoatherosclerosis have been validated against histology only in one study with limited sample size. Finally, patients in the ACS group often had red thrombus that can impair the assessment of the neointima. Nevertheless, the use of thrombus aspiration and rheolytic thrombectomy in these patients enhanced the visualization of the thrombosed region.

Conclusions

The incidence and morphological characteristics of neoatherosclerosis are similar between bare metal stents and first generation drug-eluting stents with a longer interval since implantation. Our findings suggest a time-dependent pattern in the incidence of neoatherosclerosis in first generation DES with a follow-up interval of 2-11 years.

Acknowledgements

Antonios Karanasos would like to acknowledge the funding support of the Hellenic Heart Foundation.

References

1. Inoue K, Abe K, Ando K, Shirai S, Nishiyama K, Nakanishi M, Yamada T, Sakai K, Nakagawa Y, Hamasaki N, Kimura T, Nobuyoshi M, Miyamoto TA. Pathological analyses of long-term intracoronary Palmaz-Schatz stenting; Is its efficacy permanent? Cardiovascular pathology: the official journal of the Society for Cardiovascular Pathology 2004;**13**(2):109-115.

2. Nakazawa G, Otsuka F, Nakano M, Vorpahl M, Yazdani SK, Ladich E, Kolodgie FD, Finn AV, Virmani R. The pathology of neoatherosclerosis in human coronary implants bare-metal and drug-eluting stents. Journal of the American College of Cardiology 2011;**57**(11):1314-1322.

3. Karanasos A, Ligthart JMR, Regar E. In-stent neoatherosclerosis: a cause of late stent thrombosis in a patient with "full metal jacket" 15 years after implantation: insights from optical coherence tomography. JACC. Cardiovascular interventions 2012;**5**(7):799-800.

4. Miyazaki S, Hiasa Y, Takahashi T, Yano Y, Minami T, Murakami N, Mizobe M, Tobetto Y, Nakagawa T, Chen P-M, Ogura R, Miyajima H, Yuba K, Hosokawa S, Kishi K, Ohtani R. In vivo optical coherence tomography of very late drug-eluting stent thrombosis compared with late in-stent restenosis. Circulation journal: official journal of the Japanese Circulation Society 2012;**76**(2):390-398.

5. Yamaji K, Inoue K, Nakahashi T, Noguchi M, Domei T, Hyodo M, Soga Y, Shirai S, Ando K, Kondo K, Sakai K, Iwabuchi M, Yokoi H, Nosaka H, Nobuyoshi M, Kimura T. Bare metal stent thrombosis and in-stent neoatherosclerosis. Circulation. Cardiovascular interventions 2012;**5**(1):47-54.

6. Park S-J, Kang S-J, Virmani R, Nakano M, Ueda Y. In-stent neoatherosclerosis: a final common pathway of late stent failure. Journal of the American College of Cardiology 2012;**59**(23):2051-2057.

7. Davlouros PA, Karantalis V, Xanthopoulou I, Mavronasiou E, Tsigkas G, Toutouzas K, Alexopoulos D. Mechanisms of non-fatal stent-related myocardial infarction late following coronary stenting with drug-eluting stents and bare metal stents. Insights from optical coherence tomography. Circulation journal: official journal of the Japanese Circulation Society 2011;**75**(12):2789-2797.

8. Karanasos A, Ligthart J, Witberg K, van Soest G, Bruining N, Regar E. Optical Coherence Tomography: Potential Clinical Applications. Current cardiovascular imaging reports 2012;**5**(4):206-220.

9. Nakano M, Vorpahl M, Otsuka F, Taniwaki M, Yazdani SK, Finn AV, Ladich ER, Kolodgie FD, Virmani R. Ex vivo assessment of vascular response to coronary stents by optical frequency domain imaging. JACC. Cardiovascular imaging 2012;**5**(1):71-82.

10. Prati F, Cera M, Ramazzotti V, Imola F, Giudice R, Albertucci M. Safety and feasibility of a new non-occlusive technique for facilitated intracoronary optical coherence tomography (OCT) acquisition in various clinical and anatomical scenarios. EuroIntervention: journal of EuroPCR in collaboration with the Working Group on Interventional Cardiology of the European Society of Cardiology 2007;**3**(3):365-370.

11. Tearney GJ, Regar E, Akasaka T, Adriaenssens T, Barlis P, Bezerra HG, Bouma B, Bruining N, Cho J-m, Chowdhary S, Costa MA, de Silva R, Dijkstra J, Di Mario C, Dudek D, Dudeck D, Falk E, Falk E, Feldman MD, Fitzgerald P, Garcia-Garcia HM, Garcia H, Gonzalo N, Granada JF, Guagliumi G, Holm NR, Honda Y, Ikeno F, Kawasaki M, Kochman J, Koltowski L, Kubo T, Kume T, Kyono H, Lam CCS, Lamouche G, Lee DP, Leon MB, Maehara A, Manfrini O, Mintz GS, Mizuno K, Morel M-a, Nadkarni S, Okura H, Otake H, Pietrasik A, Prati F, Räber L, Radu MD, Rieber J, Riga M, Rollins A, Rosenberg M, Sirbu V, Serruys PWJC, Shimada K, Shinke T, Shite J, Siegel E, Sonoda S, Sonada S, Suter M, Takarada S, Tanaka A, Terashima M, Thim T, Troels T, Uemura S, Ughi GJ, van Beusekom HMM, van der Steen AFW, van Es G-A, van Es G-A, van Soest G, Virmani R, Waxman S,

Weissman NJ, Weisz G. Consensus standards for acquisition, measurement, and reporting of intravascular optical coherence tomography studies: a report from the International Working Group for Intravascular Optical Coherence Tomography Standardization and Validation. Journal of the American College of Cardiology 2012;**59**(12):1058-1072.

12. Yonetsu T, Kato K, Kim SJ, Xing L, Jia H, McNulty I, Lee H, Zhang S, Uemura S, Jang Y, Kang SJ, Park SJ, Lee S, Yu B, Kakuta T, Jang IK. Predictors for Neoatherosclerosis: A Retrospective Observational Study From the Optical Coherence Tomography Registry. Circulation: Cardiovascular Imaging 2012;**5**(5):660-666.

13. Yonetsu T, Kim JS, Kato K, Kim SJ, Xing L, Yeh RW, Sakhuja R, McNulty I, Lee H, Zhang S, Uemura S, Yu B, Kakuta T, Jang IK. Comparison of incidence and time course of neoatherosclerosis between bare metal stents and drug-eluting stents using optical coherence tomography. Am J Cardiol 2012;**110**(7):933-9.

14. Kang S-J, Mintz GS, Akasaka T, Park D-W, Lee J-Y, Kim W-J, Lee S-W, Kim Y-H, Lee CW, Park S-W, Park S-J. Optical Coherence Tomographic Analysis of In-Stent Neoatherosclerosis After Drug–Eluting Stent ImplantationClinical Perspective. Circulation 2011;**123**(25):2954-2963.

15. Kang S-J, Song H-G, Ahn J-M, Kim W-J, Lee J-Y, Park D-W, Lee S-W, Kim Y-H, Lee CW, Park S-W, Park S-J. OCT-Verified Neoatherosclerosis in BMS Restenosis at 10 Years. JACC. Cardiovascular imaging 2012;**5**(12):1267-1268.

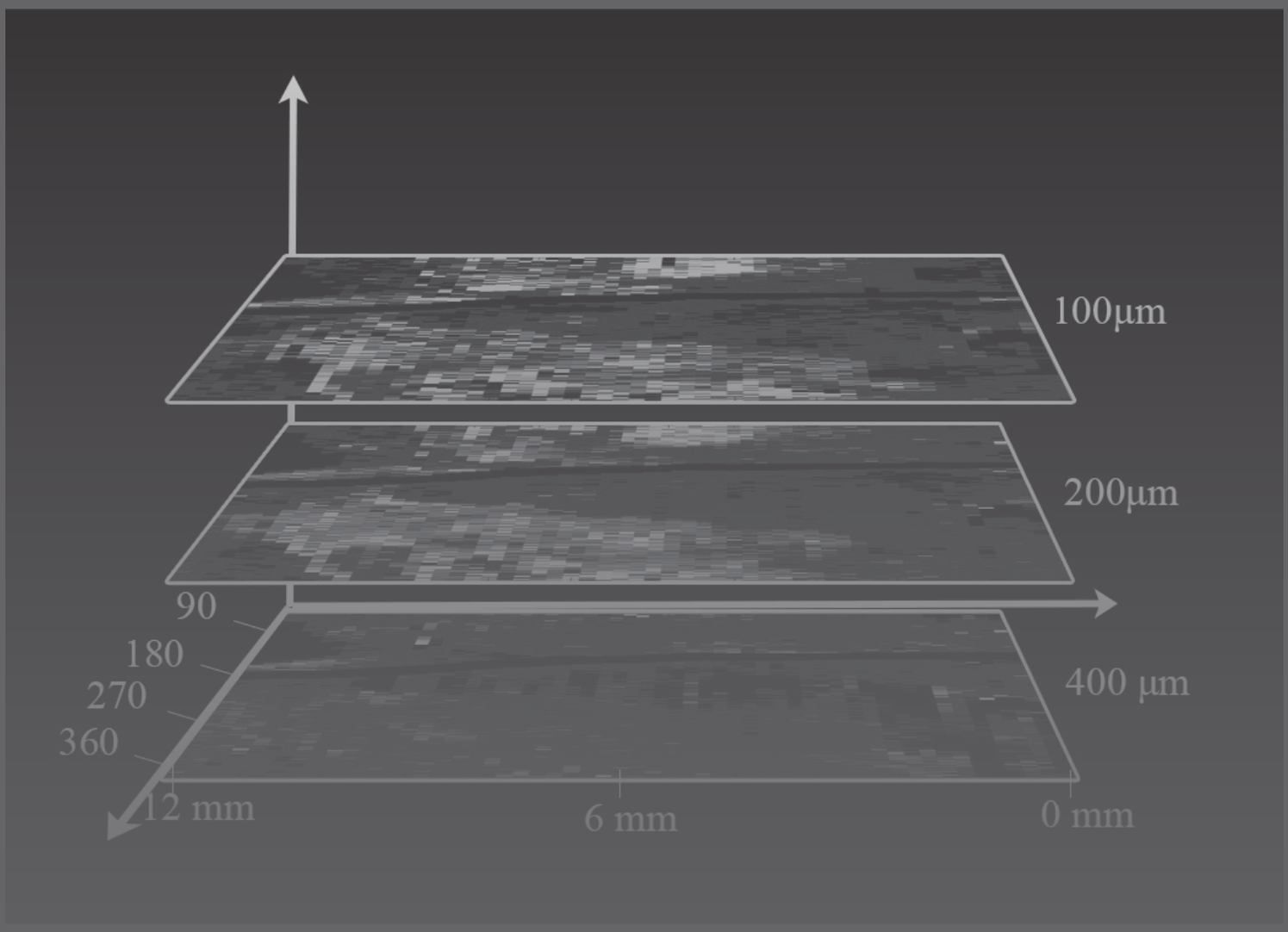
100µm
200µm
400 µm
90
180
270
360
12 mm
6 mm
0 mm

PART IV

OCT assessment of the long-term vascular healing after bioresorbable scaffold implantation

Chapter 4.1

Five-year optical coherence tomography follow-up of an everolimus-eluting bioresorbable vascular scaffold: changing the paradigm of coronary stenting?

Karanasos A, Simsek C, Serruys P, Ligthart J, Witberg K, van Geuns RJ, Sianos G, Zijlstra F, Regar E

Circulation. 2012 Aug 14;126(7):e89-91

Images in Cardiovascular Medicine

Five-Year Optical Coherence Tomography Follow-Up of an Everolimus-Eluting Bioresorbable Vascular Scaffold

Changing the Paradigm of Coronary Stenting?

Antonios Karanasos, MD; Cihan Simsek, MD; Patrick Serruys, MD, PhD; Jurgen Ligthart, BSc; Karen Witberg, CCRN; Robert-Jan van Geuns, MD, PhD; George Sianos, MD, PhD; Felix Zijlstra, MD, PhD; Evelyn Regar, MD, PhD

A 58-year-old man, included in cohort A of the Bioabsorbable Vascular Solutions First in Man Clinical Investigation: A Clinical Evaluation of the Bioabsorbable Vascular Solutions Everolimus Eluting Coronary Stent System in the Treatment of Patients With Single de Novo Native Coronary Artery Lesions (ABSORB) trial,[1] had undergone implantation of a bioresorbable everolimus-eluting scaffold (BVS; Abbott Vascular, Santa Clara, CA) in June 2006 because of stable angina class III with a positive exercise test (Figure 1). He had a positive family history for coronary artery disease. At implantation, his total cholesterol was 207 mg/dL, his low-density lipoprotein level was 130 mg/dL, and his high-density lipoprotein level was 71 mg/dL. Coronary angiography revealed a single lesion at the middle left anterior descending artery that was treated with a 3.0×12 mm BVS, and he was discharged on a treatment regimen of dual antiplatelet therapy (aspirin clopidogrel) for 6 months and atorvastatin 20 mg. His lipid profile 2 years after implantation showed a total cholesterol of 144.3 mg/dL, a low-density lipoprotein level of 65 mg/dL, and a high-density lipoprotein level of 60 mg/dL.

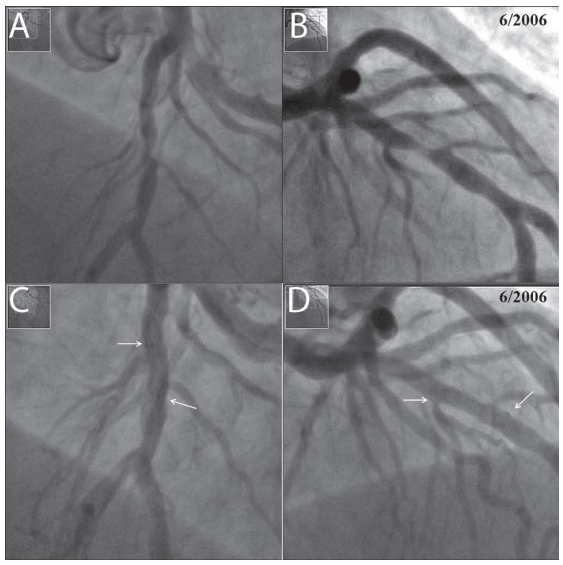

Figure 1. Coronary angiography of the left anterior descending artery before (**A** and **B**) and after (**C** and **D**) intervention at baseline. White arrows in panels **C** and **D** indicate the radio-opaque markers at the edge of the stent.

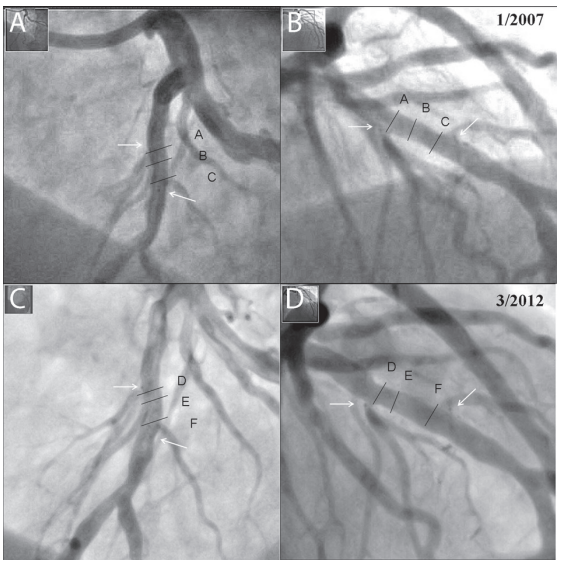

Figure 2. Repeat angiography demonstrating the site of implantation in the left anterior descending artery at 6 months (**A** and **B**) and 5 years (**C** and **D**) after implantation. White arrows indicate the radio-opaque markers at the edge of the stent, and the black lines indicate the sites corresponding to the cross-sectional images of Figure 3.

The patient was asymptomatic with a negative exercise test at a 5-year follow-up in March 2012. Repeat coronary angiography as part of a local study protocol did not demon-

From the Department of Interventional Cardiology, Thoraxcentre, Erasmus University Medical Centre, Rotterdam, The Netherlands.

The online-only Data Supplement is available with this article at http://circ.ahajournals.org/lookup/suppl/doi:10.1161/CIRCULATIONAHA.112.110122/-/DC1.

Correspondence to Evelyn Regar, MD, PhD, Department of Cardiology, Thoraxcentre, BA-585, Erasmus University Medical Centre, 's Gravendijkwal 230, 3015 CE Rotterdam, The Netherlands. E-mail e.regar@erasmusmc.nl

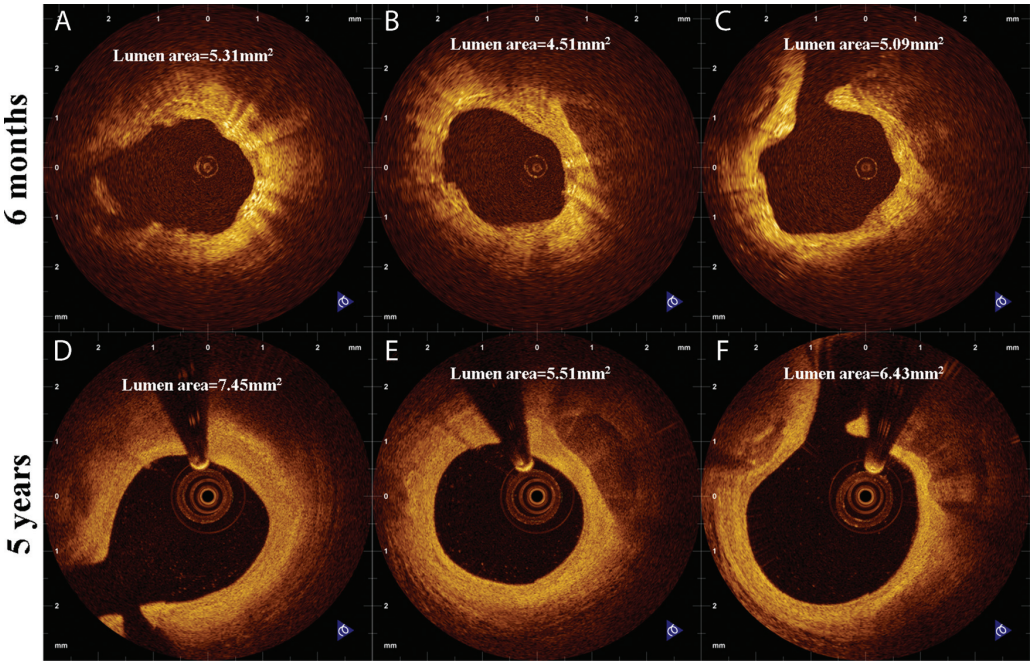

Figure 3. Optical coherence tomography images from matched sites at 6 months (both St. Jude/Lightlab M3 time domain optical coherence tomography [OCT] system; **A** and **C**) and 5 years (**D** and **F**) after stent implantation (St. Jude/Ligthlab C7XR Fourier domain OCT system). Panel **B** represents the site of the minimal lumen area (4.51 mm^2) at 6 months, whereas panel **E** represents the site of the minimal lumen area at 5 years (5.51 mm^2). Lumen area also was increased at the matched sites from 6 months to 5 years (5.31 mm^2 [**A**] versus 7.45 mm^2 [**D**]; 5.09 mm^2 [**C**] versus 6.43 mm^2 [**F**]). Note the complete disappearance of the scaffold struts at the 5-year follow-up, as well as the regular contour of the lumen as opposed to the 6-month follow-up.

strate any significant lesions at the site of the previous BVS implantation in the left anterior descending (Figure 2C and 2D). Optical coherence tomography evaluation of the target segment did not reveal any struts at the vascular wall (Movie I in the online-only Data Supplement). Minimal lumen area inside the scaffold had increased by 22.1% (4.51 to 5.51 mm^2) from 6 months to 5 years (Figure 3). Reference vessel diameter had increased from 2.96 mm at 6 months to 3.02 mm at 5 years. Evaluation of specific regions over the site of a calcified plaque showed complete resorption of struts at 5 years that had showed an open box or bright box appearance at 6 months' follow-up, whereas the thickness of the intimal layer shielding the calcified tissue from the lumen had significantly increased (baseline, 10 μm; 6 months, 260 μm; 5 years, 200 μm) (Figure 4). Using dedicated online software (qAngioOCT, Medis Medical Imaging Systems bv, Leiden, Netherlands), 3-dimensional optical coherence tomography rendering illustrates the patent, smooth lumen surface throughout the treated vessel segment (Figure 5 and Movie II in the online-only Data Supplement).

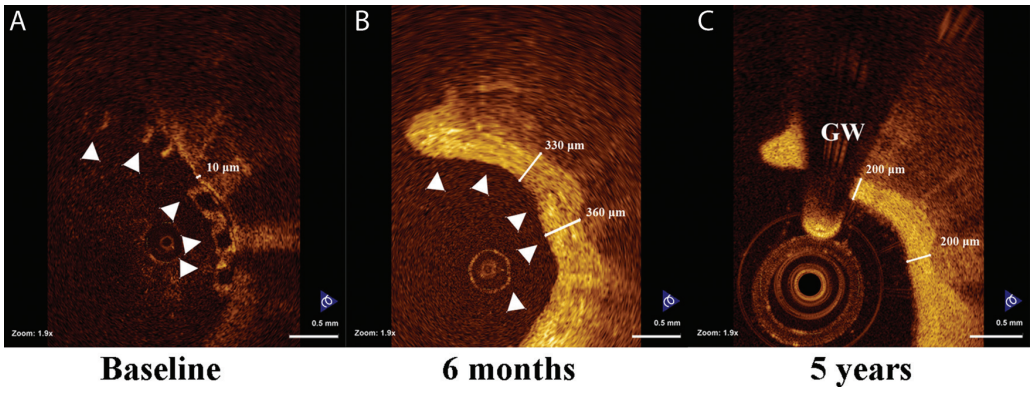

Figure 4. Images acquired from a matched site (panels C and F of Figure 3) at baseline (**A**), 6 months (**B**), and 5 years (**C**). The amount of tissue overlying the calcific deposition has increased from baseline to 6 months because of scaffold implantation and the associated neointimal response. At 5 years, the scaffold struts and neointima have merged into a thick layer of tissue covering the underlying plaque. Arrowheads indicate scaffold struts. GW indicates guide wire artifact.

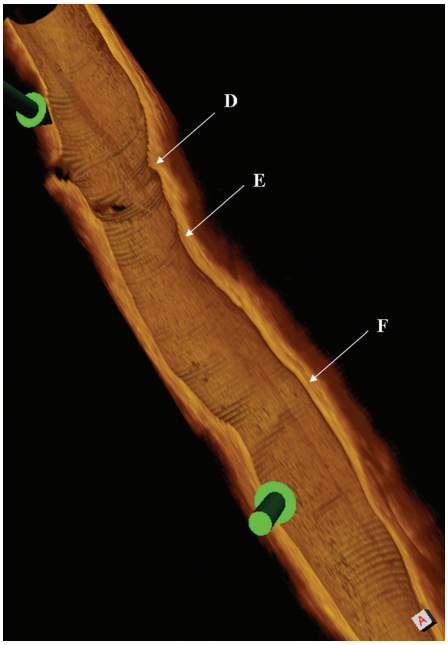

Figure 5. Three-dimensional reconstruction of cross-sectional images corresponding to the segment where the scaffold was placed (green markers). Arrows indicate the location of the cross-sectional images of Figure 3.

This is the first human case demonstrating the complete resorption in vivo of a BVS scaffold 5 years after implantation. Using optical coherence tomography, we observed the complete absence of struts in the vascular wall together with an increase of the minimal lumen area by 22.1%. This is in line with previous human studies that have demonstrated the temporal course of the polymer degradation at 6 months and 2 years,[1] as well as an increase in luminal area due to a decrease in plaque size without change in vessel size, whereas studies in a porcine experimental model have demonstrated complete resorption of the polymer 4 years after implantation.[2]

Importantly, we observed in our patient the development of a homogenous, bright, signal-intense layer shielding the persistent signal-poor, sharply delineated calcified plaque toward the lumen. Conceptually, such tissue growth could be protective because it potentially could diminish the risk of plaque erosion or rupture and prevent thrombogenic plaque components (such as calcified nodules, as in our patient, or necrotic core) from coming in direct contact with the blood stream.[3] Of note, this effect on the vascular wall did not come at the cost of lumen narrowing in our patient; luminal dimensions in the target segment increased from 6 months to 5 years. Such potentially favorable tissue response, as witnessed in this case, might hold promise for the future, evoking the utopia of a passivation of potentially unstable plaques by local therapeutic intervention.

Disclosures

None.

References

1. Serruys PW, Ormiston JA, Onuma Y, Regar E, Gonzalo N, Garcia-Garcia HM, Nieman K, Bruining N, Dorange C, Miquel-Hebert K, Veldhof S, Webster M, Thuesen L, Dudek D. A bioabsorbable everolimus-eluting coronary stent system (ABSORB): 2-year outcomes and results from multiple imaging methods. *Lancet*. 2009;373:897–910.
2. Onuma Y, Serruys PW, Perkins LE, Okamura T, Gonzalo N, Garcia-Garcia HM, Regar E, Kamberi M, Powers JC, Rapoza R, van Beusekom H, van der Giessen W, Virmani R. Intracoronary optical coherence tomography and histology at 1 month and 2, 3, and 4 years after implantation of everolimus-eluting bioresorbable vascular scaffolds in a porcine coronary artery model: an attempt to decipher the human optical coherence tomography images in the ABSORB trial. *Circulation*. 2010; 122:2288–2300.
3. Virmani R, Burke AP, Farb A, Kolodgie FD. Pathology of the vulnerable plaque. *J Am Coll Cardiol*. 2006;47:C13–C18.

Chapter 4.2

Long-term invasive follow-up of the everolimus-eluting bioresorbable vascular scaffold: five-year results of multiple invasive imaging modalities

Simsek C, **Karanasos A**, Magro M, Garcia-Garcia HM, Onuma Y, Regar E, Boersma E, Serruys PW, van Geuns RJ

EuroIntervention. 2014 Oct 28. pii: 20130724-03. doi: 10.4244/EIJY14M10_12

Long-term invasive follow-up of the everolimus-eluting bioresorbable vascular scaffold: five-year results of multiple invasive imaging modalities

Cihan Simsek[1], MD; Antonios Karanasos[1], MD; Michael Magro[1], MD; Hector M. Garcia-Garcia[2], MD, PhD; Yoshinobu Onuma[2], MD; Evelyn Regar[1], MD, PhD; Eric Boersma[1], PhD; Patrick W. Serruys[1,2], MD, PhD; Robert J. van Geuns[1]*, MD, PhD

1. Thoraxcenter, Erasmus Medical Center, Rotterdam, The Netherlands; 2. Cardialysis, Rotterdam, The Netherlands

GUEST EDITOR: Manel Sabaté, MD, PhD; *Servicio de Cardiología, Clínic Hospital, Barcelona, Spain*

KEYWORDS

- bioresorbable vascular scaffold
- percutaneous coronary intervention

Abstract

Aims: Invasive imaging modalities have shown restoration of vasomotion, prevention of restenosis and, most importantly, increase in lumen area between six months and two years after first-generation everolimus-eluting bioresorbable vascular scaffold (Absorb BVS) implantation. Our aim was to assess whether these positive findings were sustained in the long term.

Methods and results: Patients included in the ABSORB cohort A from the Thoraxcenter Rotterdam cohort underwent coronary catheterisation including angiography, intravascular ultrasound (IVUS), virtual histology, optical coherence tomography (OCT) and vasomotion testing at five years. Eight out of 16 patients underwent catheterisation and scaffold assessment with multiple imaging modalities. A trend towards an increase in minimum luminal diameter was observed between two and five years by angiography (1.95±0.37 mm vs. 2.14±0.38 mm; p=0.09). IVUS data showed an increase in mean lumen area at five years (6.96±1.13 mm^2) compared to six months (6.17±0.74 mm^2; p=0.06) and two years (6.56±1.16 mm^2; p=0.12), primarily due to a persistent reduction in plaque area size between six months and five years (9.17±1.86 mm^2 vs. 7.57±1.63 mm^2; p=0.03). The necrotic core area was reduced at five years compared to post-procedural results. In OCT, an increase in mean and minimal luminal area was observed. Moreover, no scaffold struts could be identified and a smooth endoluminal lining was observed. The scaffolded coronary segment did not show signs of endothelial dysfunction with acetylcholine testing.

Conclusions: At five years, the Absorb BVS is no longer discernible by any invasive imaging method and endothelial function is restored. Late luminal enlargement persists up to five years of follow-up without adaptive vessel remodelling.

**Corresponding author: Department of Cardiology, Thoraxcenter, Room Ba 585, Erasmus Medical Center, Dr. Molewaterplein 40, 3015 RD Rotterdam, The Netherlands. E-mail: r.vangeuns@erasmusmc.nl*

Introduction

Permanent metallic stents embedded in a coronary artery could preclude coronary revascularisation options, jail side branches, impair (long-term) endothelial function, impair non-invasive imaging and, most importantly, are associated with late and very late stent thrombosis[1]. Conceptually, a bioresorbable scaffold could help overcome these long-term pitfalls of metallic scaffolds.

The first-generation everolimus-eluting bioresorbable vascular scaffold (Absorb BVS; Abbott Vascular, Santa Clara, CA, USA) demonstrated safety and efficacy in 30 patients included in the BVS cohort A study[1]. At angiographic follow-up, the luminal late loss was 0.43±0.37 mm at six months and 0.48±0.28 mm at two years[1,2]. Intravascular ultrasound (IVUS) analysis revealed a decrease in scaffold area in the first six months together with low neointimal hyperplasia resulting in an overall reduction of 16.8% of the luminal area[3]. Interestingly, both IVUS and optical coherence tomography (OCT) showed a luminal area enlargement between six months and two years due to a reduction in plaque size without change in vessel size[2]. One third of the scaffold struts could not be visualised by OCT at two years. Moreover, there was an optically homogeneous vessel wall structure suggesting healing of the coronary artery[2].

Until now, the long-term scaffold biodegradation and vascular response following BVS implantation has not been systematically evaluated in human subjects. We aimed to assess the long-term vascular response of the first-generation everolimus-eluting BVS by multiple invasive imaging modalities, including IVUS, IVUS virtual histology (IVUS-VH), OCT and vasomotion testing.

Methods

PATIENT POPULATION

The design of the ABSORB cohort A study has already been published[1]. For the present study, we included patients from the Thoraxcenter Rotterdam cohort of the ABSORB cohort A study (n=16). All living patients (n=14; two patients died from a non-cardiac cause at 706 and 808 days post procedure, one from duodenal perforation and one from Hodgkin's disease) were asked to participate in this study. Eight out of 16 patients of the Rotterdam cohort of the ABSORB A trial provided written informed consent and underwent catheterisation and scaffold assessment with multiple imaging modalities between March 8 and July 20, 2012 **(Figure 1)**.

The long-term single-centre follow-up imaging data (quantitative coronary angiography, vasomotion test, greyscale intravascular ultrasound, virtual histology) were analysed by an independent core laboratory (Cardialysis BV, Rotterdam, The Netherlands) and compared to previous core laboratory data-on-file from the ABSORB cohort A study. OCT image analysis was performed by an independent researcher in the Erasmus Medical Center (AK).

STUDY PROCEDURES

The definitions of individual parameters have already been described in a prior manuscript[2]. The clinical endpoints included cardiac death, myocardial infarction, stent thrombosis and ischaemia-driven target lesion revascularisation according to the definitions

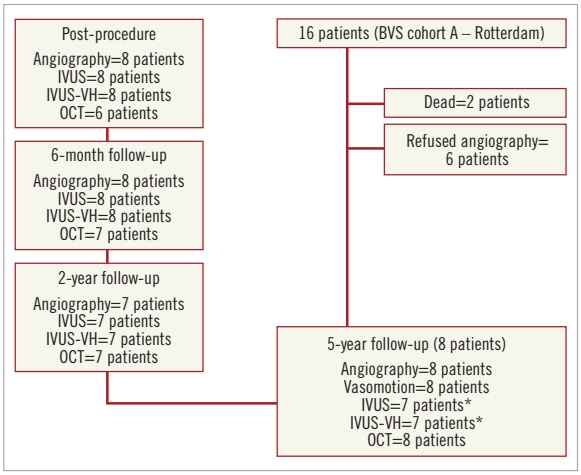

Figure 1. *Flow chart showing the patients included in the five-year follow-up study. *IVUS data could not be acquired for one the included patients at five-year follow-up.*

from the Academic Research Consortium[4]. Endothelium-dependent and endothelium-independent coronary vasomotion were studied using standard protocols[5]. Endothelial dysfunction was defined as vasoconstriction of >3% in mean vessel diameter between baseline and maximum dose acetylcholine (Ach).

IVUS acquisitions were performed using an Eagle Eye® catheter (Volcano Corp., Rancho Cordova, CA, USA) with automated continuous pullback at 0.5 mm/sec. IVUS-VH utilises backscattering of radiofrequency signals to provide information about tissue composition of the vessel wall. Four different plaque compositions, i.e., fibro-fatty, fibrous tissue, dense calcium and necrotic core were assessed on each cross-section and expressed as percentage (with each area totalling 100%). The polymeric scaffold struts were detected as dense calcified areas surrounded by necrotic core due to the strong backscattering properties of the polymer. The changes of these areas between implantation and follow-up were used as a surrogate marker to assess the polymer bioabsorption process. The methodology of OCT image acquisition for the baseline, six-month and two-year follow-up, using a first-generation OCT system with occlusive technique, has been previously described[1,2]. At five-year follow-up, all eight subjects underwent second-generation, non-occlusive OCT imaging using the commercially available C7 XR imaging console and the Dragonfly™ intravascular imaging catheter (both St. Jude Medical, St. Paul, MN, USA). Image acquisition has been previously described[6].

Scaffolds were assessed for the presence of incomplete apposition, intra-scaffold dissection and irregular lumen shape. Incomplete strut apposition was defined as the complete separation between strut and vessel wall with a distance larger than the strut thickness. Scaffolds with at least one incompletely apposed strut were considered incompletely apposed. Incompletely apposed struts located in front of side branch ostia, were considered side branch-related

struts and analysed separately. The number of side branches per scaffold with side branch-related incomplete strut apposition was recorded. Irregular lumen shape was defined as the presence of multiple intimal protrusions. Plaque morphology in each frame at five years was characterised, according to definitions used for native atherosclerosis, as fibrous, fibrocalcific and fibroatheromatous[6]. In the case of fibroatheromas, fibrous cap thickness was assessed and fibroatheromas with cap thickness <65 µm were classified as thin-cap fibroatheromas[7].

STATISTICAL ANALYSIS

This study was designed to provide preliminary observations and generate hypotheses for future studies. Baseline and procedural variables are presented as mean (±standard deviation [SD]) for continuous variables and as percentages for categorical variables. Paired comparisons of measurements performed after the procedure and in the different follow-up intervals were done by a Wilcoxon's signed rank test. No statistical adjustment was applied on the data set since no formal hypothesis testing was planned. The p-values represent exploratory analysis only and should therefore be interpreted with caution. All reported p-values are two-sided and regarded as statistically significant if ≤0.05. Statistical analysis was performed with SPSS for Windows version 15 (SPSS Inc., Chicago, IL, USA).

Results

The baseline characteristics of the population are shown in **Table 1**. At five years, there were no cardiac deaths, stent thromboses or myocardial infarctions, and only one patient had a target vessel revascularisation (TVR) at 106 days and 1,780 days and a target lesion revascularisation (TLR) at 2,218 days. At 106 days, the patient underwent catheterisation due to persistent chest pain. The Absorb BVS in the distal circumflex coronary artery was patent; however, the proximal circumflex coronary artery showed a narrowing with occlusive spasm on further testing with methergine. A paclitaxel-eluting stent was placed in the proximal circumflex coronary which was 7 mm from the proximal edge of the Absorb BVS. At 1,780 days, the patient had a repeat angiography for recurrence of stable angina. This time an everolimus-eluting stent was used to treat a significant *de novo* lesion in the intermediate branch. At 2,218 days, the angiographic follow-up performed because of this study showed a significant lesion distal of the Absorb BVS scaffold with a fractional flow reserve of 0.79. This lesion was located within 5 mm of the distal marker of the Absorb BVS and treated with a Tryton bifurcation stent (Tryton Medical, Inc., Durham, NC, USA) and an everolimus-eluting stent.

At five-year angiography, there was no evidence of significant stenosis in the coronary artery segments scaffolded by the Absorb BVS as identified by the proximal and distal radiopaque markers. All patients showed an increase in minimum luminal diameter (MLD) compared to the previous invasive follow-up at two years (except for one patient who did not have angiographic follow-up at two years). The patient-level data regarding MLD are depicted in **Table 2**. Overall, there was a trend towards an increase in MLD at five years (2.14±0.38 mm) compared to two years (1.95±0.37 mm; p=0.09), resulting in a decrease in late loss (0.22±0.34 mm vs. 0.39±0.31 mm; p=0.09; respectively).

Table 1. Baseline and procedural characteristics.

Number of patients (n=8)		BVS
Demographic characteristics	Age, years (±SD)	65.1 (±8.6)
	Male, %	75 (6/8)
Cardiac history (%)	Prior target vessel intervention	12.5 (1/8)
	Prior myocardial infarction	12.5 (1/8)
Risk factors (%)	Current smoking	12.5 (1/8)
	Hypertension	50 (4/8)
	Hypercholesterolaemia	37.5 (3/8)
	Diabetes	12.5 (1/8)
Treated vessel (%)	RCA	12.5 (1/8)
	LAD	37.5 (3/8)
	LCX	50.0 (4/8)
ACC lesion type (%)	A	0 (0/8)
	B1	50 (4/8)
	B2	50 (4/8)
	C	0 (0/8)
QCA	Mean reference vessel diameter, mm (±SD)	3.0 (±0.6)
	Minimum luminal diameter, mm (±SD)	1.1 (±0.3)
	Diameter stenosis, % (±SD)	64.6 (±10.7)
	Lesion length, mm (±SD)	10.8 (±4.0)

Data are presented as percentages or means (±SD). SD: standard deviation; RCA: right coronary artery; LAD: left anterior descending coronary artery; LCX: left circumflex coronary artery.

Table 2. Quantitative coronary angiography.

Quantitative coronary angiography	Before procedure	After procedure	6 months	2 years	5 years	*p*-value after procedure vs. 5 years	*p*-value 6 months vs. 5 years	*p*-value 2 years vs. 5 years
N	8	8	8	7	8			
Reference vessel diameter (mm)	3.02 (±0.56)	3.04 (±0.20)	2.93 (±0.21)	2.78 (±0.08)	2.83 (±0.30)	0.02	0.67	0.74
In-scaffold minimum luminal diameter (mm)	1.06 (±0.30)	2.36 (±0.30)	2.10 (±0.31)	1.95 (±0.37)	2.14 (±0.38)	0.09	0.67	0.09
In-scaffold diameter stenosis (%)	64.56 (±10.66)	22.33 (±6.68)	28.19 (±10.99)	29.93 (±13.26)	24.67 (±9.77)	0.21	0.50	0.07
In-scaffold late loss (mm)	–	–	0.26 (±0.25)	0.39 (±0.31)	0.22 (±0.34)	–	0.67	0.09

In keeping with the angiographic findings, IVUS data showed a trend towards an increase in mean lumen area at five years (6.96±1.13 mm^2) compared to six months (6.17±0.74 mm^2; p=0.06) and two years (6.56±1.16 mm^2; p=0.12) **(Table 3)**. This was primarily due to a persistent reduction in plaque size between six months and five years (9.17±1.86 mm^2 vs. 7.57±1.63 mm^2; p=0.03), resulting in an increased lumen area with no evidence of vessel dilatation/ectasia. Dense calcium area and necrotic core area were significantly reduced at five years when compared to baseline **(Table 3)**. The dense calcium area significantly decreased from 1.32±0.75 mm^2 to 0.52±0.51 mm^2 (p=0.03), whereas the necrotic core area decreased from 1.79±0.80 mm^2 to 0.74±0.66 mm^2 (p=0.03). The greatest reduction in these components occurred within two years after Absorb BVS implantation. No changes in plaque composition were observed between two and five years.

At five-year follow-up, mean and minimum luminal area by OCT were significantly increased compared to the six-month and the two-year follow-up, while there was no significant difference from baseline measurements immediately after the index procedure **(Figure 2, Table 4)**. No scaffold struts could be identified by OCT at five years, providing evidence of a continued and completed resorption process from the second year on. Morphological assessment is represented in **Table 4**. Multiple luminal protrusions which caused a corrugated ring appearance in all patients at six months were no longer evident in any patient by five years. All baseline intra-scaffold dissections (n=5) were healed by five years. Two patients showed a focally irregular lumen contour, one of whom had a short intimal dissection, not present at earlier investigations, at the overlap between the BVS and a metallic stent implanted at baseline as a bail-out procedure. There was no incomplete scaffold apposition in any case, as scaffold struts could not be detected. Side branch-related incomplete scaffold apposition was identified in seven out of eight scaffolds at previous follow-ups, while, at the five-year follow-up of the same patients, tissue bridges/neocarina **(Figure 3)** were evident at the site of previously detected side branch-related struts.

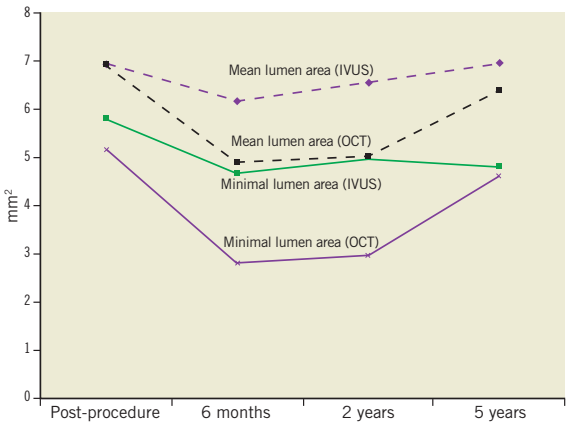

Figure 2. *Mean and minimum luminal area of IVUS and OCT analysis.*

Endothelium-dependent vasomotion was present in the proximal and distal scaffold coronary segment as the mean lumen diameter decreased by 3.2% (from 2.53 mm to 2.45 mm) and 5.2% (from 2.49 mm to 2.36 mm), respectively, after maximum dose Ach compared to baseline angiography. Endothelium-independent vasomotion was not observed in the proximal or distal segment. Neither endothelium-dependent nor endothelium-independent vasomotion was observed in the scaffolded coronary segment, due to a heterogeneous response of four patients showing vasoconstriction and four patients showing vasodilatation on maximum dose Ach. A detailed individual response is depicted in **Figure 4**.

Table 3. Intravascular ultrasound and intravascular ultrasound virtual histology.

	After procedure	6 months	2 years	5 years	*p*-value after procedure vs. 5 years	*p*-value 6 months vs. 5 years	*p*-value 2 years vs. 5 years
N	8	8	7	7			
Greyscale IVUS							
Vessel area (mm^2)	15.72 (±3.00)	15.34 (±2.00)	14.09 (±1.66)	14.52 (±1.81)	0.60	0.40	0.75
Average lumen area (mm^2)	6.95 (±0.63)	6.17 (±0.74)	6.56 (±1.16)	6.96 (±1.13)	0.75	0.06	0.12
Plaque area (mm^2)	8.78 (±2.83)	9.17 (±1.86)	7.54 (±1.24)	7.57 (±1.63)	0.60	0.03	0.92
Minimum lumen area (mm^2)	5.81 (±0.62)	4.67 (±0.77)	4.96 (±1.08)	4.81 (±2.04)	0.60	0.74	0.75
IVUS-VH							
Dense calcium (%)	23.31 (±8.40)	18.85 (±7.59)	15.43 (±6.89)	14.40 (±6.18)	0.03	0.40	0.46
Dense calcium area (mm^2)	1.32 (±0.75)	1.01 (±0.40)	0.55 (±0.31)	0.52 (±0.51)	0.03	0.09	0.12
Fibro-fatty (%)	5.31 (±3.28)	6.33 (±4.15)	8.05 (±5.86)	10.43 (±3.19)	0.03	0.13	0.25
Fibro-fatty area (mm^2)	0.34 (±0.28)	0.36 (±0.30)	0.28 (±0.25)	0.35 (±0.23)	0.92	0.31	0.75
Fibrous (%)	41.00 (±8.50)	51.50 (±8.85)	51.06 (±9.00)	55.31 (±9.55)	0.03	0.50	0.25
Fibrous area (mm^2)	2.48 (±1.22)	2.94 (±1.31)	1.77 (±0.47)	1.85 (±1.05)	0.60	0.06	0.92
Necrotic core (%)	30.38 (±4.71)	23.32 (±8.23)	25.46 (±9.37)	19.86 (±6.62)	0.03	0.40	0.17
Necrotic core area (mm^2)	1.79 (±0.80)	1.29 (±0.74)	0.90 (±0.43)	0.74 (±0.66)	0.03	0.18	0.03

Table 4. Quantitative and qualitative OCT findings.

Table measurements	After procedure	6 months	2 years	5 years	*p*-value after procedure vs. 5 years	*p*-value 6 months vs. 5 years	*p*-value 2 years vs. 5 years
N	6	7	7	8			
Minimal lumen area, mm²	5.16±0.74	2.81±1.57	2.97±1.26	4.62±1.44	0.60	0.02	0.02
Mean lumen area, mm²	6.91±0.88	4.89±1.29	5.03±1.24	6.39±1.18	0.46	0.03	0.02

Table patient level	Incomplete scaffold apposition			Side branches with side branch struts or tissue bridges (n)				Intra-scaffold dissection				Irregular lumen shape			Plaque characterisation*
Months since implantation	0	6	24	0	6	24	60	0	6	24	60	6	24	60	60
Patient 1	–	–	–	1	1	1	1	+	–	–	–	+	–	–	Fibroatheroma/fibrous
Patient 2	N/A	–	–	N/A	3	3	3	N/A	+	–	–	+	–	–	Fibrous/fibroatheroma/ fibrocalcific
Patient 3	–	–	–	2	2	2	1	+	–	–	–	+	–	–	Fibrous/fibroatheroma
Patient 4	+	+	–	1	1	1	1	–	–	–	–	+	–	–	Thin-cap fibroatheroma/ fibrous
Patient 5	–	–	N/A	2	2	N/A	2	–	–	N/A	–	+	N/A	–	Fibrocalcific/fibroatheroma
Patient 6	–	–	–	2	2	2	2	+	+	–	–	+	+	–	Fibrous/fibroatheroma
Patient 7	–	–	–	0	0	0	0	+	+	–	–	+	+	–	Fibrous
Patient 8	N/A	N/A	–	N/A	N/A	3	3	N/A	N/A	–	–	N/A	–	–	Fibrous/fibrocalcific/ fibroatheroma

Data are presented as mm² (±SD). The table consists of quantitative (top) and individual qualitative OCT findings (beneath) at different follow-up intervals. +positive; –: negative; N/A: not available

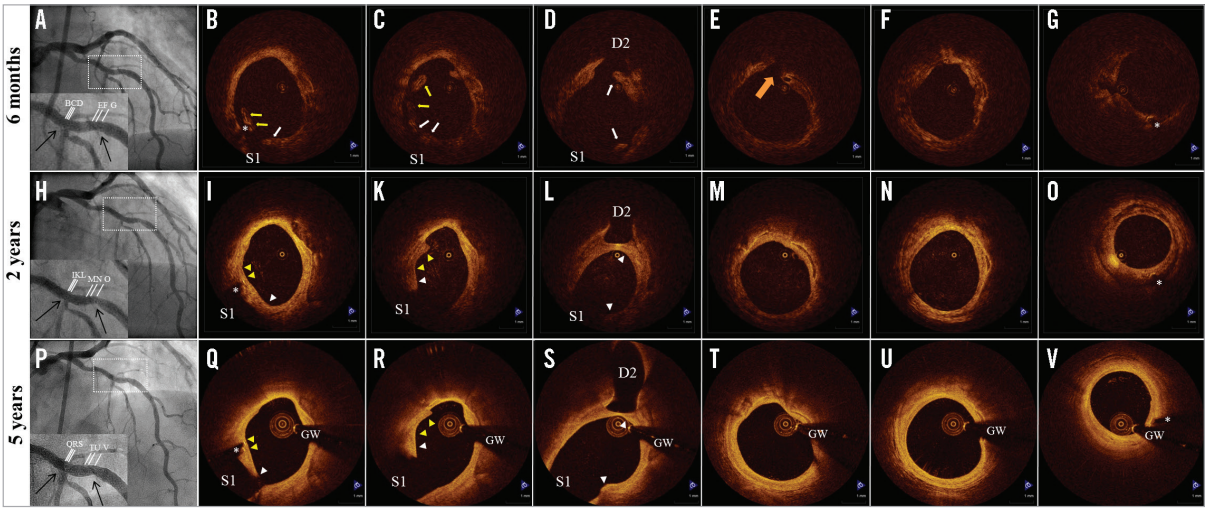

Figure 3. *Serial assessment of scaffold-vascular wall interaction by optical coherence tomography (OCT) in patient 2. A) Coronary angiography six months after BVS implantation at the mid left anterior descending artery. Arrows indicate position of the radiopaque markers at the extremities of the scaffold. B-G) OCT assessment six months after BVS implantation. Incompletely apposed struts (yellow arrows) and side branch-related struts (white arrows) in front of diagonal and septal branches were visualised. Intra-scaffold dissection (orange arrow) and irregular lumen shape can be identified in panels E and F, respectively. H) Coronary angiography 24 months after BVS implantation. I-O) OCT assessment 24 months after BVS implantation. Previously incompletely apposed struts (yellow arrowheads) were integrated into the vessel wall (panels I-K), while side branch-related struts (white arrowheads) were connected by neointimal tissue bridges (panels I-L). Healing of the intra-scaffold dissection and recovery of regular lumen shape. P) Coronary angiography 74 months after BVS implantation. Q-V) OCT assessment 74 months after BVS implantation. Complete disappearance of the struts from the vascular wall and replacement by a signal-rich intimal layer that is separating the underlying plaque (fibrocalcific plaque - fibroatheroma) from the lumen. Note also the complete biodegradation of side branch-related struts and the thinning of tissue bridges. Asterisks indicate stent markers, GW indicates guidewire artefact, S1 indicates ostium of the septal branch and D2 of the diagonal branch.*

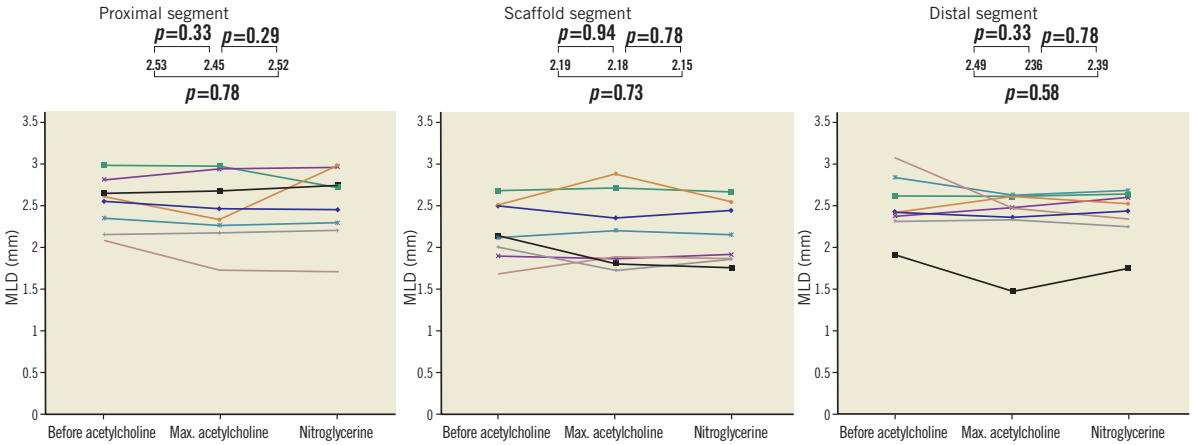

Figure 4. *Vasomotion testing. In these graphs you can see the individual changes of the patients in the proximal coronary segment, scaffold segment and distal segment. At the top, the MLD with the p-values are presented.*

Discussion

The main findings of the current study are the following. 1) The bioresorption process of the Absorb BVS has been completed, as no scaffold struts could be identified by OCT and dense calcium area and necrotic core area by IVUS-VH were significantly reduced at five years compared to baseline. 2) As suggested by OCT analysis, there is no evidence of incompletely apposed struts or struts jailing side branch ostia, and all baseline dissections were healed. 3) There was a trend towards an increase in mean and minimum lumen area at five years compared to two years as assessed by angiography and IVUS, while a significant increase was observed by OCT. The increase was primarily due to a persistent reduction in plaque area up to five years with no evidence of a change in vessel size. 4) The scaffolded coronary segments did not show signs of endothelial dysfunction, whereas a heterogeneous response of the scaffolded coronary segments was observed in response to vasoactive agents. Overall, neither endothelium-dependent nor endothelium-independent vasomotion could be observed in the scaffolded coronary segment.

In the current study, four different intravascular imaging modalities demonstrated consistently that the bioresorption process of the first-generation Absorb BVS has been fully completed. There is a remarkable persistent late luminal enlargement and a reduction in plaque area without outward vessel remodelling up to five years after the first-generation Absorb BVS implantation. Recently, positive long-term findings were also reported for the non-drug-eluting fully biodegradable self-expanding Igaki-Tamai stent (Kyoto Medical Planning Co., Ltd., Kyoto, Japan; formerly, Igaki Medical Planning Co., Ltd.)[8]. In a limited cohort of 50 patients, the struts mostly disappeared within three years after implantation as assessed by IVUS data, although no other imaging modalities with higher sensitivity for detecting scaffold struts were utilised. In that study, the overall major adverse cardiac events rate was acceptable with a target lesion revascularisation rate of 28% at 10 years[8]. In our small cohort, there were no target lesion revascularisations performed in patients treated with the first-generation Absorb BVS at five-year follow-up (only one patient had a TLR at 2,218 days). This beneficial efficacy outcome of the Absorb BVS could have been caused by differences in scaffold design (such as balloon-expanding, drug-eluting, thinner strut thickness and less maximum circular unsupported scaffold area), but also due to intrinsic differences between the two scaffolds. Knowledge of the specific timeline and completion of the bioresorption process of the Absorb BVS in human coronary arteries is very important, as the scaffold should ideally provide uniform radial support for a certain period and afterwards preferably be fully bioresorbed to restore natural physiologic vasomotor function. The Absorb BVS characteristics come closer to achieving this ideal equilibrium, which may have contributed to this favourable efficacy outcome of our patient population.

Our previous published reports with a multi-imaging approach have shown that the bioresorption process of the Absorb BVS was still ongoing at two-year follow-up, as two thirds of the struts were still visible by OCT[2]. Our group recently reported that only one sixth of the struts were recognisable at four years by OCT in a porcine model[9]. In the current study, none of the struts was discernible by OCT at five years, suggesting a faster resorption process in human coronary arteries compared to porcine coronary arteries. Analysis of virtual histology data corroborates this finding, as the dense calcium area and necrotic core area, which can be used as a surrogate marker of the bioresorption process of polymeric struts, were significantly reduced at five years compared to baseline.

IVUS data showed a tendency towards an increase in mean lumen area at five years compared to six months and two years, primarily due to a persistent reduction in plaque area up to five years. A relative reduction in plaque area of 14% in five years achieved by this

local treatment has not been observed before. Therefore, it could even have better plaque-reducing capabilities than (high-intensity) statin treatment, which showed only a reduction of roughly 1% in percentage atheroma volume at two years[10]. Although all patients were on statin treatment, this observed major decrease in plaque area size is an interesting finding that needs further research.

The OCT findings are consistent with a favourable healing response and the absence of device-induced vascular wall toxicity. This is of importance as first-generation drug-eluting stents have been associated with an impaired healing response and vascular toxicity, factors contributing to very late stent thrombosis[11]. Furthermore, metallic platforms have been associated with the development of neoatherosclerosis, which can also contribute to very late stent thrombosis, reported to occur even 15 years following stent implantation[12]. In our patients, OCT revealed the complete disappearance of scaffold struts. We assume, based on the vast evidence in the literature, that this vascular reaction is favourable and potentially reduces the risk of very late stent thrombosis. We further speculate that the observed development of a homogeneous tissue layer over the underlying plaque together with the possibility of observed everolimus-induced autophagy of the macrophages could reduce the risk of new thrombotic events caused by plaque progression[13].

The previous two-year report observed the presence of a functionally active endothelium at the site of the scaffold implantation[2]. In fact, five out of nine patients tested showed vasodilatation with intracoronary acetylcholine. In the present study, four out of eight patients had a more than 3% increase in vessel size after maximum dose of acetylcholine. Two other patients had a less than 3% response, while two patients had more than 3% vasoconstriction (3.9%). These findings are consistent with restoration and preservation of vasomotor function in the scaffolded segment, a desirable effect observed in the absence of a rigid structure.

This study provides evidence for the first time that the beneficial effects of the bioresorbable scaffold are sustained five years after implantation, and of an ongoing lumen enlargement from two years to five years with concomitant reduction in plaque area. Further clinical evidence from ongoing BVS studies can corroborate the current hypothesis and provide a role for BVS in the treatment of coronary artery disease. Furthermore, in the light of the findings of the PROSPECT study, which concluded that specific morphological characteristics of non-culprit lesions in patients with acute coronary syndrome are associated with future events, a device with a favourable safety profile that can shield the lumen from the underlying plaque by a protective homogeneous layer without causing any luminal compromise in the long term could conceptually be used in the setting of high-risk non-stenotic lesions in the future[14].

Limitations

The current study had some limitations. It included a small number of patients and therefore the various parameters that were investigated should be considered as exploratory. Moreover, not all patients who were invited participated in this study. Whether our findings are representative of the whole cohort remains questionable. However, baseline clinical and angiographic characteristics were not different from the entire ABSORB cohort A which can be expected to behave similarly. Third, OCT was performed using a second-generation system with a non-occlusive technique, whereas previous OCT examinations were performed with a first-generation system with proximal balloon occlusion. Although second-generation OCT is associated with a better imaging quality and high reproducibility, it might have slightly overestimated luminal measurements.

Conclusions

In conclusion, the observations made in the current study suggest a highly beneficial clinical and invasive imaging outcome at long-term follow-up. In this series of patients, there was evidence of small but consistent late lumen enlargement at five years, primarily caused by a reduction of the plaque area. The complete bioresorption of the scaffold without signs of endothelial dysfunction suggests the recovery of a functional vascular wall and the elimination of a substrate for late stent complications. All these beneficial findings need to be confirmed in larger studies.

Impact on daily practice

This is the first study describing the five-year results of several imaging modalities of patients treated with first-generation bioabsorbable vascular scaffolds. The results indicate that the bioabsorption process has been fully completed with a late luminal enlargement up to five years of follow-up without signs of adaptive vessel remodelling. The increase in luminal enlargement is due to an impressive reduction in plaque area of 14% in five years, which has not been observed before. These encouraging long-term results of the first-generation bioabsorbable vascular scaffolds will pave the way for larger randomised controlled trials in the future.

Guest Editor

This paper was Guest Edited by Manel Sabaté, MD, PhD, Servicio de Cardiología, Clínic Hospital, Barcelona, Spain.

Funding

The cost for this late follow-up study was fully covered by the Erasmus Medical Center. The institute has received research grants from Abbott Vascular for other projects.

Conflict of interest statement

R.J. van Geuns has received a speaker's fee and served on the European advisory board of Abbott Vascular. Y. Onuma has received a speaker's fee from Abbott Vascular. The other authors have no conflicts of interest to declare. The Guest Editor has no conflicts of interest to declare.

References

1. Ormiston JA, Serruys PW, Regar E, Dudek D, Thuesen L, Webster MW, Onuma Y, Garcia-Garcia HM, McGreevy R, Veldhof S. A bioabsorbable everolimus-eluting coronary stent system for

patients with single de-novo coronary artery lesions (ABSORB): a prospective open-label trial. *Lancet.* 2008;371:899-907.

2. Serruys PW, Ormiston JA, Onuma Y, Regar E, Gonzalo N, Garcia-Garcia HM, Nieman K, Bruining N, Dorange C, Miquel-Hebert K, Veldhof S, Webster M, Thuesen L, Dudek D. A bioabsorbable everolimus-eluting coronary stent system (ABSORB): 2-year outcomes and results from multiple imaging methods. *Lancet.* 2009;373:897-910.

3. Tanimoto S, Bruining N, van Domburg RT, Rotger D, Radeva P, Ligthart JM, Serruys PW. Late stent recoil of the bioabsorbable everolimus-eluting coronary stent and its relationship with plaque morphology. *J Am Coll Cardiol.* 2008;52:1616-20.

4. Cutlip DE, Windecker S, Mehran R, Boam A, Cohen DJ, van Es GA, Steg PG, Morel MA, Mauri L, Vranckx P, McFadden E, Lansky A, Hamon M, Krucoff MW, Serruys PW; Academic Research Consortium. Clinical end points in coronary stent trials: a case for standardized definitions. *Circulation*. 2007;115:2344-51.

5. Ludmer PL, Selwyn AP, Shook TL, Wayne RR, Mudge GH, Alexander RW, Ganz P. Paradoxical vasoconstriction induced by acetylcholine in atherosclerotic coronary arteries. *N Engl J Med.* 1986;315:1046-51.

6. Tearney GJ, Regar E, Akasaka T, Adriaenssens T, Barlis P, Bezerra HG, Bouma B, Bruining N, Cho JM, Chowdhary S, Costa MA, de Silva R, Dijkstra J, Di Mario C, Dudek D, Falk E, Feldman MD, Fitzgerald P, Garcia-Garcia HM, Gonzalo N, Granada JF, Guagliumi G, Holm NR, Honda Y, Ikeno F, Kawasaki M, Kochman J, Koltowski L, Kubo T, Kume T, Kyono H, Lam CC, Lamouche G, Lee DP, Leon MB, Maehara A, Manfrini O, Mintz GS, Mizuno K, Morel MA, Nadkarni S, Okura H, Otake H, Pietrasik A, Prati F, Räber L, Radu MD, Rieber J, Riga M, Rollins A, Rosenberg M, Sirbu V, Serruys PW, Shimada K, Shinke T, Shite J, Siegel E, Sonoda S, Suter M, Takarada S, Tanaka A, Terashima M, Thim T, Uemura S, Ughi GJ, van Beusekom HM, van der Steen AF, van Es GA, van Soest G, Virmani R, Waxman S, Weissman NJ, Weisz G; International Working Group for Intravascular Optical Coherence Tomography (IWG-IVOCT). Consensus standards for acquisition, measurement, and reporting of intravascular optical coherence tomography studies: a report from the International Working Group for Intravascular Optical Coherence Tomography Standardization and Validation. *J Am Coll Cardiol.* 2012;59:1058-72. Erratum in *J Am Coll Cardiol.* 2012;59:1662.

7. Virmani R, Burke AP, Kolodgie FD, Farb A. Vulnerable plaque: the pathology of unstable coronary lesions. *J Interv Cardiol.* 2002:15:439-46.

8. Nishio S, Kosuga K, Igaki K, Okada M, Kyo E, Tsuji T, Takeuchi E, Inuzuka Y, Takeda S, Hata S, Takeuchi Y, Kawada Y, Harita T, Seki J, Akamatsu S, Hasegawa S, Bruining N, Brugaletta S, de Winter S, Muramatsu T, Onuma Y, Serruys PW, Ikeguchi S. Long-term (>10 years) clinical outcomes of first-in-human biodegradable poly-l-lactic acid coronary stents: Igaki-Tamai stents. *Circulation*. 2012;125:2343-53.

9. Onuma Y, Serruys PW, Perkins LE, Okamura T, Gonzalo N, Garcia-Garcia HM, Regar E, Kamberi M, Powers JC, Rapoza R, van Beusekom H, van der Giessen W, Virmani R. Intracoronary optical cohorence tomography and histology at 1 month and 2, 3, and 4 years after implantation of everolimus-eluting bioresorbable vascular scaffolds in a porcine coronary artery model: an attempt to decipher the human optical coherence tomography images in the ABSORB trial. *Circulation*. 2010;122:2288-300.

10. Nicholls SJ, Ballantyne CM, Barter PJ, Chapman MJ, Erbel RM, Libby P, Raichlen JS, Uno K, Borgman M, Wolski K, Nissen SE. Effect of two intensive statin regimens on progression of coronary disease. *N Engl J Med.* 2011;365:2078-87.

11. Nakazawa G, Finn AV, Vorpahl M, Ladich ER, Kolodgie FD, Virmani R. Coronary responses and differential mechanisms of late stent thrombosis attributed to first-generation sirolimus- and paclitaxel-eluting stents. *J Am Coll Cardiol.* 2011;57:390-8.

12. Karanasos A, Ligthart JM, Regar E. In-stent neoatherosclerosis: a cause of late stent thrombosis in a patient with "full metal jacket" 15 years after implantation: insights from optical coherence tomography. *JACC Cardiovasc Interv.* 2012;5:799-800.

13. Karanasos A, Simsek C, Serruys P, Ligthart J, Witberg K, van Geuns RJ, Sianos G, Zijlstra F, Regar E. Five-year optical coherence tomography follow-up of an everolimus-eluting bioresorbable vascular scaffold: changing the paradigm of coronary stenting. *Circulation*. 2012;126:e89-91.

14. Stone GW, Maehara A, Lansky AJ, de Bruyne B, Cristea E, Mintz GS, Mehran R, McPherson J, Farhat N, Marso SP, Parise H, Templin B, White R, Zhang Z, Serruys PW; PROSPECT Investigators. A prospective natural-history study of coronary atherosclerosis. *N Engl J Med.* 2011;364:226-35.

Chapter 4.3

OCT Assessment of the Long-Term Vascular Healing Response 5 Years After Everolimus-Eluting Bioresorbable Vascular Scaffold

Karanasos A, Simsek C, Gnanadesigan M, van Ditzhuijzen NS, Freire R, Dijkstra J, Tu S, Van Mieghem N, van Soest G, de Jaegere P, Serruys PW, Zijlstra F, van Geuns RJ, Regar E

J Am Coll Cardiol. 2014 Dec 9;64(22):2343-56

OCT Assessment of the Long-Term Vascular Healing Response 5 Years After Everolimus-Eluting Bioresorbable Vascular Scaffold

Antonios Karanasos, MD,* Cihan Simsek, MD,* Muthukarrupan Gnanadesigan, MSc,†
Nienke S. van Ditzhuijzen, MSc,* Raphael Freire, MD,* Jouke Dijkstra, PhD,‡ Shengxian Tu, PhD,‡
Nicolas Van Mieghem, MD,* Gijs van Soest, PhD,† Peter de Jaegere, MD, PhD,* Patrick W. Serruys, MD, PhD,*
Felix Zijlstra, MD, PhD,* Robert-Jan van Geuns, MD, PhD,* Evelyn Regar, MD, PhD*

ABSTRACT

BACKGROUND Although recent observations suggest a favorable initial healing process of the everolimus-eluting bioresorbable vascular scaffold (BVS), little is known regarding long-term healing response.

OBJECTIVES This study assessed the in vivo vascular healing response using optical coherence tomography (OCT) 5 years after elective first-in-man BVS implantation.

METHODS Of the 14 living patients enrolled in the Thoraxcenter Rotterdam cohort of the ABSORB A study, 8 patients underwent invasive follow-up, including OCT, 5 years after implantation. Advanced OCT image analysis included luminal morphometry, assessment of the adluminal signal-rich layer separating the lumen from other plaque components, visual and quantitative tissue characterization, and assessment of side-branch ostia "jailed" at baseline.

RESULTS In all patients, BVS struts were integrated in the vessel and were not discernible. Both minimum and mean luminal area increased from 2 to 5 years, whereas lumen eccentricity decreased over time. In most patients, plaques were covered by a signal-rich, low-attenuating layer. Minimum cap thickness over necrotic core was 155 ± 90 μm. One patient showed plaque progression and discontinuity of this layer. Side-branch ostia were preserved with tissue bridge thinning that had developed in the place of side-branch struts, creating a neo-carina.

CONCLUSIONS At long-term BVS follow-up, we observed a favorable tissue response, with late luminal enlargement, side-branch patency, and development of a signal-rich, low-attenuating tissue layer that covered thrombogenic plaque components. The small size of the study and the observation of a different tissue response in 1 patient warrant judicious interpretation of our results and confirmation in larger studies. (J Am Coll Cardiol 2014;64:2343–56) © 2014 by the American College of Cardiology Foundation.

Metallic stents for percutaneous revascularization have been associated with late complications, such as neoatherosclerosis, late restenosis, and thrombosis (1). Bioresorbable vascular scaffolds (BVS) could help overcome such pitfalls. In the ABSORB A study (ABSORB [A bioabsorbable everolimus-eluting coronary stent system] Clinical Investigation, Cohort A), the first-generation

From the *Department of Interventional Cardiology, Thoraxcenter, Erasmus University Medical Center, Rotterdam, the Netherlands; †Department of Biomedical Engineering, Thoraxcenter, Erasmus University Medical Center, Rotterdam, the Netherlands; and the ‡Division of Image Processing, Department of Radiology, Leiden University Medical Center, Leiden, the Netherlands. The Thoraxcenter receives unrestricted grants from Abbott and St. Jude Medical. Dr. Karanasos has received funding support from Hellenic Heart Foundation and St. Jude Medical. Dr. Simsek and Mr. Gnanadesigan were supported by research grants from "Nederlandse Hartstichting" (2009B091 to Dr. Simsek and 2010B064 to Mr. Gnanadesigan). Dr. Tu is employed by Medis Medical Imaging Systems; and has a research appointment at the Leiden University Medical Center. Dr. van Geuns has received speaker fees and research grants from Abbott Vascular. All other authors have reported that they have no relationships relevant to the contents of this paper to disclose.
Listen to this manuscript's audio summary by *JACC* Editor-in-Chief Dr. Valentin Fuster.
You can also listen to this issue's audio summary by *JACC* Editor-in-Chief Dr. Valentin Fuster.

Manuscript received March 7, 2014; revised manuscript received August 28, 2014, accepted September 5, 2014.

ABBREVIATIONS AND ACRONYMS

BVS = bioresorbable vascular scaffold(s)
ICC = intraclass correlation coefficient
IQR = interquartile range
IVUS = intravascular ultrasound
OCT = optical coherence tomography
SB = side branch

everolimus-eluting BVS (Absorb BVS 1.0; Abbott Vascular, Santa Clara, California) was associated with a good long-term clinical outcome after 2 and 5 years (2,3). Plaque regression from 2 to 5 years and recovery of vasomotion in the scaffolded segment were documented in a patient subset (4). Moreover, recent clinical observations of a signal-rich layer separating potentially thrombogenic plaque components from the lumen (5,6) suggest a favorable long-term healing response with potential plaque sealing.

We aimed to provide a comprehensive optical coherence tomography (OCT) analysis of the vascular healing response in the longest follow-up available to date (5 years) in the first series of patients who received everolimus-eluting BVS.

METHODS

PATIENT POPULATION. The study population (4) and index procedure (2) have been described (Online Appendix). Briefly, all 14 living patients from the Thoraxcenter Rotterdam cohort of ABSORB A were asked to participate. Eight consented and were included. The protocol was approved by the institutional ethics committee and conformed to the Declaration of Helsinki.

OCT IMAGE ACQUISITION. All 8 subjects underwent frequency-domain OCT at the 5-year invasive follow-up (7). Six patients at baseline, 7 patients at 6-month follow-up, and 7 patients at 2-year follow-up had undergone occlusive time-domain OCT per the study protocol, with serial OCT imaging at all intervals available for 5 patients. For details, see the Online Appendix.

DEFINITIONS. OCT analysis of bioresorbable scaffolds reveals essential differences from metal stents (**Figure 1**). With metal stents, struts are preserved and neointimal area is clearly defined as the area between stent and lumen contour. In BVS, when scaffold struts are still discernible, the neointimal area can be assessed similarly to metal stents. However, at long-term follow-up, BVS scaffold struts are no longer visible, and the area corresponding to struts and neointima has similar optical properties as the underlying fibrous layer (5,8). Consequently, it is impossible to distinguish between strut area, neointimal area, and underlying plaque.

Therefore, the vascular structure observed at the scaffolded segment, a product of the consolidation of underlying plaque, biodegraded struts, and neointima, resembled a native atherosclerotic plaque and was defined as neoplaque (**Figure 1**).

Because OCT cannot distinguish the scaffold area, and thus neointimal area, from the underlying plaque, neointimal thickness cannot be assessed directly. Hence, we aimed to provide an indirect assessment that focused on the signal-rich layer, which consisted of the neointimal layer, resorbed struts, and pre-existing fibrous tissue. We analyzed this signal-rich layer, between the lumen border and internal elastic lamina, for providing a measure of separation of the lumen from underlying plaque components (5,6). In situations in which signal-poor regions (e.g., calcifications, necrotic core, deeply located fibrous plaque) obscured delineation of the internal elastic lamina, the signal-rich layer was delineated between lumen border and the boundary of signal-rich and signal-poor regions (**Figures 1 and 2**).

OCT IMAGE ANALYSIS. The platinum scaffold markers defined the region of interest. Quantitative and qualitative 5-year OCT image analysis was performed per frame. Analysis included the assessment of discernible struts, lumen morphometry, signal-rich layer thickness measurement, neoplaque characterization, attenuation analysis, and ostial side-branch (SB) assessment. Metal stents implanted in the same vessels were also analyzed (1).

LUMINAL MEASUREMENTS AND VARIABILITY ANALYSIS. For details, see the Online Appendix. Measurements included mean and minimum lumen area and eccentricity, calculated as: ratio (maximum lumen diameter – minimum lumen diameter)/maximum lumen diameter (7). Lumen measurements were assessed for intraobserver, interobserver, and intra-study variability.

QUANTIFICATION OF SIGNAL-RICH LAYER THICKNESS. The signal-rich layer was quantified following segmentation of its luminal and abluminal contour by measuring minimum, mean, and maximum thickness and symmetry (ratio of minimal to maximal thickness) (**Figure 2**). Signal-rich layer measurements were assessed for variability.

NEOPLAQUE CHARACTERIZATION. Neoplaque morphology was assessed per frame at 5 years, according to native atherosclerosis definitions (7), and the arc of calcifications, necrotic core, and mixed plaque were measured with QCU-CMS (LKEB, Leiden University, the Netherlands; research version of QIvus, Medis medical imaging systems, Leiden, the Netherlands). Fibrous cap contours were traced over necrotic core with mean and minimum cap thickness calculated per patient. Spread-out maps representing neoplaque morphology and cap thickness

throughout the scaffolded segment were generated (**Figure 3**) and color-coded by plaque type. The presence of sharply delineated signal-poor voids, which corresponded to intimal microchannels (7), was recorded. In neoplaques with necrotic core, OCT images were compared with previous follow-ups to look for de novo accumulation of necrotic core of adluminal origin, possibly corresponding to neoatherosclerosis.

ATTENUATION ANALYSIS. We used attenuation analysis for quantitative tissue characterization of the signal-rich layer and the neoplaque (**Figure 4**). In ex vivo validation experiments, highly attenuating regions (attenuation coefficient $\mu_t \geq 8$ mm^{-1}) have been associated with necrotic core or macrophages. Conversely, $\mu_t < 6$ mm^{-1} were associated with healthy vessel, intimal thickening, or calcified plaque (9,10). Attenuation was quantified circumferentially at different depths from the lumen surface by custom-made software (11). Results were plotted in spread-out maps demonstrating: 1) maximum attenuation coefficient per A-line throughout the pullback; and 2) attenuation coefficient values in different depths from the vessel surface.

SB ASSESSMENT. To assess anatomic SB jailing over time, 3-dimensional images of SB ostia were obtained by volume-rendering software (INTAGE Realia, KGT, Tokyo, Japan) (12). No struts were identifiable by OCT, but neointimal bridges had developed in their place and were classified based on their relative location to the ostium as proximal, distal, proximal and distal, or crossing (**Figure 5**). Mean and minimal thickness was measured in matched frames at 2- and 5-year follow-up with QCU-CMS (Online Figure 1).

SB ostium area was assessed with dedicated software (QAngioOCT 1.0, Medis Specials, Leiden, the Netherlands). After 3-dimensional reconstruction, a cut-plane perpendicular to the SB centerline was selected and SB ostium planimetry performed (**Figure 6**) (13).

STATISTICAL ANALYSIS. Continuous variables are presented as mean ± SD or median (interquartile range [IQR]) and nominal variables as n (%). Significance level was set at $p < 0.05$. Luminal measurements were compared by Wilcoxon signed-rank test. All other paired comparisons were performed by paired Student *t* test. No corrections were made for multiple comparisons. Variability was assessed with intraclass correlation coefficients (ICCs) for absolute agreement and Bland-Altman statistics. Statistical analysis was performed with SPSS version 20.0 (IBM, Armonk, New York).

FIGURE 1 Long-Term Vascular Healing Response in Metal Stents and Bioresorbable Scaffolds

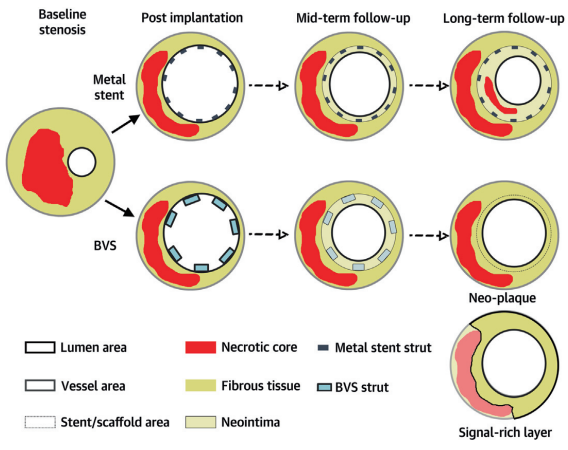

After metal stent implantation, struts are preserved and the neointimal area clearly delineated between stent and lumen contour even at long-term follow-up, with possible development of neoatherosclerosis within the neointima. Conversely, in long-term follow-up of bioresorbable scaffolds, neointimal boundaries are unclear after bioresorption **(dotted line)**, and the intima resembles native plaque, defined as *neoplaque*. The signal-rich layer is the layer that separates the underlying plaque components from the lumen. BVS = bioresorbable vascular scaffold.

RESULTS

LUMEN AND STRUT MEASUREMENTS. No binary restenosis was witnessed in the 5-year angiograms. In all patients, scaffold struts were no longer discernible as a result of complete bioresorption, and lumen area increased significantly from 2 to 5 years (**Figure 7**). Lumen eccentricity declined over time (baseline 0.24 ± 0.13; 6-month follow-up 0.29 ± 0.12; 2-year follow-up 0.21 ± 0.08; 5-year follow-up 0.15 ± 0.02; $p<0.05$ for all comparisons vs. previous studies).

The total strut count was reduced in 5 patients with serial observations: 278 struts at baseline, 248 at 6 months, 174 at 2 years, and no visible struts at 5 years. Two cases with incomplete scaffold apposition at baseline or 6 months demonstrated complete resolution of incomplete scaffold apposition at 2 years and complete strut bioresorption at 5 years.

QUANTIFICATION OF SIGNAL-RICH LAYER. Median values (IQR) for mean, minimum, and maximum signal-rich layer thickness and symmetry were 330 μm (290 to 378 μm), 150 μm (120 to 190 μm), 570 μm (500 to 640 μm), and 0.26 (0.20 to 0.33), respectively.

FIGURE 2 Quantifying Signal-Rich Layer Thickness in Different Plaque Types

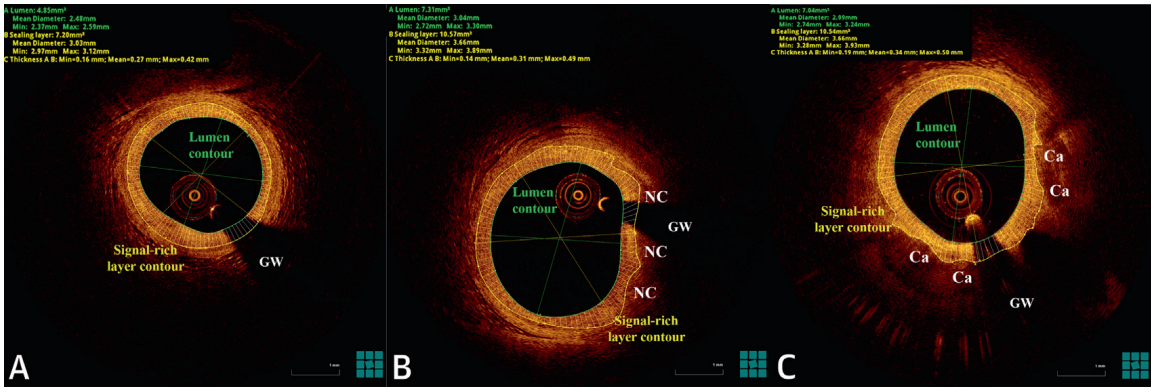

In the absence of attenuating intimal regions, the contour is traced at the internal elastic lamina **(A)**. In plaques with necrotic core, the abluminal contour is traced at the attenuating region boundary **(B)**. In plaques with calcifications, the signal-rich layer is segmented at the calcification edge **(C)**. Ca = calcium; GW = guidewire; NC = necrotic core.

FIGURE 3 Plaque Characterization and Cap Tracing

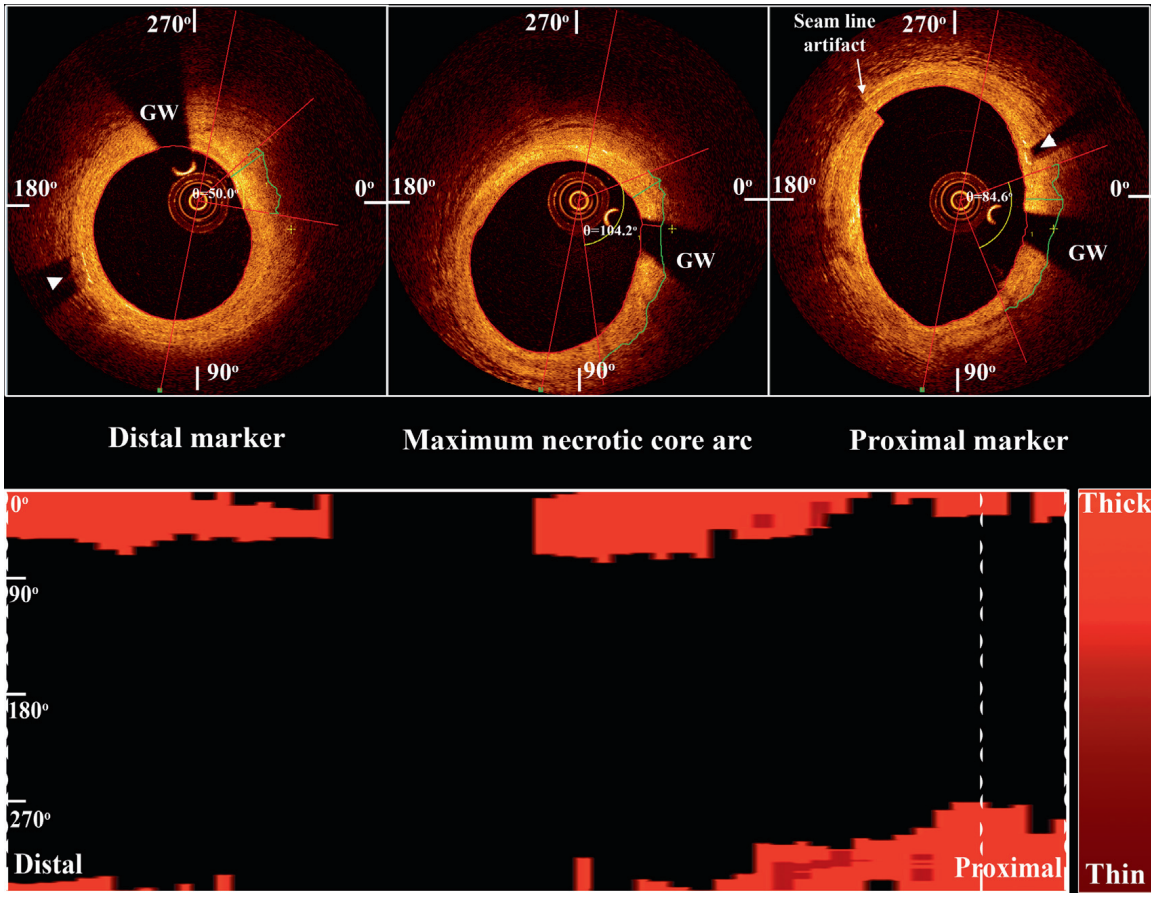

In frames with necrotic core, calcifications, or mixed plaque within the scaffolded segment, the overlying fibrous cap was segmented and minimum thicknesses were recorded. A spread-out map was generated that showed the component distribution within the neoplaque, with lighter colors corresponding to thicker caps. **Arrowhead** indicates scaffold marker. GW = guidewire.

FIGURE 4 Example of Attenuation Analysis

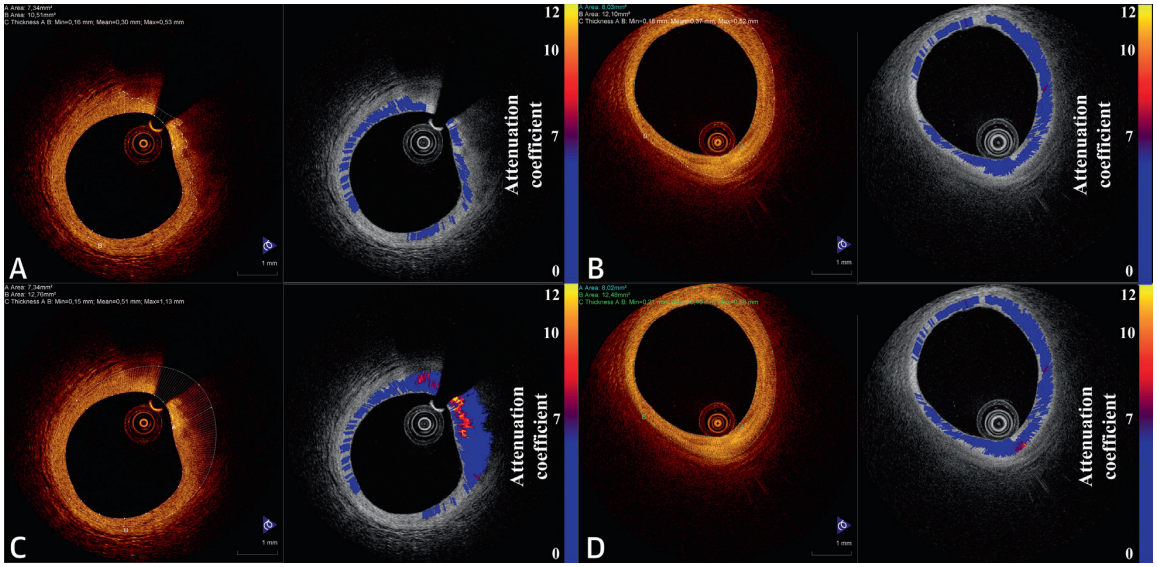

In all frames, tissue attenuation properties within adluminal and abluminal contour were measured and displayed on a color scale (**blue** represents low-attenuation regions, whereas **red** and **yellow** represent high-attenuation regions). Analysis was performed in the signal-rich layer **(A, B)**, as defined in Figure 2, and in the entire neoplaque, up to the internal elastic lamina **(C, D)**. Note the lack of highly attenuating regions within the signal-rich layer **(A, B)**, whereas attenuation properties deeper in the neoplaque depended on tissue type (high attenuation in necrotic core; **C**). For intimal thickness <200 μm, as in 6 to 7 o'clock in **A** and **C** and 8 to 9 o'clock in **B** and **D**, analysis was not performed because of lack of a sufficient imaging window. Abbreviations as in Figure 2.

FIGURE 5 Different Types of Tissue Bridges Overlying Side Branches

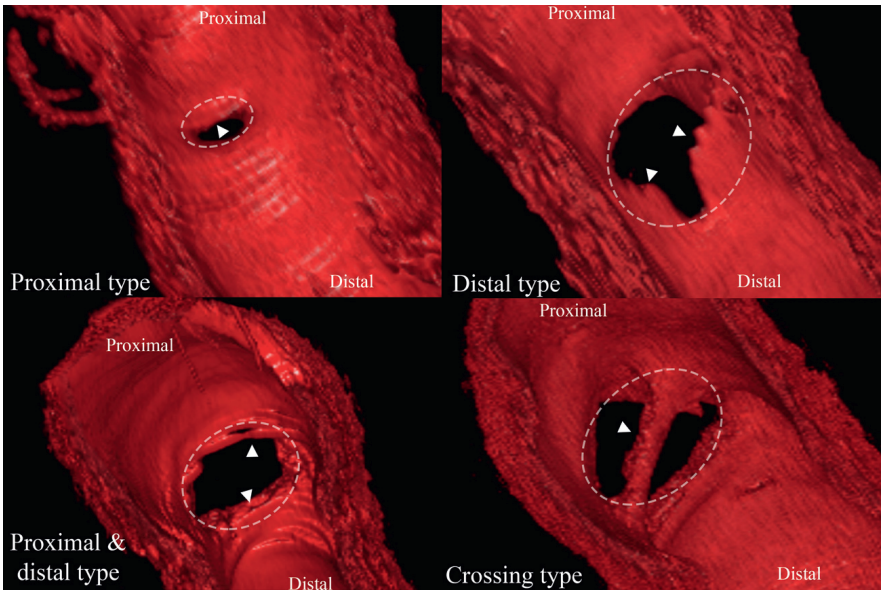

Classification was based on the relative location with the side-branch ostium. Four different types could be identified: proximal, distal, proximal and distal, or crossing. **Dotted lines** indicate side-branch ostia; **arrowhead** indicates tissue bridge.

FIGURE 6 Side-Branch Ostium Area Measurement by Cut-Plane Analysis

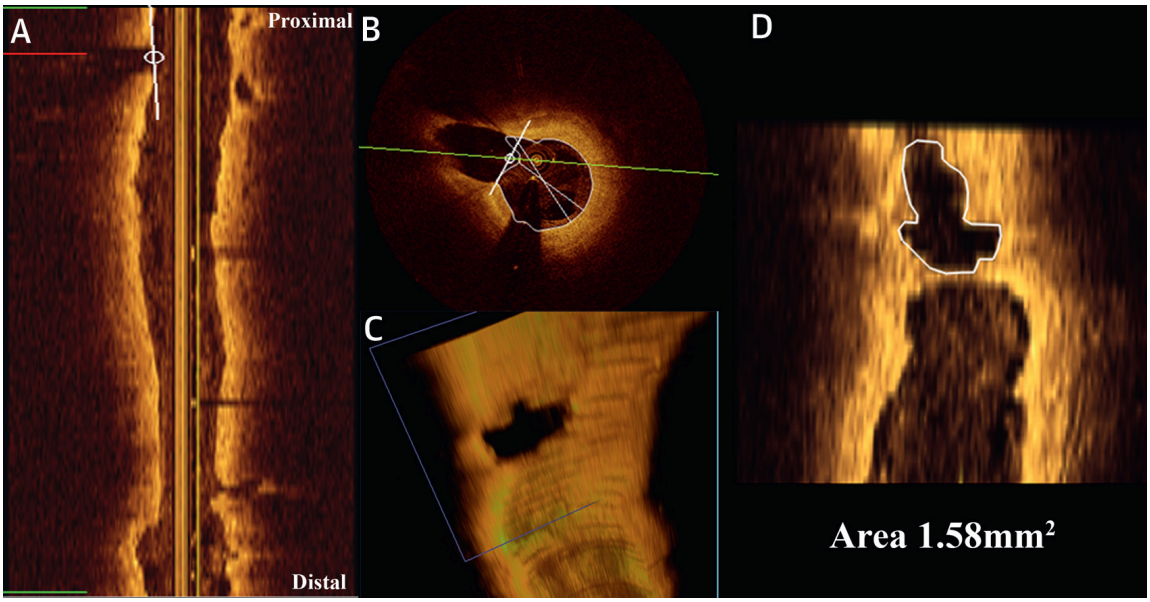

After 3-dimensional rendering, side-branch ostium area could be measured in a cut plane perpendicular to the side-branch ostium: L-mode display **(A)**; cross-sectional image **(B)**; 3-dimensional rendering **(C)**; derived perpendicular cut plane **(D)**.

Online Figure 2 demonstrates frequency distributions of these thickness measurements.

NEOPLAQUE CHARACTERIZATION. Figure 8 presents spread-out neoplaque maps. The mean value of minimum cap thickness was 310 ± 113 μm, whereas the minimum value was 155 ± 90 μm. Mean and maximum values were 92° ± 49° and 156° ± 72° for necrotic core arc, 80° and 104° for calcification arc, and 104° ± 145° and 146° ± 80° for mixed-plaque arc.

Microchannels were identified in 7 of 8 patients and in 66 of 468 frames (14.1%). Per the neoplaque maps, necrotic core or mixed plaque >1 quadrant was observed in 7 patients. Comparison with previous follow-ups did not reveal evidence of de novo necrotic core accumulation of adluminal origin.

Two patients had a focally irregular lumen contour. Patient #8 had a short intimal dissection, not present at earlier investigations, at the overlap between BVS and a metallic stent implanted at baseline. This minor, angiographically not visible dissection was most likely iatrogenic, induced by the guidewire. In Patient #4, a thin-cap fibroatheroma was observed at the distal scaffold segment with cap disruption and small thrombus (Figure 9). Post-hoc revision of previous OCT examinations revealed possible scaffold discontinuity near the distal edge at 4 months, with the scaffold being dislocated opposite to the rupture site.

ATTENUATION ANALYSIS. Mean per-patient attenuation within the signal-rich layer was 1.77 ± 0.32 mm^{-1}, and the median was 1.28 ± 0.25 mm^{-1} (Online Figure 3). This value was higher within the entire neoplaque (mean per patient 2.87 ± 0.54 mm^{-1}; median per patient 2.33 ± 0.49 mm^{-1}; $p < 0.001$) (Online Figure 4). Spread-out attenuation maps at different depths from the luminal surface are displayed in Figure 10. The surface layers (first 200 μm) had low attenuation, overlying high-attenuation areas located deeper in the plaque.

SB ASSESSMENT. All SBs were patent with TIMI (Thrombolysis In Myocardial Infarction) flow grade 3. Overall, 14 SBs were associated with incompletely apposed struts at previous examinations. Neointimal bridges at 5 years were identified in 13 SBs, whereas in 1, no bridge was visible (Table 1).

Minimal and mean thickness of neointimal bridges overlying SBs were respectively reduced from 241 ± 92 μm and 341 ± 106 μm at 2 years to 161 ± 107 μm and 227 ± 119 μm at 5 years ($p < 0.001$) (Online Figure 5).

METAL DRUG-ELUTING STENT ANALYSIS. Metal drug-eluting stent (DES) analysis is presented in Online Table 1 and Figure 11. In all metal stents, coverage was >95%, without malapposed struts, whereas neoatherosclerosis was identified in all.

VARIABILITY ANALYSIS. Interobserver and intraobserver variability for both frame- and patient-level analysis was low (interobserver: difference 0.23 ± 0.29 mm, ICC = 0.98; interobserver [core laboratory]: difference 0.13 ± 0.32 mm, ICC = 0.98; intraobserver: difference 0.17 ± 0.19 mm, ICC = 0.99) (Online Table 2, Online Figure 6). As seen in the Bland-Altman plots, there were few measurements with significant differences, all of which were in the polygon of confluence of larger SBs with complex geometry lacking a priori definitions for contour tracing. ICCs for mean and minimal signal-rich layer thickness were respectively 0.95 and 0.86 for intraobserver variability and 0.80 and 0.80 for interobserver variability.

DISCUSSION

We present the first in vivo long-term OCT data after BVS implantation. Despite the small sample size, these first patients treated with BVS offer a unique opportunity to study the long-term vascular response after BVS implantation (**Figure 12**). Our main findings are that 5 years after BVS 1.0 implantation: 1) there is late lumen enlargement with simultaneous increase in luminal symmetry; 2) all struts have disappeared and have been integrated within the neointima and underlying plaque, forming a homogeneous, signal-rich, low-attenuating layer; 3) this signal-rich layer separates the lumen from the underlying plaque with a minimum thickness of 150 μm (IQR: 120 to 190 μm); 4) this effect is not universal, with 1 case showing thinning and disruption of the signal-rich layer; 5) jailed SB ostia are preserved, whereas SB-related struts have been replaced by thin tissue bridges; and 6) metal DES in the same vessels are lacking a distinct signal-rich layer and show neoatherosclerosis despite good coverage and apposition (**Central Illustration**).

In our series, we observed a consistent luminal enlargement from 2 to 5 years in all patients. Late luminal enlargement in bioresorbable scaffolds has been attributed to outward remodeling in animal studies (14) and plaque burden reduction in clinical trials (4,15). Our findings echo larger-scale intravascular ultrasound (IVUS) observations of lumen area increases from 6 months to 2 years after BVS implantation (2,15). IVUS observations in our study population were consistent with our findings, displaying a trend for further lumen enlargement from 2 to 5 years, driven by a persistent decrease in plaque size from 6 months to 2 years caused by either true plaque regression or pseudoregression from strut resorption (2,4). A similar trend was observed in the 5-year multislice computed tomography follow-up of ABSORB A (3). We observed recovery of luminal symmetry, a finding of unclear significance. Simultaneous observations of strut bioresorption and signal-rich layer development suggest a potentially favorable biological effect, which parallels IVUS studies showing increased plaque rupture in eccentric vessels (16). The observed complete strut bioresorption tracks with vasomotion findings demonstrating a lack of mechanical vessel constraint, with positive acetylcholine response in 4 patients, negative response in 2 patients, and absence of significant change in 2 patients (4).

FIGURE 7 Serial Luminal Measurements

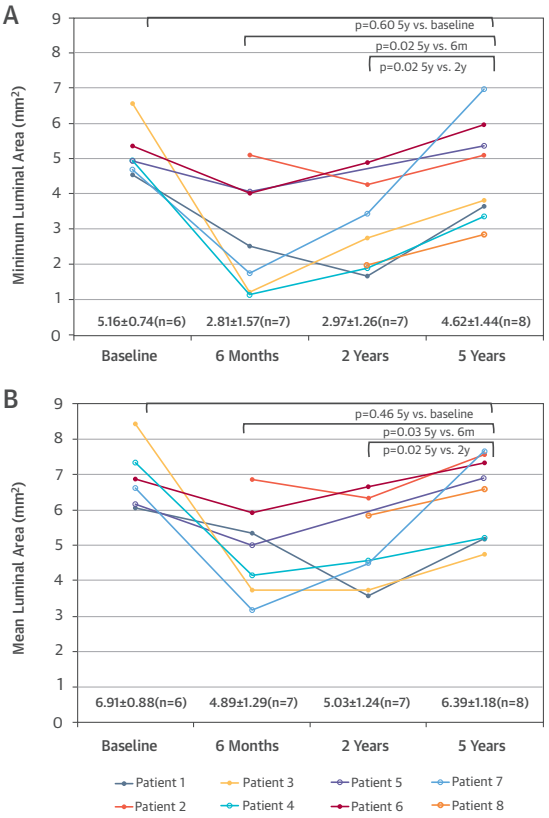

Despite an initial decrease in lumen dimensions from baseline to 6 months, minimal **(A)** and mean **(B)** lumen areas were increased at 5 years compared with previous follow-ups and were not significantly different from baseline.

FIGURE 8 Neoplaque Morphology

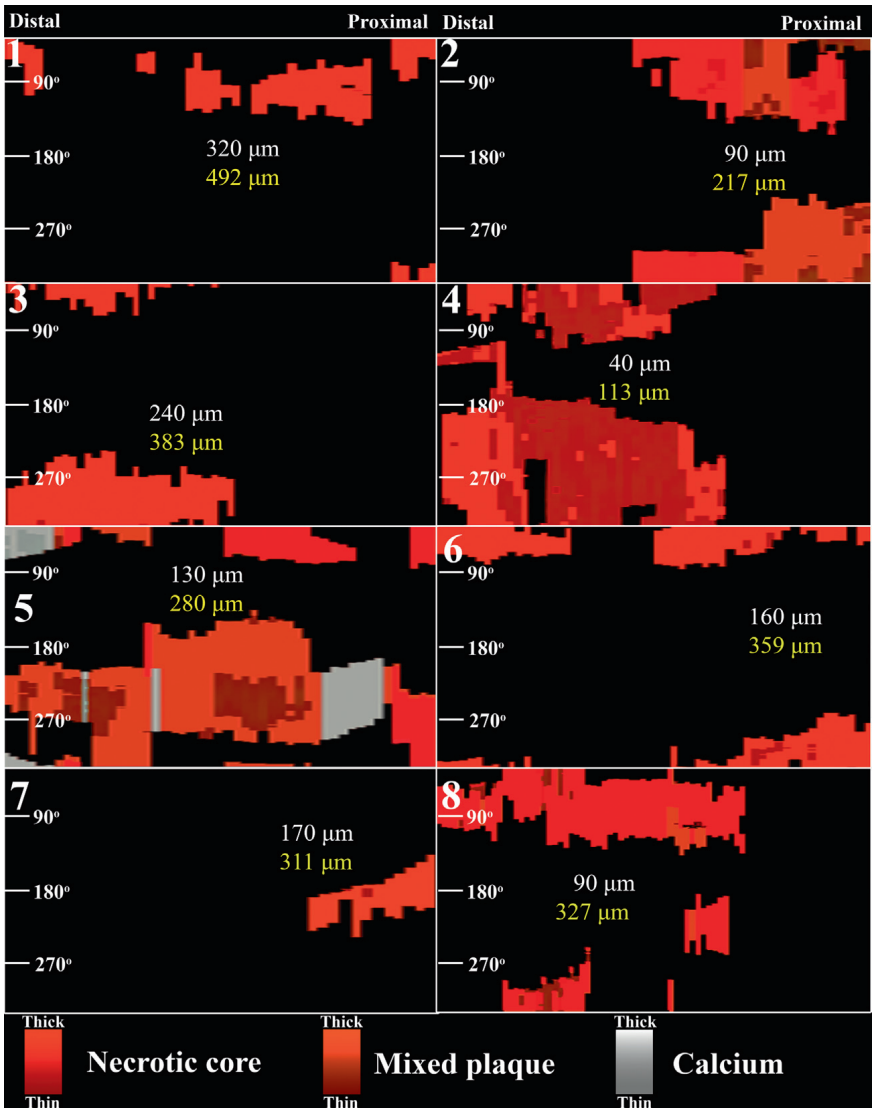

Spread-out maps from all patients demonstrating neoplaque composition. **Red** represents necrotic core; **orange**, mixed plaque; and **white**, calcification. **Lighter colors** indicate a thicker fibrous cap (>250 μm). The minimum and mean values of minimum cap thickness per patient are presented in **white** and **yellow**, respectively.

It has been suggested that neointimal growth after BVS resorption could serve as a mechanical barrier that prevents potentially thrombogenic plaque components from reaching the bloodstream, a concept dubbed "plaque sealing" or "recapping the plaque" (5,6). With this hypothesis in mind, we scrutinized BVS morphology in our cohort, using sophisticated algorithms for in-depth analysis. We focused on the developed adluminal signal-rich layer, which corresponds to neointima, bioresorbed struts, and fibrous components of the underlying plaque. The minimum signal-rich layer thickness was 150 μm, and the minimum cap thickness over necrotic core was 155 ± 90 μm, both well beyond the 65-μm threshold generally accepted as high risk for plaque rupture (17), which suggests that this layer could reliably separate the lumen from potentially thrombogenic plaque components. Importantly, this layer showed remarkable homogeneity in the attenuation analysis, with low attenuation values hinting at the absence of high-risk wall components such as necrotic core and macrophages (9,10). This signal-rich layer could be protective against very late scaffold thrombosis or de novo thrombosis by plaque progression and rupture (1,17).

The complete scaffold integration into the vascular wall has shaped a neoplaque phenotype that resulted from the complex interaction of pre-existing plaque, morphological changes of the pre-existing plaque subject to dynamic local rheological factors (18,19), strut resorption, and neointima formation (8). We visually characterized neoplaque using standardized OCT criteria (7). Quantitative attenuation analysis corroborated these qualitative findings, revealing colocalization of necrotic core regions with high attenuation regions (Online Figure 7), generally located deeper in the vessel wall and rarely observed within the first 200 μm from luminal surface. Of note, most patients were receiving intensive medical therapy (statins, 75%; beta-blockers, 75%; angiotensin receptor blockers, 62.5%), which possibly contributed to this favorable phenotype.

Metal stents covered with well-organized and functional neointima can likewise present a mechanical barrier between underlying plaque and lumen. However, neointimal proliferation and neoatherosclerosis development over time have been reported for bare-metal stents and are even more accelerated for DES. The permanent nature of the metallic structure further limits the vessel's capacity for remodeling, plaque regression, and lumen enlargement over time. Consequently, lumen narrowing develops inevitably over time, and indeed, 3 metal DES in our cohort showed adluminal neoatherosclerosis, with minimum cap thickness ranging from 70 to 110 μm. This is notable because thin fibrous cap emerges as a risk factor for neointimal rupture and acute coronary syndrome not only in native atherosclerosis but also in neoatherosclerosis (1).

We analyzed the fate of SBs "jailed" by BVS, because high strut thickness and tissue bridge formation have raised questions regarding long-term patency (12). Three-dimensional rendering demonstrated SB patency, allowed reliable ostial measurements, and identified different intimal bridge patterns. Strut integration into these tissue bridges was completed, accompanied by bridge thinning from 341 ± 106 μm at 2 years to 227 ± 119 μm at 5 years. Together with the angiographically confirmed absence of flow impairment, we consider these findings a favorable long-term outcome. However, the implications of BVS over large SBs or in true bifurcation lesions remain unknown (20,21), because these were excluded per protocol.

Overall, our long-term OCT observations suggest a favorable vascular healing response with late lumen enlargement, increased luminal symmetry, SB patency, complete strut resorption, and formation of a potentially protective tissue layer, giving an appearance consistent with the hypothetical concept of plaque sealing. Patient #4 did show a different response, which captured our attention. We observed target-lesion progression, with OCT findings consistent with macrophage infiltration, abluminal necrotic core accumulation, fibrous cap thinning, and plaque rupture at follow-up, while the patient was treated only with aspirin and clopidogrel. This patient had diffuse disease that necessitated non-target-lesion revascularization with a metal

FIGURE 9 Vascular Response in Patient #4

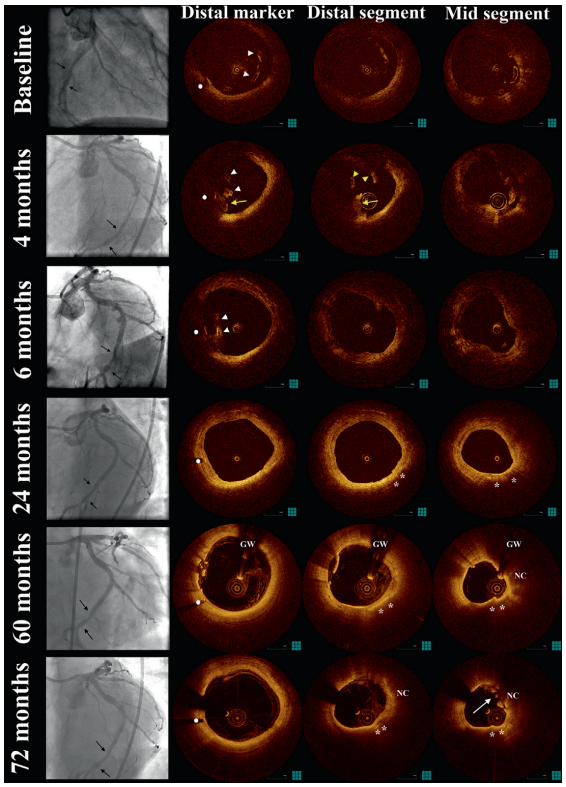

At baseline, there was malapposition **(white arrowheads)** at the distal segment. At 106-day follow-up, scaffold collapse **(white arrowheads)** at the site of the distal marker **(white bullet)**, overhanging struts **(yellow arrowheads)**, and thrombus **(yellow arrow)** were observed that suggested late scaffold discontinuity. At 6 months, a tissue bridge was formed **(white arrowheads)** at the site of the collapsed scaffold and integrated into the vascular wall by 24 months. Note the macrophage accumulation **(white asterisks)** at the opposite side at 24 months. At 60-month follow-up, lesion progression with macrophages and necrotic core was evident, as well as intimal disruption. At 72-month follow-up, there was further luminal narrowing and plaque rupture with thrombus **(white arrow)**. **Black arrows** indicate scaffold markers. Abbreviations as in **Figure 2**.

FIGURE 10 Attenuation Spread-Out Maps

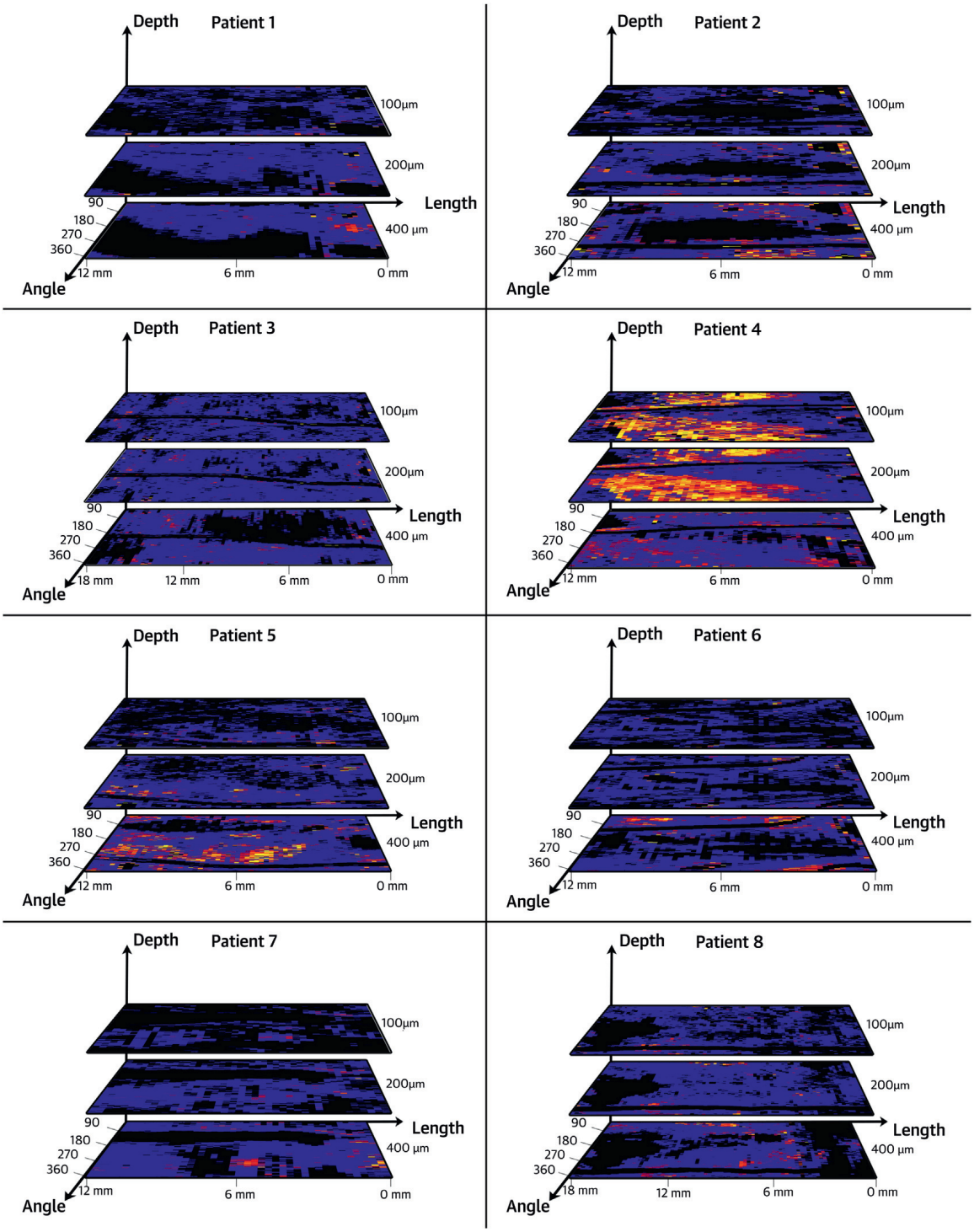

Spread-out maps demonstrating attenuation coefficient in pre-defined depths from the vessel surface (100, 200, and 400 μm) per patient. In most patients, there was a low-attenuating layer of 200 μm separating the underlying plaque (starting at ~400 μm) from the lumen. In Patient #4, this layer was absent, and attenuating areas were close to the lumen.

TABLE 1 Side-Branch Analysis

	Bifurcation Type	SB Ostium Area (mm^2)	Jailing Pattern
Patient #1: SB 1	OM-LCx	4.81	Proximal and distal
Patient #2: SB 1	LAD-septal	6.22	Crossing
Patient #2: SB 2	LAD-diagonal	1.14	Distal
Patient #2: SB 3	LAD-septal	1.89	Proximal
Patient #3: SB 1	LAD-diagonal	1.58	Distal
Patient #3: SB 2	LAD-septal	1.42	N/A*
Patient #4: SB 1	LCx-OM	1.11	Proximal and distal
Patient #5: SB 1	LAD-septal	1.93	Crossing
Patient #5: SB 2	LAD-diagonal	0.46	Distal
Patient #6: SB 1	LCx-OM	1.37	Crossing
Patient #6: SB 2	OM-LCx	2.23	Distal
Patient #8: SB 1	LCx-OM	N/A†	Proximal
Patient #8: SB 2	LCx-posterolateral	0.3	Proximal
Patient #8: SB 3	LCx-OM	0.78	Proximal

*The bridge was not present at 5 years; distal location at previous studies. †Exact area not measurable.

LAD = left anterior descending coronary artery; LCx = left circumflex coronary artery; N/A = not available; OM = obtuse marginal branch; SB = side branch.

paclitaxel-eluting stent in the same artery 106 days after BVS implantation. This stent developed subsequent neoatherosclerosis with neointimal disruption and microthrombus formation (Figure 11). This evidence of accelerated atherosclerosis, combined with mechanical factors (baseline incomplete scaffold apposition followed by late structural discontinuity), might have contributed to the adverse neoplaque phenotype. Notably, the patient did not have a clinically apparent acute coronary syndrome regardless of these impressive findings.

Despite the limited scale of our study, it provides crucial information on the long-term vascular response 5 years after BVS implantation. Although we consider the overall vascular response to be favorable and in line with larger-scale clinical reports, there might be lessons to learn from observations in the single patient who showed a different biological reaction, with recurring plaque rupture after BVS implantation. This finding might underscore the need

FIGURE 11 Representative Optical Coherence Tomography Images of Metal Drug-Eluting Stents

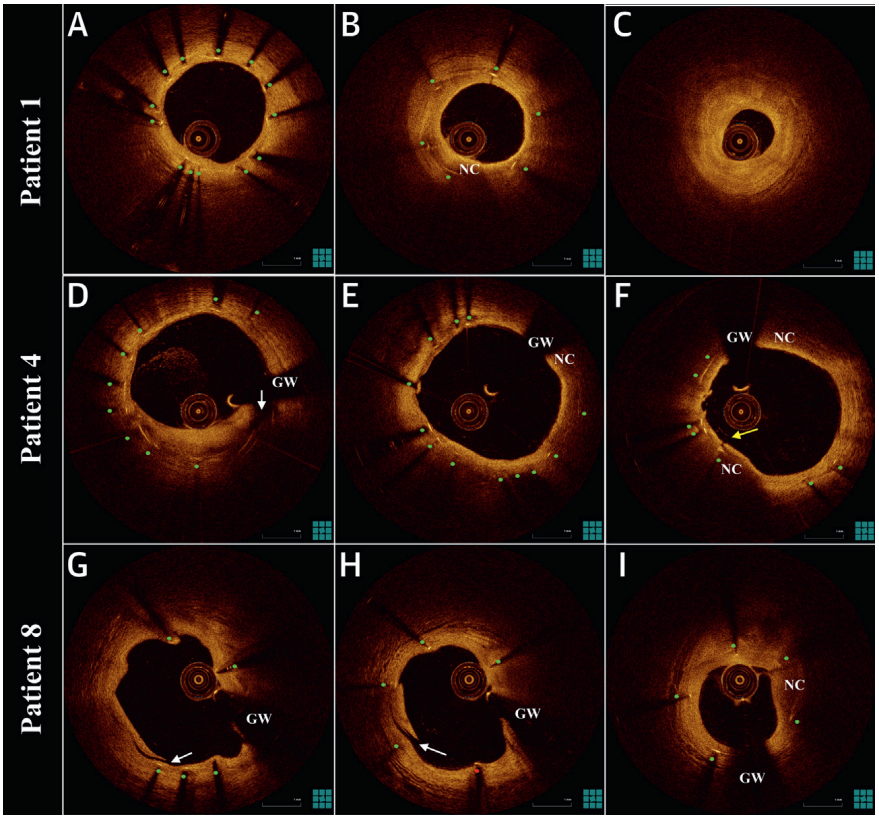

Covered struts **(A, green bullet)**; neoatherosclerosis **(B)**; distal edge stenosis **(C)** (area = 1.74 mm^2); heterogeneous neointima with discontinuity **(D, white arrow)**; neoatherosclerosis **(E)**; neointimal disruption **(yellow arrow)** over necrotic core with mural micro-thrombi **(F)**; evaginations-neointimal discontinuity **(white arrow)** possibly iatrogenic **(G)**; uncovered strut **(H, red bullet)**; neoatherosclerosis **(I)**. Abbreviations as in Figure 2.

FIGURE 12 Serial Assessment of Vascular Response

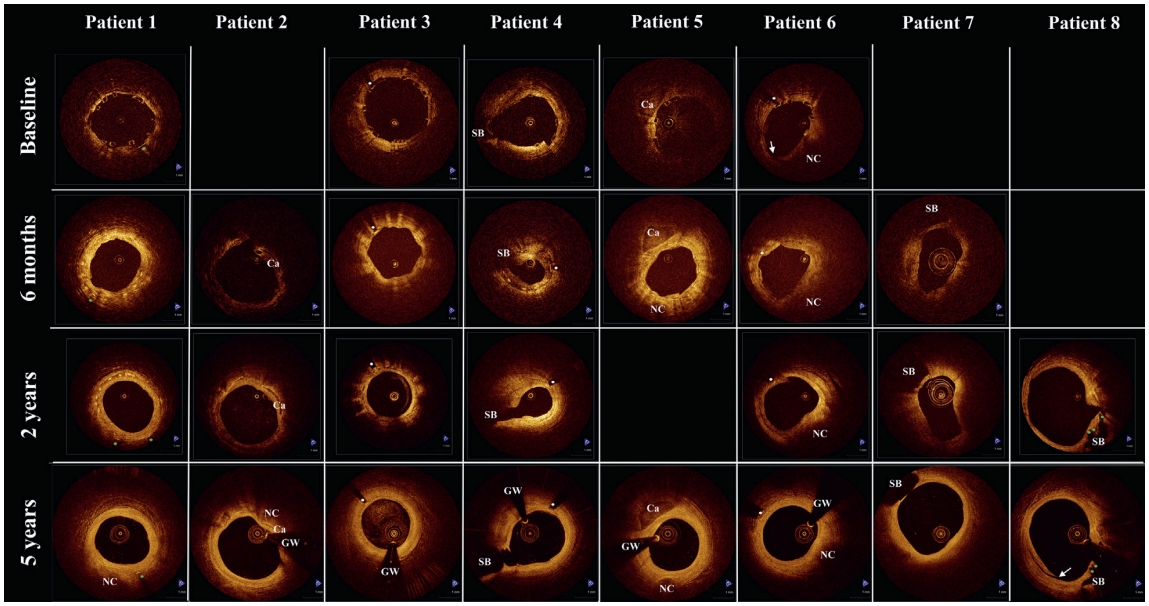

Matched representative images from serial examinations of all patients. Note the complete strut integration at 5 years, together with lumen enlargement, compared with 6-month and 2-year follow-ups. In Patient #8, intimal discontinuity **(arrow)**, presumably iatrogenic, was observed. **Green bullets** indicate metal struts; **white bullets** indicate scaffold markers. SB = side branch; other abbreviations as in Figure 2.

CENTRAL ILLUSTRATION Long-term Vascular Healing in Bioresorbable Scaffolds

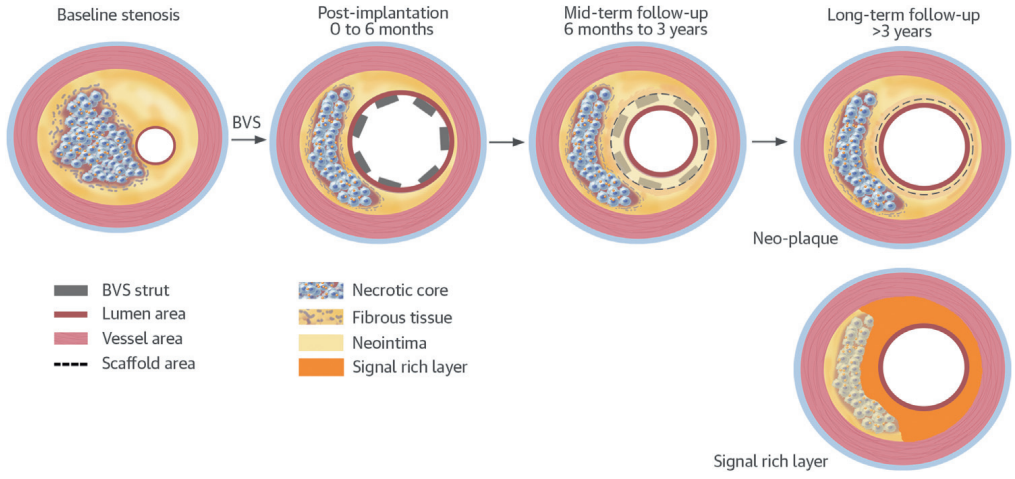

Karanasos, A. et al. J Am Coll Cardiol. 2014; 64(22):2343-56.

At long-term follow-up, bioresorbable vascular scaffolds (BVS) disappear, leaving behind late luminal enlargement, side-branch patency, and a signal-rich, low-attenuating tissue layer that covers the thrombogenic plaque components.

for an optimal acute mechanical result with optimal lesion coverage, while simultaneously raising questions regarding a possible responder/nonresponder reaction to BVS and the need for intensified secondary prevention in selected patients (22). As such, our findings might guide further research for optimizing the clinical efficacy of BVS in light of the 1.1 version modifications and herald observations in more complex populations (23).

STUDY LIMITATIONS. This is a small first-in-man study, so selection bias cannot be excluded, although the baseline clinical and angiographic characteristics were not different from the entire ABSORB A cohort. The BVS 1.0 assessed in our study differs in geometry and resorption rate from the currently used BVS 1.1, which might affect the temporal course and pattern of the healing response.

Attenuation analysis has only been validated in ex vivo specimens of native atherosclerosis and not in device-induced tissue responses. However, because attenuation is an optical property of tissue components, we expect the absence of high-attenuating regions to correspond to absence of necrotic core or macrophages in this setting.

Five-year OCT follow-up was performed with a nonocclusive frequency-domain system; previous OCT examinations were performed with an occlusive time-domain system. Frequency-domain OCT offers better image quality and higher dynamic range, which allows superior visualization of deeply located plaques (24). Because of these limitations of time-domain systems, serial assessment of plaque morphology was not performed systematically and was only examined with reference to possible neoatherosclerosis, although changes over time would be expected (19). Occlusive time-domain OCT slightly underestimates lumen area (25). Nevertheless, 4 patients in our study underwent additional nonocclusive OCT imaging at 2-year follow-up. When we compared nonocclusive data at 2 and 5 years, findings of late lumen enlargement were consistent, albeit not reaching significance because of the smaller sample size (minimum lumen area 3.54 ± 1.43 mm^2 at 2 years vs. 4.06 ± 1.33 mm^2 at 5 years; $p = 0.14$; mean lumen area 5.12 ± 1.62 mm^2 at 2 years vs. 5.95 ± 1.20 mm^2 at 5 years; $p = 0.07$).

CONCLUSIONS

At long-term follow-up 5 years after BVS implantation, we observed a favorable tissue response with late luminal enlargement, complete strut bioresorption, and development of a low-attenuating, signal-rich layer that covered the underlying potentially thrombogenic plaque components. The small scale of our study and the observation of a different tissue response in 1 patient warrant judicious interpretation of our results and further confirmation in larger studies.

ACKNOWLEDGMENTS The authors would like to thank Dr. George Sianos for his role in the ABSORB A trial, Prof. Johan Reiber and Joan Tuinenburg of ClinFact Core-Lab for the external validation of the 5-year measurements, and Prof. Guillermo Tearney for his expert review of neoplaque morphology.

REPRINT REQUESTS AND CORRESPONDENCE: Dr. Evelyn Regar, Erasmus University Medical Center, Department of Cardiology, Thoraxcenter, BA-585, Gravendijkwal 230, 3015 CE Rotterdam, the Netherlands. E-mail: e.regar@erasmusmc.nl.

PERSPECTIVES

COMPETENCY IN MEDICAL KNOWLEDGE: Strut resorption and vascular healing after bioresorbable vascular scaffold implantation are associated with late lumen enlargement, increased lumen symmetry, side-branch patency, and formation of a potentially protective tissue layer over the long term.

COMPETENCY IN PATIENT CARE: Occasional observations of unfavorable healing response after bioresorbable scaffold implantation suggest a need for both optimum lesion coverage and continued secondary prevention strategies after deployment of bioresorbable vascular scaffolds.

TRANSLATIONAL OUTLOOK: Additional long-term follow-up studies are needed to more completely characterize the patterns of biodegradation associated with favorable and unfavorable changes in plaque morphology and clinical outcomes after implantation of bioresorbable vascular scaffolds.

REFERENCES

1. Karanasos A, Ligthart J, Witberg K, et al. Association of neointimal morphology by optical coherence tomography with rupture of neoatherosclerotic plaque very late after coronary stent implantation. Proc. SPIE 8565, Photonic Therapeutics and Diagnostics IX, 856542 (March 8, 2013). http://dx.doi.org/10.1117/12.2006331.

2. Serruys PW, Ormiston JA, Onuma Y, et al. A bioabsorbable everolimus-eluting coronary stent system (ABSORB): 2-year outcomes and results from multiple imaging methods. Lancet 2009;373:897–910.

3. Onuma Y, Dudek D, Thuesen L, et al. Five-year clinical and functional multislice computed tomography angiographic results after coronary implantation of the fully resorbable polymeric everolimus-eluting scaffold in patients with de novo coronary artery disease: the ABSORB cohort A trial. J Am Coll Cardiol Intv 2013;6:999–1009.

4. Simsek C, Karanasos A, Magro M, et al. Long-term invasive follow-up of the everolimus-eluting bioresorbable vascular scaffold: five-year results

of multiple invasive imaging modalities. EuroIntervention 2014 Oct 28 [E-pub ahead of print].

5. Karanasos A, Simsek C, Serruys P, et al. Five-year optical coherence tomography follow-up of an everolimus-eluting bioresorbable vascular scaffold changing the paradigm of coronary stenting? Circulation 2012;126:e89–91.

6. Brugaletta S, Radu MD, Garcia-Garcia HM, et al. Circumferential evaluation of the neointima by optical coherence tomography after ABSORB bioresorbable vascular scaffold implantation: can the scaffold cap the plaque? Atherosclerosis 2012;221:106–12.

7. Tearney GJ, Regar E, Akasaka T, et al. consensus standards for acquisition, measurement, and reporting of intravascular optical coherence tomography studies: a report from the International Working Group for Intravascular Optical Coherence Tomography Standardization and Validation [published correction appears in J Am Coll Cardiol 2012;59:1662]. J Am Coll Cardiol 2012;59:1058–72.

8. Onuma Y, Serruys PW, Perkins LE, et al. Intracoronary optical coherence tomography and histology at 1 month and 2, 3, and 4 years after implantation of everolimus-eluting bioresorbable vascular scaffolds in a porcine coronary artery model: an attempt to decipher the human optical coherence tomography images in the ABSORB trial. Circulation 2010;122:2288–300.

9. van Soest G, Goderie T, Regar E, et al. Atherosclerotic tissue characterization in vivo by optical coherence tomography attenuation imaging. J Biomed Opt 2010;15:011105.

10. Ughi GJ, Adriaenssens T, Sinnaeve P, Desmet W, D'Hooge J. Automated tissue characterization of in vivo atherosclerotic plaques by intravascular optical coherence tomography images. Biomed Opt Express 2013;4:1014–30.

11. Gnanadesigan M, van Soest G, White S, et al. Effect of temperature and fixation on the optical properties of atherosclerotic tissue: a validation study of an ex-vivo whole heart cadaveric model. Biomed Opt Express 2014;5:1038–49.

12. Okamura T, Onuma Y, García-García HM, et al. 3-Dimensional optical coherence tomography assessment of jailed side branches by bioresorbable vascular scaffolds: a proposal for classification. J Am Coll Cardiol Intv 2010;3:836–44.

13. Karanasos A, Tu S, van Ditzhuijzen NS, et al. A novel method to assess coronary artery bifurcations by OCT: cut-plane analysis for side-branch ostial assessment from a main vessel pullback. Eur Heart J Cardiovasc Imaging 2014 Sep 16 [E-pub ahead of print].

14. Strandberg E, Zeltinger J, Schulz DG, Kaluza GL. Late positive remodeling and late lumen gain contribute to vascular restoration by a non-drug eluting bioresorbable scaffold: a four-year intravascular ultrasound study in normal porcine coronary arteries. Circulation Cardiovasc Interv 2012;5:39–46.

15. Serruys PW, Onuma Y, Garcia-Garcia HM, et al. Dynamics of vessel wall changes following the implantation of the absorb everolimus-eluting bioresorbable vascular scaffold: a multi-imaging modality study at 6, 12, 24 and 36 months. EuroIntervention 2014;9:1271–84.

16. von Birgelen C, Klinkhart W, Mintz GS, et al. Plaque distribution and vascular remodeling of ruptured and nonruptured coronary plaques in the same vessel: an intravascular ultrasound study in vivo. J Am Coll Cardiol 2001;37:1864–70.

17. Virmani R, Burke AP, Farb A, Kolodgie FD. Pathology of the vulnerable plaque. J Am Coll Cardiol 2006;47 Suppl:C13–8.

18. Wentzel JJ, Schuurbiers JC, Gonzalo Lopez N, et al. In vivo assessment of the relationship between shear stress and necrotic core in early and advanced coronary artery disease. EuroIntervention 2013;9:989–95.

19. Kubo T, Maehara A, Mintz GS, et al. The dynamic nature of coronary artery lesion morphology assessed by serial virtual histology intravascular ultrasound tissue characterization. J Am Coll Cardiol 2010;55:1590–7.

20. Ruzsa Z, van der Linden M, Van Mieghem NM, et al. Culotte stenting with bioabsorbable everolimus-eluting stents. Int J Cardiol 2013;168:e35–7.

21. van Mieghem NM, Wilschut J, Ligthart J, Witberg K, van Geuns RJ, Regar E. Modified T-technique with bioresorbable scaffolds ensures complete carina coverage: an optical coherence tomography study. J Am Coll Cardiol Intv 2014;7:e109–10.

22. Karanasos A, van Geuns RJ, Zijlstra F, Regar E. Very late bioresorbable scaffold thrombosis after discontinuation of dual antiplatelet therapy. Eur Heart J 2014;35:1781.

23. Diletti R, Karanasos A, Muramatsu T, et al. Everolimus-eluting bioresorbable vascular scaffolds for treatment of patients presenting with ST-segment elevation myocardial infarction: BVS STEMI first study. Eur Heart J 2014;35:777–86.

24. Manfrini O, Mont E, Leone O, et al. Sources of error and interpretation of plaque morphology by optical coherence tomography [published correction appears in Am J Cardiol 2007;99:1350]. Am J Cardiol 2006;98:156–9.

25. Gonzalo N, Serruys PW, García-García HM, et al. Quantitative ex vivo and in vivo comparison of lumen dimensions measured by optical coherence tomography and intravascular ultrasound in human coronary arteries. Rev Esp Cardiol 2009;62:615–24.

KEY WORDS percutaneous coronary intervention, plaque, stents

APPENDIX For supplemental material, please see the online version of this article.

SUPPLEMENTAL MATERIAL

Supplemental Methods

Patient population

The population of this study has been previously described[1]. Briefly, all living patients of the Thoraxcenter Rotterdam cohort of the ABSORB Cohort A study (n=14) were asked to participate, with the exclusion of patients with any of the following: hypersensitivity or contra-indication to treatment with heparin or contrast that could not be adequately pre-medicated, left ventricular ejection fraction<30%, renal insufficiency (serum creatinine >2.5 mg/dL or patient on dialysis), bleeding diathesis or coagulopathy and stroke within the past year. Eight patients gave final consent and were finally enrolled in the study. Invasive follow-up including OCT imaging was performed between March 8, and July 20, 2012.

Study device

The study device is a first-generation bioresorbable everolimus-eluting scaffold (BVS version 1.0; 3.0x12 mm; Abbott Vascular, Santa Clara, CA, USA), consisting of out-of-phase circumferential zig-zag poly-L-lactic acid struts (150 μm thickness) with a poly-D-L-lactic acid coating containing everolimus (98 $\mu g/cm^2$ of surface area).

OCT image acquisition

The ABSORB study included optional OCT imaging at baseline, six-months and two-years. Methodology of OCT image acquisition for these studies, using a first-generation OCT system (M2/M3®, Lightlab Imaging/St. Jude Medical, St. Paul, Minnesota, USA) with occlusive technique, has been previously described[2]. For the population of the current study, serial OCT pullbacks with good quality images were available for a total of 8 patients, specifically 6 patients at baseline, 7 patients at 6-month follow-up and 7 patients at 2-year up. All 8 subjects underwent second-generation OCT at the time of the 5-year invasive follow-up. OCT was performed with the C7XR® imaging console and the Dragonfly® intravascular imaging catheter (Lightlab Imaging/St. Jude Medical, St. Paul, Minnesota, USA), as previously described[3]. Briefly, after positioning the OCT catheter distally to the scaffold area, the catheter is pulled back automatically at 20mm/sec with simultaneous infusion by a power injector (flush rate 3-4 ml/s) of contrast (Iodixanol 370, Visipaque™, GE Health Care, Ireland) warmed at 37°C.

Luminal measurements and variability analysis

Lumen area and diameters for all time points were measured at ~200μm intervals in the region of interest, and mean and minimum cross-sectional areas were calculated. Lumen eccentricity was

calculated as the ratio (maximum lumen diameter – minimum lumen diameter)/maximum lumen diameter[3]. The analysis was performed with the proprietary LightLab/St. Jude software for off-line analysis. The z-offset was checked and corrected if necessary in all the pullbacks before any measurement. The lumen contour was obtained with an automated detection algorithm and additional manual corrections, if necessary.

Intra-observer variability was assessed by re-analysis of 5-year lumen area measurements by the same observer 3 weeks later. Inter-observer variability analysis was performed by re-analysis of 5-year lumen area measurements by 1) a second observer and 2) by an independent core-lab (Clinfact, Leiden, Netherlands) blinded to the study content. In all cases, analysis was performed with the same pre-defined region of interest. The second observer used the same offline analysis software as the first observer, with individual adjustment of the z-offset. Analysis by the core-lab was performed by offline software (QCU-CMS; LKEB, Leiden University, The Netherlands which is the research version of QIvus, Medis medical imaging systems bv, Leiden, The Netherlands) with automated contour detection and manual correction when necessary4. Inter-study variability was assessed by analysis of a second OCT pullback by the same observer, in 4 of the cases in which a second OCT pullback was available.

Variability was assessed on a frame-level and on a scaffold-level basis. In the frame-level analysis, area measurements from each frame in the region of interest were assessed for intra- and inter-observer variability. In the scaffold-level analysis, mean and minimal lumen area measurements were assessed for intra-, inter-observer and inter-study variability.

Intra- and inter-observer variability of signal-rich layer thickness measurements was assessed by re-analysis of representative images taken in 2mm intervals from all patients (total of 54 images) by the same observer at a later interval and a second observer, respectively.

Analysis of metal first-generation drug eluting stents (DES).

Although the ABSORB A study was a single-arm study, the implantation of metal sirolimus-eluting stents (SES) was allowed as a bail-out procedure. Thus, two patients had SES implanted at the index BVS implantation, both distally overlapping the BVS. Moreover, another patient had a paclitaxel-eluting stent implantation 7mm proximally to the scaffolded segment in the left circumflex artery, 106 days after BVS implantation. Metal stents were analysed on a frame-level basis, including volumetric measurements of stented segments and assessment of strut coverage and apposition. The presence of neoatherosclerosis and neointimal rupture was recorded, and in stents with neoatherosclerosis the lipid core arc and the minimum fibrous cap thickness were measured[5].

Supplemental References

1. Simsek C, Karanasos A, Magro M et al. Long-term Invasive Follow-Up of the Everolimus-Eluting Bioresorbable Vascular Scaffold: Five-year Results of Multiple Invasive Imaging Modalities. EuroIntervention 2014;in press

2. Serruys PW, Ormiston JA, Onuma Y et al. A bioabsorbable everolimus-eluting coronary stent system (ABSORB): 2-year outcomes and results from multiple imaging methods. The Lancet 2009;373:897-910.

3. Tearney GJ, Regar E, Akasaka T et al. Consensus Standards for Acquisition, Measurement, and Reporting of Intravascular Optical Coherence Tomography Studies: A Report From the International Working Group for Intravascular Optical Coherence Tomography Standardization and Validation. J Am Coll Cardiol 2012;59:1058-1072.

4. Okamura T, Gonzalo N, Gutiérrez-Chico JL et al. Reproducibility of coronary Fourier domain optical coherence tomography: quantitative analysis of in vivo stented coronary arteries using three different software packages. EuroIntervention 2010;6:371-379.

5. Karanasos A, Ligthart J, Witberg K et al. Association of neointimal morphology by optical coherence tomography with rupture of neoatherosclerotic plaque very late after coronary stent implantation. SPIE conference proceedings, 2013:856542-856542-13.

Supplemental Table 1. Assessment of metal drug-eluting stents at 5 years follow-up

	Patient 1	**Patient 4**	**Patient 8**
Type of stent	SES 3.0x13mm, distal overlap, implanted at baseline	PES 3.5x20mm, non-overlapping, implanted 106 days post BVS implantation	3 overlapping SES 3.0x13mm, distal overlap, implanted at baseline
Minimum luminal area (mm^2)	2.38	7.05	2.07
Mean luminal area (mm^2)	5.59	9.44	5.67
Minimum stent area (mm^2)	6.11	10.34	3.76
Mean stent area (mm^2)	7.16	12.89	7.13
Mean neointimal thickness (μm)	193	249	178
Uncovered/total struts n, (%)	1/627 (0.16)	25/920 (2.71)	5/1434 (0.34)
Incompletely apposed struts n, (%)	0/630 (0)	0/920 (0)	0/1434 (0)
Cross-sections with >30% uncovered struts/total n, (%)	0/59 (0)	0/103 (0)	0/146 (0)
Cross-sections with incompletely apposed struts/total n, (%)	0/59 (0)	0/103 (0)	0/ 146 (0)
Neoatherosclerosis	Yes	Yes	Yes
Neointimal rupture	No	Yes	No
Thrombus	No	Yes	No
Maximum necrotic core arc in neointima (°)	160	170	67
Minimum cap thickness in neoatherosclerosis (μm)	110	70	80

Abbreviations: SES=sirolimus-eluting stents, PES=paclitaxel eluting stents, BVS=bioresorbable scaffold

Supplemental Table 2. Variability analysis

Study-level inter- and intra-observer variability (n=8)										
	Observer 1 Measurement 1	**Observer 2**	**Difference (Observer 1 – Observer 2)**	**ICC**	**Core lab measurements**	**Difference (Observer 1 – Core lab)**	**ICC**	**Observer 1 Measurement 2**	**Difference (Measurement 1 – Measurement 2)**	**ICC**
Mean lumen area (mm^2)	6.39±1.18	6.16±1.29	0.23±0.29	0.98	6.26±1.15	0.13±0.32	0.98	6.22±1.32	0.17±0.19	0.99
Minimum lumen area (mm^2)	4.62±1.44	4.55±1.51	0.07±0.23	0.99	4.59±1.48	0.03±0.25	0.99	4.55±1.51	0.07±0.20	0.99

Inter-study variability (n=4)				
	Pullback 1	**Pullback 2**	**Difference (Pullback 1 – Pullback 2)**	**ICC**
Mean lumen area (mm^2)	6.93±1.18	6.74±1.42	0.20±0.32	0.98
Minimum lumen area (mm^2)	5.41±1.40	5.38±1.56	0.03±0.34	0.98

Frame-level inter- and intra-observer variability (n=468)										
	Observer 1 Measurement 1	**Observer 2**	**Difference (Observer 1 – Observer 2)**	**ICC**	**Core lab measurements**	**Difference (Observer 1 – Core lab)**	**ICC**	**Observer 1 Measurement 2**	**Difference (Measurement 1 – Measurement 2)**	**ICC**
Lumen area (mm^2)	6.23±2.19	6.00±2.18	0.23±0.62	0.95	6.14±2.07	0.08±0.54	0.97	6.06±2.26	0.16±0.30	0.99

Abbreviations: ICC=intraclass correlation coefficient

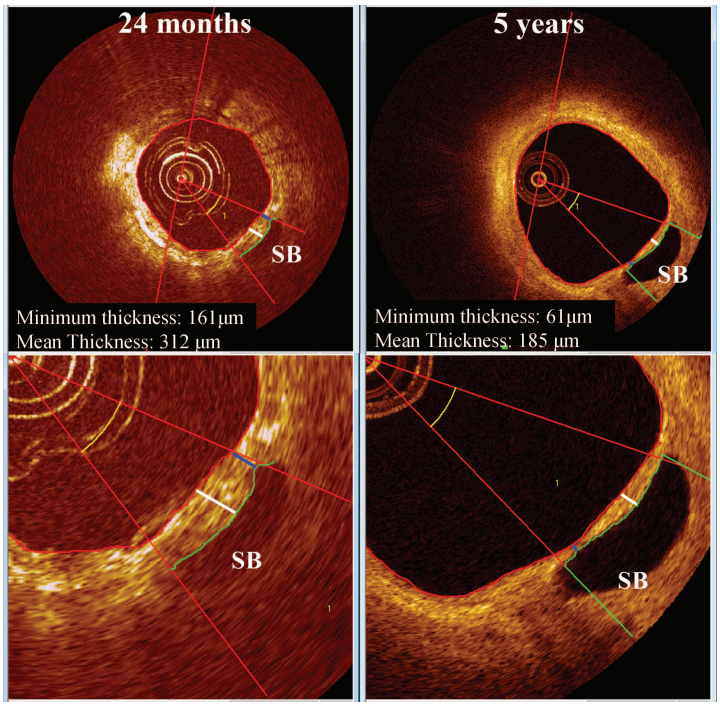

Supplementary Figure 1. Measurement of thickness of tissue bridges associated with side-branch ostia.

The tissue bridge is manually segmented at the adluminal (red line) and abluminal (green line) contour, and minimum and mean thickness are measured. Note the presence of scaffold struts at the 24-month follow-up. Blue line indicates minimum thickness and white line indicates maximum thickness. Annotations: SB=side-branch

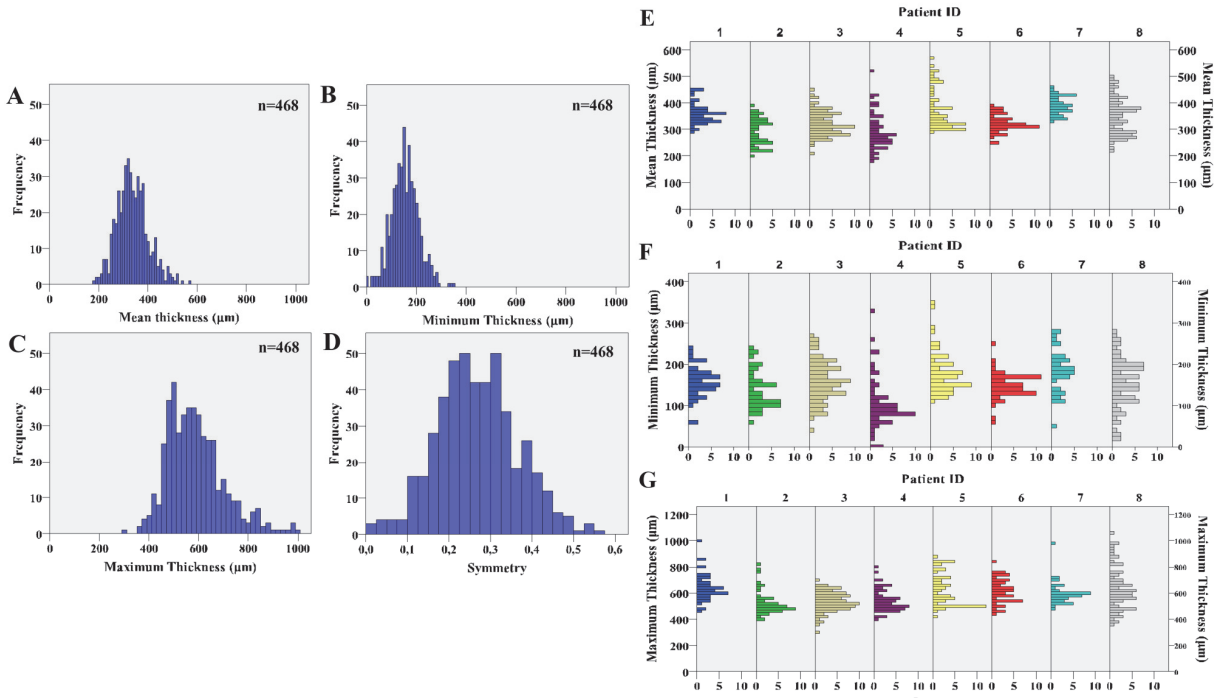

Supplementary Figure 2. Frequency distribution of signal-rich layer thickness.

Frequency distribution of (A) mean, (B) minimum, and (C) maximum signal-rich layer thickness, as well as (D) thickness symmetry in all analysed frames. Distributions of (E) mean, (F) minimum, and (G) maximum signal-rich layer thickness are also presented per individual patient.

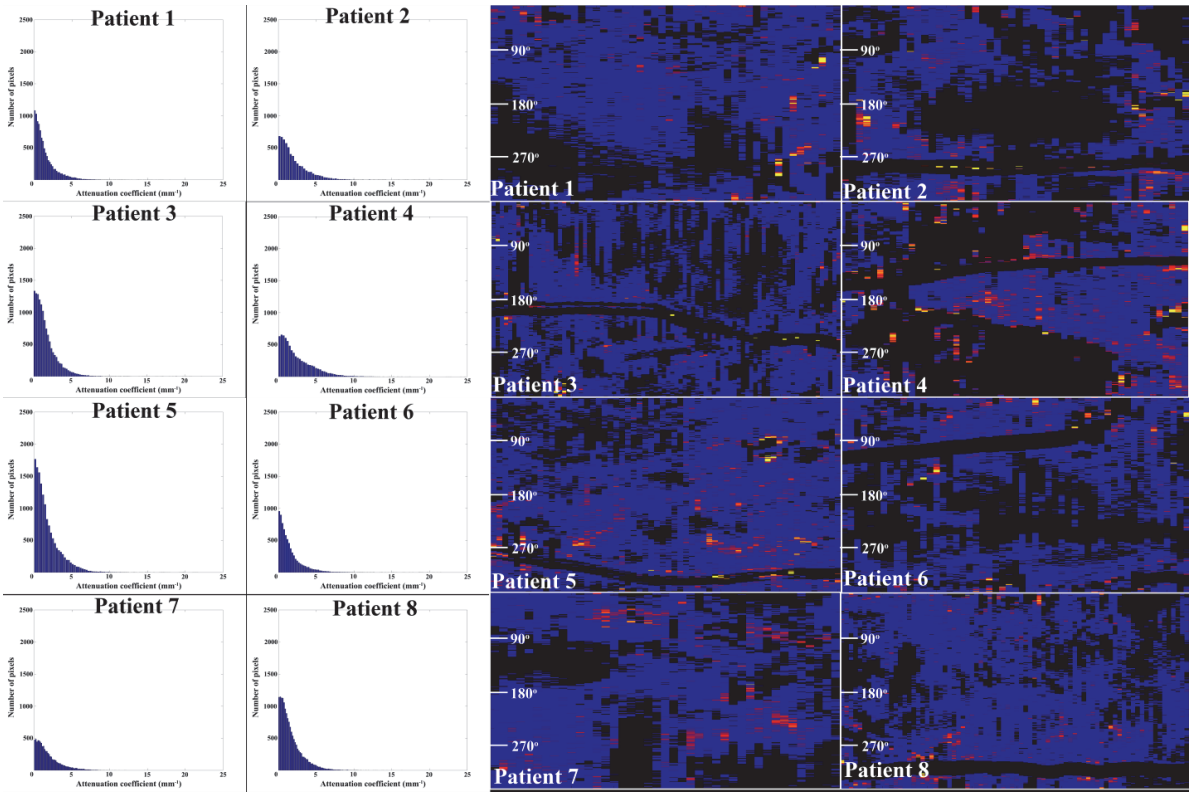

Supplementary Figure 3. Frequency distribution of attenuation coefficient and maximum attenuation maps at the signal-rich layer.

Left panels. Frequency distribution of all attenuation values in the signal-rich layer in all frames per patient. The attenuation values are low, with the 90th percentile ≤4mm^{-1}, with the exception of patient 4.

Right panels. Spread-out maps demonstrating the maximum attenuation per A-line in the signal-rich layer. There is mainly blue colour indicating low-attenuation regions. Note that in cases of signal-rich layer thickness <200μm, the region is displayed as black due to the lack of sufficient imaging window for the analysis

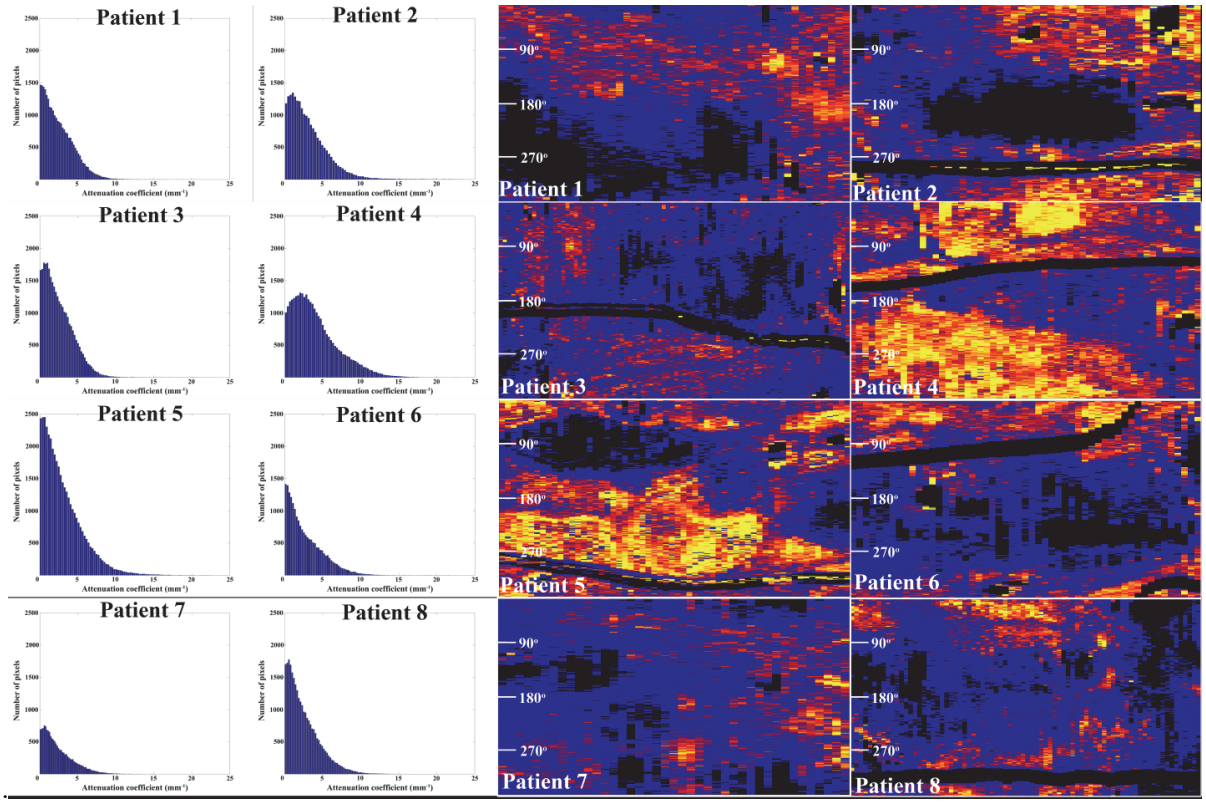

Supplementary Figure 4. Frequency distribution of attenuation coefficient and maximum attenuation maps in the 'neo-plaque' region.

Left panels. Frequency distribution of all attenuation values in the 'neo-plaque' region in all frames per patient. Attenuation values vary depending on plaque type. **Right panels**. Spread-out maps demonstrating the maximum attenuation per A-line in the 'neo-plaque' region. Regions with yellow or red colour indicate highly attenuating areas corresponding to plaque. Similarly to Supplementary Figure 3, 'neo-plaque' regions with intimal thickness <200μm are displayed as black.

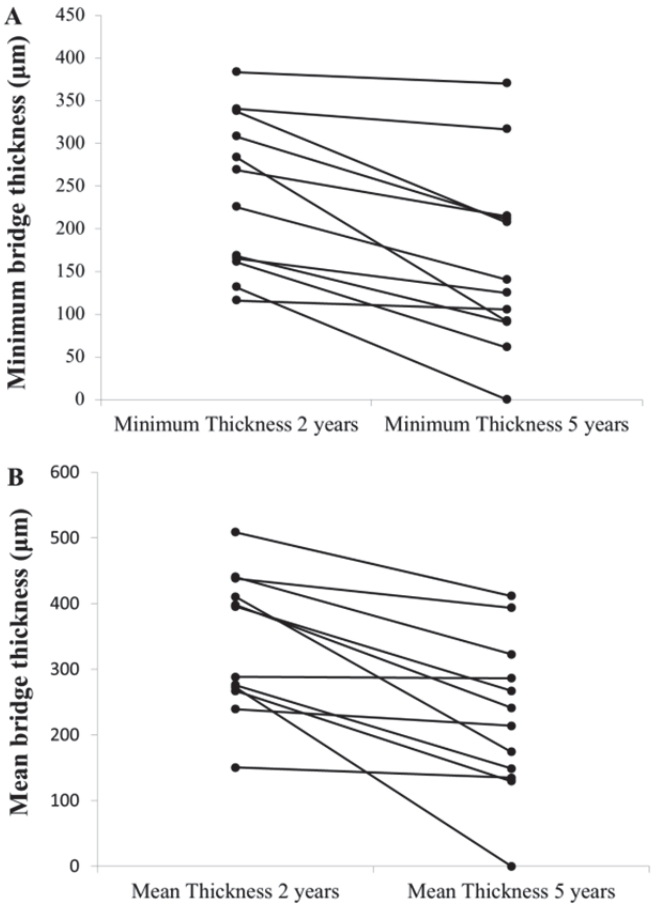

Supplementary Figure 5. Thickness of tissue bridges overlying side-branches at 2 years and 5 years.

There is a decrease of the (A) minimal and (B) mean thickness of tissue bridges associated with side-branches in almost all cases (Minimum: 241±92µm at 2 years versus 161±107µm at 5 years, p<0.001; mean: 341±106µm at 2 years versus 227±119µm at 5 years, p=0.001).

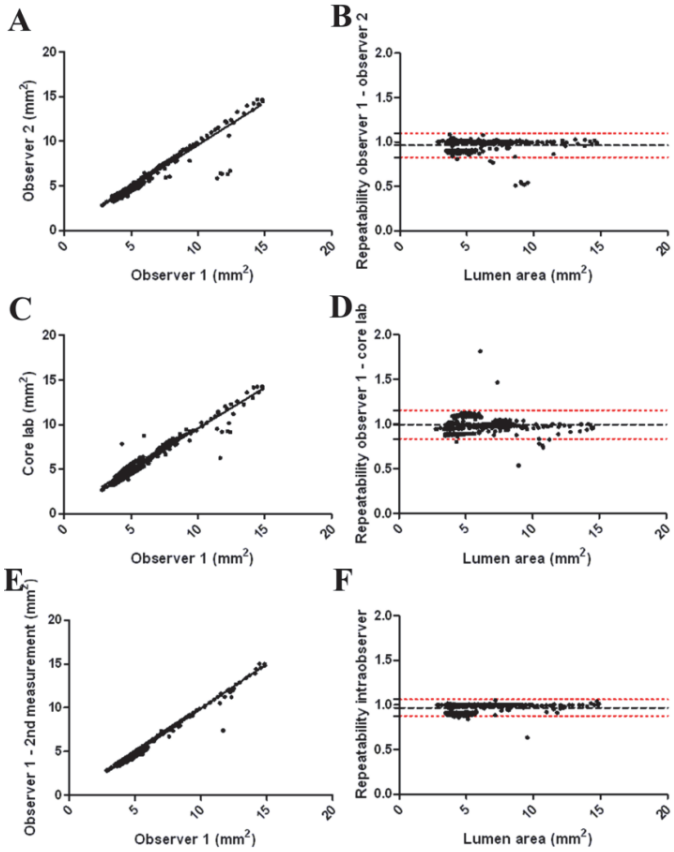

Supplementary Figure 6. Correlation and Bland-Altman plots for inter- and intra-observer variability in a frame-level analysis.

Correlation plots and Bland-Altman repeatability plots for (A, B) interobserver variability, (C, D) interobserver variability with core-lab measurements, and (E, F) intraobserver variability. Note the presence of outliers, corresponding to contour tracing discrepancies in regions of side-branch ostia. Black striped line corresponds to mean repeatability and red striped lines to 95% limits of agreement (mean ± 2standard deviations).

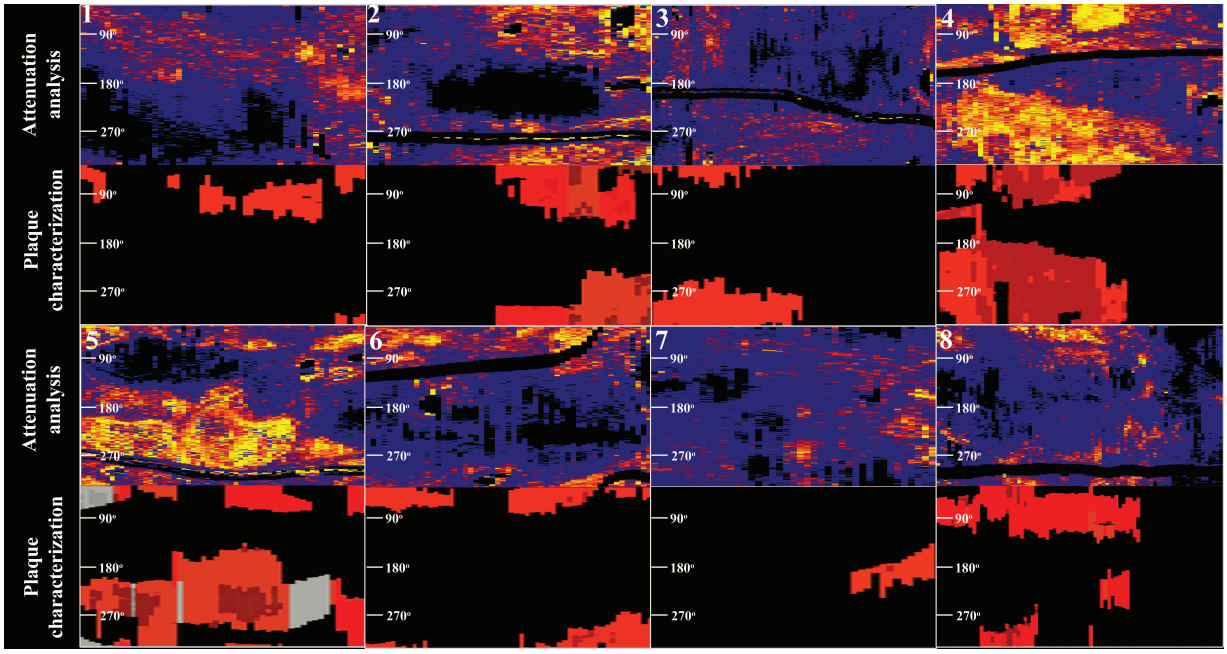

Supplementary Figure 7. Comparison of quantitative attenuation analysis with visual plaque characterization.

Spread-out maps generated by visual plaque characterization and maximum attenuation analysis of the entire plaque in all patients. Note the spatial correspondence of necrotic core sites with regions of high attenuation.

PART V

Impact of hemodynamic environment on vascular healing response of bioresorbable scaffolds

Chapter 5.1

Is it safe to implant bioresorbable scaffolds in ostial side-branch lesions? Impact of 'neo-carina' formation on main-branch flow pattern. Longitudinal clinical observations

Karanasos A*, Li Y,* Tu S, Wentzel JJ, Reiber JH, van Geuns RJ, Regar E

* indicates equal contribution

Atherosclerosis. 2014 Nov 18;238(1):22-25

Is it safe to implant bioresorbable scaffolds in ostial side-branch lesions? Impact of 'neo-carina' formation on main-branch flow pattern. Longitudinal clinical observations

Antonios Karanasos [a, 1], Yingguang Li [b, 1], Shengxian Tu [c, b, *], Jolanda J. Wentzel [d], Johan H.C. Reiber [b], Robert-Jan van Geuns [a], Evelyn Regar [a]

[a] *Department of Interventional Cardiology, Thoraxcenter, Erasmus University Medical Center, Rotterdam, Netherlands*
[b] *Division of Image Processing, Department of Radiology, Leiden University Medical Center, Leiden, Netherlands*
[c] *Biomedical Instrument Institute, School of Biomedical Engineering, Shanghai Jiao Tong University, Shanghai, PR China*
[d] *Department of Biomedical Engineering, Thoraxcenter, Erasmus University Medical Center, Rotterdam, Netherlands*

ARTICLE INFO

Article history:
Received 22 September 2014
Received in revised form
25 October 2014
Accepted 9 November 2014
Available online 18 November 2014

Keywords:
Optical coherence tomography
Bioresorbable vascular scaffold
Primary percutaneous coronary intervention
Computational fluid dynamics
Bifurcation intervention
Atherosclerosis progression

ABSTRACT

Formation of a 'neo-carina' has been reported after bioresorbable vascular scaffolds (BVS) implantation over side-branches. However, as this 'neo-carina' could protrude into the main-branch, its hemodynamic impact remains unknown. We present two cases of BVS implantation for ostial side-branch lesions, and investigate the flow patterns at follow-up and their potential impact. Computational fluid dynamics analysis was performed, using a 3D mesh created by fusion of 3-dimensional angiogram with optical coherence tomography images. In our first case, mild disturbances were seen when 'neo-carina' did not protrude perpendicularly into the main branch. In the second case, extensive flow re-distribution was observed due to a more pronounced protrusion of the 'neo-carina'. Importantly, these areas of hemodynamic disturbance were observed together with lumen narrowing in a non-stenotic vessel segment. Our case observations highlight the importance of investigating the hemodynamic consequences of BVS implantation in bifurcation lesions and illustrate a novel method to do so *in vivo*.

Bioresorbable vascular scaffolds (BVS) are a new treatment for coronary artery disease associated with a favorable long-term healing response with complete strut resorption and restoration of the vascular phenotype [1]. Despite a common misconception that BVS implantation over side-branches is associated with eventual disappearance of jailing struts, morphological changes of side-branch ostia have been reported, with tissue bridge formation resembling a 'neo-carina' [1–3]. 'Neo-carina' formation could be an appealing alternative to metal stents for bifurcation or ostial lesions [4], where non-apposed side-branch struts have been associated with incomplete healing and thrombosis [5,6]. However in ostial lesions, this 'neo-carina' may protrude into the main-branch, potentially influencing the local hemodynamic environment, and especially the main branch flow pattern. We present two cases of BVS implantation for ostial side-branch lesions, and investigate the patterns of flow distribution at follow-up and their potential implications.

For all patients and follow-ups, a 3-dimensional angiogram was created from two angiographic projections using QAngioXA 3D RE (Medis Specials bv, Leiden, Netherlands). In the first patient, selected planes for the 3D angiogram were (1 LAO, 32 Cranial) and (32 LAO, 29 Cranial), and in the second patient (35 RAO, 37 Cranial) and (54 LAO, 26 Cranial). Angle measurement was performed in both cases in the reconstructed 3D angiograms. Computational fluid dynamics (CFD) analysis was subsequently performed, using a 3D mesh created by fusion of the 3-dimensional angiogram with the OCT images [7]. For the CFD simulations, blood was modeled as incompressible Newtonian fluid. The volumetric flow, derived from TIMI frame count and 3D quantitative coronary angiography, was used as the boundary condition at the inlet, while outflow (fully-developed flow) condition was applied at the outlets [8]. Both

* Corresponding author. Room123, Med-X Research Institute, 3 Teaching Building, Shanghai Jiao Tong University, No. 1954, Hua Shan Road, Shanghai 200030, PR China.
E-mail address: sxtu@sjtu.edu.cn (S. Tu).
[1] These authors contributed equally to this work.

subjects have provided informed consent, and the study complies with the declaration of Helsinki.

1. Narrow bifurcation angle

A 73-year old gentleman presenting with acute myocardial infarction received a 2.5 mm × 18 mm BVS at the ostium of a diagonal branch (Fig. 1). OCT showed mild protrusion of the proximal scaffold into the LAD, in the presence of a narrow LAD-diagonal bifurcation angle (31°). CFD analysis performed without taking the protruding struts into consideration showed an evenly distributed flow profile in the mid LAD, with the average flow velocity in the mid LAD being slightly higher than in the diagonal branch. Follow-up OCT was performed 9 months later in the context of a research protocol, while the patient was asymptomatic. OCT showed a good overall healing response and tissue coverage of the protruding struts, leading to formation of a 'neo-carina'. CFD analysis was performed using the 9-month 3D-angiography and OCT fusion model, demonstrating a slightly changed mid LAD flow profile compared to baseline, indicating a modest influence of the 'neo-carina'. Changes included mild flow acceleration near the center of the lumen and mild deceleration at the region of the vessel wall located at the back-side of the 'neo-carina', co-localizing with areas of low wall shear stress.

2. Wide bifurcation angle

A 52 year-old gentleman with acute myocardial infarction received a 2.5 mm × 18 mm BVS at the ostium of the second diagonal branch (Fig. 2). The bifurcation angle (60°) was wider than in the previous case. OCT imaging post-implantation showed, also in this case, an extensive and perpendicular protrusion of the proximal scaffold segment into the LAD. CFD performed in the 3D mesh created by fusion of 3D-angiography and OCT without taking protruding struts into consideration demonstrated even distribution of flow velocities in the two branches. Follow-up OCT was performed 1 year later for a research protocol, while the patient remained asymptomatic. OCT demonstrated extensive tissue coverage of these protruding struts, creating the morphological appearance of a 'neo-carina'. CFD analysis performed using the 12-month fusion model showed a significantly altered flow profile of the mid LAD. Specifically, high flow acceleration was observed opposite to the side-branch ostium [in a relatively narrowed lumen (lumen area: 6.54 mm^2) due to the protrusion of the 'neo-carina' into the main vessel], whereas regions of slow flow velocities and re-circulation were observed at the back-side of the 'neo-carina' and associated with an extensive region of low shear stress at the corresponding wall segments. Importantly, this altered hemodynamic profile was observed in conjunction with lesion progression, consisting of lumen narrowing at the LAD segment distally to the bifurcation.

Contrary to the common misconception that BVS are ideal for bifurcations as they "eventually disappear", 'neo-carina' formation has been described in follow-up of BVS overlying side-branches, as a consequence of tissue coverage and gradual polymer bioresorption [1,2]. At initial stages this 'neo-carina' is comprised by struts covered by tissue in front of the side-branch ostium, whereas at later stages, after complete strut resorption, the 'neo-carina' consists of thin tissue bridges, with signal-rich appearance by OCT [1]. Formation of such 'neo-carinas' has been regarded as potentially favorable, compared to the permanent side-branch jailing from metal stents, considering that the latter has been associated with delayed healing and risk for thrombosis [6]. Nevertheless, the physiological significance of these 'neo-carinas' has not been investigated so far.

Our cases demonstrate for the first time, that 'neo-carina' development after ostial BVS implantation could have adverse hemodynamic consequences by acting as flow dividers that alter the hemodynamics of the main vessel downstream to the bifurcation. Such changes can range widely depending on the extent of protrusion in the main-branch, which is subject to several factors, including bifurcation angle, side-branch diameter, and length of scaffold protrusion. In our cases, both the side-branch diameter and the length of scaffold protrusion were similar (distal reference diameter by 3D-QCA: 3.04 mm and 3.06 mm, respectively; length of protrusion by 2D-OCT: 2.4 mm in both cases), with the bifurcation angle being the main factor differing significantly between cases. In our first case, mild disturbances were seen when 'neo-carina' did not protrude perpendicularly into the main branch, due to a narrow bifurcation angle. In the second case, extensive flow redistribution regions were observed because of the more perpendicular protrusion of the 'neo-carina' as a consequence of a wider bifurcation angle. Of note, these areas of hemodynamic disturbance were observed together with lumen narrowing in a non-stenotic vessel segment, providing pilot observations of a potential impact of device-induced hemodynamic changes on atherosclerosis progression. This observation is in accordance with prospective studies

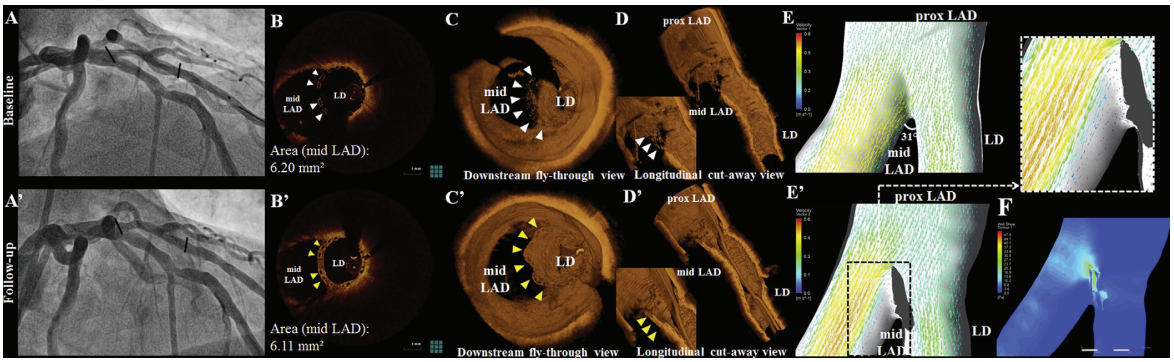

Fig. 1. A–E. (A) Angiogram, (B) 2D-OCT, (C–D) 3D-OCT images, and (E) computational fluid dynamics (CFD) analysis post-implantation. After ostial scaffold implantation at the diagonal branch (LD), scaffold protrusion into the main vessel is observed in cross-sectional and 3D images (white arrowheads), while CFD demonstrates symmetrical flow distribution in the mid left anterior descending artery (LAD). A′–E′. (A′) Angiogram, (B′) 2D-OCT, (C′–D′) 3D-OCT images, and (E′) CFD analysis at 9-month follow-up. (yellow arrowheads). CFD shows a mild increase of flow velocity in mid LAD opposite to the 'neo-carina', with regions of flow deceleration at the backside of the 'neo-carina' (gray area). F. Shear stress profile at 9-month follow-up. (For interpretation of the references to color in this figure legend, the reader is referred to the web version of this article.)

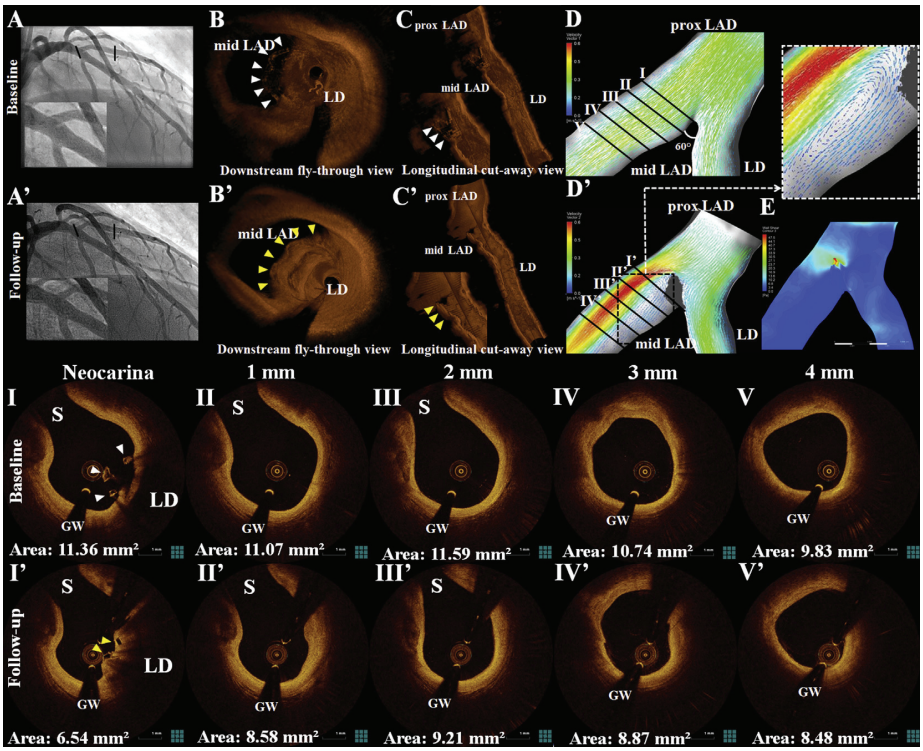

Fig. 2. A–D. (A) Angiogram, (B–C) 3D-OCT images, and (D) computational fluid dynamics (CFD) analysis post-implantation. After ostial scaffold implantation at the diagonal branch (LD), perpendicular scaffold protrusion into the main vessel is observed in the 3D images (white arrowheads), while the CFD analysis demonstrates the symmetrical distribution of flow downstream of the bifurcation. A′–D′. (A′) Angiogram, (B′–C′) 3D-OCT images, and (D′) CFD analysis at 12-month follow-up. Tissue growth over protruding struts has resulted in 'neo-carina' formation (yellow arrowheads). CFD shows substantial flow acceleration opposite to the side-branch ostium in mid LAD, due to the perpendicular 'neo-carina' protrusion (gray area). Conversely, at the backside of the 'neo-carina' there are extensive areas of slow flow and re-circulation. F. Shear stress profile at 12-month follow-up I–V′. Matched 2-dimensional OCT images from a mid-LAD segment downstream to the bifurcation (see D–D′) (I–V) post-implantation and (I′–V′) at 12-month follow-up showing luminal narrowing over time. S = septal, LD = diagonal, GW = guidewire, white arrowheads = protruding struts at baseline, yellow arrowheads = protruding struts at follow-up. (For interpretation of the references to color in this figure legend, the reader is referred to the web version of this article.)

showing the important role of hemodynamic parameters such as low and oscillatory shear stress in lesion progression [9–11].

3. Limitations

Although, our cases suggest the possible contribution of bifurcation angle in determining the extent of 'neo-carina' protrusion into the main branch, larger studies are needed for identifying the exact predictors of excessive protrusion. As our study aimed to investigate the hemodynamic consequences after 'neo-carina' formation, CFD at baseline was performed without considering the protruding struts, in an attempt to demonstrate differences between 'optimal' flow conditions in the absence of any protrusion and actual flow conditions in the presence of the 'neo-carina'. A meticulous modeling incorporating the impact of protruding struts on flow could provide further insight into the mechanisms of 'neo-carina' formation, as hemodynamic factors have been associated with BVS coverage [12]. In any case, the observed follow-up flow patterns are not affected by this amendment in the baseline analysis.

Overall, our case observations highlight the clinical importance of investigating the hemodynamic consequences of BVS implantation in bifurcation lesions and illustrate a novel method to do so *in vivo*. Insights gained from such studies could have a significant impact on treatment strategy selection in bifurcation lesions.

Funding sources

Antonios Karanasos would like to acknowledge the funding support of the Hellenic Heart Foundation and St Jude Medical. Shengxian Tu would like to acknowledge the funding support of the Natural Science Foundation of China under Grant 61271155.

Disclosures

Y Li is employed by Medis Specials bv and has a research appointment at the Leiden University Medical Center (LUMC). S Tu was employed by Medis Specials bv until June 2014. JHC Reiber is the CEO of Medis Specials bv, and has a part-time appointment at Leiden University Medical Center as Professor of Medical Imaging.

References

[1] A. Karanasos, C. Simsek, M. Gnanadesigan, N.S. van Ditzhuijzen, R. Freire, J. Dijkstra, S. Tu, N.M. Van Mieghem, G. van Soest, P. De Jaegere, P.W. Serruys, F. Zijlstra, R.J. Van Geuns, E. Regar, Optical coherence tomography assessment of the long-term vascular healing response 5 years after first-in-man implantation of the everolimus-eluting bioresorbable vascular scaffold, J. Am. Coll. Cardiol. 64 (2014) 2343–2356.

[2] T. Okamura, Y. Onuma, H.M. Garcia-Garcia, E. Regar, J.J. Wykrzykowska, J. Koolen, L. Thuesen, S. Windecker, R. Whitbourn, D.R. McClean, J.A. Ormiston, P.W. Serruys, 3-dimensional optical coherence tomography assessment of

jailed side branches by bioresorbable vascular scaffolds: a proposal for classification, JACC Cardiovasc. Interventions 3 (2010) 836–844.
[3] T. Okamura, P.W. Serruys, E. Regar, Cardiovascular flashlight. The fate of bioresorbable struts located at a side branch ostium: serial three-dimensional optical coherence tomography assessment, Eur. Heart J. 31 (2010) 2179.
[4] V. Dzavik, A. Colombo, The absorb bioresorbable vascular scaffold in coronary bifurcations: insights from bench testing, JACC Cardiovasc. Interventions 7 (2014) 81–88.
[5] A. Farb, A.P. Burke, F.D. Kolodgie, R. Virmani, Pathological mechanisms of fatal late coronary stent thrombosis in humans, Circulation 108 (2003) 1701–1706.
[6] J.L. Gutierrez-Chico, E. Regar, E. Nuesch, T. Okamura, J. Wykrzykowska, C. di Mario, S. Windecker, G.A. van Es, P. Gobbens, P. Juni, P.W. Serruys, Delayed coverage in malapposed and side-branch struts with respect to well-apposed struts in drug-eluting stents: in vivo assessment with optical coherence tomography, Circulation 124 (2011) 612–623.
[7] S. Tu, S.A. Pyxaras, Y. Li, E. Barbato, J.H. Reiber, W. Wijns, In vivo flow simulation at coronary bifurcation reconstructed by fusion of 3-dimensional X-ray angiography and optical coherence tomography, Circ. Cardiovasc. Interventions 6 (2013) e15–17.
[8] S. Tu, E. Barbato, Z. Koszegi, J. Yang, Z. Sun, N.R. Holm, B. Tar, Y. Li, D. Rusinaru, W. Wijns, J.H. Reiber, Fractional flow reserve calculation from 3-dimensional quantitative coronary angiography and TIMI frame count: a fast computer model to quantify the functional significance of moderately obstructed coronary arteries, JACC Cardiovasc. Interventions 7 (2014) 768–777.
[9] P.H. Stone, S. Saito, S. Takahashi, Y. Makita, S. Nakamura, T. Kawasaki, A. Takahashi, T. Katsuki, A. Namiki, A. Hirohata, T. Matsumura, S. Yamazaki, H. Yokoi, S. Tanaka, S. Otsuji, F. Yoshimachi, J. Honye, D. Harwood, M. Reitman, A.U. Coskun, M.I. Papafaklis, C.L. Feldman, Prediction of progression of coronary artery disease and clinical outcomes using vascular profiling of endothelial shear stress and arterial plaque characteristics: the PREDICTION Study, Circulation 126 (2012) 172–181.
[10] Y.S. Chatzizisis, A.U. Coskun, M. Jonas, E.R. Edelman, C.L. Feldman, P.H. Stone, Role of endothelial shear stress in the natural history of coronary atherosclerosis and vascular remodeling: molecular, cellular, and vascular behavior, J. Am. Coll. Cardiol. 49 (2007) 2379–2393.
[11] J.J. Wentzel, Y.S. Chatzizisis, F.J. Gijsen, G.D. Giannoglou, C.L. Feldman, P.H. Stone, Endothelial shear stress in the evolution of coronary atherosclerotic plaque and vascular remodelling: current understanding and remaining questions, Cardiovasc. Res. 96 (2012) 234–243.
[12] C.V. Bourantas, M.I. Papafaklis, A. Kotsia, V. Farooq, T. Muramatsu, J. Gomez-Lara, Y.J. Zhang, J. Iqbal, F.G. Kalatzis, K.K. Naka, D.I. Fotiadis, C. Dorange, J. Wang, R. Rapoza, H.M. Garcia-Garcia, Y. Onuma, L.K. Michalis, P.W. Serruys, Effect of the endothelial shear stress patterns on neointimal proliferation following drug-eluting bioresorbable vascular scaffold implantation: an optical coherence tomography study, JACC Cardiovasc. Interventions 7 (2014) 315–324.

Chapter 5.2

Association of wall shear stress with long-term vascular healing response following bioresorbable vascular scaffold implantation

Karanasos A, Schuurbiers JCH, Garcia-Garcia HM, Simsek C, Zijlstra F, van Geuns RJ, Regar E, Wentzel JJ

Int J Cardiol. 2015 Jul 15;191:279-83

Letter to the Editor

Association of wall shear stress with long-term vascular healing response following bioresorbable vascular scaffold implantation

Antonios Karanasos [a], Johan C.H. Schuurbiers [b], Hector M. Garcia-Garcia [a], Cihan Simsek [a], Yoshinobu Onuma [a], Patrick W. Serruys [a], Felix Zijlstra [a], Robert-Jan van Geuns [a], Evelyn Regar [a,*], Jolanda J. Wentzel [b]

[a] Department of Interventional Cardiology, Erasmus MC, Rotterdam, The Netherlands
[b] Department of Biomedical Engineering, Erasmus MC, Rotterdam, The Netherlands

ARTICLE INFO

Article history:
Received 12 February 2015
Received in revised form 27 April 2015
Accepted 30 April 2015
Available online 1 May 2015

Keywords:
Bioresorbable vascular scaffold
Optical coherence tomography
Intravascular ultrasound
Coronary hemodynamics

Bioresorbable vascular scaffolds (BVS) could potentially overcome pitfalls of metal stents, such as late failure and neoatherosclerosis [1]. At the long-term follow-up of the everolimus-eluting BVS (Absorb BVS 1.0; Abbott Vascular, Santa Clara, CA), complete strut bioresorption accompanied by late luminal enlargement and development of a signal-rich layer covering underlying thrombogenic plaque components were observed by optical coherence tomography (OCT) 5 years after implantation [1,2]. The vascular architecture after bioresorption resembled a native non-obstructive atherosclerotic plaque with varying morphology among subjects [1]. Regional hemodynamic factors have been implicated in the pathogenesis of atherosclerosis [3], and plaque progression and destabilization [4]. However, data regarding the association of wall shear stress (WSS) with vascular healing after BVS implantation are limited [5]. We explored the association between WSS 2 years after BVS implantation and the 5-year scaffolded segment morphology.

The study population has been reported in detail [2]. Briefly, 8/14 living patients of the Thoraxcenter Rotterdam cohort of ABSORB study Cohort A consented and underwent invasive 5-year follow-up including greyscale intravascular ultrasound (IVUS), virtual histology (IVUS-VH) and optical coherence tomography (OCT) imaging. The protocol was approved by the local ethics committee and conforms to the declaration of Helsinki. The wall shear stress (WSS) 2 years post implantation was calculated by fusion of multi-slice computed tomography (MSCT) and IVUS, as previously described [6]. In specific, MSCT studies were mandated in all patients at 18 months post-BVS implantation as per ABSORB A study protocol [7]. Invasive imaging follow-up had been performed at 24 months in the context of ABSORB A study, and ECG-gated IVUS pullbacks were available for 7/8 patients. Fusion of the 3D vessel centerline derived from the 18-month MSCT study with lumen information derived from the 24-month IVUS studies was performed, in order to create a three-dimensional reconstruction of the scaffolded segment (Fig. 1). Computational fluid dynamics (CFD) calculations were performed based on these reconstructions and WSS was calculated. WSS values were then evaluated with relation to plaque morphology by OCT and IVUS-VH, and morphometric vessel measurements by OCT and greyscale IVUS on two levels: a) segment level and b) plaque level.

IVUS and IVUS-VH assessment of the scaffolded vessel segments were performed at 2-year and 5-year follow-up with phased-array intravascular ultrasound catheters (EagleEye; Volcano Corporation, Rancho Cordova, CA) with automated pullback at 0.5 mm/s. The lumen and external elastic membrane (EEM) contours were semi-automatically delineated within the scaffolded segment in ECG-gated cross-sectional IVUS images by offline software [8]. Greyscale IVUS analysis included analysis of lumen, plaque, and vessel area. Offline IVUS-VH analysis included measurement of the area of four discrete plaque compositions i.e. fibrous tissue, fibro-fatty, necrotic core and dense calcium in each cross-section [2,7].

Eight patients underwent second-generation OCT with the C7XR® imaging console and the Dragonfly® catheter (Lightlab Imaging/St. Jude Medical, St. Paul, MN) at the 5-year invasive follow-up, as previously described [1,2]. OCT image analysis at 5 years has been described in detail [1]. Measurements included difference in mean lumen area and eccentricity—defined as the ratio [(maximum lumen diameter − minimum lumen diameter)/maximum lumen diameter]—from 2 years to 5 years, mean and maximum necrotic core arc, and minimum and average fibrous cap thickness.

For the fusion of MSCT and IVUS images [6], IVUS images were analyzed using a semi-automatic segmentation program (QCU-CMS, Medis medical imaging bv, Leiden, Netherlands) to obtain the lumen

Abbreviations: BVS, bioresorbable vascular scaffold; OCT, optical coherence tomography; WSS, wall shear stress; MSCT, multi-slice computed tomography; IVUS, intravascular ultrasound; CFD, computational fluid dynamics; IVUS-VH, virtual histology.

* Corresponding author at: Department of Cardiology, Thoraxcenter, BA-585, Erasmus MC's, Gravendijkwal 230, 3015CE Rotterdam, The Netherlands.
E-mail address: e.regar@erasmusmc.nl (E. Regar).

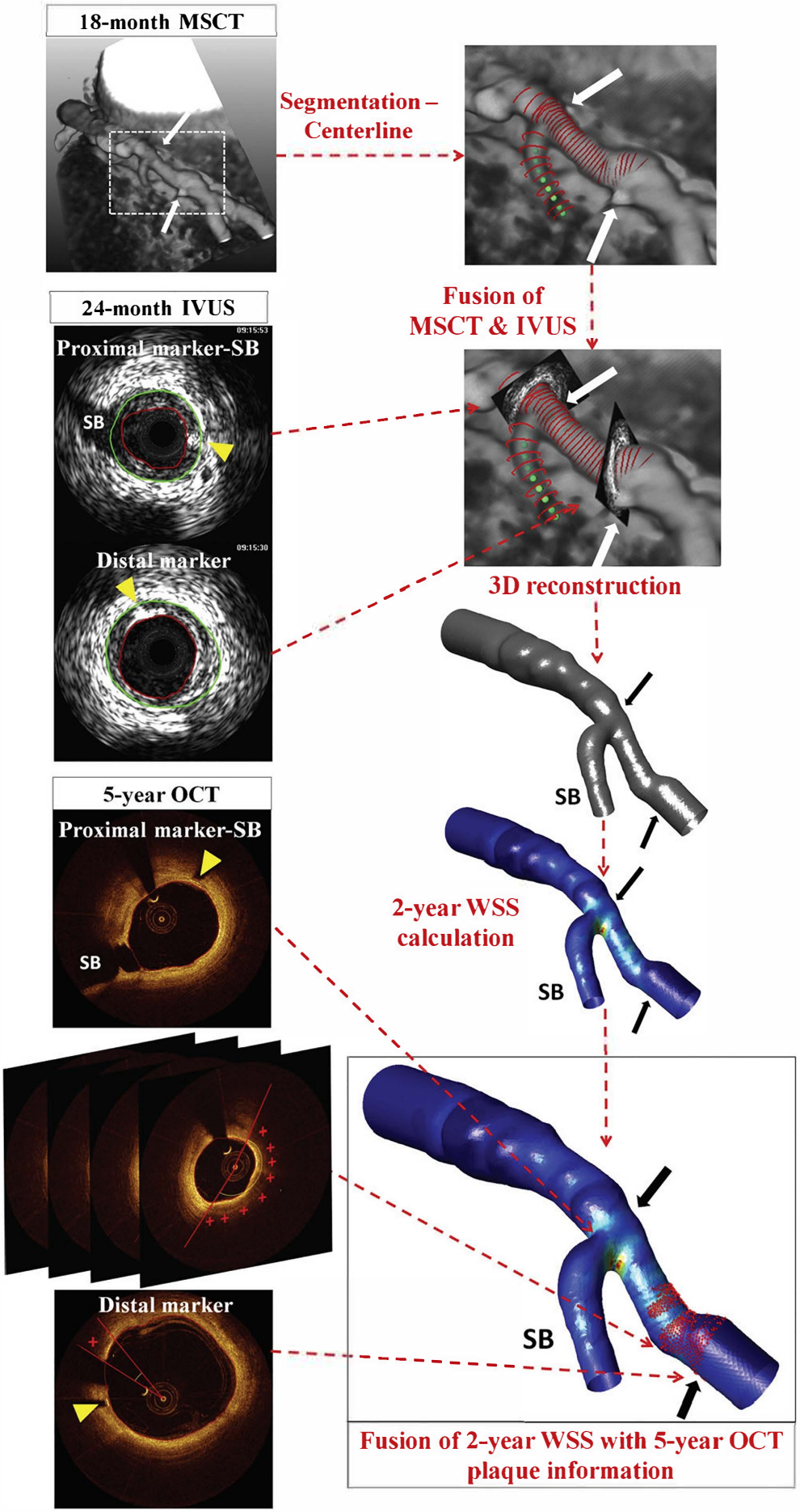
18-month MSCT
Segmentation – Centerline
24-month IVUS
Proximal marker-SB
SB
Distal marker
Fusion of MSCT & IVUS
3D reconstruction
SB
2-year WSS calculation
SB
5-year OCT
Proximal marker-SB
SB
Distal marker
SB
Fusion of 2-year WSS with 5-year OCT plaque information

and media-adventitia contours. The IVUS contours were positioned on the MSCT-extracted 3D centerline. Anatomic (side-branches, calcifications) and device-specific (scaffold markers) landmarks were used to register the IVUS contours to the MSCT data. In cases where the scaffolded segment was located near a side-branch which could influence the shear stress distribution, these branches were included and obtained by MSCT segmentation. The resulting 3D lumen contours were reconstructed for WSS calculation (Fig. 1).

The max inflow velocity (stationary flow) used to prescribe a parabolic inflow profile was based on a mean WSS of 1.2 Pa [9]. In cases of bifurcations, flow split was based on empirical flow distribution patterns, as described by van der Giessen et al. [9]. The geometry was assumed to have a rigid surface and no slip boundary conditions and a stress-free parabolic outflow were prescribed. Blood was modeled as an incompressible non-Newtonian fluid and a shear rate-dependent viscosity model was applied. CFD computations using standard numerical techniques to determine shear stress distribution were performed with Fidap 8.7.4 (Ansys Inc., PN, USA).

Segment-level analysis evaluated whether differences in mean WSS between two equal segments of the scaffold would translate to differences in vascular morphology or vessel morphometry between these two segments. The scaffolded region was divided in two equal segments (proximal and distal segment). The relative differences in WSS were calculated as the percent difference of WSS in the distal versus the proximal segment divided by the average WSS of the entire scaffolded segment. All the variables derived by the OCT, IVUS and IVUS-VH analysis were assessed separately for the distal and the proximal segment and differences were calculated. Subsequently, the correlation of relative WSS differences with differences in plaque characteristics and vessel dimensions was assessed.

Plaque-level analysis examined whether there were differences is WSS values in regions within the scaffold with and without necrotic core by OCT at 5 years. The lumen and plaque contours at areas of necrotic core or mixed plaque within the scaffolded segment were segmented in the OCT images with the QCU-CMS software and exported for co-registration with the 3D IVUS-derived reconstruction. Co-registration of these OCT-derived contours images was performed using the same landmarks used for IVUS-MSCT fusion, in order to assess the spatial correspondence of WSS patterns with OCT morphology (Fig. 1). Thereby, WSS differences in regions with necrotic core by OCT versus regions without necrotic core were assessed. Additionally, spread-out maps were generated for the visual assessment of this spatial correspondence.

Continuous variables are presented as mean ± SD and nominal variables as n (%). The Kolmogorov–Smirnov test assessed normality of distribution. Within-patient differences were assessed with paired *t*-test or Wilcoxon test, as appropriate. The correlations of relative WSS differences with differences in OCT morphometric and morphologic measurements were assessed with linear regression. Statistical analysis was performed with SPSS 20 (SPSS inc., Chicago, Illinois, USA).

Seven 3D reconstructions were generated by fusion of MSCT and IVUS images, in which CFD was successfully performed. For the segment-level analysis, changes in vessel morphometry by OCT and IVUS, and plaque morphology by OCT and IVUS-VH were assessed separately for distal and proximal segments (Supplemental Table 1). Within a scaffold, relative WSS differences in distal versus proximal segments were positively correlated to differences in minimum cap thickness ($r^2 = 0.76$, $p = 0.03$) (Fig. 2A), with a trend for negative correlation with differences in maximum necrotic core arc by OCT ($r^2 = 0.51$; $p = 0.07$). There was no correlation between WSS and changes in lumen, vessel, or plaque area from 2 to 5 years (Table 1, Supplemental Table 2). Change of IVUS-VH dense calcium area from 2 to 5 years was the only IVUS-VH variable showing a positive correlation with relative WSS differences ($r^2 = 0.73$; $p = 0.03$). For the plaque-level analysis, seven spread-out WSS maps co-registered with plaque maps were created and are presented in Fig. 2B. WSS values were numerically lower in regions with OCT necrotic core versus regions without OCT necrotic core, albeit not reaching significance (1.49 ± 1.27 Pa versus 1.83 ± 1.72 Pa; $p = 0.21$).

We present the association of WSS with the long-term vascular healing response in a small first-in-man cohort of BVS-treated patients. Our study findings suggest an impact of WSS on the long-term morphology, with a positive correlation of WSS at 2 years with minimum cap thickness of the scaffolded segment at 5 years. As the long-term BVS healing response results in a favorable morphological phenotype resembling native atherosclerosis [1], we hypothesized a potential role of WSS in configuration of vascular morphology in the scaffolded segment. Indeed, within the same scaffold, the segment with lower 2-year WSS had thinner fibrous cap at 5 years, with the magnitude of the difference correlated with the relative difference in WSS. Flow-dependent increased matrix-degrading enzyme expression could be a potential mechanism [10], as the recovery of vasomotion in the scaffolded segment [2] implies the presence of functioning endothelium, able to respond to hemodynamic stimuli, as in native atherosclerosis [3,4]. Decrease in VH calcium, an indirect marker of bioresorption, was more pronounced in segments with lower WSS, a finding that considering the complete strut resorption at 5-year OCT [2], could mirror an earlier resorption in high WSS regions.

Our study underscores the potentially significant role of hemodynamics in configuration of the long-term BVS healing response. Accordingly, this association of WSS with cap thickness after resorption identified in the current study warrants examination in larger populations. As the presence of low WSS appears to be associated with a less favorable long-term plaque phenotype, that could even consist of asymptomatic plaque rupture [1], screening of patients for regions of very low shear stress might be able to identify patients with a suboptimal healing response, which could benefit from intensive treatment with agents known to increase the thickness of fibrous caps, such as statins [11].

This is a small study, aiming to provide hypotheses for the role of WSS in the long-term BVS healing response. Motion artifacts could result in discrepancies in matching between WSS and OCT. For minimizing them, we only assessed within-scaffold WSS differences: 1) in necrotic core versus non-necrotic core regions and 2) in two equal segments per scaffold, circumventing potential errors from point-by-point co-registration. Finally, boundary conditions were computed assuming 1.2 Pa WSS at the inlet, as exact flow calculations were not available, but since relative within-scaffold differences were examined, absolute flow values are less important and unlikely to affect our results.

WSS 2 years after BVS implantation is associated with the vascular healing response by OCT at 5 years. Specifically, within a scaffold, regions with lower WSS are associated with thinner fibrous cap. Our study underscores the need of better understanding the role of hemodynamics in order to optimize the BVS healing response and presents a framework for evaluating the association of WSS with healing response over time.

Fig. 1. Multislice computed tomography (MSCT) images 18 months after implantation were segmented and the centreline was extracted. Segmented intravascular ultrasound (IVUS) images 24 months after implantation were then superimposed on the MSCT-derived centerline, using side-branches and platinum markers as landmarks, in order to reconstruct a three-dimensional model that can be used for calculating the 2-year wall shear stress (WSS) by computational fluid dynamics (CFD). Optical coherence tomography (OCT) images 5 years after implantation were segmented, and the presence of necrotic core in the plaque was denoted (red crosses). These images were then co-registered with the three-dimensional model encompassing WSS information, resulting in a fusion allowing the assessment of the spatial correspondence of WSS values with OCT necrotic core in a plaque-level analysis. Arrows and arrowheads indicate the platinum scaffold markers; SB: side-branch.

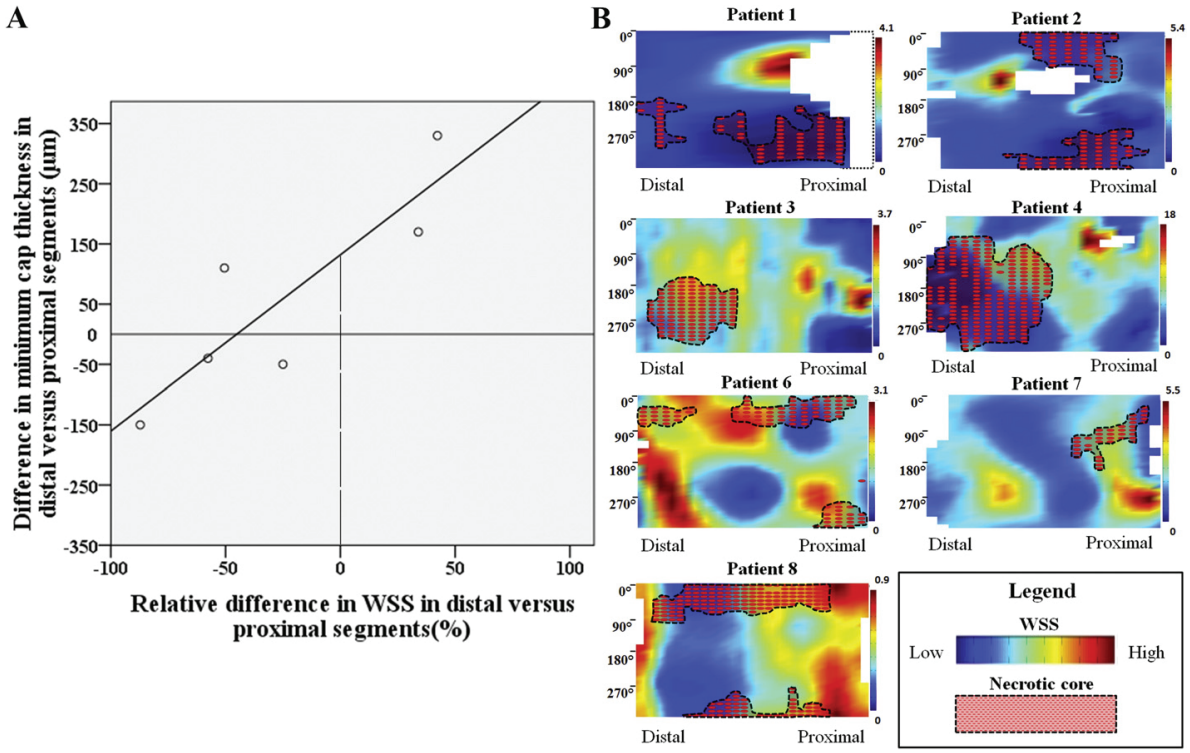

Fig. 2. A. Correlation plot of relative WSS differences in wall shear stress 2 years post-bioresorbable scaffold implantation between distal versus proximal segments with differences in minimum cap thickness of the treated segment by OCT at 5 years ($r^2 = 0.76$). Note the intercept (132 µm) suggesting that although the mean relative WSS difference between the distal and proximal segments is negative ($-21.4 \pm 47.7\%$), the mean difference in minimum cap thickness between the distal and proximal segments will be positive (62 ± 175 µm). B. Co-registration of the 2-year WSS with necrotic core regions by OCT at 5 years. Individual patient spread-out maps demonstrate the spatial correspondence of WSS values at 2 years with the presence of necrotic core by OCT at 5 years.

Conflict of interest

The authors report no relationships that could be construed as a conflict of interest.

Disclosures

AK has received research support from St Jude Medical. JJW is supported by ERC starters grant (BioCCora, ♥310457). Funding sources were not involved in any stage of the study. All authors have approved the final article.

Appendix A. Supplementary data

Supplementary data to this article can be found online at http://dx.doi.org/10.1016/j.ijcard.2015.04.231.

References

[1] A. Karanasos, C. Simsek, M. Gnanadesigan, et al., OCT assessment of the long-term vascular healing response 5 years after everolimus-eluting bioresorbable vascular scaffold, J. Am. Coll. Cardiol. 64 (2014) 2343–2356.
[2] C. Simsek, A. Karanasos, M. Magro, et al., Long-term invasive follow-up of the everolimus-eluting bioresorbable vascular scaffold: five-year results of multiple invasive imaging modalities, EuroIntervention (2014); http://dx.doi.org/10.4244/EIJY14M10_12.
[3] J.J. Wentzel, Y.S. Chatzizisis, F.J.H. Gijsen, G.D. Giannoglou, C.L. Feldman, P.H. Stone, Endothelial shear stress in the evolution of coronary atherosclerotic plaque and vascular remodelling: current understanding and remaining questions, Cardiovasc. Res. 96 (2012) 234–243.
[4] Y.S. Chatzizisis, R. Blankstein, P. Libby, Inflammation goes with the flow: implications for non-invasive identification of high-risk plaque, Atherosclerosis 234 (2014) 476–478.
[5] C.V. Bourantas, M.I. Papafaklis, A. Kotsia, et al., Effect of the endothelial shear stress patterns on neointimal proliferation following drug-eluting bioresorbable vascular scaffold implantation: an optical coherence tomography study, JACC Cardiovasc. Interv. 7 (2014) 315–324.
[6] A.G. van der Giessen, M. Schaap, F.J.H. Gijsen, et al., 3D fusion of intravascular ultrasound and coronary computed tomography for in-vivo wall shear stress analysis: a feasibility study, Int. J. Cardiovasc. Imaging 26 (2010) 781–796.

Table 1
Association of relative WSS differences in distal versus proximal segments with OCT measurements (n = 7).

Relative WSS differences in distal versus proximal segment (1% increase)	Differences in characteristics in distal versus proximal segment					
	Lumen area increase (5 years–2 years) (mm^2)	Lumen eccentricity increase (5 years–2 years)	5-year minimum cap thickness (µm) (n = 6)*	5-year average cap thickness (µm) (n = 6)*	5-year mean necrotic core arc (°)	5-year maximum necrotic core arc (°)
b	0.004	−0.001	2.922	1.746	−0.456	−0.814
95% CI	(−0.021–0.029)	(−0.002–0.000)	(0.610–5.235)	(0.279–3.213)	(−1.250–0.339)	(−1.731–0.103)
p-Value	0.71	0.16	0.03	0.03	0.20	0.07
r-Square	0.03	0.36	0.76	0.73	0.30	0.51

* Cap thickness was not available in one segment, as there was no necrotic core by OCT. Abbreviations: CI = confidence intervals.

[7] P.W. Serruys, J.A. Ormiston, Y. Onuma, et al., A bioabsorbable everolimus-eluting coronary stent system (ABSORB): 2-year outcomes and results from multiple imaging methods, Lancet 373 (2009) 897–910.
[8] G. Koning, J. Dijkstra, C. von Birgelen, et al., Advanced contour detection for three-dimensional intracoronary ultrasound: a validation—in vitro and in vivo, Int. J. Cardiovasc. Imaging 18 (2002) 235–248.
[9] A.G. van der Giessen, H.C. Groen, P.-A. Doriot, et al., The influence of boundary conditions on wall shear stress distribution in patients specific coronary trees, J. Biomech. 44 (2011) 1089–1095.
[10] R.D. Kenagy, J.W. Fischer, M.G. Davies, et al., Increased plasmin and serine proteinase activity during flow-induced intimal atrophy in baboon PTFE grafts, Arterioscler. Thromb. Vasc. Biol. 22 (2002) 400–404.
[11] K. Komukai, T. Kubo, H. Kitabata, et al., Effect of atorvastatin therapy on fibrous cap thickness in coronary atherosclerotic plaque as assessed by optical coherence tomography: the EASY-FIT study, J. Am. Coll. Cardiol. 64 (2014) 2207–2217.

SUPPLEMENTAL MATERIAL

Supplemental Table 1. Differences of WSS, IVUS, IVUS-VH and OCT characteristics between distal and proximal segments (n=7).

	Proximal segment	Distal segment	Absolute difference (distal - proximal)
WSS (Pa)	1.97±2.04	1.48±1.03	-0.48±1.18
OCT characteristics (n=7)			
Lumen area increase (5 years-2 years) (mm^2)	1.48±0.87	1.11±1.19	-0.37±1.06
Lumen eccentricity increase (5 years-2 years)	-0.09±0.07	-0.04±0.08	0.05±0.07
Minimum cap thickness (μm)*	190±98	255±162	62±175
Average cap thickness (μm)*	323±127	344±133	18±106
Mean necrotic core arc (°)	93±37	87±69	-6±40
Maximum necrotic core arc (°)	141±54	125±98	-16±55
Greyscale IVUS characteristics (n=6)			
Lumen area increase (5 years-2 years) (mm^2)	0.88±0.93	0.66±1.12	-0.22±1.70
Plaque area increase (5 years-2 years) (mm^2)	-0.86±2.07	0.25±2.21	1.11±1.65
Vessel area increase (5 years-2 years) (mm^2)	-0.06±1.25	0.91±3.28	0.97±2.60
IVUS-VH measurements (n=6)			
VH fibrous area increase (5 years-2 years) (mm^2)	-0.37±1.51	0.38±0.98	0.75±1.05
VH fibrofatty area increase (5 years-2 years) (mm^2)	0.00±0.35	-0.09±0.17	-0.09±0.31
VH necrotic core area increase (5 years-2 years) (mm^2)	-0.28±0.60	0.20±0.84	0.49±0.43
VH dense calcium area increase (5 years-2 years) (mm^2)	-0.21±0.18	-0.01±0.47	0.21±0.35

*Cap thickness was not available in one of the distal segments, as there was no necrotic core by OCT. Abbreviations: WSS=wall shear stress, IVUS=intravascular ultrasound, IVUS-VH=virtual histology, OCT=optical coherence tomography.

Supplemental Table 2. Association of relative WSS differences in distal versus proximal with differences in lumen measurements and plaque morphology by IVUS and IVUS-VH (n=6).

Relative WSS differences in distal versus proximal segment (per 1% increase)	Differences in characteristics in distal versus proximal segment						
	Mean lumen area increase (5 years - 2 years) (mm^2)	Plaque area increase (5 years -2 years) (mm^2)	Vessel area increase (5 years-2 years) (mm^2)	VH fibrous area increase (5 years-2 years) (mm^2)	VH fibrofatty area increase (5 years-2 years) (mm^2)	VH necrotic core area increase(5 years-2 years) (mm^2)	VH dense calcium area increase (5 years-2 years) (mm^2)
b	0.008	0.019	0.025	0.002	0.001	0.004	0.007
95%CI	(-0.047-0.062)	(-0.029-0.066)	(-0.052-0.102)	(-0.032-0.036)	(-0.009-0.011)	(-0.008-0.017)	(0.001-0.013)
p-value	0.71	0.34	0.42	0.86	0.78	0.41	0.03
r-square	0.04	0.23	0.17	0.01	0.02	0.17	0.73

Abbreviations: WSS=wall shear stress, IVUS=intravascular ultrasound, IVUS-VH=virtual histology, CI=confidence intervals.

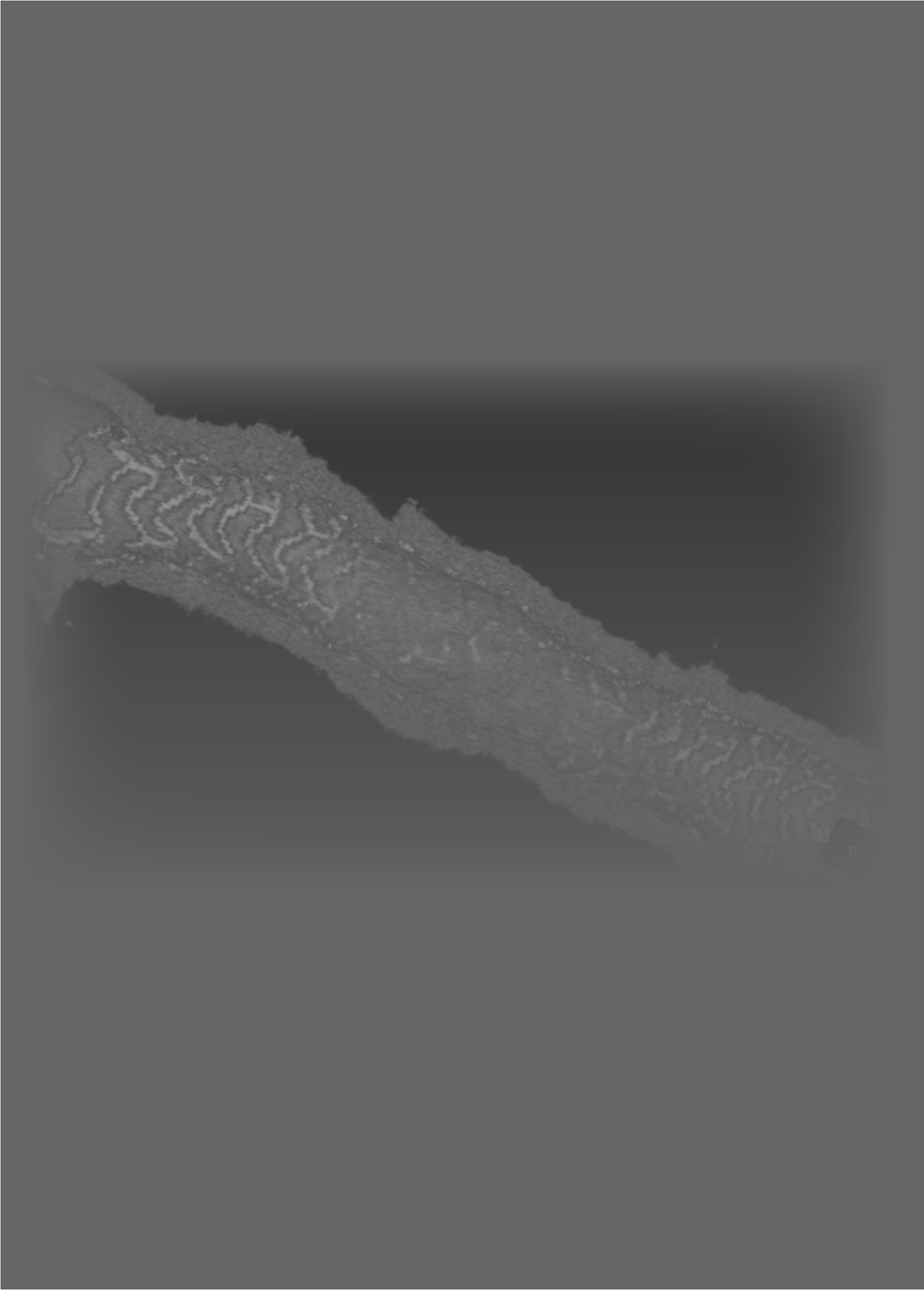

PART VI

Optical coherence tomography assessment of bioresorbable scaffolds in myocardial infarction

Chapter 6.1

Early and late optical coherence tomography findings following everolimus-eluting bioresorbable vascular scaffold implantation in myocardial infarction. A preliminary report

Karanasos A, Muramatsu T, Diletti R, Nauta S, Onuma Y, Lenzen M, Nakatani S, Van Mieghem NM, Schultz C, de Jaegere P, Serruys PW, Zijlstra F, Regar E, van Geuns RJ

Hellenic J Cardiol 2015 Mar-Apr;56(2):125-35

Early and Late Optical Coherence Tomography Findings Following Everolimus-Eluting Bioresorbable Vascular Scaffold Implantation in Myocardial Infarction: A Preliminary Report

Antonios Karanasos, Takashi Muramatsu, Roberto Diletti, Sjoerd Nauta, Yoshinobu Onuma, Mattie Lenzen, Shimpei Nakatani, Nicolas M. van Mieghem, Carl Schultz, Peter P. de Jaegere, Patrick W. Serruys, Felix Zijlstra, Evelyn Regar, Robert-Jan van Geuns

Thoraxcenter, Erasmus Medical Center, Rotterdam, the Netherlands

Key words:
Bioresorbable vascular scaffold, optical coherence tomography, ST-elevation myocardial infarction, non-ST-elevation myocardial infarction.

Introduction: Although bioresorbable vascular scaffolds (BVS) have been used with promising results in patients with stable and unstable angina, little is known about the acute vascular response following BVS implantation in myocardial infarction. We present angiographic and OCT findings from the first patients undergoing bioresorbable vascular scaffold (BVS) implantation for non-ST-elevation myocardial infarction (NSTEMI) or ST-elevation myocardial infarction (STEMI) in our institution.

Methods: The first 5 patients with NSTEMI and the first 5 patients with STEMI who underwent BVS implantation in our institution, followed by optical coherence tomography (OCT) imaging of the treated culprit vessel, were included in this series. All patients underwent angiographic analysis pre- and post- BVS implantation, as well as OCT analysis, including qualitative and quantitative assessment.

Results: Implantation was successful in all cases, as assessed by angiography and OCT. There were no cases with coronary spasm, distal embolization or no-reflow. No adverse clinical events were recorded in any patient at the 6-month follow up. Specific illustrative cases demonstrating the challenges of BVS implantation in myocardial infarction are presented.

Conclusions: BVS implantation can potentially be used in the setting of thrombotic lesions encountered in myocardial infarction; however, the role of this treatment approach warrants systematic evaluation in prospective studies.

Manuscript received:
May 30, 2014;
Accepted:
September 8, 2014.

Address:
Robert-Jan van Geuns

Department of Cardiology, Thoraxcenter Room Ba585, Erasmus Medical Center Molewaterplein 40 3015 RD, Rotterdam The Netherlands
r.vangeuns@erasmusmc.nl

Implantation of metallic platform drug-eluting stents constitutes the mainstay of revascularization in acute myocardial infarction.[1] However, their use has been associated with an impaired vascular healing response, while concerns have been raised over their long-term performance. Bioresorbable vascular scaffolds (BVS) could help overcome such long-term pitfalls of metallic platforms.[2] Although bioresorbable scaffolds have shown promising results in stable and unstable angina,[3,4] the acute vascular response following BVS implantation in myocardial infarction has not been extensively studied.[5-7]

As of September 1st, 2012, the ABSORB™ BVS (Abbott Vascular, Santa Clara, CA, USA) has been commercially available in the Netherlands. Based on available evidence,[3,4] our department selected these devices as the first option for younger patients presenting for percutaneous coronary intervention (PCI) in every-

day clinical practice. As lesions in these patients might be more complex compared to those of trial investigational patients, the BVS-EXPAND registry was initiated. In this registry, follow-up data are collected as part of the hospital routine for monitoring outcomes after PCI and the introduction of a different generation of stent or scaffold. The BVS-EXPAND includes patients with stable disease, but also patients with unstable angina or non-ST-elevation myocardial infarction (NSTEMI). After the first experience with acute patients and an interim analysis, a decision was made to extend BVS utilization to the treatment of ST-elevation myocardial infarction (STEMI).

To assess the safety and procedural success of a BVS strategy in STEMI, optical coherence tomography (OCT) imaging was performed, according to clinical judgment, in patients with STEMI and BVS implantation, for a more comprehensive evaluation of the acute procedural outcome by the operator. OCT is a high-resolution intravascular imaging modality that enables visualization of the acute vascular response after stent implantation.[8-11] Specifically, OCT can accurately evaluate scaffold expansion and apposition, and can also assess vascular trauma and residual thrombotic burden.[11-13]

We previously reported on a systematic analysis of the OCT findings post BVS implantation in STEMI.[6] In the current report, we present patient-level angiographic and OCT findings from the first five patients of BVS-EXPAND presenting with NSTEMI and imaged by OCT, and the first five patients who underwent BVS implantation for STEMI followed by OCT imaging, in our institution, in an attempt to illustrate the main challenges of BVS implantation in thrombotic lesions.

Methods

Study population

The current series comprised 1) the first five patients of BVS-EXPAND presenting with NSTEMI and imaged by OCT, and 2) the first five patients who underwent BVS implantation for STEMI followed by OCT imaging, in our institution. The STEMI patients were not a part of BVS-EXPAND.

Procedure and OCT image acquisition

Patients with NSTEMI typically underwent coronary angiography within 24-72 hours from symptom onset, according to the regional protocol, followed by urgent PCI after discussion in the HeartTeam, while patients with STEMI underwent primary PCI upon hospital arrival. Interventional management, including the use of thrombectomy, pre-dilation and post-dilation, was performed according to the operator's discretion. OCT was performed after BVS implantation using the C7™ imaging system and the Dragonfly™ catheter (both St. Jude Medical, St. Paul, Minnesota, USA), as previously described.[11] In several cases, OCT findings guided further procedural optimization (i.e. additional scaffold implantation and/or post-dilation). In these cases, a new OCT pullback was performed at the end of the procedure. The patients were contacted by telephone 6 months after the procedure, and adverse events (death, myocardial infarction, any unplanned revascularization), according to the Academic Research Consortium definitions, were recorded.[14]

Angiographic and OCT analysis

Quantitative coronary angiography (QCA) analyses were performed offline by an experienced observer (TM) using CAAS 5.10 (Pie Medical Imaging, Maastricht, Netherlands) according to a previously reported methodology.[13] Intracoronary thrombus was identified angiographically and scored in five grades, as previously described.[13] Complications such as dissection, spasm, distal embolization and no-reflow were also recorded. OCT analysis was performed offline by an experienced observer in fixed 1-mm longitudinal intervals within the treated culprit segment, after exclusion of frames with <75% lumen contour visibility. Quantitative analysis included measurement of the minimal lumen and the minimal scaffold area, according to a previously described methodology.[15] Qualitative assessment included evaluation of in-scaffold and edge dissections, tissue prolapse and in-scaffold thrombus. Dissections were defined as the presence of intimal discontinuity, with or without flap formation, either within the scaffolded segment (intra-scaffold dissection), or within 5-mm-long proximal or distal edge segments (edge dissections).[16] Tissue prolapse was defined as the projection of tissue into the lumen between stent struts after implantation.[16] Incomplete strut apposition (ISA) was defined as a clear lack of contact between scaffold strut and vascular wall;[15] apposition was assessed at a scaffold-level basis, using a definition of malapposed scaffold as a scaffold with >5% malapposed struts.

Ethics

This was an observational study, performed according to the privacy policy of Erasmus MC and the Erasmus MC regulations for the appropriate use of data in patient-oriented research. These are based on international regulations, including the declaration of Helsinki. A waiver from the Ethical Committee of Erasmus MC was obtained for written informed consent, as—according to Dutch law—written consent is not required if patients do not undergo procedures other than as part of their regular treatment. Invasive follow up in two of the patients was performed as part of an ethical committee-approved, single-center, investigator-driven, observational study (BVS-STEMI first) for which written informed consent was obtained from the patients.

Results

The median patient age was 56 years (range 40-75 years). Baseline characteristics are presented in Table 1, while angiographic data are presented in Table 2. There were no cases with spasm, distal embolization or no-reflow. No in-hospital events were recorded. Table 3 summarizes the OCT findings. Clinical follow-up at 6 months was available for all patients, showing an absence of adverse clinical events. Specific illustrative cases demonstrating the challenges of BVS implantation in NSTEMI and STEMI are presented below.

Patient 2 (Figure 1)

A 56-year-old man with no prior cardiovascular history, who presented with NSTEMI, had a total occlusion of the proximal left circumflex artery (LCx) with collateral filling from the left anterior descending artery (LAD), as documented by coronary angiography. OCT imaging performed after thrombus aspiration and predilation with a 2.0 × 20 mm compliant Trek™ balloon (Abbott Vascular) revealed a thrombosed, severely stenotic lesion with plaque rupture and intimal tears, probably induced by balloon predilation (Panels A-D). After additional predilation with a 3.0 × 20 mm Trek™ compliant balloon inflated at 14 atm (maximum diameter 3.11 mm; just below the maximum luminal diameter by QCA), a 3.0 × 18 mm BVS was implanted in the culprit lesion (inflation pressure 16 atm). Following this strategy, post-implantation OCT showed no edge dissections or residual stenosis. There were, however, several sites with moderate tissue prolapse/thrombus within the scaffold (panels A'-C'), for which no additional treatment was applied.

Patient 5 (Figures 2-3)

A 56-year-old man was admitted with NSTEMI and referred for PCI after HeartTeam consensus. Coronary angiography had demonstrated three-vessel disease: a lesion in the proximal LCx, a diffuse calcified lesion of the mid LAD, and a diffusely diseased right

Table 1. Baseline and procedural characteristics.

Patient	Age	Sex	Clinical syndrome	Lesions treated (n)	BVS implanted (n)	Thrombus aspiration	Balloon predilation	BVS size	Balloon post-dilation	Side-branch dilation
Patient 1	59	♀	NSTEMI	1	4	No	3 × 15	3 × 28, 3 × 28, 3 × 18, 2.5 × 28	3 × 12, 3.5 × 15	No
Patient 2	56	♂	NSTEMI	1	1	Yes	3 × 20	3 × 18	No	No
Patient 3	75	♂	NSTEMI	1	3	No	3 × 15	3.5 × 18, 3 × 18, 2.5 × 18	No	1.5 × 8
Patient 4	57	♀	NSTEMI	1	1	No	2.5 × 20	3 × 28	No	No
Patient 5	56	♂	NSTEMI	2	3	No	3 × 15 (LCx) 3 × 20 (LAD)	3.5 × 18, 3.5 × 12 (LCx) 3.5 × 28 (LAD)	No (LCx) 3.75 × 15 (LAD)	No
Patient 6	56	♀	STEMI	1	1	Yes	2.5 × 20	3 × 28	3.25 × 15	No
Patient 7	40	♂	STEMI	1	1	Yes	2.5 × 15	3.5 × 18	No	No
Patient 8	53	♂	STEMI	1	1	No	2 × 8	2.5 × 18	No	No
Patient 9	65	♂	STEMI	1	2	Yes	No	3.5 × 12, 3.5 × 12	4 × 8	No
Patient 10	58	♂	STEMI	1	2	Yes	3 × 12	3.5 × 18, 3.5 × 18	3.5 × 15	1.5 × 15

BVS – bioresorbable vascular scaffold; NSTEMI – non-ST-elevation myocardial infarction; STEMI – ST-elevation myocardial infarction; LCx – left circumflex artery; LAD – left anterior descending artery.

Table 2. Angiographic characteristics.

Patient	Culprit vessel	Pre procedure		Pre BVS implantation				Post implantation (in-scaffold)				
		Total Occlusion	Thrombus burden	Dmax (mm)	RVD (mm)	MLD (mm)	DS (%)	RVD (mm)	MLD (mm)	DS (%)	Final TIMI flow	Dissection
Patient 1	RCA	Yes	5	3.6	2.64	1.04	61	2.76	2.22	20	II	Yes
Patient 2	LCx	Yes	5	3.22	2.74	2.1	23	3.15	3	5	III	No
Patient 3	LAD	No	2	3.16	2.18	1.56	28	2.51	2.32	8	III	No
Patient 4	LAD	No	1	3.09	2.74	1.22	55	2.79	2.46	12	III	No
Patient 5, Lesion 1	LCx	No	0	3.44	2.96	1.39	53	2.71	2.36	13	III	No
Patient 5, Lesion 2	LAD	No	0	3.28	3.27	1.27	61	2.81	2.54	10	III	No
Patient 6	RCA	Yes	5	3.44	2.89	0.96	67	2.85	2.42	15	III	Yes
Patient 7	LAD	No	2	3.16	2.68	2.16	19	2.92	2.92	0	II	Yes
Patient 8	LD	Yes	5	2.55	2	0.51	74	2.47	2.05	17	III	No
Patient 9	RCA	Yes	5	3.97	3.52	1.4	60	3.17	2.39	25	III	No
Patient 10	LAD	No	3	3.63	2.29	0.9	61	2.58	1.93	25	III	No

Dmax – maximum diameter; RVD – reference vessel diameter; MLD – minimum lumen diameter; DS – diameter stenosis; RCA – right coronary artery; LD – diagonal branch. Other abbreviations as in Table 1.

coronary artery (RCA). It was decided to proceed with LCx and LAD revascularization, and staged revascularization of the RCA one month later.

The proximal LCx lesion (Panel 2I) was treated by 3.5 × 18 mm BVS implantation and post-dilation with a 3.0 × 15 mm compliant Trek™ balloon (Panel 2II). Subsequently, lumen narrowing with haziness was observed proximally, corresponding to an edge dissection by OCT (Panels 2A-B). The dissection was treated by implantation of an overlapping 3.5 × 12 mm BVS with a good angiographic result (panel 2III). A final OCT pullback showed focal under-expansion due to calcification, as well as sites with mild tissue prolapse and in-stent thrombus (Panels 2A'-D').

The LAD lesion (Panel 3I) was treated by 3.0 × 20 mm Trek™ balloon predilation, 3.5 × 28 mm BVS implantation and post-dilation with a 3.75 × 15mm Trek™ non-compliant balloon (Panels 3II-III). OCT following predilation revealed a heavily calcified vessel without intracoronary thrombus. Post-implantation OCT demonstrated good scaffold apposition, moderate pinching of the ostium of the diagonal (Panel 3A'), focal under-expansion at sites with heavy calcification (Panel 3C'), lack of tissue prolapse, and a small distal edge dissection (Panel 3D').

Patient 7 (Figure 4)

A 40-year-old man with diabetes and no known cardiovascular history was admitted with anterior STEMI. Angiography demonstrated a stenotic LAD lesion with angiographic haziness (Panel I). The lesion was treated by thrombus aspiration, 2.5 × 15 mm Trek™ compliant balloon pre-dilation and 3.5 × 18 mm BVS implantation (Panels II-III). A small edge dissection was visible by angiography after implantation. OCT confirmed the diagnosis of distal edge dissection extending for ~5 mm, which was left untreated (Panels D-E). The scaffold was well-expanded and apposed with moderate tissue prolapse and in-scaffold thrombus at the middle segment (Panels A-C). The patient underwent invasive follow up, including OCT imaging, 9 months post implantation for study purposes (Panel IV). The follow-up OCT showed a good healing response, without late ISA, high strut coverage (Panels A'-C') and complete healing of the dissection with integration of the dissection flap in the vessel wall (Panels D'-E').

Patient 8 (Figure 5)

A 52-year-old man with an unremarkable cardiovascular history was admitted with anterolateral STEMI. Angiography demonstrated total occlusion of the second diagonal branch (Panel I). The lesion was treated by 2.0 × 8 mm Trek™ compliant balloon dilation and 2.5 × 18 mm BVS implantation (Panels II-III). OCT showed a well-expanded and apposed scaffold with no vascular trauma at the middle and distal segments, and mild tissue prolapse and thrombus near the vessel ostium (Panels C-D). Scaffold struts were visible at the polygon of confluence of

Table 3. Optical coherence tomography (OCT) findings.

Patient	ISA	Minimal lumen area (mm^2)	Minimal scaffold area (mm^2)	Intraprocedural findings	Final OCT findings
Patient 1	Yes	Proximal BVS: 6.63	Proximal BVS: 7.85	Extensive intra-scaffold dissections with ISA in proximal scaffold, treated with post-dilation	• Improvement of scaffold apposition after post-dilation. • Minimal tissue prolapse.
Patient 2	No	7.60	8.34	-	• Good expansion and apposition. • No edge dissections • Moderate tissue prolapse/thrombus.
Patient 3	Yes	4.42	4.97	Side-branch compromise, treated with balloon dilation	• Distal and middle scaffolds well-expanded without tissue prolapse or thrombus. • ISA in the proximal and middle scaffolds due to eccentric calcium and intra-scaffold dissections. • Mild tissue prolapse in the proximal scaffold. • No evident scaffold fracture at the level of the side-branch.
Patient 4	No	6.05	6.57	-	• Good expansion and apposition without edge dissections. • Short segment with moderate tissue prolapse/thrombus
Patient 5	LCx: Yes LAD: No	LCx: 6.28 mm^2 LAD: 4.98 mm^2	LCx: 6.28 mm^2 LAD: 5.36 mm^2	Proximal dissection in LCx, treated with 2nd BVS	• LCx: mild tissue prolapse/thrombus in both scaffolds. • Sub-optimal expansion and ISA focally. • LAD: good apposition with sub-optimal expansion focally due to calcium. • Small distal edge dissection.
Patient 6	Yes	6.27	7.07	Extensive intra-scaffold dissection with ISA, treated with post-dilation.	• Reduction of dissection cavity size and malapposition distance after post-dilation. • Mild tissue prolapse and in-scaffold thrombus ISA.
Patient 7	No	7.55	8.33	-	• Distal edge dissection ~5 mm long. • Sites with moderate tissue prolapse/in-scaffold thrombus proximally.
Patient 8	No	4.21	4.76	-	• Well-expanded and apposed scaffold with minimal tissue prolapse/thrombus. • Scaffold protrusion into the main branch for ~1 mm.
Patient 9	Yes	5.72	7.6	Stenosis in distal RCA after BVS implantation in RPL, treated with 2nd BVS.	• ISA proximally due to scaffold-lumen dimensions mismatch. • Minimal overlap at the crux with moderate tissue prolapse. • Presence of struts at the RPD ostium and residual red thrombus.
Patient 10	No	6.77	7.15	Small edge dissection and residual lesion distally (MLA: 1.71 mm^2), treated with 2nd BVS - Side-branch compromise, treated with balloon dilation	• Good expansion and apposition with minimal overlap. • Mild tissue prolapse/thrombus in both scaffolds. • No evident scaffold fracture at the level of the side-branch.

ISA – incomplete scaffold apposition; RPL – right posterolateral branch; RPD – right posterior descending branch; MLA – minimal lumen area. Other abbreviations as in Tables 1 and 2.

the LAD-diagonal bifurcation, with minimal protrusion of the scaffold into the LAD (Panels A, B, G). Invasive follow up with OCT imaging was performed 1 year post implantation for study purposes (Panel IV). The follow-up OCT revealed a good healing response without ISA and a low number of uncovered struts (Panels A'-D'). Dense tissue coverage was also observed at the side-branch-related struts located in the vessel ostium, resulting in the development of a neo-carina (Panel H).

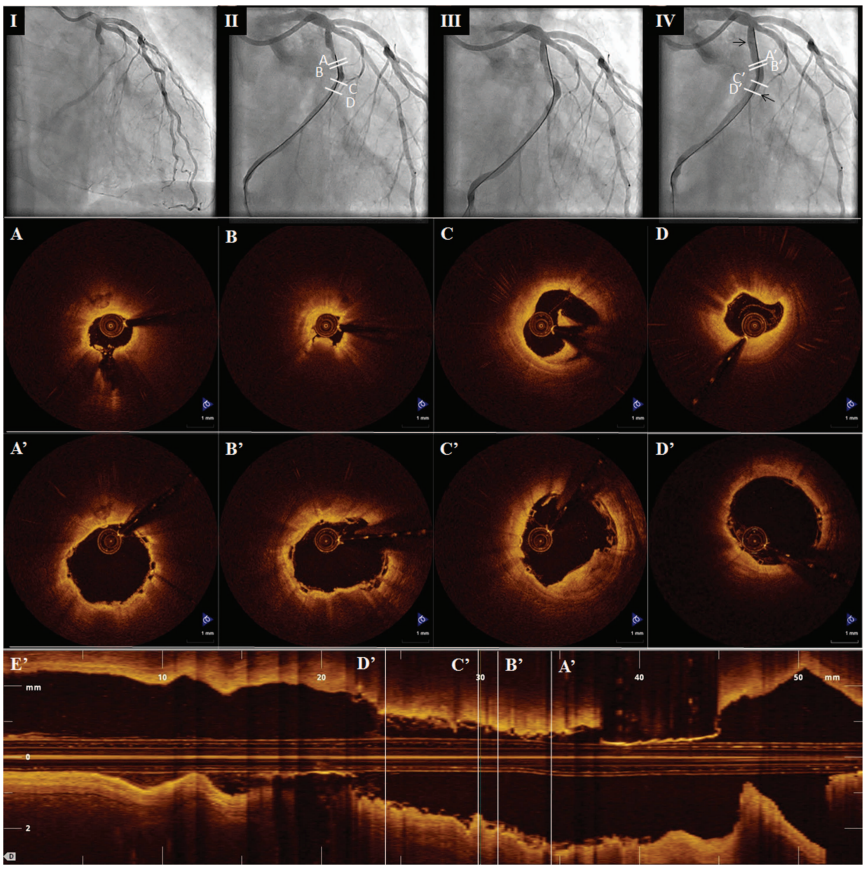

Figure 1. Top panels: Coronary angiography demonstrating the culprit lesion of the proximal left circumflex artery (I) pre-intervention, (II) after 2.0 mm balloon predilation, (III) after 3.0 mm balloon predilation, and (IV) after 3.0 × 18 mm bioresorbable vascular scaffold (BVS) implantation. Black arrows indicate scaffold markers, and white lines the sites corresponding to the bottom panels. Bottom panels: Culprit lesion optical coherence tomography images of matched sites (A-D) after 2.0 mm balloon dilation and (A'-D') after BVS implantation. Pre-implantation images demonstrate (A) plaque rupture with cavity, (B) minimal lumen area with red thrombus, (C) dissection flap, and (D) distal segment with macrophage infiltration. Findings after BVS implantation include (A') mild tissue prolapse at the cavity site, (B') residual compressed red thrombus, (C') tissue prolapse at the site of the flap, and (D') good expansion and apposition without tissue prolapse/thrombus.

Discussion

The current series of patients provides real-life insights into the acute vascular response after BVS implantation in myocardial infarction. In order to assess the efficacy of BVS implantation, OCT imaging was employed. OCT-derived parameters can potentially be used as surrogate markers for assessing the acute outcome of BVS implantation in patients with myocardial infarction. In particular, in addition to the assessment of luminal dimensions and scaffold expansion, OCT allows a comprehensive assessment of the scaffold-vessel wall interaction, providing detailed information about scaffold apposition, vascular trauma (intra-scaffold and edge dissections, tissue prolapse), and residual thrombotic burden. The clinical impact of such OCT parameters has not been established; however, their evaluation in studies of BVS implantation in myocardial infarction could be of significance, considering i) the increased incidence of incomplete apposition after metal stent implantation in myocardial infarction,[17] ii) the need for more aggressive lesion preparation with BVS, and iii) the association of increased residual thrombus with impaired reperfusion after metal stent implantation in myocardial infarction.[18]

In the ABSORB B study, in a relatively non-complex lesion subset of patients with stable and unstable

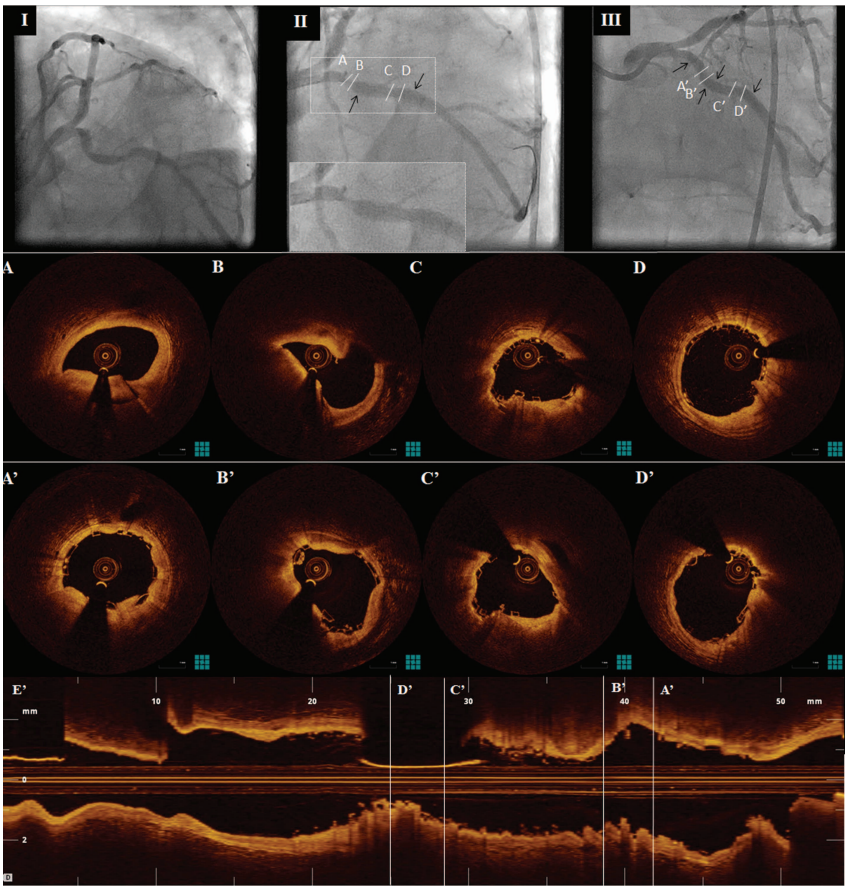

Figure 2. Top panels: Coronary angiography demonstrating the left circumflex artery lesion (I) pre-intervention, and (II) after 3.5 × 18 mm bioresorbable vascular scaffold (BVS) implantation. Because of proximal dissection a 3.5 × 12 mm scaffold was implanted (III). Black arrows indicate scaffold markers, and white lines the sites corresponding to the bottom panels. Bottom panels: Culprit lesion optical coherence tomography images of matched sites after (A-D) first and (A'-D') second BVS implantation. In the proximal scaffold, there is tissue prolapse at the sites of the dissection flaps with a small amount of intraluminal thrombus (A-A', B-B'). Mild under-expansion over a calcified plate (C-C') and mild tissue prolapse/in-stent thrombus (D-D') are observed at the distal scaffold.

angina, the BVS has shown adequate expansion, with a minimum scaffold area of 6.31 ± 1.25 mm^2.[15] In our series of patients with myocardial infarction, good scaffold expansion was observed in all but one case, in which case the implanted scaffolds were focally under-expanded because of heavy calcification (Panels 2C' and 3C'). In all other patients the implanted scaffolds were well expanded, including a case with direct BVS implantation in STEMI (Patient 9).

Apposition was not optimal in all cases, with causes for incomplete apposition including extensive intra-scaffold dissections and in one case mismatch of lumen and scaffold dimensions after bail-out BVS implantation in a proximal segment (Patient 9). The selection of scaffold size during the acute phase of myocardial infarction can be challenging, as the increased thrombus burden and the enhanced vascular tone can hamper evaluation of the true vessel size.[12] Post-dilation guided by OCT imaging – always in agreement with scaffold compliance and respecting the recommended maximum scaffold diameter – helped improve scaffold apposition in most cases. Still, the future course of scaffold apposition remains elusive. In the two patients in our series who underwent invasive follow up, no late incomplete scaffold apposition was observed. Although implantation of metal stents during primary PCI is associated with higher incomplete apposition at follow up compared to stable angina,[8,17] possibly due to resolution of vasoconstriction and thrombus,[12] no such data are currently available for the follow up of BVS implanted in myocardial infarction. Thus, longer-term follow up and prospective

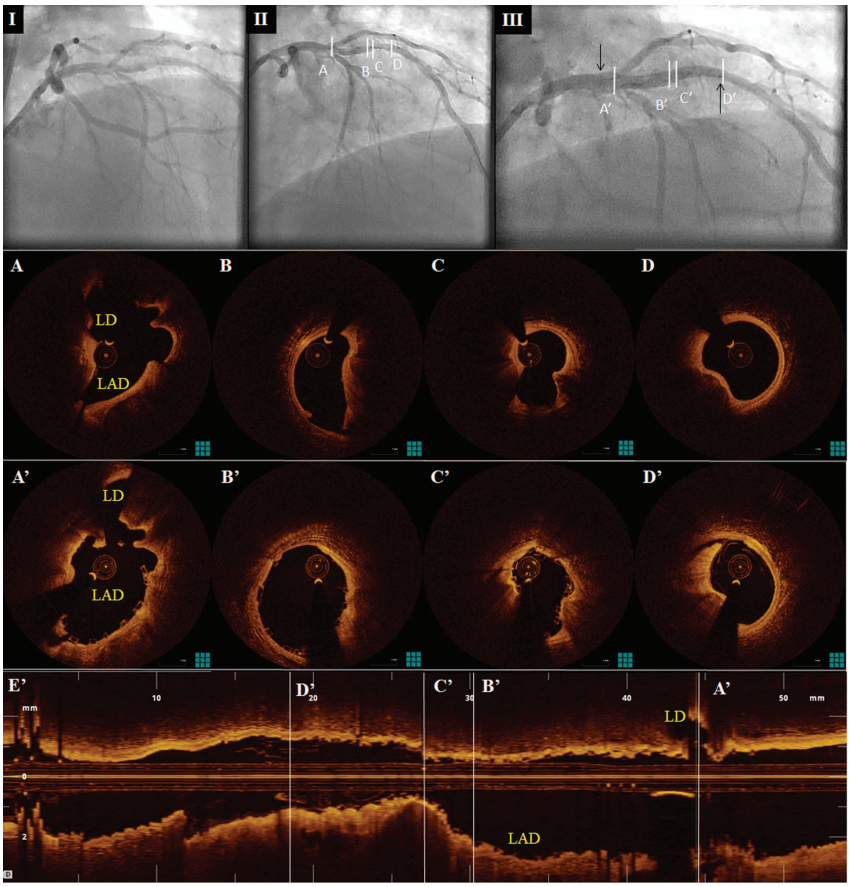

Figure 3. Top panels: Coronary angiography demonstrating the LAD lesion (I) pre-intervention, (II) after 3.0 mm balloon dilation, and (III) after 3.5 × 28 mm bioresorbable vascular scaffold (BVS) implantation and post-dilation with 3.75 mm non-compliant balloon. Black arrows demonstrate scaffold markers and white lines the sites corresponding to the bottom panels. Bottom panels: Culprit lesion optical coherence tomography images of matched sites after (A-D) pre-dilation and (A'-D') BVS implantation. (A-A') Small thrombus formation and pinching of the diagonal ostium post-implantation. (B-B') Good expansion and apposition at the site of a dissected eccentric calcified plaque. (C-C') Suboptimal scaffold expansion due to the presence of two protruding calcified plates at a site without dissection. (D-D') Small distal edge dissection at the site of a calcified nodule. LAD – left anterior descending branch; LD – diagonal branch.

studies are warranted to assess the true extent of incomplete scaffold apposition in myocardial infarction and its clinical implications at follow up.

Despite their similar pathophysiological mechanisms, NSTEMI and STEMI exhibit differences in lesion morphology and disease severity.[19,20] In our series, high disease heterogeneity was observed in NSTEMI. Two of the cases with NSTEMI (Patients 1 and 2) presented with total occlusion. Implantation was successful in both cases with a good final result, demonstrating the potential of BVS implantation in a highly thrombogenic setting, similar to STEMI. Indeed, the vascular response after BVS implantation in STEMI resembled these NSTEMI cases. The other end of the NSTEMI spectrum also includes patients with multiple lesions, increased calcification and minimal thrombus, as in Patient 5. Conversely, all STEMI cases in our series were associated with angiographic thrombus, dictating the use of thrombus aspiration in all but one case.

The different lesion substrate could have implications for the extent of vascular trauma and residual thrombotic burden. Both lesion morphology and unstable presentation have been associated with periprocedural vascular trauma.[9] In cases with heavy calcification, as in Patient 5, aggressive lesion preparation could help optimize scaffold expansion. However, lesion preparation should be performed with caution, as it may as well induce extensive vascular trauma, as in Patients 1 and 6.[21] Predilation has been associated with increased distal embolization in the setting of metal stent implantation for myocardial in-

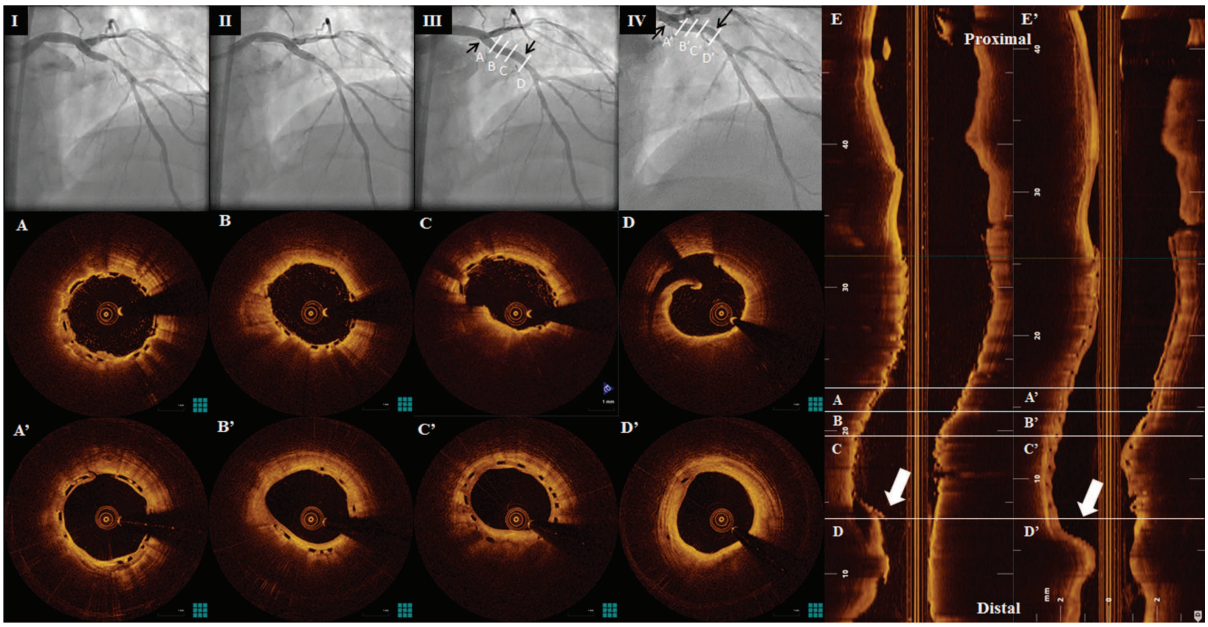

Figure 4. Top panels: Coronary angiography demonstrating the culprit left anterior descending artery lesion (I) pre-intervention, (II) post thrombus aspiration/2.5 mm balloon predilation, (III) post 3.5 × 18 mm BVS implantation, and (IV) at 9-month follow up. Black arrows indicate scaffold markers and white lines the sites corresponding to the bottom panels. Bottom panels: Optical coherence tomography of the treated lesion. Panels A-C disclose the presence of varying degrees of tissue prolapse/intra-scaffold thrombus, and Panel D an intra-scaffold dissection. Nine-month follow-up images show a favorable healing response with the absence of late incomplete apposition, symmetric coverage of the bioresorbable vascular scaffold (A'-C'), and the complete healing of the edge dissection (D'). L-mode images at baseline (E) and follow up (E') demonstrate the longitudinal morphology of the healed dissection (arrow).

farction,[22] however such data are not available for BVS. In our series, although distal embolization was not angiographically documented, OCT revealed varying degrees of tissue prolapse and/or residual thrombus in all cases. Importantly, increased tissue prolapse and/or residual thrombus have been associated with impaired reperfusion following stenting for STEMI.[18] Therefore, it is important to evaluate such findings systemically in BVS and to assess their significance and differences with metal platform stents.[6]

Another important aspect is the presence of culprit bifurcation lesions. In cases of ostial side-branch disease, as in Patients 8 and 9, BVS implantation constitutes an appealing option, given the favorable response observed in side-branch-related scaffold struts, with their gradual replacement by tissue bridges and development of a neo-carina,[23] Conversely, in metal stents, the permanent stent layer jailing side-branches is often characterized by impaired healing,[24] providing a potential substrate for thrombosis. In the case of culprit lesions with large side-branch involvement, however, a high thrombus burden can cause underestimation of the side-branch involvement, potentially resulting in side-branch compromise post-procedurally, as in Patients 3 and 10. The good angiographic result after side-branch dilation and the absence of scaffold fracture by OCT suggest a potential role for this approach in the treatment of side-branch compromise.

It is important to note that the current series represents a preliminary report of a single-center experience with BVS implantation in myocardial infarction. The current report did not aim to conduct a systematic analysis of the OCT findings, but instead gives patient-specific descriptions of the acute vascular response, aiming to provide initial observations and demonstrate challenges and differences with stable disease. The impact of a thrombotic substrate on the vascular response following BVS implantation still needs to be systematically evaluated in larger patient cohorts with a longer follow up.

Conclusions

In the current series, we presented angiographic and OCT findings following BVS implantation in myocardial infarction. Implantation was successful both in thrombotic culprit lesions of NSTEMI patients and in culprit lesions of STEMI patients, with a similar acute vascular response by OCT. The incidence of incom-

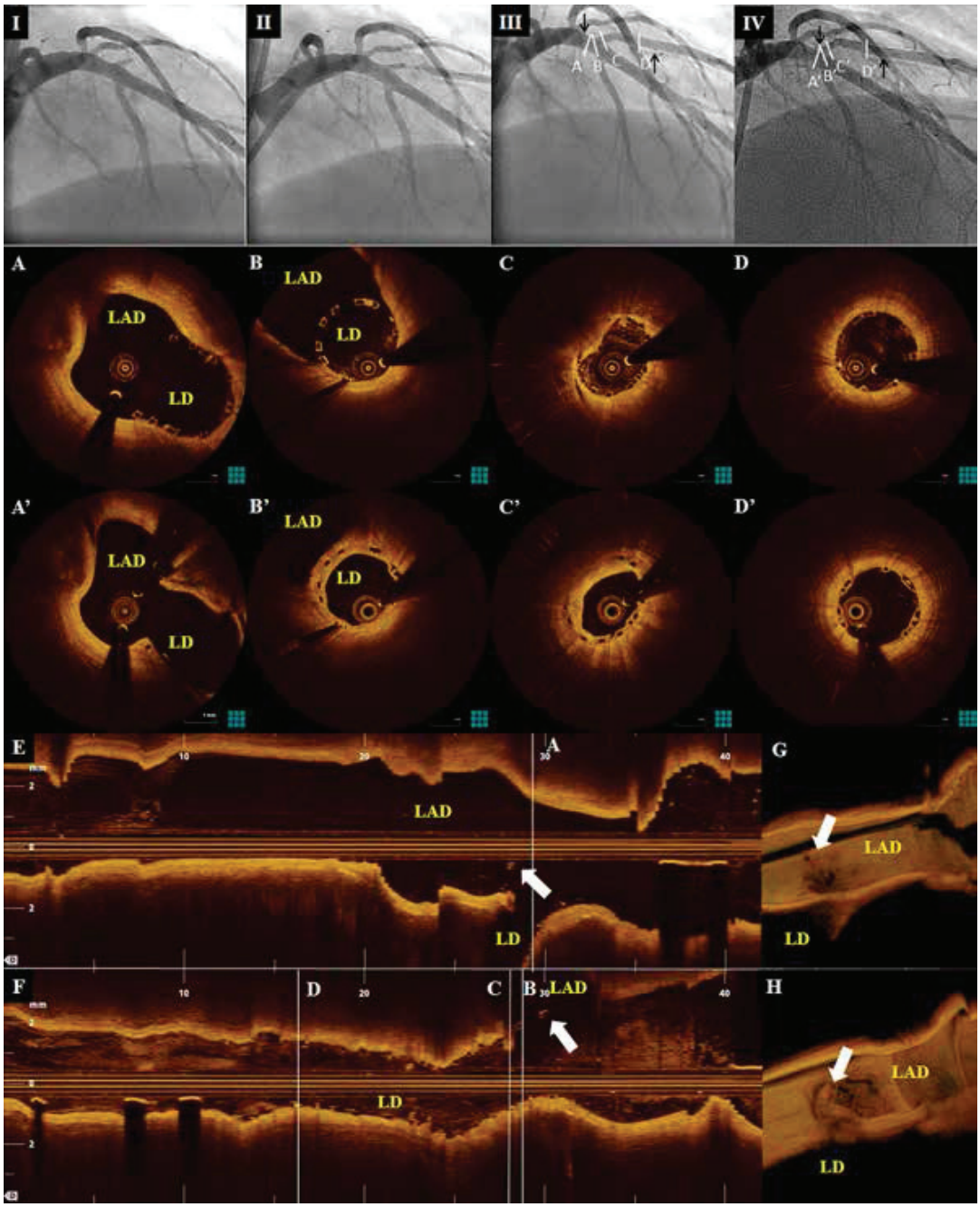

Figure 5. Top panels: Coronary angiography demonstrating (I) total occlusion of the LD, and the angiographic result after (II) 2.0 mm balloon predilation and (III) 2.5 × 18 mm bioresorbable vascular scaffold implantation. Panel IV shows the angiography at 12-month follow up. Black arrows indicate scaffold markers and white lines the sites corresponding to the bottom panels. Bottom panels: Optical coherence tomography (OCT) of the culprit diagonal branch lesion. Scaffold struts are protruding into the polygon of confluence of the LAD-diagonal bifurcation, as can appreciated from both the LAD (A, E) and the diagonal pullback (B, F). There is mild tissue prolapse and thrombus near the vessel ostium (C), but minimal prolapse in the middle and distal scaffold segments, with good expansion and apposition (D). Follow-up OCT images at matched sites are presented in panels A'-D', showing coverage of the implanted scaffold, absence of incomplete apposition, and the development of tissue bridges in relation to side-branch-related struts. Three-dimensional renderings illustrate the development of a neo-carina at the site of scaffold protrusion into the LAD (E, E'). LAD – left anterior descending branch; LD – diagonal branch.

plete scaffold apposition at follow up, the role of the pathological substrate in the selection of lesion preparation strategy, and the impact of periprocedural trauma and residual thrombus post-intervention remain open questions regarding BVS implantation in myocardial infarction that warrant systematic evaluation in prospective studies.

References

1. Stone GW, Lansky AJ, Pocock SJ, et al. Paclitaxel-eluting stents versus bare-metal stents in acute myocardial infarction. N Engl J Med. 2009; 360: 1946-1959.
2. Karanasos A, Simsek C, Serruys P, et al. Five-year optical coherence tomography follow-up of an everolimus-eluting bioresorbable vascular scaffold: changing the paradigm of coronary stenting? Circulation. 2012; 126: e89-91.
3. Ormiston JA, Serruys PW, Onuma Y, et al. First serial assessment at 6 months and 2 years of the second generation of absorb everolimus-eluting bioresorbable vascular scaffold: a multi-imaging modality study. Circ Cardiovasc Interv. 2012; 5: 620-632.
4. Serruys PW, Ormiston JA, Onuma Y, et al. A bioabsorbable everolimus-eluting coronary stent system (ABSORB): 2-year outcomes and results from multiple imaging methods. Lancet. 2009; 373: 897-910.
5. Gori T, Schulz E, Hink U, et al. Early outcome after implantation of Absorb bioresorbable drug-eluting scaffolds in patients with acute coronary syndromes. 2014; 9: 1036-1041.
6. Diletti R, Karanasos A, Muramatsu T, et al. Everolimus-eluting bioresorbable vascular scaffolds for treatment of patients presenting with ST-segment elevation myocardial infarction: BVS STEMI first study. Eur Heart J. 2014; 35: 777-786.
7. Kočka V, Malý M, Toušek P, et al. Bioresorbable vascular scaffolds in acute ST-segment elevation myocardial infarction: a prospective multicentre study "Prague 19". Eur Heart J. 2014; 35: 787-794.
8. Guagliumi G, Costa MA, Sirbu V, et al. Strut coverage and late malapposition with paclitaxel-eluting stents compared with bare metal stents in acute myocardial infarction: optical coherence tomography substudy of the Harmonizing Outcomes with Revascularization and Stents in Acute Myocardial Infarction (HORIZONS-AMI) Trial. Circulation. 2011; 123: 274-281.
9. Kubo T, Imanishi T, Kitabata H, et al. Comparison of vascular response after sirolimus-eluting stent implantation between patients with unstable and stable angina pectoris: a serial optical coherence tomography study. JACC Cardiovasc Imaging. 2008; 1: 475-484.
10. Karanasos A, Ligthart J, Witberg K, van Soest G, Bruining N, Regar E. Optical Coherence Tomography: Potential Clinical Applications. Curr Cardiovasc Imaging Rep. 2012; 5: 206-220.
11. Tearney GJ, Regar E, Akasaka T, et al. Consensus standards for acquisition, measurement, and reporting of intravascular optical coherence tomography studies: a report from the International Working Group for Intravascular Optical Coherence Tomography Standardization and Validation. J Am Coll Cardiol. 2012; 59: 1058-1072.
12. van Geuns RJ, Tamburino C, Fajadet J, et al. Self-expanding versus balloon-expandable stents in acute myocardial infarction: results from the APPOSITION II study: self-expanding stents in ST-segment elevation myocardial infarction. JACC Cardiovasc Interv. 2012; 5: 1209-1219.
13. Onuma Y, Thuesen L, van Geuns RJ, et al. Randomized study to assess the effect of thrombus aspiration on flow area in patients with ST-elevation myocardial infarction: an optical frequency domain imaging study – TROFI trial. Eur Heart J. 2013; 34: 1050-1060.
14. Cutlip DE, Windecker S, Mehran R, et al. Clinical end points in coronary stent trials: a case for standardized definitions. Circulation. 2007; 115: 2344-2351.
15. Serruys PW, Onuma Y, Ormiston JA, et al. Evaluation of the second generation of a bioresorbable everolimus drug-eluting vascular scaffold for treatment of de novo coronary artery stenosis: six-month clinical and imaging outcomes. Circulation. 2010; 122: 2301-2312.
16. Gonzalo N, Serruys PW, Okamura T, et al. Optical coherence tomography assessment of the acute effects of stent implantation on the vessel wall: a systematic quantitative approach. Heart. 2009; 95: 1913-1919.
17. Gonzalo N, Barlis P, Serruys PW, et al. Incomplete stent apposition and delayed tissue coverage are more frequent in drug-eluting stents implanted during primary percutaneous coronary intervention for ST-segment elevation myocardial infarction than in drug-eluting stents implanted for stable/unstable angina: insights from optical coherence tomography. JACC Cardiovasc Interv. 2009; 2: 445-452.
18. Magro M, Regar E, Gutiérrez-Chico JL, et al. Residual atherothrombotic material after stenting in acute myocardial infarction - An optical coherence tomographic evaluation. Int J Cardiol. 2013; 167: 656-663.
19. Toutouzas K, Karanasos A, Tsiamis E, et al. New insights by optical coherence tomography into the differences and similarities of culprit ruptured plaque morphology in non-ST-elevation myocardial infarction and ST-elevation myocardial infarction. Am Heart J. 2011; 161: 1192-1199.
20. Ferrara LA, Russo BF, Gente R, Esposito G, Rapacciuolo A, de Simone G. STEMI and NSTEMI: A mono versus a multivessel disease? Int J Cardiol. 2013; 168: 2905-2906.
21. Karanasos A, Regar E, Geeve P, van Mieghem NM. Bioresorbable scaffold in myocardial infarction: has the time come? Int J Cardiol. 2013; 167: e17-19.
22. Loubeyre C, Morice MC, Lefèvre T, Piéchaud JF, Louvard Y, Dumas P. A randomized comparison of direct stenting with conventional stent implantation in selected patients with acute myocardial infarction. J Am Coll Cardiol. 2002; 39: 15-21.
23. Okamura T, Onuma Y, García-García HM, et al. 3-Dimensional Optical Coherence Tomography Assessment of Jailed Side Branches by Bioresorbable Vascular Scaffolds: A Proposal for Classification. JACC: Cardiovasc Interv. 2010; 3: 836-844.
24. Gutiérrez-Chico JL, Regar E, Nüesch E, et al. Delayed coverage in malapposed and side-branch struts with respect to well-apposed struts in drug-eluting stents: in vivo assessment with optical coherence tomography. Circulation. 2011; 124: 612-623.

Chapter 6.2

Everolimus-eluting bioresorbable vascular scaffolds for treatment of patients presenting with ST-segment elevation myocardial infarction: BVS STEMI first study

Diletti R, **Karanasos A**, Muramatsu T, Nakatani S, Van Mieghem NM, Onuma Y, Nauta ST, Ishibashi Y, Lenzen MJ, Ligthart J, Schultz C, Regar E, de Jaegere PP, Serruys PW, Zijlstra F, van Geuns RJ

Eur Heart J. 2014 Mar;35(12):777-86

Everolimus-eluting bioresorbable vascular scaffolds for treatment of patients presenting with ST-segment elevation myocardial infarction: BVS STEMI first study

Roberto Diletti, Antonios Karanasos, Takashi Muramatsu, Shimpei Nakatani, Nicolas M. Van Mieghem, Yoshinobu Onuma, Sjoerd T. Nauta, Yuki Ishibashi, Mattie J. Lenzen, Jurgen Ligthart, Carl Schultz, Evelyn Regar, Peter P. de Jaegere, Patrick W. Serruys, Felix Zijlstra, and Robert Jan van Geuns*

Thoraxcenter, Erasmus MC, 's-Gravendijkwal 230, 3015 CE Rotterdam, the Netherlands

Received 11 September 2013; revised 6 November 2013; accepted 26 November 2013; online publish-ahead-of-print 6 January 2014

See page 753 for the editorial comment on this article (doi:10.1093/eurheartj/ehu005)

Aims We evaluated the feasibility and the acute performance of the everolimus-eluting bioresorbable vascular scaffolds (BVS) for the treatment of patients presenting with ST-segment elevation myocardial infarction (STEMI).

Methods and results The present investigation is a prospective, single-arm, single-centre study, reporting data after the BVS implantation in STEMI patients. Quantitative coronary angiography and optical coherence tomography (OCT) data were evaluated. Clinical outcomes are reported at the 30-day follow-up. The intent-to-treat population comprises a total of 49 patients. The procedural success was 97.9%. Pre-procedure TIMI-flow was 0 in 50.0% of the patients; after the BVS implantation, a TIMI-flow III was achieved in 91.7% of patients and the post-procedure percentage diameter stenosis was 14.7 $\pm$ 8.2%. No patients had angiographically visible residual thrombus at the end of the procedure. Optical coherence tomography analysis performed in 31 patients showed that the post-procedure mean lumen area was 8.02 $\pm$ 1.92 mm^2, minimum lumen area 5.95 $\pm$ 1.61 mm^2, mean incomplete scaffold apposition area 0.118 $\pm$ 0.162 mm^2, mean intraluminal defect area 0.013 $\pm$ 0.017 mm^2, and mean percentage malapposed struts per patient 2.80 $\pm$ 3.90%. Scaffolds with $>$5% malapposed struts were 7. At the 30-day follow-up, target-lesion failure rate was 0%. Non-target-vessel revascularization and target-vessel myocardial infarction (MI) were reported. A non-target-vessel non-Q-wave MI occurred. No cases of cardiac death or scaffold thrombosis were observed.

Conclusion In the present series, the BVS implantation in patients presenting with acute MI appeared feasible, with high rate of final TIMI-flow III and good scaffold apposition. Larger studies are currently needed to confirm these preliminary data.

Keywords Bioresorbable vascular scaffolds • ST-segment elevation myocardial infarction • Optical coherence tomography

Introduction

Primary percutaneous coronary intervention has been demonstrated to be superior to thrombolytic strategy and is currently the treatment of first choice for patients presenting with ST-segment elevation myocardial infarction (STEMI) in experienced centres with limited time delay.[1] First-generation drug-eluting stents (DES) have been shown to reduce the need for repeat revascularization compared with bare-metal stents (BMS),[2–4] and the newer-generation DES with improved biocompatibility of polymers may lower the rate of clinical events also in acute patients.[5,6] However, the implantation of metal devices is not devoid of important limitations, such as permanent caging of the vessel with permanent impairment of coronary vasomotion, side branch jailing, impossibility of late lumen

*Corresponding author. Tel: +31 10 4635260(33348), Fax: +31 10 4369154, Email: r.vangeuns@erasmusmc.nl

enlargement, non-invasive imaging and future surgical revascularization of stented segments.[7] Moreover, in spite of the beneficial effect of neointimal inhibition, the antiproliferative drug elution has been shown to interfere with the vascular healing processes providing the background for delayed strut coverage and persistent or acquired malapposition.[8,9] The above-mentioned limitations can be proposed for both stable and acute patients; however, primary stenting has additional specific characteristics that should be highlighted. Stent placement in acute thrombotic lesions has been reported to be an independent predictor of late stent malapposition after the BMS[10] or DES[11] implantation. Possible explanations for this phenomenon could be the thrombus sequestration behind the struts—which subsequently resolves—and the vasoconstriction during the acute phase. Both these factors may predispose to stent underdeployment, malapposition and finally to stent thrombosis. The everolimus-eluting bioresorbable vascular scaffold (BVS) has been designed to overcome the general limitations of the metallic stents and recently has been shown to provide excellent results for the treatment of stable patients.[12,13] However, so far very limited data are available on the use of this novel device in patients with acute coronary syndromes (ACS).[14,15] Given this background, a pilot study investigating the feasibility and acute performance of the BVS for the treatment of patients presenting with STEMI was initiated.

Methods

Rationale

As of 1 September 2012, the BVS (ABSORB; Abbott Vascular, Santa Clara, CA, USA) has been commercially available in the Netherlands. Based on previous experience and available evidence, reported in ABSORB Cohort A and B Trial[13,16] our institution initiated the use of BVS for the treatment of patients presenting for PCI in everyday clinical practice, with a preference for patients with a good life expectancy as demonstrated by the presence of limited co-morbidities. As these patients might have more complex lesions compared with the ABSORB study patients[16,17] the BVS-EXPAND registry was initiated. The BVS-EXPAND also included patients with ACS (unstable angina or non-STEMI). After the first experience with ACS patients and an interim analysis, a decision was made to extend BVS utilization to the treatment of STEMI.

As an additional measure for assessing the safety of a treatment approach with BVS in STEMI, optical coherence tomography (OCT) imaging was performed, according to clinical judgement, for a more comprehensive evaluation of the acute procedural outcome.

Study design

The present report is an investigator initiated, prospective, single-arm, single-centre study to assess feasibility and performance of the second-generation everolimus-eluting BVS for the treatment of patients presenting with STEMI.

Subjects enrolled were patients of $\geq$18-year-old admitted with STEMI, defined as at least 1 mm ST-segment elevation in two or more standard leads or at least 2 mm in two or more contiguous precordial leads or new left bundle branch block within 12 h after the onset of symptoms. Culprit lesions were located in vessels within the upper limit of 3.8 mm and the lower limit of 2.0 mm by online quantitative coronary angiography (QCA). The absorb BVS was implanted according to the manufacturer's indication on target-vessel diameter ranges and absorb BVS diameters to be used. The absorb BVS with a nominal diameter of 2.5 mm was implanted in vessels $\geq$2.0 and $\leq$3.0 mm by online QCA; the 3.0 mm BVS was implanted in vessels $\geq$2.5 and $\leq$3.3 mm by online QCA; the 3.5 mm BVS was implanted in vessels $\geq$3.0 and $\leq$3.8 mm. Given the manufacturer's indication on maximum scaffold expansion, for each nominal diameter a further expansion of 0.5 mm was allowed. Enrolled subjects were willing to comply with specified follow-up evaluation and to be contacted by telephone. Exclusion criteria comprise pregnancy, known intolerance to contrast medium, uncertain neurological outcome after cardiopulmonary resuscitation, previous percutaneous coronary intervention with the implantation of a metal stent, left main (LM) disease previous coronary artery bypass grafting (CABG), age superior to 75 years, and participation to another investigational drug or device study before reaching the primary endpoints. The enrolment period started on 1 November 2012 and ended on 30 March 2013. Dual antiplatelet therapy after the BVS implantation was planned to have a duration of 12 months. Baseline and post-BVS implantation QCA analysis, OCT analyses at post-BVS implantation, and clinical outcomes at the 30-day follow-up were evaluated.

Definitions

Success rates were defined as follows: device success was the attainment of $<$30% final residual stenosis of the segment of the culprit lesion covered by the BVS, by angiographic visual estimation. Procedure success was defined as device success and no major periprocedural complications (Emergent CABG, coronary perforation requiring pericardial drainage, residual dissection impairing vessel flow—TIMI-flow II or less). Clinical success was defined as procedural success and no in-hospital major adverse cardiac events (MACE). All deaths were considered cardiac unless an undisputed non-cardiac cause was identified. Myocardial infarction (MI) and scaffold thrombosis were defined according to the Academic Research Consortium definition.[18] Target-lesion revascularization (TLR) was defined as clinically driven if at repeat angiography the diameter stenosis was $>$70%, or if a diameter stenosis $>$50% was present in association with (i) presence of recurrent angina pectoris, related to the target vessel; (ii) objective signs of ischaemia at rest (ECG changes) or during exercise test, related to the target vessel; and (iii) abnormal results of any functional diagnostic test.

The device-oriented endpoint target-lesion failure was defined as the composite of cardiac death, target-vessel MI, or ischaemia-driven TLR. Major adverse cardiac events defined as the composite of cardiac death, any re-infarction (Q- or non-Q-wave), emergent bypass surgery (CABG), or clinically driven TLR. Target-vessel failure (TVF) was defined as cardiac death, target-vessel MI, or clinically driven TVR.

Ethics

This is an observational study, performed according to the privacy policy of the Erasmus MC and to the Erasmus MC regulations for the appropriate use of data in patient-oriented research, which are based on international regulations, including the declaration of Helsinki. The BVS received the CE mark for clinical use, indicated for improving coronary lumen diameter in patients with ischaemic heart disease due to *de novo* native coronary artery lesions with no

restriction in terms of clinical presentation. Therefore, the BVS can be currently used routinely in Europe in different settings comprising the acute MI without a specific written informed consent in addition to the standard informed consent to the procedure. Given this background, a waiver from the hospital Ethical Committee was obtained for written informed consent, as according to Dutch law written consent is not required, if patients are not subject to acts other than as part of their regular treatment.

Study device

The second-generation everolimus-eluting BVS is a balloon expandable device consisting of a polymer backbone of poly-L-lactide acid (PLLA) coated with a thin layer of amorphous matrix of poly-D and -L-lactide acid (PDLLA) polymer (strut thickness 157 μm). The PDLLA controls the release of the antiproliferative drug everolimus (100 μg/cm^2), 80% of which is eluted within the first 30 days. Both PLLA and PDLLA are fully bioresorbable. The polymers are degraded via hydrolysis of the ester bonds and the resulting lactate and its oligomers are metabolized by the Krebs cycles. Small particles (<2 μm in diameter) may be also phagocytized and degraded by macrophages.[19] According to preclinical studies, the time for complete bioresorption of the polymer backbone is ~2–3 years.[20] The BVS edges contain two platinum markers for accurate visualization during angiography or other imaging modalities.

Quantitative coronary angiography analysis

Quantitative coronary angiography (QCA) analyses were performed using the Coronary Angiography Analysis System (Pie Medical Imaging, Maastricht, Netherlands).

Analyses were performed at pre-procedure, after thombectomy, after balloon dilatation, and after the BVS implantation with a methodology already reported.[21]

In case of thrombotic total occlusion, pre-procedure QCA analysis was performed as proximally as possible from the occlusion (in case of a side branch distally to the most proximal take off of the side branch). Intracoronary thrombus was angiographically identified and scored in five grades as previously described.[22] Thrombus grade was assessed before procedure and after thombectomy.

The QCA measurements included reference vessel diameter (RVD)—calculated with interpolate method—percentage diameter stenosis, minimal lumen diameter (MLD), and maximal lumen diameter (D_{max}). Acute gain was defined as post-procedural MLD minus pre-procedural MLD (MLD value equal to zero was applied when culprit vessel was occluded pre-procedurally). Complications occurring any time during the procedure, such as dissection, spasm, distal embolization, and no-reflow were reported. As additional information, MI SYNTAX I and MI SYNTAX II scores providing long-term risk stratification for mortality and MACE in patients presenting with STEMI were assessed.[23]

Optical coherence tomography image acquisition and analysis

Optical coherence tomography imaging after the BVS implantation was encouraged in all patients but was not mandatory, subordinated to device availability and left at the operator's discretion.

Therefore, OCT imaging of the culprit lesion after treatment was performed in a subset of the population. The image acquisition was performed with C7XR imaging console and the Dragonfly intravascular imaging catheter (both St. Jude Medical, St. Paul, MN, USA). Image acquisition has been previously described.[24] Briefly, after positioning the OCT catheter distally to the most distal scaffold marker, the catheter is pulled back automatically at 20 mm/s with simultaneous contrast infusion by a power injector (flush rate 3–4 mL/s). In cases where the entire scaffold region was not imaged in one pullback, a second more proximal pullback was performed for complete visualization. Images were stored and analysed offline.

Analysis of the OCT images was performed with the St Jude/Lightlab offline analysis software (St. Jude Medical), using previously described methodology for BVS analysis.[17] Analysis was performed in 1-mm longitudinal intervals within the treated culprit segment, after exclusion of frames with <75% lumen contour visibility. Lumen, scaffold, and incomplete scaffold apposition (ISA) area were calculated in accordance with standard methodology for analysis of bioresorbable scaffolds[17] (*Figure 1A* and *B*), while in sites with overlapping scaffolds, analysis was performed using previously suggested modifications[25] (*Figure 1D*). Specifically, the lumen contour is traced at the lumen border and in the abluminal (outer) side of apposed struts, while in the case of malapposed struts the contour is traced behind the malapposed struts. In cases where the scaffold struts are completely covered by tissue or thrombus, the lumen contour is traced above the prolapsing tissue (*Figure 1C*). The scaffold area is traced following interpolation of points located in the mid-point of the abluminal border of the black core in apposed struts and the mid-point of the abluminal strut frame border in malapposed or side branch-related struts, so that the scaffold area is identical to the lumen area in the absence of ISA and tissue prolapse. Incomplete scaffold apposition area is traced in the case of malapposed struts as the area delineated between the lumen and scaffold contours (*Figure 1B*).

A special consideration should be mentioned concerning BVS analysis in MI with the presence of increased tissue prolapse and residual thrombus post-implantation[21,26] (*Figures 1C* and *2*). Tissue prolapse area can be quantified as the difference between the scaffold and the lumen area. For the calculation of prolapse area, in the case that one or more scaffold struts are completely covered by thrombus or tissue, the total black core area of these struts is also measured. Prolapse area is then calculated as [scaffold area + ISA area − lumen area − embedded black core area]. The area of non-attached intraluminal defects (e.g. thrombus) is also measured. Atherothrombotic area is then calculated as the sum of prolapse area and intraluminal defect area and normalized as a percent ratio of the scaffold area (atherothrombotic burden, ATB).[21,26] It should be noted that in the case of bioresorbable scaffolds where measurements of the scaffold area are performed using the abluminal side of the scaffold struts, ATB is overestimated compared with metal platform stents where measurements of the stent area are performed from the adluminal (inner) side of the struts. Additionally, flow area was assessed as [scaffold area + ISA area − atherothrombotic area − total strut area] and the minimal flow area was recorded.

A scaffold strut is defined as incompletely apposed when there is no contact between the abluminal border of the strut and the vessel wall. This does not include struts located in front of side branches or their ostium (polygon of confluence region), which are

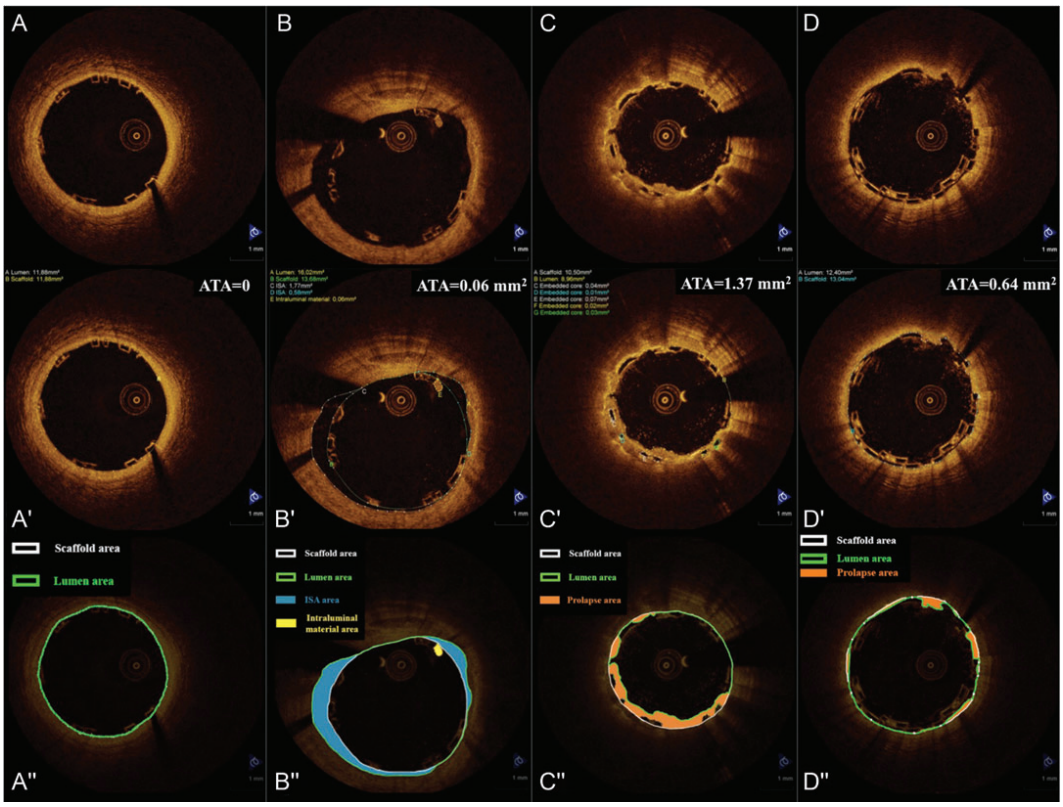

Figure 1 Methodology of optical coherence tomography analysis. (*A*) Good scaffold apposition and absence of incomplete scaffold apposition or tissue prolapse, (*B*) incomplete scaffold apposition, (*C*) sites with high tissue prolapse and struts completely covered by thrombus, and (*D*) overlapping scaffolds. Upper panel shows baseline images, middle panel shows quantitative measurements, and lower panel shows methodology for analysis. ISA, incomplete scaffold apposition; ATA, atherothrombotic area.

defined as side branch-related struts. Intraluminal struts that are part of adjacent clusters of apposed struts in overlapping scaffolds are also not considered malapposed.[25] For illustrative proposes, OCT bi-dimensional images are reported by three-dimensional rendering by dedicated software (Intage Realia, KGT, Kyoto, Japan)[17] (*Figures 2* and *3*).

Statistical analysis

Continuous variables are presented as mean and standard deviation, and categorical variables are reported as count and percentages. Descriptive statistics was provided for all variables. The present study is intended to be a 'first experience investigation' evaluating feasibility and acute performance of the everolimus-eluting BVS for the treatment of patients presenting with STEMI. A patient population of at least 30 patients was planned to be included in the present study. Comparisons among multiple means were performed with analysis of variance (one-way ANOVA). Score (Wilson) confidence intervals were reported for measures of success. Type A intraclass correlation coefficients (ICCs) for absolute agreement were used for assessing intra- and interobserver agreement, while measurement error and 95% limits of agreement were assessed by Bland–Altman analysis. The ICCs were computed with a two-way random effects model (single measures). All statistical tests were performed with SPSS, version 15.0 for windows (IL, USA).

Results

From 1 November 2012 to 30 April 2013, a total of 267 patients presented with acute MI. Twenty-one of those patients were treated percutaneously without any stent implantation (thrombectomy or balloon dilatation alone). Seventy-four had a culprit lesion located in a coronary vessel with a vessel diameter out of the range availability of the BVS (i.e. RVD >4.0 mm). Out of the remaining 172 patients, 125 were meeting the inclusion and none of the exclusion criteria of the present study (47 patients excluded for age, previous PCI or CABG, left main disease). Seventy-six of those patients were treated with metal stents and 49 cases (48 implanted with BVS) were enrolled in the present study (*Figure 4*, *Table 1*). Therefore, the patients implanted with BVS constitute the ~38% of the patients eligible for the present investigation.

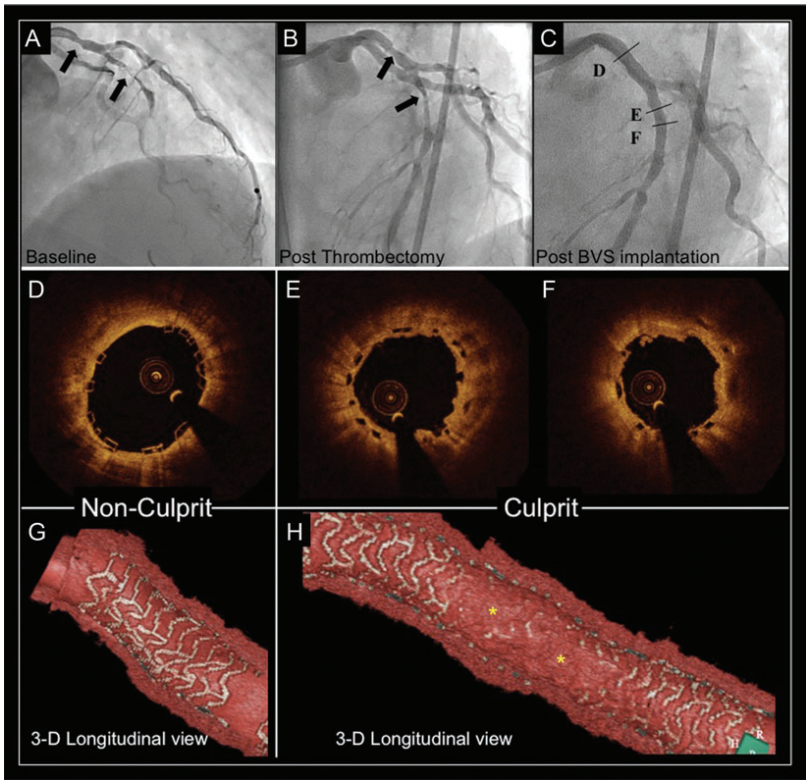

Figure 2 Bioresorbable vascular scaffolds implantation in a culprit and a non-culprit lesion in myocardial infarction. (*A*) Coronary angiography demonstrating a stenotic lesion in proximal LAD (proximal non-culprit lesion) and a total occlusion of the mid-LAD (culprit lesion). (*B*) Angiography following thrombus aspiration. (*C*) Angiography following implantation of a 3.5 × 12 mm bioresorbable vascular scaffolds at the proximal LAD lesion and a 3.0 × 28 mm bioresorbable vascular scaffolds at the mid-LAD lesion. (*D*) Optical coherence tomography image from the proximal non-culprit lesion showing absence of tissue prolapse and thrombus in the 3.5 × 12 mm scaffold. (*E* and *F*) Optical coherence tomography images from the culprit lesion showing complete coverage of the bioresorbable vascular scaffolds by tissue prolapse and presence of small amount of intraluminal defect. (*G*) Three-dimensional optical coherence tomography rendering in the proximal non-culprit lesion with complete scaffold visualization indicating the absence of prolapsing material. (*H*) Conversely, in the three-dimensional rendering of the culprit lesion, the morphology of the bioresorbable vascular scaffolds cannot be fully visualized due to high levels of tissue prolapse (*).

Baseline clinical characteristics of the 172 patients (49 patients included in the intent-to-treat population and 123 patients implanted with metal stents) with vessels size in the range of the BVS availability are reported in *Table 1*. In the intent-to-treat population thirty-eight patients were male (77.6%), mean age was 58.9 ± 10.5 years. Lesions were distributed as follows: left anterior descending 21 (42.9%), right coronary artery 22 (44.9%), and circumflex 6 (12.2%). Baseline clinical data of the enrolled patients were compared with the general population presenting with acute MI and implanted with a metal stent in vessels theoretically suitable for BVS implantation. Minimal differences were observed between the two groups. Namely, age 58.9 ± 10.5 vs. 66.4 ± 12.2, $P < 0.001$ and previous PCI 0% vs. 12.2%, $P = 0.007$. All the other clinical characteristics of the two populations did not show any significant difference.

Mean door-to-balloon time was 31.3 ± 19.5 min. All patients were treated with unfractionated heparin at the dose of 70–100 UI/kg and dual antiplatelet therapy (aspirin plus, prasugrel in 45 patients or clopidogrel in 4 patients). Manual thrombectomy was performed in 38 patients. In 16 cases, direct stenting was performed; a total of 65 scaffolds were implanted (12 patients received overlapping scaffolds—overlap was systematically intended to be minimal). The scaffolds lengths used were 12, 18, and 28 mm, with scaffolds diameters 2.5, 3.0, and 3.5 mm. Mean scaffold length per-lesion was 26.40 ± 13.86 mm, mean scaffold diameter per-lesion was 3.2 ± 34 mm. A highly supportive wire was used in five cases and radial approach was performed in 26 patients (53.0%) (*Table 2*). The procedural success was 97.9% (48/49 patients); in one patient, the delivery of the BVS was unsuccessful (due to the remarkable vessel tortuosity was not

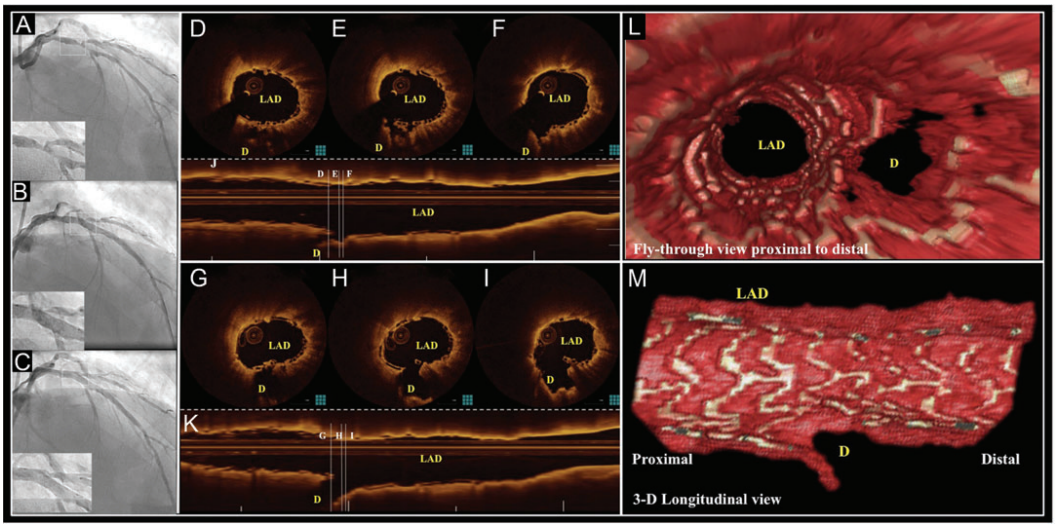

Figure 3 Bioresorbable vascular scaffold implantation in a thrombotic bifurcation lesion treated with provisional approach. (*A*) Coronary angiography pre-intervention. (*B*) Angiography following bioresorbable vascular scaffold implantation in the LAD, showing pinching of the ostium of the diagonal (D). (*C*) Final angiographic result following side branch dilation with 2.0 × 15 mm balloon. (*D–F* and *J*) Optical coherence tomography cross-sectional images and l-mode after bioresorbable vascular scaffolds implantation showing the compromise of the side branch after implantation and presence of thrombus at the side branch ostium. (*G–I* and *K*) Optical coherence tomography cross-sectional images and l-mode after side branch dilation, showing the opening of the carina of the side branch. (*L* and *M*) Three-dimensional reconstructions confirm the opening of the side branch ostium.

possible to advance the BVS at the site of the lesion) and a metallic DES was implanted. Clinical success was 97.9% (48/49 patients).

Quantitative coronary angiography analysis

The QCA is reported only in patients implanted with BVS. In 50.0% of those patients, pre-procedure TIMI-flow was 0 and the RVD was 2.94 ± 0.77 mm. In the non-totally occluded vessels, the RVD was 2.62 ± 0.63 mm, with an MLD of 0.75 ± 0.44 mm and a mean diameter stenosis of 70.8 ± 12.5%. After thrombectomy and balloon dilatation, TIMI-flow grade 0 was present in 2.5 and 0.0% of patients, respectively, and TIMI-flow III in 52.5 and 59.3% of the cases, respectively. After the scaffold implantation, there were no cases of TIMI-flow 0, and a TIMI-flow III was achieved in 91.7% of patients, the mean post-procedure in-scaffold % diameter stenosis was 14.7 ± 8.2%, in-scaffold MLD was 2.44 ± 0.49 mm (*Table 3*). No angiographically visible residual thrombus was observed at post-procedure.

Optical coherence tomography findings

Optical coherence tomography analysis was performed in a subgroup of 31 patients implanted with BVS. Mean lumen area was 8.02 ± 1.92 mm^2, minimum lumen area 5.95 ± 1.61 mm^2, and minimum flow area 5.62 ± 1.66 mm^2. Incomplete scaffold apposition (ISA) was observed in 20 patients with a mean ISA area of 0.118 ± 0.162 mm^2 and a mean percentage of malapposed struts per patients equal to 2.80 ± 3.90%. The mean prolapse area was 0.60 ± 0.26 mm^2, and the mean intraluminal defect area was 0.013 ± 0.017 mm^2. Scaffolds with >5% malapposed struts were 7 (*Table 4*). The OCT analysis stratified by scaffold size (5 BVS 2.5 mm, 13 BVS 3.0 mm, 24 BVS 3.5 mm) showed different lumen, scaffold, and flow areas, but similar amounts of incomplete stent apposition, plaque prolapse, and intraluminal mass areas (*Table 5*). In three cases, the observation of scaffold malapposition by OCT, guided an additional post-dilatation and in one patient the visualization of considerable intraluminal thrombus as assessed by OCT led to a repeated thrombus aspiration.

Intra-observer variability was excellent. Intraclass correlation coefficients were 0.999 for lumen area and 0.999 for scaffold area, and the corresponding measurement errors and limits of agreement were 0.01 mm^2 (−0.12 to 0.15 mm^2) for lumen area and −0.01 mm^2 (−0.20 to 0.17 mm^2) for scaffold area. Similarly, inter-observer intraclass correlation coefficients were 0.997 for lumen area and 0.987 for scaffold area, and the corresponding measurement errors and limits of agreement were −0.01 mm^2 (−0.30 to 0.28 mm^2) for lumen area and −0.22 mm^2 (−0.68 to 0.24 mm^2) for scaffold area.

Clinical outcomes

At the 30-day follow-up, the rate of the device-oriented endpoint, target-lesion failure, was 0%. None of the patients experienced target-vessel re-infarction, emergent bypass surgery, or clinically driven TLR. No cases of cardiac death or scaffold thrombosis were reported. The MACE rate was 2.6% as one patient, after discharge developed a non-Q-wave MI related to a non-target-vessel lesion and underwent a non-target-vessel revascularization within the

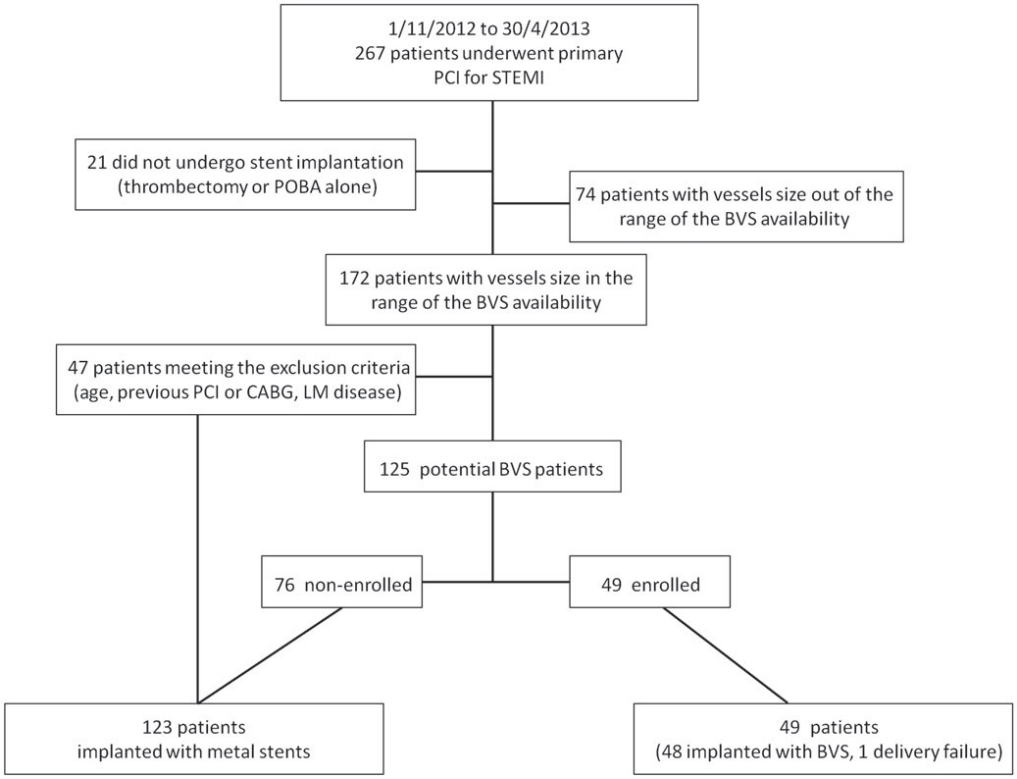

Figure 4 Flow-chart of the study. From 1 November 2012 to 30 April 2013, a total of 267 patients presented with acute myocardial infarction. Twenty-one of those patients were treated percutaneously but without any stent implantation (thrombectomy or balloon dilatation alone). Seventy-four had a culprit lesion located in a coronary vessel with a vessel diameter out of the range availability of the bioresorbable vascular scaffolds (i.e. reference vessel diameter >4.0 mm). Out of the remaining 172 patients, 125 were meeting the inclusion and none of the exclusion criteria of the present study (47 patients excluded for age, previous PCI or CABG, left main disease). Seventy-six of those patients were treated with metal stents and 49 cases (48 implanted with BVS) were included in the present study.

30 days post-procedure. This was the only event reported in the studied population (*Table 6*).

Discussion

The everolimus-eluting BVS has been tested so far only in elective patients with stable, unstable angina, or silent ischaemia;[16,17,27–29] showing promising results up to 4-year follow-up[30] for the first-generation and up to 2 years for the second-generation BVS.[12,13,31] The present study represents an early investigation reporting clinical and angiographic data on the use of the second-generation BVS for the treatment of patients presenting with STEMI and evaluating acute results with high-resolution intracoronary imaging (OCT).

A high device, procedural, and clinical success rates were observed with all the scaffolds achieving a residual stenosis <30% and no in-hospital MACE. Such data are supportive of feasibility and good acute performance of the BVS for the treatment of patients with acute MI.

Angiographic data

The everolimus-eluting BVS was implanted in patients presenting with ST-segment elevation and a thrombus burden 4 or 5 in 63.0% of the cases. A theoretical concern related to the implantation of the BVS in such thrombotic lesions is the fact that scaffold positioning and placement may need a more aggressive lesion preparation (pre-dilatation) compared with standard metal devices, due to its slightly higher profile. We hypothesized that this strategy might be prone to an increase in distal embolization following balloon inflations, favouring no-reflow and reducing the rate of final TIMI-flow III.

However, the analysis of the post-procedural angiographies revealed a TIMI-flow III in 91.7% of the cases; such results are in line with recently reported large trials evaluating the performance of metallic stents in patients presenting with acute MI.[5,6] Less thrombus embolization may result from a different pattern of thrombus dislodgment and compression to the arterial wall after deployment of a device with a larger strut width (157 μm) compared with currently available metallic stents. The percentage of vessel wall area

Table 1 **Baseline clinical characteristics intent-to-treat population and patients treated with metallic stent in the enrolment period**

Clinical characteristics	BVS (*N* = 49)	Metal stents (*N* = 123)	*P*-value
Age (year)	58.9 ± 10.5	66.4 ± 12.2	<0.001
Male, *n* (%)	38 (77.6)	93 (75.6)	0.845
Hypertension, *n* (%)	19 (38.8)	53/105 (50.5)	0.225
Hypercholesterolemia, *n* (%)	11 (22.4)	30/100 (30.0)	0.435
Diabetes, *n* (%)	4 (8.2)	14/116 (12.1)	0.590
Smoke, *n* (%)	27 (69.2)	46/116 (39.7)	0.120
Family history of CAD, *n* (%)	12 (24.5)	31/95 (32.6)	0.343
Peripheral vascular disease, *n* (%)	1 (2.0)	8 (6.5)	0.449
Kidney disease, *n* (%)	1 (2.0)	7 (5.7)	0.442
Prior MI, *n* (%)	1 (2.0)	14 (11.4)	0.070
Prior PCI, *n* (%)	0 (0.0)	15 (12.2)	0.007
Prior CABG, *n* (%)	0 (0.0)	3 (2.4)	0.559
COPD, *n* (%)	2 (4.1)	5 (4.1)	1.000
Culprit vessel			0.624
LM, *n* (%)	0 (0)	2 (1.6)	
LAD, *n* (%)	21 (42.9)	52 (42.3)	
RCA, *n* (%)	22 (44.9)	46 (37.4)	
LCX, *n* (%)	6 (12.2)	21 (17.1)	
SVG, *n* (%)	0 (0)	2 (1.6)	

Patients with vessels diameters not feasible for BVS implantation (i.e. reference vessel diameter ≥4.0 mm) were excluded.
Data are expressed as mean ± SD or number and proportion, *n* (%).
CAD, coronary artery disease; MI, myocardial infarction; PCI, percutaneous coronary intervention; CABG, coronary artery bypass graft; COPD, chronic obstructive pulmonary disease; LM, left main; LAD, left anterior descending; RCA, right coronary artery; LCX, circumflex; SVG, saphenous vein graft.

Table 2 **Procedural data intent-to-treat population**

Procedural data	*N* = 49
Medications	
Aspirin, *n* (%)	49 (100)
Prasugrel, *n* (%)	45 (91.8)
Clopidogrel, *n* (%)	4 (8.2)
Glycoprotein IIb/IIIa antagonists, *n* (%)	17 (34.7)
Unfractionated heparin, *n* (%)	49 (100)
Mean door-to-balloon time (min)	31.3 ± 19.5
Manual thrombectomy, *n* (%)	38 (77.5)
Direct stenting, *n* (%)	16 (32.7)
Pre-dilatation, *n* (%)	33 (67.3)
Mean pre-dilatation balloon diameter per-lesion (mm)	2.6 ± 0.67
Post-dilatation, *n* (%)	10 (20.4)
Mean post-dilatation balloon diameter per-lesion (mm)	3.5 ± 0.47
Overlapping, *n* (%)	12 (24.5)
Overlap scaffolds diameters 3.5 mm–3.5 mm, *n* (%)	5 (10.2)
Overlap scaffolds diameters 3.5 mm – 3 mm *n* (%)	5 (10.2)
Overlap scaffolds diameters 3.5 mm–2.5 mm, *n* (%)	1 (2.0)
Overlap scaffolds diameters, 3 mm–2.5 mm, *n* (%)	1 (2.0)
Total number of scaffolds, *n*.	65
Mean scaffolds per-lesion, *n*.	1.35 ± 0.60
Mean scaffold length per-lesion (mm)	26.40 ± 13.86
Mean scaffold diameter per-lesion (mm)	3.2 ± 34
Supportive wire, *n*. (%)	5 (10.2)
Radial approach, *n*. (%)	26 (53.0)

Data are expressed as mean ± SD or number and proportion, *n* (%).

covered by the BVS polymer (scaffold/vessel ratio) has been previously evaluated to be 26%,[32] a value considerably higher compared with what observed for conventional metallic DES (i.e. EES provides a percentage stent/vessel ratio equal to 12%).[32] This characteristic of the BVS might be associated to an increased capacity of capturing debris and thrombotic material behind the struts before embolization to distal microcirculation. This so-called snow racket concept (entrapment of thrombotic material between the stent and the vessel) is currently the basis for the design of novel devices and clinical studies.[33]

Optical coherence tomography findings

Given its high resolution, OCT allows the assessment of *in vivo* strut apposition and presence of thrombus.[24,34–36]

The present analysis was performed at 1 mm intervals in the OCT pullback. Although, the possibility for a more strict assessment of OCT analysis in thrombotic lesion may be considered,[21] this methodology is the current standard applied in our institution for clinical studies, and the most commonly used in the literature.

Previous reports defined a stent malapposed if at least 5% of struts were observed to be malapposed;[37,38] in the present investigation, only seven scaffolds (22.6%) investigated with OCT showed a strut malapposition of >5%, with an overall mean struts malapposition equal to 2.8 ± 3.90%. A recently reported study using a similar methodology to investigate malapposition after metallic balloon expandable stent implantation in STEMI patients showed a total of 37.1% malapposed stents (stents with >5% malapposition) with a mean percentage of strut malapposition equal to 5.99 ± 7.28%.[38] In addition, the mean ISA area was 0.118 ± 0.162 mm^2, a value in line with data reported for metallic stent implantation in patients presenting with STEMI.[21,38] Similarly, the amount of intraluminal defect after scaffold implantation was minimal and comparable with what is observed in metallic stents.[21] Notably, these results were consistent among different scaffold sizes.

Clinical outcomes

In the present series, none of patients treated with BVS experienced a clinical event related to the treated vessel at the 30-day follow-up. These observations support the feasibility of BVS implantation in patients presenting with acute STEMI.

Table 3 Angiographic analysis in patients implanted with bioresorbable vascular scaffolds

Angiographic data	*N* = 48
Pre-procedure	
TIMI-flow, % (*n*)	
0	50.0% (23/46)
1	15.2% (7/46)
2	21.7% (10/46)
3	13.0% (6/46)
Thrombus burden, % (*n*)	
0	0.0% (0/46)
1	6.5% (3/46)
2	17.4% (8/46)
3	13.0% (6/46)
4	13.0% (6/46)
5	50.0% (23/46)
Total occlusion (*N* = 23)	
RVD (mm)	2.94 ± 0.77
Non-total occlusion (*N* = 23)	
RVD (mm)	2.62 ± 0.63
MLD (mm)	0.75 ± 0.44
Diameter stenosis (%)	70.8 ± 12.5
After thrombectomy	
TIMI-flow, % (*n*)	
0	2.5% (1/40)
1	7.5% (3/40)
2	37.5% (15/40)
3	52.5% (21/40)
Thrombus burden, % (*n*)	
0	0.0% (0/40)
1	30.0% (12/40)
2	35.0% (14/40)
3	22.5% (9/40)
4	10.0% (4/40)
5	2.5% (1/40)
After pre-dilatation	
TIMI-flow, % (*n*)	
0	0.0% (0/27)
1	7.4% (2/27)
2	33.3% (9/27)
3	59.3% (16/27)
Before BVS implantation	
RVD (mm)	2.63 ± 0.53
MLD (mm)	1.21 ± 0.46
Diameter stenosis (%)	53.2 ± 16.1
D_{max} (mm)	3.01 ± 0.52
Post-procedure	
TIMI-flow, % (*n*)	
0	0.0% (0/48)
1	0.0% (0/48)
2	8.3% (4/48)
3	91.7% (44/48)
In-scaffold	
RVD (mm)	2.86 ± 0.52
MLD (mm)	2.44 ± 0.49
Diameter stenosis (%)	14.7 ± 8.2
In-segment	
RVD (mm)	2.74 ± 0.59
MLD (mm)	2.20 ± 0.53
Diameter stenosis (%)	21.8 ± 12.0
MI syntax score I[a]	10.0 (7.0–15.0)
MI syntax score II[a]	7.0 (4.25–10.0)
Dominant right coronary artery, % (*n*)	93.8% (45/48)
Scaffold-to-artery ratio	1.19 ± 0.24
Complications occurring any time during the procedure, % (*n*)	
Dissection	6.3% (3/48)
Spasm	4.2% (2/48)
Distal embolism	14.6% (7/48)
No-reflow	2.1% (1/48)

Data are expressed as mean ± SD or proportion (%).
[a]MI syntax scores I and II are expressed as median (interquartile range).

Table 4 Optical coherence tomography findings post-implantation in patients implanted with bioresorbable vascular scaffolds

OCT variables	*N* = 31
Analysed length (mm)	28.16 ± 13.29
Analysed struts, *n*	245 ± 135
Minimum lumen area (mm^2)	5.95 ± 1.61
Mean lumen area (mm^2)	8.02 ± 1.92
Lumen volume (mm^3)	225.78 ± 113.63
Minimum scaffold area (mm^2)	6.69 ± 1.94
Mean scaffold area (mm^2)	8.54 ± 1.97
Scaffold volume (mm^3)	240.07 ± 118.48
Minimum flow area (mm^2)	5.62 ± 1.66
ISA area (mm^2) (*N* = 20)	0.118 ± 0.162
Mean prolapse area (mm^2)	0.60 ± 0.26
Mean intraluminal defect area (mm^2)	0.013 ± 0.017
Maximum intraluminal defect area (mm^2)	0.094 ± 0.077
Mean atherothrombotic area (mm^2)	0.61 ± 0.27
Mean atherothrombotic burden (%)	7.29 ± 3.12
Malapposed struts per patient (%)	2.80 ± 3.90
Scaffolds with at least 1 malapposed strut, *n* (%)	20 (64.5)
Scaffolds with >5% malapposed struts, *n* (%)	7 (22.6)

ISA, incomplete scaffold apposition.
Data are expressed as mean ± SD or number and proportion, *n* (%).

Table 5 **Optical coherence tomography findings post-implantation stratified by scaffold size in patients implanted with bioresorbable vascular scaffolds**

OCT variables				
Scaffold size	**2.5 mm (*N* = 5)**	**3.0 mm (*N* = 13)**	**3.5 mm (*N* = 24)**	***P***
Analysed length (mm)	18.80 ± 1.30	22.23 ± 6.46	21.33 ± 7.38	0.628
Minimum lumen area (mm^2)	4.08 ± 0.24	5.60 ± 0.93	7.18 ± 1.58	0.001
Mean lumen area (mm^2)	5.42 ± 0.75	7.18 ± 1.03	9.25 ± 1.72	0.001
Minimum scaffold area (mm^2)	4.53 ± 0.51	6.13 ± 1.02	8.06 ± 1.82	0.001
Mean scaffold area (mm^2)	5.62 ± 0.28	7.66 ± 0.88	9.82 ± 1.70	0.001
Minimum flow area (mm^2)	3.84 ± 0.28	5.17 ± 0.86	6.77 ± 1.60	0.001
ISA area (mm^2) (*N* = 25)	0.190 ± 0.318 (*N* = 3)	0.063 ± 0.072 (*N* = 10)	0.133 ± 0.177 (*N* = 12)	0.429
Mean prolapse area (mm^2)	0.40 ± 0.19	0.54 ± 0.27	0.62 ± 0.29	0.246
Mean intraluminal defect area (mm^2)	0.007 ± 0.008	0.016 ± 0.021	0.012 ± 0.018	0.628
Maximum intraluminal defect area (mm^2)	0.072 ± 0.081	0.102 ± 0.086	0.068 ± 0.065	0.096
Mean atherothrombotic area (mm^2)	0.40 ± 0.19	0.56 ± 0.27	0.64 ± 0.30	0.237
Mean atherothrombotic burden (%)	6.00 ± 4.66	7.42 ± 3.79	6.20 ± 3.39	0.594

ISA, incomplete scaffold apposition.
Data are expressed as mean ± SD or number and proportion, *n* (%).

Table 6 **Clinical outcomes at the 30-day follow-up intent-to-treat population**

Clinical events	*N* = 49	95% CI
Target-lesion failure	(0/49) 0%	(0–7.41)
TVF	(0/49) 0%	(0–7.41)
Cardiac death	(0/49) 0%	(0–7.41)
Target-vessel MI	(0/49) 0%	(0–7.41)
Q-wave MI	(0/49) 0%	(0–7.41)
Non Q-wave MI	(0/49) 0%	(0–7.41)
Clinically driven target-vessel revascularization	(0/49) 0%	(0–7.41)
Any MI	(1/49) 2.6%	(0–10.69)
Q-wave MI	(0/49) 0%	(0–7.41)
Non Q-wave MI	(1/49) 2.6%	(0–10.69)
Major adverse cardiac events	(1/49) 2.6%	(0–10.69)
Non-target-vessel revascularization	(1/49) 2.6%	(0–10.69)
Definite or probable scaffold thrombosis	(0/49) 0%	(0–7.41)

Data are expressed number and proportion, *n* (%). 95% CI, 95% confidence interval.

Data showed in the present report with optimal acute performance in terms of final TIMI-flow and scaffold apposition may suggest that everolimus-eluting BVS could be considered for the treatment of patients presenting with STEMI, however, due to the limited number of patients and events, caution should be made in reaching firm conclusions. Further larger studies are needed to fully evaluate the performance of the present device in STEMI patients.

Limitations

The present study represents a feasibility study with a limited number of patients. The small sample size does not allow reaching conclusions in terms of clinical outcomes. The lack of a head-to-head comparison with the current standard of care is a major limitation of the present study. A longer follow-up is needed to fully evaluate the performance of this novel device in patients presenting with acute MI. During the enrolment period, the implantation of either metallic stent or BVS in STEMI patients was left to the operator's discretion; this methodology may be prone to selection bias. Therefore, these data should not stimulate at the current state of knowledge the use of BVS in patients presenting with acute MI. Larger randomized studies are needed to confirm these preliminary observations.

Conclusion

In the present investigation, the implantation of the everolimus-eluting BVS was observed to be feasible in patients presenting with STEMI with optimal acute performance. These data are preliminary and need further confirmation in randomized controlled trials to define the true role of BVS for the treatment of patients presenting with acute myocardial infarction.

Funding

Conflict of interest: Dr R.J. van Geuns received speakers fee from Abbott Vascular. Abbott Vascular is providing institution research grant for the Erasmus MC. Antonios Karanasos received funding support from the Hellenic Heart Foundation and St Jude Medical.

References

1. Task Force on Myocardial Revascularization of the European Society of C, the European Association for Cardio-Thoracic S, European Association for Percutaneous

Cardiovascular I, Wijns W, Kolh P, Danchin N, Di Mario C, Falk V, Folliguet T, Garg S, Huber K, James S, Knuuti J, Lopez-Sendon J, Marco J, Menicanti L, Ostojic M, Piepoli MF, Pirlet C, Pomar JL, Reifart N, Ribichini FL, Schalij MJ, Sergeant P, Serruys PW, Silber S, Sousa Uva M, Taggart D. Guidelines on myocardial revascularization. *Eur Heart J* 2010;**31**:2501–2555.

2. Spaulding C, Henry P, Teiger E, Beatt K, Bramucci E, Carrie D, Slama MS, Merkely B, Erglis A, Margheri M, Varenne O, Cebrian A, Stoll HP, Snead DB, Bode C, Investigators T. Sirolimus-eluting versus uncoated stents in acute myocardial infarction. *N Engl J Med* 2006;**355**:1093–1104.
3. Stone GW, Lansky AJ, Pocock SJ, Gersh BJ, Dangas G, Wong SC, Witzenbichler B, Guagliumi G, Peruga JZ, Brodie BR, Dudek D, Mockel M, Ochala A, Kellock A, Parise H, Mehran R, Investigators H-AT. Paclitaxel-eluting stents versus bare-metal stents in acute myocardial infarction. *N Engl J Med* 2009;**360**:1946–1959.
4. Brar SS, Leon MB, Stone GW, Mehran R, Moses JW, Brar SK, Dangas G. Use of drug-eluting stents in acute myocardial infarction: a systematic review and meta-analysis. *J Am Coll Cardiol* 2009;**53**:1677–1689.
5. Raber L, Kelbaek H, Ostojic M, Baumbach A, Heg D, Tuller D, von Birgelen C, Roffi M, Moschovitis A, Khattab AA, Wenaweser P, Bonvini R, Pedrazzini G, Kornowski R, Weber K, Trelle S, Luscher TF, Taniwaki M, Matter CM, Meier B, Juni P, Windecker S, Investigators CAT. Effect of biolimus-eluting stents with biodegradable polymer vs bare-metal stents on cardiovascular events among patients with acute myocardial infarction: the COMFORTABLE AMI randomized trial. *JAMA* 2012; **308**:777–787.
6. Sabate M, Cequier A, Iniguez A, Serra A, Hernandez-Antolin R, Mainar V, Valgimigli M, Tespili M, den Heijer P, Bethencourt A, Vazquez N, Gomez-Hospital JA, Baz JA, Martin-Yuste V, van Geuns RJ, Alfonso F, Bordes P, Tebaldi M, Masotti M, Silvestro A, Backx B, Brugaletta S, van Es GA, Serruys PW. Everolimus-eluting stent versus bare-metal stent in ST-segment elevation myocardial infarction (EXAMINATION): 1 year results of a randomised controlled trial. *Lancet* 2012;**380**:1482–1490.
7. Serruys PW, Garcia-Garcia HM, Onuma Y. From metallic cages to transient bioresorbable scaffolds: change in paradigm of coronary revascularization in the upcoming decade? *Eur Heart J* 2012;**33**:16–25b.
8. Finn AV, Joner M, Nakazawa G, Kolodgie F, Newell J, John MC, Gold HK, Virmani R. Pathological correlates of late drug-eluting stent thrombosis: strut coverage as a marker of endothelialization. *Circulation* 2007;**115**:2435–2441.
9. Joner M, Finn AV, Farb A, Mont EK, Kolodgie FD, Ladich E, Kutys R, Skorija K, Gold HK, Virmani R. Pathology of drug-eluting stents in humans: delayed healing and late thrombotic risk. *J Am Coll Cardiol* 2006;**48**:193–202.
10. Hong MK, Mintz GS, Lee CW, Kim YH, Lee SW, Song JM, Han KH, Kang DH, Song JK, Kim JJ, Park SW, Park SJ. Incidence, mechanism, predictors, and long-term prognosis of late stent malapposition after bare-metal stent implantation. *Circulation* 2004;**109**: 881–886.
11. Hong MK, Mintz GS, Lee CW, Park DW, Park KM, Lee BK, Kim YH, Song JM, Han KH, Kang DH, Cheong SS, Song JK, Kim JJ, Park SW, Park SJ. Late stent malapposition after drug-eluting stent implantation: an intravascular ultrasound analysis with long-term follow-up. *Circulation* 2006;**113**:414–419.
12. Ormiston JA, Serruys PW, Onuma Y, van Geuns RJ, de Bruyne B, Dudek D, Thuesen L, Smits PC, Chevalier B, McClean D, Koolen J, Windecker S, Whitbourn R, Meredith I, Dorange C, Veldhof S, Hebert KM, Rapoza R, Garcia-Garcia HM. First serial assessment at 6 months and 2 years of the second generation of absorb everolimus-eluting bioresorbable vascular scaffold: a multi-imaging modality study. *Circ Cardiovasc Interv* 2012;**5**:620–632.
13. Serruys PW, Onuma Y, Dudek D, Smits PC, Koolen J, Chevalier B, de Bruyne B, Thuesen L, McClean D, van Geuns RJ, Windecker S, Whitbourn R, Meredith I, Dorange C, Veldhof S, Hebert KM, Sudhir K, Garcia-Garcia HM, Ormiston JA. Evaluation of the second generation of a bioresorbable everolimus-eluting vascular scaffold for the treatment of de novo coronary artery stenosis: 12-month clinical and imaging outcomes. *J Am Coll Cardiol* 2011;**58**:1578–1588.
14. Kajiya T, Liang M, Sharma RK, Lee CH, Chan MY, Tay E, Chan KH, Tan HC, Low AF. Everolimus-eluting bioresorbable vascular scaffold (BVS) implantation in patients with ST-segment elevation myocardial infarction (STEMI). *EuroIntervention* 2013;**9**: 501–504.
15. Kocka V, Lisa L, Tousek P, Budesinsky T, Widimsky P. ST elevation myocardial infarction treated with bioresorbable vascular scaffold: rationale and first cases. *Eur Heart J* 2013;**34**:2073.
16. Ormiston JA, Serruys PW, Regar E, Dudek D, Thuesen L, Webster MW, Onuma Y, Garcia-Garcia HM, McGreevy R, Veldhof S. A bioabsorbable everolimus-eluting coronary stent system for patients with single de-novo coronary artery lesions (ABSORB): a prospective open-label trial. *Lancet* 2008;**371**:899–907.
17. Serruys PW, Onuma Y, Ormiston JA, de Bruyne B, Regar E, Dudek D, Thuesen L, Smits PC, Chevalier B, McClean D, Koolen J, Windecker S, Whitbourn R, Meredith I, Dorange C, Veldhof S, Miquel-Hebert K, Rapoza R, Garcia-Garcia HM. Evaluation of the second generation of a bioresorbable everolimus drug-eluting vascular scaffold for treatment of de novo coronary artery stenosis: six-month clinical and imaging outcomes. *Circulation* 2010;**122**:2301–2312.
18. Cutlip DE, Windecker S, Mehran R, Boam A, Cohen DJ, van Es GA, Steg PG, Morel MA, Mauri L, Vranckx P, McFadden E, Lansky A, Hamon M, Krucoff MW, Serruys PW, Academic Research C. Clinical end points in coronary stent trials: a case for standardized definitions. *Circulation* 2007;**115**:2344–2351.
19. Onuma Y, Serruys PW. Bioresorbable scaffold: the advent of a new era in percutaneous coronary and peripheral revascularization? *Circulation* 2011;**123**:779–797.
20. Onuma Y, Serruys PW, Perkins LE, Okamura T, Gonzalo N, Garcia-Garcia HM, Regar E, Kamberi M, Powers JC, Rapoza R, van Beusekom H, van der Giessen W, Virmani R. Intracoronary optical coherence tomography and histology at 1 month and 2, 3, and 4 years after implantation of everolimus-eluting bioresorbable vascular scaffolds in a porcine coronary artery model: an attempt to decipher the human optical coherence tomography images in the ABSORB trial. *Circulation* 2010;**122**:2288–2300.
21. Onuma Y, Thuesen L, van Geuns RJ, van der Ent M, Desch S, Fajadet J, Christiansen E, Smits P, Ramsing Holm N, Regar E, van Mieghem N, Borovicanin V, Paunovic D, Senshu K, van Es GA, Muramatsu T, Lee IS, Schuler G, Zijlstra F, Garcia-Garcia HM, Serruys PW, Investigators T. Randomized study to assess the effect of thrombus aspiration on flow area in patients with ST-elevation myocardial infarction: an optical frequency domain imaging study – TROFI trial. *Eur Heart J* 2013;**34**:1050–1060.
22. Sianos G, Papafaklis MI, Daemen J, Vaina S, van Mieghem CA, van Domburg RT, Michalis LK, Serruys PW. Angiographic stent thrombosis after routine use of drug-eluting stents in ST-segment elevation myocardial infarction: the importance of thrombus burden. *J Am Coll Cardiol* 2007;**50**:573–583.
23. Magro M, Nauta S, Simsek C, Onuma Y, Garg S, van der Heide E, van der Giessen WJ, Boersma E, van Domburg RT, van Geuns RJ, Serruys PW. Value of the SYNTAX score in patients treated by primary percutaneous coronary intervention for acute ST-elevation myocardial infarction: The MI SYNTAXscore study. *Am Heart J* 2011;**161**:771–781.
24. Tearney GJ, Regar E, Akasaka T, Adriaenssens T, Barlis P, Bezerra HG, Bouma B, Bruining N, Cho JM, Chowdhary S, Costa MA, de Silva R, Dijkstra J, Di Mario C, Dudek D, Falk E, Feldman MD, Fitzgerald P, Garcia-Garcia HM, Gonzalo N, Granada JF, Guagliumi G, Holm NR, Honda Y, Ikeno F, Kawasaki M, Kochman J, Koltowski L, Kubo T, Kume T, Kyono H, Lam CC, Lamouche G, Lee DP, Leon MB, Maehara A, Manfrini O, Mintz GS, Mizuno K, Morel MA, Nadkarni S, Okura H, Otake H, Pietrasik A, Prati F, Raber L, Radu MD, Rieber J, Riga M, Rollins A, Rosenberg M, Sirbu V, Serruys PW, Shimada K, Shinke T, Shite J, Siegel E, Sonoda S, Suter M, Takarada S, Tanaka A, Terashima M, Thim T, Uemura S, Ughi GJ, van Beusekom HM, van der Steen AF, van Es GA, van Soest G, Virmani R, Waxman S, Weissman NJ, Weisz G, International Working Group for Intravascular Optical Coherence T. Consensus standards for acquisition, measurement, and reporting of intravascular optical coherence tomography studies: a report from the International Working Group for Intravascular Optical Coherence Tomography Standardization and Validation. *J Am Coll Cardiol* 2012;**59**:1058–1072.
25. Farooq V, Onuma Y, Radu M, Okamura T, Gomez-Lara J, Brugaletta S, Gogas BD, van Geuns RJ, Regar E, Schultz C, Windecker S, Lefevre T, Brueren BR, Powers J, Perkins LL, Rapoza RJ, Virmani R, Garcia-Garcia HM, Serruys PW. Optical coherence tomography (OCT) of overlapping bioresorbable scaffolds: from benchwork to clinical application. *EuroIntervention* 2011;**7**:386–399.
26. Magro M, Regar E, Gutierrez-Chico JL, Garcia-Garcia H, Simsek C, Schultz C, Zijlstra F, Serruys PW, van Geuns RJ. Residual atherothrombotic material after stenting in acute myocardial infarction – an optical coherence tomographic evaluation. *Int J Cardiol* 2013;**167**:656–663.
27. Serruys PW, Ormiston JA, Onuma Y, Regar E, Gonzalo N, Garcia-Garcia HM, Nieman K, Bruining N, Dorange C, Miquel-Hebert K, Veldhof S, Webster M, Thuesen L, Dudek D. A bioabsorbable everolimus-eluting coronary stent system (ABSORB): 2-year outcomes and results from multiple imaging methods. *Lancet* 2009;**373**:897–910.
28. Diletti R, Onuma Y, Farooq V, Gomez-Lara J, Brugaletta S, van Geuns RJ, Regar E, de Bruyne B, Dudek D, Thuesen L, Chevalier B, McClean D, Windecker S, Whitbourn R, Smits P, Koolen J, Meredith I, Li D, Veldhof S, Rapoza R, Garcia-Garcia HM, Ormiston JA, Serruys PW. 6-month clinical outcomes following implantation of the bioresorbable everolimus-eluting vascular scaffold in vessels smaller or larger than 2.5 mm. *J Am Coll Cardiol* 2011;**58**:258–264.
29. Diletti R, Serruys PW, Farooq V, Sudhir K, Dorange C, Miquel-Hebert K, Veldhof S, Rapoza R, Onuma Y, Garcia-Garcia HM, Chevalier B. ABSORB II randomized controlled trial: a clinical evaluation to compare the safety, efficacy, and performance of the absorb everolimus-eluting bioresorbable vascular scaffold system against the XIENCE everolimus-eluting coronary stent system in the treatment of subjects with ischemic heart disease caused by de novo native coronary artery lesions: rationale and study design. *Am Heart J* 2012;**164**:654–663.
30. Dudek D, Onuma Y, Ormiston JA, Thuesen L, Miquel-Hebert K, Serruys PW. Four-year clinical follow-up of the ABSORB everolimus-eluting bioresorbable vascular scaffold in patients with de novo coronary artery disease: the ABSORB trial. *EuroIntervention* 2012;**7**:1060–1061.

31. Diletti R, Farooq V, Girasis C, Bourantas C, Onuma Y, Heo JH, Gogas BD, van Geuns RJ, Regar E, de Bruyne B, Dudek D, Thuesen L, Chevalier B, McClean D, Windecker S, Whitbourn RJ, Smits P, Koolen J, Meredith I, Li X, Miquel-Hebert K, Veldhof S, Garcia-Garcia HM, Ormiston JA, Serruys PW. Clinical and intravascular imaging outcomes at 1 and 2 years after implantation of absorb everolimus eluting bioresorbable vascular scaffolds in small vessels. Late lumen enlargement: does bioresorption matter with small vessel size? Insight from the ABSORB cohort B trial. *Heart* 2013;**99**:98–105.
32. Muramatsu T, Onuma Y, Garcia-Garcia HM, Farooq V, Bourantas CV, Morel MA, Li X, Veldhof S, Bartorelli A, Whitbourn R, Abizaid A, Serruys PW, Investigators A-E. Incidence and short-term clinical outcomes of small side branch occlusion after implantation of an everolimus-eluting bioresorbable vascular scaffold: an interim report of 435 patients in the ABSORB-EXTEND single-arm trial in comparison with an everolimus-eluting metallic stent in the SPIRIT first and II trials. *JACC Cardiovasc Interv* 2013;**6**:247–257.
33. Stone GW, Abizaid A, Silber S, Dizon JM, Merkely B, Costa RA, Kornowski R, Abizaid A, Wojdyla R, Maehara A, Dressler O, Brener SJ, Bar E, Dudek D. Prospective, randomized, multicenter evaluation of a polyethylene terephthalate micronet mesh-covered stent (MGuard) in ST-segment elevation myocardial infarction: the MASTER trial. *J Am Coll Cardiol*. 2012;**60**:1975–1984.
34. Otake H, Shite J, Ako J, Shinke T, Tanino Y, Ogasawara D, Sawada T, Miyoshi N, Kato H, Koo BK, Honda Y, Fitzgerald PJ, Hirata K. Local determinants of thrombus formation following sirolimus-eluting stent implantation assessed by optical coherence tomography. *JACC Cardiovasc Interv* 2009;**2**:459–466.
35. Prati F, Guagliumi G, Mintz GS, Costa M, Regar E, Akasaka T, Barlis P, Tearney GJ, Jang IK, Arbustini E, Bezerra HG, Ozaki Y, Bruining N, Dudek D, Radu M, Erglis A, Motreff P, Alfonso F, Toutouzas K, Gonzalo N, Tamburino C, Adriaenssens T, Pinto F, Serruys PW, Di Mario C, Expert's OCTRD. Expert review document part 2: methodology, terminology and clinical applications of optical coherence tomography for the assessment of interventional procedures. *Eur Heart J* 2012;**33**:2513–2520.
36. Prati F, Regar E, Mintz GS, Arbustini E, Di Mario C, Jang IK, Akasaka T, Costa M, Guagliumi G, Grube E, Ozaki Y, Pinto F, Serruys PW, Expert's OCTRD. Expert review document on methodology, terminology, and clinical applications of optical coherence tomography: physical principles, methodology of image acquisition, and clinical application for assessment of coronary arteries and atherosclerosis. *Eur Heart J* 2010;**31**:401–415.
37. Barlis P, Regar E, Serruys PW, Dimopoulos K, van der Giessen WJ, van Geuns RJ, Ferrante G, Wandel S, Windecker S, van Es GA, Eerdmans P, Juni P, di Mario C. An optical coherence tomography study of a biodegradable vs. durable polymer-coated limus-eluting stent: a LEADERS trial sub-study. *Eur Heart J* 2010; **31**:165–176.
38. van Geuns RJ, Tamburino C, Fajadet J, Vrolix M, Witzenbichler B, Eeckhout E, Spaulding C, Reczuch K, La Manna A, Spaargaren R, Garcia-Garcia HM, Regar E, Capodanno D, Van Langenhove G, Verheye S. Self-expanding versus balloon-expandable stents in acute myocardial infarction: results from the APPOSITION II study: self-expanding stents in ST-segment elevation myocardial infarction. *JACC Cardiovasc Interv* 2012;**5**:1209–1219.

Chapter 6.3

OCT assessment of the mid-term vascular healing after everolimus-eluting bioresorbable scaffold implantation in STEMI (BVS-STEMI-FIRST). A comparison with metallic drug-eluting stents

Karanasos A, Van Mieghem N, Garcia-Garcia HM, Diletti R, Felix C, van der Sijde JN, Ishibashi Y, Fam JM, de Jaegere PP, van der Ent M, Holm NR, Serruys PW, OnumaY, Zijlstra F, Regar E, van Geuns RJ

Submitted for publication.

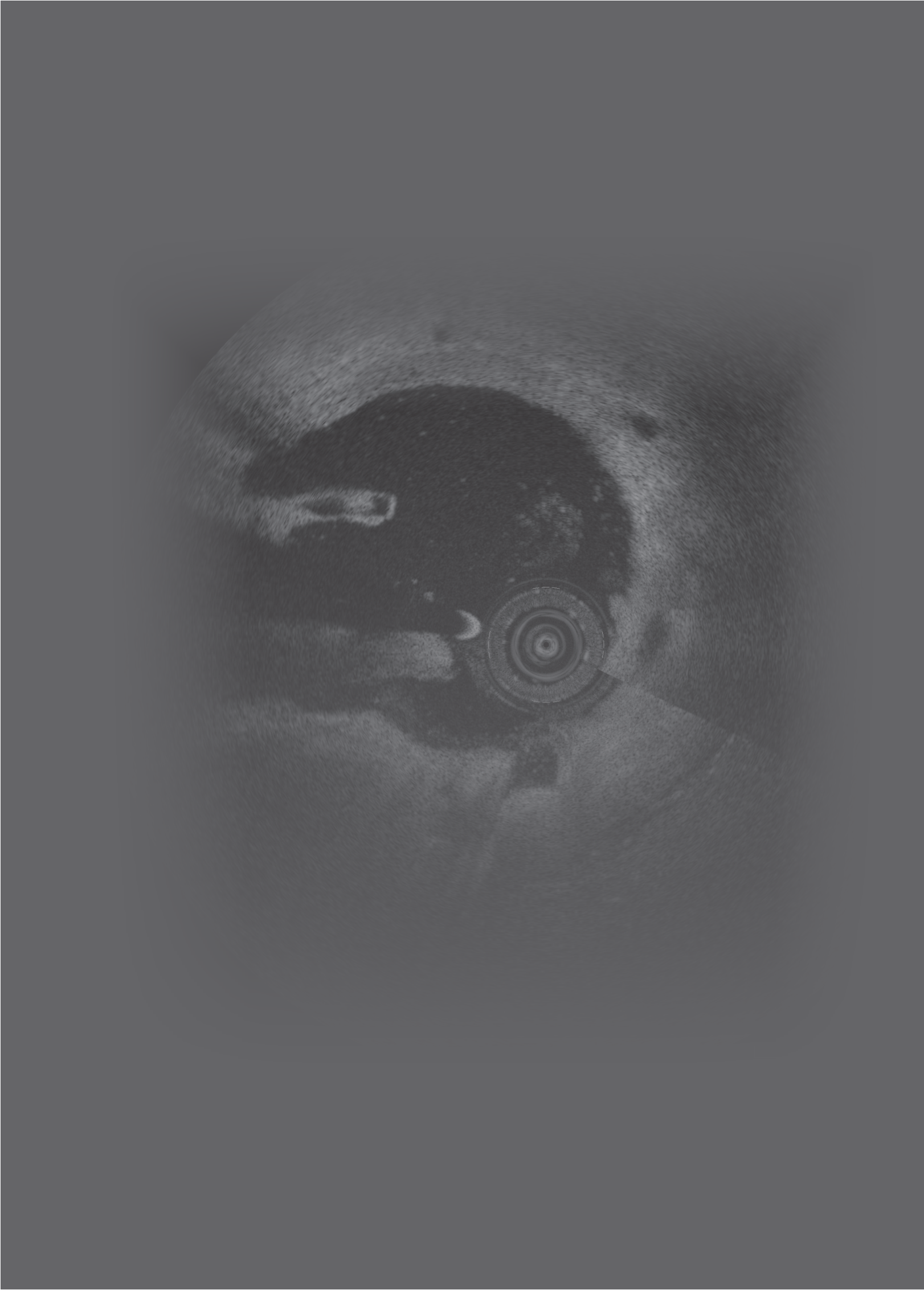

PART VII

Optical coherence tomography assessment of bioresorbable scaffold thrombosis

Chapter 7.1

Very late bioresorbable scaffold thrombosis after discontinuation of dual antiplatelet therapy

Karanasos A, van Geuns RJ, Zijlstra F, Regar E

Eur Heart J. 2014 Jul 14;35(27):1781

CARDIOVASCULAR FLASHLIGHT

Very late bioresorbable scaffold thrombosis after discontinuation of dual antiplatelet therapy

Antonios Karanasos, Robert-Jan van Geuns, Felix Zijlstra, and Evelyn Regar*

Department of Interventional Cardiology, Thoraxcentre, BA-585, Erasmus University Medical Centre, 's Gravendijkwal 230, 3015 CE, Rotterdam, the Netherlands

* Corresponding author. Tel: +31 107035232, Fax: +31 107035046, Email: e.regar@erasmusmc.nl

A 57-year-old gentleman was admitted with unstable angina with dynamic ECG changes (E), 4 days after discontinuation of dual antiplatelet therapy (DAT) with aspirin and clopidogrel. He had undergone staged percutaneous coronary intervention with bioresorbable vascular scaffold (BVS; ABSORB 1.1, Abbott Vascular, Santa Clara, CA, USA) implantation in the ostial left circumflex artery (LCx) 2 years ago (*Panels A–D*), followed by everolimus-eluting metal stent implantation in the distal left main and proximal left anterior descending artery, with balloon dilation of the LCx ostium. Fractional flow reserve of the LCx post-intervention was 0.88.

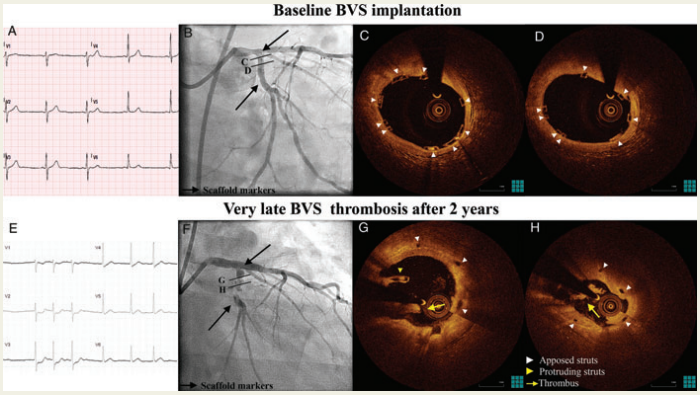

At presentation, angiography showed a filling defect in the scaffolded segment (*Panel F*). Optical coherence tomography revealed intracoronary thrombus and scaffold pattern irregularities (*Panels G* and *H*). The patient was treated with thrombectomy and everolimus-eluting metal stent implantation and discharged on aspirin and prasugrel.

To our knowledge, this is the first reported case of very late BVS thrombosis. Bioresorbable scaffolds have been suggested as an alternative to metal platform drug-eluting stents, aiming to reduce very late stent complications, by providing transient support and being completely integrated into the vascular wall after this period. Although, at 24 months significant bioresorption is expected to have occurred with restoration of local vasomotion, there is still evidence of scaffold struts. In our case, scaffold thrombosis was observed together with scaffold pattern irregularities. The possibility that the observed irregularities were induced by the balloon dilation performed during left main metal stent implantation, subsequently leading to thrombosis, cannot be excluded. Importantly, the event occurred 4 days after DAT discontinuation, suggesting a need for individualized duration of DAT in complex cases treated with BVS.

Funding: Funding to pay the Open Access publication charges for this article was provided by Thoraxcentre, Erasmus University, Rotterdam, NL.

Chapter 7.2

Late and very late scaffold thrombosis

Karanasos A, Zhang BC, van der Sijde J, Fam JM, van Geuns RJ, Regar E

In: Textbook on Bioresorbable Scaffolds: from Basic concept to clinical application. (Book chapter) (In press)

Chapter 7.3

Angiographic and optical coherence tomography insights into bioresorbable scaffold thrombosis. A single-centre experience

Karanasos A, Van Mieghem NM, van Ditzhuijzen N, Felix C, Daemen J, Autar A, Onuma Y, Kurata M, Diletti R, Valgimigli M, Kauer F, van Beusekom H, de Jaegere P, Zijlstra F, van Geuns RJ, Regar E

Circ Cardiovasc Intv 2015 May;8(5). pii: e002369

Coronary Interventions

Angiographic and Optical Coherence Tomography Insights Into Bioresorbable Scaffold Thrombosis

Single-Center Experience

Antonios Karanasos, MD, PhD; Nicolas Van Mieghem, MD, PhD; Nienke van Ditzhuijzen, MSc; Cordula Felix, MD; Joost Daemen, MD, PhD; Anouchska Autar, MD; Yoshinobu Onuma, MD, PhD; Mie Kurata, MD, PhD; Roberto Diletti, MD; Marco Valgimigli, MD, PhD; Floris Kauer, MD; Heleen van Beusekom, MD, PhD; Peter de Jaegere, MD, PhD; Felix Zijlstra, MD, PhD; Robert-Jan van Geuns, MD, PhD; Evelyn Regar, MD, PhD

Background—As bioresorbable vascular scaffolds (BVSs) are being increasingly used in complex real-world lesions and populations, BVS thrombosis cases have been reported. We present angiographic and optical coherence tomography (OCT) findings in a series of patients treated in our center for definite bioresorbable scaffold thrombosis.

Methods and Results—Up to June 2014, 14 patients presented with definite BVS thrombosis in our center. OCT was performed in 9 patients at the operator's discretion. Angiographic and OCT findings were compared with a control group comprising 15 patients with definite metallic stent thrombosis. In the BVS group, time interval from index procedure to scaffold thrombosis ranged from 0 to 675 days. Incomplete lesion coverage by angiography was identified in 4 of 14 cases, malapposition by OCT in 5 of 9 cases, strut discontinuity in 2 of 9 cases, and underexpansion in 2 of 9 cases. Five patients had discontinued dual antiplatelet therapy, and in 3 of them discontinued dual antiplatelet therapy discontinuation had occurred the week preceding the event. There were no significant differences in angiographic or OCT findings between BVS and metallic stent thrombosis.

Conclusions—Suboptimal implantation with incomplete lesion coverage, underexpansion, and malapposition comprises the main pathomechanism for both early and late BVS thrombosis, similar to metallic stent thrombosis. Dual antiplatelet therapy discontinuation seems to also be a secondary contributor in several late events. Our observations suggest that several potential triggers for BVS thrombosis could be avoided. **(*Circ Cardiovasc Interv*. 2015;8:e002369. DOI: 10.1161/CIRCINTERVENTIONS.114.002369.)**

Key Words: bioabsorbable implants ■ coronary artery disease ■ drug-eluting stents ■ tomography, optical coherence

Metallic drug-eluting stents (DESs) are the current standard for invasive treatment of coronary artery disease. However, metallic DES have been associated with late complications such as neoatherosclerosis and incomplete healing that can lead to failure even at long-term follow-up.[1–3] Bioresorbable vascular scaffolds (BVSs) are a new treatment for coronary artery disease that could potentially alleviate such problems.[4,5] To date, bioresorbable scaffolds have been evaluated in first-in-man or highly selected study cohorts with simple lesions in low-risk patient populations,[4–7] whereas vascular response in lesions of real-world patients might differ. As BVSs are being increasingly used in more complex lesions, several cases of BVS thrombosis have been reported.[8–10]

In metallic DES, intravascular imaging has elucidated pathophysiologic mechanisms of stent thrombosis, underscoring the significance of procedural factors such as inadequate stent expansion and vascular trauma for acute thrombosis[11,12] or delayed healing and neoatherosclerosis for late thrombosis.[1,2] Whether BVS thrombosis is amenable to the same factors remains unknown.

We aimed to present angiographic and optical coherence tomography (OCT) findings in a series of patients with definite bioresorbable scaffold thrombosis treated in our catheterization laboratory and compare them with a control group of patients with definite metallic stent thrombosis.

Methods

Study Population

The everolimus-eluting BVS (Absorb; Abbott Vascular, Santa Clara, CA) has been used in clinical trials in our center since 2006.[4–7] Since

Received September 24, 2014; accepted April 13, 2015.

From the Departments of Interventional Cardiology (A.K., N.V.M., N.v.D., C.F., J.D., Y.O., R.D., M.V., F.K., P.d.J., F.Z., R.-J.v.G., E.R.) and Experimental Cardiology (A.A., M.K., H.v.B.), Thoraxcenter, Erasmus MC, Rotterdam, The Netherlands.

The Data Supplement is available at http://circinterventions.ahajournals.org/lookup/suppl/doi:10.1161/CIRCINTERVENTIONS.114.002369/-/DC1.

Correspondence to Evelyn Regar, MD, PhD, Thoraxcenter, BA-585, Erasmus MC, 's Gravendijkwal 230, 3015CE Rotterdam, The Netherlands. E-mail e.regar@erasmusmc.nl

WHAT IS KNOWN

- Bioresorbable scaffolds are a new treatment for coronary artery disease with a favorable long-term healing response that could potentially alleviate long-term complications of metallic stents such as neoatherosclerosis and incomplete healing.
- Several real-world registries have demonstrated relatively high rates of scaffold thrombosis, driven mainly by increased rates of acute and subacute scaffold thrombosis.

WHAT THE STUDY ADDS

- The main pathomechanisms for both early and late bioresorbable scaffold thrombosis are similar to those of metallic stents and consist of suboptimal implantation with underexpansion, malapposition, and incomplete lesion coverage.
- Addition to suboptimal implantation and similar to metallic stents, the absence of appropriate antiplatelet therapy administration is also an important contributor to bioresorbable scaffold thrombosis.

September 2012, Absorb BVS was approved for commercial use in Netherlands and has been used in our center also in more complex patients and lesions, while outcomes of these patients are recorded in the Expanded Clinical Use of Everolimus Eluting Bioresorbable Vascular Scaffolds for Treatment of Coronary Artery Disease (BVS-Expand) and Everolimus-Eluting Bioresorbable Vascular Scaffolds for Treatment of Patients Presenting With ST-Segment–Elevation Myocardial Infarction (BVS-STEMI) registries.[13,14] Up to June 1, 2014, a total of 733 everolimus-eluting BVS had been implanted in 469 patients in our center.

Since 2006 and up to June 2014, 14 patients were admitted to our laboratory because of definite BVS thrombosis. Definite BVS thrombosis was identified using the Academic Research Consortium definition requiring both angiographic evidence of scaffold thrombosis (including 5-mm edge segments) and clinical evidence of acute coronary syndrome and were classified as acute, subacute, late, or very late.[15] Treatment of BVS thrombosis, including thrombus aspiration or invasive imaging, was performed at the operator's discretion. All patients have provided informed consent.

To understand potential differences and similarities between BVS and metallic stent thrombosis, we used consecutive patients with definite metallic stent thrombosis as control. Between September 1, 2012 and June 1, 2014, 55 patients presented with definite metallic stent thrombosis. We excluded patients with stent thrombosis in left main or in graft (n=4), as these typically large vessels are not suited for BVS with its currently limited diameter range, and patients with very late stent thrombosis >2 years since implantation (n=36), as the available follow-up period in BVS does not allow a meaningful comparison of very late thrombosis at that interval. Thus, 15 patients with definite metallic stent thrombosis were included as control (2 acute, 4 subacute, 5 late, and 4 very late between 1 and 2 years).

Angiographic Analysis

Angiographic analysis was performed for baseline implantation and for stent/scaffold thrombosis, including quantitative coronary angiography and assessment of intraprocedural complications. Incomplete lesion coverage (also called geographical miss) was defined as the longitudinal mismatch between implantation site and diseased coronary segment or coronary segment subjected to balloon dilatation, and its identification required a consensus characterization by 2 observers that reviewed the baseline angiography, applying established methodology.[16] Angiographic analysis at the event included assessment of thrombolysis in myocardial infarction flow grade, thrombus burden,[17] and quantitative coronary angiography measurements.

OCT Image Acquisition

OCT was performed at the operator's discretion, after thrombus aspiration, in 9 patients with BVS thrombosis and in 5 patients with metallic stent thrombosis. OCT acquisition was performed with the Lightlab/St Jude (C7XR/Illumien, St Jude/Lightlab, St Paul, MN) or the Terumo Lunawave (Terumo Corporation, Tokyo, Japan) frequency-domain imaging systems, as previously described.[4,14]

OCT Image Analysis

OCT image analysis was performed offline in 1-mm intervals within the treated segment, including proximal and distal 5-mm long edge segments, after excluding frames with <75% lumen contour visibility, as previously described.[1,7,14] Scaffold struts were defined malapposed in the absence of contact with the vessel wall, whereas metallic stent struts were malapposed when the distance of the adluminal strut reflection from the vessel wall exceeded the nominal strut thickness (metal backbone plus coating). These definitions do not include struts in front of side-branches or their ostium (polygon of confluence), which are defined as side-branch–related struts. Intraluminal struts belonging to adjacent clusters of apposed struts in overlapping scaffolds were not considered malapposed. Thrombus was defined as irregular endoluminal or mural mass and scaffold discontinuity (in BVS) as struts overhanging each other at the same angular sector, with or without malapposition, or isolated struts at the luminal center without obvious connection to other surrounding struts,[7,18] further classified as fracture (present at baseline and follow-up) or late discontinuity (present only at follow-up). OCT findings in BVS thrombosis were compared between frames with and without thrombus.

Statistical Analysis

All analyses were performed with SPSS 20.0 (IBM, Chicago, IL). Continuous variables are presented as mean±SD, median [interquartile range], or estimated means (95% confidence interval), whereas categorical variables are reported as count and percentages. Differences in continuous baseline or angiographic variables were assessed with *t* test, whereas in categorical variables with the χ^2 or Fisher exact test. Differences in OCT variables were assessed with Mann–Whitney and paired comparisons with Wilcoxon, because of the small sample size and skewed nature of these variables. Frame- or strut-level analysis was performed with mixed linear or logistic regression, as struts are clustered within each frame within each patient. Strut-level malapposition was assessed by mixed logistic regression using within-frame and within-patient intercepts as random effects. Frame-level differences were assessed with mixed linear or logistic regression analysis using within-patient intercepts as random effect. All *P* values are 2-sided with a value <0.05 indicating significance.

Results

Baseline Characteristics and Concomitant Therapy

Baseline characteristics for BVS (n=14) and metallic stents (n=15) are reported in Table 1. There were no significant differences in baseline characteristics with the exception of a higher proportion of men in BVS (100% versus 67%; *P*=0.042).

At the time of BVS thrombosis, 5 patients were not receiving dual antiplatelet therapy (DAPT) (2 with premature discontinuation <1 year and 3 with planned discontinuation >1 year). In three patients, DAPT discontinuation had occurred the week preceding the event. In metallic stents, complete DAPT discontinuation <1 year was confirmed in 1 patient and suspected in 2, whereas 4 patients with very late thrombosis after 1 year were only receiving aspirin.

Table 1. Clinical and Demographic Characteristics

	BVS (n=14)	Metal (n=15)	*P* Value
Age, y	60.2±10.5	64.2±11.6	0.35
Male, n (%)	14 (100)	10 (66.7)	0.042
Type, n (%)			0.70
Acute	4 (28.6)	2 (13.3)	
Subacute	2 (14.3)	4 (26.7)	
Late	5 (35.7)	5 (33.3)	
Very late	3 (21.4)	4 (26.7)	
Time to event, d	152.6±210.1	232.0±237.9	0.35
Clinical syndrome (baseline)			0.79
Stable angina, n (%)	5 (35.7)	3 (20.0)	
Unstable angina, n (%)	1 (7.1)	2 (13.3)	
NSTEMI, n (%)	3 (21.4)	4 (26.7)	
STEMI, n (%)	5 (35.7)	6 (40.0)	…
Clinical syndrome (scaffold/stent thrombosis)			0.48
UA, n (%)	0 (0)	1 (6.7)	
NSTEMI, n (%)	7 (50.0)	5 (33.3)	
STEMI, n (%)	7 (50.0)	9 (60.0)	
Antiplatelet therapy at scaffold/stent thrombosis*			
Aspirin, n (%)	11 (78.6)	12 (92.3)	0.99
P2Y12 inhibitor, n (%)			0.58
Clopidogrel	3 (21.4)	5 (38.5)	
Prasugrel	5 (35.7)	3 (23.1)	
Ticagrelor	1 (7.1)	0 (0)	
Oral anticoagulation, n (%)	3 (21.4)	1 (6.7)	0.33
CAD risk factors			
Hypertension, n (%)	9 (64.3)	5 (35.7)	0.26
Dyslipidemia, n (%)	6 (42.9)	7 (50.0)	0.99
Diabetes mellitus, n (%)	1 (7.1)	6 (42.9)	0.08
Smoking, n (%)	6 (42.9)	2 (14.3)	0.21
Family history of CAD, n (%)	5 (35.7)	5 (35.7)	0.99
Comorbidities			
Prior cerebrovascular accident, n (%)	3 (21.4)	2 (13.3)	0.60
Peripheral vascular disease, n (%)	1 (7.1)	0 (0)	0.99
Kidney disease, n (%)	0 (0.0)	2 (14.3)	0.48
Prior MI, n (%)	2 (14.3)	5 (35.7)	0.39
Prior PCI, n (%)	2 (14.3)	4 (28.6)	0.65
Prior CABG, n (%)	0 (0.0)	0 (0)	…
COPD, n (%)	1 (7.1)	1 (7.1)	0.99

Values are presented as mean±SD or n (%). BVS indicates bioresorbable vascular scaffold; CABG, coronary artery bypass graft; CAD, coronary artery disease; COPD, chronic obstructive pulmonary disease; MI, myocardial infarction; NSTEMI, non–ST-segment–elevation myocardial infarction; PCI, percutaneous coronary intervention; STEMI, ST-segment–elevation myocardial infarction; and UA, unstable angina.

*For 2 patients in the metallic stent group, poor compliance was suspected but not confirmed.

Angiographic and Procedural Characteristics

Angiographic and procedural characteristics of baseline and repeat procedure are reported in Tables 2 and 3, respectively. Pre- and postdilation was used more frequently in

Table 2. Angiographic and Procedural Characteristics at Baseline Implantation

Angiographic Characteristics	BVS (n=14)	Metal (n=15)	*P* Value
Vessel, n (%)			0.37
LAD	9 (64.3)	6 (40.0)	
LCx	3 (21.4)	4 (26.7)	
RCA	2 (14.3)	5 (33.3)	
Bifurcation	3 (21.4)	4 (26.7)	0.99
Ostial LAD/LCx lesion	6 (42.9)	5 (33.3)	0.71
AHA/ACC classification			0.17
A/B1	4 (28.6)	1 (6.7)	
B2/C	10 (71.4)	14 (93.3)	
Preprocedure			
TIMI flow grade, n (%)			0.57
0	5 (35.7)	5 (33.3)	
1	0 (0)	2 (13.3)	
2	1 (7.1)	1 (6.7)	
3	8 (57.1)	7 (46.7)	
Total occlusion (n=10)			
RVD, mm	2.98±0.22	2.66±0.59	0.30
Non-total occlusion (n=19)			
RVD, mm	2.61±0.35	2.60±0.66	0.95
Minimal lumen diameter, mm	0.94±0.26	0.96±0.29	0.89
Diameter stenosis, %	64.1±9.8	61.8±10.9	0.64
Lesion length, mm	19.38±9.04	24.16±10.72	0.25
Postprocedure			
TIMI flow grade, n (%)			0.99
0	0 (0)	0 (0)	
1	0 (0)	0 (0)	
2	0 (0)	1 (7.1)	
3	14 (100)	13 (92.9)	
RVD, mm	2.62±0.33	2.56±0.59	0.71
Minimal lumen diameter, mm	2.32±0.22	2.23±0.36	0.44
Diameter stenosis, %	10.9±9.5	11.7±10.5	0.82
Acute gain, mm	1.29±0.38	1.45±0.35	0.35
Dissection, n (%)	2 (14.3)	3 (21.4)	0.99
Side-branch occlusion	1 (7.1)	1 (7.1)	0.99
Procedural data			
Predilation, n (%)	13 (92.9)	7 (50.0)	0.033
Postdilation, n (%)	7 (50.0)	0 (0)	0.006
Thrombus aspiration, n (%)	4 (28.6)	5 (35.7)	0.99
OCT guidance, n (%)	5 (35.7)	0 (0)	0.041
Overlap, n (%)	3 (21.4)	4 (26.7)	0.99
Bifurcation intervention, n (%)			0.99
T-stenting	1 (7.1)	1 (6.7)	
Balloon dilation of side-branch ostium	1 (7.1)	1 (6.7)	
Mean scaffolds/stents per patient, n	1.4±0.6	1.4±0.5	0.84
Total scaffold/stent length per patient, mm	28.57±14.56	30.29±15.91	0.77
Mean scaffold/stent diameter per patient, mm	3.18±0.27	2.90±0.47	0.06

All values presented as n (%) or mean±SD. ACC indicates American College of Cardiology; AHA, American Heart Association; BVS, bioresorbable vascular scaffold; LAD, left anterior descending artery; LCx, left circumflex artery; OCT, optical coherence tomography; RCA, right coronary artery; RVD, reference vessel diameter; and TIMI, thrombolysis in myocardial infarction.

Table 3. Angiographic Characteristics at Thrombosis

Angiographic Characteristics	BVS (n=14)	Metal (n=15)	*P* Value
TIMI flow grade, n (%)			0.47
0	9 (64.3)	10 (66.7)	
1	2 (14.3)	3 (20.0)	
2	2 (14.3)	0 (0)	
3	1 (7.1)	2 (13.3)	
Thrombus burden index, n (%)			0.47
0	0 (0)	0 (0)	
1	0 (0)	0 (0)	
2	2 (14.3)	1 (6.7)	
3	3 (21.4)	2 (13.3)	
4	0 (0)	2 (13.3)	
5	9 (64.3)	10 (66.7)	
Total occlusion (n=19)			
RVD, mm	2.93±0.32	2.37±0.69	0.042
Non-total occlusion (n=10)			
RVD, mm	2.42±0.66	2.61±0.36	0.59
Minimal lumen diameter, mm	0.90±0.17	0.94±0.97	0.93
Diameter stenosis, %	60.0±15.0	66.0±33.5	0.73

All values presented as n (%) or mean±SD. BVS indicates bioresorbable vascular scaffold; RVD, reference vessel diameter; and TIMI, thrombolysis in myocardial infarction.

BVS compared with metallic stents (predilation: 92.9% versus 50.0%; *P*=0.033 and postdilation: 50.0% versus 0%; *P*=0.006), with a trend for higher scaffold diameter in BVS (3.18±0.27 versus 2.90±0.47; *P*=0.06). OCT post implantation had been performed in 5 of 14 patients in BVS and in none of the metallic stents.

Incomplete lesion coverage was observed in four BVS cases, and in one case with metallic stent. Two patients with BVS had an angiographically visible edge dissection (one proximal, one distal) after baseline implantation, left untreated.

OCT Findings

OCT at thrombosis was performed in 9 of 14 patients with BVS and in 5 of 15 patients with metallic stents. There was no significant difference in OCT findings between BVS and metallic stent thrombosis (Table 4). In (very) late thrombosis, the incidence of malapposed struts was 1.9%±2.2% for BVS versus 5.6%±6.2% for metallic stents (*P*=0.31), and malapposition distance 486±225 μm for BVS versus 265±151 μm for metallic stents (*P*=0.17).

In BVS thrombosis, frames with thrombus had lower lumen (4.35 mm^2 [2.61–6.08 mm^2] versus 5.84 mm^2 [4.11–7.58 mm^2]; *P*<0.001) and scaffold area (7.63 mm^2 [6.32–8.95 mm^2] versus 8.14 mm^2 [6.83–9.46 mm^2]; *P*<0.001) compared with frames without thrombus (Table I in the Data Supplement). No difference was found in frame-level malapposition incidence (*P*=0.75), whereas malapposition area was numerically higher in frames with thrombus, without reaching significance (1.54 mm^2 [0–3.44 mm^2] versus 0.44 mm^2 [0.00–6.70 mm^2]; *P*=0.18).

Table 4. OCT Findings at Thrombosis

	BVS (n=9)	Metal (n=5)	*P* Value
Baseline characteristics in OCT subgroup			
Age, y	60.3 [53.1–67.3]	64.0 [59.0–73.0]	0.44
Male, n (%)	9 (100)	3 (60.0)	0.11
Type, n (%)			0.40
Acute	1 (11.1)	0 (0)	
Subacute	1 (11.1)	2 (40.0)	
Late	5 (55.6)	3 (60.0)	
Very late	2 (22.2)	0 (0)	
Time to event, d	129.0 [24.5–319.5]	139.0 [6.5–227.5]	0.99
OCT variables			
Analyzed struts, n	222 [76.5–310.5]	202 [81.5–514.5]	0.80
Minimum lumen area, mm^2	1.87 [0.92–3.23]	1.42 [0.98–3.25]	0.90
Mean lumen area, mm^2	4.77 [3.72–6.83]	5.33 [3.87–5.72]	0.90
Minimum scaffold/stent area, mm^2	6.88 [5.10–7.24]	4.87 [2.97–5.72]	0.07
Mean scaffold/stent area, mm^2	7.59 [6.86–8.95]	6.49 [5.10–7.23]	0.11
Ratio of minimum scaffold/stent area to reference area	0.93 [0.73–1.12]	0.82 [0.52–1.36]	0.54
Ratio of minimum scaffold/stent diameter to nominal diameter	0.87 [0.84–0.89]	0.83 [0.66–0.89]	0.53
Malapposition area, mm^2	0.13 [0.04–0.26]	0.05 [0–0.31]	0.86
Mean neointimal/attached thrombus area, mm^2	1.70 [1.28–2.63]	1.48 [0.93–2.19]	0.34
Malapposed struts, %	2.50±3.27	4.63±4.70	0.48*
Malapposition distance, μm	293±257	287±271	0.36*
Scaffolds/stents with any malapposed strut, n (%)	5 (55.6)	4 (80.0)	0.58
Scaffolds/stents with >5% malapposed struts, n (%)	2 (22.2)	1 (20.0)	0.99
Thrombus, n (%)	8 (88.8)	5 (100)	0.99
Scaffold discontinuity, n (%)	2 (22.2)		

Values presented as n (%), median [IQR], or mean±SD. BVS indicates bioresorbable vascular scaffold; IQR, interquartile range; and OCT, optical coherence tomography.

**P* values calculated with multilevel regression using within-patient and within-frame intercepts as random effects.

Patient-Specific Substrates of Thrombosis

Tables II and III in the Data Supplement present patient-specific clinical, procedural, angiographic and OCT characteristics in BVS thrombosis.

(Sub)acute Thrombosis

In (sub)acute scaffold thrombosis, suboptimal implantation was the main mechanism. Incomplete lesion coverage was observed in three patients (Figure I in the Data Supplement), either because of mismatch of the predilated segment and the scaffolded segment or because of incomplete coverage of the thrombosed segment in ST-segment–elevation myocardial infarction (Figure 1). In 2 cases with BVS implantation in ostial left anterior descending artery, angiography demonstrated scaffold protrusion into left main suggesting malapposition, also with underexpansion in one. Finally, in 1 case, thrombus was observed in a long overlap segment (7 mm by

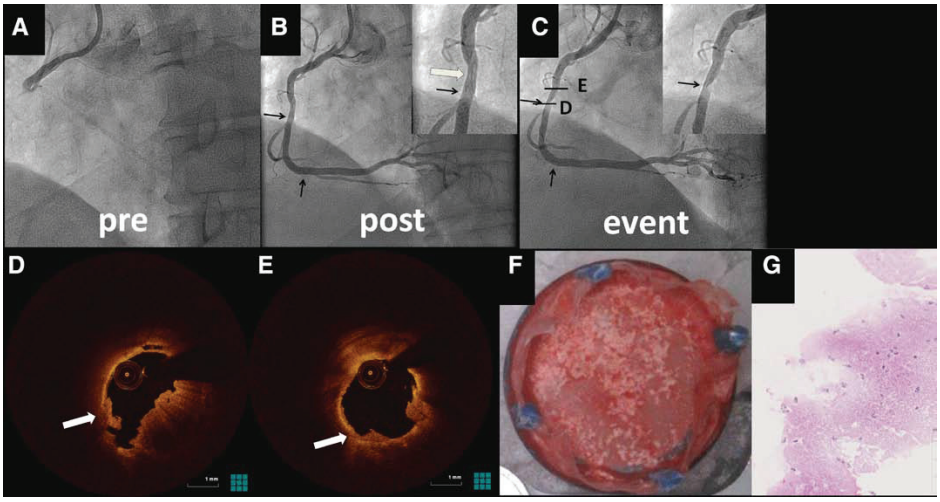

Figure 1. Acute thrombosis because of incomplete lesion coverage. **A**, Preprocedural and (**B**) postprocedural angiogram after bioresorbable vascular scaffold implantation in a ST-segment–elevation myocardial infarction patient undergoing primary percutaneous coronary intervention. Mild haziness at the proximal edge postprocedure (arrow). **C**, Angiogram at event after thrombus aspiration. Red and white thrombus at the proximal scaffold segment (**D**) and proximal edge segment (**E**) extending >5 mm. The thrombus is overlying a thin-cap fibroatheroma, with possible rupture (arrow). Thrombus aspirate histology (**F** and **G**) demonstrates platelet-rich thrombus.

OCT), together with compact fibrin and Zahn-lines in aspirate histology (Figure 2), despite good expansion and apposition. In metallic stents, (sub)acute thrombosis was attributed to edge dissections in 3 cases, strut protrusion into left main with associated malapposition in 1 case, and extensive underexpansion in 1 case (minimal stent area, 1.19 mm^2). In 1 case, there were no findings suggesting suboptimal implantation, but there was suspicion of poor compliance with DAPT.

(Very) Late Thrombosis

In 1 case, despite meeting Academic Research Consortium criteria for definite thrombosis, OCT disclosed the absence of thrombus and occlusive edge restenosis as substrate (Figure

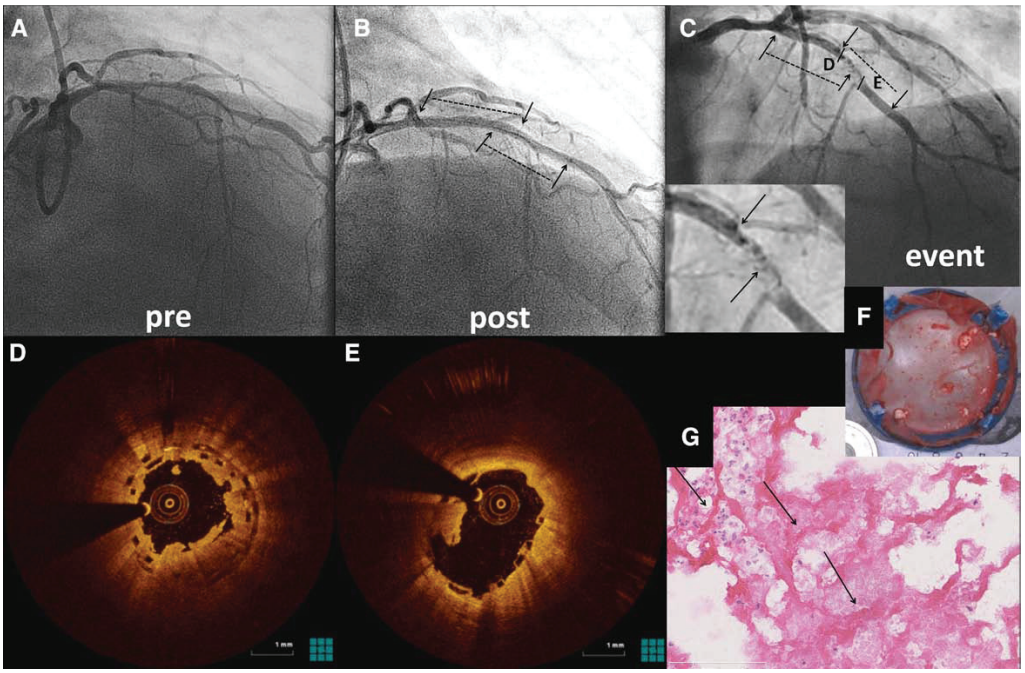

Figure 2. Subacute bioresorbable vascular scaffold thrombosis in extensive strut overlap. **A**, Preprocedural and (**B**) postprocedural angiogram at baseline. **C**, Angiogram at event showing contrast deficit in the scaffolded segment. **D** and **E**, Optical coherence tomography demonstrates thrombus mainly at the overlap (**D**). **F** and **G**, Thrombus aspirate histology shows compact fibrin with Zahn-lines (arrows).

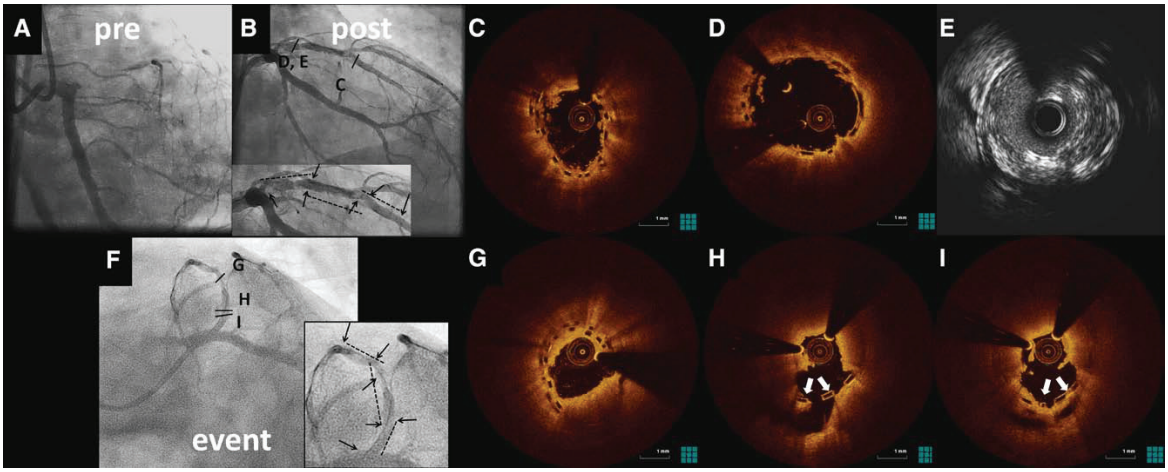

Figure 3. Late bioresorbable vascular scaffold (BVS) thrombosis and malapposition. BVS implantation in a total left anterior descending artery occlusion with postdilation (**A**), resulting in acceptable angiographic result with mild haziness (**B**), but residual thrombus by optical coherence tomography (OCT; **C** and **D**) and residual plaque burden by intravascular ultrasound (**E**). Postdilation was not repeated, considering the risk of side-branch occlusion. **F**, Angiogram at event after thrombus aspiration. **G** through **I**, OCT shows massive red thrombus, and late malapposition (arrows).

II in the Data Supplement). In most patients, (very) late BVS thrombosis was observed in the presence of regional suboptimal flow conditions, such as strut malapposition, scaffold fracture, and underexpansion. Four of 7 patients with (very) late BVS thrombosis undergoing OCT had malapposed struts. In 2 patients, malapposition was observed in the absence of scaffold discontinuity (Figure 3), also with underexpansion and restenosis in one of them. In the other 2 patients, malapposition was observed because of strut discontinuity: 1 with late discontinuity and intraluminal thrombus,[19] possibly resulting from balloon dilation of the scaffolded segment after the index procedure, whereas acute fracture had been detected in a second case. In this second case, late thrombosis occurred 2 days after both aspirin and clopidogrel discontinuation; however, there was no thrombus in the fracture site, but in an underexpanded long overlap segment (Figure 4). In 3 cases, the substrate was not clearly identified: 1 very late thrombosis case where late discontinuity was suspected but not clearly identified because of thrombus (Figure III in the Data Supplement), 1 very late thrombosis case with extensive baseline

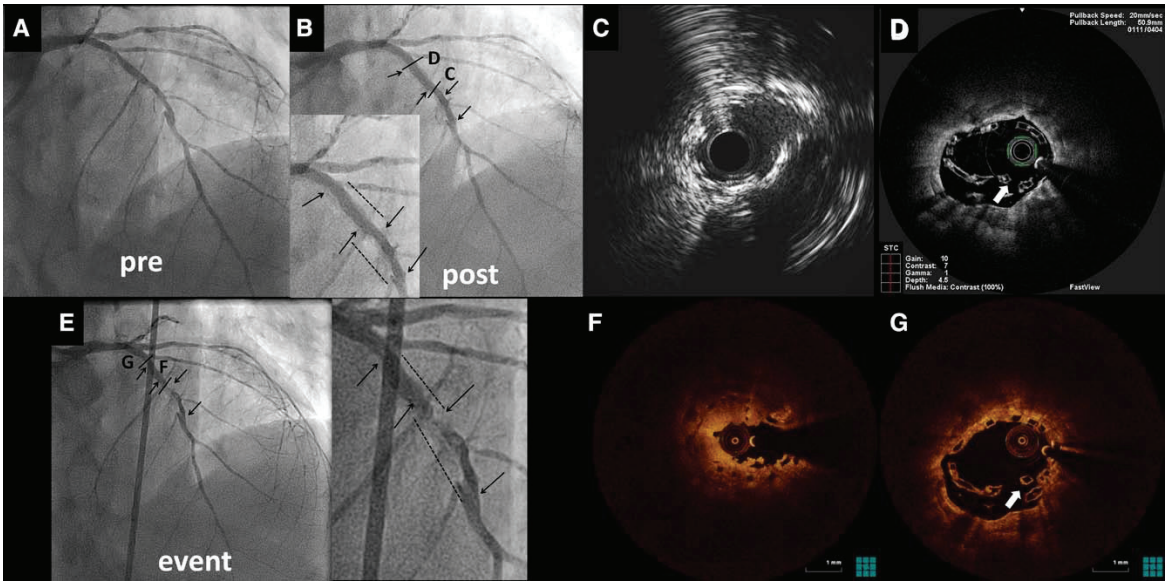

Figure 4. Late scaffold thrombosis after dual antiplatelet therapy discontinuation in overlapping bioresorbable vascular scaffold (BVS) with underexpansion. Overlapping BVS implantation in a diffuse calcified left anterior descending artery lesion (**A**), with acceptable angiographic result (**B**), but underexpansion by intravascular ultrasound (**C**), and scaffold fracture at the proximal edge by optical coherence tomography (OCT; **D**), possibly because of deep catheter intubation. The patient experienced late thrombosis 161 days post implantation (**E**), 2 days after aspirin and clopidogrel discontinuation. OCT shows thrombosis mainly at the overlap region, with low minimal scaffold area (4.21 mm^2; **F**), whereas the fracture site remains free of thrombus (**G**).

malapposition (8.6% malapposed struts) and intrascaffold dissections (no imaging at the event), and 1 late thrombosis case with T-stenting with BVS in a left anterior descending artery-diagonal bifurcation. The 2 latter patients were not receiving any antiplatelet agent at the time of late scaffold thrombosis. In metallic stents, late thrombosis was associated with malapposition in 2 cases and with strut protrusion into left main in another case. Complete DAPT discontinuation was confirmed in an additional patient and suspected in another with late thrombosis. In 4 patients with very late metallic stent thrombosis, baseline or follow-up angiography did not suggest any mechanical issues, while intravascular imaging was not performed.

Discussion

This real-world case series provides unique insights in the mechanisms of BVS thrombosis. The main findings of our study are (1) device thrombosis remains an issue with BVS, with the timing of the event evenly distributed from acute to very late thrombosis; (2) similar to metallic stents, acute and subacute BVS thrombosis is predominantly associated with suboptimal implantation; and (3) late and very late scaffold thrombosis is frequently observed in the presence of regional suboptimal flow conditions, often in combination with cessation of DAPT.

Notwithstanding promising results from first-in-man studies showing favorable BVS long-term healing response[4,7] and clinical results comparable with metallic DES,[5,6] little is known about vascular healing after BVS implantation in complex lesions. Real-world registries have reported high 6-month BVS thrombosis rates, driven mainly by increased early thrombosis,[8,9] implying a possible role of suboptimal implantation. In our series, we report on 14 cases of definite BVS thrombosis at different intervals since implantation and compare the imaging findings with a control group of metallic stents with definite stent thrombosis from the same time period, thus providing imaging insights into this complication. Importantly, suboptimal implantation was identified in both groups in a similar extent, suggesting that achieving an optimal implantation result might be more crucial than the type of implanted device in avoiding device thrombosis.

(Sub)acute BVS Thrombosis: Impact of Suboptimal Implantation

In acute and subacute BVS thrombosis, suboptimal implantation, comprising incomplete lesion coverage, malapposition, and underexpansion, was identified as the leading morphological substrate. This finding is in line with established substrates for metallic stent thrombosis[12] and confirmed by observations in our control group. As the current BVS generation has a relatively high crossing profile, BVSs require rigorous lesion preparation, potentially translating to higher risk for incomplete coverage of the injured segment, compared with direct stenting often applied with metallic stents. Thus, our findings might urge the operator to specifically ensure complete coverage of the lesion and injured segments, including angiographically apparent edge dissections.

Furthermore, the development of acute and subacute BVS thrombosis in 2 ST-segment–elevation myocardial infarction patients, after BVS implantation in ostial left anterior descending artery with scaffold protrusion into the left main, raises speculation that hemodynamic disturbances resulting from the protrusion and the associated malapposition could be a substrate for thrombosis.[20–22] This was also documented by OCT in 2 metallic stent thrombosis cases, suggesting a similar contribution of this mechanism.

Finally, 1 case of subacute thrombosis occurred despite good expansion and apposition, in the presence of long strut overlap. The high strut thickness of Absorb BVS (150 μm) and bench observations of increased thrombogenicity of thick-strut stents which is more pronounced at overlap sites,[21] together with histological observations of Zahn-lines in the aspirates, indicate a potential involvement of flow disturbances induced by long overlap and make a case for minimizing overlap length in treatment of long lesions by BVS. Whether this increased strut thickness could translate to increased thrombogenicity in vivo in the presence of an optimal implantation result remains unknown.

These findings underscore the significance of a meticulous BVS implantation technique, potentially including invasive imaging guidance, which has proven advantages over angiography for achieving optimal lesion treatment, in terms of coverage and expansion.[23] It is important however to note that imaging guidance during the procedure might drive the operator to excessive postdilation, potentially leading to scaffold fracture. Therefore, thorough lesion evaluation before implantation might help avoid situations with pronounced mismatch between scaffold and artery size.

Late and Very Late BVS Thrombosis: Prominent Role of Suboptimal Flow Conditions

(Very) late thrombosis events in our series were attributed to factors potentially affecting flow conditions. These include underexpansion and pronounced strut protrusion into the lumen as a result of malapposition, bifurcation intervention, or strut discontinuity. Underexpansion has been identified as an important predictor of metallic DES thrombosis.[3,12] The significance of optimal expansion in avoiding BVS thrombosis is underscored by the finding of lower scaffold area in sites with thrombus compared with sites without thrombus.

The role of malapposition in late metallic DES thrombosis is debated[24]; however, there is high prevalence in patients with events,[1] and late malapposition in first-generation DES has been identified as predictor of very long-term adverse outcome.[25] In our series, malapposition in (very) late BVS thrombosis (1.9±2.2%) did not differ significantly from late metallic stent thrombosis and was higher than the range reported for follow-up of second-generation metallic DES.[26] Likewise, malapposition distance (486±225 μm) was similar to metallic stents (265±151 μm) and at the range of previously reported values in metallic DES thrombosis (mean: 350 μm).[1] Therefore, malapposition of such extent, either persistent or late-acquired, might contribute to (very) late scaffold thrombosis.

As opposed to metallic DES, extensive malapposition in BVS might also result from strut discontinuity, which was associated with extensive thrombosis in a very late event in our series, possibly triggered by DAPT cessation.[19] Whether small

discontinuities, resulting from normal scaffold resorption, are associated with thrombosis is unclear. Notwithstanding this poorly documented association of discontinuity with thrombosis,[18] precautionary measures such as respecting the postdilation limits and cautious catheter recrossing or reintervention at later time points should be considered.

Role of DAPT Discontinuation

In addition to suboptimal implantation, DAPT cessation seems to play a role in BVS thrombosis, as in metallic DES.[27] In 3 cases, there was a close temporal association of DAPT cessation with clinical manifestation of BVS thrombosis, tracking with observations in first-generation metallic DES, where scheduled P2Y12 inhibitor withdrawal was associated with increased ischemic events.[28] As we assume concomitant suboptimal flow conditions in these patients, caused by underexpansion or extensive malapposition, we speculate on a possible synergistic effect of these factors in scaffold thrombosis. Consequently, these observations might raise questions about the need for platelet reactivity testing in patients with complex procedures or where optimal expansion cannot be achieved. Furthermore, the impact of DAPT cessation could be more pronounced when both aspirin and P2Y12 inhibitor are withdrawn in patients receiving chronic oral anticoagulation, as in 3 patients in our BVS series. Therefore, considering our observations of ongoing thrombotic risk even beyond 1 year, BVS implantation in such patients should be accompanied by adequate antiplatelet therapy or avoided in case of high bleeding risk.

Clinical Implications

Collectively, our findings underscore the significance of an optimal implantation result for minimizing the incidence of BVS thrombosis. Intravascular imaging at baseline could allow for early recognition and treatment of incomplete lesion coverage, better procedural planning in ostial lesions,[29] and optimal BVS sizing and postdilating, thus avoiding underexpansion[23] or scaffold fracture. Moreover, similar to metallic DES, proper DAPT administration must be emphasized.[27] Therefore, future studies should focus on optimal DAPT duration in patients with BVS, whereas platelet reactivity testing might be considered in selected patients with suboptimal implantation or complex intervention. Finally, in patients concomitantly receiving anticoagulants, administration of at least 1 antiplatelet agent until resorption or for life should be considered, pending appropriate studies.

Limitations

This study is focusing on a mechanistic understanding of BVS thrombosis. The study design and its single-center nature preclude firm estimations of BVS thrombosis incidence and predictors in real-world populations, considering the inclusion of patients treated for BVS thrombosis in our center, leading to possible underestimation. As OCT was not systematically performed, it was only available for 9 of 14 patients. Routine OCT use could have provided further insights into the pathomechanisms of BVS thrombosis, whereas the small number of patients undergoing OCT might be a limitation in the mixed model analysis of OCT variables. Moreover, the lack of a control group of BVS without thrombosis precludes assessment of morphological predictors of BVS thrombosis. Residual thrombus might have underestimated our results, hampering complete substrate visualization, while precluding coverage assessment, which is based on thickness measurements for BVS, that are inaccurate in the presence of attached thrombus, rather than on visual confirmation of overlying tissue as in metallic stents.[1,7] Therefore, a possible contribution of incomplete strut coverage could not be systematically evaluated. Finally, no platelet function tests were performed that could evaluate a possible contribution of increased platelet reactivity to BVS thrombosis.

Conclusions

Suboptimal implantation with underexpansion, malapposition, and incomplete lesion coverage comprised the main pathomechanisms for both early and late BVS thrombosis in our series, similar to metallic stent thrombosis. DAPT discontinuation seems to also be a secondary contributor in several late events. Our observations suggest that a number of potential triggers for BVS thrombosis could be avoided and might warrant prospective validation.

Acknowledgments

Dr Karanasos acknowledges the funding support of St Jude Medical.

Sources of Funding

Thoraxcenter receives unrestricted grants from the Abbott Vascular and St. Jude Medical.

Disclosures

None.

References

1. Guagliumi G, Sirbu V, Musumeci G, Gerber R, Biondi-Zoccai G, Ikejima H, Ladich E, Lortkipanidze N, Matiashvili A, Valsecchi O, Virmani R, Stone GW. Examination of the *in vivo* mechanisms of late drug-eluting stent thrombosis: findings from optical coherence tomography and intravascular ultrasound imaging. *JACC Cardiovasc Interv*. 2012;5:12–20. doi: 10.1016/j.jcin.2011.09.018.
2. Amabile N, Souteyrand G, Ghostine S, Combaret N, Slama MS, Barber-Chamoux N, Motreff P, Caussin C. Very late stent thrombosis related to incomplete neointimal coverage or neoatherosclerotic plaque rupture identified by optical coherence tomography imaging. *Eur Heart J Cardiovasc Imaging*. 2014;15:24–31. doi: 10.1093/ehjci/jet052.
3. Alfonso F, Dutary J, Paulo M, Gonzalo N, Pérez-Vizcayno MJ, Jiménez-Quevedo P, Escaned J, Bañuelos C, Hernández R, Macaya C. Combined use of optical coherence tomography and intravascular ultrasound imaging in patients undergoing coronary interventions for stent thrombosis. *Heart*. 2012;98:1213–1220. doi: 10.1136/heartjnl-2012-302183.
4. Karanasos A, Simsek C, Gnanadesigan M, van Ditzhuijzen NS, Freire R, Dijkstra J, Tu S, Van Mieghem N, van Soest G, de Jaegere P, Serruys PW, Zijlstra F, van Geuns RJ, Regar E. OCT assessment of the long-term vascular healing response 5 years after everolimus-eluting bioresorbable vascular scaffold. *J Am Coll Cardiol*. 2014;64:2343–2356. doi: 10.1016/j.jacc.2014.09.029.
5. Serruys PW, Chevalier B, Dudek D, Cequier A, Carrié D, Iniguez A, Dominici M, van der Schaaf RJ, Haude M, Wasungu L, Veldhof S, Peng L, Staehr P, Grundeken MJ, Ishibashi Y, Garcia-Garcia HM, Onuma Y. A bioresorbable everolimus-eluting scaffold versus a metallic everolimus-eluting stent for ischaemic heart disease caused by de-novo native coronary artery lesions (ABSORB II): an interim 1-year analysis of clinical and procedural secondary outcomes from a randomised controlled trial. *Lancet*. 2015;385:43–54. doi: 10.1016/S0140-6736(14)61455-0.

6. Abizaid A, Costa JR Jr, Bartorelli AL, Whitbourn R, van Geuns RJ, Chevalier B, Patel T, Seth A, Stuteville M, Dorange C, Cheong WF, Sudhir K, Serruys PW. The ABSORB EXTEND study: preliminary report of the twelve-month clinical outcomes in the first 512 patients enrolled. *EuroIntervention*. 2015;10:1396–1401. doi: 10.4244/EIJV10I12A243.
7. Serruys PW, Onuma Y, Garcia-Garcia HM, Muramatsu T, van Geuns RJ, de Bruyne B, Dudek D, Thuesen L, Smits PC, Chevalier B, McClean D, Koolen J, Windecker S, Whitbourn R, Meredith I, Dorange C, Veldhof S, Hebert KM, Rapoza R, Ormiston JA. Dynamics of vessel wall changes following the implantation of the absorb everolimus-eluting bioresorbable vascular scaffold: a multi-imaging modality study at 6, 12, 24 and 36 months. *EuroIntervention*. 2014;9:1271–1284. doi: 10.4244/EIJV9I11A217.
8. Capodanno D, Gori T, Nef H, Latib A, Mehilli J, Lesiak M, Caramanno G, Naber C, Di Mario C, Colombo A, Capranzano P, Wiebe J, Araszkiewicz A, Geraci S, Pyxaras S, Mattesini A, Naganuma T, Münzel T, Tamburino C. Percutaneous coronary intervention with everolimus-eluting bioresorbable vascular scaffolds in routine clinical practice: early and mid-term outcomes from the European multicentre GHOST-EU registry. *EuroIntervention*. 2015;10:1144–1153. doi: 10.4244/EIJY14M07_11.
9. Kraak RP, Hassell ME, Grundeken MJ, Koch KT, Henriques JP, Piek JJ, Baan J Jr, Vis MM, Arkenbout EK, Tijssen JG, de Winter RJ, Wykrzykowska JJ. Initial experience and clinical evaluation of the Absorb bioresorbable vascular scaffold (BVS) in real-world practice: the AMC Single Centre Real World PCI Registry. *EuroIntervention*. 2015;10:1160–1168. doi: 10.4244/EIJY14M08_08.
10. Ishibashi Y, Onuma Y, Muramatsu T, Nakatani S, Iqbal J, Garcia-Garcia HM, Bartorelli AL, Whitbourn R, Abizaid A, Serruys PW; ABSORB EXTEND Investigators. Lessons learned from acute and late scaffold failures in the ABSORB EXTEND trial. *EuroIntervention*. 2014;10:449–457. doi: 10.4244/EIJV10I4A78.
11. Regar E, Lemos PA, Saia F, Degertekin M, Tanabe K, Lee CH, Arampatzis CA, Hoye A, Sianos G, de Feyter P, van der Giessen WJ, Smits PC, van Domburg RT, Serruys PW. Incidence of thrombotic stent occlusion during the first three months after sirolimus-eluting stent implantation in 500 consecutive patients. *Am J Cardiol*. 2004;93:1271–1275. doi: 10.1016/j.amjcard.2004.02.013.
12. Choi SY, Witzenbichler B, Maehara A, Lansky AJ, Guagliumi G, Brodie B, Kellett MA Jr, Dressler O, Parise H, Mehran R, Dangas GD, Mintz GS, Stone GW. Intravascular ultrasound findings of early stent thrombosis after primary percutaneous intervention in acute myocardial infarction: a Harmonizing Outcomes with Revascularization and Stents in Acute Myocardial Infarction (HORIZONS-AMI) substudy. *Circ Cardiovasc Interv*. 2011;4:239–247. doi: 10.1161/CIRCINTERVENTIONS.110.959791.
13. Van Geuns RJ, De Jaegere P, Diletti R, Karanasos A, Muramatsu T, Nauta ST, Onuma Y, Regar E, Schultz CJ, Serruys PW, Van Mieghem NM, Zijlstra F. Short- and intermediate- term clinical outcomes after implantation of everolimus-eluting bioresorbable scaffold in complex lesions: a prospective single-arm study - ABSORB Expand trial. *J Am Coll Cardiol*. 2013;62:B133–B133.
14. Diletti R, Karanasos A, Muramatsu T, Nakatani S, Van Mieghem NM, Onuma Y, Nauta ST, Ishibashi Y, Lenzen MJ, Ligthart J, Schultz C, Regar E, de Jaegere PP, Serruys PW, Zijlstra F, van Geuns RJ. Everolimus-eluting bioresorbable vascular scaffolds for treatment of patients presenting with ST-segment elevation myocardial infarction: BVS STEMI first study. *Eur Heart J*. 2014;35:777–786. doi: 10.1093/eurheartj/eht546.
15. Cutlip DE, Windecker S, Mehran R, Boam A, Cohen DJ, van Es GA, Steg PG, Morel MA, Mauri L, Vranckx P, McFadden E, Lansky A, Hamon M, Krucoff MW, Serruys PW; Academic Research Consortium. Clinical end points in coronary stent trials: a case for standardized definitions. *Circulation*. 2007;115:2344–2351. doi: 10.1161/CIRCULATIONAHA.106.685313.
16. Sianos G, Kay IP, Costa MA, Regar E, Kozuma K, de Feyter PJ, Boersma E, Disco C, Serruys PW. Geographical miss during catheter-based intracoronary beta-radiation: incidence and implications in the BRIE study. Beta-Radiation In Europe. *J Am Coll Cardiol*. 2001;38:415–420.
17. Sianos G, Papafaklis MI, Daemen J, Vaina S, van Mieghem CA, van Domburg RT, Michalis LK, Serruys PW. Angiographic stent thrombosis after routine use of drug-eluting stents in ST-segment elevation myocardial infarction: the importance of thrombus burden. *J Am Coll Cardiol*. 2007;50:573–583. doi: 10.1016/j.jacc.2007.04.059.
18. Onuma Y, Serruys PW, Muramatsu T, Nakatani S, van Geuns RJ, de Bruyne B, Dudek D, Christiansen E, Smits PC, Chevalier B, McClean D, Koolen J, Windecker S, Whitbourn R, Meredith I, Garcia-Garcia HM, Veldhof S, Rapoza R, Ormiston JA. Incidence and imaging outcomes of acute scaffold disruption and late structural discontinuity after implantation of the absorb Everolimus-Eluting fully bioresorbable vascular scaffold: optical coherence tomography assessment in the ABSORB cohort B Trial (A Clinical Evaluation of the Bioabsorbable Everolimus Eluting Coronary Stent System in the Treatment of Patients With De Novo Native Coronary Artery Lesions). *JACC Cardiovasc Interv*. 2014;7:1400–1411. doi: 10.1016/j.jcin.2014.06.016.
19. Karanasos A, van Geuns RJ, Zijlstra F, Regar E. Very late bioresorbable scaffold thrombosis after discontinuation of dual antiplatelet therapy. *Eur Heart J*. 2014;35:1781. doi: 10.1093/eurheartj/ehu031.
20. Foin N, Gutiérrez-Chico JL, Nakatani S, Torii R, Bourantas CV, Sen S, Nijjer S, Petraco R, Kousera C, Ghione M, Onuma Y, Garcia-Garcia HM, Francis DP, Wong P, Di Mario C, Davies JE, Serruys PW. Incomplete stent apposition causes high shear flow disturbances and delay in neointimal coverage as a function of strut to wall detachment distance: implications for the management of incomplete stent apposition. *Circ Cardiovasc Interv*. 2014;7:180–189. doi: 10.1161/CIRCINTERVENTIONS.113.000931.
21. Kolandaivelu K, Swaminathan R, Gibson WJ, Kolachalama VB, Nguyen-Ehrenreich KL, Giddings VL, Coleman L, Wong GK, Edelman ER. Stent thrombogenicity early in high-risk interventional settings is driven by stent design and deployment and protected by polymer-drug coatings. *Circulation*. 2011;123:1400–1409. doi: 10.1161/CIRCULATIONAHA.110.003210.
22. Karanasos A, Li Y, Tu S, Wentzel JJ, Reiber JH, van Geuns RJ, Regar E. Is it safe to implant bioresorbable scaffolds in ostial side-branch lesions? Impact of 'neo-carina' formation on main-branch flow pattern. Longitudinal clinical observations. *Atherosclerosis*. 2015;238:22–25. doi: 10.1016/j.atherosclerosis.2014.11.013.
23. Witzenbichler B, Maehara A, Weisz G, Neumann FJ, Rinaldi MJ, Metzger DC, Henry TD, Cox DA, Duffy PL, Brodie BR, Stuckey TD, Mazzaferri EL Jr, Xu K, Parise H, Mehran R, Mintz GS, Stone GW. Relationship between intravascular ultrasound guidance and clinical outcomes after drug-eluting stents: the assessment of dual antiplatelet therapy with drug-eluting stents (ADAPT-DES) study. *Circulation*. 2014;129:463–470. doi: 10.1161/CIRCULATIONAHA.113.003942.
24. Karanasos A, Regar E. Standing on solid ground?: Reassessing the role of incomplete strut apposition in drug-eluting stents. *Circ Cardiovasc Interv*. 2014;7:6–8. doi: 10.1161/CIRCINTERVENTIONS.114.001173.
25. Cook S, Eshtehardi P, Kalesan B, Räber L, Wenaweser P, Togni M, Moschovitis A, Vogel R, Seiler C, Eberli FR, Lüscher T, Meier B, Jüni P, Windecker S. Impact of incomplete stent apposition on long-term clinical outcome after drug-eluting stent implantation. *Eur Heart J*. 2012;33:1334–1343. doi: 10.1093/eurheartj/ehr484.
26. Papayannis AC, Cipher D, Banerjee S, Brilakis ES. Optical coherence tomography evaluation of drug-eluting stents: a systematic review. *Catheter Cardiovasc Interv*. 2013;81:481–487. doi: 10.1002/ccd.24327.
27. McFadden EP, Stabile E, Regar E, Cheneau E, Ong AT, Kinnaird T, Suddath WO, Weissman NJ, Torguson R, Kent KM, Pichard AD, Satler LF, Waksman R, Serruys PW. Late thrombosis in drug-eluting coronary stents after discontinuation of antiplatelet therapy. *Lancet*. 2004;364:1519–1521. doi: 10.1016/S0140-6736(04)17275-9.
28. Garratt KN, Weaver WD, Jenkins RG, Pow TK, Mauri L, Kereiakes DJ, Winters KJ, Christen T, Allocco DJ, Lee DP. Prasugrel plus aspirin beyond 12 months is associated with improved outcomes after TAXUS Liberté paclitaxel-eluting coronary stent placement. *Circulation*. 2015;131:62–73. doi: 10.1161/CIRCULATIONAHA.114.013570.
29. Patel Y, Depta JP, Patel JS, Masrani SK, Novak E, Zajarias A, Kurz HI, Lasala JM, Bach RG, Singh J. Impact of intravascular ultrasound on the long-term clinical outcomes in the treatment of coronary ostial lesions [published online ahead of print June 1, 2013]. *Catheter Cardiovasc Interv*. doi: 10.1002/ccd.25034.

SUPPLEMENTAL MATERIAL

Supplementary Methods

Quantitative coronary angiography

Quantitative coronary angiography was performed using CAAS 5.11 (Pie Medical Imaging, Maastricht, Netherlands) and included reference vessel diameter (RVD), diameter stenosis (DS%), and minimal lumen diameter (MLD).

Histopathological analysis of thrombus aspirates

Thrombus aspiration was attempted in thirteen cases. However, aspiration samples were successfully retrieved only in four (30.8%) and were collected after filtering (40μm cell strainer BD Biosciences), snap-frozen and stored at -80°C. Macroscopic characteristics such as color, size and number of particles were documented. The frozen samples were cryosectioned (5μm serial sections), fixed with buffered paraformaldehyde 4%, and stained with hematoxylin-eosin as a routine stain, rosorcin-fuchin as an elastin stain and alcian blue for proteoglycans. Polarized light was used to detect birefringence.

Supplementary Results

Histopathological findings of thrombus aspirates

Four thrombus aspirates were submitted for histopathology analysis. One sample did not contain any thrombus. One case contained only micro-thrombi [mean length 36μm (25-52μm)] without cellular elements. Two cases contained overt thrombi: one being platelet-rich and one containing compact fibrin with Zahn-lines. Eosinophilic granulocytes were observed in both but comprised <10% of all granulocytes, reflecting normal distribution. There was no evidence of hypersensitivity towards scaffold material. Vessel wall components and atheroma were not observed. There was no birefringence indicative of polymeric scaffold material in the aspirates.

Treatment of BVS thrombosis

At the discretion of the operator, thrombus aspiration was performed in 13/14 patients. Glycoprotein IIb/IIIa inhibitors were administered in 9/14 cases (64.3%). Seven of 14 patients were treated by implantation of a metallic DES. Two patients with edge problems were treated by additional BVS implantation. Four patients were treated by combination of thrombus aspiration and balloon dilation, while in one patient the attempt for treatment of acute thrombosis failed.

This patient developed a large myocardial infarction (CK_{peak}: 4358U/L), which led to poor left ventricular systolic function and implantation of an implantable cardioverter-defibrillator for non-sustained ventricular tachycardia. In all patients, antiplatelet therapy after thrombosis was recommended for at least one year, continued by aspirin alone, including patients concomitantly receiving oral anticoagulation.

Repeated OCT pullbacks were available for 5/7 patients that underwent additional metallic stent implantation, and for 1/2 patients with additional scaffold implantation for the treatment of BVS failure: in these 6 patients, the mean lumen area was increased from 4.40mm² [2.80-6.43mm²] to 8.34mm² [7.43-8.88mm²] (p=0.028), mean scaffold area increased non-significantly from 7.49mm² [6.99-9.29mm²] to 9.21mm² [7.51-9.89mm²] (p=0.29), mean prolapse/neointimal area decreased non-significantly from 1.94mm² [1.13-2.98mm²] to 0.83mm² [0.47-1.22mm²] (p=0.07), and the percentage of malapposed struts was non-significantly decreased from 3.1% [0-6.4%] to 0.6% [0.2-1.6%] (p=0.17).

Clinical outcome after treatment of BVS thrombosis

In 11 patients, follow-up was uneventful, while 3 patients suffered a recurrent event: One patient died of cardiac cause 4 days after the procedure. The second patient receiving a metallic DES for the treatment of BVS thrombosis, had an invasive follow-up 6 months follow-up. OCT showed an overall good expansion and healing result with nevertheless sporadic clusters of uncovered struts. This patient suffered recurrent thrombosis, one year after the initial event, and 5 days after scheduled prasugrel discontinuation. The third patient had a repeat target vessel revascularization 4 months after thrombosis by coronary artery bypass graft (CABG), due to restenosis of the metal DES implanted for the treatment of BVS thrombosis.

Supplementary Table 1. OCT findings in BVS thrombosis in frames with and without thrombus

	Frames with thrombus (n=140)	Frames without thrombus (n=112)	p-value
Lumen area, mm^2	4.35 (2.61-6.08)	5.84 (4.11-7.58)	<0.001*
Scaffold area, mm^2	7.63 (6.32-8.95)	8.14 (6.83-9.46)	<0.001*
Malapposition area, mm^2 (n=16)	1.54 (0-3.44)	0.44 (0.00-6.70)	0.18*
Frames with malapposition, %	5.3 (1.8-15.1)	6.3 (2.0-17.9)	0.75*
Frames with overlap, %	4.8 (1.4-15.4)	2.3 (0.5-9.3)	0.20*

All values presented as estimated means (95% confidence intervals).

*P-values and estimated means were calculated with multilevel regression analysis using within-patient intercepts as random effects.

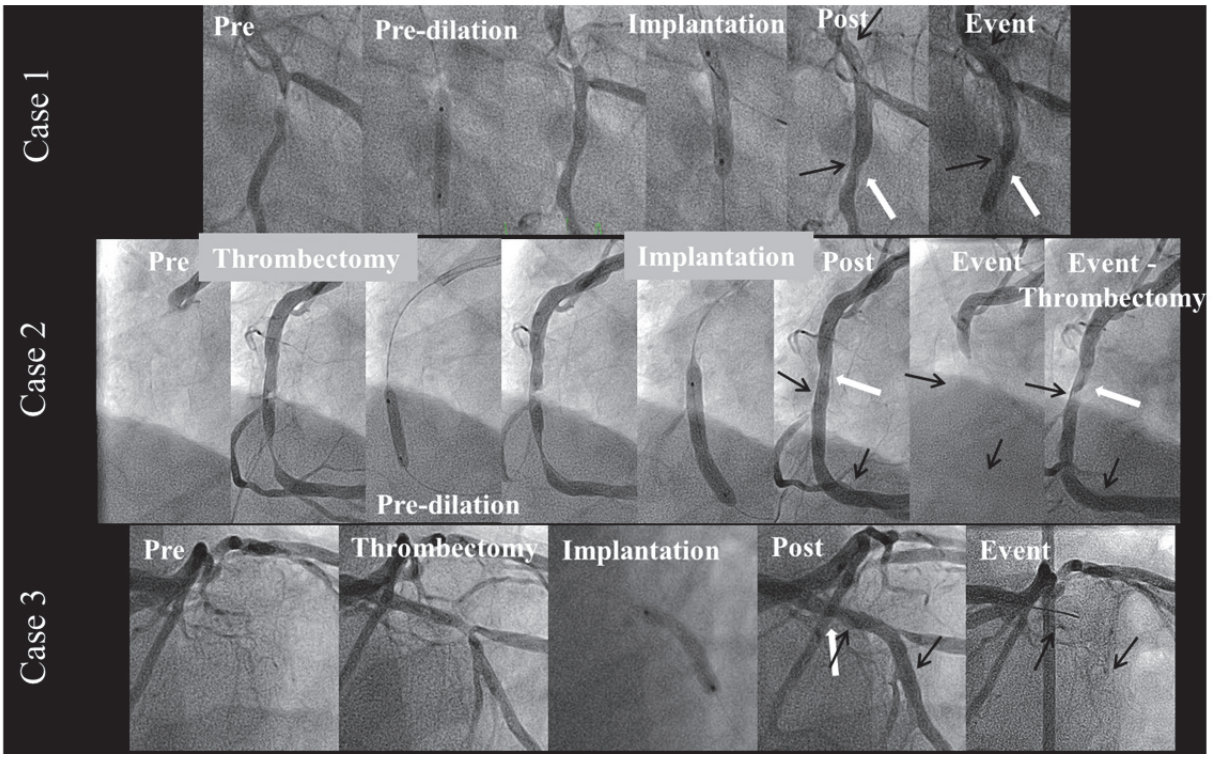

Supplementary Figure 1. Summary of the cases with acute thrombosis due to incomplete lesion coverage

Black arrows indicate the scaffold markers and white arrows indicate the uncovered edge segment.

Supplementary Table 2. Patient-level characteristics

Case	Baseline and procedural characteristics												Scaffold thrombosis				
	Age	ACS	Prescribed P2Y12 inhibitor	Treated vessel	AHA/ ACC class	Bifurcation	Ostial LAD/ LCx lesion	No of BVS	Total BVS length	OCT guided	Pre-dilation	Post-dilation	Type	Time (days)	ASA	P2Y12 inh	OAC
1	50	Yes	clopidogrel	LCX	C	No	No	1	18	No	Yes	No	Acute	0	Yes	Yes	No
2	51	Yes	ticagrelor	RCA	B1	No	No	1	28	No	Yes	No	Acute	0	Yes	Yes	No
3	59	Yes	prasugrel	LAD	C	No	No	1	18	No	No	No	Acute	1	Yes	Yes	No
4	62	Yes	prasugrel	LAD	B1	No	Yes	1	18	No	Yes	No	Acute	1	Yes	Yes	No
5	49	Yes	prasugrel	LAD	B2	No	Yes	1	18	No	Yes	Yes	Subacute	17	Yes	Yes	No
6	45	No	clopidogrel	LAD	B2	No	No	2	56	No	Yes	Yes	Subacute	2	Yes	Yes	No
7	65	Yes	prasugrel	LAD	B2	Yes	No	1	18	No	Yes	Yes	Late	142	Yes	Yes	No
8	69	Yes	clopidogrel	LAD	C	Yes	Yes	3	64	Yes	Yes	Yes	Late	47	Yes	Yes	No
9	59	No	prasugrel	LAD	C	No	Yes	1	28	No	Yes	Yes	Late	112	Yes	Yes	No
10	55	No	clopidogrel	LCX	A	No	Yes	1	18	Yes	Yes	No	Very late	675	Yes	No	No
11	71	No	clopidogrel	LAD	C	No	No	2	36	Yes	Yes	Yes	Late	161	No	No	Yes
12	62	Yes	prasugrel	RCA	C	No	No	1	28	Yes	Yes	No	Very late	478	Yes	No	No
13	86	Yes	clopidogrel	LCX	C	No	Yes	1	28	Yes	Yes	No	Very late	371	No	No	Yes
14	60	No	clopidogrel	LAD	C	Yes	No	2	24	No	Yes	Yes	Late	129	No	No	Yes

Abbreviations: ACS=acute coronary syndrome, BVS=bioresorbable vascular scaffold, OCT=optical coherence tomography, ASA=acetylsalicylic acid, OAC=oral anticoagulation

Supplementary Table 3. Patient-level angiographic and OCT findings

Case	Type	Time (days)	Incomplete lesion coverage	Malappo-sition	Reste-nosis	Disconti-nuity	Under-expansion	Other baseline findings	Other follow-up findings	Recent DAPT disconti-nuation	DAPT disconti-nuation <1 year
1	Acute	0	Dissection	N/A	No	No	No	No	No	No	No
2	Acute	0	Thrombosed segment	Yes	No	No	No	No	No	No	No
3	Acute	1	Thrombosed segment	N/A	No	No	No	No	No	No	No
4	Acute	1	No	Suspected (angio)	No	No	No	No	No	No	No
5	Subacute	17	No	Suspected (angio)	No	No	Suspected (angio)	No	No	No	No
6	Subacute	2	No	No	No	No	No	No	Thrombus overlying extensive overlap region (7mm)	No	No
7	Late	142	Dissection	No	Edge	No	No	No	Occlusive proximal edge restenosisNo no thrombus	No	No
8	Late	47	No	Yes (late malapposition)	No	No	No	Residual plaque burden/ residual thrombus	No	No	No

9	Late	112	No	Yes	Yes	No	Yes	No	No	No	No
10	Very late	675	No	Yes (late malapposition)	No	Late discontinuity	No	No	No	Yes	No
11	Late	161	No	Yes (Fracture)	No	Fracture	Yes	No	Thrombus in underexpanded long overlap region(~5mm)	Yes	Yes
12	Very late	478	No	Possible	No	Possible late discontinuity	No	No	No	No	No
13	Very late	371	No	Yes (Baseline)	No	No	No	Extensive intra-scaffold dissections	No	Yes	No
14	Late	129	No	No	No	No	No	No	Uncovered struts protruding at the bifurcation	No	Yes

Abbreviations: OCT=optical coherence tomography, DAPT=dual antiplatelet therapy

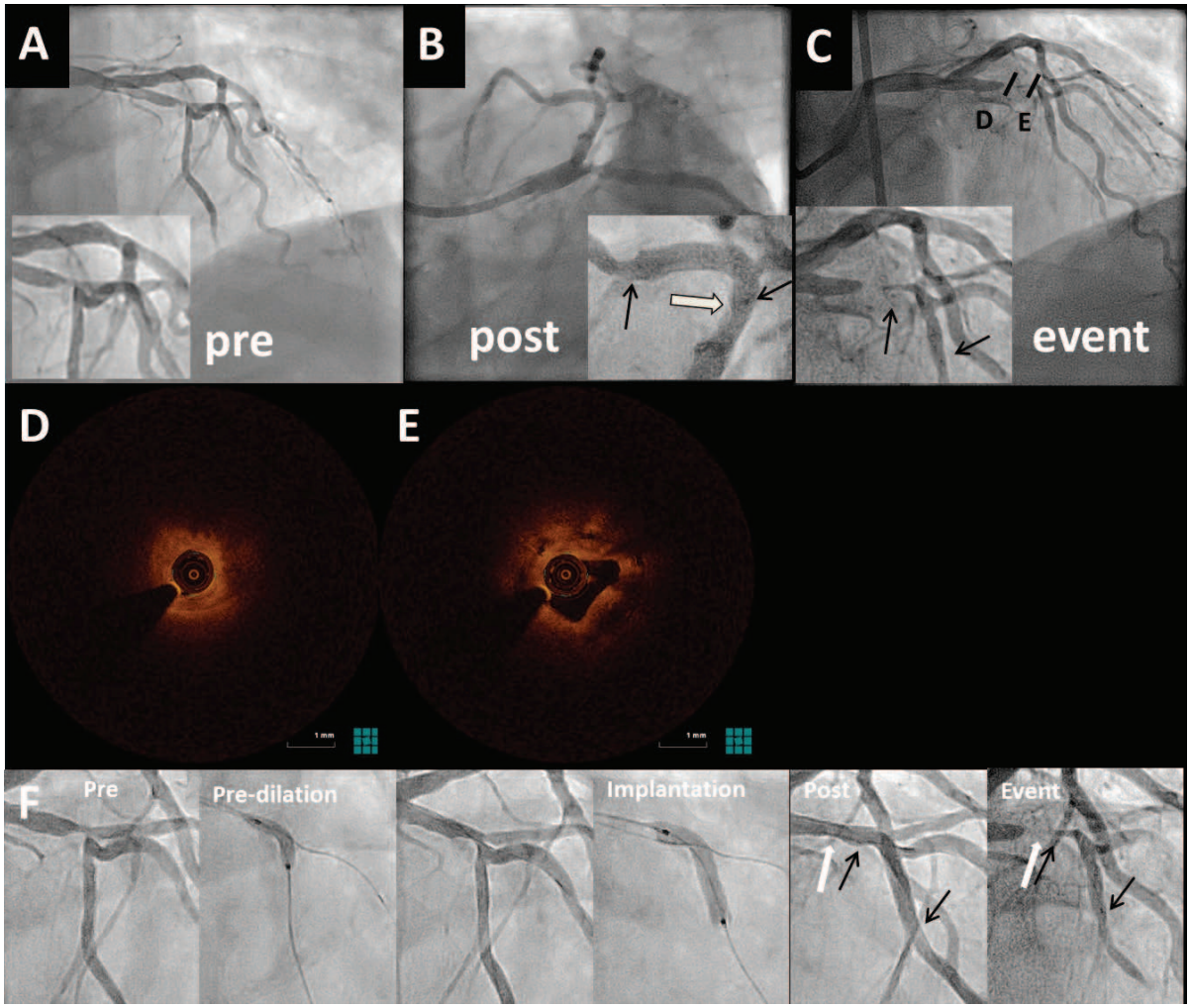

Supplementary Figure 2. Late stent thrombosis re-classified by OCT as edge restenosis resulting from incomplete lesion coverage.

A. Pre-procedural and B. post-procedural angiogram at baseline showing proximal edge dissection (white arrow). C. Angiogram at event (142 days) shows contrast deficit at the proximal edge, extending within the scaffold with TIMI I flow. OCT discloses occlusive edge restenosis (D) and restenosis within the scaffold with layered pattern (E), without luminal thrombus. F. Angiographic review demonstrating incomplete lesion coverage. Black arrows indicate the scaffold markers and white arrows the uncovered edge segment.

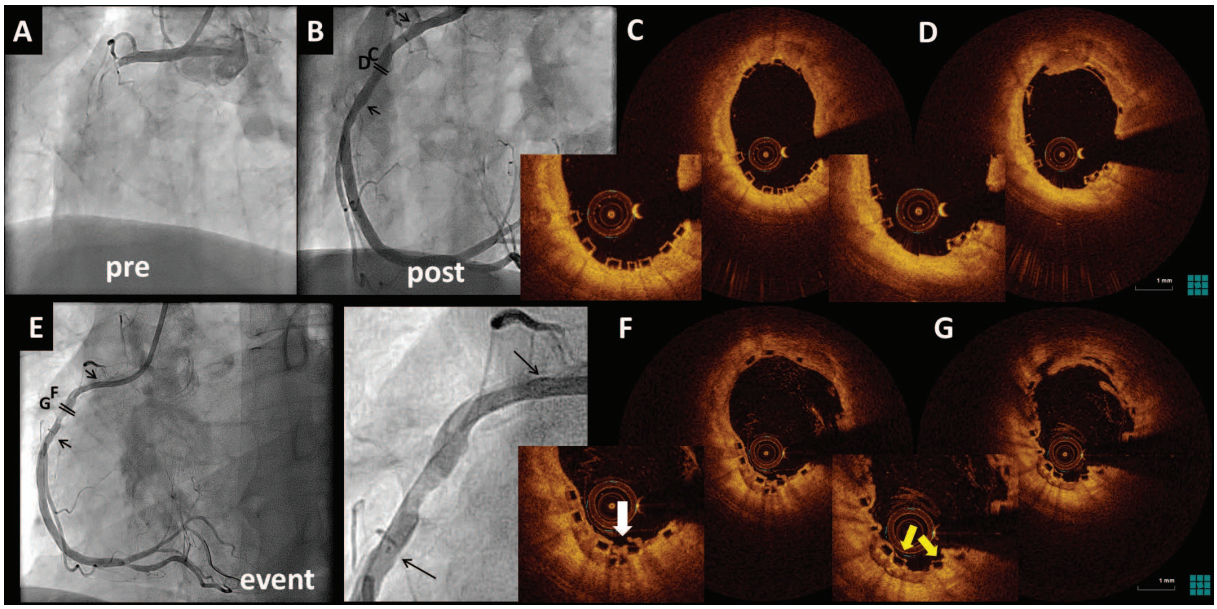

Supplementary Figure 3. Very late scaffold thrombosis without definite substrate.

BVS implantation in a proximal RCA lesion due to STEMI (A), with good post-procedural angiographic (B) and OCT (C-D) result. The patient suffered very late scaffold thrombosis 478 days post implantation, while only on aspirin (E). OCT shows suspected scaffold discontinuity (F; white arrow) and uncovered and possibly malapposed struts (G; yellow arrow) proximally to the thrombosed segment.

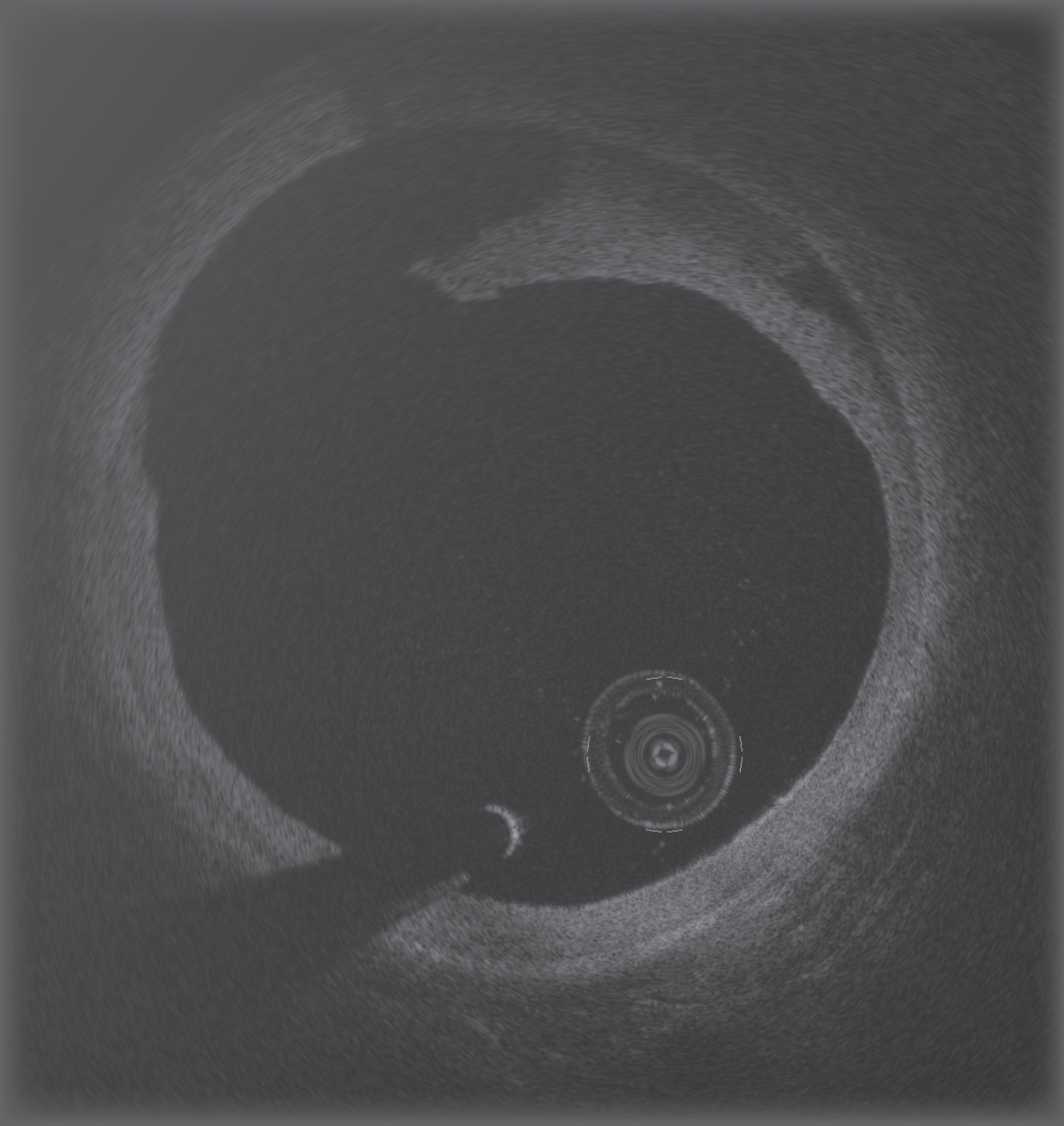

PART VIII

Intravascular imaging assessment in renal denervation

Chapter 8.1

Validation of renal artery dimensions measured by magnetic resonance angiography in patients referred for renal sympathetic denervation

van Kranenburg M, **Karanasos A**, Chelu RG, van der Heide E, Ouhlous M, Nieman K, van Mieghem N, Krestin G, Niessen W, Zijlstra F, van Geuns RJ, Daemen J

Acad Radiol 2015. 2015 Sep;22(9):1106-14

Validation of Renal Artery Dimensions Measured by Magnetic Resonance Angiography in Patients Referred for Renal Sympathetic Denervation

Matthijs van Kranenburg, MD, Antonis Karanasos, MD, Raluca Gabriela Chelu, MD, Elco van der Heide, Mohamed Ouhlous, MD, PhD, Koen Nieman, MD, PhD, Nicolas van Mieghem, MD, Gabriel Krestin, MD, PhD, Wiro Niessen, PhD, Felix Zijlstra, MD, PhD, Robert-Jan van Geuns, MD, PhD, Joost Daemen, MD, PhD

Rationale and Objectives: Magnetic resonance angiography (MRA) is a well-established modality for the assessment of renal artery stenosis. Using dedicated quantitative analyses, MRA can become a useful tool for assessing renal artery dimensions in patients referred for renal sympathetic denervation (RDN) and for providing accurate measurements of vascular response after RDN. The purpose of this study was to test the reproducibility of a novel MRA quantitative imaging tool and to validate these measurements against intravascular ultrasound (IVUS).

Materials and Methods: In nine patients referred for renal denervation, renal artery dimensions were measured. Bland–Altman analysis was used to assess the intraobserver and interobserver reproducibility.

Results: Mean lumen diameter was 5.8 ± 0.7 mm, with a very good intraobserver and interobserver variability of 0.7% (reproducibility: bias, 0 mm; standard deviation [SD], 0.1 mm) and 1.2% (bias, 0 mm; SD, 0.1 mm), respectively. Mean total lumen volume was 1035.3 ± 403.6 mm^3 with good intraobserver and interobserver variability of 2.9% (bias, −9.7 mm^3; SD, 34.0 mm^3) and 2.8% (bias, −11.4 mm^3; SD, 42.4 mm^3). The correlation (Pearson *R*) between mean lumen diameter measured with MRA and IVUS was 0.750 (*P* = .002).

Conclusions: Using a novel MRA quantitative imaging tool, renal artery dimensions can be measured with good reproducibility and accuracy. MRA-derived diameters and volumes correlated well with IVUS measurements.

Key Words: Renal artery; percutaneous renal sympathetic denervation; magnetic resonance angiography; intravascular ultrasound.

Percutaneous renal sympathetic denervation (RDN) is currently being studied as a potential treatment to lower sympathetic nerve activity in a broad spectrum of diseases (1,2). At present, more than 53 devices are available to disrupt renal afferent and efferent nerves traveling along the renal arterial wall. Besides the fact that initial promising, but noncontrolled studies on clinical efficacy in patients with therapy-resistant hypertension were recently challenged by a negative randomized controlled trial, data on long-term safety are mainly limited to the use of the first-generation radiofrequency devices (3–5). The currently available data on the incidence of renal artery stenosis, mostly derived from duplex ultrasound findings, are showing a low rate of adverse events, both at short and longer term follow-up (4,6). Published data from computed tomography angiography (CTA) or magnetic resonance angiography (MRA) report only binary outcomes (7), precluding firm conclusion on the true vascular response to RDN itself. As new renal denervation systems are being introduced, there is a need for dedicated volumetric noninvasive imaging tools to accurately assess renal artery integrity at the medium to long term (8). Furthermore, balloon-based RDN devices require accurate sizing to avoid complications due to oversizing (9). The aim of the present study was to evaluate a new software tool allowing automated vessel

Acad Radiol 2015; ■:1–9

From the Department of Cardiology, Erasmus Medical Center, P.O. Box 2040, Rotterdam 3000 CA, The Netherlands (M.v.K., A.K., R.G.C., E.v.d.H., K.N., N.v.M., F.Z., R.-J.v.G., J.D.); and [b]Departments of Radiology (M.v.K., R.G.C., M.O., K.N., G.K., W.N., R.-J.v.G.) and [c]Medical Informatics (W.N.), Erasmus Medical Center, Rotterdam, The Netherlands. Received December 15, 2014; accepted March 18, 2015. Conflicts of Interest: A.K. has received research support from St Jude Medical; K.N. has received institutional research support from Siemens Medical Solutions, GE Healthcare, and Bayer Healthcare; W.N. is co-founder, scientific director, and share holder of Quantib BV; G.K. received institutional research support from GE Healthcare, Siemens AG, and Bayer Healthcare. He received payment for lectures from EISAI Japan. All other authors have reported that they have no relationships relevant to the contents of this article to disclose. **Address correspondence to**: J.D. e-mail: j.daemen@erasmusmc.nl

http://dx.doi.org/10.1016/j.acra.2015.03.014

segmentation for quantitative renal artery lumen dimension assessment. Intraobserver and interobserver reproducibility were studied, and MRA-derived measurements were validated with intravascular ultrasound (IVUS).

MATERIALS AND METHODS

Patient Selection

Nine consecutive patients underwent both MRA and preprocedural IVUS at the time of the renal denervation procedure. Because of an early trifurcation in the vessel in one patient, automated segmentation with MRA was not successful in one artery. For the MRA analyses, 17 vessels were used. For the correlation analyses between MRA and IVUS, MRA vessel length was determined and manually adjusted on the basis of the length of the IVUS pullback with either the ostium or bifurcation as landmark. Because of a lack of IVUS measurement in 1 vessel and a lack of visualization of either bifurcation or ostium, a total of 16 arteries in which both MRA and IVUS data were available were used for validation of MRA against IVUS measurements. The study was approved by the hospital ethics committee and conforms to the declaration of Helsinki. All patients provided written informed consent before inclusion.

Magnetic Resonance Angiography Acquisition

MRA was performed on a 1.5T MRI scanner (Discovery MR450; GE Medical systems, Milwaukee, WI). Patients were positioned in supine position, and an eight-channel cardiac coil was placed on the thorax and upper abdomen. A dedicated RDN-MRI protocol was used. As part of this MRI protocol, a three-dimensional (3D) Vasc Fast time of flight (TOF) spoiled gradient-echo sequence was used to acquire images of the renal vasculature, after a test bolus procedure. Images were acquired during a breath-hold. The following parameters were used: field of view, 46 cm × 41.4 cm; matrix, 320 × 192, upsampled to 512 × 512; number of excitations, 0.75; pixel size, 0.89 × 0.89 mm; flip angle, 17°; slice thickness, 1.6 mm; location per slab, 28 upsampled to 56 with ZIP2; repetition time, 3.2 milliseconds; echo time, 1.2 milliseconds; bandwidth, 83.33 Hz. Approximately, 20 seconds was the duration of the breath-hold, depending on the locations per slab. A power injector (Medrad Spectris, Warrendale, PA) was used to inject gadobutrol (Gadovist 1.0 mmol/mL; Bayer, Mijdrecht, The Netherlands). Gadovist was injected, around 18 seconds before acquisition, with a dose of 0.1 mmol/kL ml into an antecubital vein followed by 15 mL of saline at a rate of 2.5 mL/s to visualize the renal arteries.

MRA Analysis

Renal arteries were analyzed with CAAS MRA version 1.0 (Pie Medical Imaging B.V, Maastricht, The Netherlands). The segmentation was initialized by placing four delimiter points on the volumetric rendered contrast-enhanced MRA view; root delimiter point at the thoracic aorta, abdominal aorta, and finally two points distal of the bifurcation of the renal artery (Supplementary Figure 1). Ray tracing was used to extract the 3D position of the user-defined delimiter points within the rendered volume. The acquired position was centralized within the lumen by image processing techniques. The 3D segmentation used a deformable model algorithm (10) that iteratively optimized the location of the surface toward the luminal border based on image gradients while simultaneously maintaining local smoothness of the 3D segmented surface. After segmentation, the center lines of the 3D segmentation were extracted as the minimum path of maximal inscribed spheres from the root delimiter point to the distal delimiter points (11). Within this process, the diameter of the spheres resembled the minimum diameter along the center line of the 3D segmentation (Supplementary Figure 2). The ostium and bifurcation of the renal arteries were automatically detected, by generation of a polygon of confluence (POC) (12). The center line splits in the POC from the proximal main vessel splits in the renal artery and the bifurcation of the renal artery. Outside the POC, the cross-sectional area was defined perpendicular to the lumen wall along each position of the center line. Based on the cross-sectional area, the lumen diameter was defined as the equivalent diameter on the basis of the assumption of circularity. For analysis, the arteria renal was selected, which is the single vessel segment between the ostial POC and the bifurcation POC. In case of failure of this method, only the bifurcation of the renal artery was selected manually. The automatically segmented arteries were inspected, and borders were manually corrected if necessary in the stretched multiplanar rendering and perpendicular view. Vessel length of the renal arteries was defined as the distance between the automatically defined ostium and bifurcation of the renal artery (Fig 1). Minimal lumen diameter, mean lumen diameter, and total lumen volume were based on semiautomatic segmentation. To compare and validate MRA with IVUS, images were matched and MRA dimensions were measured again with use of IVUS references. IVUS-derived borders were used as a reference. To be able to validate the MRA volumetric measurements with IVUS, the segment of interest was matched by using either the ostium or bifurcation of the renal artery as a landmark. MRA borders were adjusted according to the vessel length measured with IVUS. In this way, we were able to validate the volume measurements of the renal artery segment between MRA and IVUS.

IVUS Acquisition

Renal arteries were examined with an IVUS system with automatic pullback at 0.5 mm/s (Atlantis SR Pro Imaging Catheter; Boston Scientific, Natick, MA) before renal denervation in all vessels. Spatial resolution was 100 μm. A total dose of 200 μg of nitrates was locally administered before invasive imaging to prevent catheter-induced spasm.

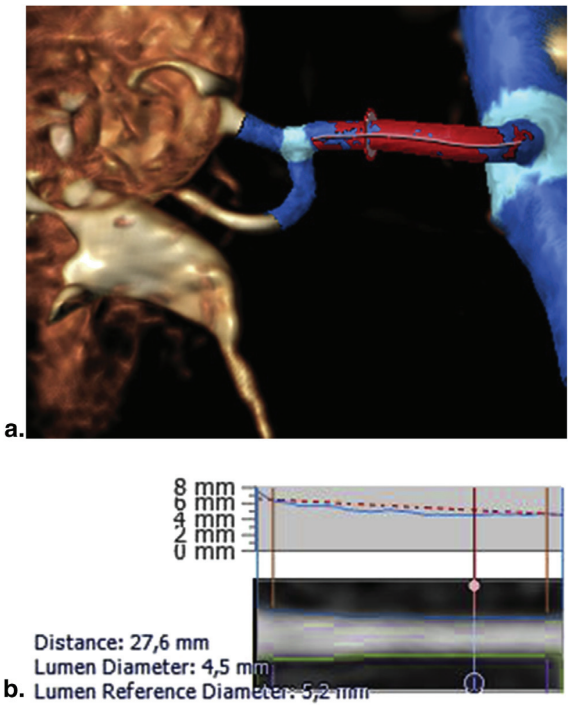

Figure 1. **(a)** Example renal artery measured with MRA. **(b)** Typical longitudinal cross-section of an analyzed renal artery. *Blue lines* represent renal artery borders. The *pink line* can be manually moved to measure luminal dimensions at a specific cross section. *Orange lines* represents reference lines for stenosis measurements. MRA, magnetic resonance angiography. (Color version of figure is available online.)

Retrieved IVUS images were digitally stored and analyzed offline.

IVUS Analysis

Volumetric analysis of the region of interest was performed at 0.5-mm fixed intervals throughout the segment between the renal artery ostium and the first major bifurcation using dedicated software (QCU-CMS, LKEB, Leiden University, The Netherlands). In cases where the guiding catheter was located deeper than the anatomic renal artery ostium or that the first major bifurcation was not visualized, IVUS analysis was performed in the entire pullback. In analyzed frames, the lumen contour was segmented with the help of a semiautomatic algorithm, using manual corrections where necessary (Fig 2). As in MRA, mean diameter was calculated in each frame by the lumen area, as the equivalent diameter based on the assumption of circularity.

Statistical Analysis

Continuous data with normal distribution are presented as mean ± standard deviation (SD). Bland–Altman plots were drawn to assess intraobserver and interobserver variability of MRA and IVUS measurements. Intraobserver and interobserver variability was calculated as the absolute value of the difference between two measurements divided by the average value of the pairs of interest. Associations of MRA measurements with IVUS measurements were estimated with the Pearson correlation coefficient. Paired *t* tests were performed to test significant differences between the means values for MRA and IVUS measurements. Statistical analyses were performed using the IBM SPSS Statistics, version 20.0.01 (SPSS, Chicago, IL). Bland–Altman plots were made with GraphPad PrisM version 4.00 (GraphPad Software Inc, La Jolla, CA).

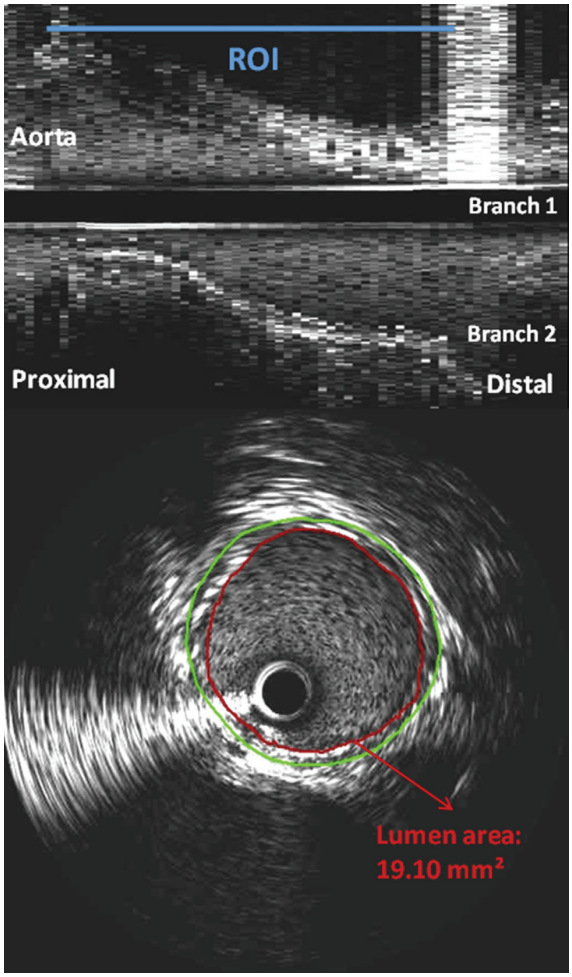

Figure 2. Intravascular ultrasound renal artery. *Black line* represents intravascular ultrasound catheter. *White band* is guidewire artifact. *Red line* represents the lumen area. *Green line* represents the external elastic membrane. ROI, region of interest. (Color version of figure is available online.)

RESULTS

Segmentation Algorithm and Renal Artery Dimensions

In nine patients, 17 renal arteries were analyzed to study intraobserver and interobserver reproducibility. In three renal

TABLE 1. Renal Artery Dimensions After Adjustments with IVUS References

Parameter	MRA, Mean ± SD; *n* = 14	MRA Range	IVUS, Mean ± SD; *n* = 14	IVUS Range	*P* Value
Minimum lumen diameter (mm)	5.2 ± 0.7	4.1–6.4	5.2 ± 0.7	4.2–6.7	.947
Mean lumen diameter (mm)	5.8 ± 0.7	4.6–7.1	5.9 ± 0.6	4.7–7.0	.485
Total lumen volume (mm^3)	861.9 ± 407.3	406.20–1687.2	902.9 ± 369.4	471.3–1527.5	.248

IVUS, intravascular ultrasound; MRA, magnetic resonance angiography; SD, standard deviation.
A paired *t* test is used to test differences between the mean values for MRA and IVUS.

arteries by observer 1 and in 3 renal arteries by observer 2, the bifurcation was selected manually. The segmentation was not possible in two matched renal arteries. Minimum lumen diameter, mean lumen diameter, and total lumen volume measured by MRA and IVUS are summarized in Table 1 and Supplementary Tables 1 and 2.

Intraobserver Reproducibility MRA

Mean minimum lumen diameter was 5.1 ± 0.8 mm. Bias of minimum lumen diameter was 0 mm; standard deviation (SD) of bias, 0.1 mm (95% limits of agreement, −0.1 to 0.1 mm). Intraobserver variability was 0.8%. Mean lumen diameter was 5.8 ± 0.7 mm. Bias of mean lumen diameter was 0 mm; SD of bias, 0.1 mm (95% limits of agreement, −0.1 to 0.1 mm). Intraobserver variability was 0.7%. Mean vessel length was 39.4 ± 12.3 mm. Bias of vessel length was 0.1 mm; SD of bias, 1.2 mm (95% limits of agreement, −2.2 to 2.4 mm). Intraobserver variability was 2.5%. Mean total lumen volume was 1035.3 ± 403.6 mm^3. Bias of total lumen volume was −9.7 mm^3; SD of bias, 34.0 mm^3 (95% limits of agreement, −76.4 to 57.0 mm^3). Intraobserver variability was 2.9%. Bland–Altman plots are shown in Figure 3.

Interobserver Reproducibility MRA

Mean minimum lumen diameter was 5.0 mm ± 0.8 mm. Bias of minimum lumen diameter was 0.1 mm; SD of bias, 0.3 mm (95% limits of agreement, −0.5 to 0.7 mm). Interobserver variability was 3.2%. Mean lumen diameter was 5.7 ± 0.7 mm. Bias of mean lumen diameter was 0 mm; SD of bias, 0.1 mm (95% limits of agreement, −0.2 to 0.3 mm). Interobserver variability was 1.2%. Mean vessel length was 39.8 ± 12.0 mm. Bias of vessel length was −0.9 mm; SD of bias, 2.8 mm (95% limits of agreement, −6.4 to 4.6 mm). Interobserver variability was 2.8%. Mean total lumen volume was 1041.0 ± 397.1 mm^3. Bias of total lumen volume was −11.4 mm^3; SD of bias, 42.4 mm^3 (95% limits of agreement, −94.5 to 71.7 mm^3). Interobserver variability was 2.8%. Bland–Altman plots are shown in Figure 4.

Validation of MRA Dimensions Against IVUS

Mean vessel length measured with MRA was 32.3 ± 11.4 and measured with IVUS 32.8 ± 11.4. Mean minimum lumen diameter was 5.2 ± 0.7 mm. Bias of minimum lumen diameter was 0 mm; SD, 0.5 mm (95% limits of agreement, −0.9 to 0.9 mm). Minimum lumen diameter measured by MRA was correlated with minimum lumen diameter measured by IVUS (*R* value, 0.771; *P* = .001). Mean lumen diameter was 5.8 ± 0.6 mm. Bias of mean lumen diameter was −0.1 mm; SD, 0.5 mm (95% limits of agreement, −1.1 to 0.9 mm). Mean lumen diameter measured by MRA was correlated with mean lumen diameter measured by IVUS (*R* value, 0.750; *P* = .002). Mean total lumen volume was 882.4 ± 383.6 mm^3. Bias of total lumen volume was −40 mm^3; SD, 126.7 mm^3 (95% limits of agreement, −289.4 to 207.5 mm^3). Total lumen volume measured by MRA was correlated with the IVUS measurement (*R* value, 0.951; *P* < .001). Bland–Altman and correlation plots are shown in Figures 5 and 6.

DISCUSSION

Our study demonstrates that quantitative MRA can measure the renal artery dimensions (vessel length, minimum lumen diameter, mean lumen diameter, and renal artery volumes) reproducibly and with good intraobserver and interobserver variability. Intraobserver variability using semiautomatic MRA analysis was excellent for minimum lumen diameter and mean lumen diameter (0.8% and 0.7%, respectively). For vessel, length and total lumen volume was slightly higher but were still well (2.5% and 2.9%, respectively). Interobserver variability was excellent for minimum lumen diameter and mean lumen diameter (3.2% and 1.2%, respectively) and good for vessel length and total lumen volume (2.8% and 2.8%, respectively).

MRA Technique

Automatic analysis of MRA and CTA (13–15) has been developed over the last years. The described quantitative MRA software requires minimal of user interaction to

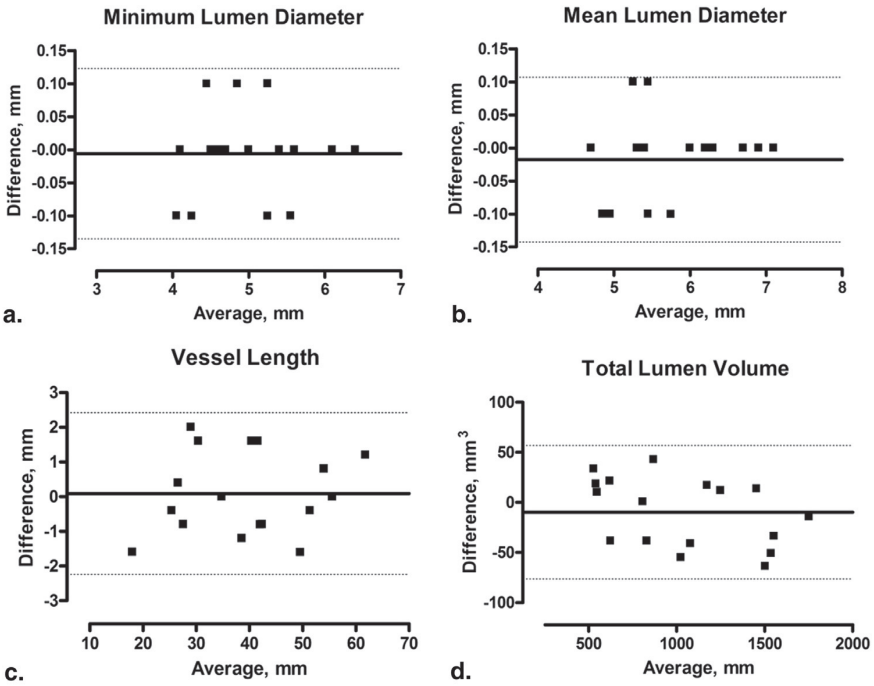

	Minimum Lumen Diameter	Mean Lumen Diameter	Vessel Length	Total Lumen Volume
Bias	0 mm	0 mm	0.1 mm	-9.7 mm^3
SD of Bias	0.1 mm	0,1 mm	1.2 mm	34.0 mm^3
95% Limits of Agreement	-0.1 – 0.1 mm	-0,1 – 0,1 mm	-2.2 – 2.4 mm	-76.4 – 57.0 mm^3

Figure 3. Bland–Altman plots of minimum lumen diameter **(a)**, mean lumen diameter **(b)**, vessel length **(c)**, and total lumen volume **(d)** of the renal arteries measured by magnetic resonance angiography. *Dotted lines* show 95% limits of agreement.

select the vessel segment of interest. By standardizing marker points for ostium and bifurcation identification, the used algorithm achieves excellent reproducibility which is important when baseline and follow-up imaging have to be compared. As well as CTA, renal duplex ultrasound, and invasive renal angiography, MRA is widely used for the detection of RAS (16). The advantage of MRA is that it does not require the use of ionizing radiation or iodinated contrast material that are required by CTA (17,18), nor is MRA hampered by a higher body mass as may the case with duplex ultrasound. Various magnetic resonance imaging techniques have been developed to visualize the aorta and its branches, including "black blood" sequences, 2D and 3D TOF methods, phase-contrast techniques, and 3D contrast-enhanced methods using a gadolinium-based agent (19,20). The most commonly used sequences are the 2D TOF MRA and 3D contrast-enhanced methods. Nevertheless, the quality of the images in MRA depends on proper breath-hold and accurate timing of the contrast bolus. MRA cannot be performed in patients with implanted devices or claustrophobia.

Validation with IVUS

To the best of our knowledge, this is the first study validating MRA measurements of the renal arteries against IVUS measurements. Because of difficulties in engaging the tip of the IVUS catheter beyond the first large renal artery bifurcation (53% of the cases) and inability to fully visualize the ostium of the renal artery due to engagement of the tip of the guiding catheter (47%), IVUS pullback length was on average 5.9 mm shorter than the length of renal artery as assessed by MRA. To be able to validate the MRA volumetric measurements with IVUS, the segment of interest was matched by using either the ostium or bifurcation of the renal artery as a land mark. In this way, we were able to validate the volume measurements of the renal artery segment between MRA and IVUS. Quantitative MRA renal artery measurements correlated well with IVUS, with a Pearson $R > 0.5$ for all measurements. MRA slightly underestimated vessel dimensions compared with IVUS, but the mean differences were small and not significant. One potential cause could have been the use of perprocedural intra-arterial nitrates directly before the IVUS pullback.

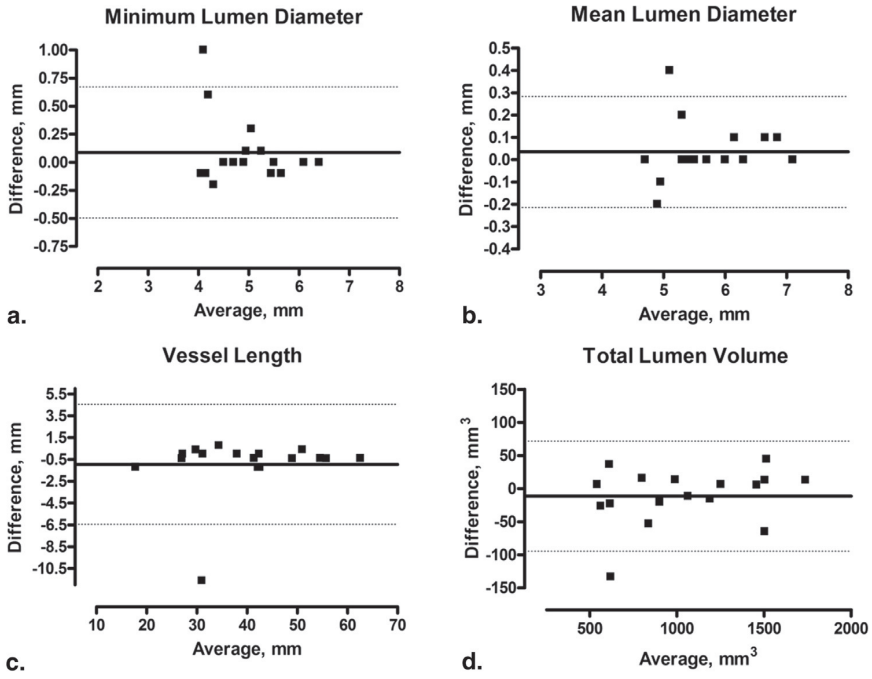

	Minimum Lumen Diameter	Mean Lumen Diameter	Vessel Length	Total Lumen Volume
Bias	0.1 mm	0 mm	-0.9 mm	-11.4 mm^3
SD of Bias	0.3 mm	0.1 mm	2.8 mm	42.4 mm^3
95% Limits of Agreement	-0.5 – 0.7 mm	-0.2 – 0.3 mm	-6.4 – 4.6 mm	-94.5 - 71.7 mm^3

Figure 4. Interobserver variability magnetic resonance angiography (MRA). Bland–Altman plots of minimum lumen diameter **(a)**, mean lumen diameter **(b)**, vessel length **(c)**, and total lumen volume **(d)** of the renal arteries measured by MRA. *Dotted lines* show 95% limits of agreement.

Clinical Applicability

Noninvasive quantitative measurements of renal artery dimension might be useful in preprocedural planning. The significance of the proper assessment of luminal dimensions has been demonstrated by recent data showing that oversizing with balloon-based RDN devices significantly increases the risk of intimal dissections of the renal artery as detected by OCT. Particularly, the measurement of minimum lumen diameter can be helpful in helping the treating physician in selecting the proper device and especially in selecting the balloon size to avoid oversizing (9). MRA may thus be important to the selection of patients for RDN procedure.

Quantitative MRA analyses might allow accurate follow-up of renal arteries after renal artery interventions, allowing precise estimates of the vascular lumen and possible stenoses. The latter supports the use of MRA over duplex ultrasound, which is known to be highly operator dependent and which has a diagnostic accuracy in detecting stenosis that ranges from 60% to 90% (21). MRA, in contrast, has a sensitivity of 93% and specificity of 91% to detect renal artery stenosis compared with digital subtraction arteriography with invasive measurements (22).

Current rates of stenosis after RDN depend strongly on the definitions and the methods of follow-up. For example, the Symplicity HTN-3 trial (which used the Medtronic Symplicity Flex RDN system) showed that the occurrence of RAS (defined as >70%) was low (1 of 332 [0.3%]) within 6 months after renal denervation. Conversely, an emerging number of case reports have been published on RAS related to RDN (23–25), and recent data on the use of optical coherence tomography after RDN showed dissections in up to 35% of the arteries (9).

In our study, MRA measurements demonstrated a low intraobserver variability of 0.8% for minimum lumen diameter, 2.9% for total lumen volume, and low interobserver variability of 3.2% for minimum lumen diameter, and 2.8% for total lumen volume. This allows the assessment of changes well in the range of a 10–40% change in luminal dimensions that might be clinically relevant at the long term. This dedicated quantitative analyses software requires minimal user input and might help to examine subtle changes renal artery integrity after RDN.

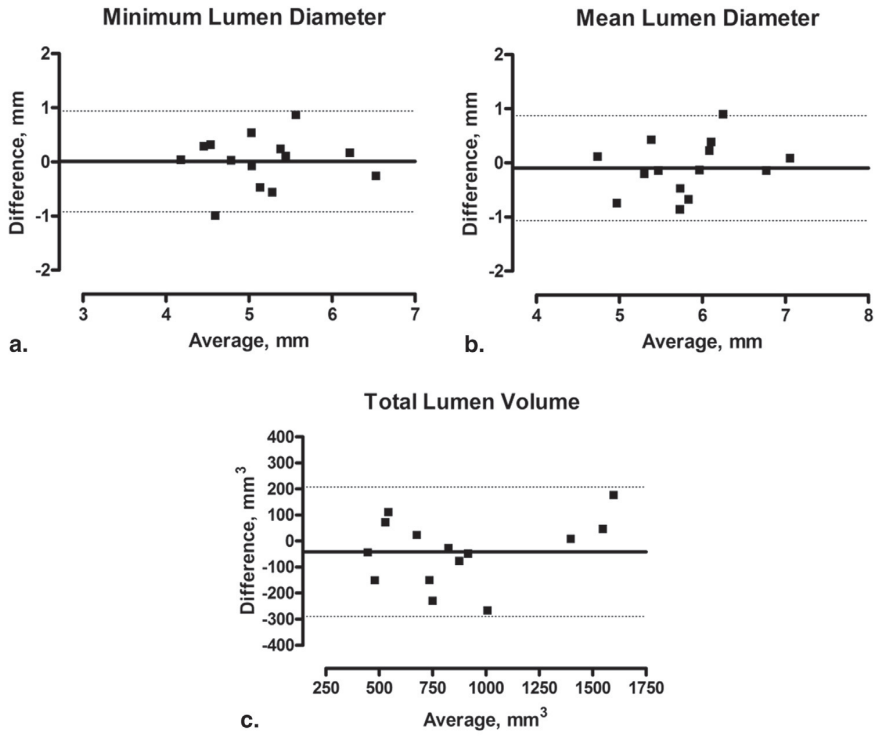

	Minimum Lumen Diameter	Mean Lumen Diameter	Total Lumen Volume
Bias	0 mm	-0.1 mm	-40 mm^3
SD of Bias	0.5 mm	0.5 mm	126.7 mm^3
95% Limits of Agreement	-0.9 – 0.9 mm	-1.1 – 0.9 mm	-289.4 – 207.5 mm^3

Figure 5. Bland–Altman plots of minimum lumen diameter **(a)**, mean lumen diameter **(b)**, and total lumen volume **(c)** in mm^3 of the renal arteries measured by magnetic resonance angiography and intravascular ultrasound. *Dotted lines* show 95% limits of agreement.

The presented technology could help to achieve a more accurate evaluation of renal artery integrity at the medium- and long-term after renal artery interventions, especially in an era with an emerging number of newer generation devices.

Limitations

Our study has several limitations. First, interstudy variability was not tested by performing repeated MRAs. Second, as we were unable to treat small renal arteries with the current generation devices used in our site, patients with a renal artery diameter <4 mm were not included in this study. Our results might therefore not be applicable to arteries <4 mm.

A total dose of 200 μg of nitrates was locally administered before IVUS to prevent catheter-induced spasm. This might change the artery size and might be an explanation for the small differences in renal artery dimensions. The slice thickness of 1.6 mm without overlap is a limitation of the acquisition but inherent to breath-hold period of 20 seconds used in our protocol. Different MRA protocols and interstudy repeatability of the renal artery dimension were not tested as we were interested in the segmentation algorithm. Another contrast-agent injection on a second day would also have been more invasive. A double dose (0.2 mmol/kg) of contrast agent for CE-MRA might have an impact on signal intensity (20). We opted for a single dose of contrast agent because kidney perfusion was part of the MRI protocol, which requires another 0.1 mmol/kg of contrast agent.

CONCLUSIONS

Renal artery dimensions acquired with MRA can be quantified with good reproducibility, and these measurements

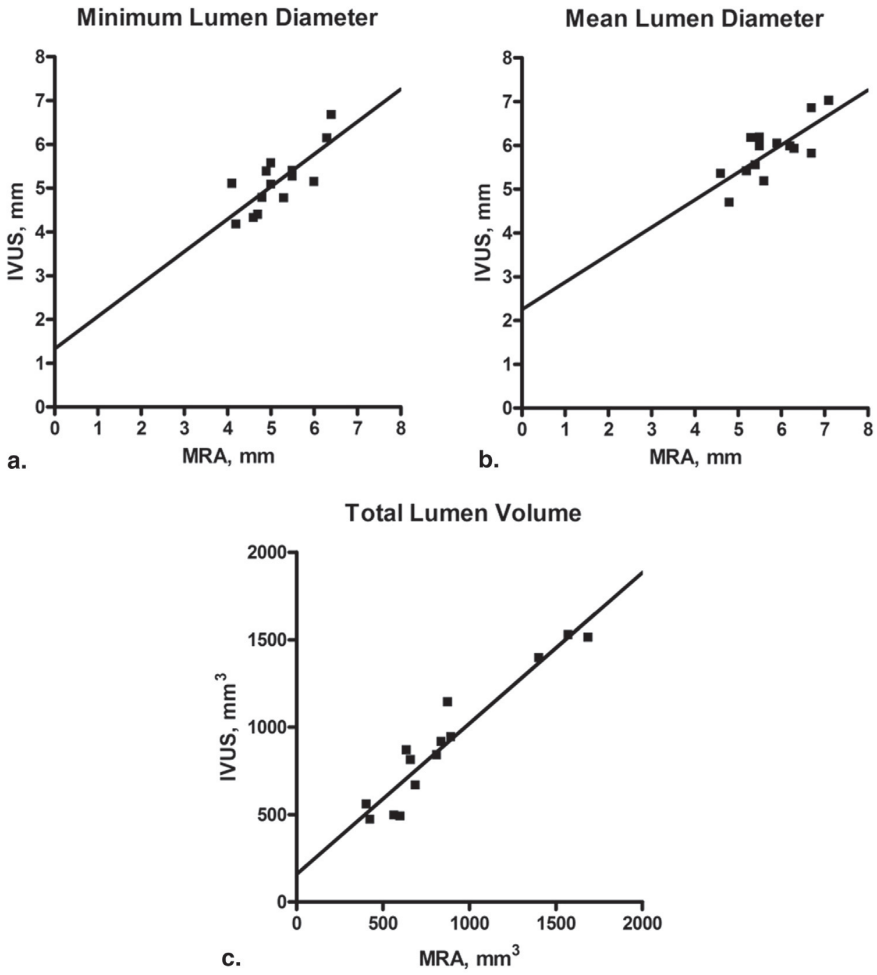

	Minimum Lumen Diameter	Mean Lumen Diameter	Total Lumen Volume
R value	0.771	0.750	0.951
P value	0.001	0.002	< 0.001

Figure 6. Correlation of MRA dimensions with IVUS. Correlation of minimum lumen diameter **(a)**, correlation of mean lumen diameter **(b)**, correlation of total lumen volume **(c)**. MRA, magnetic resonance angiography; IVUS, intravascular ultrasound.

correlated well with IVUS measurements. . The software is a promising tool to assess changes in renal artery dimension after renal artery intervention and for the selection of the proper device before the procedure.

ACKNOWLEDGMENTS

The authors thank Jean-Paul Aben, Pie Medical Imaging, Maastricht, The Netherlands, for his help with the detailed description of the segmentation algorithm.

SUPPLEMENTARY DATA

Supplementary data related to this article can be found at http://dx.doi.org/10.1016/j.acra.2015.03.014.

REFERENCES

1. Bohm M, Linz D, Ukena C, et al. Renal denervation for the treatment of cardiovascular high risk-hypertension or beyond? Circ Res 2014; 115(3): 400–409.
2. Daemen J, Mahfoud F. Renal denervation: expanding the indication. Eurointervention 2013; 9(Suppl R):R101–R104.

3. Davis MI, Filion KB, Zhang D, et al. Effectiveness of renal denervation therapy for resistant hypertension: a systematic review and meta-analysis. J Am Coll Cardiol 2013; 62(3):231–241.
4. Bhatt DL, Kandzari DE, O'Neill WW, et al. A controlled trial of renal denervation for resistant hypertension. N Engl J Med 2014; 370(15):1393–1401.
5. Symplicity HTNI, Esler MD, Krum H, et al. Renal sympathetic denervation in patients with treatment-resistant hypertension (The Symplicity HTN-2 Trial): a randomised controlled trial. Lancet 2010; 376(9756): 1903–1909.
6. Krum H, Schlaich MP, Sobotka PA, et al. Percutaneous renal denervation in patients with treatment-resistant hypertension: final 3-year report of the Symplicity HTN-1 study. Lancet 2014; 383(9917):622–629.
7. Papademetriou V, Tsioufis CP, Sinhal A, et al. Catheter-based renal denervation for resistant hypertension: 12-month results of the EnligHTN I First-in-Human Study using a multielectrode ablation system. Hypertension 2014; 64(3):565–572.
8. Karanasos A, Van Mieghem NM, Regar E, et al. Serial imaging observations of vascular healing in a denervation-induced renal artery dissection. Eur Heart J 2015; 36(17):1040.
9. Antonis Karanasos, Nicolas Van Mieghem, Jurgen Ligthart, Elco van der Heiden, Evelyn Regar, Joost Daemen, editor. Multi-modality intra-arterial imaging assessment of the vascular trauma induced by four different catheter-based renal sympathetic denervation systems. *Circ Cardiovasc Interv* (in press).
10. Delingette. General object reconstruction based on simplex meshes. Int J Comput. Vision 1999; 32:111–142.
11. Antiga L, Steinman DA. Robust and objective decomposition and mapping of bifurcating vessels. IEEE Trans Med Imaging 2004; 23(6):704–713.
12. Girasis C, Schuurbiers JC, Muramatsu T, et al. Advanced three-dimensional quantitative coronary angiographic assessment of bifurcation lesions: methodology and phantom validation. Eurointervention 2013; 8(12):1451–1460.
13. van 't Klooster R, de Koning PJ, Dehnavi RA, et al. Automatic lumen and outer wall segmentation of the carotid artery using deformable three-dimensional models in MR angiography and vessel wall images. J Magn Reson Imaging 2012; 35(1):156–165.
14. White JH, Bartlett ES, Bharatha A, et al. Reproducibility of semi-automated measurement of carotid stenosis on CTA. Can J Neurol Sci 2010; 37(4): 498–503.
15. Ahmed S, Zimmerman SL, Johnson PT, et al. MDCT interpretation of the ascending aorta with semiautomated measurement software: improved reproducibility compared with manual techniques. J Cardiovasc Comput Tomogr 2014; 8(2):108–114.
16. Lao D, Parasher PS, Cho KC, et al. Atherosclerotic renal artery stenosis—diagnosis and treatment. Mayo Clin Proc 2011; 86(7):649–657.
17. Schoenberg SO, Rieger J, Weber CH, et al. High-spatial-resolution MR angiography of renal arteries with integrated parallel acquisitions: comparison with digital subtraction angiography and US. Radiology 2005; 235(2): 687–698.
18. Vasbinder GB, Nelemans PJ, Kessels AG, et al. Accuracy of computed tomographic angiography and magnetic resonance angiography for diagnosing renal artery stenosis. Ann Intern Med 2004; 141(9):674–682; discussion 82.
19. Leiner T, de Haan MW, Nelemans PJ, et al. Contemporary imaging techniques for the diagnosis of renal artery stenosis. Eur Radiol 2005; 15(11): 2219–2229.
20. Heverhagen JT, Wright CL, Schmalbrock P, et al. Dose comparison of single versus double dose in contrast-enhanced magnetic resonance angiography of the renal arteries: intra-individual cross-over blinded trial using Gd-DTPA. Eur Radiol 2009; 19(1):67–72.
21. Zhang HL, Sos TA, Winchester PA, et al. Renal artery stenosis: imaging options, pitfalls, and concerns. Prog Cardiovasc Dis 2009; 52(3):209–219.
22. Eklof H, Ahlstrom H, Magnusson A, et al. A prospective comparison of duplex ultrasonography, captopril renography, MRA, and CTA in assessing renal artery stenosis. Acta Radiol 2006; 47(8):764–774.
23. Kaltenbach B, Id D, Franke JC, et al. Renal artery stenosis after renal sympathetic denervation. J Am Coll Cardiol 2012; 60(25):2694–2695.
24. Jaen Aguila F, Mediavilla Garcia JD, Molina Navarro E, et al. Bilateral renal artery stenosis after renal denervation. Hypertension 2014; 63(5):e126–e127.
25. Pucci G, Battista F, Lazzari L, et al. Progression of renal artery stenosis after renal denervation. Impact on 24-hour blood pressure. Circ J 2014; 78(3):767–768.

Supplementary Table 1. Individual renal artery dimensions, MRA

Patient	Renal Artery	Vessel Length (mm)	Minimum Lumen Diameter (mm)	Mean Lumen Diameter (mm)	Total Lumen Volume (mm^3)	Vessel Length (mm)	Minimum Lumen Diameter (mm)	Mean Lumen Diameter (mm)	Total Lumen Volume (mm^3)	Vessel Length (mm)	Minimum Lumen Diameter (mm)	Mean Lumen Diameter (mm)	Total Lumen Volume (mm^3)
		Day 1 Observer 1	Day 1 Observer 1	Day 1 Observer 1	Day 1 Observer 1	Day 2 Observer 1	Day 2 Observer 1	Day 2 Observer 1	Day 2 Observer 1	Observer 2	Observer 2	Observer 2	Observer 2
#1	Left	41.2	4.9	5.3	889.8	39.6	4.8	5.2	847.0	41.6	4.9	5.3	910.2
	Right	34.8	4.7	5.5	807.6	34.8	4.7	5.4	806.7	34.0	4.7	5.5	792.0
#2	Left	48.8	5.6	6.3	1471.2	50.4	5.6	6.3	1534.9	49.2	5.7	6.3	1536.1
	Right	54.4	5.0	5.4	1254.9	53.6	5.0	5.5	1243.0	54.8	4.9	5.4	1248.5
#3	Left	38.0	6.4	7.1	1536.2	39.2	6.4	7.1	1569.8	38.0	6.4	7.1	1491.7
	Right	55.6	5.3	6.3	1744.2	55.6	5.2	6.3	1758.6	56.0	5.2	6.3	1731.3
#4	Left	17.2	6.1	6.7	604.5	18.8	6.1	6.7	642.9	18.4	6.1	6.6	627.5
	Right	N.A.	N.A.	N.A.	N.A.	N.A.	N.A.	N.A.	N.A.	N.A.	N.A.	N.A.	N.A.
#5	Left	25.2	4.6	5.3	552.3	25.6	4.6	5.3	542.1	36.8	3.6	4.9	685.6
	Right	26.8	4.5	5.4	629.8	26.4	4.4	5.4	608.3	27.2	3.9	5.2	593.4
#6	Left	41.6	5.2	5.7	1057.1	42.4	5.3	5.8	1098.1	42.8	4.9	5.7	1068.5
	Right	62.4	4.5	5.4	1460.6	61.2	4.5	5.5	1446.8	62.8	4.5	5.4	1455.3
#7	Left	27.2	6.4	6.9	996.2	28.0	6.4	6.9	1051.1	27.2	6.4	6.8	982.7
	Right	51.2	5.5	6.2	1510.9	51.6	5.6	6.2	1561.7	50.8	5.5	6.1	1498.1
#8	Left	42.4	5.4	6.0	1180.9	40.8	5.4	6.0	1163.8	42.4	5.5	6.0	1196.7
	Right	42.0	4.1	4.9	810.7	42.8	4.1	5.0	849.2	43.2	4.2	5.0	863.9
#9	Left	31.2	4.0	4.7	544.0	29.6	4.1	4.7	510.3	31.2	4.1	4.7	537.7
	Right	30.0	4.2	4.8	549.3	28.0	4.3	4.9	530.7	29.6	4.4	5.0	575.5
Mean ± SD		39.3 ± 12.5	5.1 ± 0.7	5.8 ± 0.7	1021.4 ± 421.9	39.3 ± 12.2	5.1 ± 0.8	5.8 ± 0.7	1045.0 ± 418.3	40.3 ± 11.9	5.0 ± 0.8	5.7 ± 0.7	1046.7 ± 391.7

Abbreviations: MRA=magnetic resonance angiography, N.A=data not available.

Supplementary Table 2. Individual renal artery dimensions, IVUS

Patient	Renal Artery	Vessel Length (mm)	Minimum Lumen Diameter (mm^2)	Mean Lumen Diameter (mm)	Total Lumen Volume (mm^3)	Visualization Aorta	Visualization bifurcation
#1	Left	39.69	4.78	5.41	916.48	No	Yes
	Right	28.85	5.38	5.98	812.45	No	Yes
#2	Left	32.51	7.59	8.62	1906.62	No	No
	Right	28.96	5.57	6.17	867.58	Yes	No
#3	Left	36.07	6.67	7.02	1396.23	Yes	No
	Right	53.71	4.77	5.92	1512.03	Yes	Yes
#4	Left	18.54	5.14	5.81	490.62	Yes	No
	Right						
#5	Left	18.76	4.32	5.55	471.32	Yes	No
	Right	23.33	4.39	5.18	495.14	Yes	Yes
#6	Left	37.82	5.08	6.18	1142.82	Yes	No
	Right	53.50	2.81	5.70	1309.00	No	No
#7	Left	22.84	6.14	6.85	840.30	Yes	Yes
	Right	54.34	5.27	5.98	1527.48	No	Yes
#8	Left	32.85	5.40	6.04	943.05	Yes	No
	Right	38.56	4.17	4.69	667.22	No	Yes
#9	Left	24.84	5.10	5.35	558.06	No	Yes
	Right	N.A.	N.A.	N.A.	N.A.	N.A.	N.A.
Mean ± SD		34.1 ± 11.8	5.2 ± 1.1	6.0 ± 0.9	991.0 ± 433.8	9/16	8/16

Abbreviations: IVUS=intravascular ultrasound; N.A=data not available.

Chapter 8.2

Multi-modality intra-arterial imaging assessment of the vascular trauma induced by four different renal denervation systems

Karanasos A, Van Mieghem NM, Bergmann M, Hartman E, Ligthart J, van der Heide E, Heeger C, Ouhlous M, Zijlstra F, Regar E, Daemen J

Circ Cardiovasc Intv 2015 Jul;8(7):e002474

New Techniques

Multimodality Intra-Arterial Imaging Assessment of the Vascular Trauma Induced by Balloon-Based and Nonballoon-Based Renal Denervation Systems

Antonios Karanasos, MD, PhD; Nicolas Van Mieghem, MD, PhD; Martin W. Bergmann, MD, PhD; Eline Hartman, MD; Jurgen Ligthart, BSc; Elco van der Heide, MSc; Christian-H. Heeger, MD; Mohamed Ouhlous, MD, PhD; Felix Zijlstra, MD, PhD; Evelyn Regar, MD, PhD; Joost Daemen, MD, PhD

Background—Renal denervation is a new treatment considered for several possible indications. As new systems are introduced, the incidence of acute renal artery wall injury with relation to the denervation method is unknown. We investigated the acute repercussion of renal denervation on the renal arteries of patients treated with balloon-based and nonballoon-based denervation systems by quantitative angiography, intravascular ultrasound, and optical coherence tomography (OCT).

Methods and Results—Twenty-five patients (50 renal arteries) underwent bilateral renal denervation with 5 different systems, 3 of which balloon-based (Paradise [n=5], Oneshot [n=6], and Vessix V2 [n=5)]) and 2 nonballoon-based (Symplicity [n=6] and EnligHTN [n=3]). Analysis included quantitative angiography and morphometric intravascular ultrasound measurements pre and post procedure and assessment of vascular trauma (dissection, edema, or thrombus) by OCT after denervation. A significant reduction in lumen size by quantitative angiography and intravascular ultrasound was observed in nonballoon denervation but not in balloon denervation. By postdenervation OCT, dissection was seen in 14 arteries (32.6%). The percentage of frames with dissection was higher in balloon-based denervation catheters. Thrombus and edema were detected in 35 (81.4%) and 32 (74.4%) arteries, respectively. In arteries treated with balloon-based denervation that had dissection by OCT, the balloon/artery ratio was higher (1.24 [1.17–1.32] versus 1.10 [1.04–1.18]; $P<0.01$).

Conclusions—A varying extent of vascular injury was observed after renal denervation in all systems; however, different patterns were identified in balloon-based and in nonballoon-based denervation systems. In balloon denervation, the presence of dissections by OCT was associated with a higher balloon/artery ratio. **(*Circ Cardiovasc Interv*. 2015;8:e002474. DOI: 10.1161/CIRCINTERVENTIONS.115.002474.)**

Key Words: angiography ■ arteries ■ denervation ■ hypertension resistant to conventional therapy ■ renal artery ■ tomography, optical coherence ■ ultrasound, interventional

Renal denervation has been recently studied as a potential new treatment for resistant hypertension and is currently considered for several other indications. Besides the fact that initial success stories were recently challenged by a negative randomized controlled trial, data on long-term safety are scarce.[1–3] Currently, available data on safety, mostly derived from duplex ultrasound findings, show a low rate of adverse events, both at short- and long-term follow-ups.[2,4] However, the number of patients scrutinized for renal artery integrity post procedure is remarkably low, and several reports of renal artery stenosis have been published.[4–6] Moreover, procedure-induced vascular trauma has been demonstrated in animals[7] and in patients treated with renal denervation.[8,9] As new systems are being introduced,[10] there is a paucity of knowledge on the incidence of acute vascular wall injury with relation to the denervation method.

Intravascular imaging enables the assessment of procedure-mediated injury. Intravascular ultrasound (IVUS) can provide comprehensive volumetric measurements of lumen, external elastic membrane (EEM), and intima-and-media area, whereas optical coherence tomography (OCT) can visualize the superficial arterial wall layers with near-histological resolution (≈15 μm) and detect intraluminal structures with high accuracy.[11]

The aim of this study was to assess the acute vascular injury after renal sympathetic denervation with 5 different

Received June 17, 2014; accepted June 2, 2015.

From the Department of Interventional Cardiology, Thoraxcenter, Erasmus Medical Center (A.K., N.V.M., E.H., J.L., E.v.d.H., F.Z., E.R., J.D.), Department of Radiology (M.O.), Rotterdam, The Netherlands; and Department of Interventional Cardiology, St. Georg Asklepios Klinik, Hamburg, Germany (M.W.B., C.-H.H.).

The Data Supplement is available at http://circinterventions.ahajournals.org/lookup/suppl/doi:10.1161/CIRCINTERVENTIONS.115.002474/-/DC1.

Correspondence to Joost Daemen, MD, PhD, Department of Cardiology, Erasmus University Medical Center, PO Box 2040, 3000CA Rotterdam, The Netherlands. E-mail j.daemen@erasmusmc.nl

WHAT IS KNOWN

- Renal denervation has been associated with renal artery trauma in animal models and in human clinical studies.

WHAT THE STUDY ADDS

- In patients undergoing renal denervation using 5 different devices, OCT revealed that a varying extent of vascular injury characterized by dissection, thrombus or edema was observed after renal denervation with all systems.
- Nonballoon-based denervation is associated with a low incidence and extent of vessel dissection but with acute lumen narrowing and vessel wall thickening accompanied by a moderately higher thrombus area.
- Balloon-based denervation is associated with a higher longitudinal extent of dissection, thrombus, and intimal protrusions in the absence of significant changes in the luminal or vessel diameter during the procedure.
- In balloon-based denervation, a high balloon-to-artery ratio is associated with a higher incidence of dissection.
- Post-procedural angiographic luminal irregularities are associated with the extent of dissection in balloon-based denervation.

devices by quantitative angiography, IVUS, and OCT and explore a potential difference between balloon-based and nonballoon-based denervation devices.

Methods

This is a 2-center, prospective, observational study, including 25 patients, 19 enrolled in Thoraxcenter Rotterdam and 6 enrolled in Asklepios Klinik, St. Georg, Hamburg, who underwent bilateral renal denervation with 5 different renal denervation systems. Three systems were balloon-based (Paradise [Recor Medical, Palo Alto, CA; n=5], Oneshot [Covidien, Campbell, CA; n=6], and Vessix V2 [Boston Scientific, Natick, MA; n=5]) and 2 were nonballoon-based (Symplicity [Medtronic, Minneapolis, MN; n=6], EnligHTN [St Jude, St Paul, MN; n=3]). Patients in both centers underwent postdenervation OCT, and 16 patients enrolled in Thoraxcenter Rotterdam underwent predenervation and postdenervation IVUS (Figure I in the Data Supplement). Offline image analysis included quantitative angiography pre and post procedure, morphometric lumen and vessel measurements by IVUS pre and post procedure, and postprocedural assessment of vascular trauma by OCT. This study was approved by the hospital ethics committee and conforms to the declaration of Helsinki. All patients provided written informed consent before inclusion.

Study Population

The study population consisted of patients undergoing renal denervation in clinical trials or for treatment of resistant hypertension[12] or patients included in clinical trials assessing safety and efficacy of renal denervation for heart failure or atrial fibrillation. All patients underwent noninvasive preprocedural renal artery imaging and were discussed in a multidisciplinary team, including interventional cardiologists, radiologists, and hypertension specialists. Device selection was not mandated by the current study protocol and depended on the inclusion criteria of the clinical trial in which the patient was enrolled. Invasive imaging was performed in small consecutive series of patients treated with a specific device.

Denervation Procedure

All patients were preloaded with 300 mg aspirin, if naive, and advised to continue aspirin for at least 1 month. Preprocedurally, 100 IU heparin/kg were administered to achieve an active clotting time of >250 s. A total of 200 μg nitrates were locally administered before invasive imaging. Procedures were performed according to device-specific instructions for use[10,12] under conscious sedation with midazolam and fentanyl. Balloon size selection in balloon-based devices was based on online measurement of maximal diameter by quantitative angiography (Data Supplement).

IVUS and OCT Image Acquisition

Targeted renal arteries were examined with an IVUS system with automatic pullback at 0.5 mm/s (Boston Scientific, Natick, MA) pre and post renal denervation. Retrieved IVUS images were stored and analyzed offline.

OCT was performed after renal denervation. Images were acquired using the Illumien/C7XR system and Dragonfly or Dragonfly Duo catheter (all Lightlab/St Jude, Minneapolis, MN). The catheter was positioned distally to first major bifurcation and automatically pulled back at 20 mm/s, acquiring images at 100 m/s, with simultaneous isoosmolar contrast (Iodixanol 370, Visipaque, GE Healthcare, Ireland) administration at a flow rate of 4 to 6 mL/s, depending on artery size.

Angiographic Analysis

Angiographic analysis was performed offline (Data Supplement material). In balloon catheters, the balloon/artery ratio was calculated as the ratio of nominal balloon diameter to mean luminal diameter by offline quantitative angiography.

IVUS Analysis

IVUS analysis was blinded to the device used. Volumetric analysis of the region of interest was performed in fixed 0.5-mm intervals within the segment between the renal artery ostium and the first major bifurcation using dedicated software (QCU-CMS, LKEB, Leiden University, NL). Morphometric analysis included EEM measurements and lumen measurements. Two volumetric intima-and-media indices, normalized total atheroma volume and percent atheroma volume (PAV), were also derived from these measurements. These indices have been used in coronary atherosclerosis regression studies and are defined as follows:

$$\mathrm{nTAV} = \frac{\sum\left(\mathrm{EEM_{area}} - \mathrm{lumen_{area}}\right)}{\text{no. of analyzed images in the pullback}} \times \text{median no. of analyzed images}$$

and

$$\mathrm{PAV} = \frac{\sum\left(\mathrm{EEM_{area}} - \mathrm{lumen_{area}}\right)}{\sum \mathrm{EEM_{area}}} \times 100$$

where $\mathrm{EEM_{area}}$ is the cross-sectional EEM area and $\mathrm{lumen_{area}}$ is the cross-sectional lumen area.[13]

In our study, where arteries had minimal atherosclerosis with low plaque burden, differences in these indices post minus predenervation were used as surrogates for a possible increase in the intima-and-media area by procedure-induced edema. Considering a relatively high variability in volumetric IVUS measurements,[14] only relative changes >5% were considered relevant.

OCT Analysis

OCT analysis was blinded to device used and performed offline by an experienced analyst in Thoraxcenter Rotterdam on frame level (every 0.2 mm).

As the range of OCT is limited (scan diameter, 10–11 mm) and the blood removal required for imaging can be challenging in 5- to 7 mm-vessels, the entire vessel periphery is not always visualized, especially in eccentric catheter position or suboptimal flushing. Therefore, acquired images were screened for quality (Figure II in the Data Supplement). Images with <50% perimeter visualization were scored as poor quality, those with 50% to 75% perimeter visualization as fair, and those with >75% perimeter visualization as good. Fair and good quality images were included in the analysis.

OCT analysis included assessment of vascular trauma post-denervation, comprising dissection, thrombus, and edema.[9] Dissections were defined as endothelial or intimal disruptions (Figure 1A–1C). Although dissections in renal arteries that have minimal atherosclerosis might differ from coronaries, where edge dissections after stent implantation often develop in vessels with advanced atherosclerosis, the basic morphological patterns in our study resembled coronary stent edge dissections. Therefore, we applied previously described methodology for analysis of coronary edge dissections.[15] Four dissection types were observed: (1) dissections with formation of flap protruding into the lumen (Figure 1A); (2) dissections with intimal lining separation and cavity formation (Figure 1B); (3) dissections with double lumen morphology (false lumen formation underneath the intima; Figure 1C); and (4) intramural hematomas (blood accumulation within the media, displacing the internal elastic membrane inward; Figure 1D). In all dissections, the circumferential extent was quantified as arc (°) of vessel wall discontinuity (Figure 1E and 1F). Furthermore, in flap-type dissections, the flap opening was quantified as the distance from flap tip to lumen border, along a line projected through the gravitational lumen center (Figure 1E). The dissection depth was quantified based on vessel wall layer involvement as (1) intimal (disruption confined to intima; Figure 1G); (2) medial (disruption extends to media; Figure 1H); and (3) adventitial (disruption extends beyond media; Figure 1I). Thrombus was defined as mural or intraluminal signal-rich mass (Figure 1J). In all frames with thrombus, thrombus area was measured. Finally, edema was defined as any significant endothelial–intimal notch of the luminal surface (Figure 1K).[9]

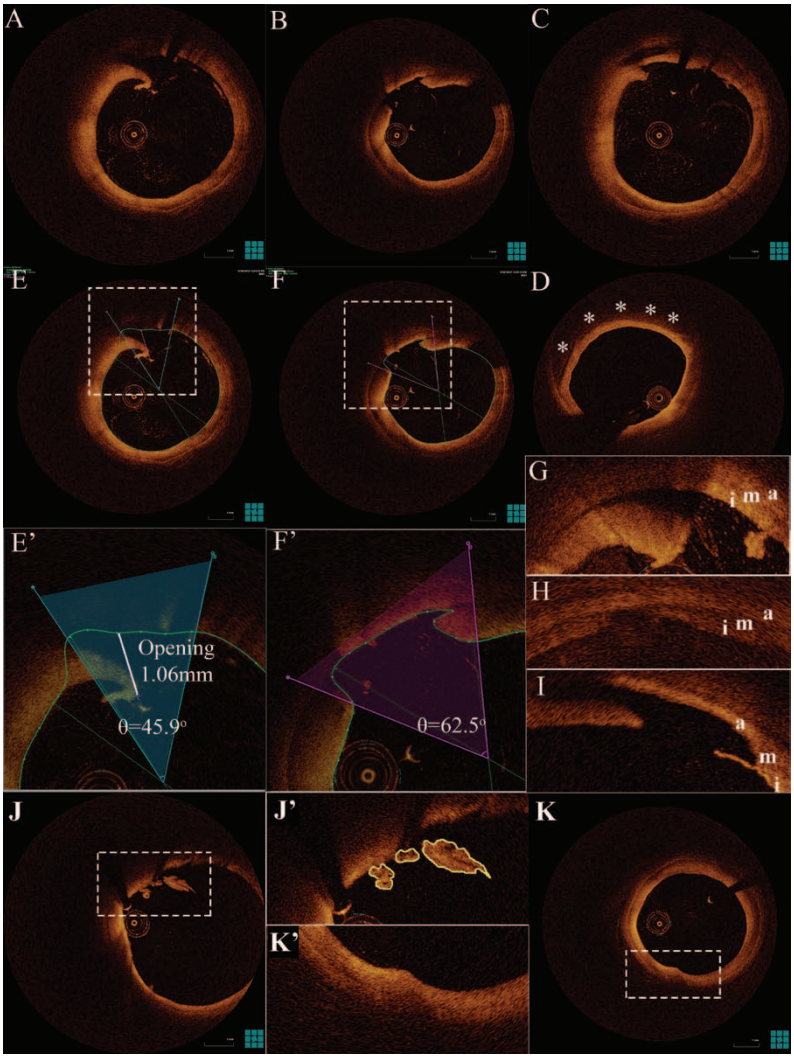

Figure 1. Optical coherence tomography analysis. **A**–**D**, Morphological classification of OCT dissection: (**A**) flap; (**B**) cavity; (**C**) double lumen; (**D**) intramural hematoma. **E** and **F**, Measurement of dissection angle and opening in (**E**) flap-type and (**F**) cavity-type. **G**–**I**, Assessment of dissection depth: (**G**) intimal; (**H**) medial; (**I**) adventitial. **J** and **J′**, Intraluminal thrombus. **K** and **K′**, Edema. * indicates hematoma; a, adventitia; i, intima; and m, media.

Statistical Analysis

This study is exploratory, and statistical analysis is principally hypothesis-generating. All analyses were performed with SPSS 20.0 (IBM, Chicago, IL). Nominal variables are presented as n (%) and continuous as mean±SD. Estimates in clustered variables are presented as estimated mean (95% confidence intervals [CIs]). The Kolmogorov–Smirnov test assessed normality of distribution. All continuous variables had a normal distribution. Between-group differences in patient-level characteristics were examined using χ^2 or Fisher exact test for nominal variables and with *t* test or ANOVA for quantitative variables. As vessel-level characteristics are clustered within each patient and frame-level characteristics are clustered within each vessel within each patient, these characteristics were compared by multilevel linear or logistic regression, using within-patient intercepts as random effects for vessel level, and within-patient and within-vessel intercepts for frame level.[16] A receiver operating characteristic analysis was performed to evaluate the ability of several variables for predicting dissection; to adjust for data clustering, receiver operating characteristic analysis was repeated using predicted probabilities derived from a multilevel model using within-patient intercepts as random effects. A 2-sided *P* value of <0.05 indicated statistical significance.

Results

Baseline Characteristics

There were no significant between-group differences in baseline characteristics (Table 1; Table I in the Data Supplement). The balloon/artery ratio did not differ significantly among balloon catheters (Paradise: 1.21 [1.13–1.30], Oneshot: 1.11 [1.04–1.19], and Vessix V2: 1.11 [1.03–1.19]; *P*=0.11). Procedural success was achieved in all but one patient who underwent bilateral renal artery stenting because of bilateral renal artery dissection postdenervation (Figure 2).

Angiographic Analysis

Angiographic analysis is summarized in Table 2 and Table II in the Data Supplement. Six angiographic projections (3 predenervation and 3 postdenervation) were excluded from analysis. Before denervation, all arteries were angiographically normal with smooth contour and no signs of atherosclerosis. Post procedure, lumen contour irregularities were observed in 18 arteries (38.3%) with no difference between groups (Figures 3–4). In 3 patients (4 arteries), all treated with balloon-based catheters, dissections were visualized angiographically. Two patients were treated conservatively (Figure 5), whereas the other patient with bilateral dissection was treated with bilateral stent implantation (Figure 2).

No significant differences were observed for reference lumen diameter and minimal lumen diameter (MLD) postdenervation compared with predenervation for the overall cohort, whereas percent diameter stenosis (DS%) had a mild increase (ΔDS%: 4.7% [1.2%–8.3%]; *P*=0.01). MLD was significantly decreased in nonballoon denervation (−0.45 [−0.85 to −0.05] mm; *P*=0.03) but not in balloon denervation (0.02 [−0.27 to 0.31] mm; *P*=0.87).

IVUS Analysis

IVUS pullbacks were available for 16 patients, in 31 arteries predenervation and in 32 arteries postdenervation. IVUS analysis is summarized in Table 3 and Tables III to V in the Data Supplement. In the overall population, there was a significant lumen volume decrease and PAV increase postdenervation compared with predenervation (Δlumen volume: −68.17 [−133.23 to −4.22] mm^3, *P*=0.04; ΔPAV: 2.20% [0.88%–3.52%], *P*<0.01]. In the nonballoon denervation group, both minimum lumen and minimum EEM area significantly decreased postdenervation (Δmin lumen area: −3.27 [−5.70 to −0.85] mm^2, *P*=0.03; Δmin EEM area: −3.82 [−6.50 to −1.14] mm^2, *P*=0.02); these changes were not significant for the balloon denervation group.

OCT Analysis

OCT pullbacks were available in 25 patients and 43 arteries. A total of 6530 frames were retrieved, from which 5260 (80.6%) had fair-to-good quality and were analyzed (Table 4; Table VI in the Data Supplement).

Dissections were detected in 12 patients (14 arteries), mainly with balloon-based denervation catheters (42.9%

Table 1. Baseline Characteristics

	All Patients, n=25	Balloon-Based Devices, n=16	Nonballoon-Based Devices, n=9	*P* Value
Age, y	63.4±10.1	61.7±8.6	66.6±12.3	0.25
Male, sex, n (%)	14 (56.0)	9 (56.3)	5 (55.6)	0.99
Cardiovascular risk factors, n (%)				
Dyslipidemia	15 (60.0)	9 (56.3)	6 (66.7)	0.69
Smoking	8 (32.0)	5 (31.3)	3 (33.3)	0.99
Diabetes mellitus	7 (28.0)	3 (18.8)	4 (44.4)	0.21
Family history for CAD	13 (52.0)	8 (50.0)	5 (55.6)	0.99
CAD	10 (40.0)	7 (43.8)	3 (33.3)	0.69
Previous infarction, n (%)	5 (20.0)	4 (25.0)	1 (11.1)	0.62
Previous stroke, n (%)	2 (8.0)	0 (0.0)	2 (22.2)	0.13
Systolic BP before ablation, mm Hg	168.9±29.7	172.5±32.8	162.6±23.3	0.43
Diastolic BP before ablation, mm Hg	91.6±12.8	92.2±13.5	90.6±12.0	0.76
eGFR before ablation, mL/min per 1.73 m^2	69.5±19.1	71.1±19.6	66.8±19.1	0.60

Values are expressed as mean±SD or n (%). BP indicates blood pressure; CAD, coronary artery disease; and eGFR, estimated glomerular filtration rate.

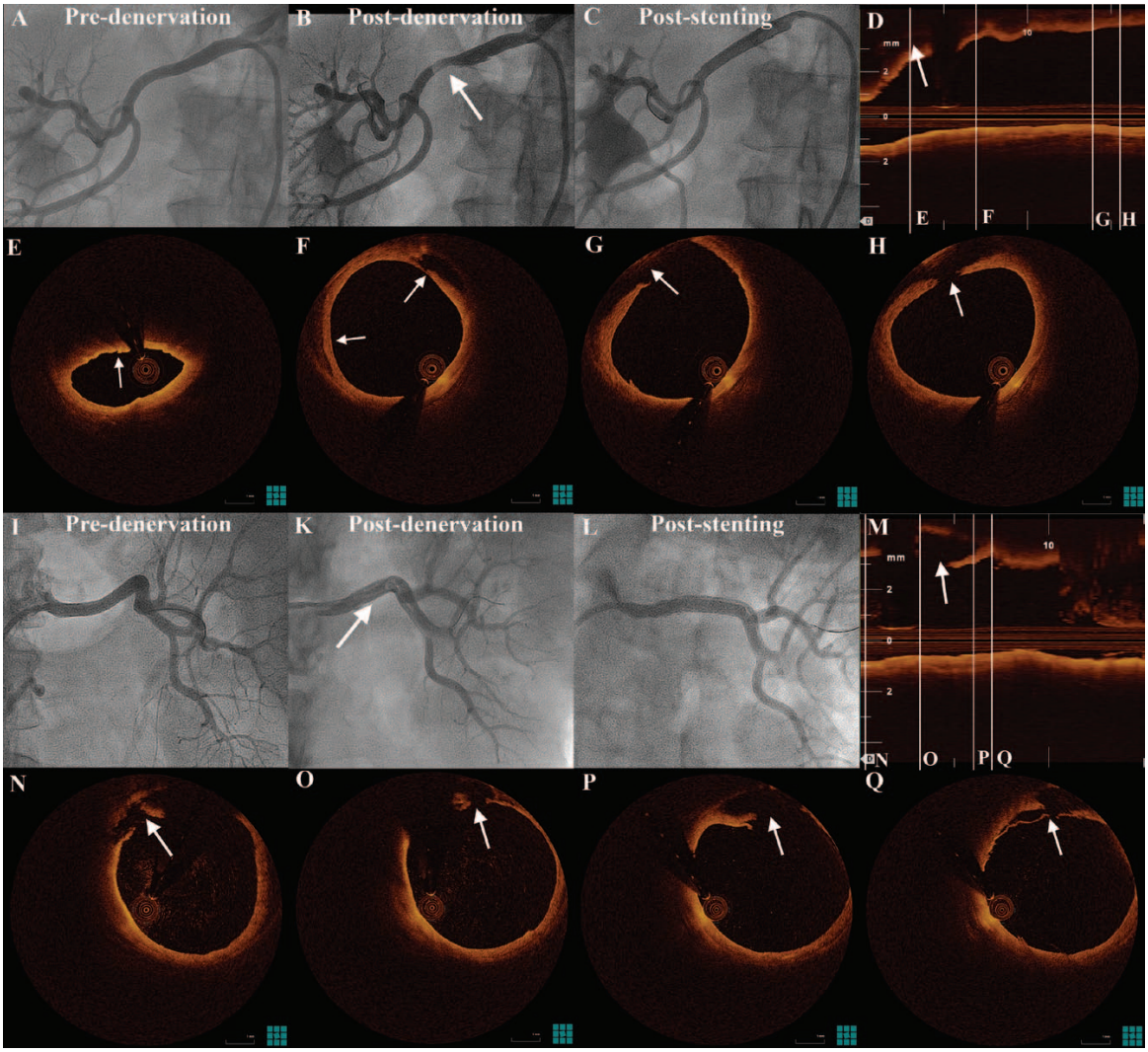

Figure 2. Bilateral renal artery dissection treated with stent implantation. **A**–**C**, Right renal artery angiogram: (**A**) predenervation, (**B**) postdenervation with the Oneshot system, and (**C**) after 2 stent implantation for treatment of the dissection. White arrow indicates the contrast deficit. **D**–**H**, Optical coherence tomography (OCT) images demonstrating the dissection (white arrows). Note the hematoma in (**E**) and (**F**), whereas the tear is visualized more proximally. **I**–**L**, Left renal artery angiogram: (**I**) predenervation, (**K**) postdenervation, and (**L**) after 2 stent implantation for treatment of the dissection. White arrow indicates the dissection extending to the distal branches. **M**–**Q**, OCT images demonstrating the dissection (white arrows).

[n=10] for balloon denervation versus 13.3% [n=2] for nonballoon denervation; *P*=0.07). The percentage of frames with dissection was higher for balloon versus nonballoon denervation (*P*=0.03). Within cases with dissection, the circumferential extent was similar between balloon and nonballoon denervation with a dissection angle of 40.0° (13.6°–66.5°). Similarly, dissection opening was 0.47 (0–1.03) mm, with no significant differences between the groups. All dissections are described in detail in Table 5.

Thrombus was detected in 23 of 25 patients (92.0%) and 35 of 43 arteries (81.4%). In most cases, thrombi were very small with a mean area of 0.08 (0.06–0.11) mm^2. Although the percentage of frames with thrombus was similar in the 2 groups, thrombus area was lower in balloon denervation compared with nonballoon denervation (0.06 [0.04–0.09] mm^2 versus 0.11 [0.07–0.14] mm^2; *P*=0.04). Finally, edema was observed in 18 of 25 patients (72.0%) and 32 of 43 arteries (74.4%). There were no significant differences in edema between balloon denervation and nonballoon denervation.

Association of Angiographic With Intravascular Imaging Findings

By quantitative angiography, vessels with lumen irregularities or dissection had higher decrease of MLD and higher increase of DS% postprocedure (ΔMLD: −0.64 [−0.95 to −0.32] mm versus 0.25 [−0.04 to 0.54] mm, *P*<0.01; ΔDS%: 11.3% [6.9%–15.6%] versus 0.0% [−4.0% to 4.0%]; *P*<0.01). By IVUS, the decrease in minimal lumen area and increase in PAV were higher

Table 2. Quantitative Angiography Measurements and Qualitative Findings

	All Vessels (n=48)	Balloon-Based Devices (n=32)	Nonballoon-Based Devices (n=16)	*P* Value
Predenervation, n=47				
RVD, mm	5.35 (5.03 to 5.67)	5.14 (4.76 to 5.52)*	5.56 (5.04 to 6.08)	0.19
MLD, mm	4.86 (4.55 to 5.18)	4.63 (4.26 to 5.00)*	5.10 (4.59 to 5.60)	0.14
DS, %	9.0 (6.7 to 11.3)	9.9 (7.5 to 12.6)*	8.1 (4.4 to 11.8)	0.41
Postdenervation, n=47				
RVD, mm	5.38 (4.98 to 6.07)	5.34 (4.87 to 5.82)*	5.42 (4.78 to 6.07)	0.84
MLD, mm	4.63 (4.23 to 5.03)	4.63 (4.16 to 5.11)*	4.63 (3.98 to 5.27)	0.98
DS, %	14.2 (10.0 to 18.4)	12.9 (7.9 to 17.9)*	15.5 (8.7–22.2)	0.53
Difference (postdenervation–predenervation), n=46				
RVD, mm	0.14 (–0.09 to 0.36)	0.24 (–0.02 to 0.51)†	–0.07 (–0.44 to 0.29)	0.18
MLD, mm	–0.14 (–0.39 to 0.11)	0.02 (–0.26 to 0.31)†	–0.45 (–0.86 to 0.05)‡	0.09
DS, %	4.7 (1.2 to 8.3)‡	3.2 (–0.9 to 7.4)†	7.8 (2.1 to 13.5)‡	0.01
Qualitative assessment postdenervation, n=47				
Dissection, n (%)	4 (8.5)	4 (12.9)*	0 (0)	0.99§
Contour irregularities, n (%)	18 (38.3)	10 (32.3)*	8 (50.0)	0.17§

Values expressed as estimated mean (95% confidence interval) or n (%). DS indicates diameter stenosis; MLD, minimum lumen diameter; and RVD, reference vessel diameter.

*n=31.

†n=30.

‡*P*<0.05 for postdenervation versus predenervation.

§*P* values derived from multilevel logistic regression using within-patient intercepts as random effects.

in vessels with such abnormal angiographic findings compared with those without (ΔMLA: −4.22 [−6.18 to −2.25] mm^2 versus 1.05 [–0.72 to 2.82] mm^2, *P*<0.01; ΔPAV: 4.07% [2.26%–5.90%] versus 0.78% [–0.78% to 2.36%], *P*<0.01). Similarly by OCT, the percentage of frames with dissection after procedure was higher in vessels with abnormal angiographic findings (*P*<0.01). This association was observed in balloon-based denervation (*P*<0.01) but not in nonballoon-based denervation

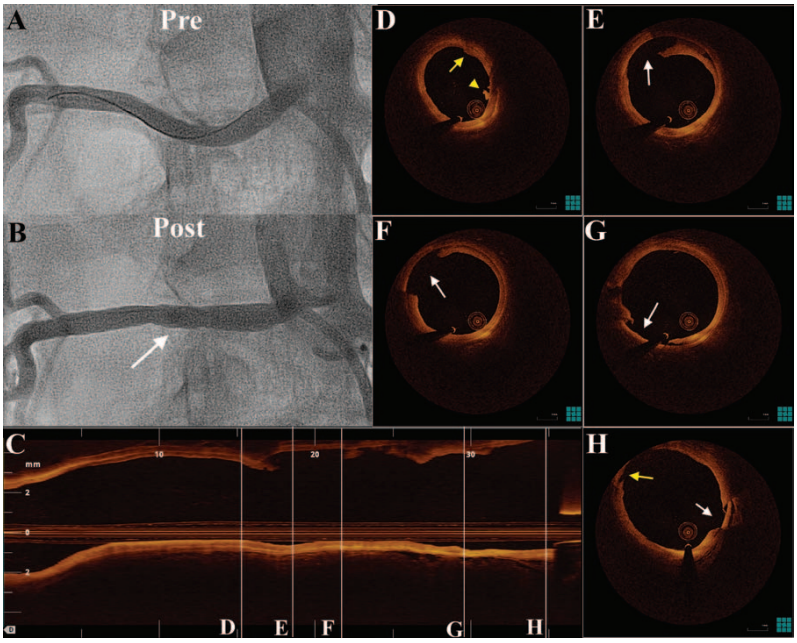

Figure 3. Renal artery trauma after balloon catheter denervation. **A** and **B**, Renal angiography predenervation and postdenervation with the Paradise system (balloon/artery ratio, 1.56). White arrow indicates lumen contour irregularities in the postdenervation angiogram. **C**–**H**, Optical coherence tomography images demonstrating dissection (white arrows), edema (yellow arrows), and thrombus (yellow arrowhead) at multiple sites.

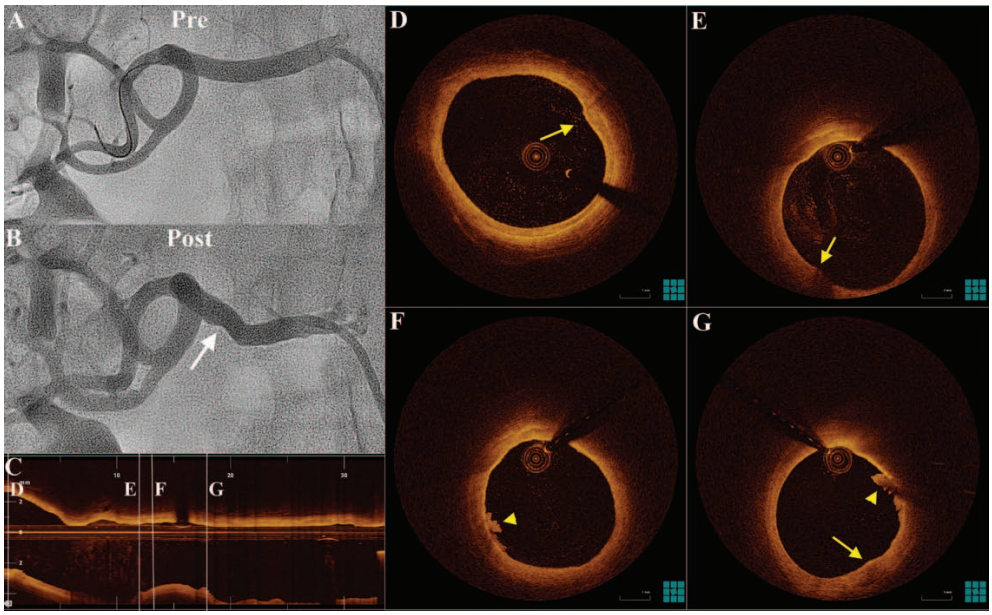

Figure 4. Renal artery trauma after nonballoon catheter denervation. **A** and **B**, Renal angiography predenervation and postdenervation with the Symplicity system. White arrow indicates lumen contour irregularities in the postdenervation angiogram. Minimal lumen area by intravascular ultrasound was reduced from 13.65 to 10.54 mm^2, whereas percent atheroma volume was increased from 23.5% to 26.0%. **C**–**G**, Optical coherence tomography images demonstrating edema (yellow arrows) and thrombus (yellow arrowhead) at multiple sites.

(*P*=0.99). There was a significant negative correlation of ΔMLD by quantitative angiography with the percentage of frames with edema by OCT (*b*=–0.016; 95% CI, –0.027 to –0.004; *P*<0.01) but no significant correlation between ΔMLD and percentage of frames with dissection or thrombus.

Balloon/Artery Ratio and Vascular Trauma

Among vessels treated with balloon denervation, dissection by OCT was associated with a higher balloon/artery ratio (1.24 [1.17–1.32] versus 1.10 [1.04–1.18]; *P*<0.01). In balloon denervation, balloon/artery ratio had a good discriminative ability for predicting dissection by OCT (unadjusted receiver operating characteristic: 0.81 [95% CI, 0.65–0.97], *P*<0.01; adjusted receiver operating characteristic: 0.89 [95% CI, 0.75–1.00]), with a value of >1.19 predicting dissection with 58.3% sensitivity and 87.5% specificity (Figure 6). The balloon/artery ratio had a significant positive correlation with the percentage of frames with dissection (*b*=92.248; 95% CI, 24.164–160.332; *P*=0.01). Conversely, preinterventional lumen measurements by angiography or IVUS, or the absolute balloon size had no significant association with the presence of dissection or percentage of frames with dissection.

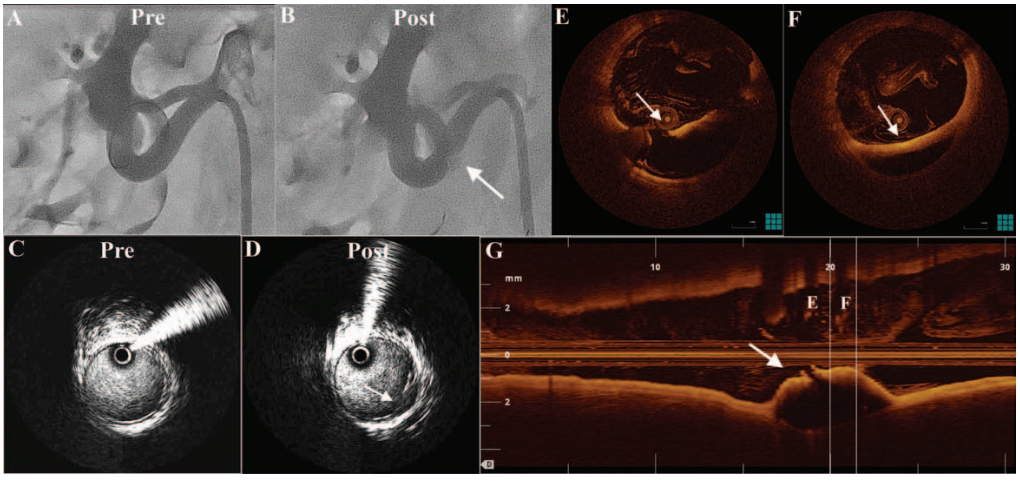

Figure 5. Renal artery dissection visualized by angiography, intravascular ultrasound (IVUS), and optical coherence tomography (OCT). **A** and **B**, Renal angiography pre- and postdenervation with the Oneshot system (balloon/artery ratio, 1.16). Angiography shows a contrast deficit (white arrow) indicative of dissection. **C** and **D**, Predenervation and postdenervation IVUS images at the contrast deficit site. Postdenervation image shows wall discontinuity with cavity and flap (arrow). **E**–**G**, OCT images demonstrating the dissection.

Table 3. Difference in Intravascular Ultrasound Measurements, Postdenervation–Predenervation

	All Vessels, n=31	Balloon-Based Devices, n=20	Nonballoon-Based Devices, n=11	*P* Value
Difference (postdenervation–predenervation)				
Mean lumen area, mm^2	–1.42 (–3.13 to 0.29)	–0.29 (–2.26 to 1.67)	–3.54 (–6.20 to –0.88)*	0.04
Min lumen area, mm^2	–1.38 (–2.91 to 0.15)	–0.36 (–2.13 to 1.41)	–3.27 (–5.70 to –0.85)*	0.03
Mean EEM area, mm^2	–1.14 (–3.11 to 0.82)	–0.79 (–3.03 to 1.46)	–2.91 (–6.23 to 0.42)	0.19
Min EEM area, mm^2	–1.43 (–3.13 to 0.28)	–0.15 (–2.11 to 1.81)	–3.82 (–6.50 to –1.14)*	0.03
Lumen volume, mm^3	–68.7 (–133.2 to –4.2)*	–33.9 (–108.7 to 40.8)	–134.6 (–236.3 to –33.0)*	0.05
EEM volume, mm^3	–74.0 (–151.2 to 3.3)	–34.9 (–124.7 to 46.00)	–148.2 (–270.4 to –26.0)*	0.10
PAV, %	2.20 (0.88 to 3.52)*	1.31 (–0.19 to 2.81)	3.86 (1.84 to 5.88)*	<0.01
nTAV, mm^3	3.3 (–6.9 to 13.5)	7.0 (–5.4 to 19.4)	–3.8 (–20.8 to 13.2)	0.47

Values are expressed as estimated mean (95% confidence interval). EEM indicates external elastic membrane; min, minimal; nTAV, normalized total atheroma volume; and PAV, percent atheroma volume.

*P<0.05 for postdenervation versus predenervation.

Discussion

The main findings of our study are that in patients undergoing renal denervation using 5 different devices: (1) a varying extent of vascular injury by OCT with the presence of dissection, thrombus, or edema was observed after renal denervation with all systems; (2) balloon-based denervation was associated with higher longitudinal extent of dissection, whereas nonballoon-based denervation was associated with higher thrombus area; (3) vessel dissections in arteries treated with balloon-based denervation catheters were associated with higher balloon/artery ratio; (4) in arteries treated with nonballoon-based denervation, a significant reduction in postprocedural vessel dimensions was observed by both angiography and IVUS, which was not observed in balloon-based denervation; and (5) postprocedural angiographic lumen irregularities were associated with reduction in lumen dimensions and in the case of balloon-based denervation with dissection by OCT.

As the debate concerning the efficacy of renal denervation is ongoing, safety data are relatively limited, whereas its effect on renal artery integrity is largely unknown.[1,2,4] Pilot studies have shown angiographic lumen irregularities post procedure (string-of-pearls sign) that tend to disappear at follow-up,[3] whereas renal artery stenosis development has been occasionally reported.[4–6] In our series, we observed such lumen wall irregularities in 38.3% of the arteries and angiographically visible dissections in 4 arteries, 2 of which treated with stent implantation. In the total cohort, these findings mirrored a reduction of lumen dimensions by angiography and IVUS. Of note, specifically in balloon-based devices, these abnormalities were also associated with the percentage of frames with dissection by OCT. Consequently, in balloon-based devices, the finding of postprocedural angiographic abnormalities should raise the suspicion of vascular injury.

Moreover, quantitative angiography and IVUS consistently showed a lack of change in lumen and vessel dimensions in

Table 4. Optical Coherence Tomography Findings Postdenervation

	All Vessels, n=43	Balloon-Based Devices, n=28	Nonballoon-Based Devices, n=15	*P* Value
Vessel-level analysis				
No. of frames, n	157.9 (141.3–174.5)	154.9 (135.2–174.5)	161.0 (134.3–187.6)	0.71
Fair-to-good quality, n	126.6 (106.8–146.4)	116.5 (93.0–140.1)	136.7 (104.8–168.5)	0.31
Any dissection, n (%)	14 (32.6)	12 (42.9)	2 (13.3)	0.07‡
Max dissection opening, mm*	0.59 (0.11–1.06)	0.98 (0.59–1.36)	0.20 (0–1.07)	0.10
Any edema, n (%)	32 (74.4)	19 (67.9)	13 (86.7)	0.27‡
Any thrombus, n (%)	35 (81.4)	23 (82.1)	12 (80.0)	0.75‡
Frame-level analysis				
Frames with dissection, %	0.6 (0.1–2.4)	2.8 (0.6–11.2)	0.1 (0.1–1.4)	0.03
Dissection angle, °*	40.0 (13.6–66.5)	61.3 (41.0–81.5)	18.8 (0–67.8)	0.11
Dissection opening, mm*	0.47 (0–1.03)	0.67 (0.31–1.00)	0.28 (0–1.36)	0.47
Frames with thrombus, %	6.8 (4.3–10.6)	7.5 (4.3–12.6)	6.1 (2.9–12.6)	0.68
Thrombus area, mm^2†	0.08 (0.06–0.11)	0.06 (0.04–0.09)	0.11 (0.07–0.14)	0.04
Frames with edema, %	9.3 (4.8–17.3)	5.7 (2.4–12.6)	14.8 (5.3–35.1)	0.15

Values are expressed as estimated as n (%) or estimated mean (95% Confidence interval). Max indicates maximal.

*Calculated in pullbacks with dissection (balloon-based devices: n=12; nonballoon-based devices: n=2).

†Calculated in pullbacks with thrombus (balloon-based devices: n=23; nonballoon-based devices: n=12).

‡*P* values derived from multilevel logistic regression using within-patient intercepts as random effects.

Table 5. Morphological Description of Dissections by Optical Coherence Tomography

Renal Artery	System	Balloon/Artery Ratio	Dissection Depth	Dissection Type	Total Dissection Length	Mean Dissection Angle	Max Flap Opening	Description
Right	Oneshot	1.16	Adventitial	Flap-double lumen	7 mm	105°	2.36 mm	Large intimal detachment creating a double lumen appearance with visible entry points (Figure 5)
Right	Vessix V2	1.11	Medial adventitial	Cavity-flap	10.2 mm	60°	0.58 mm	Cavity-type medial dissections at 4 different sites along the artery; in one of the sites, there is also a flap-type adventitial dissection
Right	Paradise	1.25	Intimal	Flap	10 mm	40°	1.05 mm	Long intimal dissection with flap protruding into the lumen
Left	Paradise	1.17	Intimal	Cavity	0.8 mm	18°	n/a	Focal intimal disruption in contact with the guiding catheter
Right	Paradise	1.20	Adventitial	Flap-double lumen	12 mm	50°	0.77 mm	2 discrete adventitial dissections with flap and endothelial denudation
Right	Paradise	1.41	Intimal–medial adventitial	Flap–cavity-double lumen	14 mm	64°	1.53 mm	3 discrete dissections with varying morphology along the artery with or without adjacent thrombus
Right	Paradise	1.56	Intimal–medial adventitial	Flap–cavity-double lumen	18 mm	73°	1.08 mm	Long dissection with flap and several shorter cavity-type dissections (Figure 3)
Right	Vessix V2	1.24	Intimal	Cavity	0.4 mm	21°	n/a	Focal separation of the intimal layer near the renal artery bifurcation
Left	Oneshot	1.14	Adventitial	Flap–cavity	8 mm	57°	1.40 mm	Long adventitial dissection with flap formation, also visible in angiogram, extending to the distal branches (Figure 2)
Right	Oneshot	1.17	Medial	Flap–cavity-hematoma	18 mm	136°	1.23 mm	Extensive medial dissection with intramural hematoma causing lumen compromise (Figure 2)
Right	Symplicity	n/a	Intimal	Cavity	1 mm	21°	n/a	Small, focal cavity-type dissection adjacent to the guide catheter
Right	Oneshot	1.23	Intimal	Flap	7.2 mm	39°	0.85 mm	Separation of a thin intimal flap from the vessel surface
Right	Vessix V2	1.22	Medial	Flap–hematoma	4.6 mm	51°	0.30 mm	Intimal flap also visible in IVUS with possible hematoma at the abluminal side
Right	EnligHTN	n/a	Intimal	Flap–cavity	4.2 mm	17°	0.39 mm	Focal small intimal separations at different sites throughout the vessel

IVUS indicates intravascular ultrasound; max, maximal; and n/a, not applicable.

patients treated with balloon denervation. Conversely, such a reduction was identified by both modalities in patients treated with nonballoon denervation, also accompanied by a significant increase of PAV (3.86% [1.84–5.88%]; relative increase >15%). This increase might reflect oedematous medial cell swelling induced by energy delivery, a finding described in animal studies of the Symplicity catheter, where it subsided several days after treatment.[7] These findings are in accordance with previous studies showing a significant reduction of vessel dimensions in patients treated with nonballoon catheters,[9] but lack of significant change postdenervation in studies of balloon catheters.[8,17]

Our OCT findings add to the current understanding of denervation-induced renal artery trauma, showing that with a variety of denervation devices and irrespectively of the energy delivery method, there are findings of edema and intraluminal thrombus, and also a high incidence of dissections by OCT (over one third of treated arteries). This tracks with previous studies demonstrating acute vascular injury after renal denervation with some of the systems used in this study,[7–9,18] without, however, prominent findings at short-term follow-up.[7,19] Preclinical studies of nonballoon denervation catheters have shown tissue damage, including media fibrosis, mild EEM disruption, endothelial denudation, thrombus formation, and oedematous medial cell swelling,[7,18] whereas clinical studies demonstrated thrombus formation, development of focal convex-shaped intimal protrusions, attributed to edema, and in 13% of cases, minor dissections or detachment of the superficial endothelial layer,[9] similar to the percentage found for nonballoon-based devices in our study. Thrombus and dissection have also been observed with balloon-based denervation in similar frequency as in our study,[8] whereas less renounced injury was reported in another study where sizing was carefully performed.[17] Overall, the inclusion of patients treated both with balloon-based and nonballoon-based catheters allowed us to observe 2 distinct patterns of renal injury: (1) in nonballoon-based denervation, a response with low incidence and extent of dissection, but with acute lumen narrowing and vessel wall thickening, accompanied by a significantly but moderately higher thrombus area and a numerically

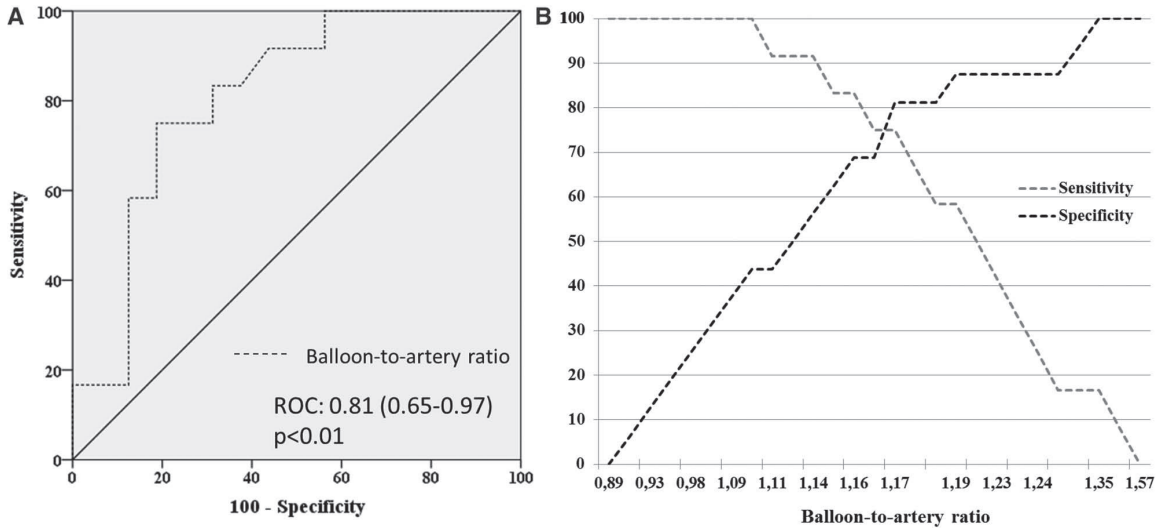

Figure 6. Receiver operating characteristic (v) curve and sensitivity–specificity curves for the prediction of dissection by the balloon/artery ratio.

higher percentage of frames with intimal protrusions; and (2) in balloon-based denervation, a response with a higher longitudinal extent of dissection, also with thrombus and intimal protrusions, in the absence of significant lumen or vessel size changes during the procedure.

Our study does not allow to directly differentiate whether the identified trauma was a result of denervation catheters themselves or iatrogenic because of the procedure. Nevertheless, all procedures were performed by experienced interventional cardiologists, skilled in intravascular imaging, with strict adhesion to denervation device–specific instructions. Although small ostial dissections might have occurred because of guiding catheter or guidewire manipulation, no evidence of vascular trauma or spasm was observed in preprocedural IVUS and was only observed after the actual denervation. This highly suggests that the denervation devices were the most likely cause of the observed injuries. In addition to thermal injury because of energy delivery, barotrauma could be potentially implicated in the pathogenesis of the observed dissections, despite low-pressure balloon dilations considered atraumatic, whereas device properties such as cooling could act protectively. Although our study did not specifically investigate the cause of these dissections, the percentage of frames with dissection was higher in balloon-based denervation, and dissection was associated with the balloon/artery ratio. This supports a role for barotrauma, possibly in synergy with the other factors.

The short- and long-term implications of such dissections remain elusive. In 1 patient, the flow was bilaterally impaired by dissections, leading to bilateral stent implantation. With the exception of this patient, dissections were of small extent relative to the vessel size (mean maximum dissection opening, 0.59 mm with mean angiographic MLD, 4.63 mm), in contrast to the coronary arteries where flow can often be significantly impaired.[20] Moreover, 6-month noninvasive imaging follow-up of 13 patients in our study treated in Thoraxcenter Rotterdam, in the context of a research protocol, did not show any significant renal artery stenosis. In addition, OCT follow-up in 1 patient demonstrated a complete healing of denervation-induced dissections.[21] However, given the well-defined relationship of vessel injury and cellular proliferation in percutaneous coronary intervention,[22] a possible association with late development of renal artery stenosis cannot be excluded, and measures for avoiding dissection, such as adaptation of a conservative strategy for balloon sizing, could prove beneficial.

Clinical Implications

Although renal denervation for resistant hypertension has not been widely adopted after the negative randomized sham-controlled Symplicity-HTN3 trial,[2] questions have been raised about the procedural efficacy of the Symplicity Flex system,[23] and several new devices are currently under investigation to address these technical limitations. Hence, our findings may have important clinical implications, as they report on vascular trauma from several different denervation devices and might help illuminate several procedural aspects. We demonstrated that small-scale dissections are not uncommon after renal denervation by balloon-expandable devices. Importantly, the significant association of balloon/artery ratio with the dissection extent dictates a judicious selection of balloon size, without excessive oversizing (balloon/artery ratio>1.20). Furthermore, postprocedural angiographic abnormalities in balloon-based devices should alert for possible dissection by OCT. Finally, as subclinical dissections and thrombus are not uncommon; strategies focusing on preventing thrombus formation, such as the current practice of 1-month aspirin administration to all patients undergoing renal denervation, seem justified in this setting, whereas a potential benefit of adding a P2Y12 agent needs to be clarified by further studies.

Limitations

As mentioned, this is an observational study in a limited number of patients, providing preliminary observations about the vascular trauma by these devices. Therefore, our study is not

powered to detect differences between individual devices, not allowing to make firm statements about the effect of cooling capacities of the OneShot and Paradise catheters on local vascular damage. Accordingly, our findings need to be confirmed by larger studies with follow-up to also address the prognostic effect of OCT markers of vascular trauma postdenervation. As there is currently no established measure for adequacy of denervation, differences in vascular trauma between technically successful or unsuccessful denervation could not be assessed. Moreover, analysis was feasible in ≈80% of OCT images, because of inherent limitations of OCT in assessment of large vessels, which could slightly underestimate our findings. Finally, at the time of the study, only 6-mm and 8-mm balloon catheters were available for the Paradise system. The introduction of 5-mm and 7-mm balloon sizes could allow for less pronounced balloon-artery mismatch and possibly lower incidence of dissections.

Conclusions

A varying extent of vascular injury was observed after renal denervation with all systems; however, different patterns of vessel injury were identified in balloon-based and nonballoon-based denervation systems. In balloon denervation, the presence of dissections by OCT was associated with a higher balloon/artery ratio and vessel wall irregularities on postprocedural angiogram. Our findings suggest that in these devices, postprocedural angiographic abnormalities should not be disregarded and raise suspicion of vascular injury, while a conservative approach on balloon selection could be considered.

Disclosures

Dr Karanasos received financial support for optical coherence tomography–related research from St Jude Medical. The other authors report no conflicts.

References

1. Davis MI, Filion KB, Zhang D, Eisenberg MJ, Afilalo J, Schiffrin EL, Joyal D. Effectiveness of renal denervation therapy for resistant hypertension: a systematic review and meta-analysis. *J Am Coll Cardiol*. 2013;62:231–241. doi: 10.1016/j.jacc.2013.04.010.
2. Bhatt DL, Kandzari DE, O'Neill WW, D'Agostino R, Flack JM, Katzen BT, Leon MB, Liu M, Mauri L, Negoita M, Cohen SA, Oparil S, Rocha-Singh K, Townsend RR, Bakris GL; SYMPLICITY HTN-3 Investigators. A controlled trial of renal denervation for resistant hypertension. *N Engl J Med*. 2014;370:1393–1401. doi: 10.1056/NEJMoa1402670.
3. Esler MD, Krum H, Sobotka PA, Schlaich MP, Schmieder RE, Bohm M. Renal sympathetic denervation in patients with treatment-resistant hypertension (the symplicity htn-2 trial): a randomised controlled trial. *Lancet*. 2010;376:1903–1909.
4. Krum H, Schlaich MP, Sobotka PA, Böhm M, Mahfoud F, Rocha-Singh K, Katholi R, Esler MD. Percutaneous renal denervation in patients with treatment-resistant hypertension: final 3-year report of the Symplicity HTN-1 study. *Lancet*. 2014;383:622–629. doi: 10.1016/S0140-6736(13)62192-3.
5. Kaltenbach B, Id D, Franke JC, Sievert H, Hennersdorf M, Maier J, Bertog SC. Renal artery stenosis after renal sympathetic denervation. *J Am Coll Cardiol*. 2012;60:2694–2695. doi: 10.1016/j.jacc.2012.09.027.
6. Pucci G, Battista F, Lazzari L, Dominici M, Boschetti E, Schillaci G. Progression of renal artery stenosis after renal denervation. Impact on 24-hour blood pressure. *Circ J*. 2014;78:767–768.
7. Steigerwald K, Titova A, Malle C, Kennerknecht E, Jilek C, Hausleiter J, Nährig JM, Laugwitz KL, Joner M. Morphological assessment of renal arteries after radiofrequency catheter-based sympathetic denervation in a porcine model. *J Hypertens*. 2012;30:2230–2239. doi: 10.1097/HJH.0b013e32835821e5.
8. Stabile E, Ambrosini V, Squarcia R, Salemme L, Popusoi G, Esposito G, Trimarco B, Rubino P. Percutaneous sympathectomy of the renal arteries: the OneShot Renal Denervation System is not associated with significant vessel wall injury. *EuroIntervention*. 2013;9:694–699. doi: 10.4244/EIJV9I6A113.
9. Templin C, Jaguszewski M, Ghadri JR, Sudano I, Gaehwiler R, Hellermann JP, Schoenenberger-Berzins R, Landmesser U, Erne P, Noll G, Lüscher TF. Vascular lesions induced by renal nerve ablation as assessed by optical coherence tomography: pre- and post-procedural comparison with the Simplicity catheter system and the EnligHTN multi-electrode renal denervation catheter. *Eur Heart J*. 2013;34:2141–2148, 2148b. doi: 10.1093/eurheartj/eht141.
10. Daemen J. Current technologies: an introduction. *EuroIntervention*. 2013;9(suppl R):R75–R82. doi: 10.4244/EIJV9SRA13.
11. Karanasos A, Ligthart J, Witberg K, van Soest G, Bruining N, Regar E. Optical coherence tomography: potential clinical applications. *Curr Cardiovasc Imaging Rep*. 2012;5:206–220. doi: 10.1007/s12410-012-9140-x.
12. Tsioufis C, Mahfoud F, Mancia G, Redon J, Damascelli B, Zeller T, Schmieder RE. What the interventionalist should know about renal denervation in hypertensive patients: a position paper by the ESH WG on the interventional treatment of hypertension. *EuroIntervention*. 2014;9:1027–1035. doi: 10.4244/EIJV9I9A175.
13. Mintz GS, Garcia-Garcia HM, Nicholls SJ, Weissman NJ, Bruining N, Crowe T, Tardif JC, Serruys PW. Clinical expert consensus document on standards for acquisition, measurement and reporting of intravascular ultrasound regression/progression studies. *EuroIntervention*. 2011;6:1123–1130, 1139. doi: 10.4244/EIJV6I9A195.
14. von Birgelen C, de Vrey EA, Mintz GS, Nicosia A, Bruining N, Li W, Slager CJ, Roelandt JR, Serruys PW, de Feyter PJ. ECG-gated three-dimensional intravascular ultrasound: feasibility and reproducibility of the automated analysis of coronary lumen and atherosclerotic plaque dimensions in humans. *Circulation*. 1997;96:2944–2952.
15. Chamié D, Bezerra HG, Attizzani GF, Yamamoto H, Kanaya T, Stefano GT, Fujino Y, Mehanna E, Wang W, Abdul-Aziz A, Dias M, Simon DI, Costa MA. Incidence, predictors, morphological characteristics, and clinical outcomes of stent edge dissections detected by optical coherence tomography. *JACC Cardiovasc Interv*. 2013;6:800–813. doi: 10.1016/j.jcin.2013.03.019.
16. Lingsma H, Nauta S, van Leeuwen N, Borsboom G, Bruining N, Steyerberg E. Tools & Techniques: analysis of clustered data in interventional cardiology: current practice and methodological advice. *EuroIntervention*. 2013;9:162–164. doi: 10.4244/EIJV9I1A23.
17. Versaci F, Trivisonno A, Olivieri C, Caranci F, Brunese L, Prati F. Vascular response after percutaneous sympathectomy: not all devices are equal. *Int J Cardiol*. 2014;174:406–407. doi: 10.1016/j.ijcard.2014.04.049.
18. Rippy MK, Zarins D, Barman NC, Wu A, Duncan KL, Zarins CK. Catheter-based renal sympathetic denervation: chronic preclinical evidence for renal artery safety. *Clin Res Cardiol*. 2011;100:1095–1101. doi: 10.1007/s00392-011-0346-8.
19. Stefanadis C, Toutouzas K, Synetos A, Tsioufis C, Karanasos A, Agrogiannis G, Stefanis L, Patsouris E, Tousoulis D. Chemical denervation of the renal artery by vincristine in swine. A new catheter based technique. *Int J Cardiol*. 2013;167:421–425. doi: 10.1016/j.ijcard.2012.01.002.
20. Holmes DR Jr, Holubkov R, Vlietstra RE, Kelsey SF, Reeder GS, Dorros G, Williams DO, Cowley MJ, Faxon DP, Kent KM. Comparison of complications during percutaneous transluminal coronary angioplasty from 1977 to 1981 and from 1985 to 1986: the National Heart, Lung, and Blood Institute Percutaneous Transluminal Coronary Angioplasty Registry. *J Am Coll Cardiol*. 1988;12:1149–1155.
21. Karanasos A, Van Mieghem NM, Regar E, Daemen J. Serial imaging observations of vascular healing in a denervation-induced renal artery dissection. *Eur Heart J*. 2015;36:1040. doi: 10.1093/eurheartj/ehu430.
22. Toutouzas K, Karanasos A, Stefanadis C. Inflammatory mechanisms of adverse reactions to BMS. *Curr Vasc Pharmacol*. 2013;11:379–391.
23. Vink EE, Goldschmeding R, Vink A, Weggemans C, Bleijs RL, Blankestijn PJ. Limited destruction of renal nerves after catheter-based renal denervation: results of a human case study. *Nephrol Dial Transplant*. 2014;29:1608–1610. doi: 10.1093/ndt/gfu192.

SUPPLEMENTAL MATERIAL

Supplementary Methods

Balloon size selection. Balloon size selection for Vessix V2™ was based on maximal artery diameter on on-line quantitative angiography using a 4mm balloon for arteries with maximal diameter 3.0-4.0mm, a 5mm balloon for arteries with maximal diameter 3.8-5.0mm, a 6mm balloon for arteries with maximal diameter 4.7-6.0mm, and a 7mm balloon for arteries with maximal diameter 5.6-7.0mm. A similar principle was used for sizing with the Oneshot™ –with 5, 6, and 7mm balloon sizes available for Oneshot™- and with the Paradise™ system. However, at the time of the study, only 6 and 8mm balloon sizes were available for Paradise™.

Angiographic analysis. Quantitative angiographic analysis was performed offline in Thoraxcenter Rotterdam, using dedicated software (CAAS 5.9.2, Pie medical, Maastricht, Netherlands). Measurements included reference vessel diameter (RVD), minimal lumen diameter (MLD), mean luminal diameter, and percent diameter stenosis (DS%).

Angiographic images were also qualitatively assessed for lumen contour irregularities and dissection. Dissection was defined as an intraluminal filling defect or a persistent parietal radiopacity, in line with angiographic definitions for coronaries[1].

Supplementary references

1. Holmes DR, Holubkov R, Vlietstra RE, Kelsey SF, Reeder GS, Dorros G, Williams DO, Cowley MJ, Faxon DP, Kent KM, Bentivoglio LG, Detre K. Comparison of complications during percutaneous transluminal coronary angioplasty from 1977 to 1981 and from 1985 to 1986: The national heart, lung, and blood institute percutaneous transluminal coronary angioplasty registry. *J Am Coll Cardiol.* 1988;12:1149-1155

Supplementary Tables

Supplementary Table 1. Baseline characteristics by device

	Symplicity ™ (n=6)	Paradise™ (n=5)	Oneshot™ (n=6)	Vessix V2™ (n=5)	EnligHTN ™ (n=3)	p-value
Age (years)	68.2±14.6	63.0±11.3	64.3±7.7	57.2±5.9	63.3±6.7	0.54
Male gender n, (%)	3 (50.0)	1 (20.0)	3 (50.0)	5 (100)	2 (66.7)	0.14
Cardiovascular risk factors n, (%)						
Hypertension	6 (100)	5 (100)	6 (100)	5 (100)	3 (100)	1.00
Dyslipidaemia	4 (66.7)	3 (60.0)	3 (50.0)	3 (60.0)	2 (66.7)	0.98
Smoking	2 (33.3)	0 (0)	2 (33.3)	3 (60.0)	1 (33.3)	0.38
Diabetes mellitus	3 (50.0)	2 (40.0)	1 (16.7)	0 (0)	1 (33.3)	0.38
Family history for CAD	2 (33.3)	4 (80.0)	1 (16.7)	3 (60.0)	3 (100)	0.08
CAD	2 (33.3)	3 (60.0)	2 (33.3)	2 (40.0)	1 (33.3)	0.89
Prior infarction n, (%)	1 (16.7)	2 (40.0)	0 (0)	2 (40.0)	0 (0)	0.31
Prior stroke n, (%)	1 (16.7)	0 (0)	0 (0)	0 (0)	1 (33.3)	0.36
Systolic BP pre ablation (mm Hg)	159.5±22.5	185.6±21.0	179.3±30.4	151.2±40.0	168.7±28.7	0.33
Diastolic BP pre ablation (mm Hg)	85.2±7.5	97.1±11.0	89.9±9.7	90.1±20.0	101.3±13.3	0.38
eGFR pre ablation (ml/min/1.73m^2)	66.3±19.6	67.6±20.1	71.7±21.6	73.8±20.5	67.7±22.2	0.97

Values are expressed as mean±SD or n,(%). CAD=coronary artery disease; BP=blood pressure; eGFR=estimated glomerular filtration rate

Supplementary Table 2. Quantitative angiography measurements and qualitative findings by device

	Symplicity™ (n=10)	Paradise™ (n=10)	Oneshot™ (n=12)	Vessix V2™ (n=10)	EnligHTN™ (n=6)	p-value
Pre-denervation (n=47)						
RVD (mm)	5.50 (4.89 - 6.11)	5.11 (4.45 - 5.76)*	4.82 (4.24 - 5.41)	5.55 (4.85 - 6.49)	5.67 (4.85 - 6.49)	0.30
MLD (mm)	5.10 (4.52 - 5.68)	4.46 (3.84 - 5.09)*	4.34 (3.79 - 4.90)	5.11 (4.51 - 5.72)	5.10 (4.32 - 5.88)	0.17
DS (%)	6.9 (2.5 - 11.3)	12.1 (7.5 – 16.7)*	10.1 (6.1 - 14.1)	7.8 (3.4 - 12.2)	10.0 (4.3 - 15.7)	0.50
Post-denervation (n=47)						
RVD (mm)	5.42 (4.69 - 6.14)	4.90 (4.14 - 5.67)	5.11 (4.42 - 5.81)	6.08 (5.30 - 6.86)*	5.44 (4.46 - 6.42)	0.25
MLD (mm)	4.82 (4.03 - 5.60)	4.47 (3.64 - 5.29)	4.63 (3.88 - 5.38)	4.81 (3.97 - 5.66)*	4.28 (3.21 - 5.34)	0.89
DS (%)	11.6 (4.6 - 18.7)	9.1 (1.7 - 16.5)	9.5 (2.8 - 16.2)	21.2 (13.6 - 28.7)*	22.8 (13.3 - 32.3)	0.04
Difference (Post-denervation – pre-denervation) (n=46)						
RVD (mm)	−0.07 (−0.49 - 0.35)	−0.14 (−0.58 - 0.30)*	0.24 (−0.15 - 0.62)	0.70 (0.22 - 1.17)*,†	−0.06 (−0.66 - 0.53)	0.07
MLD (mm)	−0.32 (−0.79 - 0.15)	0.06 (−0.42 - 0.54)*	0.26 (−0.16 - 0.69)	−0.36 (−0.88 - 0.16)*	−0.77 (−1.43 - −0.10)†	0.08
DS (%)	4.2 (−1.4 - 9.7)	−1.8 (−7.4 - 3.8)*	−0.2 (−5.3 - 4.9)	14.4 (8.2 - 20.6)*,†	15.6 (7.8 - 23.3)†	<0.01
Qualitative assessment post-denervation (n=47)						
Dissection n, (%)	0 (0)	0 (0)	3 (25.0)	1 (11.1)*	0 (0)	0.99‡
Contour irregularities n, (%)	4 (40.0)	4 (40.0)	1 (8.3)	5 (55.6)*	4 (66.7)	0.22‡

Values are expressed as estimated means (95% confidence intervals) or n, (%). RVD=reference vessel diameter; MLD=minimum lumen diameter; DS=diameter stenosis

*n=9; †p<0.05 for post-denervation versus pre-denervation; ‡p-values derived from multilevel logistic regression using within-patient intercepts as random effects.

Supplementary Table 3. Intravascular ultrasound measurements in balloon and non-balloon-based systems pre- and post-denervation

	All vessels (n=32)	Balloon-based devices (n=20)	Non-balloon-based devices (n=12)	p-value
Pre-denervation (n=31)				
Analyzed length (mm)	29.1 (24.7 - 33.5)	27.0 (21.6 - 32.3)	31.2 (24.2 - 38.3)	0.32
Mean lumen area (mm^2)	25.66 (21.12 - 30.20)	25.12 (19.62 - 30.62)	26.19 (18.97 - 33.42)	0.81
Min lumen area (mm^2)	20.42 (16.78 - 24.07)	19.23 (14.83 - 23.62)	21.62 (15.82 - 27.43)	0.50
Mean EEM area (mm^2)	34.43 (28.57 - 40.29)	33.48 (26.39 - 40.58)	35.37 (26.04 - 44.71)	0.74
Min EEM area (mm^2)	28.41 (23.67 - 33.15)	26.90 (21.17 - 32.62)	29.92 (22.36 - 37.48)	0.51
Lumen volume (mm^3)	771.7 (573.7 - 969.7)	694.1 (453.4 - 934.7)	849.4 (534.8 - 1163.9)	0.42
EEM volume (mm^3)	1035.7 (768.7 - 1302.7)	921.2 (596.5 - 1245.8)	1150.3 (726.2 - 1574.3)	0.38
PAV (%)	25.16 (23.21 - 27.11)	25.46 (23.11 - 27.82)	24.85 (21.74 - 27.95)	0.74
nTAV (mm^3)	253.2 (107.7 - 298.6)	241.2 (186.2 - 296.1)	265.2 (192.7 - 337.7)	0.58
Post-denervation (n=32)				
Analyzed length (mm)	28.0 (24.1 - 32.0)	26.0 (21.1 - 30.9)	30.1 (23.8 - 36.4)	0.29
Mean lumen area (mm^2)	23.69 (18.97 - 28.41)	24.90 (19.12 - 30.68)	22.48 (15.02 - 29.94)	0.59
Min lumen area (mm^2)	18.44 (14.26 - 22.62)	18.85 (13.73 - 23.98)	18.03 (11.42 - 24.64)	0.84
Mean EEM area (mm^2)	32.60 (26.46 - 38.74)	33.71 (26.19 - 41.23)	31.48 (26.19 - 41.23)	0.71
Min EEM area (mm^2)	26.13 (20.68 - 31.57)	26.74 (20.07 - 33.41)	25.51 (16.91 - 34.12)	0.82
Lumen volume (mm^3)	690.9 (494.9 - 886.8)	667.2 (427.2 - 907.3)	714.5 (404.6 - 1024.4)	0.80
EEM volume (mm^3)	948.0 (688.5 - 1207.6)	896.7 (578.9 - 1214.6)	999.3 (589.0- 1409.7)	0.68
PAV (%)	27.57 (25.30 - 29.84)	26.80 (24.02 - 29.59)	28.34 (24.74 - 31.93)	0.49
nTAV (mm^3)	252.3 (203.4 - 301.2)	249.7 (189.8 - 309.5)	254.9 (177.6 - 332.2)	0.91

Values are expressed as estimated means (95% confidence intervals). EEM=external elastic membrane; PAV=percent atheroma volume; nTAV=normalized total atheroma volume

Supplementary Table 4. Intravascular ultrasound measurements pre- and post-denervation by device

	Symplicity™ (n=6)	Paradise™ (n=4)	Oneshot™ (n=6)	Vessix V2™ (n=10)	EnligHTN™ (n=6)	p-value
Pre-denervation (n=31)						
Analyzed length (mm)	31.7 (23.5-39.9)*	17.1 (7.7-26.5)	24.2 (16.5-31.9)	32.6 (26.6-38.5)	31.1 (23.4-38.8)	0.06
Mean lumen area (mm²)	26.28 (16.08-36.48)*	22.86 (10.81-34.90)	28.26 (18.43-38.10)	24.14 (16.52-31.75)	26.13 (16.30-35.96)	0.94
Min lumen area (mm²)	22.17 (14.05-30.28)*	17.03 (7.57-26.50)	22.55 (14.82-30.27)	18.11 (12.13-24.10)	21.15 (13.42-28.88)	0.77
Mean EEM area (mm²)	34.97 (21.74-48.20)*	30.23 (14.64-45.81)	37.10 (24.38-49.83)	32.62 (22.76-42.47)	35.76 (23.04-48.48)	0.95
Min EEM area (mm²)	30.45 (19.81-41.09)*	23.38 (10.99-35.76)	30.64 (20.53-40.58)	26.05 (18.22-33.89)	29.47 (19.36-39.59)	0.82
Lumen volume (mm³)	811.7 (387.4-1235.9)*	389.4 (0-894.2)	734.1 (321.9-1146.2)	791.9 (472.7-1111.2)	886.3 (474.1-1298.4)	0.58
EEM volume (mm³)	1076.6 (506.5-646.6)*	513.0 (0-1193.7)	965.2 (410.2-1520.2)	1058.0 (628.1-1487.9)	1221.9 (666.9-1776.9)	0.54
PAV (%)	24.27 (19.86-28.68)*	24.01 (18.85-29.17)	25.22 (21.01-29.43)	26.19 (22.93-29.45)	23.37 (21.16-29.58)	0.93
nTAV (mm³)	251.4 (147.9-354.9)*	212.5 (91.3-333.7)	254.8 (155.9-353.8)	244.4 (167.7-321.1)	277.7 (178.7-376.6)	0.93
Post-denervation (n=32)						
Analyzed length (mm)	31.4 (24.9-37.8)	17.2 (9.3-25.0)	22.3 (15.9-28.7)	31.7 (26.7-36.7)	28.8 (22.4-35.3)	0.02
Mean lumen area (mm²)	23.94 (13.57-34.31)	22.18 (9.48-34.87)	27.05 (16.68-37.41)	24.71 (16.68-32.74)	21.02 (10.65-31.38)	0.92
Min lumen area (mm²)	19.64 (10.59-28.69(	17.19 (6.1-28.72)	22.03 (12.98-31.08)	17.61 (10.60-24.62)	16.42 (7.37-25.47)	0.89
Mean EEM area (mm²)	32.31 (18.74-45.88)	30.04 (13.43-46.66)	36.04 (22.47-49.61)	33.78 (23.27-44.29)	30.65 (17.08-44.22)	0.97
Min EEM area (mm²)	26.90 (15.06-38.75)	23.68 (9.17-38.19)	30.71 (18.86-42.55)	25.58 (16.40-34.76)	24.13 (12.28-35.97)	0.91
Lumen volume (mm³)	761.0 (352.0-1170.1)	380.0 (0-880.9)	642.4 (233.3-1051.4)	797.0 (480.2-1113.9)	668.0 (258.9-1077.0)	0.66
EEM volume (mm³)	1028.4 (486.7-1570.0)	511.9 (0-1175.3)	857.5 (315.8-1399.2)	1074.2 (654.6-1493.8)	970.3 (428.6-1512.0)	0.64
PAV (%)	25.53 (20.94-30.13)	26.53 (20.90-32.16)	26.07 (21.48-30.67)	27.35 (23.79-30.91)	31.14 (26.55-35.74)	0.41
nTAV (mm³)	237.5 (129.7-345.3)	223.3 (91.3-355.4)	255.4 (147.6-363.2)	256.7 (173.2-340.2)	272.2 (164.48-380.0)	0.97

Values are expressed as estimated means (95% confidence intervals). EEM=external elastic membrane; PAV=percent atheroma volume; nTAV=normalized total atheroma volume

*n=5

Supplementary Table 5. Difference in intravascular ultrasound measurements post-denervation minus pre-denervation by device

	Symplicity™ (n=5)	Paradise™ (n=4)	Oneshot™ (n=6)	Vessix V2™ (n=10)	EnligHTN™ (n=6)	p-value
			Difference (Post-denervation – pre-denervation)			
Mean lumen area (mm²)	−1.56 (−5.10 - 1.97)	−0.90 (−4.88 - 3.08)	−0.95 (−4.21 - 2.31)	0.42 (−2.25 - 3.09)	−5.52 (−9.08 - −1.97)*	0.07
Min lumen area (mm²)	−1.27 (−4.47 - 1.93)	0.01 (−3.63 - 3.64)	−0.38 (−3.35 - 2.59)	−0.51 (−2.93 - 1.92)	−5.30 (−8.55 - −2.05)*	0.06
Mean EEM area (mm²)	−1.46 (−5.60 - 2.67)	−0.45 (−5.10 - 4.20)	−0.82 (−4.63 - 2.98)	0.95 (−2.17 - 4.07)	−5.52 (−9.67 - −1.36)*	0.17
Min EEM area (mm²)	−2.10 (−5.73 - 1.53)	0.26 (−3.85 - 4.38)	0.09 (−3.27 - 3.45)	−0.50 (−3.24 - 2.25)	−5.56 (−9.24 - −1.88)*	0.08
Lumen volume(mm³)	−31.1 (−159.0 - 96.8)	−32.9 (−176.7 - 110.9)	−92.8 (−210.5 - 24.8)	6.1 (−90.2 - 102.3)	−240.7 (−369.1 - −112.3)*	0.01
EEM volume(mm³)	−20.1 (−172.4 - 132.3)	−29.36 (−200.3 - 29.8)	−110.0 (−249.9 - 29.8)	14.7 (−99.7 - 129.2)	−279.7 (−432.4- −127.1)*	0.02
PAV (%)	1.51 (−0.99 - 4.00)	2.40 (−0.48 - 5.29)	0.86 (−1.50 - 3.22)	1.12 (−0.81 - 3.05)	6.40 (3.82 - 8.98)*	<0.01
nTAV (mm³)	−1.2 (−24.9 - 22.5)	10.2 (−16.5 - 36.8)	0.7 (−21.1 - 22.5)	9.8 (−8.0 - 27.6)	−6.3 (−30.2 - 17.5)	0.82

Values are expressed as estimated means (95% confidence intervals). EEM=external elastic membrane; PAV=percent atheroma volume; nTAV=normalized total atheroma volume

*p<0.05 for post-denervation versus pre-denervation

Supplementary Table 6. Optical coherence tomography findings post-denervation by device

	Symplicity™ (n=10)	Paradise™ (n=7)	Oneshot™ (n=11)	Vessix V2™ (n=10)	EnligHTN™ (n=5)	p-value
Vessel-level analysis						
Number of frames, (n)	167.0 (137.6 - 196.4)	178.5 (143.9 - 213.0)	130.7 (102.4 - 159.1)	163.2 (133.2 - 193.2)	149.5 (107.9 - 191.1)	0.23
Fair-to-good quality, (n)	135.5 (101.6 - 169.5)	163.4 (124.2 - 202.6)	99.4 (66.4 - 132.3)	97.3 (62.1 - 132.5)	140.1 (92.1 - 188.2)	0.07
Any dissection n, (%)	1 (10)	5 (71.4)	4 (36.4)	3 (30.0)	1 (20.0)	0.29‡
Max dissection opening (mm)*	-	1.00 (0.58 - 1.42)	1.49 (1.01 - 1.98)	0.37 (0 - 0.86)	0.39 (0 - 1.26)	0.01
Any thrombus n, (%)	7 (70.0)	6 (85.7)	10 (90.9)	7 (70.0)	5 (100.0)	0.89‡
Any oedema n, (%)	8 (80.0)	6 (85.7)	4 (36.4)	9 (90)	5 (100)	0.36‡
Frame-level analysis						
Frames with dissection,%	0 (0-1.9)	10.4 (0.7-66.9)	2.0 (0.2-22.4)	0.9 (0.1-14.1)	0.3 (0-15.8)	0.21
Dissection angle (°)*	20.8 (0 - 92.2)	50.6 (19.3 - 81.9)	84.2 (49.6 - 118.9)	46.7 (5.6 - 87.8)	17.0 (0 - 86.5)	0.24
Dissection opening (mm)*	-	0.65 (0.12 - 1.17)	0.98 (0.37 - 1.59)	0.31 (0 - 0.93)	0.28 (0 - 1.33)	0.35
Frames with thrombus,%	4.4 (1.6-11.3)	9.5 (3.3-24.5)	9.8 (4.0-21.9)	4.1 (1.4-11.3)	10.9 (3.0-32.6)	0.51
Thrombus area (mm^2)†	0.13 (0.09 - 0.17)	0.07 (0.03 - 0.11)	0.06 (0.02 - 0.10)	0.05 (0 - 0.11)	0.07 (0.01 - 0.12)	0.11
Frames with oedema,%	13.0 (3.6-37.3)	7.4 (1.7-26.9)	1.3 (0.3-5.8)	16.3 (4.3-45.9)	19.0 (3.3-61.3)	0.08

Values are expressed as n, (%) or estimated means (95% confidence intervals).
*Calculated among pullbacks with dissection (Symplicity™: n=1, Paradise™: n=5, Oneshot™: n=4, Vessix V2™: n=3, EnligHTN™: n=1); †Calculated among pullbacks with thrombus (Symplicity™: n=7, Paradise™: n=6, Oneshot™: n=10, Vessix V2™: n=7, EnligHTN™: n=5); ‡p-values derived from multilevel logistic regression using within-patient intercepts as random effects.

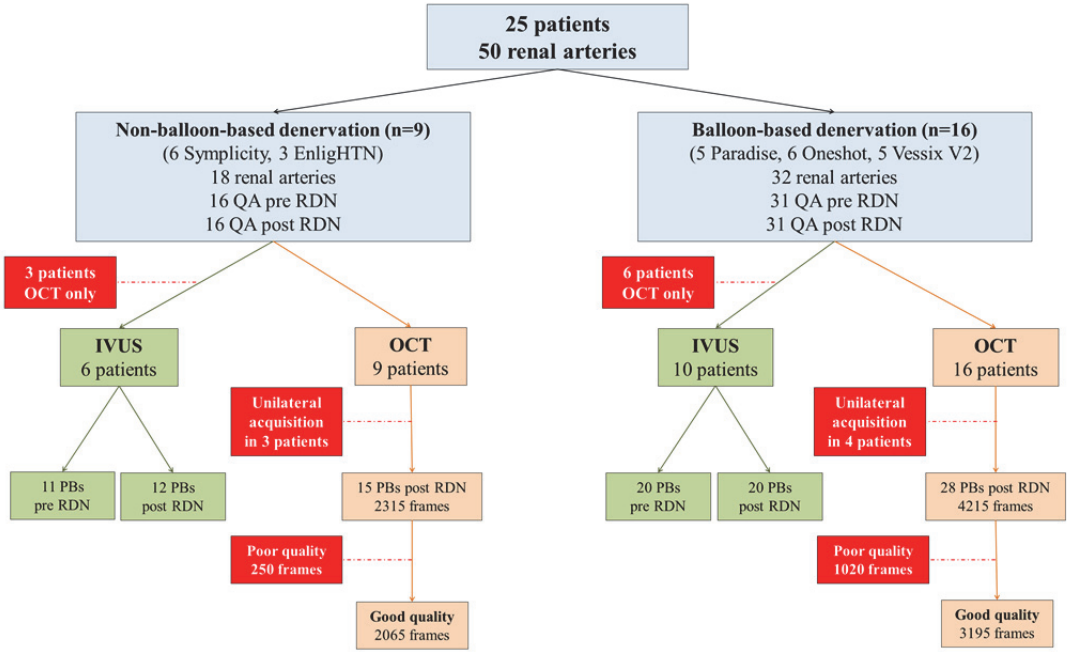

Supplementary Figure 1. Study flowchart.

Abbreviations: QA=quantitative angiography; RDN=renal denervation; IVUS=intravascular ultrasound; OCT=optical coherence tomography; PB=pullback

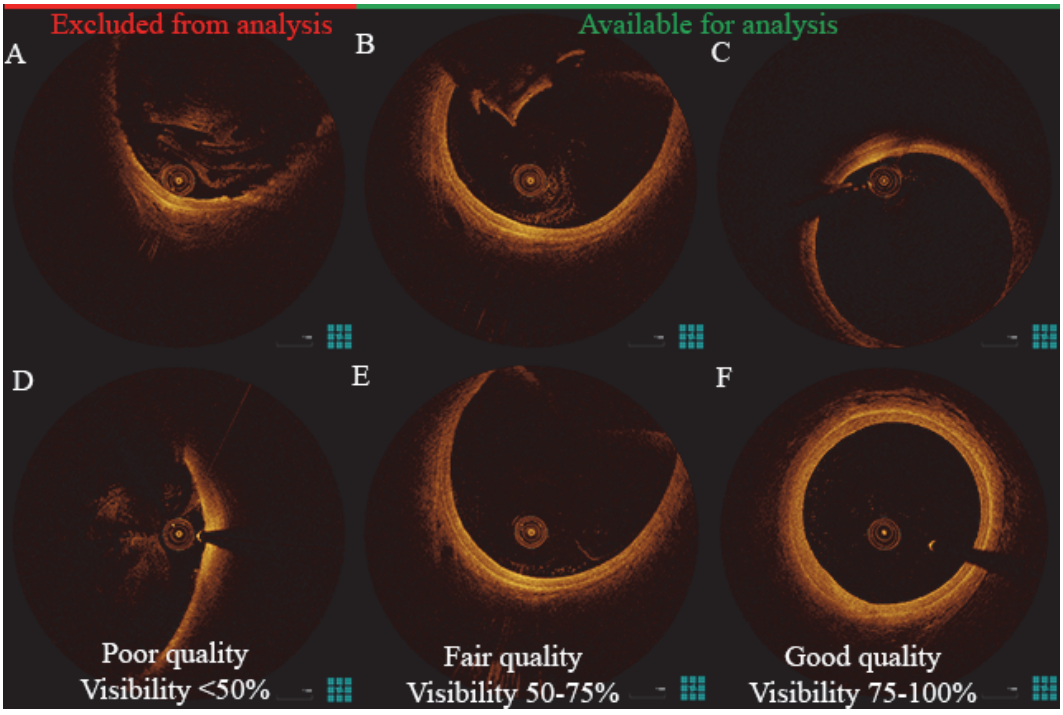

Supplementary Figure 2. Optical coherence tomography (OCT) image quality screening

Images were screened for image quality by measuring the percentage of lumen contour visibility. Frames with poor quality (visibility <50% [180°]) were excluded from analysis.

Chapter 8.3

Serial imaging observations of vascular healing in a denervation-induced renal artery dissection

Karanasos A, Van Mieghem NM, Regar E, Daemen J

Eur Heart J. 2015;36:1040

CARDIOVASCULAR FLASHLIGHT

Serial imaging observations of vascular healing in a denervation-induced renal artery dissection

Antonios Karanasos, Nicolas M. Van Mieghem, Evelyn Regar, and Joost Daemen*

Department of Cardiology, Thoraxcenter, Erasmus MC, Rotterdam, The Netherlands

* Corresponding author. Tel: +31 10 703 52 60, Fax: +31 10 703 52 54, Email: j.daemen@erasmusmc.nl

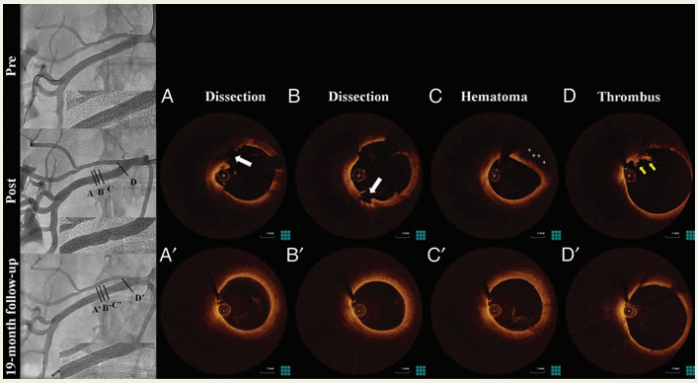

A 75-year-old woman underwent bilateral renal denervation with an ultrasound-based balloon denervation system (Paradise™; Recor Medical, Palo Alto, CA, USA) due to resistant hypertension. The procedure was successfully completed without clinical adverse events; however, the post-procedural right renal artery angiogram showed non-flow limiting lumen irregularities, associated with micro-thrombi and dissections with intramural hematoma formation by optical coherence tomography (OCT). No further treatment was performed and the patient was discharged on aspirin for 1 month. Six-month follow-up magnetic resonance angiography (MRA) showed no signs of stenosis. At 1 year, severe refractory hypertension persisted (mean office 193/93 mmHg) and the patient suffered a cerebrovascular accident. In view of the persistent elevated blood pressure, a repeat procedure was performed 19 months after the baseline procedure. Prior to the repeat procedure, OCT was performed in the right renal artery demonstrating no evidence of vascular trauma with complete healing of the dissections and resolution of the hematoma.

Although small dissections and micro-thrombi have been reported as direct vascular consequences of renal denervation with several different devices, their clinical significance remains unclear. We present for the first time the follow-up of a denervation-induced dissection showing a completed healing process with no evidence of persistent vascular trauma or development of stenosis.

Angiographic and optical coherence tomography (OCT) images from the right renal artery from pre-denervation, post-denervation, and at the repeat procedure. Follow-up angiography demonstrates the resolution of lumen irregularities, while OCT images disclose the complete healing of dissections and intramural hematoma. White arrow, dissection; yellow arrow, thrombus; cross, hematoma.

A.K. has received support for OCT-related research from St Jude.

Summary and conclusions

Summary and conclusions

Since the introduction of percutaneous coronary intervention, coronary angiography has been the tool for assessing the presence of coronary artery lesions, as well as for assessing the outcome of interventions. The advent of intravascular imaging has opened a new chapter in coronary lesion and intracoronary device assessment, enabling the transition from assessment of the lumen to the direct assessment of plaque and vessel morphology and the evaluation of the vessel wall response to stenting. During the recent decade, optical coherence tomography (OCT) has gained increasing popularity for the assessment of atherosclerosis and cardiovascular interventions. OCT is a light-based intravascular imaging method that has the advantage of providing high resolution (5–15 μm) images of the vascular wall and intracoronary devices[1]. The development of the second generation, frequency domain OCT allowed for a widespread implementation of this imaging modality in the clinical practice, by simplifying the procedure of image acquisition, shortening the required time, and having reduced requirements for flashing[2]. Consequently, OCT comprises an ideal tool for assessing atherosclerotic plaque morphology and the acute and chronic vascular effects of interventions with a variety of devices.

Overall, this thesis describes the clinical use of OCT in percutaneous coronary intervention with the main focus on the assessment of the acute and chronic vascular effects of intravascular interventions.

Assessment of coronary atherosclerosis and use of OCT in coronary intervention.

In **Part I** the potential for utilization of OCT imaging in the practice of a catheterization laboratory is analyzed. **Chapter 1.1** proposes several potential applications for OCT in percutaneous coronary intervention. Such applications include evaluation for the presence of a lesion, pre-procedural lesion assessment for the guidance of percutaneous coronary intervention, post-procedural assessment of the acute outcome of percutaneous coronary intervention, and the follow-up intracoronary device evaluation, including the assessment of the pathomechanisms of stent failure.

Chapter 1.2 reviews the current experience from OCT imaging in acute myocardial infarction and summarizes current insights into the association of atherosclerotic plaque morphology and pathomechanisms of myocardial infarction, as assessed by in vivo OCT imaging. Moreover, the role of OCT in the assessment of myocardial infarction after stent implantation is further analyzed. Simultaneously, the use of OCT for the assessment of the treatment effect in

myocardial infarction is reviewed, and pilot studies referring to a potential clinical utility of OCT for guidance of treatment in myocardial infarction are referenced.

Chapter 1.3 reports on a large single-registry investigating the safety and feasibility of OCT in an unselected population. In a series of 1,142 patients in different clinical settings and with varying indications for imaging, second generation OCT was successfully performed with a low incidence of imaging-related complications (0.6%). Importantly, this incidence was similar to the incidence of imaging-related complications observed in a series of 2,476 patients undergoing IVUS during the same study period in the same center, while the observed complications were self-limiting after retrieval of the imaging catheter or easily treatable in the catheterization laboratory. These findings indicate that second generation optical coherence tomography is safe to use in percutaneous coronary intervention in a variety of clinical settings with a very low event rate.

Methodological aspects of OCT analysis in challenging settings.

Part II discusses several methodological considerations in quantitative and qualitative analysis of OCT images. The impact of longitudinal catheter displacement during image acquisition on the quantitative assessment of bioresorbable scaffolds was examined in an experimental setting, using a swine model which is associated with exaggerated vessel motion (**Chapter 2.1**). Indeed variation in the assessment of the imaged scaffold length was exceedingly high. Although, this did no significantly affect global measurements such as mean lumen, mean scaffold and mean coverage area, measurements in specific scaffold regions were significantly affected, hampering serial evaluation of matched cross-sections. Importantly, longitudinal catheter displacement due to coronary artery motion has also been described in human, suggesting that such quantitative measurements are also vulnerable to errors in human studies. Therefore, dedicated analysis methodology with meticulous per frame analysis or segment matching with the use of software allowing synchronized inspection of matched segments would be more suitable for serial analysis in specific scaffold regions in the presence of extensive vessel motion.

Chapter 2.2 deals with the issue of atherosclerotic plaque evaluation and specifically with cap thickness measurement in human fibroatheromas. Variability in the assessment of cap thickness could pose a problem in the reliable assessment of these plaques[3], a problem that becomes more imminent considering the critical significance of cap thickness in the pathomechanism of plaque rupture[4-7]. Therefore, an algorithm for the automated segmentation of cap thickness is proposed. The performance of the proposed algorithm was good, with the error

in the assessment of cap thickness being comparable to the inter-observer variability. Consequently, implementation of this algorithm for the assessment of fibrous cap thickness can allow for a fast, objective and reliable assessment of cap thickness in OCT studies of human fibroatheromas.

Challenges in the analysis of bifurcation lesions by OCT are described in **Chapter 2.3**. Specifically, the problem of the measurement of a side-branch ostium from a contralateral branch pullback is analyzed. By using measurements from the side-branch as a reference, the error in the assessment of the ostial side-branch area from a main branch pullback was higher than 0.4 mm in 50% of the cases. This error could have important implications in a therapeutic approach leading to suboptimal sizing when side-branch treatment is required. A new approach is thus proposed for this problem, that includes the use of dedicated offline software with three-dimensional rendering. This approach allows for the selection of a plane perpendicular to the side-branch take-off and the performance of measurements at the anatomical ostium of the side-branch. Thereby, the absolute error in the assessment of side-branch ostium area is reduced from 1.50 ± 1.31 to 0.56 ± 0.45 mm², while the analysis is robust with a low intra- and inter-observer variability. This reliable side-branch assessment from a main-branch pullback has the potential to limit side-branch instrumentation and might significantly reduce procedural complexity, improve treatment strategy planning and potentially improve outcome of bifurcation lesions in the future.

Assessment of very late metallic stent failure by OCT – the role of neoatherosclerosis.

Part III deals with one of the major pitfalls of metallic stents which is late stent failure. Although with the current generation of metallic stents used in clinical practice, short- and mid-term clinical results are excellent, observations of late failure with these devices are recorded even at very long intervals after implantation, both with bare metal stents and drug-eluting stents[8-10]. The potential of OCT to discern intracoronary thrombus and in-stent structures with high resolution gives OCT a pivotal role in the assessment of the pathomechanism of very late stent failure. **Chapter 3.1** illustrates a case of very late thrombosis of a bare metal stent occurring 15 years after implantation. OCT after restoration of flow revealed the pathological background of this complication, which was the development of atherosclerosis within the stented segment, called neoatherosclerosis. The necrotic core accumulation within the stent was succeeded by intra-stent plaque rupture and thrombosis, which triggered the clinical event. Importantly, a variety of morphological characteristics could be identified within the neoatherosclerotic segment, which had a similar OCT appearance as morphological characteristics of native atherosclerosis.

Chapter 3.2 provides a comprehensive summary of current insights into neoatherosclerosis by OCT. In specific, there is reference to the OCT appearance of morphological characteristics of neoatherosclerosis and different neointimal patterns, which are discussed with relation to histological evidence. Moreover, prevalence of neoatherosclerosis by OCT in the late follow-up of both bare metal stents and drug-eluting stents and the associated factors are reviewed. The chapter also discusses the association of neoatherosclerosis with very late stent restenosis or thrombosis, and highlights the contribution of intravascular imaging in changing the current paradigm of late failure by disclosing that neoatherosclerosis is a common pathomechanism in both late restenosis and thrombosis. Traditionally, stent restenosis had been considered rather benign and associated with stable symptoms, while stent thrombosis life-threatening and associated with acute presentation. However, the presence of common imaging findings, in different extent, such as in-stent necrotic core, neointimal rupture and thrombus in both entities implies that these two presentations can occur as different manifestations of the same unfavorable healing process.

The association of neoatherosclerosis with clinical presentation is further explored in **Chapter 3.3**. In a two-center registry of 74 patients undergoing OCT for the assessment of very late failure or assessment of very long-term vascular healing response we investigated the differences in the prevalence of neoatherosclerosis with regard to the clinical presentation. Both stent restenosis and stent thrombosis had a higher prevalence of neoatherosclerosis compared to the asymptomatic group, however the prevalence of neointimal rupture was higher in stent thrombosis. Notably, the presence of plaque rupture was associated with specific morphological characteristics of the neointimal plaque, such as thin fibrous cap and macrophage infiltration, in analogy to the paradigm of vulnerable plaque in native atherosclerosis. These findings collectively imply the active contribution of neoatherosclerosis in the pathogenesis of late stent failure, while underscoring the significance of in-stent plaque instability for the development of acute coronary syndrome after stent implantation.

Chapter 3.4 investigates the differences in prevalence and morphology of neoatherosclerosis between bare metal stents and first-generation drug-eluting stents at a very late follow-up. A time-dependent pattern was observed in the prevalence of neoatherosclerosis in first-generation drug-eluting stents, with the development of neoatherosclerosis being associated with a higher interval since implantation. Interestingly, there were no differences in prevalence or morphology of neoatherosclerosis between bare metal stents and first-generation drug-eluting stents, despite the latter having a lower interval from implantation. These findings indicate that the development of neoatherosclerosis is a common problem in bare metal stents and first-

generation metal drug-eluting stents, with pathologic studies also hinting to a similar incidence of neoatherosclerosis in second-generation drug-eluting stents[11].

OCT examination of the long-term vascular healing response of bioresorbable scaffolds.

The ongoing failure observed with permanent metallic DES, has therefore created a need for platforms allowing the restoration of the vessel morphology and physiology after providing temporary mechanical support post intervention. Bioresorbable scaffolds are new platforms which could potentially fulfill this need[12], however experience with these devices is limited and there is a need to better understand the process of the vascular healing after bioresorbable scaffold implantation. Thus, intravascular imaging by OCT has a central role in the assessment of the vascular healing response after bioresorbable scaffold implantation, and parts IV to VII focus on the use of OCT for the assessment of bioresorbable scaffolds. **Part IV** examines the long-term vascular healing after bioresorbable scaffold implantation. In **Chapter 4.1**, findings from the late invasive follow-up by OCT of one the first patients that underwent bioresorbable scaffold implantation are presented and discussed, shaping a hypothesis supporting that bioresorbable scaffolds can induce the development of a homogeneous layer that can shield the lumen from potentially thrombogenic plaque component, without causing lumen narrowing.

Chapter 4.2 reports on the comprehensive multi-modality imaging assessment of the long-term vascular response after bioresorbable scaffold implantation. By using quantitative coronary angiography, vasomotion, intravascular ultrasound, virtual histology, and OCT we evaluated the long-term vascular healing five years after first-in-man bioresorbable scaffold implantation. In this report, we documented the complete resorption of bioresorbable scaffold struts, the presence of vasomotion with heterogeneous response among the patients -implying the lack of permanent jailing of the scaffolded segment-, late lumen enlargement driven by a reduction in plaque burden, and patency of small side-branches that were jailed post implantation.

The vascular healing process was further documented by a rigorous analysis of the OCT findings in the same cohort **(Chapter 4.3)**. Implantation of the bioresorbable scaffold led to a restoration of the vascular phenotype at long term by configuration of a non-obstructive plaque, created by the consolidation of the underlying plaque, neointima, and resorbed struts. Tissue characterization of the formed 'neo-plaque' was performed both by a human analyst and automated software assessing tissue attenuation. Both assessments were consistent, showing in the majority of the cases, the formation of a stable plaque phenotype with low amount of

necrotic core that was covered by a signal-rich tissue layer separating the underlying thrombogenic plaque components from the lumen, potentially shielding the plaque. However, this favorable response was not universal and the observation of a patient with recurrent asymptomatic plaque rupture suggested a need for both optimum lesion coverage and continued secondary prevention strategies after deployment of bioresorbable vascular scaffolds in order to optimize vascular healing.

Impact of hemodynamics on bioresorbable scaffold vascular healing.

We further examined the dynamic interaction between hemodynamic environment and vascular healing response of bioresorbable scaffolds **(Part V)**. Regional hemodynamic factors have been implicated in the pathogenesis of atherosclerosis[13], plaque progression and destabilization[14, 15], and vascular healing after metallic stent implantation[16]. However, as data regarding the association of wall shear stress with vascular healing after BVS implantation and the impact of BVS implantation on local hemodynamics are limited, we focused on investigating this association. **Chapter 5.1** focuses on the hemodynamic consequences of implantation of bioresorbable scaffolds in side-branch ostia and investigates the impact of the neocarina formation on the main branch flow patterns. By using a new methodology for the fusion of OCT images with three-dimensional angiography, a three-dimensional model was created that allowed the investigation of main vessel flow patterns at baseline and at follow-up after neo-carina formation. It was shown that the extensive protrusion of the neo-carina, which can be caused by a wider bifurcation angle, might significantly affect main-branch flow patterns by creating zones with turbulent flow and re-circulation. This change in flow patterns should not be disregarded, as it might coincide with lumen narrowing due to progression of non-culprit lesions located downstream of the bifurcation.

The relationship between the wall shear stress 2 years after bioresorbable scaffold implantation and the long-term vascular healing after bioresorption is examined in **Chapter 5.2**. After fusion of multi-slice computer tomography and intravascular ultrasound studies performed 2 years after implantation, using previously described methodology[17], a three-dimensional model of the scaffolded segment was created and the 2-year wall shear stress in this region was calculated. The three-dimensional model was then registered to the plaque information by OCT at 5 years and a spatial co-registration of regions with necrotic core and wall shear stress was achieved. Although a significant association between wall shear stress and necrotic core was not identified, there was an association between the wall shear stress 2 years after implantation and

the thickness of the fibrous cap in the scaffolded segment. Specifically, within a scaffold regions with a lower shear stress at 2 years had thinner fibrous cap at 5 years. These findings are suggestive of a complex interplay between hemodynamics and bioresorbable scaffold healing, which warrants further investigation.

OCT assessment of bioresorbable scaffolds in ST-elevation myocardial infarction.

The first-in-man studies of bioresorbable scaffolds had focused on relatively simple lesions[18, 19]. Nonetheless, after commercial application of bioresorbable scaffolds, the use of bioresorbable scaffolds has been extended to more complex lesions that are more reflective of the daily catheterization laboratory practice. One of the current questions is the healing response after implantation of bioresorbable scaffolds in thrombotic lesions, such as the culprit lesions of patients with STEMI. Considerations about the implantation of bioresorbable scaffolds in STEMI, acute outcome and mid-term healing response are being discussed in **Part VI**. **Chapter 6.1** presents patient-level data from the first patients with STEMI and NSTEMI treated in our institution and demonstrates the challenges regarding the implantation of these stents in STEMI. Such challenges include the increased incidence of incomplete apposition associated with myocardial infarction, the unclear role of post-dilation as optimization of scaffold expansion needs to be weighed over the potential for distal embolization, and the need to minimize plaque prolapse and residual thrombotic burden, factors associated with impaired reperfusion after metal stent implantation in myocardial infarction[20].

In **Chapter 6.2**, a systematic assessment of the acute outcome of bioresorbable scaffold implantation in myocardial infarction is performed. In a series of 49 patients with STEMI treated with bioresorbable scaffolds, high device, procedural, and clinical success rates were observed with all the scaffolds achieving a residual stenosis <30% and no in-hospital major adverse events. Importantly, OCT in a subgroup of 31 patients confirmed a good procedural outcome with acceptable scaffold expansion, low rates of incomplete scaffold apposition, and a low prolapse and in-stent thrombotic material. These data together with other reports on bioresorbable scaffold implantation in acute coronary syndromes demonstrate the feasibility of this treatment approach in STEMI[21, 22].

In addition to acute outcome, vascular healing is another open question regarding the use of bioresorbable scaffolds in myocardial infarction. Although pilot studies in stable patients have shown a good healing response for bioresorbable scaffolds with low rates of uncovered and malapposed struts, it is not clear whether the healing response would be similar in STEMI, that

has been associated with delayed healing compared to stable syndromes in metallic DES[23, 24]. Therefore, a follow-up OCT study of 39 patients was performed in order to document the mid-term vascular healing response after bioresorbable scaffold implantation in STEMI (**Chapter 6.3)**. Findings from this study were compared to findings from a historical cohort of 49 patients reporting on the healing response of a contemporary metallic biolimus-eluting stent with bioresorbable polymer. There were no cases with lumen compromise or scaffold recoil in bioresorbable scaffolds. The incidence of malapposed struts was low in both groups, while the incidence of uncovered struts was lower for bioresorbable scaffolds. We further documented the natural history of incomplete scaffold apposition in BVS, and we found evidence of resolution of strut malapposition in the majority of cases, with only a few cases demonstrating persistence of malapposition. Interestingly, the incidence of late-acquired incomplete scaffold apposition was non-negligible, as it was detected in 30% of the cases, a finding that needs to be better elucidated in terms of pathomechanism and potential clinical sequences. Nonetheless, the overall low incidence of malapposed struts and the more complete strut coverage observed are indicative of a favourable mid-term healing process after bioresorbable scaffold implantation in STEMI which needs to be validated by large randomized trials comparing bioresorbable scaffolds with current state-of-the-art metallic DES in order to prove a potential benefit for bioresorbable scaffolds in the long-term.

OCT findings in bioresorbable scaffold thrombosis.

Although first-in-man studies of bioresorbable scaffolds did not report any cases with scaffold thrombosis, implantation of bioresorbable scaffolds in more complex 'real-world' lesions has given rise to several reports of bioresorbable scaffold thrombosis[25, 26]. The utility of OCT in assessing the pathomechanisms of this complication is discussed in **Part VII**. In **Chapter 7.1**, we present images from the first reported case of very late bioresorbable scaffold thrombosis occurring 2 years after implantation. The event took place soon after dual antiplatelet therapy discontinuation, in a lesion where a complex staged procedure had taken place. This case highlights the fact that an ongoing risk of thrombosis does not only exist in metallic implants, but also in bioresorbable devices, at least until polymer resorption, and suggests a need for extended duration of antiplatelet therapy in patients with increased thrombotic risk due to complex interventions.

Current evidence regarding late and very late bioresorbable scaffold thrombosis is further discussed in **Chapter 7.2.** Previous lessons from metallic stents underscore the multifactorial

nature of late and very late thrombosis[27, 28], which could also apply in the case of bioresorbable scaffolds. Yet, despite the report of a number of cases with bioresorbable scaffold thrombosis, the exact pathomechanisms of this complication remain poorly understood. Current hypotheses include increased thrombogenicity due to high strut thickness (150μm)[29], the presence of adverse hemodynamic environment with impaired flow condition[30], and in some cases the contribution of suboptimal platelet inhibition.

Angiography and OCT from a series of cases with both early and late bioresorbable scaffold thrombosis provide some new insights in the mechanisms of this complication (**Chapter 7.3**). In 14 patients treated for definite bioresorbable scaffold thrombosis in our institution, angiographic and OCT findings were analyzed and compared to a matched series of cases with metallic stent thrombosis. Overall, we found similar mechanisms in bioresorbable scaffold and metallic stent thrombosis, with the main pathomechanisms for both early and late bioresorbable scaffold thrombosis being underexpansion, malapposition, and incomplete lesion coverage. In addition to suboptimal implantation, the absence of appropriate antiplatelet therapy administration was also found to be an important contributor to bioresorbable scaffold thrombosis.

OCT assessment of vascular trauma after renal denervation.

Renal denervation is a new method recently studied as a potential treatment for resistant hypertension and is currently considered for several other indications. Besides the fact that initial success stories were recently challenged by a negative randomized controlled trial, not much is known regarding the impact of this procedure on renal artery integrity[31-34]. Intravascular imaging can therefore be utilized for the in vivo assessment of the vascular effects of renal denervation, and it its use is described in **Part VIII**. As device selection in renal denervation is closely related to renal artery anatomy and size, there is a need for an accurate estimation of renal artery dimensions[35]. Although invasive evaluation remains the golden standard for the evaluation of the renal artery dimensions, non-invasive tools are needed that can provide accurate assessment both pre procedure and at follow-up. The validation of measurements of renal artery dimensions by magnetic resonance angiography against intravascular ultrasound measurements is presented in **Chapter 8.1.** Measurement of mean lumen diameter by magnetic resonance angiography was achieved with very low inter- and intra-observer variability, while it had high agreement with the intravascular ultrasound derived measurements with a bias of −0.1mm and 95% limits of agreement ranging from −1.1mm to 0.9 mm. The robustness of the measurements by the studied

non-invasive modality could find application in the evaluation of renal artery integrity at medium- and long-term follow-up intervals after renal artery interventions, especially in an era with an increasing number of emerging newer generation devices.

Chapter 8.2 reports on the multimodality imaging assessment of the renal artery trauma induced by five different renal denervation devices. Although several studies have demonstrated the development of vascular trauma by renal denervation, there is a paucity of knowledge on the incidence of acute vascular wall injury with relation to the denervation method. Quantitative angiography, intravascular ultrasound and OCT were performed in fifty vessels undergoing renal denervation with either balloon-based or non-balloon-based renal denervation catheters. A varying extent of vascular injury by OCT with the presence of dissection, thrombus, or edema was observed after renal denervation with all systems. The inclusion of patients treated both with balloon-based and non-balloon-based catheters allowed us to observe 2 distinct patterns of renal injury: (1) in non-balloon-based denervation, a response with low incidence and extent of dissection, but with acute lumen narrowing and vessel wall thickening, accompanied by a moderately higher thrombus area and a numerically higher percentage of frames with intimal protrusions; and (2) in balloon-based denervation, a response with a higher longitudinal extent of dissection, also with thrombus and intimal protrusions, in the absence of significant lumen or vessel size changes during the procedure. Moreover, in balloon-based denervation we observed an association of dissection by OCT with a higher balloon/artery ratio and vessel wall irregularities on post-procedural angiogram, suggesting that in these devices, post-procedural angiographic abnormalities should not be disregarded and raise suspicion of vascular injury, while a conservative approach in balloon selection could be considered.

Nevertheless, the short- and long-term implications of such small-scale dissections, which are unlikely to impair flow in most cases, remain elusive. The observation of complete vascular healing of a denervation-induced dissection one and a half year after the procedure, without development of renal artery stenosis, supports the hypothesis of a rather benign prognosis **(Chapter 8.3)**. This is further corroborated by the absence of significant stenosis demonstrated in the 6-month non-invasive imaging follow-up of 13 patients of our study.

Discussion and future outlook

Clinical and research perspectives for OCT imaging. The role of technological innovations.

In **Part I** of the thesis, the current experience with OCT imaging in clinical practice was summarized, while potential pitfalls hampering an objective interpretation of OCT images were discussed in **Part II**. Although OCT today is being used in a large number of catheterization laboratories and indications for clinical use, namely optimizing stent implantation and evaluating stent failure, have been proposed[36], a routine use of OCT in guidance of PCI is not currently supported on the basis of outcome data. Nevertheless, OCT has been shown to have an impact on periprocedural decision making[37], while optimization of stent expansion is similar to the one achieved by IVUS[38]. Moreover, several post-procedural findings of suboptimal implantation by OCT have been associated with adverse prognosis at follow-up[39], and there is evidence from non-randomized studies that there might be a potential for improved outcome in patients undergoing an OCT-guided strategy over an angiography-guided strategy[40]. Hence, randomized studies of OCT guidance versus angiographic guidance are warranted for defining the role of OCT in clinical practice.

Furthermore, for enhancing the prognostic potential of OCT identification of plaque morphology, we need to overcome methodological shortcomings of current analysis methods and be able to provide a better classification of plaque morphology by OCT. The development of tools for automated assessment of plaque morphology and user-independent measurement of cap thickness can help a more objective characterization of atherosclerotic plaques, and reduce errors due to human variability[41, 42]. Moreover, the extraction of information regarding the local hemodynamic environment from an OCT pullback allows the simultaneous assessment of morphological information and local hemodynamic stimuli[43, 44], possibly providing an improved risk profiling of the atherosclerotic plaque[45]. Seeing that catheter movement might have an important adverse effect on the accurate estimation of lumen measurements throughout a coronary artery, as demonstrated in **Chapter 2.1**, which can lead to significant errors in hemodynamic calculations by computational fluid dynamics analysis, the development of ultra-high-speed OCT catheters can help improve this kind of assessment[46]. Furthermore, as our knowledge of the characteristics of high-risk plaques is expanding, new morphological factors that might be associated with adverse outcome are being identified[47]. Ongoing innovations in OCT-based technologies that allow the assessment of structural information of the plaques, or of

intraplaque biochemical activity, or of cellular-sized plaque features can possibly improve the prognostic capability of OCT plaque characterization[48-50].

Pitfalls of permanent stent platforms and the need for transient stent platforms.

Current second-generation drug-eluting stents are the current standard of revascularization, with excellent clinical results[51]. However, complications such as very late stent failure and development of neoatherosclerosis are not uncommon also with these devices[11]. Therefore, the introduction of bioresorbable scaffolds in clinical practice could conceptually help alleviate these long-term complications[12]. We demonstrated in a pilot study that bioresorbable scaffolds are associated with a favorable healing response at a very long-term follow-up. However, this hypothesis needs to be further supported by clinical studies showing that this healing response translates to a better clinical outcome at long term. The non-inferiority of bioresorbable scaffolds to metallic stents in relatively selected non-complex lesions has been demonstrated in a number of studies[52-56]. However, the implementation of such a technology at clinical practice needs confirmation of superiority at long term and also better performance at complex lesions. The randomized ABSORB IV trial (NCT02173379) will try to prove the potential superiority of bioresorbable scaffolds over the current standard of metallic everolimus-eluting stents with a fluoropolymer at a 5-year follow-up. Regarding the use in more complex population there are currently conflicting reports from registries with several of them showing increased rates of scaffold thrombosis[25]. Our study, which is the first human study assessing the pathomechanisms of bioresorbable scaffold thrombosis in vivo, demonstrates that suboptimal implantation is the main substrate for bioresorbable scaffold thrombosis, thus highlighting a need for optimal lesion preparation and possibly for use of invasive imaging in order to optimize implantation. Improvements in bioresorbable scaffold technology with thinner struts or bioresorbable metallic platforms could prove advantageous in achieving optimal implantation. Finally, in patients with myocardial infarction, the observation of a favorable healing response at a mid-term follow-up, comparable with current state-of-the-art metallic DES implicates that bioresorbable scaffolds are a viable option also for this complex population subset[55], although larger randomized studies focused on outcome are needed to support their use also in this population, while the distinct healing patterns observed in our study need to be better understood.

Long-term renal vascular integrity in renal denervation

Initial enthusiasm over the results of renal denervation for resistant hypertension was soon substituted with skepticism after the negative result of a randomized sham-controlled study[31]. However, as inadequate efficacy of the catheter used in this study could not be excluded, numerous new devices have been developed in an attempt to resolve the efficacy issue. As this debate for efficacy of this technique for resistant hypertension is ongoing, several potential new indications such as heart failure and atrial fibrillation have also been proposed. Nevertheless, data regarding safety are sparse. By OCT, we demonstrated the presence of acute vascular injury with renal denervation, with discrete patterns between different categories of devices. Longer term follow-up with high-resolution non-invasive imaging such as the magnetic resonance angiography imaging that we validated versus intravascular imaging measurements will demonstrate whether this procedure has a long-term negative impact on renal vascular integrity, or whether the effect is transient and self-limiting.

Samenvatting en conclusies

Sinds de introductie van percutane coronaire interventie is coronaire angiografie de standaard geweest ter beoordeling van de aanwezigheid van coronaire laesies en van het resultaat van interventies. De komst van intravasculaire beeldvorming heeft een nieuw hoofdstuk geopend voor coronaire laesie en intracoronaire stent evaluatie, waardoor naast de beoordeling van het lumen, ook de directe beoordeling van plaque en vaatmorfologie en de evaluatie van de vaatwand respons op stenting mogelijk werd. In de afgelopen tien jaar heeft optische coherentie tomografie (OCT) toenemende populariteit gekregen voor de beoordeling van atherosclerose en cardiovasculaire interventies. OCT is een op licht gebaseerde intravasculaire beeldvormende modaliteit die het voordeel heeft van het maken van zeer hoge resolutie (5-15 pm) beelden van de vaatwand en van intracoronaire stents[1]. De ontwikkeling van de tweede generatie, frequentiedomein OCT heeft een grootschalige toepassing van deze beeldvormende modaliteit in de klinische praktijk mogelijk gemaakt, door vereenvoudiging van de procedure van beeldacquisitie, verkorten van de vereiste tijd en met lagere eisen voor het flushing[2]. Dientengevolge lijkt OCT een ideaal instrument voor de beoordeling van atherosclerotische plaque morfologie en van de acute en chronische vasculaire effecten van interventies met diverse stents.

Kortom, dit proefschrift beschrijft het klinisch gebruik van OCT in percutane coronaire interventie met de nadruk op de beoordeling van de acute en chronische vasculaire effecten van intravasculaire interventies.

Evaluatie van coronaire atherosclerose en het gebruik van OCT in coronaire interventie.

In **Deel I** wordt het potentiele nut van OCT beeldvorming in de praktijk van een katheterisatielaboratorium geanalyseerd. **Hoofdstuk 1.1** stelt verschillende mogelijke toepassingen van OCT in percutane coronaire interventie voor. Dergelijke toepassingen omvatten evaluatie voor de aanwezigheid van een laesie, pre-procedurele laesie beoordeling voor de begeleiding van percutane coronaire interventie, post-procedurele evaluatie van de acute resultaat van percutane coronaire interventie, en de follow-up evaluatie van intracoronaire stents, inclusief de beoordeling van de pathomechanismen van stent failure.

Hoofdstuk 1.2 bevat een overzicht van de huidige ervaringen van OCT beeldvorming tijdens een acuut myocardinfarct en van de huidige inzichten in de vereniging van atherosclerotische plaque morfologie en pathomechanismen van myocardinfarct, zoals beoordeeld door in vivo OCT beeldvorming. Bovendien wordt de rol van OCT in de beoordeling van een myocardinfarct na stentimplantatie verder geanalyseerd. Tegelijkertijd wordt het gebruik van OCT ter beoordeling van het behandelingseffect van een myocardinfarct beschreven en worden pilotstudies die focussen op een potentiële klinische toepassing van OCT guidance in de behandeling van myocardinfarct verder besproken.

Hoofdstuk 1.3 rapporteert over een grote single-center registry onderzoek naar de veiligheid en de haalbaarheid van OCT in een niet-geselecteerde populatie. In een reeks van 1142 patiënten in verschillende klinische settingen en met verschillende indicaties voor beeldvorming, werd de tweede generatie OCT succesvol uitgevoerd met een lage incidentie van beeldvorming gerelateerde complicaties (0.6%). Belangrijk is dat deze incidentie vergelijkbaar was met de incidentie van beeldvorming gerelateerde complicaties waargenomen bij een reeks van 2476 patiënten die IVUS in dezelfde onderzoeksperiode in hetzelfde centrum hebben ondergaan. De waargenomen complicaties waren zelflimiterend na de verwijdering van de beeldvormende katheter, of gemakkelijk te behandelen in het katheterlaboratorium. Deze bevindingen geven aan dat de tweede generatie optische coherentie tomografie veilig is voor gebruik in percutane coronaire interventie in diverse klinische settingen met een zeer lage incidentie van complicaties.

Methodologische aspecten van OCT analyse in bijzondere instellingen.

Deel II behandelt verschillende methodologische overwegingen in kwantitatieve en kwalitatieve analyse van OCT afbeeldingen. Het effect van longitudinale verplaatsing van de katheter tijdens beeldacquisitie op de kwantitatieve beoordeling van oplosbare stents werd onderzocht in een experimentele setting, met een varkensmodel die bekend is met versneld beweging van de coronair **(Hoofdstuk 2.1).** Variatie in de beoordeling van de afgebeelde stent lengte was inderdaad buitengewoon hoog. Hoewel dit geen significante invloed op de globale metingen, zoals gemiddelde lumenoppervlak, gemiddelde stentoppervlak en gemiddelde dekkingsoppervlak heeft gehad, werden metingen in specifieke stentregio's significant beïnvloed, waardoor de seriële evaluatie van gematcht cross-secties belemmert zou kunnen worden. Belangrijk is dat de longitudinale verplaatsing van de katheter als gevolg van coronaire beweging, ook in mensen is beschreven, wat suggereert dat deze kwantitatieve metingen ook kwetsbaar voor fouten in

humane studies zijn. Daarom zou speciale methodologie met nauwgezette per frame analyse of matching van segmenten met gebruik van software waarmee gesynchroniseerde inspectie van bijpassende segmenten mogelijk is, geschikter zijn voor seriële analyse van specifieke oplosbare stent gebieden in de aanwezigheid van uitgebreide bloedvatbeweging.

Hoofdstuk 2.2 gaat over de beoordeling van de atherosclerotische plaque en in het bijzonder over cap diktemeting in menselijke fibroatheromas. Variabiliteit in de beoordeling van de cap dikte kan een probleem opleveren bij de betrouwbare beoordeling van deze plaques[3]. Dit betreft een probleem met bijzondere implicaties gezien de kritieke rol van cap dikte in het pathomechanisme van plaqueruptuur[4-7]. Derhalve wordt een algoritme voor automatische segmentatie van cap dikte voorgesteld. De prestatie van het voorgestelde algoritme was goed, met een fout in de beoordeling van de kap dikte die vergelijkbaar is met de variabiliteit tussen de menselijke onderzoekers. Derhalve kan toepassing van dit algoritme voor de beoordeling van de fibreuze cap dikte zorgen voor een snelle, objectieve en betrouwbare beoordeling van cap dikte in OCT studies van humane fibroatheromas.

Uitdagingen in de analyse van de bifurcatie laesies met OCT worden beschreven in **hoofdstuk 2.3.** Specifiek wordt het probleem van de meting van een zijtak ostium via een OCT pullback van de contralaterale tak geanalyseerd. Door metingen van de zijtak als referentie te gebruiken, werd gezien dat de meetfout in de oppervlakte van de ostium zijtak door een hoofdtak pullback was groter dan 0.4mm in meer dan 50% van de gevallen. Deze fout kan belangrijke gevolgen hebben in een therapeutische aanpak, met als gevolg suboptimale dimensionering als zijtak behandeling nodig is. Een nieuwe aanpak wordt derhalve voorgesteld om dit probleem, die het gebruik van speciale software met offline driedimensionale weergave omvat. Deze benadering maakt de selectie mogelijk van een vlak loodrecht op het begin van de zijtak en het uitvoeren van metingen op het echte anatomische ostium van de zijtak. Daardoor wordt de absolute fout in de beoordeling van het zijtak ostium oppervlak verlaagd van 1.50 ± 1.31 tot 0.56 ± 0.45 mm^2, met een robuuste analyse met een lage intra- en inter-observer variabiliteit. Deze betrouwbare zijtak evaluatie van een hoofdtak pullback heeft het potentieel om zijtak instrumentatie te beperken en kan een aanzienlijke vermindering van de procedurele complexiteit, het verbeteren van de behandeling strategie planning en het verbeteren van de resultaten van bifurcatie laesie interventie in de toekomst mogelijk maken.

Beoordeling van zeer laat metalen stent failure door OCT - de rol van neoatherosclerose.

Deel III gaat over één van de belangrijkste valkuilen van metalen stents, namelijk late stent failure. Hoewel met de huidige generatie metalen stents die gebruikt worden in de klinische praktijk, op korte en middellange termijn klinische resultaten uitstekend zijn, zijn observaties van late failure van deze apparaten waargenomen in zeer lange intervallen na implantatie, zowel met bare metal als met drug-eluerende stents[8-10]. Het potentieel van OCT om intracoronaire trombus en in-stent structuren te onderscheiden met een hoge resolutie geeft OCT een centrale rol bij de beoordeling van het pathomechanisme van zeer late stent failure. **Hoofdstuk 3.1** illustreert een geval van zeer late trombose van een bare metal stent die 15 jaar na implantatie is gebeurt. OCT na herstel van stroming toonde de pathologische achtergrond van deze complicatie, namelijk de ontwikkeling van atherosclerose in het gestente segment was, oftwel neoatherosclerose. De necrotische kern accumulatie binnen de stent werd opgevolgd door intra-stent plaque ruptuur en trombose, die de klinische gebeurtenis heeft getriggerd. Een verscheidenheid aan morfologische kenmerken binnen het neoatherosclerotisch segment konden worden geïdentificeerd, met vergelijkbare OCT morfologische kenmerken als natieve atherosclerose.

Hoofdstuk 3.2 geeft een uitgebreid overzicht van de huidige inzichten in neoatherosclerose van OCT. In het bijzonder is er een verwijzing naar de morfologische OCT kenmerken van neoatherosclerose en verschillende neointima patronen, die worden besproken met in relatie tot histologisch bewijs. Bovendien wordt de prevalentie van neoatherosclerose met OCT in de late follow-up van zowel de bare metal stents en drug-eluerende stents en de daarmee samenhangende factoren beoordeeld. Het hoofdstuk bespreekt ook de associatie van neoatherosclerose met zeer late stent restenose of trombose, en wijst op de bijdrage van de intravasculaire beeldvorming in het veranderen van de huidige paradigma van late failure door de bekendmaking dat neoatherosclerose een gemeenschappelijk pathomechanisme is in zowel late restenose als in trombose. Traditioneel werd stent restenose beschouwd als tamelijk goedaardig en in verband gebracht met stabiele symptomen, terwijl stent trombose als levensbedreigend werd gezien en in verband gebracht met een acute presentatie. De aanwezigheid van overeenkomstige beeldvorming bevindingen in verschillende omvang, zoals een in-stent necrotische kern, neointima ruptuur en trombus in beide entiteiten impliceert dat deze twee vormen kunnen voorkomen als verschillende manifestaties van hetzelfde ongunstige genezingsproces.

De associatie van neoatherosclerose met de klinische presentatie wordt verder onderzocht in **hoofdstuk 3.3.** In een twee-center register van 74 patiënten die OCT ondergingen voor de beoordeling van zeer late failure of beoordeling van zeer late vasculaire genezingsrespons, onderzochten wij de verschillen in de prevalentie van neoatherosclerose met betrekking tot de klinische presentatie. Zowel stent restenose en stent trombose hadden een hogere prevalentie van neoatherosclerose ter opzichte van de asymptomatische groep, maar de prevalentie van neointima ruptuur was hoger bij stent trombose. Met name de aanwezigheid van plaque ruptuur werd geassocieerd met specifieke morfologische kenmerken van de neo-intimale

plaque, zoals dunne fibreuze cap en macrofaag infiltratie, vergelijkbaar met het paradigma van kwetsbare plaque in native atherosclerose. Deze bevindingen samen impliceren de actieve bijdrage van neoatherosclerose in de pathogenese van late stent failureen benadrukken het belang van in-stent plaque instabiliteit voor de ontwikkeling van een acuut coronair syndroom na stent implantatie.

Hoofdstuk 3.4 onderzoekt de verschillen in prevalentie en morfologie van neoatherosclerose tussen bare metal stents en de eerste generatie drug-eluting stents met een zeer lange follow-up. Een tijdsafhankelijke patroon werd waargenomen in de prevalentie van neoatherosclerose in eerste generatie drug-eluting stents, waar de ontwikkeling van neoatherosclerose met een hogere interval sinds implantatie was geassocieerd. Interessant genoeg waren er geen verschillen in de prevalentie of morfologie van neoatherosclerose tussen bare metal stents en eerste generatie drug-eltuing stents, hoewel deze een langer interval na implantatie hadden. Deze bevindingen geven aan dat de ontwikkeling van neoatherosclerose een veelvoorkomend probleem is in bare metal stents en de eerste generatie metal-drug-eluting stents, met pathologische studies die een soortgelijke incidentie van neoatherosclerose in de tweede generatie drug-eluerende stents laten doorschemeren[11].

OCT onderzoek naar de langdurige vasculaire genezingrespons van oplosbare stents.

De voortdurende failure waargenomen bij permanente metalen DES, heeft daarom een behoefte gecreëerd voor platforms die de vaatmorfologie en fysiologie restaureren na het verstrekken van een tijdelijke mechanische ondersteuning na de interventie. Oplosbare stents zijn nieuwe platforms die zou kunnen voldoen aan deze behoefte[12], maar ervaring met deze apparaten is beperkt en het proces van de vasculaire genezing na implantatie van een biologisch oplosbare stent moet verduidelijkt worden. Dus, intravasculaire beeldvorming met OCT heeft een centrale rol in de beoordeling van de vasculaire genezing respons na oplosbare stent implantatie en delen IV tot en met VII focussen op het gebruik van OCT voor de beoordeling van oplosbare stents. **Deel IV** onderzoekt de lange termijn vasculaire genezing na oplosbare stent implantatie. In **hoofdstuk 4.1** worden bevindingen vermeld en besproken uit de late invasieve follow-up door OCT van een van de eerste patiënten die implantatie van een biologisch oplosbare stent heeft ondergaan, die een hypothese vormt dat oplosbare stents de ontwikkeling van een homogene laag kunnen induceren die het lumen kan beschermen tegen potentieel trombogene plaque componenten, zonder lumen vernauwing.

Hoofdstuk 4.2 rapporteert over de veelomvattende multi-modaliteit beeldvorming evaluatie van de late vasculaire genezingsrespons na implantatie van biologisch oplosbare stent. Door het gebruik van kwantitatieve coronaire angiografie, vatbeweging studies, intravasculair ultrageluid, virtuele histologie en OCT evalueren we de lange termijn vasculaire genezing vijf jaar na de eerste-in-man oplosbare stent implantatie. In dit rapport hebben we een reportage over de

volledige resorptie van oplosbaar stent struts, de aanwezigheid van vasomotie met heterogene respons bij de patiënten –die impliceert het gebrek aan permanente opsluiting van het gestente segment-, late lumen vergroting gedreven door een vermindering van de plaque oppervlak, en doorgankelijkheid van kleine zijtakken die werden gejaild na de implantatie.

De vasculaire genezingsproces werd verder gedocumenteerd door een grondige analyse van de OCT bevindingen in hetzelfde cohort **(Hoofdstuk 4.3).** Implantatie van de biologisch oplosbare stent leidde tot de herstel van de vasculaire fenotype op lange termijn met de configuratie van een niet-obstructieve plaque, gevormd door de consolidatie van de onderliggende plaque, neointima en geresorbeerd struts. Weefsel karakterisering van de gevormde 'neo-plaque' werd uitgevoerd, zowel door een menselijke analist en geautomatiseerde software gericht op het beoordelen van weefsel demping. Beide evaluaties waren consistent, in de meeste gevallen de vorming van een stabiele plaque fenotype aantonend met een lage hoeveelheid necrotische kern die bedekt werd door een signaal-rijke weefsellaag die zich onderscheidde van de onderliggende trombogene plaque componenten van het lumen, met een mogelijk afschermende werking. Echter, deze gunstige respons was niet universeel en de observatie van een patiënt met recidiverende asymptomatische plaquerupturen suggereerde een noodzaak voor zowel een optimale laesie dekking alshet voortzetten van preventiestrategieën na implantatie van oplosbare vasculaire stents om de vasculaire genezing te optimaliseren.

Invloed van de hemodynamiek op de vasculaire genezingsrespons van oplosbare stents.

Wij onderzochten verder de dynamische interactie tussen hemodynamische milieu en vasculaire genezingsrespons van oplosbare stents **(Deel V)**. Regionale hemodynamische factoren zijn betrokken bij de pathogenese van atherosclerose[13], plaque progressie en destabilisatie[14, 15], en genezing na metalen stentimplantatie[16]. Gezien het feit dat gegevens met betrekking tot de associatie van shear stress met vasculaire genezing na BVS implantatie en de impact van de BVS implantatie op de lokale hemodynamiek beperkt zijn, hebben we ons gericht op het onderzoeken van dit verband. **Hoofdstuk 5.1** richt zich op de hemodynamische gevolgen van de implantatie van oplosbare stents in zijtak ostia en onderzoekt de impact van de neocarina formatie op de hoofdtak stromingspatronen. Door een nieuwe methode voor de fusie van OCT beelden met driedimensionale angiografie, werd een driedimensionaal model gemaakt dat het onderzoek van de stromingspatronen van het hoofdvat op baseline en bij follow-up na neocarina formatie heeft toegestaan. Er werd aangetoond dat het grote uitsteeksen van de neo-carina, die kan worden veroorzaakt door een grotere vertakking hoek, een significante invloed op de stromingspatronen van de hoofdtak zou kunnen hebben door het creëren van zones met turbulente stroming en recirculatie. Deze verandering in stromingspatronen mag worden genegeerd, aangezien dat het lumen vernauwing zou kunnen veroorzaken vanwege de progressie van non-culprit laesies distaal van de vertakking.

De relatie tussen de wand shear stress 2 jaar na oplosbare stent implantatie en de lange termijn vasculaire genezing na bioresorptie wordt onderzocht in **Hoofdstuk 5.2.** Na fusie van multi-slice computer tomografie en intravasculaire ultrasound studies 2 jaar na de implantatie met behulp van eerder beschreven werkwijze[17], werd een driedimensionaal model van het gestente segment gemaakt en werd de 2-jaar shear stress in dit gebied berekend. Het driedimensionale model werd vervolgens geregistreerd op de plaque informatie van OCT op 5 jaar en een ruimtelijk co-registratie van gebieden met necrotische kern en shear stress werd bereikt. Hoewel een significant verband tussen shear stress en necrotische kern niet werd geïdentificeerd, was er een associatie tussen de shear stress 2 jaar na implantatie en de dikte van de fibreuze cap van het scaffolded segment. Binnen een stent, regio's met een lagere shear stress 2 jaar na implantatie hadden een dunnere fibreuze cap op 5 jaar. Deze bevindingen suggereren een complex samenspel tussen hemodynamiek en de genezing van biologisch oplosbare stents, die verder onderzoek rechtvaardigen.

OCT beoordeling van oplosbare stents in ST-elevatie myocardinfarct.

De eerstestudie in mensen naar oplosbare stents richtte zich op relatief eenvoudige letsels[18, 19]. Niettemin, is na de commerciële beschikbaarheid van biologisch oplosbare stents het gebruik uitgebreid tot complexere laesies die een meer realistische afspiegeling van de dagelijkse klinische praktijk zijn. Een van de huidige vragen gaat over de genezingsrespons na implantatie van biologisch oplosbare stents in trombotische laesies, zoals de culprit laesies van patiënten met STEMI. Overwegingen betreffende de implantatie van oplosbare stents in STEMI, acute uitkomst en middellange termijn genezingsrespons worden besproken in **Deel VI. Hoofdstuk 6.1** presenteert de gegevens van de eerste patiënten met STEMI en NSTEMI behandeld in onze instelling en toont de uitdagingen met betrekking tot de implantatie van deze stents in STEMI. Zulke uitdagingen omvatten de verhoogde incidentie van onvolledige appositie geassocieerd met myocardiaal infarct, de onduidelijke rol van post-dilatatie ter optimalisering van stent expansie moet afgewogen worden tegen mogelijke distale embolisatie, en de noodzaak om plaque verzakking en residuele trombotische last te verminderen, factoren geassocieerd met een verminderde reperfusie na metalen stent implantatie in myocardinfarct[20].

Hoofdstuk 6.2 geeft een systematische beoordeling weer van de acute uitkomst van oplosbaar stent implantatie in myocardinfarct. In een serie van 49 patiënten met STEMI behandeld met oplosbare stents, hoge device, procedurele en klinisch slagingskansen werden waargenomen met alle stents resulterend in een resterende stenose <30%, zonder belangrijk complicaties tijdens ziekenhuisopname. Belangrijker nog, OCT in een subgroep van 31 patiënten bevestigde een goede procedurele uitkomst met aanvaardbare stent expansie, lage percentages van onvolledige stent appositie, en een lage prolaps en in-stent trombose materiaal. Deze

gegevens en andere rapporten over biologisch oplosbare stent implantatie bij acute coronaire syndromen bewijzen de haalbaarheid van deze benadering in STEMI[21, 22].

Naast acute uitkomst, is wondgenezing een open vraag over het gebruik van oplosbare stents in myocardinfarct. Hoewel eerste studies bij stabiele patiënten een goede genezingsrespons voor biologisch oplosbare stents hebben laten zien met een laag percentage van ongedekte en malapposed struts, is het niet duidelijk of de genezingsrespons vergelijkbaar is in STEMI, welke mogelijk geassocieerd is met vertraagde genezing in vergelijking met stabiele syndromen in metalen DES[23, 24]. Daarom is een follow-up studie van 39 OCT patiënten uitgevoerd om de vasculaire genezingsrespons na oplosbare stent implantatie in STEMI op middellange termijn te documenteren (**Hoofdstuk 6.3**)**.** De bevindingen van deze studie zijn vergeleken met bevindingen vanuit een historisch cohort van 49 patiënten rapporterend over de genezingsrespons van een hedendaagse metalen biolimus-elutinge stent met oplosbare polymeer. Er waren geen gevallen met lumen vernauwing of "stent recoil" in oplosbare stents. De incidentie van malapposed struts was laag in beide groepen, terwijl de incidentie van ongedekte struts lager was voor oplosbaar stents. We documenteerden verder het natuurlijke beloop van onvolledige stent appositie in BVS, en we vonden bewijs van de resolutie van de strut malappositie in de meeste gevallen, met slechts een paar gevallen met persistentie van malappositie. Interessant is dat de incidentie van late stent malappositie niet te verwaarlozen was en werd gedetecteerd in 30% van de gevallen, een bevinding die moet beter worden toegelicht in termen van pathomechanisme en potentiële klinische sequenties. Niettemin, de over het algemeen lage incidentie van malapposed struts en de vollediger strut dekking wijzen op een gunstig middellange termijn genezingsproces na implantatie van biologisch oplosbare stents in STEMI, die moet worden bevestigd door grote gerandomiseerde studies die biologisch oplosbare stents vergelijken met huidige state-of- the-art metalen DES ten einde mogelijke baten van biologisch oplosbare stents op lange termijn te bewijzen.

OCT bevindingen in oplosbare stent trombose.

Hoewel de eerste studies van oplosbare stents geen gevallen met stent trombose hebben gemeld, heeft implantatie van oplosbare stents in meer complexe 'real-world' laesies aanleiding gegeven tot enige rapporten over oplosbare stent trombose[25, 26]. Het nut van OCT bij de beoordeling van het pathomechanisme van deze complicatie wordt besproken in **Deel VII.** In **Hoofdstuk 7.1** presenteren we beelden van het eerste gerapporteerde geval van zeer late biologisch oplosbare stent trombose 2 jaar na implantatie. Deze gebeurtenis vond plaats kort na staken van de dubbele antiplatelet therapie, in een laesie waar een complexe gefaseerde procedure had plaatsgevonden. Deze casus benadrukt het feit dat een voortdurende risico op trombose bestaat, niet alleen in metalen implantaten, maar ook in oplosbare stents, tenminste tot polymeer resorptie, en

suggereert een mogelijk belang van het verlengen van de duur van antiplatelet therapie bij patiënten met een verhoogd risico op trombose als gevolg van complexe interventies.

De huidige gegevens over late en zeer late oplosbare stent trombose worden verder besproken in **Hoofdstuk 7.2.** Vorige lessen van metalen stents onderstrepen de multifactoriële aard van de late en zeer late trombose[27, 28], die ook van toepassing zou kunnen zijn op oplosbare stents. Ondanks de rapportage van een aantal gevallen met oplosbare stent trombose, blijven precieze pathomechanismen van deze complicatie slecht begrepen. Huidige hypothesen omvatten verhoogde trombogeniciteit door hoge strut dikte (150μm)[29], de aanwezigheid van schadelijke hemodynamische milieu met verminderde stroming[30], en in sommige gevallen de bijdrage van suboptimale bloedplaatjesremming.

Angiografie en OCT uit een serie van casussen met zowel vroege als late oplosbare stent trombose bieden een aantal nieuwe inzichten in de mechanismen van deze complicatie (**Hoofdstuk 7.3**). In 14 patiënten behandeld voor definitieve oplosbare stent trombose in onze instelling, werden angiografische en OCT bevindingen geanalyseerd en vergeleken met een gematchte reeks van casussen met metalen stent trombose. Over het algemeen vonden we soortgelijke mechanismen in oplosbare stent en metalen stent trombose, met de belangrijkste pathomechanismen voor zowel vroege en late oplosbaar stent trombose bestaande uit onderexpansie, malappositie en incomplete laesie dekking. Naast suboptimale implantatie, werd het gebrek aan geschikte antibloedplaatjestherapie toediening ook gevonden als een belangrijke bijdrage aan biologisch oplosbare stent trombose te zijn.

OCT evaluatie van vasculaire trauma na renale denervatie.

Renale denervatie is een nieuwe methode die recent bestudeerd is als potentiële behandeling voor resistente hypertensie en wordt momenteel overwogen voor verschillende andere indicaties. Naast het feit dat de eerste succesverhalen onlangs in twijfel zijn getrokken door een negatief gerandomiseerd onderzoek, zijn er niet veel bekend over de gevolgen van deze procedure op de nierslagader integriteit[31-34]. Intravasculaire beeldvorming kan derhalve worden toegepast voor de in vivo beoordeling van de vasculaire effecten van renale denervatie, en het gebruik ervan wordt beschreven in **Deel VIII.** Doordat apparaatselectie in renale denervatie nauw verwant is aan nierslagader anatomie en grootte, is er een behoefte aan een nauwkeurige schatting van de nierslagader afmetingen[35]. Hoewel invasieve evaluatie de gouden standaard blijft voor de evaluatie van de nierslagader afmetingen, zijn non-invasieve instrumenten vereist die nauwkeurige evaluatie zowel vóór behandeling als bij follow-up kunnen leveren. De validatie van metingen van de nierslagader afmetingen door middel van magnetische resonantie angiografie in vergelijking met intravasculaire ultrasone metingen wordt gepresenteerd in **Hoofdstuk 8.1.** Meting van de gemiddelde lumendiameter door magnetische resonantie angiografie werd bereikt met een zeer lage inter- en intra-observer variabiliteit, terwijl het een hoge overeenkomst had met de

intravasculair ultrageluid afgeleide metingen met een fout van -0.1mm en de 95% grenzen van de overeenkomst variërend van -1.1mm tot 0.9 mm. De robuustheid van de metingen van de bestudeerde niet-invasieve modaliteit zou toepassing kunnen vinden bij de evaluatie van de nierslagader integriteit bij middellange en lange tijd follow-up intervallen na nierslagader ingrepen, met name in een tijdperk met een toenemend aantal opkomende nieuwere generatie apparaten.

Hoofdstuk 8.2 rapporteert over de multimodale beeldvormende beoordeling van de nierslagader trauma, veroorzaakt door vijf verschillende renale denervatie apparaten. Hoewel verschillende studies de ontwikkeling van vasculaire trauma door renale denervatie hebben aangetoond, is er een gebrek aan kennis over de incidentie van acute vaatwand schade met betrekking tot de denervatie methode. Kwantitatieve angiografie, intravasculair ultrageluid en OCT werden in vijftig vaten uitgevoerd die renale denervatie hebben ondergaan met hetzij ballon-gebaseerde of non-ballon-gebaseerde renale denervatie katheters. Een verschillende ernst van vasculaire schade op OCT met de aanwezigheid van dissectie, trombus of oedeem is na renale denervatie bij alle systemen waargenomen. Het opnemen van patiënten behandeld met zowel ballon-gebaseerde en niet-ballon-gebaseerde katheters liet 2 verschillende patronen van nierbeschadiging zien: (1) in niet-ballon-gebaseerde denervatie, een respons met lage incidentie en mate van dissectie, maar met acuut lumen vernauwing en vaatwand verdikking, gepaard met een licht groter trombus oppervlakte en een numeriek hoger percentage van frames met intimale protrusies; en (2) in de ballon-gebaseerde denervatie, een respons met een hogere mate van longitudinale dissectie, ook met trombus en intimale protrusies, met afwezigheid van significante lumen of vaat grootte veranderingen tijdens de procedure. Bovendien hebben we in de ballon-gebaseerde denervatie een relatie van dissecties op OCT met zowel een hogere ballon/arterie ratio als vaatwand onregelmatigheden op post-procedurele angiogram waargenomen, suggererend dat met deze apparaten, post-procedurele angiografische afwijkingen niet moeten worden genegeerd. Deze bevindingen duiden op de aanwezigheid van vasculaire trauma, terwijl een conservatieve benadering in ballon selectie zou kunnen worden beschouwd.

Toch blijven de korte en lange termijn gevolgen van dergelijke kleinschalige dissecties, die in de meeste gevallen waarschijnlijk geen invloed op de bloeddoorstroming hebben, ongrijpbaar. De waarneming van volledige vasculaire genezing van een denervatie-geïnduceerde dissectie anderhalf jaar na de procedure, zonder ontwikkeling van nierarteriestenose, ondersteunt de hypothese van een tamelijk goedaardige prognose (**Hoofdstuk 8.3**). Dit wordt verder bevestigd door de afwezigheid van significante stenosen in de 6 maanden follow-up met niet-invasieve beeldvorming van 13 patiënten in onze studie.

Discussie en vooruitzichten

Klinisch en onderzoeksperspectieven voor OCT beeldvorming. De rol van technologische innovaties.

In **Deel I** van het proefschrift werden de huidige ervaringen met OCT beeldvorming in de klinische praktijk samengevat. Mogelijke valkuilen die een objectieve en realistische interpretatie van OCT afbeeldingen belemmeren zijn in **Deel II** besproken. Hoewel OCT tegenwoordig in een groot aantal catheterisatie laboratoria wordt gebruikt en indicaties voor klinisch gebruik, namelijk het optimaliseren van stentimplantatie en het evalueren van stentfailure, zijn voorgesteld[36], wordt routinematig gebruik van OCT voor de begeleiding van PCI momenteel niet ondersteund door het ontbreken van gegevens met harde uitkomsten. Toch blijkt OCT een invloed op periprocedural besluitvorming te hebben[37], en optimalisatie van stent expansie is vergelijkbaar als met IVUS kan worden bereikt[38]. Bovendien hebben een aantal post-procedurele bevindingen van suboptimale implantatie op OCT een associatie met een ongunstige prognose bij follow-up[39], en er is bewijs uit niet-gerandomiseerde studies dat er een potentieel betere uitkomst zou kunnen zijn voor patiënten met een OCT-geleide strategie ten opzichte van patiënten met een angiografie-geleide strategie[40]. Vandaar dat gerandomiseerde studies gericht op OCT begeleiding versus angiografie begeleiding nodig zijn voor het definiëren van de rol van OCT in de klinische praktijk.

Bovendien, moeten we voor het verbeteren van het prognostisch potentieel van OCT van identificatie van plaque morfologie methodologische tekortkomingen van de huidige analysemethoden overwinnen en een betere classificatie van plaque morfologie op basis van OCT kunnen hebben. De ontwikkeling van instrumenten voor geautomatiseerde evaluatie van de plaque morfologie en gebruiker-onafhankelijke meting van de cap dikte kunnen helpen tot een meer objectieve karakterisering van atherosclerotische plaques, en fouten als gevolg van menselijke variabiliteit verminderen[41, 42]. Bovendien maakt extractie van informatie over de lokale hemodynamische omgeving vanuit een OCT pullback de gelijktijdige beoordeling van de morfologische informatie en lokale hemodynamische stimuli mogelijk[43, 44], wellicht zorgend voor een verbeterde risicoprofilering van de atherosclerotische plaque[45]. Aangezien katheter beweging een belangrijke negatieve invloed op de nauwkeurige schatting van lumen metingen in een kransslagader kan hebben, zoals aangetoond in **Hoofdstuk 2.1,** wat kan leiden tot significante fouten bij hemodynamische berekeningen van computationele vloeistofdynamica analyse. De ontwikkeling van ultra-high-speed OCT katheters kan helpen bij het verbeteren van dit soort onderzoeken[46]. Bovendien kunnen, nu onze kennis van de kenmerken van hoog risico plaques aan het uitbreiden is, nieuwe morfologische factoren die worden geassocieerd met negatieve uitkomst worden geïdentificeerd[47]. Lopende innovaties in op OCT-gebaseerde technologieën gericht op de beoordeling van structurele informatie van plaques, of plaque biochemische

activiteit, of van cellulaire-sized plaque kenmerken kunnen eventueel het prognostische vermogen van OCT plaque karakterisering verbeteren[48-50].

Valkuilen van permanente stent platforms en de noodzaak voor transiënte stent platforms.

Huidige tweede generatie drug-eluting stents zijn de huidige standaard van revascularisatie, met uitstekende klinische resultaten[51]. Echter, complicaties zoals zeer late stent failure en ontwikkeling van neoatherosclerose zijn ook bij deze stents niet ongewoon[11]. Daarom kan de invoering van oplosbare stents in de klinische praktijk conceptueel helpen deze lange termijn complicaties te vermijden[12]. We toonden in een pilotstudie aan dat oplosbare stents op een lange termijn follow-up met een gunstige genezeningsrespons worden geassocieerd. Echter, deze hypothese moet verder worden ondersteund door klinische studies die aantonen dat de genezingsrespons zich vertaalt in beter klinisch uitkomst op lange termijn. De non-inferioriteit van oplosbare stents ten opzichte van metalen stents in relatief geselecteerde niet-complex laesies is aangetoond in een aantal studies[52-56]. De implementatie van een dergelijke technologie in de klinische praktijk moet echter bevestiging van de superioriteit op lange termijn hebben met tevens betere prestaties in complexe laesies. De gerandomiseerde ABSORB IV trial (NCT02173379) zal proberen om de potentiële superioriteit van oplosbare stents ten opzichte van de huidige standaard van metallic-everolimus eluting stents met een fluorpolymeer te bewijzen bij een follow-up duur van 5-jaar. Ten aanzien van het gebruik in meer complexe bevolking zijn er momenteel tegenstrijdige rapporten van studies, een aantal van hen tonen verhoogde percentages van stent trombose[25]. Onze studie, die de eerste menselijke studie naar de in vivo pathomechanismen van biologisch oplosbare stent trombose is, heeft aangetoond dat suboptimale implantatie het belangrijkste substraat is voor biologisch oplosbare stent trombose. Dit benadrukt de behoefte aan optimale laesie voorbereiding en mogelijk het gebruik van invasieve beeldvorming om implantatie te optimaliseren. Verbeteringen in oplosbare stent technologie met dunnere struts of oplosbare metalen platforms zouden voordelig kunnen blijken in het bereiken van optimale implantatie. Tot slot toont de gunstige genezingsreactie in patiënten met een hartinfarct met een middellange termijn follow-up, vergelijkbaar met the huidige state-of-the-art metalen DES, dat oplosbare stents een haalbare optie zijn voor deze complexe patiëntengroep[55]. Grotere gerandomiseerde studies gericht op harde eindpunten zijn echter nodig zijn om hun gebruik ook bij deze populatie te ondersteunen, terwijl de waargenomen genezingspatronen in ons onderzoek beter moeten worden onderzocht.

Lange termijn renale vasculaire integriteit in renale denervatie

Aanvankelijke enthousiasme over de resultaten van renale denervatie voor resistente hypertensie werd al snel vervangen met scepsis na het negatieve resultaat van een gerandomiseerde placebo-gecontroleerde studie[31]. Aangezien onvoldoende werkzaamheid van de katheter in deze studie niet kon worden uitgesloten, zijn talrijke nieuwe apparaten ontwikkeld in een poging om het probleem ten aanzien van werkzaamheid op te lossen. Aangezien de discussie over de effectiviteit van deze techniek voor resistente hypertensie nog open is, zijn diverse potentiële nieuwe indicaties zoals hartfalen en atriale fibrillatie ook voorgesteld. Toch zijn gegevens over de veiligheid schaars. Middels OCT hebben we de aanwezigheid van acute vasculaire verwonding met renale denervatie aangetoond, met discrete patronen tussen de verschillende categorieën van apparaten. Langere termijn follow-up met een hoge resolutie niet-invasieve beeldvormende techniek, zoals magnetische resonantie imaging die we valideerde middels metingen met intravasculaire beeldvorming, zal aantonen of deze procedure op lange termijn een negatief effect op de renale vasculaire integriteit heeft, of van voorbijgaande aard is.

Bibliography

1. Tearney GJ, Regar E, Akasaka T, Adriaenssens T, Barlis P, Bezerra HG, Bouma B, Bruining N, Cho J-m, Chowdhary S, Costa MA, de Silva R, Dijkstra J, Di Mario C, Dudeck D, Falk E, Feldman MD, Fitzgerald P, Garcia H, Gonzalo N, Granada JF, Guagliumi G, Holm NR, Honda Y, Ikeno F, Kawasaki M, Kochman J, Koltowski L, Kubo T, Kume T, Kyono H, Lam CCS, Lamouche G, Lee DP, Leon MB, Maehara A, Manfrini O, Mintz GS, Mizuno K, Morel M-a, Nadkarni S, Okura H, Otake H, Pietrasik A, Prati F, Räber L, Radu MD, Rieber J, Riga M, Rollins A, Rosenberg M, Sirbu V, Serruys PWJC, Shimada K, Shinke T, Shite J, Siegel E, Sonada S, Suter M, Takarada S, Tanaka A, Terashima M, Troels T, Uemura S, Ughi GJ, van Beusekom HMM, van der Steen AFW, van Es G-A, van Soest G, Virmani R, Waxman S, Weissman NJ, Weisz G. Consensus Standards for Acquisition, Measurement, and Reporting of Intravascular Optical Coherence Tomography Studies: A Report From the International Working Group for Intravascular Optical Coherence Tomography Standardization and Validation. J Am Coll Cardiol 2012;**59**(12):1058-1072.

2. Gonzalo N, Tearney GJ, Serruys PW, van Soest G, Okamura T, Garcia-Garcia HM, Jan van Geuns R, van der Ent M, Ligthart J, Bouma BE, Regar E. Second-generation optical coherence tomography in clinical practice. High-speed data acquisition is highly reproducible in patients undergoing percutaneous coronary intervention. Rev Esp Cardiol 2010;**63**(8):893-903.

3. Kim SJ, Lee H, Kato K, Yonetsu T, Xing L, Zhang S, Jang IK. Reproducibility of in vivo measurements for fibrous cap thickness and lipid arc by OCT. JACC Cardiovasc Imaging 2012;**5**(10):1072-4.

4. Narula J, Nakano M, Virmani R, Kolodgie FD, Petersen R, Newcomb R, Malik S, Fuster V, Finn AV. Histopathologic characteristics of atherosclerotic coronary disease and implications of the findings for the invasive and noninvasive detection of vulnerable plaques. J Am Coll Cardiol 2013;**61**(10):1041-51.

5. Toutouzas K, Karanasos A, Tsiamis E, Riga M, Drakopoulou M, Synetos A, Papanikolaou A, Tsioufis C, Androulakis A, Stefanadi E, Tousoulis D, Stefanadis C. New insights by optical coherence tomography into the differences and similarities of culprit ruptured plaque morphology in non–ST-elevation myocardial infarction and ST-elevation myocardial infarction. Am Heart J 2011;**161**(6):1192-1199.

6. Virmani R, Burke AP, Farb A, Kolodgie FD. Pathology of the vulnerable plaque. J Am Coll Cardiol 2006;**47**(8 Suppl):C13-8.

7. Yonetsu T, Kakuta T, Lee T, Takahashi K, Kawaguchi N, Yamamoto G, Koura K, Hishikari K, Iesaka Y, Fujiwara H, Isobe M. In vivo critical fibrous cap thickness for rupture-prone coronary plaques assessed by optical coherence tomography. Eur Heart J 2011;**32**(10):1251-9.

8. Yamaji K, Kimura T, Morimoto T, Nakagawa Y, Inoue K, Soga Y, Arita T, Shirai S, Ando K, Kondo K, Sakai K, Goya M, Iwabuchi M, Yokoi H, Nosaka H, Nobuyoshi M. Very long-term (15 to 20 years) clinical and angiographic outcome after coronary bare metal stent implantation. Circ Cardiovasc Interv 2010;**3**(5):468-75.

9. Räber L, Magro M, Stefanini GG, Kalesan B, Domburg RTv, Onuma Y, Wenaweser P, Daemen J, Meier B, Jüni P, Serruys PW, Windecker S. Very Late Coronary Stent Thrombosis of a Newer-Generation Everolimus-Eluting Stent Compared With Early-Generation Drug-Eluting Stents A Prospective Cohort Study. Circulation 2012;**125**(9):1110-1121.

10. Daemen J, Wenaweser P, Tsuchida K, Abrecht L, Vaina S, Morger C, Kukreja N, Jüni P, Sianos G, Hellige G, van Domburg RT, Hess OM, Boersma E, Meier B, Windecker S, Serruys PW. Early and late coronary stent thrombosis of sirolimus-eluting and paclitaxel-eluting stents in routine clinical practice: data from a large two-institutional cohort study. Lancet 2007;**369**(9562):667-678.

11. Otsuka F, Vorpahl M, Nakano M, Foerst J, Newell JB, Sakakura K, Kutys R, Ladich E, Finn AV, Kolodgie FD, Virmani R. Pathology of second-generation everolimus-eluting stents versus first-generation sirolimus- and paclitaxel-eluting stents in humans. Circulation 2014;**129**(2):211-23.

12. Serruys PW, Garcia-Garcia HM, Onuma Y. From metallic cages to transient bioresorbable scaffolds: change in paradigm of coronary revascularization in the upcoming decade? Eur Heart J 2012;**33**(1):16-25b.

13. Wentzel JJ, Chatzizisis YS, Gijsen FJ, Giannoglou GD, Feldman CL, Stone PH. Endothelial shear stress in the evolution of coronary atherosclerotic plaque and vascular remodelling: current understanding and remaining questions. Cardiovasc Res 2012;**96**(2):234-43.

14. Chatzizisis YS, Blankstein R, Libby P. Inflammation goes with the flow: implications for non-invasive identification of high-risk plaque. Atherosclerosis 2014;**234**(2):476-8.

15. Stone PH, Saito S, Takahashi S, Makita Y, Nakamura S, Kawasaki T, Takahashi A, Katsuki T, Namiki A, Hirohata A, Matsumura T, Yamazaki S, Yokoi H, Tanaka S, Otsuji S, Yoshimachi F, Honye J, Harwood D, Reitman M, Coskun AU, Papafaklis MI, Feldman CL. Prediction of progression of coronary artery disease and clinical outcomes using vascular profiling of endothelial shear stress and arterial plaque characteristics: the PREDICTION Study. Circulation 2012;**126**(2):172-81.

16. Wentzel JJ, Gijsen FJ, Schuurbiers JC, van der Steen AF, Serruys PW. The influence of shear stress on in-stent restenosis and thrombosis. EuroIntervention 2008;**4 Suppl C**:C27-32.

17. van der Giessen AG, Schaap M, Gijsen FJH, Groen HC, van Walsum T, Mollet NR, Dijkstra J, van de Vosse FN, Niessen WJ, Feyter PJd, van der Steen AFW, Wentzel JJ. 3D fusion of intravascular ultrasound and coronary computed tomography for in-vivo wall shear stress analysis: a feasibility study. Int J Cardiovasc Imaging 2010;**26**(7):781-796.

18. Serruys PW, Onuma Y, Garcia-Garcia HM, Muramatsu T, van Geuns RJ, de Bruyne B, Dudek D, Thuesen L, Smits PC, Chevalier B, McClean D, Koolen J, Windecker S, Whitbourn R, Meredith I, Dorange C, Veldhof S, Hebert KM, Rapoza R, Ormiston JA. Dynamics of vessel wall changes following the implantation of the absorb everolimus-eluting bioresorbable vascular scaffold: a multi-imaging modality study at 6, 12, 24 and 36 months. EuroIntervention 2014;**9**(11):1271-84.

19. Serruys PW, Ormiston JA, Onuma Y, Regar E, Gonzalo N, Garcia-Garcia HM, Nieman K, Bruining N, Dorange C, Miquel-Hébert K, Veldhof S, Webster M, Thuesen L, Dudek D. A bioabsorbable everolimus-eluting coronary stent system (ABSORB): 2-year outcomes and results from multiple imaging methods. The Lancet 2009;**373**(9667):897-910.

20. Magro M, Regar E, Gutierrez-Chico JL, Garcia-Garcia H, Simsek C, Schultz C, Zijlstra F, Serruys PW, van Geuns RJ. Residual atherothrombotic material after stenting in acute myocardial infarction--an optical coherence tomographic evaluation. Int J Cardiol 2013;**167**(3):656-63.

21. Gori T, Schulz E, Hink U, Wenzel P, Post F, Jabs A, Munzel T. Early outcome after implantation of Absorb bioresorbable drug-eluting scaffolds in patients with acute coronary syndromes. EuroIntervention 2014;**9**(9):1036-41.

22. Kocka V, Maly M, Tousek P, Budesinsky T, Lisa L, Prodanov P, Jarkovsky J, Widimsky P. Bioresorbable vascular scaffolds in acute ST-segment elevation myocardial infarction: a prospective multicentre study 'Prague 19'. Eur Heart J 2014;**35**(12):787-94.

23. Gonzalo N, Barlis P, Serruys PW, Garcia-Garcia HM, Onuma Y, Ligthart J, Regar E. Incomplete stent apposition and delayed tissue coverage are more frequent in drug-eluting stents implanted during primary

percutaneous coronary intervention for ST-segment elevation myocardial infarction than in drug-eluting stents implanted for stable/unstable angina: insights from optical coherence tomography. JACC Cardiovasc Interv 2009;**2**(5):445-52.

24. Guagliumi G, Costa MA, Sirbu V, Musumeci G, Bezerra HG, Suzuki N, Matiashvili A, Lortkipanidze N, Mihalcsik L, Trivisonno A, Valsecchi O, Mintz GS, Dressler O, Parise H, Maehara A, Cristea E, Lansky AJ, Mehran R, Stone GW. Strut Coverage and Late Malapposition With Paclitaxel-Eluting Stents Compared With Bare Metal Stents in Acute Myocardial Infarction: Optical Coherence Tomography Substudy of the Harmonizing Outcomes With Revascularization and Stents in Acute Myocardial Infarction (HORIZONS-AMI) Trial. Circulation 2011;**123**(3):274-281.

25. Capodanno D, Gori T, Nef H, Latib A, Mehilli J, Lesiak M, Caramanno G, Naber C, Di Mario C, Colombo A, Capranzano P, Wiebe J, Araszkiewicz A, Geraci S, Pyxaras S, Mattesini A, Naganuma T, Munzel T, Tamburino C. Percutaneous coronary intervention with everolimus-eluting bioresorbable vascular scaffolds in routine clinical practice: early and midterm outcomes from the European multicentre GHOST-EU registry. EuroIntervention 2015;**10**(10):1144-53.

26. Ishibashi Y, Nakatani S, Onuma Y. Definite and probable bioresorbable scaffold thrombosis in stable and ACS patients. EuroIntervention 2014.

27. Holmes Jr DR, Kereiakes DJ, Garg S, Serruys PW, Dehmer GJ, Ellis SG, Williams DO, Kimura T, Moliterno DJ. Stent Thrombosis. J Am Coll Cardiol 2010;**56**(17):1357-1365.

28. Windecker S, Meier B. Late Coronary Stent Thrombosis. Circulation 2007;**116**(17):1952-1965.

29. Kolandaivelu K, Swaminathan R, Gibson WJ, Kolachalama VB, Nguyen-Ehrenreich KL, Giddings VL, Coleman L, Wong GK, Edelman ER. Stent thrombogenicity early in high-risk interventional settings is driven by stent design and deployment and protected by polymer-drug coatings. Circulation 2011;**123**(13):1400-9.

30. Foin N, Gutierrez-Chico JL, Nakatani S, Torii R, Bourantas CV, Sen S, Nijjer S, Petraco R, Kousera C, Ghione M, Onuma Y, Garcia-Garcia HM, Francis DP, Wong P, Di Mario C, Davies JE, Serruys PW. Incomplete stent apposition causes high shear flow disturbances and delay in neointimal coverage as a function of strut to wall detachment distance: implications for the management of incomplete stent apposition. Circ Cardiovasc Interv 2014;**7**(2):180-9.

31. Bhatt DL, Kandzari DE, O'Neill WW, D'Agostino R, Flack JM, Katzen BT, Leon MB, Liu M, Mauri L, Negoita M, Cohen SA, Oparil S, Rocha-Singh K, Townsend RR, Bakris GL. A controlled trial of renal denervation for resistant hypertension. N Engl J Med 2014;**370**(15):1393-401.

32. Davis MI, Filion KB, Zhang D, Eisenberg MJ, Afilalo J, Schiffrin EL, Joyal D. Effectiveness of Renal Denervation Therapy for Resistant Hypertension: A Systematic Review and Meta-Analysis. J Am Coll Cardiol 2013;**62**(3):231-241.

33. Esler MD, Krum H, Sobotka PA, Schlaich MP, Schmieder RE, Bohm M. Renal sympathetic denervation in patients with treatment-resistant hypertension (The Symplicity HTN-2 Trial): a randomised controlled trial. Lancet 2010;**376**(9756):1903-9.

34. Templin C, Jaguszewski M, Ghadri JR, Sudano I, Gaehwiler R, Hellermann JP, Schoenenberger-Berzins R, Landmesser U, Erne P, Noll G, Luscher TF. Vascular lesions induced by renal nerve ablation as assessed by optical coherence tomography: pre- and post-procedural comparison with the Simplicity catheter system and the EnligHTN multi-electrode renal denervation catheter. Eur Heart J 2013;**34**(28):2141-8, 2148b.

35. Tsioufis C, Mahfoud F, Mancia G, Redon J, Damascelli B, Zeller T, Schmieder RE. What the interventionalist should know about renal denervation in hypertensive patients: a position paper by the ESH WG on the interventional treatment of hypertension. EuroIntervention 2014;**9**(9):1027-1035.

36. Windecker S, Kolh P, Alfonso F, Collet JP, Cremer J, Falk V, Filippatos G, Hamm C, Head SJ, Juni P, Kappetein AP, Kastrati A, Knuuti J, Landmesser U, Laufer G, Neumann FJ, Richter DJ, Schauerte P, Sousa Uva M, Stefanini GG, Taggart DP, Torracca L, Valgimigli M, Wijns W, Witkowski A. 2014 ESC/EACTS Guidelines on myocardial revascularization: The Task Force on Myocardial Revascularization of the European Society of Cardiology (ESC) and the European Association for Cardio-Thoracic Surgery (EACTS)Developed with the special contribution of the European Association of Percutaneous Cardiovascular Interventions (EAPCI). Eur Heart J 2014;**35**(37):2541-619.

37. Wijns W, Shite J, Jones MR, Lee SW, Price MJ, Fabbiocchi F, Barbato E, Akasaka T, Bezerra H, Holmes D. Optical coherence tomography imaging during percutaneous coronary intervention impacts physician decision-making: ILUMIEN I study. Eur Heart J 2015.

38. Maehara A, Ben-Yehuda O, Ali Z, Wijns W, Bezerra HG, Shite J, Genereux P, Nichols M, Jenkins P, Witzenbichler B, Mintz GS, Stone GW. Comparison of Stent Expansion Guided by Optical Coherence Tomography Versus Intravascular Ultrasound: The ILUMIEN II Study (Observational Study of Optical Coherence Tomography [OCT] in Patients Undergoing Fractional Flow Reserve [FFR] and Percutaneous Coronary Intervention). JACC Cardiovasc Interv 2015;**8**(13):1704-14.

39. Prati F, Romagnoli E, Burzotta F, Limbruno U, Gatto L, La Manna A, Versaci F, Marco V, Di Vito L, Imola F, Paoletti G, Trani C, Tamburino C, Tavazzi L, Mintz GS. Clinical Impact of OCT Findings During PCI: The CLI-OPCI II Study. JACC Cardiovasc Imaging 2015;**8**(11):1297-305.

40. Prati F, Di Vito L, Biondi-Zoccai G, Occhipinti M, La Manna A, Tamburino C, Burzotta F, Trani C, Porto I, Ramazzotti V, Imola F, Manzoli A, Materia L, Cremonesi A, Albertucci M. Angiography alone versus angiography plus optical coherence tomography to guide decision-making during percutaneous coronary intervention: the Centro per la Lotta contro l'Infarto-Optimisation of Percutaneous Coronary Intervention (CLI-OPCI) study. EuroIntervention 2012;**8**(7):823-9.

41. Gnanadesigan M, van Soest G, White S, Scoltock S, Ughi GJ, Baumbach A, van der Steen AF, Regar E, Johnson TW. Effect of temperature and fixation on the optical properties of atherosclerotic tissue: a validation study of an ex-vivo whole heart cadaveric model. Biomed Opt Express 2014;**5**(4):1038-49.

42. Ughi GJ, Adriaenssens T, Sinnaeve P, Desmet W, D'Hooge J. Automated tissue characterization of in vivo atherosclerotic plaques by intravascular optical coherence tomography images. Biomed Opt Express 2013;**4**(7):1014-30.

43. Toutouzas K, Chatzizisis YS, Riga M, Giannopoulos A, Antoniadis AP, Tu S, Fujino Y, Mitsouras D, Doulaverakis C, Tsampoulatidis I, Koutkias VG, Bouki K, Li Y, Chouvarda I, Cheimariotis G, Maglaveras N, Kompatsiaris I, Nakamura S, Reiber JH, Rybicki F, Karvounis H, Stefanadis C, Tousoulis D, Giannoglou GD. Accurate and reproducible reconstruction of coronary arteries and endothelial shear stress calculation using 3D OCT: comparative study to 3D IVUS and 3D QCA. Atherosclerosis 2015;**240**(2):510-9.

44. Papafaklis MI, Bourantas CV, Yonetsu T, Vergallo R, Kotsia A, Nakatani S, Lakkas LS, Athanasiou LS, Naka KK, Fotiadis DI, Feldman CL, Stone PH, Serruys PW, Jang IK, Michalis LK. Anatomically correct three-dimensional coronary artery reconstruction using frequency domain optical coherence tomographic and angiographic

data: head-to-head comparison with intravascular ultrasound for endothelial shear stress assessment in humans. EuroIntervention 2015;**11**(4):407-15.

45. Vergallo R, Papafaklis MI, Yonetsu T, Bourantas CV, Andreou I, Wang Z, Fujimoto JG, McNulty I, Lee H, Biasucci LM, Crea F, Feldman CL, Michalis LK, Stone PH, Jang IK. Endothelial shear stress and coronary plaque characteristics in humans: combined frequency-domain optical coherence tomography and computational fluid dynamics study. Circ Cardiovasc Imaging 2014;**7**(6):905-11.

46. Wang T, Wieser W, Springeling G, Beurskens R, Lancee CT, Pfeiffer T, van der Steen AF, Huber R, van Soest G. Intravascular optical coherence tomography imaging at 3200 frames per second. Opt Lett 2013;**38**(10):1715-7.

47. Toutouzas K, Benetos G, Karanasos A, Chatzizisis YS, Giannopoulos AA, Tousoulis D. Vulnerable plaque imaging: updates on new pathobiological mechanisms. Eur Heart J 2015.

48. Nadkarni SK, Pierce MC, Park BH, de Boer JF, Whittaker P, Bouma BE, Bressner JE, Halpern E, Houser SL, Tearney GJ. Measurement of collagen and smooth muscle cell content in atherosclerotic plaques using polarization-sensitive optical coherence tomography. J Am Coll Cardiol 2007;**49**(13):1474-81.

49. Liu L, Gardecki JA, Nadkarni SK, Toussaint JD, Yagi Y, Bouma BE, Tearney GJ. Imaging the subcellular structure of human coronary atherosclerosis using micro-optical coherence tomography. Nat Med 2011;**17**(8):1010-4.

50. Wang H, Gardecki JA, Ughi GJ, Jacques PV, Hamidi E, Tearney GJ. Ex vivo catheter-based imaging of coronary atherosclerosis using multimodality OCT and NIRAF excited at 633 nm. Biomed Opt Express 2015;**6**(4):1363-75.

51. Raber L, Magro M, Stefanini GG, Kalesan B, van Domburg RT, Onuma Y, Wenaweser P, Daemen J, Meier B, Juni P, Serruys PW, Windecker S. Very late coronary stent thrombosis of a newer-generation everolimus-eluting stent compared with early-generation drug-eluting stents: a prospective cohort study. Circulation 2012;**125**(9):1110-21.

52. Ellis SG, Kereiakes DJ, Metzger DC, Caputo RP, Rizik DG, Teirstein PS, Litt MR, Kini A, Kabour A, Marx SO, Popma JJ, McGreevy R, Zhang Z, Simonton C, Stone GW. Everolimus-Eluting Bioresorbable Scaffolds for Coronary Artery Disease. N Engl J Med 2015;**373**(20):1905-15.

53. Gao R, Yang Y, Han Y, Huo Y, Chen J, Yu B, Su X, Li L, Kuo HC, Ying SW, Cheong WF, Zhang Y, Xu B, Popma JJ, Stone GW. Bioresorbable Vascular Scaffolds Versus Metallic Stents in Patients with Coronary Artery Disease: ABSORB China trial. J Am Coll Cardiol 2015.

54. Kimura T, Kozuma K, Tanabe K, Nakamura S, Yamane M, Muramatsu T, Saito S, Yajima J, Hagiwara N, Mitsudo K, Popma JJ, Serruys PW, Onuma Y, Ying S, Cao S, Staehr P, Cheong WF, Kusano H, Stone GW. A randomized trial evaluating everolimus-eluting Absorb bioresorbable scaffolds vs. everolimus-eluting metallic stents in patients with coronary artery disease: ABSORB Japan. Eur Heart J 2015.

55. Sabate M, Windecker S, Iniguez A, Okkels-Jensen L, Cequier A, Brugaletta S, Hofma SH, Raber L, Christiansen EH, Suttorp M, Pilgrim T, Anne van Es G, Sotomi Y, Garcia-Garcia HM, Onuma Y, Serruys PW. Everolimus-eluting bioresorbable stent vs. durable polymer everolimus-eluting metallic stent in patients with ST-segment elevation myocardial infarction: results of the randomized ABSORB ST-segment elevation myocardial infarction-TROFI II trial. Eur Heart J 2015.

56. Serruys PW, Chevalier B, Dudek D, Cequier A, Carrie D, Iniguez A, Dominici M, van der Schaaf RJ, Haude M, Wasungu L, Veldhof S, Peng L, Staehr P, Grundeken MJ, Ishibashi Y, Garcia-Garcia HM, Onuma Y. A bioresorbable everolimus-eluting scaffold versus a metallic everolimus-eluting stent for ischaemic heart disease

caused by de-novo native coronary artery lesions (ABSORB II): an interim 1-year analysis of clinical and procedural secondary outcomes from a randomised controlled trial. Lancet 2015;**385**(9962):43-54.

Acknowledgements

This last part of the thesis proves to be one of the most difficult to compose, as additionally to the difficulties in acknowledging the contribution of numerous persons over several years in a short piece, it is the part that is ‘reviewed’ by all readers and there is always the anxiety that not everybody that has contributed is properly credited.

This thesis represents the summary of research work performed during the last 4 years in Thoraxcenter Rotterdam. After having arrived in Rotterdam from Athens on a cold January afternoon almost 4 years ago, it was hard to envision that I would still be in Rotterdam today. My wish to do additional research on the field of invasive imaging turned to a long stay and, eventually, to the composition of this thesis. Of course, this scientific publication cannot be credited to one person alone. It is actually the product of numerous fruitful collaborations among several departments. Therefore, this section is just a small token of my gratitude for everybody that has helped in the creation of this thesis.

To my promotor, professor **Felix Zijlstra** for being the right man at the right place. He is a solid and inspiring leader that has managed to successfully run things in an extremely demanding environment such as the Thoraxcenter, with a tradition of an outstanding cathlab. Despite the extremely busy schedule required by his position, it was always possible to find some time for me when the circumstances would demand it, and for that I would like to thank him.

To my co-promotor, **Evelyn Regar**, which is the person that has provided invaluable guidance during the performance of this thesis, and has always been of assistance with everything since my first moment in Rotterdam even when it comes to plain logistic matters. I can still remember our first encounter, when I arrived here in search of a center where I could expand my knowledge over intravascular imaging and the outcome of our discussion which was that I would try to do as much research in OCT as possible and that she would try to facilitate my efforts. With the completion of this thesis, I come to believe that this target was achieved, always with the continuous support and mentoring of Evelyn. Therefore, Evelyn I would like to personally thank you for standing behind me during this time.

To the senior physicians of the cathlab for their cooperation during my stay. Professor **Robert-Jan van Geuns** has given me the chance to collaborate with him in projects regarding the imaging of bioresorbable scaffolds and has always provided constructive feedback for my papers having a slightly different perspective than mine. I have also closely collaborated with

Nicolas Van Mieghem and **Roberto Diletti** in my research during a large part of my stay. Although I did not get the opportunity to work closely with professor **Peter de Jaegere** and **Marco Valgimigli**, I would like to thank them for their contribution in the collective work performed in several papers of this thesis. I have known **Joost Daemen** since his days in training and I would like to thank him for our excellent collaboration in the renal denervation project. I would also like to thank **Ramon** and **Bert** for the good times inside and outside the cathlab, and wish them luck with their current ventures.

Moreover, I would like to thank the assistants and senior staff of the cardiology department of Erasmus MC, for their cooperation during my clinical assignment from July 2015 and onwards.

To the cathlab staff for helping me during my visits to the cathlab in the search of data and for always being a pleasant company at the long waiting hours behind the protective panel, but also in the fun times outside the hospital. I would also like to highlight the contribution of the technicians that have acquired all this wealth of intravascular images and have helped with retrieving information and several analyses. **Angelique, Anne Marie, Elco, John, Patrick, Paul, Rob,** and **Sander,** thank you for your help. With a flawless collaboration with **Gerard, Hans, Houda, Leonie, Linda, Marianne, Marjo, Peggy**, and **Rixt** you make everything work perfectly around the cathlab. And of course, I also got valuable administrative support during my stay from the administrative staff and secretaries of the 5th floor, for which I am thankful.

Jurgen and **Karen**, a large thank you for all the useful help you have provided me during my stay. You were the first persons to turn to when I had a practical question and you would always provide me with a hint to the right answer. Your experience with analysis has always generated intriguing debates, mainly during OCT meetings. Jurgen, I can still recall our first meeting several years ago during an IVUS course, where you shared a fraction of your in-depth knowledge of IVUS interpretation.

During this thesis, I had the opportunity to collaborate with a number of engineers from various departments. I would therefore like to express my thanks to the biomedical engineering group with which we have closely collaborated. **Gijs** thank you for all the stimulating discussions and also for your role in the reading committee, and **Muthu** thanks for helping me include your innovative analysis method in my manuscripts. I will not forget the great conference trip in San Francisco. To the biomechanics laboratory, for a great

collaboration allowing me to expand my knowledge on the field of hemodynamics. **Jolanda, Frank, Jelle** and **Hans** thank you for all your help in these intriguing projects. To **Guillaume** from the image processing group for a great cooperation that will help bring the field of automated OCT analysis forward. To my collaborators from the imaging group from Leiden University for their continued support with innovative software for OCT analysis. **Jouke** thanks for all the times that you looked into our craziest requests for analysis. **Shengxian** we had a great cooperation during your time in Leiden, but I am confident that it will continue even now that you have moved to Shanghai. I know that you will continue all this innovative work.

To the international and Dutch fellows with whom I came in contact during my stay, which would be too numerous to mention. I would still line to briefly mention the clinical researchers from various departments with whom I have directly collaborated: **Ron van Domburg** from epidemiology, **Matthijs Kranenburg** from non-invasive imaging, **Heleen van Beuzekom** and **Anouchska Autar** from experimental cardiology. Also to the trial bureau and especially **Cihan Simsek** and **Cordula Felix**, and to **Hector Garcia-Garcia**, **Takashi Muramatsu**, **Shimpei Nakatani** and **Yoshi Onuma** from Cardialysis.

I would like to especially thank the fellows with whom I have shared the working environment and the pleasure of doing OCT analysis together. To my Asian friends **Bu-Chun Zhang** and **Jiang-Ming Fam** for their cooperation in several projects during the one year that they stayed in Rotterdam, but also for their friendship and the quality time. I am sure that both of you will manage to thrive at your hospitals.

To my ‘roommates’ **Jors** and **Nienke** for all the moments that we have spent doing OCT analysis. For all the great ideas and for their contribution to this thesis. For helping me to adapt more easily to the Dutch language and lifestyle, although the concept of the ‘uitdrukking van de week’ never took off. Both of you have helped in making my time in the office more pleasant. Nienke, I believe you will compile a great thesis and will have no trouble going through the internships. Jors, I am sure that you will manage to balance your time between clinical work, research work and parenthood effectively.

To my former mentor, **Kostas Toutouzas** from Hippokration Hospital, Athens Medical School for providing me the chance to get acquainted with cathlab research and in specific OCT, for his valuable guidance during my first PhD, and for pointing me to the right place for doing research in intravascular imaging.

To my girlfriend **Stella** for her support and patience during this period that I have stayed in Rotterdam. When I set out to come to Rotterdam, I had no idea of how long I would eventually stay, and it actually turned out to be an unexpectedly long time. During this interval I have received continued support from your side and you have never let me down, despite the large distance between us. For all this unconditional support, the endless Skype calls, and the numerous visits I want to thank you.

I would like to leave for last two persons that have always supported me and have been role models for me during my lifetime. To my parents, **Vassilis** and **Nouli** for bringing me up and continuously providing moral support. They have always backed my decisions, including my departure for Rotterdam although it would mean that they would have to spend a significant amount of time without seeing me in person. For all their love and support I would like to thank them.

Curriculum Vitae

Biographical information

Full Name: Antonios Karanasos

Date of Birth: 23 January 1982

Family status: Single

Nationality: Greek

Spoken languages: Greek (Native), English (Proficient), Dutch (Higher Intermediate), French (Basic)

Current Address: Nieuwe Binnenweg 214D, 3021GM, Rotterdam, Zuid Holland, Netherlands

Telephone: +31(0)627561555, +30 6955474450

e-mail: akaranasos@outlook.com; a.karanasos@erasmusmc.nl

Education and appointments

- Graduation from High School: 1999
- Medical diploma from Medical School of University of Athens: 2005

  (Grade: very good)
- March 2006 – September 2007: Primary care physician in Atalanti Medical Centre, Lamia General Hospital, Lamia, Greece
- October 2007 – February 2010: Research fellow (PhD) in First Department of Cardiology, Athens Medical School, Hippokration Hospital, Athens, Greece (PhD diploma obtained in October 2014; grade: excellent)
- March 2010-December 2011: Internal medicine resident, 2nd Department of Internal Medicine, Sismanogleio General Hospital, Athens, Greece
- January 2012-July 2015: Research fellow (PhD candidate) in Thoraxcenter, Erasmus Medical Center, Rotterdam, Netherlands

Awards

1. Recipient of the **Hellenic Heart Foundation scholarship** for the year 2011.

2. Nominated for the **Young Investigator Award in Coronary Pathophysiology and Microcirculation** at the **European Society of Cardiology Congress 2012** for the contribution: 'Karanasos A, Witberg K, Van Geuns RJ, Schultz C, van Mieghem N, De Jaegere P, Bruining N, Zijlstra F, Regar E. Morphological characteristics by optical coherence tomography of ruptured neoatherosclerotic plaques in patients with very late stent thrombosis'.

3. Top 50 poster award in **Transcatheter Cardiovascular Therapeutics Meeting 2014** for the contribution 'TCT-616. Attenuation Analysis Of The 'Sealing Effect' And Plaque Morphology 5 Years After Implantation Of The Everolimus-Eluting Bioresorbable Vascular Scaffold. An Optical Coherence Tomography Study.'

Reviewer in peer-reviewed journals

I am a reviewer for the following peer-reviewed journals:

1. Circulation: Cardiovascular Interventions
2. International Journal of Cardiology
3. Atherosclerosis
4. Eurointervention
5. International Journal of Cardiovascular Imaging
6. Heart & Vessels
7. Minerva Cardioangiologica
8. Expert Review of Cardiovascular Therapy
9. International Journal of Anatomy and Physiology
10. Current Topics in Medicinal Chemistry
11. Cardiology (Future medicine)
12. Interventional Cardiology (Future medicine)

Abstracts in international congresses

American Heart Association Annual Scientific Sessions: 14

Annual Scientific Sessions of the American College of Cardiology: 19

Congresses of the European Society of Cardiology: 45

Transcatheter Cardiovascular Therapeutics Meeting: 17

EuroPCR: 9

Peer Review Publications

Co-author in 57 peer reviewed publications, in 20 of which credited as first author and in 15 as second author (total impact factor 2014: 288)

Books

Doctoral dissertation (University of Athens). July 2014.

Antonios Karanasos

'OCT study of plaque morphology in STEMI patients undergoing thrombolysis'

Book Chapters

Co-author in 7 chapters in international textbooks.

PUBLICATION LIST

Peer-reviewed publications

1. **Karanasos A**, Ligthart J, Witberg K, van Soest G, Bruining N, Regar E. Optical Coherence Tomography: Potential Clinical Applications. ***Curr Cardiovasc Imaging Rep. 2012;5:206-220***

2. **Karanasos A**, Ligthart JM, Regar E. In-stent neoatherosclerosis: a cause of late stent thrombosis in a patient with "full metal jacket" 15 years after implantation: insights from optical coherence tomography. ***JACC Cardiovasc Interv. 2012;5:799-800 (IF 2014: 7.345)***

3. **Karanasos A**, Ligthart JM, Witberg KT, Regar E. Calcified nodules: an underrated mechanism of coronary thrombosis? ***JACC Cardiovasc Imaging. 2012;5:1071-1072 (IF 2014: 7.188)***

4. **Karanasos A**, Simsek C, Serruys P, Ligthart J, Witberg K, van Geuns RJ, Sianos G, Zijlstra F, Regar E. Five-year optical coherence tomography follow-up of an everolimus-eluting bioresorbable vascular scaffold: changing the paradigm of coronary stenting? ***Circulation. 2012;126:e89-91 (IF 2014: 14.43)***

5. **Karanasos A**, Tsiamis E, Stefanadis C. Myocardial infarction caused by ostial right coronary artery thrombus in the absence of atheromatosis. ***J Invasive Cardiol. 2012;24:E188-189 (IF 2014: 0.949)***

6. **Karanasos A**, Tu S, van der Heide E, Reiber JH, Regar E. Carina shift as a mechanism for side-branch compromise following main vessel intervention: insights from three-dimensional optical coherence tomography. ***Cardiovasc Diagn Ther. 2012;2:173-177***

7. **Karanasos A**, Tu S, van der Linden M, van Weenen S, Ligthart J, Regar E. Online 3-dimensional rendering of optical coherence tomography images for the assessment of bifurcation intervention. ***Can J Cardiol. 2012;28:759 e751-753 (IF 2014: 3.711)***

8. **Karanasos A**, Van Soest G, Ligthart J, Gnanadesigan M, del Trigo M, Regar E. Periprocedural myocardial injury unraveled: Combined assessment by optical coherence tomography, near-infrared spectroscopy and IVUS. ***J Invasive Cardiol. 2013;25:22A-23A (IF 2014: 0.949)***

9. **Karanasos A**, Regar E, Geeve P, van Mieghem NM. Bioresorbable scaffold in myocardial infarction: has the time come? ***Int J Cardiol. 2013;167:e17-19***

10. **Karanasos A**, van Geuns RJ, Zijlstra F, Regar E. Very late bioresorbable scaffold thrombosis after discontinuation of dual antiplatelet therapy. ***Eur Heart J. 2014;35:1781 (IF 2014: 15.203)***

11. **Karanasos A**, Regar E. Standing on solid ground?: Reassessing the role of incomplete strut apposition in drug-eluting stents. ***Circ Cardiovasc Interv. 2014;7:6-8 (IF 2014: 6.218)***

12. **Karanasos A**, Simsek C, Gnanadesigan M, van Ditzhuijzen NS, Freire R, Dijkstra J, Tu S, Van Mieghem N, van Soest G, de Jaegere P, Serruys PW, Zijlstra F, van Geuns RJ, Regar E. OCT assessment of the long-term vascular healing response 5 years after everolimus-eluting bioresorbable vascular scaffold. ***J Am Coll Cardiol. 2014;64:2343-2356 (IF 2014: 16.503)***

13. **Karanasos A**, Muramatsu T, Diletti R, Nauta S, Onuma Y, Lenzen M, Nakatani S, Van Mieghem NM, Schultz C, De Jaegere PP, Serruys PW, Zijlstra F, Regar E, van Geuns RJ. Early and late optical coherence tomography findings following everolimus-eluting bioresorbable vascular scaffold implantation in myocardial infarction: a preliminary report. ***Hellenic J Cardiol. 2015;56:125-135 (IF 2014: 1.229)***

14. **Karanasos A**, Tu S, van Ditzhuijzen NS, Ligthart JM, Witberg K, Van Mieghem N, van Geuns RJ, de Jaegere P, Zijlstra F, Reiber JH, Regar E. A novel method to assess coronary artery bifurcations by OCT: cut-plane analysis for side-branch ostial assessment from a main-vessel pullback. ***Eur Heart J Cardiovasc Imaging. 2015;16:177-189 (IF 2014: 4.105)***

15. **Karanasos A**, Van Mieghem N, van Ditzhuijzen N, Felix C, Daemen J, Autar A, Onuma Y, Kurata M, Diletti R, Valgimigli M, Kauer F, van Beusekom H, de Jaegere P, Zijlstra F, van Geuns RJ, Regar E. Angiographic and optical coherence tomography insights into bioresorbable scaffold thrombosis: single-center experience. ***Circ Cardiovasc Interv. 2015;8 pii: e002369. (IF 2014: 6.218)***

16. **Karanasos A**, Schuurbiers JC, Garcia-Garcia HM, Simsek C, Onuma Y, Serruys PW, Zijlstra F, van Geuns RJ, Regar E, Wentzel JJ. Association of wall shear stress with long-term vascular healing response following bioresorbable vascular scaffold implantation. ***Int J Cardiol. 2015;191:279-283 (IF 2014: 4.036)***

17. **Karanasos A**, Van Mieghem NM, Regar E, Daemen J. Serial imaging observations of vascular healing in a denervation-induced renal artery dissection. ***Eur Heart J. 2015;36:1040 (IF 2014: 15.203)***

18. **Karanasos A**, Garcia-Garcia HM, van Geuns RJ, Regar E. Fate of side-branch jailing and a malapposed platinum marker after resorption of an everolimus-eluting bioresorbable vascular scaffold: serial optical coherence tomography observations. ***JACC Cardiovasc Interv. 2015;8:e53-54 (IF 2014: 7.345)***

19. **Karanasos A**, Li Y, Tu S, Wentzel JJ, Reiber JH, van Geuns RJ, Regar E. Is it safe to implant bioresorbable scaffolds in ostial side-branch lesions? Impact of 'neo-carina' formation on main-branch flow pattern. Longitudinal clinical observations. ***Atherosclerosis. 2015;238:22-25 (IF 2014: 3.994)***

20. **Karanasos A**, Van Mieghem N, Bergmann MW, Hartman E, Ligthart J, van der Heide E, Heeger CH, Ouhlous M, Zijlstra F, Regar E, Daemen J. Multimodality Intra-Arterial Imaging Assessment of the Vascular Trauma Induced by Balloon-Based and Nonballoon-Based Renal Denervation Systems. ***Circ Cardiovasc Interv. 2015;8. pii: e002474. (IF 2014: 6.218)***

21. Toutouzas K, **Karanasos A**, Stefanadis C. Multiple plaque morphologies assessed by optical coherence tomography in a patient with acute coronary syndrome. ***Heart. 2010;96:1335-1336 (IF 2014: 5.595)***

22. Toutouzas K, **Karanasos A**, Anastasakis A, Vavuranakis M, Seggewiss H, Stefanadis C, Rigopoulos A. Optimal branch selection in alcohol septal ablation. ***Int J Cardiol. 2011;147:143-144 (IF 2014: 4.036)***

23. Toutouzas K, **Karanasos A**, Tsiamis E, Riga M, Drakopoulou M, Synetos A, Papanikolaou A, Tsioufis C, Androulakis A, Stefanadi E, Tousoulis D, Stefanadis C. New insights by optical coherence tomography into the differences and similarities of culprit ruptured plaque morphology in non-ST-elevation myocardial infarction and ST-elevation myocardial infarction. ***Am Heart J. 2011;161:1192-1199 (IF 2014: 4.463)***

24. Toutouzas K, **Karanasos A**, Riga M, Tsiamis E, Synetos A, Michelongona A, Papanikolaou A, Triantafyllou G, Tsioufis C, Stefanadis C. Optical coherence tomography assessment of the spatial distribution of culprit ruptured plaques and thin-cap fibroatheromas in acute coronary syndrome. ***Eurointervention. 2012;8:477-485 (IF 2014: 3.769)***

25. Toutouzas K, **Karanasos A**, Stathogiannis K, Synetos A, Tsiamis E, Papadopoulos D, Stefanadis C. A honeycomb-like structure in the left anterior descending coronary artery: demonstration of recanalized thrombus by optical coherence tomography. ***JACC Cardiovasc Interv. 2012;5:688-689 (IF 2014: 7.345)***

26. Toutouzas K, **Karanasos A**, Stefanadis C. Pitfalls of angiography in the assessment of atherosclerosis: the role of optical coherence tomography. ***J Invasive Cardiol. 2012;24:246-247 (IF 2014: 0.949)***

27. Toutouzas K, **Karanasos A**, Stefanadis C. Inflammatory mechanisms of adverse reactions to BMS. ***Curr Vasc Pharmacol. 2013;11:379-391 (IF 2014: 2.966)***

28. Diletti R, **Karanasos A**, Muramatsu T, Nakatani S, Van Mieghem NM, Onuma Y, Nauta ST, Ishibashi Y, Lenzen MJ, Ligthart J, Schultz C, Regar E, de Jaegere PP, Serruys PW, Zijlstra F, van Geuns RJ. Everolimus-eluting bioresorbable vascular scaffolds for treatment of patients presenting with ST-segment elevation myocardial infarction: BVS STEMI first study. ***Eur Heart J. 2014;35:777-786 (IF 2014: 15.203)***

29. Simsek C, **Karanasos A**, Magro M, Garcia-Garcia HM, Onuma Y, Regar E, Boersma E, Serruys PW, van Geuns RJ. Long-term invasive follow-up of the everolimus-eluting bioresorbable vascular scaffold: five-year results of multiple invasive imaging modalities. ***Eurointervention. 2014 pii: 20130724-03. (IF 2014: 3.769)***

30. van Ditzhuijzen NS, **Karanasos A**, Bruining N, van den Heuvel M, Sorop O, Ligthart J, Witberg K, Garcia-Garcia HM, Zijlstra F, Duncker DJ, van Beusekom HM, Regar E. The impact of Fourier-Domain optical coherence tomography catheter induced motion artefacts on quantitative measurements of a PLLA-based bioresorbable scaffold. ***Int J Cardiovasc Imaging. 2014;30:1013-1026 (IF 2014: 1.810)***

31. van Kranenburg M, **Karanasos A**, Chelu RG, van der Heide E, Ouhlous M, Nieman K, van Mieghem N, Krestin G, Niessen W, Zijlstra F, van Geuns RJ, Daemen J. Validation of Renal Artery Dimensions Measured by Magnetic Resonance Angiography in Patients Referred for Renal Sympathetic Denervation. ***Acad Radiol. 2015 pii: S1076-6332(15)00198-1. (IF 2014: 1.751)***

32. Fam JM, **Karanasos A**, Regar E, van Geuns RJ. Bioresorbable vascular scaffold for ST elevation myocardial infarction: optical coherence tomography observations at the 2-year follow-up. ***Coron Artery Dis. 2015 (IF 2014: 1.497)***

33. Zahnd G, **Karanasos A**, van Soest G, Regar E, Niessen W, Gijsen F, van Walsum T. Quantification of fibrous cap thickness in intracoronary optical coherence tomography with a contour segmentation method based on dynamic programming. ***Int J Comput Assist Radiol Surg. 2015 (IF 2014: 1.707)***

34. Zhang BC, **Karanasos A**, Royaards KJ, Ligthart J, Regar E. An unusual complication after bioresorbable scaffold implantation: Visualization of intramural hematoma by OCT. ***JACC Cardiovasc Interv. 2015:in press (IF 2014: 7.345)***

35. Zhang BC, **Karanasos A**, Regar E. OCT demonstrating neoatherosclerosis as part of the continuous process of coronary artery disease. ***Herz 2015 Sep;40(6):845-854.. (IF 2014: 0.690)***

36. Toutouzas K, Benetos G, **Karanasos A**, Chatzizisis YS, Giannopoulos AA, Tousoulis D. Vulnerable plaque imaging: updates on new pathobiological mechanisms. ***Eur Heart J. 2015 Sep 28. pii: ehv508 (IF 2014: 15.203)***

37. Toutouzas K, Synetos A, **Karanasos A**, Drakopoulou M, Tsiamis E, Lerakis S, Stefanadis C. Percutaneous coronary intervention in chronic stable angina. ***Am J Med Sci. 2010;339:568-572 (IF 2014: 1.389)***

38. Toutouzas K, Tsiamis E, **Karanasos A**, Drakopoulou M, Synetos A, Tsioufis C, Tousoulis D, Davlouros P, Alexopoulos D, Bouki K, Apostolou T, Stefanadis C. Morphological characteristics of culprit atheromatic plaque are associated with coronary flow after thrombolytic therapy: new implications of optical coherence tomography from a multicenter study. ***JACC Cardiovasc Interv. 2010;3:507-514 (IF 2014: 7.345)***

39. Synetos A, Toutouzas K, **Karanasos A**, Stathogiannis K, Triantafyllou G, Tsiamis E, Lerakis S, Stefanadis C. Differences in drug-eluting stents used in coronary artery disease. ***Am J Med Sci. 2011;342:402-408 (IF 2014: 1.389)***

40. Toutouzas K, Synetos A, **Karanasos A**, Tsiamis E, Stefanadis C. Simultaneous occlusion of two coronary arteries in a patient with acute myocardial infarction: a result of plaque rupture and plaque erosion. ***Int J Cardiol. 2011;152:e29-30 (IF 2014: 4.036)***

41. Toutouzas K, Synetos A, **Karanasos A**, Nikolaou C, Michelongona A, Panagiotakos D, Tsiamis E, Tsioufis C, Tousoulis D, Stefanadis C. Prognostic models for cardiovascular events after successful primary percutaneous coronary intervention. ***Int J Cardiol. 2012;158:168-170 (IF 2014: 4.036)***

42. Mytas D, Zairis M, **Karanasos A**, Kosma L, Arsenos P, Tentolouris C, Pitsavos C, Foussas S, Stefanadis C, Cokkinos D. Effect of statin pretreatment on the outcome of ST-segment elevation myocardial infarction in patients without prior history of coronary artery disease. ***Hellenic J Cardiol. 2013;54:422-428 (IF 2014: 1.229)***

43. Nammas W, Ligthart JM, **Karanasos A**, Witberg KT, Regar E. Optical coherence tomography for evaluation of coronary stents in vivo. ***Expert Rev Cardiovasc Ther. 2013;11:577-588***

44. Toutouzas K, Sfikakis PP, **Karanasos A**, Aggeli C, Felekos I, Kitas G, Zampeli E, Protogerou A, Stefanadis C. Myocardial ischaemia without obstructive coronary artery disease in rheumatoid arthritis: hypothesis-generating insights from a cross-sectional study. ***Rheumatology (Oxford). 2013;52:76-80 (IF 2014: 4.475)***

45. Fam JM, van der Sijde JN, **Karanasos A**, Zhang B, van Geuns RJ, Regar E. Use of Intracoronary imaging in ST Elevation Myocardial Infarction with coronary artery aneurysm and very late stent thrombosis. ***Int J Cardiol. 2015;97:296-299. (IF 2014: 4.036)***

46. Toutouzas K, Patsa C, Synetos A, **Karanasos A**, Karampelas J, Tsiamis E, Spanos A, Stefanadi E, Tousoulis D, Stefanadis C. The impact of new generation drug-eluting stent implantation on patients with chronic kidney disease and a single lesion in the proximal segment of the left anterior descending artery. ***Hellenic J Cardiol. 2011;52:103-110 (IF 2014: 1.229)***

47. Toutouzas K, Stathogiannis K, Synetos A, **Karanasos A**, Stefanadis C. Vulnerable atherosclerotic plaque: from the basic research laboratory to the clinic. ***Cardiology. 2012;123:248-253 (IF 2014: 2.177)***

48. Stefanadis C, Toutouzas K, Synetos A, Tsioufis C, **Karanasos A**, Agrogiannis G, Stefanis L, Patsouris E, Tousoulis D. Chemical denervation of the renal artery by vincristine in swine. A new catheter based technique. ***Int J Cardiol. 2013;167:421-425 (IF 2014: 4.036)***

49. Hu S, Yonetsu T, Jia H, **Karanasos A**, Aguirre AD, Tian J, Abtahian F, Vergallo R, Soeda T, Lee H, McNulty I, Kato K, Yu B, Mizuno K, Toutouzas K, Stefanadis C, Jang IK. Residual thrombus pattern in patients with ST-segment elevation myocardial infarction caused by plaque erosion versus plaque rupture after successful fibrinolysis: an optical coherence tomography study. ***J Am Coll Cardiol. 2014;63:1336-1338 (IF 2014: 16.503)***

50. Nakatani S, Onuma Y, Ishibashi Y, **Karanasos A**, Regar E, Garcia-Garcia HM, Tamburino C, Fajadet J, Vrolix M, Witzenbichler B, Eeckhout E, Spaulding C, Reczuch K, La Manna A, Capodanno D, Van Langenhove G, Verheye S, Serruys PW, van Geuns RJ. Incidence and Potential Mechanism of Resolved, Persistent and Newly Acquired Incomplete Stent Apposition 3 days after Implantation of Self-expanding or Balloon-expandable Stent in ST-elevation Myocardial Infarction Population: Insights from Optical Coherence Tomography in the APPOSITION II Study. **Eurointervention** ***2015;11: pii: 20150309-10. (IF 2014: 3.769)***

51. Diletti R, Van Mieghem NM, Valgimigli M, **Karanasos A**, Everaert BR, Daemen J, van Geuns RJ, de Jaegere PP, Zijlstra F, Regar E. Rapid exchange ultra-thin microcatheter using fibre-optic sensing technology for measurement of intracoronary fractional flow reserve. ***EuroIntervention. 2015;11. pii: 20140816-03***. ***(IF 2014: 3.769)***

52. Tsiamis E, Toutouzas K, Synetos A, Karambelas J, **Karanasos A**, Demponeras C, Drakopoulou M, Stefanadi E, Tsioufis C, Tousoulis D, Stefanadis C. Prognostic clinical and angiographic characteristics for the development of a new significant lesion in remote segments after successful percutaneous coronary intervention. ***Int J Cardiol. 2010;143:29-34 (IF 2014: 4.036)***

53. Patsa C, Toutouzas K, Tsiamis E, Tsioufis C, Spanos A, **Karanasos A**, Michelongona A, Tousoulis D, Stefanadis C. Impact of metabolic syndrome on clinical outcomes after new generation drug-eluting stent implantation: the 'obesity paradox' phenomenon is still apparent. ***Nutr Metab Cardiovasc Dis. 2013;23:307-313 (IF 2014: 3.323)***

54. Toutouzas K, Benetos G, Drakopoulou M, Bounas P, Tsekoura D, Stathogiannis K, Koutagiar I, Aggeli C, **Karanasos A**, Panagiotakos D, Siores E, Stefanadis C. Insights from a thermography-based method suggesting higher carotid inflammation in patients with diabetes mellitus and coronary artery disease. ***Diabetes Metab. 2014;40:431-438 (IF 2014: 3.267)***

55. Toutouzas K, Drakopoulou M, Aggeli C, Nikolaou C, Felekos I, Grassos H, Synetos A, Stathogiannis K, **Karanasos A**, Tsiamis E, Siores E, Stefanadis C. In vivo measurement of plaque neovascularisation and thermal heterogeneity in intermediate lesions of human carotid arteries. ***Heart. 2012;98:1716-1721 (IF 2014: 5.595)***

56. Toutouzas K, Drakopoulou M, Aggeli C, Nikolaou C, Felekos I, Grassos H, Synetos A, Stathogiannis K, **Karanasos A**, Tsiamis E, Siores E, Stefanadis C. In vivo

measurement of plaque neovascularisation and thermal heterogeneity in intermediate lesions of human carotid arteries. The authors' reply. ***Heart. 2014;100:e1 (IF 2014: 5.595)***

57. Toutouzas K, Synetos A, Tousoulis D, Latsios G, Brili S, Mastrokostopoulos A, **Karanasos A**, Sideris S, Dilaveris P, Cheong A, Yu CM, Stefanadis C. Predictors for permanent pacemaker implantation after core valve implantation in patients without preexisting ECG conduction disturbances: the role of a new echocardiographic index. ***Int J Cardiol. 2014;172:601-603 (IF 2014: 4.036)***

Book chapters

1. Intravascular Imaging: Current Applications and Research Developments

K. Toutouzas, **A. Karanasos**, C. Stefanadis: '*Research utility of optical coherence tomography'*

Editors: V. Tsakanikas, L. Michalis, D. Fotiadis, K. Naka, C. Bourantas. IGI global 2011, DOI: 10.4018/978-1-61350-095-8

2. Urgent Interventional Therapies.

K. Toutouzas, **A. Karanasos**, C. Stefanadis: '*Diagnosis of Vulnerable Plaque'*

Editors: N. Kipshidze, J. Fareed, R.T. Rosen, P.W. Serruys. Wiley-Blackwell 2014. DOI: 10.1002/9781118504499.ch3

3. Information Processing in Computer-Assisted Interventions. Lecture Notes in Computer Science,Vol. 8498

G. Zahnd, **A. Karanasos**, G. van Soest, E. Regar, WJ. Niessen, F. Gijsen, T. van Walsum '*Semi-automated Quantification of Fibrous Cap Thickness in Intracoronary Optical Coherence Tomography*'

Editors: Stoyanov, D., Collins, D.L., Sakuma, I., Abolmaesumi, P., Jannin, P. Springer International Publishing 2014

4. Myocardial infarctions: Risk factors, emergency management and long-term health outcomes.

A. Karanasos, K. Toutouzas, J. van der Sijde, N. van Ditzhuijzen, Regar E. '*Optical coherence tomography imaging in acute myocardial infarction'. pp 17-52.*

Editor: P. Wilkonson. Nova Science Publishers, Inc. 2014

5. Cardiovascular OCT imaging

N.S. van Ditzhuijzen, **A. Karanasos**, J.N. van der Sijde, G. van Soest, E. Regar**.** '*Bioabsorbable stent'* pp 179-193.

Editor: I.K. Jang. Springer International Publishing 2015

6. Textbook on Bioresorbable Scaffolds: from basic concept to clinical application.

A. Karanasos, B.C. Zhang, J. van der Sijde, J.M. Fam, R-J. van geuns, E. Regar**.** '*Late and very late scaffold thrombosis'*

J.M. Fam, N.S. van Ditzhuijzen, J. van der Sijde, B.C. Zhang, **A. Karanasos**, R-J. van Geuns, E. Regar**.** '*OCT is the way to go'*

Editors: Y. Onuma, A. Abizaid, A. Colombo, R. Gao, M. Haude, A. Lafont, J. Ormiston, T. Santoso, A. Seth, G. Stone, S. Verheye, R. Waksman, P.W. Serruys. Europa Digital & Publishing *in press*

Portfolio of awarded ECTS points

Candidate: Antonios Karanasos.
Erasmus MC Department: Cardiology
Research School: Cardiovascular Research School
Total of ECTS points: 44.7

PhD period: January 2012 – July 2015
Promotor: Felix Zijlstra
Co-promotor: Evelyn Regar

Specific courses offered by COEUR:	**Date**	**ECTS**
Cardiovascular Pharmacology	12-13/12/13	1.5
Cardiovascular imaging and diagnostics	10-11/1/13	1.5

Other courses followed:	**Date and location**	**ECTS**
3rd PCI optimization workshop	Budapest, 25-26 November 2013	0.6
OPTIS integrated system onboarding program	Rotterdam 25-26 February 2015	0.6

COEUR Research seminars:	**Date**	**ECTS**
1. New imaging strategies for the detection of atherosclerosis.	10/10/14	0.2
2. Non-invasive Imaging of Myocardial Ischemia	17/1/14	0.4
3. Biostatistics and Cardio-Thoracic Surgery: A joint (ad)venture	17/12/13	0.2
4. Coronary and Cranial Thrombosis	29/11/13	0.4
5. Hemostasis and arterial Thrombosis	14/12/12	0.4

Lectures:	**Date**	**ECTS**
1. Structural and fluid dynamics in bifurcated coronary arteries	7/2/14	0.1
2. Simulation Tailored Interventional Treatment: Dream or Reality	7/2/14	0.1
3. Biomechanics of Atherosclerotic Plaque: Site, Stability and in vivo Modeling	23/10/13	0.1

Symposia and congresses (0.3 ECTS points/day):	**Date, location and number of days:**	**ECTS**
- EuroPCR 2013	Paris, 21-24 May 2013 (4)	1.2
- EuroPCR 2014	Paris, 20-23 May 2014 (4)	1.2
- EuroPCR 2015	Paris, 17-20 May 2015 (4)	1.2
- Vulnerable plaque meeting 2012	Sounio, 24-26 June 2012 (3)	0.9
- TCT 2012	Miami, 22-26 October 2012 (5)	1.5
- TCT 2014	Washington, 13-17 September 2014 (5)	1.5
- ACC 2014	Washington, 29-31 March 2014 (3)	0.9
- SPIE Photonics West 2013	San Francisco, 2-7 February 2013 (5)	1.5
- Optics 2013	Rotterdam, 21-22 March 2013 (2)	0.6
- Optics 2015	Rotterdam, 11-13 March 2015 (3)	0.9
- Biomechanics in vascular biology and cardiovascular disease	Rotterdam, 18-19 April 2013 (2)	0.6
- Biomechanics in vascular biology and cardiovascular disease	Rotterdam, 23-24 April 2015 (2)	0.6
- ESC congress 2012	Munich 25-29 August 2012 (5)	1.5
- Cardiology & Vascular Medicine 2012	Rotterdam, 11-13 June 2012 (3)	0.9
- PCR focus group on bioresorbable scaffolds 2012	Rotterdam, 8-9 March 2012 (2)	0.6
- PCR focus group on bioresorbable scaffolds 2013	Rotterdam, 7-8 March 2012 (2)	0.6
- 19th Turkish Annual Interventional Cardiology Meeting	Antalya, 12-15 April 2012 (3)	0.9
- Bioresorbable vascular scaffolds course 2014	Boston, 25-26 July 2014 (2)	0.6

Conference presentations/lectures	Date and location	ECTS
- EuroPCR 2013 (1 oral presentation)	Paris, 21-24 May 2013	0.6
- EuroPCR 2014 (2 oral presentations, 1 poster presentation)	Paris, 20-23 May 2014	1.5
- EuroPCR 2015 (4 presentations)	Paris, 17-20 May 2015	2.4
- TCT 2012 (1 oral presentation, 2 poster presentations)	Miami, 22-26 October 2012	1.2
- TCT 2014 (1 oral presentation, 4 poster presentations)	Washington, 13-17 September 2014	1.8
- ACC 2014 (1 oral presentation, 2 poster presentations)	Washington, 29-31 March 2014	1.2
- SPIE Photonics West 2013 (2 oral presentations)	San Francisco, 2-7 February 2013	1.2
- Optics 2013 (1 lecture)	Rotterdam, 21-22 March 2013	0.6
- Optics 2015 (2 lectures)	Rotterdam, 11-13 March 2015	1.2
- ESC congress 2012 (1 oral presentation, 1 poster presentation)	Munich 25-29 August 2012	0.9
- 19th Turkish Annual Interventional Cardiology Meeting (3 lectures)	Antalya, 12-15 April 2012	1.8
- Bioresorbable vascular scaffolds course 2014 (2 lectures)	Boston, 25-26 July 2014	1.2
- 3rd PCI optimization workshop (6 lectures)	Budapest, 25-26 November 2013	3.6
- OPTIS integrated system onboarding program (course faculty)	Rotterdam, 25-26 February 2015	0.5
- Coeur research seminar: Coronary and Cranial Thrombosis (1 lecture)	Rotterdam, 29 November 2013	0.6
- COEUR Course Pathophysiology of Ischemic Heart Disease 2014 (1 lecture)	Rotterdam, 1-2 May 2014	0.6

Financial support for the printing of this thesis was kindly provided by:

Cardialysis BV

Abbott Vascular

Medis medical imaging systems bv

Servier

ABN AMRO bank

Erasmus Medical Center